

ORGANIZED BY



ICPPP20



BOOK OF ABSTRACTS

THE 20TH INTERNATIONAL CONFERENCE
ON PHOTOACOUSTIC AND PHOTOTHERMAL PHENOMENA

JULY 7-12, 2019, MOSCOW, RUSSIA

SUPPORTED BY



Contents

PLENARY SESSIONS	3
Plenary Session A1	4
Plenary Session A5	9
Plenary Session E4	17
Jubilee Session	20
Keynote Session A6+B7	24
IPPA Award Sessions S2 and S3	29
Plenary Session D4	36
ORAL CONTRIBUTIONS	39
Session A2: Cytometry and Imaging	40
Session A3: Spectroscopy I	49
Session A4: Radiometry I	60
Session B1: ND&E I / Ultrasonics I	70
Session B2: Spectroscopy II / Radiometry II	81
Session B3: Thermography II	88
Session B4: ND&E II / PA/OA and Imaging II	101
Session B5: Thermal Properties I	111
Session B6: Radiometry III / Thermal Properties II	120
Session C2: Applied Chemistry	128
Session C3: Applied / Gas Analysis	139
Session C4: Spectroscopy III	151
Session D1: Fundamentals / Phonons	161
Session D2: Thermometry / Scattering	168
Session D3: ND&E III / Thermography III	180
Session D5: ND&E IV / Ultrasonics II	190
Session E1: Thermography I / Data Handling	194
Session E2: PA/OA and imaging I	203
Session E3: Instrumentation	213
Session E5: PA/OA and Imaging III	221
POSTER CONTRIBUTIONS 225	
A Biomedical Sciences and Biophotonics	226
B Materials Science and Characterization	239
C Chemistry and Earth Sciences	291
D Fundamentals of Photothermics, PA/OA, and Related Phenomena	304
E Methodologies of Photothermics, PA/OA, and Related Techniques	342

PLENARY SESSIONS



Citius, Altius, Fortius — the rapid evolution of optoacoustic imaging technology

Daniel Razansky

1. Faculty of Medicine and Institute of Pharmacology and Toxicology, University of Zurich, Switzerland
2. Institute for Biomedical Engineering and Department of Information Technology and Electrical Engineering, ETH Zurich, Switzerland

daniel.razansky@uzh.ch

Optoacoustic imaging is increasingly attracting the attention of biomedical research community due to its excellent spatial and temporal resolution, centimeter scale penetration into living tissues, versatile endogenous and exogenous optical absorption contrast. State-of-the-art implementations of multi-spectral optoacoustic tomography (MSOT) are based on multi-wavelength excitation of tissues to visualize specific molecules within opaque tissues [1]. As a result, the MSOT technology can noninvasively deliver structural, functional, metabolic, and molecular information from living tissues. Our recent efforts in the field of optoacoustic functional and molecular imaging have established new technological platforms employing spherical matrix arrays, parallel acquisition hardware, GPU-based data processing and fast-tuning laser systems in order to enable acquisition and visualization of spectroscopic information from entire tissue volumes at video rates. This has set the stage for the so-called five dimensional (real-time three-dimensional multi-spectral) optoacoustic imaging that offers unparalleled capabilities among the existing bio-imaging modalities [2]. Biomedical applications are explored in the areas of functional neuro-imaging, fast tracking of agent kinetics and biodistribution, cardiovascular research, monitoring of therapies and drug efficacy as well as targeted molecular imaging studies [1,3]. Handheld optoacoustic systems are further transforming optical imaging by offering new level of precision for clinical diagnostics of patients in a number of indications, such as breast and skin lesions, lymph node metastases, thyroid conditions and inflammatory bowel disease [4].

Acknowledgements

The work in our lab is supported by the European Research Council (ERC) grant ERC-2015-CoG-682379, National Institute of Health (NIH) grants R21-EY026382, R21-EY028365 and UF1-NS107680, Human Frontier Science Program (HFSP) grant RGY0070/2016, and the German Research Foundation (DFG) grant RA1848/5-1.

References

1. X. L. Deán-Ben, S. Gottschalk, B. McLarney, S. Shoham, D. Razansky. Chem Soc Rev 46, 2158-2198 (2017)
2. X. L. Deán-Ben and D. Razansky. Light Sci Appl 3, e137 (2014)
3. S. Gottschalk, O. Degtyaruk, B. McLarney, J. Rebling, M.A. Hutter, X. L. Deán-Ben, S. Shoham, and D. Razansky, Nature Biomed Eng 3, 392-401 (2019)
4. F. Knieling et al. N Engl J Med 376, 1292-1294 (2017)

Optoacoustic Tomography for Diagnostic Imaging of Cancer

Alexander A. ORAEVSKY

TomoWave Laboratories, Inc. 6550 Mapleridge St. Suite 103-124, Houston, Texas 77081

AO@tomowave.com

Cancer is the most notorious disease that kills approximately 600,000 people every year in the USA alone and millions worldwide. It is well established that early detection of aggressive cancer greatly increases probability for 10-year survival. On the other hand, the present methods of diagnostic imaging have serious drawbacks when applied for detection of cancer and differentiation of malignant lesions from benign masses. Ultrasound imaging (USI), magnetic resonance imaging (MRI), X-ray computed tomography (CT) and nuclear imaging techniques, such as positron emission tomography (PET) and single photon emission computed tomography (SPECT), are being used to detect cancerous tumors in various human organs often with limited less than perfect sensitivity and poor specificity. In order to develop new clinically viable strategies for diagnostic imaging of cancer with increased sensitivity and greatly enhanced specificity, one needs to characterize not only morphological structures of tumors, but more importantly provide radiologists with functional and metabolic properties based on molecular contrast.

From its early days and pioneering works, optoacoustic tomography was developed as a modality for diagnostic imaging of breast cancer [1]. Later technology developers realized that rapid pathological development of most solid cancers involves formation of a dense angiogenesis related network of microvasculature and increased consumption of oxygen. As a consequence, clinical research in the area of diagnostic optoacoustic imaging expanded from breast cancer to prostate, ovarian, thyroid, colon and other cancers [2-5]. Owing to pioneering research of 1990s and increased research efforts in the 21st century, optoacoustic imaging has emerged as a clinically viable modality with the potential to meet the demand of radiologists in visualizing molecular content of tissue within morphological structures and measurement of functional parameters such as blood oxygen saturation. Optoacoustic tomography is uniquely suitable for visualization and measurements of the optical absorption properties of tissue at the clinically relevant depths of 25-50 mm, with the spatial resolution of better than 1 mm. The greatest challenge that remains is to achieve high quantitative accuracy of the measured optical absorption coefficients at multiple laser wavelengths, which can result in significant decrease of false positive diagnosis without missing aggressively growing cancer. Spatial and temporal coregistration of ultrasound and optoacoustic images is regarded as the most effective clinical modality for its ability to provide new functional information within readily recognizable morphological structures of the tumors and their immediate vicinity.

This review analyses the potential role of quantitative optoacoustic tomography and coregistered ultrasound plus optoacoustic imaging in clinical detection and diagnosis of various types of cancer. As examples, Fig.1 and Fig.2 show breast tumors as depicted by coregistered anatomical (ultrasound) and functional (optoacoustic) images recorded in patients with benign (Fig.1) and cancerous (Fig.2) tumors obtained with Imagio system (Seno Medical Instruments, San Antonio, Texas). These examples demonstrate the value of functional optoacoustic imaging in significant enhancement of diagnostic specificity of breast cancer detection [6]. Ultrasound B-mode image presented in Fig.1 shows heterogeneous irregularly shaped mass highly suspicious for breast carcinoma. On the other hand, the functional image of the total hemoglobin [tHb] presented in yellow shows that microvascular density within the tumor is lower than in certain areas of the adjacent normal tissue and the functional image of the blood oxygen saturation [SO₂] shows in green that the average blood oxygenation in the tumor microvasculature is normal. Thus, optoacoustic tomography shows that this tumor is benign, thereby eliminating false positive diagnosis. Surgical and microsurgical procedures performed as a consequence of false positive diagnostics account for over \$3 Billion in unnecessary medical expenses in the United States

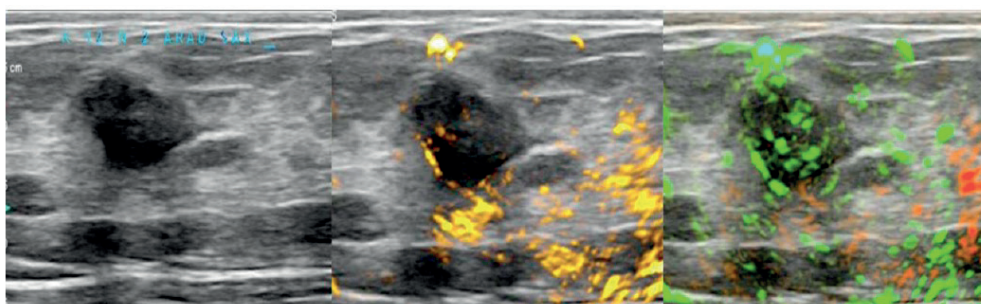


Figure 1. Coregistered ultrasound and functional optoacoustic images of a breast tumor obtained with Imagio diagnostic imaging system: ultrasound (left), functional image of [tHb] overlaid with ultrasound (center), and functional image of [SO₂] overlaid with ultrasound. Biopsy revealed benign nature of this tumor.

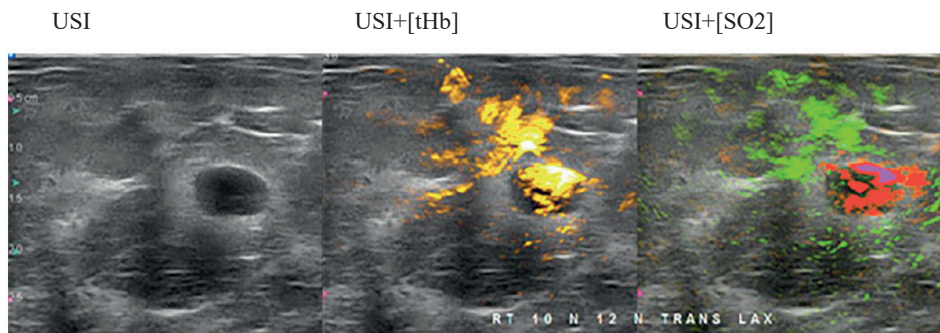


Figure 2. Coregistered ultrasound and functional optoacoustic images of a breast tumor obtained with Imagio diagnostic imaging system: ultrasound (left), functional image of [tHb] overlaid with ultrasound (center), and functional image of [SO₂] overlaid with ultrasound. Biopsy revealed invasive breast carcinoma.

Ultrasound B-mode image presented in Fig. 2 shows relatively homogeneous round shaped mass not suspicious for cancer. On the other hand, the functional image of the total hemoglobin [tHb] presented in yellow shows that microvascular density within the tumor is much higher than in the areas of the adjacent normal tissue and the functional image of the blood oxygen saturation [SO₂] shows in red that the average blood oxygenation in the tumor microvasculature is hypoxic. Thus, optoacoustic tomography shows that this tumor is a breast carcinoma. In this case false negative diagnosis of B-mode ultrasound was reverted and the probability of this patient to be cured from cancer was increased by early detection.

This review also presents examples of clinical images of other types of solid cancers and demonstrates that spatio-temporal coregistration of functional and anatomical images permits radiological assessment of the vascular pattern around tumors, microvascular density of tumors as well as the relative values of the total hemoglobin [tHb] and blood oxygen saturation [sO₂] in tumors relative to adjacent normal tissues thereby providing enhanced accuracy for estimated probability of malignancy. Pathology examinations on biopsied tissue of the imaged tumors typically found consistent with the microscopic interpretation of the OA/US image findings.

With the development of various targeted contrast agents, optoacoustic tomography will also be able to provide molecular information about the malignant tumor tissue, particularly cancer-specific protein receptors that do not have endogenous optical contrast for deeply penetrating near-infrared light. Novel contrast agents, such as biocompatible and biodegradable nontoxic nanoparticles, enable molecular optoacoustic imaging, thus facilitating further characterization of cancer pathophysiology [7].

A number of examples of molecular optoacoustic images of various types of cancer acquired *in vivo* suggest that targeted contrast agents specific to cancer and genetic reporters strongly absorbing near-infrared light have the potential to enhance detection sensitivity and diagnostic specificity of the optoacoustic imaging of cancer in clinical applications [2,8].

Acknowledgements

Financial support from the National Cancer Institute (grant R01CA167446) and from Guangdong Health and Family Planning Commission of Guangzhou Municipality (grant #20161A011092), is gratefully acknowledged. Author also would like to thank the research teams at TomoWave Laboratories and Seno Medical Instruments as well as clinical collaborators for invaluable discussions.

References

1. A.A. Oraevsky: "Optoacoustic Tomography: From Fundamentals to Diagnostic Imaging of Breast Cancer", in Biomedical Photonics Handbook, Second Edition: Fundamentals, Devices, and Techniques, ed. by T. Vo-Dinh, CRC Press, Boca Raton, Florida, Vol. PM222, Chapter 21, pp. 715-757 (2014).
2. S. Mallidi, G.P. Luke and S. Emelianov: Photoacoustic imaging in cancer: detection, diagnosis, and treatment guidance. Trends in Biotechnology 29(5); 213-221 (2011).
3. T. Shiina, M. Toi, T. Yagi: Development and clinical translation of photoacoustic mammography, Biomedical Engineering Letters, 8(2), 157-165 (2018).
4. E. Amidi, A. Mostafa, S. Nandy, G. Yang, W. Middleton, C. Siegel, Q. Zhu: Classification of human ovarian cancer using functional, spectral, and imaging features obtained from *in vivo* photoacoustic imaging. Biomedical optics express 10(5); 2203; (2019); doi: 10.1364/boe.10.002303.
5. A. Horiguchi, M. Shinchi, A. Nakamura, T. Wada, K. Ito, T. Asano, H. Shinmoto, H. Tsuda, M. Ishihara: Pilot Study of Prostate Cancer Angiogenesis Imaging Using a Photoacoustic Imaging System. Urology, 108: 212-219 (2017); doi: 10.1016/j.urology.2017.07.008.
6. A.A. Oraevsky, B. Clingman, T. Stavros, J. Parikh, W.T. Yang: Clinical Optoacoustic Imaging Combined with Ultrasound for Coregistered Functional and Anatomical Mapping of Breast Tumors, Photoacoustics 8: 2345-2351 (2018). DOI.org/10.1016/j.pacs.2018.08.003.
7. D.L. Longo, R. Stefania, S. Aime, A.A. Oraevsky: Melanin-Based Contrast Agents for Biomedical Optoacoustic Imaging and Theranostic Applications. Int. J. Mol. Sci. 2017; 18: 1719-1739.
8. Amit P. Jathoul, J. Laufer, Olumide Ogunlade, B. Treeby, B. Cox, E. Zhang, P. Johnson, A.R. Pizzey, B. Philip, T. Marafiot, M.F. Lythgoe, R.B. Pedley, M.A. Pule, P. Beard: Deep *in vivo* photoacoustic imaging of mammalian tissues using a tyrosinase-based genetic reporter, Nature Photonics 9, 239-246 (2015); DOI: 10.1038/NPHOTON.2015.22

Real-time, non-contact, non-invasive imaging of soft tissue elasticity combining light with air-coupled ultrasound

Ivan PELIVANOV^{(1)*}, Mitchel KIRBY⁽¹⁾, Łukasz AMBROZIŃSKI⁽²⁾, John PITRE⁽¹⁾, Shaozhen SONG⁽¹⁾, David LI⁽¹⁾, Liang GAO⁽¹⁾, Tueng T. SHEN⁽⁴⁾, Ruikang K. WANG⁽¹⁾ Matthew O'DONNELL⁽¹⁾

1. Department of Bioengineering, University of Washington, Seattle, WA 98195, USA

2. AGH University of Science and Technology, Krakow, Poland

3. Department of Chemical Engineering, University of Washington, Seattle, WA 98195, USA

4. Department of Ophthalmology, University of Washington, Seattle, WA 98104, USA

ivanp3@uw.edu

Scanning rates of modern OCT systems have recently reached a few MHz using swept-source lasers, enabling real-time, 3-D (i.e., 4-D) imaging of clinically relevant structures up to 2 mm below tissue surfaces. These high line rates can also be used for a different and complementary modality - Optical Coherence Elastography (OCE) - in which mechanical waves propagating in tissue are tracked in both time and space. By estimating local propagation parameters such as velocity and attenuation from these recordings, two- or even three-dimensional elastograms can be reconstructed [1, 2]. The accuracy and resolution of these elastograms has been limited by the bandwidth of propagating mechanical waves. Clearly, there is still great need for robust methods exciting high bandwidth mechanical waves for OCE to take advantage of the spatial and temporal resolution possible with modern 4-D OCT systems.

In this study, we report on our recent progress in non-contact, broadband mechanical wave excitation applied to OCE using both ultraviolet (UV) pulsed laser radiation (photoacoustic) or air-coupled focused ultrasound (US).

UV laser radiation is absorbed in a thin subsurface region of tissue, creating transient mechanical waves due to thermal expansion. This method has many advantages, such as no contact with the target, high localization defined by the beam diameter at the target surface, and rapid optical movement of the beam to any point on the target. However, laser excitation is very inefficient in converting light to mechanical waves for nearly incompressible media such as soft tissue. We tested this method with 5 ns, 263 nm UV pulses and concluded that propagating mechanical waves could be efficiently generated and tracked with phase-sensitive (PhS)-OCT only if the laser intensity approached the tissue ablation limit [3]. The same conclusion was achieved in a theoretical study [4].

An alternative approach is to use the acoustic radiation force provided by an air-coupled focused US beam reflected from the air/medium interface. This method, which we call acoustic micro-tapping (AuT), was first shown in our recent studies [2, 5, 6] to be at least two orders of magnitude more efficient than the PA method described above. The resolution of elastograms obtained with AuT is defined by the spatial width of the air-coupled beam at the tissue surface and, therefore, depends on the beam carrier frequency. In our study, we designed, built, and used a 1 MHz cylindrically focused air-coupled transducer with an ~ 350 μm beam width that efficiently excited mechanical waves in the multiple kHz range.

Tissue mimicking phantoms, porcine and human corneas and skin were used in ex vivo and in vivo experiments (see an example in Fig.1). Results strongly suggest that simple, non-contact excitation holds great promise for non-invasive characterization of soft media, in general, and for elasticity measurements in delicate soft tissues and organs (e.g., in the eye) in particular.

In this study, we also explore the best methods for elasticity reconstruction from space-time mechanical waveforms. We carefully take into account guided modes in bounded tissues and propose several different methods of tissue elasticity reconstruction with experimental data. We show that in layered media the conventional bulk shear wave assumption results in highly underestimated shear modulus reconstructions and significant structural artifacts in modulus images. We urge the OCE community to be careful in using the group velocity to evaluate tissue elasticity and to focus on developing robust reconstruction methods to accurately reconstruct images of the shear elastic modulus in bounded media.

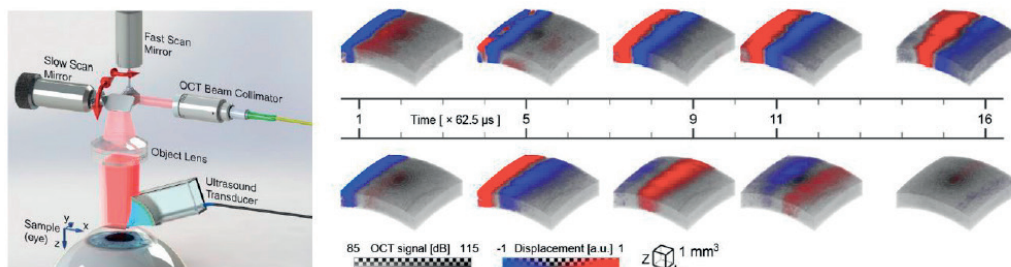


Figure 1. Schematics of the dynamic OCE method with AuT mechanical wave excitation (on the left); snapshots of mechanical wave propagation in ex-vivo porcine cornea at different IOP (10 mmHg and 40 mmHg, respectively for top and bottom images) on the right. Figure is reproduced from Ref [6].

Plenary Session A1

To conclude, we have shown that a fast scanning phase sensitive (PhS)-OCT system combined with acoustic micro-tapping (AuT) to excite mechanical waves can be used for non-contact quantitative elasticity mapping in soft tissues such as cornea and skin. Because both US and OCT are already used extensively in the clinic, there appears to be a straightforward path to translate the entire method (AuT-OCE) into a routine clinical tool.

References

1. M.A. Kirby et al. *Journal of Biomed. Opt.*, 22(12), 1-28 (2017). doi: 10.1117/1.JBO.22.12.121720
2. S. Wang, & K. V. Larin. *J. Biophotonics* 8(4), 279–302 (2015). doi: 10.1002/jbio.201400108
3. S. Song et al. *Appl. Phys. Lett.* 108, 191104 (2016). doi.org/10.1063/1.4949469
4. P. Grasland-Mongrain et al. *Appl. Phys. Lett.* 109(22), 2219011 (2016). doi:10.1063/1.4968538
5. Ł. Ambroziński et al. *Appl. Phys. Lett.* 109, 43701 (2016). doi.org/10.1063/1.4959827
6. Ł. Ambroziński, et al. *Sci. Rep.* 6, 38967 (2016). doi.org/10.1038/srep38967

A new optical imaging paradigm with Multispectral Optoacoustic Tomography

Vasilis NTZIACHRISTOS^(1,2)

1. Technical University of Munich, Munich, Germany

2. HelmholtzZentrum München, Munich, Germany

v.ntziachristos@tum.d

Optical imaging is unequivocally the most versatile and widely used visualization modality in the life sciences. Yet it has been significantly limited by photon scattering, which complicates the visualization of tissue beyond a few hundred microns. For the past few years, there has been an emergence of powerful new optical and optoacoustic imaging methods that offer high resolution imaging beyond the penetration limits of microscopic methods. The talk discusses progress in multi-spectral opto-acoustic tomography (MSOT) and mesoscopy (MSOM) that bring unprecedented optical imaging performance in visualizing anatomical, physiological and molecular biomarkers. Advances in light technology, detection methods and algorithms allow for highly performing visualization in biology and medicine through several millimetres to centimetres of tissue and real-time imaging. The talk demonstrates implementations in the time and frequency domain, showcase how it is possible to accurately solve fluence and spectral coloring issues for yielding quantitative measurements of tissue oxygenation and hypoxia and demonstrate quantitative in-vivo measurements of inflammation, metabolism, angiogenesis in label free mode.

Breaking the physical limits for early diagnostics and theranostics of deadly diseases with Cytophone

Vladimir P. ZHAROV

Arkansas Nanomedicine Center, University of Arkansas for Medical Sciences, 4301, West Markham St., Little Rock, Arkansas 72205-7199, USA.

zharovvladimirp@uams.edu

Introduction: New is well forgotten old

After discovery of the optoacoustic (OA) effect by Alexander Graham Bell in 1880, new birthday of this phenomenon called later also photoacoustic (PA) effect has been happened after the invention of laser. Under supervision of professor Vladilen Lethokov I was involved in these studies at the beginning seventies last century [e.g., 1,2] as young student that was resulted in multiple publications summarized in several books and reviews [3-6]. At that time we demonstrated one of first applications of OA/PA effects in laser spectroscopy and detection of atmosphere pollutions including OA spectroscopy of the excited molecule states using heated OA detector, OA nonlinear and multiphoton absorption using strong-focused laser beams with high spatial resolution OA detector, OA isotope analysis, OA drug injection, OA scalpel, destruction of gall stones by using OA effect, the first demonstration of OA tomography, biophotophone for diagnostic of ear's dysfunctions, the first application the pulsed photothermal (PT) radiometry for study biotissue properties and as the feedback in laser medicine, and the first demonstration of delivery simultaneously of optical and acoustic waves through the same optical fiber for microsurgery (U.S. Maiman award). We have also developed OA detectors for gas and liquid chromatography through OA detection of low concentration of molecules in gas (the State Prize of the Russian Federation) and liquid flow including identification of disease (diabetes and tuberculosis)-associated markers in exhaled air and blood testing from cancer patients as well as the study of OA effect impacts on cellular structures amplified by laser-induced nanobubbles. Latter technologies after significant improvement were recently used for breaking the physical limits and *in vivo* blood tests.

Nonlinear photoacoustic and photothermal effects to break the diffraction, spectroscopic, and detection limits

We proposed and demonstrated new applications of laser-induced nano- and microbubbles around heated absorbing nano- and microobjects. These phenomena lead to significant (10-100-fold) PT and PA signal amplifications with simultaneous spatial and spectral sharpening of PT and PA resonances from individual absorbing nanobjects [7-11]. Based on these phenomena, we developed super-resolution of PA and PT microscopy beyond the diffraction limit [10-11], super-resolution PA and PT spectroscopy spectral hole burning [7,9], and *in vivo* super-resolution PA flow cytometry [12] with PA and acoustic blood and lymph flow focusing [13] as well as PT-PA theranostics of circulating tumor cells (CTCs) and bacteria as well as PT -gene therapy [14-15]. The discovered ultrasharp (0.5-1 nm) PT and PA spectral resonances in plasmonic nanostructures are accompanied by their red and blue spectral shifting and splitting [7-8]. Our team demonstrated also the first biomedical application of spasers (plasmonic nanolasers) as the brightest labels for advanced targeted single cell diagnostics and theranostics [9].

Photoacoustic flow cytometry and photothermal theranostics of circulating cells

Cardiovascular diseases, cancer, and infections remain the main causes of death in the worldwide. The diagnosis of these and other diseases begins with a common medical procedure: the examination of blood samples. The sensitivity of current blood tests is limited by the small volume of blood collected, in which no less than one disease-specific biomarker (e.g., tumor cell, clot, or pathogen) can be detected. This can miss many thousands of abnormal cells and biomarkers in the whole blood volume (~5 liter in adults), which can be sufficient for disease progression to difficult-to-treat if not already incurable complications (e.g., metastasis, stroke, or sepsis). To solve these problems, we introduced a new platform of *in vivo* PA flow cytometry (PAFC) called advanced version Cytophone for real-time detection of circulating normal and abnormal cells, biomolecules, contrast agents, micro- and nanoparticles in various bioflows [16-19]. Cytophone can provide identification and enumeration of rare circulating biomarkers with intrinsic PA contrasts (e.g., melanin in melanoma and hemozoin in malaria) or molecularly targeted with the functionalized gold nanoparticles. The principle of PAFC is based on the irradiation of the superficial blood vessels through intact skin with near-infrared laser pulses followed by detection of laser-induced acoustic waves with small ultrasound transducer attached to skin. Recent Cytophone advances include multispectral laser array, multimodal PA-PT-Raman-fluorescent detection schematics, ultrasharp rainbow nanoparticles, molecular targeting of disease-associated circulating biomarkers, *in vivo* magnetic enrichment, and combination of PA diagnosis with PT therapy. The capacity of this technology was demonstrated by the real-time detection of circulating individual normal cells (e.g., erythrocytes and leukocytes) in different functional states (e.g., normal, apoptotic, or necrotic), CTCs (melanoma, breast, squamous), bacteria and parasites (e.g., *E. coli*, *S. aureus* and malaria), nanoparticles (e.g., gold nanorods, carbon nanotubes, magnetic, and golden carbon nanotubes), and dyes (e.g., Lymphazurin, Evans blue, and Indocyanine Green) in blood, lymphatics, bone, and plants. The assessment of large blood volume *in vivo*, potentially the patient's entire blood volume (in adults ~5 liter) significantly (10³-fold) enhances the sensitivity of CTC detection including rare cancer stem cells compared to the existing CTC assay *ex vivo*. In

particular, most cancer deaths (up to 90%) are a result of metastatic spread of cancer cells from the primary tumor to distant organs through blood system. However, current approaches have been mainly focused on the treatment of primary tumor. We introduced a new theranostic platform with focus on PA diagnosis and PT treatment of CTCs. Recent clinical trials using the portable Cytophone platform provides breakthroughs for the early detection and killing of melanoma CTCs with potential at least inhibit if not prevent development of difficult to treat metastasis [19].

References

1. A. S. Gomenyuk, V. P. Zharov, D. D. Ogurok, E. A. Ryabov, O. A. Tumanov and V. O. Shaidurov. Optoacoustic detection of low concentrations of hydrogen fluoride, nitric oxide, and carbon dioxide in gases using radiation of pulsed hydrogen fluoride laser. *Soviet Journal of Quantum Electronics* 4(8), 1001 (1975).
2. V.P. Zharov, Y.O. Simanovsky, Optoacoustic tomography of laser beams. *J Acoustics*. 35;556-558 (1989).
3. V.P. Zharov, V.S. Letokhov. *Laser Optoacoustic Spectroscopy*. Springer Series in Optical Sciences, vol.37, Springer-Verlag (Berlin Heidelberg New York), 320p (1986).
4. V.P. Zharov. Laser optoacoustic spectroscopy in chromatography. In: V.S. Letokhov VS, ed. *Laser Analytical Spectrochemistry*. The Adam Hilger Series on Optics and Optoelectronics, Boston, Mass: Bristol; 229-271 (1986).
5. V.P. Zharov. Application of power optoacoustic methods and instruments in medicine and biology. In book: *Photoacoustics and Photothermal Phenomena*, Springer Series in Optical Sciences (Springer, Berlin), 58, 533-547 (1987).
6. A.S. Latyshev, V.P. Zharov VP. Laser combined medical technologies from Russia. *J. Laser Applications*., 11, 80-90 (1999).
7. V.P. Zharov. Ultrasharp nonlinear photothermal and photoacoustic resonances and holes beyond the spectral limit. *Nat Photon*.5, 110-116 (2011).
8. Mertiri, N. Altug, M.K. Hong, P. Mehta, J. Mertz, L.D. Ziegler, S. Erramilli. Nonlinear midinfrared photothermal spectroscopy using Zharov splitting and quantum cascade lasers. *ACS Photonics*. 8, 696–702. (2014). 9. E.I. Galanzha, R. Weingold, D.A. Nedosekin, M. Sarimollaoglu, J. Nolan, W. Harrington, A.S. Kuchyanov, R.G. Parkhomenko, F. Watanabe, Z. Nima, A.S. Biris, A.I. Plekhanov, M.I. Stockman, V.P. Zharov. Spaser as a biological probe. *Nat Commun*. 8, 15528 (2017).
10. V. Zharov. Far-field photothermal microscopy beyond the diffraction limit. *Opt Lett*. 28,1314-1316 (2003).
11. D.A. Nedosekin, E.I. Galanzha, E. Dervishi, A.S. Biris, V.P. Zharov. Super-resolution nonlinear photothermal microscopy. *Small*, 10, 135-142 (2014).
12. Z.A. Nima, F.Watanabe, A.Jamshidi-Parsian, M. Sarimollaoglu, D.A.Nedosekin, M. Han, J.A Watts, A.S. Biris, V.P. Zharov, E.I. Galanzha EI. Bioinspired magnetic nanoparticles as multimodal photoacoustic, photothermal and photomechanical contrast agents. *Sci Rep*. 9 (1), 887 (2019).
13. E.I. Galanzha, V.P. Zharov. Photoacoustic flow cytometry. *Methods*, 57, 282-296 (2012).
14. E.I. Galanzha, E.V.Shashkov, T.Kelly, J-W Kim, L.Yang, V.P. Zharov. In vivo magnetic enrichment and multiplex photoacoustic detection of circulating tumour cells. *Nature of Nanotechnology*, 12, 855-860 (2009).
15. J-W Kim, E.I. Galanzha, E.V. Shashkov, H-M.Moon, V.P. Zharov VP. Golden carbon nanotubes as multimodal photoacoustic and photothermal high-contrast molecular agents. *Nature of Nanotechnology*, 4, 688-694 (2009).
16. E.I. Galanzha, M.G. Viegas, T. Malinsky, A.V. Melerzanov, M.A. Juratli, M. Sarimollaoglu, D.A. Nedosekin, V.P. Zharov. In vivo acoustic and photoacoustic focusing of circulating cells. *Scientific Reports*, 6, 21531 (2016).
17. V. Zharov, V. Galitovsky, and M. Viegas. Photothermal detection of local thermal effects during selective nanophotothermolysis. *Appl Phys Letter* 83, 4897-4899 (2003).
18. V.P. Zharov, E.N. Galitovskaya, C. Jonson, T. Kelly. Synergistic enhancement of selective nanophotothermolysis with gold nanoclusters: potential for cancer therapy. *Laser Surg Med*. 37, 219-226 (2005).
19. E.I. Galanzha, Y.A. Menayev, M. Sarimollaoglu, D.A. Nedosekin, S.F. Foster, A.J. Jamshidi-Parsian, E.R. Siegal, L. Hutchins, J.Y. Suen, I. Makhoul, V.P. Zharov. In vivo liquid biopsy using cytophone platform for photoacoustic detection of circulating tumor cells in melanoma patients. *Science Translational Medicine* 2019 (in press).

High-resolution raster-scanning optoacoustic mesoscopy (RSOM) for microvasculature imaging

Katja HAEDICKE*

iThera Medical GmbH, Munich, Germany

katja.haedicke@ithera-medical.com

Non-invasive and high-resolution imaging of microvasculature is essential not only for the diagnosis and evaluation of certain dermatological conditions but also in preclinical research to understand the development and treatment outcome in skin diseases and tumors. In clinical dermatology, so far, examinations are conducted only through visual inspection or by using dermatoscopes or capillaroscopes which illuminate and optically magnify selected areas of the skin. However, these modalities provide only superficial, subjective and not quantifiable measures as 2D images without any information about deeper structures, limiting a precise evaluation of the disease progression. In the field of tumor research, especially when it comes to anti-angiogenic therapies directly targeting the tumor vascular network, new imaging modalities are of great interest. Until recently, an evaluation of detailed tumor vascular structures was only possible by using invasive procedures like skin window chambers or skin flap models with intravital microscopy within a small field of view. Other non-invasive modalities like BOLD-MRI or fluorescence imaging are limited due to low spatial resolution.

With the introduction of the novel imaging modality of raster-scanning optoacoustic mesoscopy (RSOM), the before-mentioned limitations can be overcome. By solely using the intrinsic optical properties of hemoglobin without any additional contrast agents, non-invasive, high-resolution 3D images of the vasculature can be generated, enabling a more detailed insight and more precise evaluation of vascular changes throughout all layers of the skin. In RSOM, the tissue is illuminated in a defined raster with a fast 532 nm nanosecond-pulsed laser [1]. The absorption of the light energy by tissue chromophores leads to a short thermoelastic expansion of the excited molecules and subsequently to the generation of ultrasound waves. An ultra-wide bandwidth detector allows for the generation of high-resolution images, resolving fine structures in the lower micrometer range at several millimeters in depth. Different sized vessels can be distinguished based on the emitted ultrasound frequencies. Further specific technical parameters of the RSOM scanner are listed in table 1.

Table 1. Technical parameters of the RSOM scanner

Wavelength	532 nm
Pulse repetition rate of the laser	Up to 2000 Hz
Pulse lengths	1-2 ns
Pulse energy	<1 mJ
Ultrasound detector	50 MHz
Detected ultrasound bandwidth	10-100 MHz
Step size	20 μm
Field of view	Up to 12x12x4 mm
Axial/Lateral resolution	15/40 μm

The generated RSOM images can then be analyzed qualitatively as well as quantitatively by either evaluating whole areas of the skin or single blood vessels. Example images of the skin of a mouse leg and an ear of a mouse are illustrated in Figure 1.

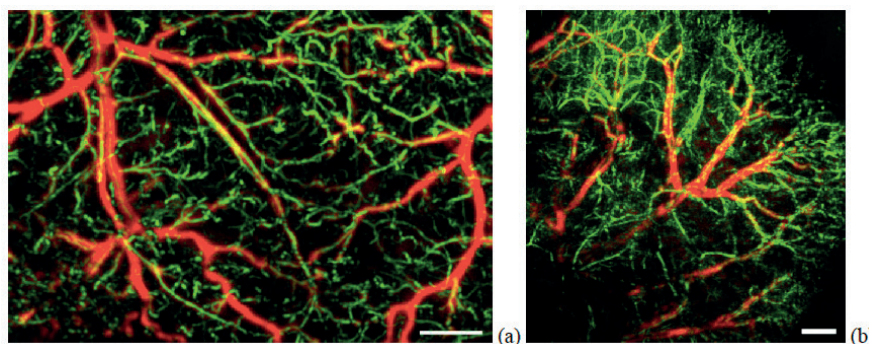


Fig. 1. RSOM maximum intensity projection images of vessels in a mouse leg (a) and mouse ear (b) with red depicting larger blood vessels (11-33 MHz) and green depicting smaller vessels (33-99 MHz). Scale bar = 1 mm.

In preclinical research, RSOM was successfully used to reveal the vascular network supporting melanoma growth over time [1] and to monitor therapy response in tumors to anti-VEGF and anti-vascular treatments like photodynamic therapy in colon carcinomas. Furthermore, first studies could depict differences in vascularization in mice ears and skin with atopic dermatitis and scleroderma. In the clinical field, RSOM could not only depict different skin layers and moles but also disease markers like thickened epidermis, larger capillary loops or alterations in the dermal vasculature with changes in blood volume for psoriasis [2]. In addition, hyperthermia induced vasodilation was studied on a single-vessel level, demonstrating the high sensitivity of RSOM [3].

In future, RSOM can be used to study tumor development and therapy mechanisms in the preclinical setup as well as human dermatological diseases like skin cancer, actinic keratosis, scleroderma, psoriasis and many more applications to improve the current evaluation standards and overall treatment efficacy. RSOM is a powerful tool to monitor blood vessels in the skin and tumor angiogenesis. With the future implementation of additional wavelengths, this modality will be able to distinguish several chromophores like melanin, oxy- and deoxy-hemoglobin, and even contrast agents at high resolution in a multispectral manner and therefore expand the opportunities for high precision imaging.

References

1. M. Omar, M. Schwarz, D. Soliman, P. Symvoulidis, V. Ntziachristos, *Neoplasia* 17 (2), (2015) doi: 10.1016/j.neo.2014.12.010
2. J. Aguirre, M. Schwarz, N. Farzorz, M. Omar, A. Buehler, K. Eyerich, V. Ntziachristos, *Nature Biomedical Engineering* 1 (68), (2017) doi: 10.1038/s41551-017-0068
3. A. Bereznoi, M. Schwarz, A. Buehler, S. V. Ovsepian, J. Aguirre, V. Ntziachristos, *Journal of Biophotonics* 11 (11), (2018) doi: 10.1002/jbio.201700359

Photothermal Readout for Microfluidics and Nanofluidics

Takehiko Kitamori

Department of Applied Chemistry, School of Engineering, The University of Tokyo

kitamori@icl.t.u-tokyo.ac.jp

There may be no need to explain that photothermal spectrometry is ultrasensitive for nonfluorescent molecules in this community. However, photothermal spectrometry has poor selectivity, and it is also not necessary to refer here. Therefore, especially for analytical applications, separation of the target molecule, that is the analyte, from admixtures is indispensable for ultrasensitive analysis applying photothermal spectrometry. This is the reason why such separation is in effective combination with the microfluidic devices which can integrate complicated chemical processes of separation chemistry like extraction, immunoassay, chromatography and so on.

We made thermal lens spectrometry possible under an optical microscope which was named thermal lens microscope TLM in 1993, and we combined the TLM with microfluidic devices as a readout detector for the isolated molecules by the microfluidic chemical separation. This combination of microfluidics and TLM worked very well, and we could demonstrate solvent extraction (wet analysis), immunoassay, chemical reaction monitoring, cell culture experiments, etc., in the early 1990's when it was almost the same time as microfluidics for electrophoresis so called m-TAS was founded. These demonstrations which notified a wide range of applications to biomedical and chemical researchers were based on pressure driven fluidic control, and our method was generalized as micro continuous chemical processing which consisted of micro unit operation MUO, and these demonstrations changed the tide of research of microfluidics from electrophoresis/electroosmosis to pressure driven fluidics, which have been a basis of today's microfluidics which have spread into bio, medical and chemical fields. However, honestly saying, such microfluidics of ours was a byproduct of TLM development in our lab. The short history of pioneering microfluidics will be also introduced in the lecture.

From the early 2000's, we turned the rudder to nanofluidics which was still unexplored at all. Our first paper of the nanofluidics was in 2002. There were many technical difficulties to make ways into nanofluidics of which channel size became one thousandth at once. Detection was also one of the difficulties. In the first place, size of nanochannels is smaller than the wavelength of light, and then, geometrical optics like thermal lensing effect itself doesn't work. Therefore, we introduced wave optics to detect the refractive index change induced by photothermal effect in a nanochannel. Concretely, a differential interference contrast DIC optics was introduced in the TLM system which was named DIC-TLM, and we succeeded in ultrasensitive detection of refractive index change induced by photothermal effect of the analyte molecules in a nanochannel in 2009. This DIC-TLM was also a powerful readout detector of our nanofluidic devices, and many applications of nanofluidics were initiated similar to microfluidics development. And now, we have developed analytical chemistry at pL, fL, and even aL levels, and the application for the ultimate analysis at single to countable molecules is available in our laboratory. In the lecture, details of the DIC-TLM and the application of nanofluidics to "stimulation released cytokine protein analysis from living single B cell at countable molecules levels" will be introduced.

Optical and Photothermal Detection of Single Molecules and Single Gold Nanoparticles

Michel ORRIT

Leiden Institute of Physics, 2300 RA Leiden, Netherlands

orrit@physics.leidenuniv.nl

I shall present several optical methods giving access to signals from single molecules and single gold nanoparticles. The latter objects are interesting because of their strong interaction with light mediated by their plasmon resonance, and because they are chemically and photochemically very stable. The experiments are based on fluorescence or photoluminescence, scattering, absorption detected by photothermal contrast, purely refractive effects leading to shifts of the plasmon resonance, or plasmon-enhanced fluorescence of weak emitters.

The optical isolation of single gold nanoparticles leads to their spectroscopic study on a single-particle basis and, through their plasmonic properties, to the study of their direct surroundings. I shall illustrate this general idea with some recent experiments from our laboratory.

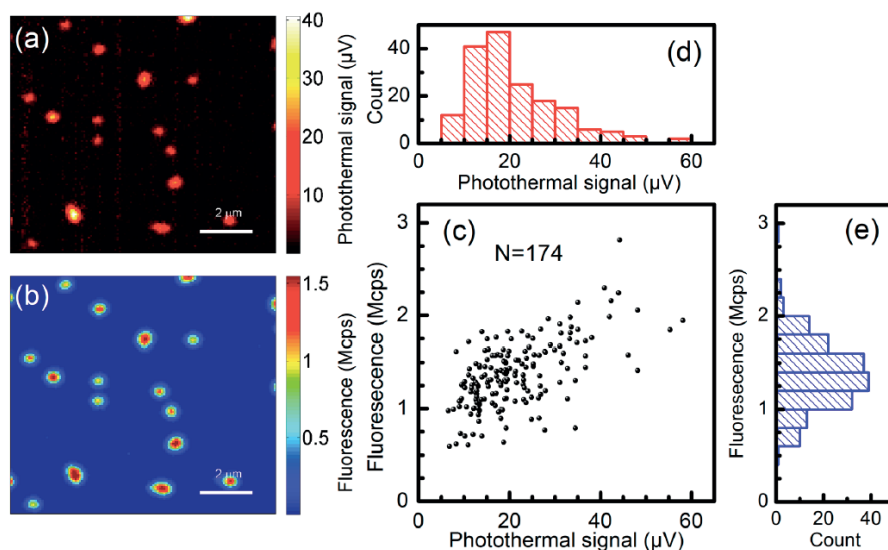
Besides fluorescence, other optical signals can provide enough contrast to detect single molecules. The sensitivity of photothermal contrast can be pushed to the detection of individual organic absorbers with negligible fluorescence yields [1]. For photosensitive objects such as single conjugated polymer molecules, the absorbed intensities often lead to photodegradation of the molecules in very short times. In that case, it is possible to reduce the illumination intensity by increasing the sensitivity of the photothermal medium. We have shown that near-critical xenon, or carbon dioxide, are convenient media to enhance the photothermal signal by more than two orders of magnitude [2]. Critical fluctuations also increase the noise on the measurements, but this detection method makes it possible to detect single molecules with light intensities much lower than in regular molecular liquids such as glycerol or methanol.

The strong optical near field close to the tips of gold nanorods enhances coupling to optical waves, both for excitation and for emission [3,4], and make the surface plasmon resonance sensitive to refractive index changes in the environment. This effect allowed us to detect individual non-absorbing proteins [3]. These biomolecules were bound to the functionalized metal surface with preferential attachment to the tips of the nanorod. The binding and unbinding of single protein molecules from the solution gave rise to sudden absorption steps, and could be of use in micro-analytical applications and in-situ sensing. More recent versions of this experiment use parallel scattering measurements of tens or hundreds of gold nanorods, which are monitored simultaneously. Single gold nanorods can also enhance the fluorescence of single molecules by enhancement of excitation and of radiative decay. This enhancement is particularly important for weakly emitting dyes, which then become observable at the single-molecule level [4].

By photothermal methods, we have monitored the nanosecond dynamics of steam nanobubbles formed in a liquid around a nanoparticle upon plasmonic heating [5]. We show that steam nanobubbles are extremely nonlinear systems that present dynamics in the nanosecond time scale and are very sensitive to perturbations. For example, a nanobubble could probe changes in pressure and act as a fast acousto-optical transducer. The strong light-matter interaction caused by plasmons opens many new experiments, such as the

manipulation of position and orientation of anisotropic gold nanoparticles in complex media.

Fig. 1. Examples of images of single molecules of the conjugated polymer MEH-PPV, recorded in photothermal microscopy (a) and in fluorescence (b). The scatter plot (c) and histograms of signal strengths (photothermal (d), and fluorescence (e)) show the partial correlation of photothermal and fluorescence signals. Figure reproduced from ref. 2.



References

1. A. Gaiduk et al., *Science* 330 (2010) 353.
2. L. Hou et al., *NanoLett.* 17 (2017) 1575-1581.
3. P. Zijlstra et al., *Nat. Nanotech.* 7 (2012) 379.
4. H. Yuan et al. *Angew. Chem.* 52 (2013) 1217.
5. L. Hou et al., *New J. Phys.* 17 (2015) 013050.

Time-resolved detection of photoinduced heating and volume changes during protein reactions

Masahide Terazima

Department of Chemistry, Graduate School of Science, Kyoto University, Kyoto, 606-8502, Japan

mterazima@kuchem.kyoto-u.ac.jp

Heating after photoexcitation to the electronic excited states is generally observed in condensed phase, and the techniques to detect the heating are called the photothermal methods. We have been using this photothermal technique, in particular, the transient grating (TG) and transient lens (TrL) methods, to understand chemical reactions of biomolecules.

The thermodynamics have been playing very important roles in revealing the nature of molecules in solution. In particular, the thermodynamics is important for revealing fluctuation. Although the most stable state of a protein exists at a global minimum of the Gibbs energy surface, there must be many local minima around the minimum, and there must be many jumps among the minima due to the thermal energy. Proteins are impossible to escape from the thermal fluctuation. The importance of fluctuation has sometimes been used to explain enzymatic reactions. However, compared with the determinations of the static structures, detection of fluctuation and in particular its relationship to the protein reaction is very difficult, and it is almost impossible to apply traditional techniques to irreversible reactions or reactions involving short-lived species. Our group has demonstrated the usefulness of the TG and TrL methods for quantitative measurements of the enthalpy change (ΔH) and the partial molar volume change (ΔV) during photochemical reactions in time-domains at one temperature without assumptions. Here we will report on the thermodynamic studies of short-lived intermediate species of a biological protein, PixD.

PixD is a relatively short protein (17 kDa) that consists of a BLUF (blue light sensors using a flavin chromophore) domain and additional short helices. PixD possesses FAD as the chromophore. PixD from the thermophilic cyanobacterium *Thermosynechococcus elongatus* BP-1 (Tll0078) is called TePixD. A crystal structure of TePixD forms a decamer that is composed of two pentamer rings (Fig.1(a)). This decameric structure is maintained in solution. The photochemical reaction of TePixD was initially studied by absorption spectroscopy. Upon blue light irradiation, the visible absorption band of FAD is red shifted by ~ 10 nm indicating creation of an intermediate (I_1) state. The kinetics of the red shift were determined by the flash photolysis method to be sub-nanoseconds

A typical TG signal is depicted in Fig.1(b). The initial decay was attributable to the thermal grating caused by the thermal energy released from the excited molecule. The second weak decay component was expressed well by a single exponential function with a time constant of 40 μ s. The rate constant was independent of the grating wavenumber, so the kinetics should represent intrinsic reaction kinetics. This component was attributed to the volume grating due to the increase of the partial molar volume of TePixD indicating creation of the second intermediate (I_2) state. The slowest rise-decay curve on the millisecond time scale was dependent on the grating wavenumber, and this peak was attributed to the molecular diffusion process. The rise and the decay parts, respectively, can be assigned to the diffusion of the reactant and a product. It was shown that this reaction is the dissociation reaction from the decamer to the pentamer. The excited TePixD returns back to the dark state with a time constant of 12 s at room temperature

We tried to measure the compressibility of the reaction intermediate. For this purpose, a high-pressure optical cell was constructed and the volume change at various pressures was measured quantitatively in the time domain. The volume property was very sensitive to pressure. From the pressure dependence of ΔV for the I_1 and I_2 intermediate states, $\Delta\kappa_T$ of I_1 and I_2 were determined to be 5.6×10^{-2} cm³/mol MPa for I_1 and 6.6×10^{-2} cm³/mol MPa for I_2 . Therefore, this result showed that the partial molar volume fluctuation of the short-lived intermediate states is enhanced transiently compared with that of the ground state. As the compressibility is related to the volume fluctuation, these intermediates fluctuate a greater extent than the ground state. We will discuss the results in more detail.

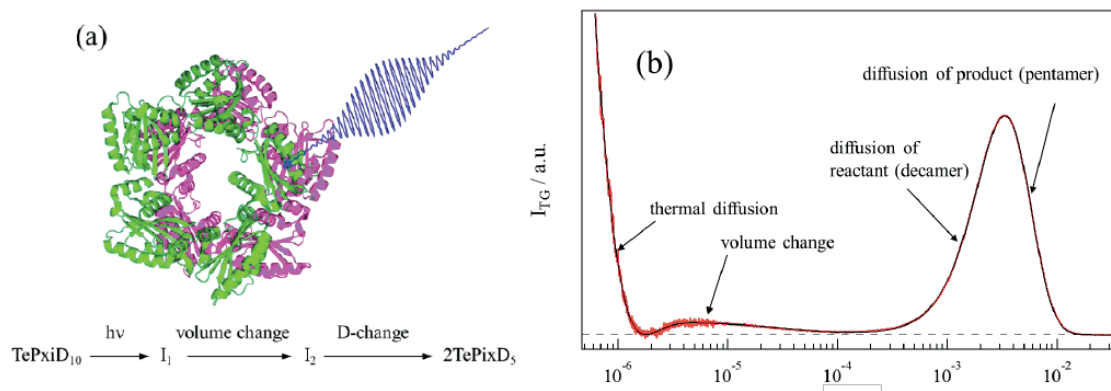


Fig.1 (a) Decamer structure of TePixD. Upper and lower tetramer rings are indicated in green and purple, respectively. (b) Typical TG signal of TePixD at 0.1 MPa. The origins of the phases of the TG components are indicated in the figure.

Photothermal Control of Micro- and Nanoobjects

Frank Cichos

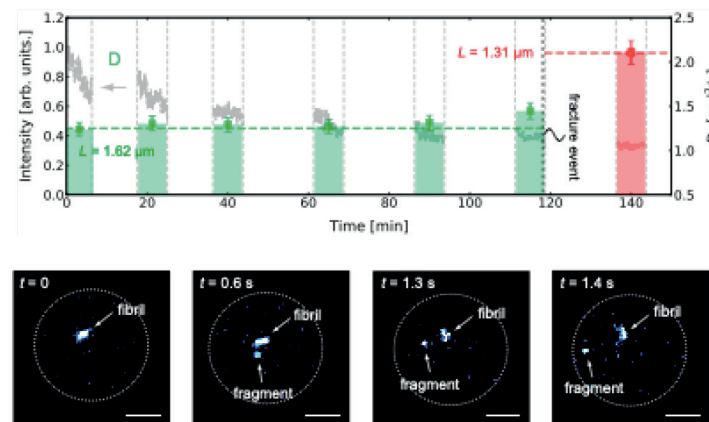
Molecular Nanophotonics Group, Peter-Debye Institute for Soft Matter Physics, University Leipzig, Leipzig Germany

cichos@physik.uni-leipzig.de

The optical generation of localized and dynamic temperature fields is accompanied by new fundamental physics. We will address three topics of thermal non-equilibrium processes around optically heated metal structures in solution to demonstrate new phenomena and new tools for the control of single molecules, particles or more complex matter in solution.

At first we will consider the case of a spherically heated metal particle in solution, where photothermal detection principles allow to study their Brownian motion [1]. The radially symmetric temperature profile around the particle will cause a viscosity gradient as well. Due to the temperature field and the viscosity profile Debye Stokes Einstein relation, which is a consequence of a fluctuation dissipation relation is as well as the equipartition theorem at question. A suitable fluctuation dissipation relation with an effective temperature and an effective friction can be recovered, if one recognizes that temperature and hydrodynamics are intimately related in what is called Hot Brownian Motion [2]. Due to this coupling of temperature field and viscous dissipation in the liquid surrounding the particle different degrees of freedom of the particle and even the configurational and kinetic temperatures i.e. the ones displayed in the diffusion coefficient and the instantaneous velocity distribution are not any more the same.

At second we refer to situations where the radial symmetry is broken and a tangential temperature gradient exists along interfaces, i.e. as generated by optically heated metal nanostructures on a substrate surface net to a liquid. In such situations the difference in the heat content along the interface goes along with an osmotic pressure difference that sets up an interfacial creep flow. This type of thermo-osmotic flow [3] is much like the flow due to an osmotic pressure difference as a result of different ion concentrations across a semipermeable membrane. The thermo-osmotic pressure difference is what drives the motion of particles and molecules from the hot to the cold regions in a liquid and what is termed thermophoresis. A photothermal control of thermo-osmotic flows and thermophoresis lets us now create a thermophoretic trap that enables the confinement of single nano-objects using heat. With the thermophoretic trap we are able to hold and compress single DNA molecules or single fibrillar aggregates of peptides which are linked to the appearance of neurodegenerative diseases like Alzheimers, Parkinson and Huntington disease. Our study of fibrillar peptide



aggregates provides for the first time access to the real-time observation of fibril growth in solution without immobilization by long time rotational diffusion measurements (Fig. 1). It also highlights for the first time directly, that processes like fibril fracture are relevant for the growth of peptide aggregates [4], an issue which has been suggested for a long time but never been observed directly.

Fig. 1. (Top) Intensity (line) as well as rotational diffusion coefficient time trace (bars) of an A β 40 peptide fibril (1.6 μm length) in buffer as a function of time. The rotational diffusion coefficient is constant over a period of more than 100 minutes before the fibril fractures spontaneously at about 120 minutes into a 1.3 μm and a 0.3 μm fragment. (Bottom) Image series for the fracture event detected in the above time trace.

As the third example, we show how photothermal effects can be used to create active matter. Artificial active matter is a model system for living matter which shares the same features of energy consumption and active response. It is also a way to prepare thermally powered micro-machines. When metal structures are combined with colloidal polymer particles, tangential temperature gradients are generated across the colloidal particle surface. The resulting thermo-osmotic flows propel the particles at a speed which is controlled by the incident light. These active particles give new insights into phase separation and structure formation under non-equilibrium conditions. The light control of the photothermal processes in these active particles also allows a feedback control [5]. With the help of this feedback control we highlight in experiments the importance of information exchange as a structure forming element, which is relevant in all kinds of assemblies of cells in terms of cell signaling up to whole organisms creating swarms and flocks [6].

References

1. M. Selmke, F. Cichos, Phys. Rev. Lett. 110 103901 (2013) doi: 10.1103/PhysRevLett.110.103901
2. D. Rings, R. Schachoff, M. Selmke, F. Cichos, K. Kroy, Phys. Rev. Lett. 105, 09060 (2010)
3. A.P. Bregulla, A. Würger, K. Günther, M. Mertig, F. Cichos, Phys. Rev. Lett. 116 (18) 188303 (2016) doi: 10.1103/PhysRevLett.116.188303

Quantitative Imaging of Optical Absorption Spectra Using Photoacoustics

Matthew O'Donnell

Department of Bioengineering, University of Washington, Seattle, WA 98195, USA

odonnell@uw.edu

Photoacoustics (PA) is rapidly bringing molecular sensitivity to ultrasound (US) imaging for many biomedical applications leveraging recent developments in molecular-scale bioconjugated contrast agents and integrated system design for multispectral imaging. However, true quantitation of absorber concentrations using multispectral measurements has been limited for *in vivo* applications due to wavelength-dependent fluence variations at depth in a medium, and by motion artifacts. In this presentation, we will explore techniques to overcome laser fluence variations and motion artifacts and demonstrate their applicability at multiple size scales. In particular, we will show how controlling laser fluence enables quantitative PA spectrophotometry even in highly scattering media, and how an integrated PAUS system can quantify wavelength-dependent fluence variations *in vivo* and correct for motion artifacts in multispectral PA images appropriate for clinical applications.

Optoelectronic Diffusion Waves in Semiconductors: Carrier Lifetime Chronotomography Imaging of Si Solar Cells

Andreas Mandelis ^{(1,2)*}, Qiming Sun ^(1,2), Alexander Melnikov ⁽¹⁾

1. Center for Advanced Diffusion-Wave and Photoacoustic Technologies (CADIPT),
University of Toronto, Toronto M5S 3G8, Canada

2. School of Optoelectronic Information, University of Electronic Science and Technology of China,
Chengdu 610054, China

mandelis@mie.utoronto.ca

Photocarriers in semiconductors excited by modulated laser sources give rise to diffusion waves that can be used to study and characterize the electronic properties of materials and devices. In this talk the concept of carrier diffusion waves will be reviewed [1]. Then, Lock-In Carrierography (LIC), a near-infrared (NIR)-camera-based quantitative diffusion-wave methodology developed in the CADIPT for non-destructive imaging of electronic materials and devices, will be presented [2]. With the recent advent of the heterodyne mode (HeLIC) [3], high-frequency imaging up to and beyond 100 kHz has been achieved, which allows hundred-Hz frame-rate NIR cameras to map out carrier-diffusion-wave microsecond-level recombination dynamics in active optoelectronic devices like solar cells. Beyond today's state-of-the-art single effective-lifetime imaging, the high-frequency information from HeLIC can help resolve multiple carrier recombination rates/lifetimes, Fig. 1. Introducing the rate-window, a resonant time-gated modality applied to decaying photocarrier diffusion-wave temporal profiles in Si solar cells, Fig. 2, the resulting time-resolved tomography (coined definition: "lifetime chronotomography") will be shown to give rise to three-dimensional space-time reconstructions of superposed multiple lifetime modes in solar cells, thus providing novel penetrating physical insights into the solar energy conversion/loss mechanisms.

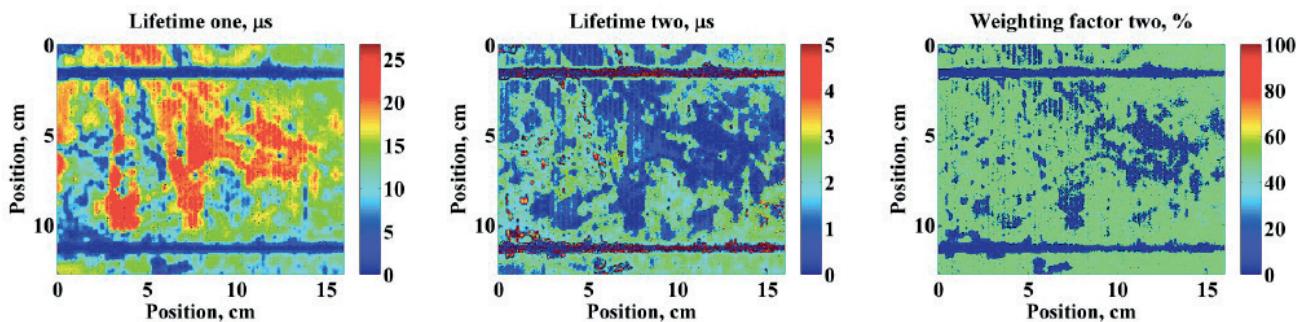


Fig. 1: Two-lifetime images and the corresponding weighting factor obtained from high-frequency HeLIC image data and a multi-lifetime model. (a) lifetime No.1; (b) lifetime No.2; and (c) weighting factor of lifetime No.2.

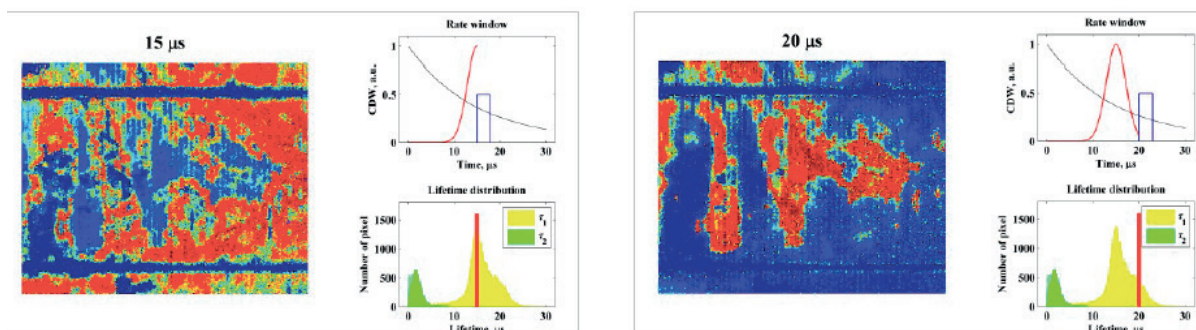


Fig. 2. Two slices of carrier lifetime chronotomography obtained from rate-window-resonance based time-domain reconstruction. (a) tomogram at 15 ms; (b) tomogram at 20 ms.

References

- [1] A. Mandelis, Diffusion-Wave Fields, Springer, New York 2001, Chap. 9.
- [2] A. Melnikov, A. Mandelis, J. Tolev, P. Chen, and S. Huq, Infrared lock-in carrierography (photocarrier radiometric imaging) of Si solar cells. *J. Appl. Phys.* 107, 114513 (2010).
- [3] Q. M. Sun, A. Melnikov, and A. Mandelis, Camera-based high frequency heterodyne lock-in carrierographic (frequency-domain photoluminescence) imaging of crystalline silicon wafers. *Phys. Status Solidi A* 213, 405-411 (2016).

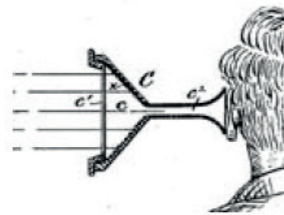
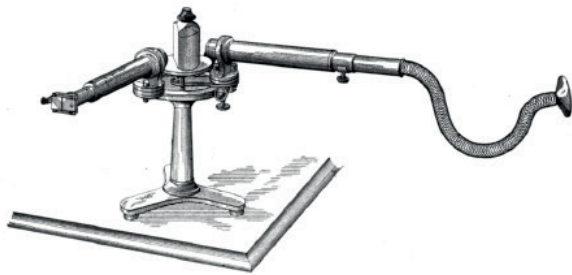
From Past through Present to Future...

Danièle Fournier

Sorbonne Université, UPMC, Univ. Paris 06, CNRS, UMR 7588, Institut des NanoSciences de Paris, 75005, Paris, France

daniele.fournier@upmc.fr

1880 Spectrophone as proposed by A G Bell



***U.S. Patent No. 241,909**, 05/24/1881 (app. 03/24/1881, no model) [DiVu205KB]
PHOTOPHONIC RECEIVER. (class: 359/150; 250/214.1; 359/154; 359/212; 359/223; 359/291)
Bell, Alexander G. and Tainter, Sumner

Thanks to Alexander Graham Bell and Allan Rosencwaig, photoacoustics took off in the 1970s and the very first conferences focused on photoacoustic and photothermal spectroscopies.

Nowadays, thanks to the sophistication of theoretical models and, above all, thanks to experimental expertises allowing us to see and listen to cells, to detect nano-emitters, to work using Gigahertz waves... the fields of photoacoustics and photothermal investigations have expanded in all areas: biomedical sciences and biophotonics, material science and characterization, chemistry and earth sciences...

But there is still a need to improve our understanding and the detection techniques. The last two topics of the 20th conference will be dedicated to it: Fundamentals and methodologies of Photothermics, Photoacoustics/Optoacoustics, and Related Techniques or Phenomena.

From Ames 1979 (Iowa, USA) to Moscow 219 (Russia), what a journey, both literally and figuratively, for ICPPP conference attendees! Connection of all the conference venues is as long as 6 times the world circumference! We have visited every continent except Oceania and Antarctica.

I propose to highlight all the photoacoustic and photothermal discoveries that have made fantastic progress in medical diagnosis, non-destructive evaluation, material characterization, nanostructure visualization... during a trip around the world.

Photoacoustic and Photothermal (time-resolved) Methods with Biomolecules. A (biased) historical perspective

Silvia E. Braslavsky

Max Planck Institute for Chemical Energy Conversion, Postfach 101365, 45413 Mülheim an der Ruhr, Germany

silvia.braslavsky@cec.mpg.de

In 1968 the first kinetic study of photoinduced processes in solution using photo(opto)acoustics was reported [1]. An amplitude-modulated high-pressure mercury lamp irradiated the solution, the acoustic wave was detected by a microphone attached to a cuvette and the signal was fed to a lock-in amplifier. Transient species with ms lifetimes could be studied. In 1969, dyes solutions were excited with μs light flashes, a capacitor microphone detected the acoustic waves and signals were averaged. Since the apparatus response was 100 μs , glycerol was the solvent in order to slow down the relaxation processes [2]. The same group studied chromatophores of photosynthetic bacteria and was the first to analyse the volume changes taking place in solution after light excitation as a sum of a thermal contribution due to the excited states relaxation plus a term due to structural changes [3], e.g., due to solvent reorganization upon photoisomerization. Several groups applied the technique of photoacoustic spectroscopy (PAS) to photosynthesis and presented their work at the “International Topical Meetings on Photoacoustic and Photothermal Phenomena” (predecessor of the International Conferences on Photoacoustic and Photothermal Phenomena). Among them, the group around Shmuel Malkin with David Cahen in Israel, who proposed light saturation of the systems to obtain an internal calorimetric reference [4, 5], Buschmann and Prehn in Germany [6], Moore et al. in Arizona, USA [7], and the group around R.M. Leblanc in Trois-Rivières, Canada [8], with strong collaboration with the group of Danuta Frackowiak in Poznan who also carried out a number of studies of PAS of photosynthetic membranes and antenna pigments with polarized light [9].

The question of the separation of the signals due to heat and to oxygen when doing PAS experiments with leaves was addressed by P. Korpium and S. Malkin in a report during the Doorwerth 7th ICPPP [10].

The laser as a source of short pulses and piezoelectric (PZT) acoustic detectors permitted improving the time resolution to several ns. In 1979 Andrew Tam and Kumar Patel used PZT detection of ultrasonic acoustic waves at low temperatures and developed a stainless-steel finger that could be clamped to the side of a regular 1-cm quartz cuvette [11]. This instrumentation opened the possibility of measuring ns to μs lifetime species under normal conditions of pressure and temperature. Zharov (Moscow, USSR) and collaborators developed several procedures for the use of pulsed lasers and piezo-detection in medical areas [12].

In Mülheim we built the equipment following Patel’s design and ns laser pulses for the study of photoinduced processes in open-chain tetrapyrroles (chromophores of phytochromes) [13], in plant phytochrome [14, 15] as well as in photosynthetic units [16]. We called the technique Laser-Induced Optoacoustic Spectroscopy (LIOAS). Using this equipment, Merten Jabben performed the first experiment in vivo with intact leaves [17]. Retinal proteins, photoactive yellow protein and flavin-bearing blue-light sensor proteins were studied [18, 19]. Structural volume changes were correlated with entropy changes associated with light-induced processes.

The group led by Kevin Peters (Boston, USA) developed a similar arrangement to study photochemical reactions and called the technique Photoacoustic Calorimetry (PAC). Jeanne Rudzki in this group presented in her PhD thesis work a procedure to deconvolute the sample signal from the transducer function and extract lifetimes of the transient species in the ns and μs time range and the volume changes associated with the formation and decay of such transients [20]. Jeanne Rudzki and Enoch Small started a company some years later (Quantum Northwest) and commercialized a thermostated cuvette and a detector using piezoelectric films as well as the software for deconvolution of sample and apparatus signals.

The application of Temperature-dependent LIOAS to photosystem II (PSII) reaction centres (RC) without the antenna, combined with ns-flash photolysis of complete PSII RC, led us to conclude that the carotene in the so-called inactive D2 branch in plant RC acts as a protector for high light-intensity situations. This work was presented at the 16-ICPPP [21].

Luis Arnaut and Dick Caldwell built a front-face cuvette with a dichroic mirror in front of the piezodetector and a flowing thin film of the sample solution. With pulsed lasers and this arrangement time resolution down to ca. 2 ns was obtained in PAC [22]. This system, however, has disadvantages for its use with proteins.

Extending the time domain of photothermal techniques to ps times for the application to biological molecules (proteins and DNA) was addressed by Dwayne Miller in a contribution on “Picosecond transient thermal phase grating spectroscopy: from proteins to surfaces” during the ICPPP Baltimore meeting and published in Science [23].

Thermal lensing (TL) is extremely accurate and sensitive. Its use for trace detection has been reported in all ICPPP meetings. In 1983 Deng, Sheng and Wang presented a TL study for trace solutes determination [24]. TL time range is much wider than with LIOAS because heat diffusion in solvents is longer than the lifetimes of the photoproducted transient species in dyes. However, light absorption by these transient species complicates matters (see below).

In 1987, we reported on the quantitative determination of singlet molecular oxygen production (and its lifetime) using time-resolved TL (TRTL) [25]. Isak, Komorowski and Eyring presented a combination of TRTL and PAC for the study of dyes in solution [26]. A related technique is Photoacoustic Deflection Spectroscopy (PDS), also called Photoacoustic Beam Deflection (PBD). Komorowski and Eyring reported a comparison of the sensitivity and time resolution between BD and acoustic detection with a polyvinylidene fluoride film (PVF2) for pulsed signals in liquids [27], and the same group presented later measurements by PBD and radiometry of thermal diffusivities in liquids, in particular in molten salts [28].

PAC/LIOAS can resolve times up to few μ s. The photoinduced cycles of biological photosensors may take minutes for completion. The longer times involve movements in optically silent regions of the protein far from the chromophore. We applied PBD to follow the cycle of bacteriorhodopsin (BR), completed in ca. 10 ms after ns-pulse excitation. This was a difficult enterprise, due to the dependence of the refractive index on the absorbance of all species in the whole spectral range (population lens explicited in the Kramers-Kronig law). P. Schulenberg, during his doctoral work, solved the problem for BR, the results were presented at the ICPPP meeting in 1994 [29]. M. Terazima presented at the same meeting an approach for the discrimination between population lens and heat lens in TRTL experiments [30]. More recently, Klauss et al. optimised the PBD technique to determine the structural volume changes in the seven steps (from μ s to several ms) taking place for water oxidation (upon pulse excitation) in the manganese centrum of PSII [31].

M. Terazima with N. Hirota have applied the technique of time-resolved thermal grating (TRTG) to study photoinduced reactions in solution, among them those of photoreceptor proteins. In the 12th ICPPP [32] M. Terazima reported on energy and volume changes induced by photoinitiated proton releasing reaction with apomyoglobin using TRTG, called it time-resolved diffusion technique and used it to compare the behaviour of cryptochrome, a blue-light sensing chromoprotein responsible for the entrainment of circadian rhythm in plants and many animals, and that of photolyase, a DNA light-induced repair protein. Although differing in function, both proteins have a similar amino acids sequence as chromophore cavity; however, different time-resolved movements were observed in both proteins [33]. With the same method, in 2018 the group reported on the photoinduced diffusion changes of a blue-light regulated enzyme involved in the photomovement of some bacteria and interpreted them as due to protein conformational changes, concluding also that this protein is a non-linear photosensor [34].

Molecular movements upon light-induced proton transfer in proteins and of protein folding can be followed by PAC/LIOAS. After laser-induced proton release, the protonation of short polypeptides and proteins gives rise to the acoustic signals [35, 36].

References

1. E. Hey, K. Gollnick, Ber. Bunsen Gesellschaft, 72, 263 (1968)
2. J.B. Callis, M. Gouterman, J.D.S. Danielson, Rev. Sc. Instr., 40, 1599 (1969)
3. J.B. Callis, M. Gouterman, W.W. Parson, Biochim. Biophys. Acta, 267, 348 (1972)
4. P. Poulet, D. Cahen, S. Malkin, Biochim. Biophys. Acta, 724, 433 (1983)
5. O. Canaani et al., Photoacoustic and Photothermal Phenomena II, eds: J.C. Murphy et al., Springer, 6th ICPPP, Baltimore, 1989, 435
6. C. Buschmann, H. Prehn, Photoacoustic and Photothermal Phenomena, eds: P. Hess, J. Pelzl, Springer, 5th ICPPP, Heidelberg, 1987, 523
7. T.A. Moore, R. Benin, R. Tom, J. Physique, 3rd ICPPP Paris, Colloque 6, C6-351, 1983
8. (a) R. Carpentier et al., J. Physique, 3rd ICPPP Paris, C6-355, 1983; (b) R.M. Leblanc, C.N. N'Soukpoé-Kossi, Photoacoustic and Photothermal Phenomena, eds: P. Hess, J. Pelzl, Springer, 5th ICPPP, Heidelberg, 1987, 514
9. D. Frackowiak et al, Photochem. Photobiol. 43, 335 (1986)
10. P. Korpiun, S. Malkin, Photoacoustic and Photothermal Phenomena III, ed: D. Bicanic, Springer, 7th ICPPP, Doorwerth, 1991, 59
11. A.C. Tam, C.K.N. Patel, Rev. Mod. Phys. 53, 517 (1981)
12. V.P. Zharov et al, Photoacoustic and Photothermal Phenomena, eds: P. Hess, J. Pelzl, Springer, 5th ICPPP, Heidelberg, 1987, 533
13. S.E. Braslavsky et al., Tetrahedron, 39, 1909 (1983)
14. M. Jabben, S.E. Braslavsky, K. Schaffner, J. Physique, 3rd ICPPP Paris, Colloque 6, C6-389, 1983
15. K. Heihoff, S.E. Braslavsky, K. Schaffner, Biochemistry 26, 1422 (1987)
16. C. Nitsch, G. Schatz, S.E.B. Biochim. Biophys. Acta 975, 88 (1989)
17. M. Jabben, K. Schaffner, Biochim. Biophys. Acta, 809, 445 (1985)
18. M.E. van Brederode, T. Gensch, W.D. Hoff, K.J. Hellingwerf, S.E. Braslavsky, Biophys. J. 68, 1101-1109 (1995)
19. A. Losi, S.E. Braslavsky, Phys. Chem. Chem. Phys., 5, 2739-2750 (2003)
20. J.E. Rudzki, J.L. Goodman, K.S. Peters, J. Am. Chem. Soc. 107, 7849 (1985)
21. S.E. Braslavsky, A.R. Holzwarth, 16th ICPPP, Merida, 2012, Int. J. Thermophysics, 33, 2021 (2012)
22. L.G. Arnaut et al., Rev. Sc. Instruments, 63, 5381 (1992),
23. R.J.D. Miller, L. Genberg, L. Richard, S.M. Gracewski, Photoacoustic and Photothermal Phenomena II, eds: J.C. Murphy et al., Springer, 6th ICPPP, Baltimore, 1989, 380; L. Genberg, L. Richard, G. McLendon, R.J. Dwayne Miller, Science, 251, 1051 (1991)
24. Y. Deng, R. Sheng, M. Wang, J. Physique, 3rd ICPPP Paris, C6-569, 1983

25. R.W. Redmond, S.E. Braslavsky, Photoacoustic and Photothermal Phenomena, eds: P. Hess, J. Pelzl, Springer, 5th ICPPP, Heidelberg, 1987, 95
26. S.J. Komorowski, S.J. Isak, E.M. Eyring, Photoacoustic and Photothermal Phenomena, eds: P. Hess, J. Pelzl, Springer, 5th ICPPP, Heidelberg, 1987, 103
27. S.J. Komorowski, E.M. Eyring, Photoacoustic and Photothermal Phenomena, eds: P. Hess, J. Pelzl, Springer, 5th ICPPP, Heidelberg, 1987, 484
28. D.P. Cobranchi, N.F. Leite, J. Isak, S.J. Komorowski, A. Erhard, E.M. Eyring, Photoacoustic and Photothermal Phenomena II, eds: J.C. Murphy et al., Springer, 6th ICPPP, Baltimore, 1989, 328,
29. P. Schulenberg, W. Gärtner, S.E. Braslavsky, J. Physique IV, Colloque C7, C7-477, 8th ICPPP, Guadeloupe, 1994, J. Phys. Chem. 99, 9617 (1995)
30. M. Terazima, J. Physique IV, Colloque C7, C7-345, 8th ICPPP, Guadeloupe, 1994
31. A. Klaus, M. Haumann, H. Dau, J. Phys. Chem. B 119, 2677 (2015)
32. J. Choi, M. Terazima, 12th ICPPP, Toronto, Canada, 2002
33. M. Kondoh, M. Terazima, Photochemistry and Photobiology 93, 15 (2017)
34. K. Shibata, Y. Nakasone and M. Terazima, Phys. Chem. Chem. Phys., 20, 8133 (2018)
35. S. Abbruzzetti, C. Viappiani, J.R. Small, L.J. Libertini, E.W. Small, Biophysical J. 79, 2714 (2000)
36. C. S. H. Jesus, P.F. Cruz, L.G. Arnaut, R.M.M. Brito, C. Serpa, J. Phys. Chem. B 122, 3790 (2018)

Photoacoustic imaging with compact handheld probes

Wiendelt Steenbergen

University of Twente, Enschede, The Netherlands

w.steenbergen@utwente.nl

Photoacoustic imaging is a promising novel modality for biomedical imaging, and is the topic of a huge research effort in the recent decade. This effort has led to a range of devices for various applications, and to novel measurement strategies and algorithms for image reconstruction. However, no potential application of photoacoustic imaging has made it to the clinic, while the images obtained are sometimes stunning. My contribution will focus on recent efforts to develop devices which are meant to bridge the gap between lab and bedside by integrating photoacoustic imaging in a normal ultrasound scanner, making use of affordable light sources.

A European consortium of industrial and academic partners has developed systems for combined PA and US imaging, in which pulsed diode lasers and laser drivers have been integrated with an ultrasound imaging array into a handheld probe. This is a unique effort which can only be undertaken by industrial-academic partnerships who join their technologies and expertise.

I will discuss the development from the first photoacoustic images made with diode lasers with pulse energies of <10 mJ [1] through a number of innovations [2], to the current generation of multiwavelength probes with pulse energies of more than 1 mJ per wavelength.

Next, I will present our efforts to improve image quality by the suppression of reflection artefacts (clutter) in various manners. Methods will be presented that make use of the ultrasound reflections by the tissue [3], along with algorithms that utilize multiwavelength responses of the tissue [4] and controlled translation of the probe.

Finally, I will discuss steps towards measuring blood flow using the photoacoustic Doppler effect [5].

References

1. R.G.M. Kolkman, W. Steenbergen, T.G. van Leeuwen, *Lasers Med Sci*, vol 21: 134 (2006) DOI 10.1007/s10103-006-0384-z
2. K. Daoudi, P. J. van den Berg, O. Rabot, A. Kohl, S. Tisserand, P. Brands, W. Steenbergen, *Optics Express* 22, 26365 (2014) <https://doi.org/10.1364/OE.22.026365>
3. M.K.A. Singh, M. Jaeger, M. Frenz, W. Steenbergen, *Biomedical Optics Express* 7, 2955 (2016) <https://doi.org/10.1364/BOE.7.002955>
4. H.N.Y. Nguyen, W. Steenbergen, *Biomedical Optics Express* 9 (10), 4613 (2018) <https://doi.org/10.1364/BOE.9.004613>
5. T.M. Bücking, P.J. van den Berg, S. Balabani, W. Steenbergen, P.C. Beard, J. Brunker, *Journal of Biomedical Optics*, 23 (2), 026009 (2018) <https://doi.org/10.1117/1.JBO.23.2.026009>

Advanced infrared nanospectroscopy using photothermal induced resonance technique, AFMIR: a versatile tool to characterize polymeric nanoparticles

Ariane Deniset-Besseau⁽¹⁾, Jérémie Mathurin⁽¹⁾, Elisabetta Pancani⁽²⁾, Seray Merve Ural⁽²⁾, Ece Aybeke1, Marie-Françoise Bernet-Camard⁽³⁾, Ruxandra Gref⁽²⁾, Alexandre Dazzi

1. Laboratoire de Chimie Physique (LCP), CNRS UMR 8000,

Univ. of Paris-Sud, Université Paris-Saclay, 91405 Orsay, France

2. ISMO, UMR 8214 CNRS, Université Paris Sud, Université Paris Saclay, Orsay, France

3. EA4043 "Unité Bactéries Pathogènes et Santé" (UBaPS), Univ. of Paris-Sud, Université Paris-Saclay, 92290 Châtenay-Malabry, France

ariane.deniset@u-psud.fr

Introduction

Since 10 years, a new instrumentation, called AFMIR, has been developed in our team at the Chemical-Physics laboratory (LCP, Université Paris-sud) to perform IR spectromicroscopy analyses at the nanoscale. This technique is based on photothermal effect [1–3] and is the result of a coupling between atomic force microscopy (AFM) and IR spectroscopy to perform local IR absorption measurements (Patent US11 / 803421, A. Dazzi). This combination makes it possible to identify at the nanoscale organic molecules without using exogenous markers. The application fields range from biomedical, to polymer science and astrochemistry.

In our team, the technique has shown its potential in the study of lipid bodies in microorganisms. Nevertheless, in its initial configuration, the instrumentation has reached a limit in term of sensitivity: the size of the smallest object (chemically pur) detectable is around 50 nm. New experimental approaches are therefore developed to solve the problems and overcome the technical constraints imposed by the system itself (configuration of illumination - sensitivity -study of soft sample...).

In particular, two changes were significant:

First, a change of configuration was done that allowed us to go down in terms of resolution and to reach tens of nanometer. This breakthrough offers new perspectives such as the study of protein fibers or nanoparticles. The second concerned the AFM imaging itself: AFM-IR was used mainly in the contact mode, thus preventing its application in soft or loosely adhered samples such as polymeric nanoparticles (NPs) of less than 200 nm. Here, we will present an application of tapping AFM-IR, which enabled addressing the limitations of the contact mode AFM, thus extending its application to unraveling the chemical and morphological features of soft, spherical samples difficult to fix on the AFM substrate [4].

Polymeric biodegradable NPs are a typical example of samples very challenging to investigate using AFM in the contact mode. For this reason, they were selected here to test the newly developed AFM-IR configuration. These particles constitute intriguing reservoirs able to release their drug cargo in a controlled manner at targeted sites in the body.

Results

We will show the possibilities to apply AFM-IR as an analytical technique for the study of polymeric nanoparticles. In the first part, the principle of the technique will be presented as well as the experimental constraints. Then we will show how the method can be used to reveal new insight about the structure of polymeric nanoparticles and the antibiotic repartition compared with low resolution methods. To conclude, we will demonstrate the use of AFM-IR as a new label free tool to study the localization of nanoparticles carrier inside fixed macrophages at the subcellular scale [3].

Discussion

We will discuss how the possibility to have acces to chemical informations at high resolution can be critical for further improvements of efficient drug nanocarriers. Indeed, elucidating the substructure without any labelling of nanoparticles loaded with antibiotic is usefull to understand the effect of various parameters on the interaction between the different components, which is crucial to the vialibility and the optimization of these systems. Furthermore, AFMIR might be an interesting tool to directly probe the chemical composition of nanoparticles within the cells, investigate their degradation and elucidate the key steps in the mechanism of drug release.

Acknowledgements

Financial support for carrying out this work was provided by the European Community through the Marie Curie ITN "CycloN Hit" Grant No. 608407. We thank the C'nano IDF DIM for funding this research through the "Nanoimagerie" grant. This work was supported by a public grant overseen by the French National Research Agency (ANR) as part of the "Investissements d'Avenir" program (Labex NanoSaclay, reference: ANR-10-LABX-0035). We are grateful to Dr K. Salim (PCAS, Longjumeau, France) for kindly donating the PLGA polymer samples.

Keynote Session A6+B7

References

1. A. Dazzi and C. B. Prater, *Chem. Rev.* 117, 5146 (2017).
2. A. Dazzi, C. B. Prater, Q. Hu, D. B. Chase, J. Rabolt, and C. Marcott, *Appl. Spectrosc.* 66, 1365 (2012).
3. A. Dazzi, F. Glotin, and R. Carminati, *J. Appl. Phys.* 107, 1 (2010).
4. J. Mathurin, E. Pancani, A. Deniset-Besseau, K. Kjoller, C. B. Prater, R. Gref, and A. Dazzi, *Analyst* 143, 5940 (2018).

Phonon-Mediated Thermal Transport Measured in Various Kinetic Regimes

Keith A NELSON

Department of Chemistry, MIT, Cambridge, MA 02139, USA

kanelson@mit.edu

Direct measurement of thermal transport on experimentally controllable length scales offers excellent prospects for detailed understanding of the kinetics in microscopic terms. For phonon-mediated heat transport, the wavevector-dependent phonon mean free paths and how they are influenced by phonon-phonon scattering and scattering due to impurities and crystalline defects are the key ingredients for a detailed description of transport kinetics. We have used transient thermal grating (TTG) measurements in which the length scale D on which thermal transport is measured is set by the interference period produced by two intersecting “excitation” laser pulses. Diffraction of probe laser light from the transient thermal grating pattern is measured, and its time-dependent decay reveals the kinetics of thermal transport. If the kinetics are diffusive, then the exponential decay time τ scales with the square-root of the transport length scale D , i.e. $D = \sqrt{\alpha\tau}$ where α is the thermal diffusivity. By varying the angle between excitation pulses at visible wavelengths, the TTG interference period can be varied and a thermal transport length scale range $D \sim 1\text{--}30\ \mu\text{m}$ range can be accessed easily.

In high-quality single crystals of Si or GaAs, deviations from diffusive kinetics are clearly observed on micron length scales even at room temperature [1]. The average phonon mean free paths are on the order of 40 nm, heavily weighted by the phonon density of states which increases proportional to the square of the wavevector magnitude q . Because very high- q , nm-wavelength phonons undergo scattering readily from each other and from even the smallest crystal defects, their role in thermal transport is not completely predominant even though they account for most of the heat capacity. Because of their longer mean free paths, phonons of intermediate wavevector magnitude play an outsize role in thermal transport. Diffusive kinetics break down on 1-10 μm length scales because phonons with micron-scale mean free paths result in a significant ballistic contribution to thermal transport on that scale. In recent work, we have studied a Si/Ge alloy with 6.6% Ge, which is sufficient to drastically reduce the thermal conductivity measured on macroscopic length scales. It could be anticipated that in such a system, with phonon mean free paths reduced substantially compared to those in pure Si, the breakdown of diffusive thermal transport kinetics would only be observed on shorter length scales than the micron range on which it was seen in pure Si. Instead, ballistic contributions to thermal transport become apparent at 10-20 μm , somewhat longer lengths than in Si. This occurs because phonons are essentially undergoing Rayleigh scattering from the Ge atomic-scale impurities, with the characteristic $1/\lambda^4$ dependence resulting in greatly reduced mean free paths for the shortest phonon wavelengths λ while having negligible effects on phonons of intermediate wavevectors. Thus the phonons with micron mean free paths are hardly affected by the impurities, while the diffusive transport contributions of higher- q phonons are reduced compared to those in Si. The appearance of ballistic contributions to the transport kinetics at greater length scales than in pure Si occurs because the relative contribution of diffusive contributions is reduced.

In general, when heat is deposited in a localized region of a solid, the heated region remains warmer than the surrounding regions even as thermal transport gradually reduces the temperature difference between them. That outcome depends on backscattering of the phonons that carry the heat, so that energy is not simply carried away from the heated region and never returned. Phonon-phonon scattering processes that result in net reversal of the propagation direction, sometimes described in terms of Umklapp scattering, are key components of thermal equilibration in crystalline solids. In rare cases, suppression of such processes has resulted in wavelike thermal transport or “second sound.” Phonon hydrodynamics of this sort have been observed in NaF and several other crystals at temperatures below 20 K [3], and recently reported [4] (and disputed [5]) in SrTiO₃ up to 40 K. Recent theoretical calculations have indicated that in some materials such as graphene and graphite [6], second sound could be observed at far higher temperatures. In recent TTG measurements on graphite, we have observed second sound at temperatures as high as 124 K [7]. TTG data show oscillatory signals, clearly indicating wavelike behavior in which the pattern of alternately heated and unheated regions is reversed – the initially heated regions becoming cooler than the initially unheated regions – then reversed again, before the signal decays. Our results, observed with TTG spatial periods of 8-18 μm , support the recent theoretical predictions which also suggest that with smaller periods second sound may persist at still higher temperatures.

The previous examples of TTG data were collected with visible light and TTG periods in the micron range. For investigation of many phenomena, key information and insights require nanoscale measurements. We have worked in collaboration with scientists at the Trieste ELETTRA soft x-ray free-electron laser system to use the extreme ultraviolet (EUV) transient grating system they have constructed for thermal transport measurements. The first results were obtained using near-UV probe light which required a small angle between the EUV excitation pulses to generate a 280-nm TG period from which the probe light could be diffracted [8]. More recently, all-EUV TG measurements were conducted and thermal transport (as well as acoustic waves) were measured with TG pe-

Keynote Session A6+B7

riods as small as 28 nm. Thermal and acoustic contributions to the signal were apparent, and on this length scale thermal transport in high-quality single crystals like Si is essentially ballistic in character. Wavevector-dependent results in partially disordered crystals and amorphous solids are more complex as thermal transport is mediated by quasi-localized vibrations as well as propagating acoustic modes. Nanoscale TG measurements will ultimately be conducted with soft and hard x-rays, providing direct access to the wavevectors associated with charge and spin-density waves, striped phases of correlated electron materials, and structural, dipolar, magnetic, and other correlation length scales.

References

1. J.A. Johnson, A.A. Maznev, J. Cuffe, J.K. Eliason, A.J. Minnich, T. Kehoe, C.M. Sotomayor Torres, G. Chen, K.A. Nelson, *Physical Review Letters* 110, 025901 (2013) doi:10.1103/PhysRevLett.110.025901
2. S. Huberman, V. Chiloyan, R. A. Duncan, L. Zeng, R. Jia, A. A. Maznev, E. A. Fitzgerald, K. A. Nelson, G. Chen, *Physical Review Materials* 1, 054601 (2017) doi/10.1103/PhysRevMaterials.1.054601
3. D. W. Pohl, V. Irniger, *Physical Review Letters* 36, 480 (1976) doi:10.1103/PhysRevLett.36.480
4. B. Hehlen, A.-L. Pérou, E. Courtens, R. Vacher, *Physical Review Letters* 75, 2416 (1995) doi:10.1103/PhysRevLett.75.2416
5. J. F. Scott, A. Chen, H. Ledbetter, *Journal of Physics and Chemistry of Solids* 61, 185 (2000) doi.org/10.1016/S0022-3697(99)00280-2
6. Z. Ding, J. Zhou, B. Song, V. Chiloyan, M. Li, T. H. Liu, G. Chen, *Nano Letters* 18, 638 (2018) doi:10.1021/acs.nanolett.7b04932
7. S. Huberman, R.A. Duncan, K. Chen, B. Song, V. Chiloyan, Z. Ding, G. Chen, K.A. Nelson, *Science* 10.1126/science.aav3548 (2019)
8. A. A. Maznev, F. Bencivenga, A. Cannizzo, F. Capotondi, R. Cucini, R. A. Duncan, T. Feurer, T. D. Frazer, L. Foglia, H.-M. Frey, H. Kapteyn, J. Knobloch, G. Knopp, C. Masciovecchio, R. Mincigrucci, G. Monaco, M. Murnane, I. Nikolov, E. Pedersoli, A. Simoncig, A. Vega-Flick, and K. A. Nelson, *Applied Physics Letters* 113, 221905 (2018).

Time-Resolved Energetics and Structural Volume Changes in Photosensor Proteins

Silvia E. BRASLAVSKY

Max Planck Institute for Chemical Energy Conversion, Postfach 101365, 45413 Mülheim an der Ruhr, Germany

silvia.braslavsky@cec.mpg.de

Photosensor proteins detect the quantity, quality (wavelength) and, in some cases, the direction of light in the environment. All biological organisms from bacteria, fungus, algae, plants, to insects, fish, reptiles, birds and mammals, need and use biological photonic signal transducers to better develop their survival strategy and secure their reproduction. These photosensors, e.g., retinal proteins, photoactive biliproteins such as phytochromes as well as flavin-containing proteins, form, in the sub-ns time scale after primary photochemistry upon light absorption, the first thermodynamically stable intermediates. The energy stored in these intermediate states drives the rest of the photocycle, which usually takes place in several thermally-controlled steps with times ranging from milliseconds to seconds, until the biological signal is produced. Time-resolved photothermal methods, such as laser-induced optoacoustics (LIOAS) have the unique ability to monitor, in real time, the energy level of transient species and the corresponding volumetric changes of non-thermal origin, i.e., due to structural changes, such as, e.g., water rearrangements induced by changes of dipolar moment caused by the photoisomerization or protein movements due to light-induced charge transfer [1–4].

LIOAS has been used to determine the energy content of nano- and microsecond species and the structural volume changes accompanying their formation and decay in several retinal proteins, photoactive yellow protein (PYP), and in plant phytochrome A (the phytochrome driving the growth of dark grown seedlings) from *Avena sativa* [2]. Lately, the 65 kDa truncated form (AsphyA) assembled with phytochromobilin and with phycocyanobilin, as well as in the diverse photochromic bilin-binding photoreceptors of prokaryotic origin have been analysed also by LIOAS [5]. This latter family of photosensors shows an extremely broad spectral versatility, novel physiological functions, and are excellent candidates for applications in modern techniques such as optogenetics and special nanoscopies. The measurements with the chromophore-binding domain of a red/green switching cyanobacteriochrome from *Synechocystis* (*Slr1393g3*), the red/far red *Synechocystis* Cph1 phytochrome, as well as full-length and truncated constructs of *Xantomonas campestris* bacteriophytochrome show a similar large prompt heat dissipation (up to 90% or 370%) in the sub-ns time scale upon formation of the first intermediate, reflecting the very low quantum yield of photoisomerization in all four chromoproteins. Plant AsphyA shows a quantum yield of 0.17 [6] and in the three bilin-binding proteins measured lately it is \approx 0.3.

The structural volume change accompanying the production of the first intermediate is positive, i.e., an expansion is produced of ca. 5-12 ml/mol, underscoring the relevance of geometric and steric effects. An exception is the green-absorbing form of *Slr1393g3* for which the prompt expansion is followed by a contraction, probably indicating a larger occupancy and more mobility of water molecules in the protein cavity in this construct.

Acknowledgements

I deeply thank all young and senior colleagues with whom I have learned and collaborated over several decades, in particular Wolfgang Gärtner. I also thank the support of the Max Planck Society and of Kurt Schaffner. The latest results with bilin-binding photosensors are from the group led by Aba Losi (Parma, Italy) and her collaborators [5].

References

1. T. Gensch, C. Viappiani, *Photochem. Photobiol. Sc.* 2, 699 (2003) doi: 10.1039/b303177b
2. Losi, S.E. Braslavsky, *Phys. Chem. Chem. Phys.*, 5, 2739 (2003) doi: 10.1039/b303848c
3. S.E. Braslavsky, G.E. Heibel, *Chem. Rev.* 92, 1381(1992) doi: 10.1021/cr00014a007
4. T. Gensch, C. Viappiani, S.E. Braslavsky, in *Encyclopedia of Spectroscopy and Spectrometry* (Jan Reedijk, Editor-in-Chief) Elsevier Reference Module. Chemical, Molecular Sciences and Engineering, (2014), <http://dx.doi.org/10.1016/B978-0-12-409547-2.10992-8>
5. A. Losi, H.R. Bonomi, R. Michael, K. Tang, K.-H. Zhao, *Photochem. Photobiol.* 93, 733 (2017) doi: 10.1111/php.12728
6. T. Gensch, S. Churio, S.E. Braslavsky, K. Schaffner, *Photochem. Photobiol.* 63, 719 (1996) doi: 10.1111/j.1751-1097.1996.tb09621.x

Ballistic thermal transport in silicon nanostructures investigated using time-domain thermoreflectance

Roman ANUFRIEV ^{(1)*}, Aymeric RAMIERE ⁽¹⁾, Jeremie MAIRE ⁽¹⁾, Sebastian VOLZ ^(1,2), Masahiro NOMURA ^(1,3)

1. Institute of Industrial Science, the University of Tokyo, Tokyo, Japan

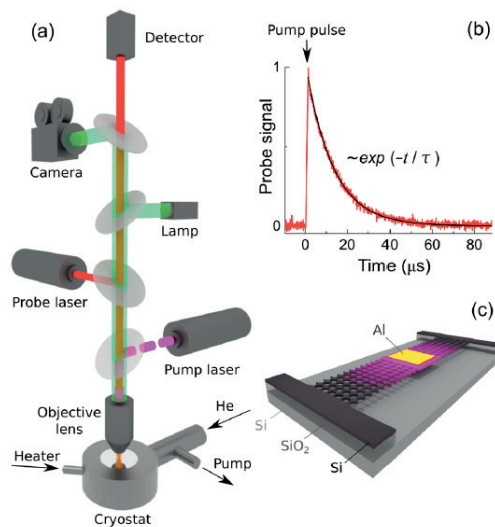
2. Laboratory for Integrated Micro Mechatronic Systems / National Center for Scientific Research-Institute of Industrial Science (LIMMS/CNRS-IIS), the University of Tokyo, Tokyo, Japan

3. CREST, Japan Science and Technology Agency, Saitama 332-0012, Japan

anufriev@iis.u-tokyo.ac.jp

Understanding of heat conduction in silicon nanostructures is crucial to modern microelectronics. Remarkably, at the nanoscale, heat can be conducted without actually heating the conductor. This phenomenon occurs because some phonons can preserve their phase as they travel over hundreds of nanometers and reflect from crystal boundaries. Due to such a long lifetime and the elastic reflections, phonons can transport energy over long distances without dissipation. In semiconductors, where phonons play the role of heat carriers, such phonon transport results in non-diffusive conduction of heat. In nanostructures, phonons can even cross without resistance the entire structure thus participating in ballistic heat conduction. However, the mechanism of such ballistic thermal transport in confined nanostructures is yet to be fully understood, whereas attempts to demonstrate this phenomenon experimentally remain controversial due to non-negligible thermal contact resistance involved in the experiments.

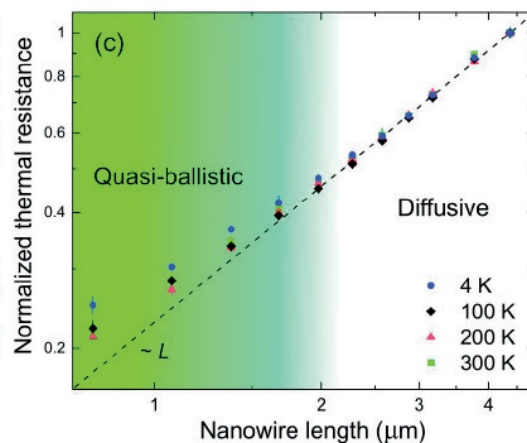
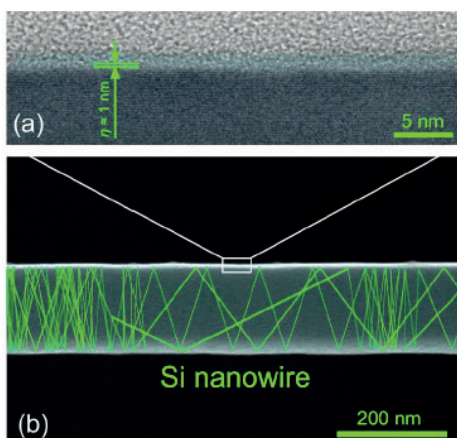
Here, we experimentally study ballistic heat conduction in silicon nanostructures using a contactless all-optical method which allows avoiding the contact resistance issues. We demonstrate ballistic effects in silicon nanowires and phononic membranes at different length scales and temperatures and discuss the underlying phonon transport mechanism.



Materials and Methods

To measure the thermal properties of our samples, we used the micro time-domain thermoreflectance technique (μ TDTR), illustrated in Fig. 1(a). In our setup, a pulsed *pump* laser periodically heats the Al pad placed in the center of each suspended sample. After the end of each pulse, heat dissipates from the center through the bridge towards the surrounding wafer, which acts as a heat sink. Since the reflectance of the Al pad changes proportionally to its temperature, we can monitor heat dissipation from the pad by continuously measuring the intensity of the second *probe* laser reflected from the Al pad. Figure 1(b) shows a typical decay curve. To quantitatively compare the decay curves, we fit them with an exponential function $\exp(-t/\tau)$, from which we can extract the decay time (τ). To convert the measured decay time into the thermal conductivity, we use FEM simulations [1,2].

Fig. 1. (a) Schematic of the micro time-domain thermoreflectance setup. (b) Typical decay signal showing the exponential thermal dissipation in a typical air-bridged sample, schematically shown in (c).



To fabricate our samples, schematically shown in Fig. 1(c), we used conventional top-down fabrication methods [3] applied to a silicon-on-insulator wafer with 145-nm-thick top Si monocrystalline layer.

Fig. 2. (a) TEM image shows low surface roughness. (b) SEM image of a silicon nanowire with simulated phonon paths. (c) The thermal resistance of short nanowires deviates from a linear diffusive trend indicating quasi-ballistic behavior.

Thermal transport in nanowires

First, we probed [2,4] the ballistic heat conduction in silicon nanowires, shown in Fig. 2(a,b). Figure 2(c) shows that measured thermal resistance deviates from a linear function of the nanowire length for the short nanowires. This implies that while heat conduction is diffusive in the long nanowire, short nanowires exhibit a quasi-ballistic behavior. The non-linearity is the strongest at the 4 K but weakens as temperature is increased. Yet, even at room temperature, quasi-ballistic heat conduction remained visible in short nanowires. To better understand this phenomenon, we probed directions and lengths of phonon flights in the nanowires [2]. Our experiments and simulations showed that the quasi-ballistic phonon motion in nanowires is essentially the Lévy walk like transport (Fig. 2(b)) with short flights between the boundaries and long ballistic leaps along the nanowire axis.

Heat guiding and focusing

Next, we studied the ballistic heat transport in silicon phononic crystals (PnCs) and a possibility to use such PnCs for directional thermal emission and heat focusing [3]. First, we fabricated and measured PnCs with aligned (Fig. 3a) and staggered (Fig. 1b) lattices of five different periods, and demonstrated that significant difference in thermal decay times (t) appears in the structures with small period (Fig. 3c) at 300 K and strengthened by factor of two at 4 K. We attributed the faster heat dissipation in the samples with aligned lattice to the presence of ballistic phonon transport in the passages between the holes.

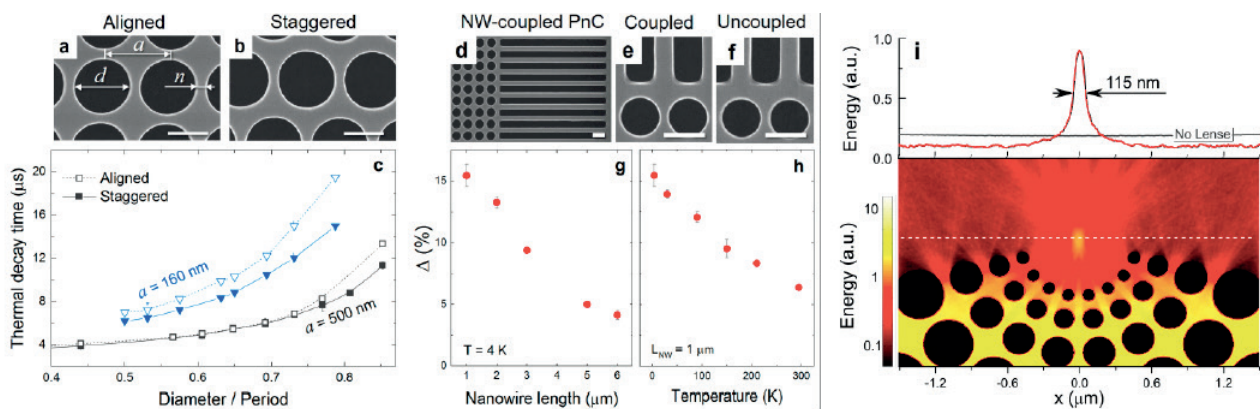


Fig. 3. SEM images of (a) aligned and (b) staggered PnCs and (c) measured decay time. SEM images of (d) a nanowire-coupled PnCs sample with (e) coupled and (f) uncoupled configurations, and the difference between their decay times as a function of (g) NW length and (h) temperature. (i) MC simulation of a thermal lens.

To prove this hypothesis, we fabricated samples of PnCs coupled with nanowires (Fig. 3(d)), in *coupled* (Fig. 3(e)) and *uncoupled* (Fig. 3(f)) configurations. We observed a significant difference between the decay time of coupled and uncoupled samples with short NWs at 4 K, due to the enhancement of ballistic transport in the coupled configuration. However, as the nanowire length or temperature were increased, the effect gradually disappeared (Fig. 1g and 1e), as heat transport became diffusive.

Finally, we proposed [3] thermal lens structure that can focus thermal energy. We demonstrate the formation of a hot spot of 115 nm (Fig. 3(i)) using MC simulations and show experimental evidence of the heat focusing. These results motivate the concept of ray-like heat manipulations at the nanoscale.

Acknowledgements

This work was supported by Kakenhi (15H05869, 17H02729, and 18K14078), CREST JST (JPMJCR19Q3), and Postdoctoral Fellowship program of Japan Society for the Promotion of Science.

References

1. R. Anufriev, R. Yanagisawa, and M. Nomura, *Nanoscale* 9, 15083 (2017).
2. R. Anufriev, S. Gluchko, S. Volz, and M. Nomura, *ACS Nano* 12, 11928 (2018).
3. R. Anufriev, A. Ramiere, J. Maire, and M. Nomura, *Nature Communications* 8, 15505 (2017).
4. J. Maire, R. Anufriev, and M. Nomura, *Scientific Reports* 7, 41794 (2017)

From optoacoustics to Lock-in thermography methods for NDE

Gerd Busse

Institute for polymer technology (IKT), University of Stuttgart, D-70569 Stuttgart / Germany

The start of my over 4 decades of thermal wave work was triggered by a talk given by Andrej Krupnov on microwave spectroscopy with acoustic detection. This optoacoustic effect depends on the spectral overlap of radiation source and detector. Every good solution fits to more than just one problem, and my problem at that time was how to tune a CO₂ laser to optical pumping of a submillimetre laser. The optoacoustic effect provided the ideal solution: A microphone mounted in the pumped laser resonator monitored the achieved spectral coincidence and allowed not only active stabilization, but also to discover new laser lines in the spectral region that is now named THz. The result was presented in 1979 at the first ICPPP conference in Ames, shortly thereafter first scans showed the potential of THz-inspection for nondestructive evaluation (NDE), but the interest came only decades later.

The arrangement was modified to an optoacoustic cell containing solid samples across which the CO₂ laser beam was scanned while the microphone signal was plotted. The optoacoustic images obtained this way were the first to be presented also in Ames.

The modulated microphone output was analyzed by a lock-in amplifier which was one channel, switched either to in-plane or to out-of-plane of signal. As I belonged to the faculty of electrical engineering (that time at University of German Armed Forces Munich), I combined two lock-ins and some analogue circuitry to give the first phase angle lock-in before it was commercially available. The advantage of phase angle optoacoustic imaging became apparent: More depth range and less sensitivity to optical surface features.

At the Ames conference it turned out that the words “optoacoustic” and “photoacoustic” were used in parallel. To avoid the permanent confusion with “acousto-optic”, the conference participants made a vote and decided in favour of “photoacoustic” used since then.

The result that phase angle images have more depth range than those obtained with amplitude were confirmed thereafter by other groups. It can be understood in terms of simple thermal wave interference. It is of interest that Luukkala in Helsinki would not believe, he re-measured and found that his data confirmed our results. That was the beginning of a permanent friendship that ended with his early death in an accident in the Baltic sea.

Phase is a specific feature for modulation. People using pulsed methods cannot use this advantage so easily. As a pulse contains a broad frequency spectrum, there is a corresponding depth range spectrum dominated by near-surface areas if a ms pulse length of a flash lamp is used. Interpretation depends on how well one is familiar with Fourier mathematics which is not the topic of this presentation. Analysis of longer pulses (“burst”) as suggested by Maldague and Balageas brings the depth range into a more NDE-relevant regime and allows for burst phase analysis used also by my team at IKT where I performed most of my thermal wave work.

Thermal wave imaging has to do with resolution. We need to consider that both optical and thermal features are involved. The quantity of interest is not only the size of the optical spot used for excitation but also the thermal wave extension around it. Their convolution determines thermal wave resolution. Microscopy images obtained at low frequencies display only optical features. Hence microscopy of thermal features requires frequencies that are too high for microphones and mechanical modulators: Piezo-electric detection and an acousto-optic laser light modulator are required. As I had access to both in Munich, Rosencwaig visited my lab so that we performed the first thermal wave microscopy of an electronic circuit at 200 kHz optical modulation, as was confirmed by the details in the phase angle image.

One NDE application of photoacoustic imaging was thickness measurement of coatings on a substrate and monitoring of subsurface contamination. Depth range and thickness resolution were adjusted by modulation frequency. However, the major restriction was that the sample needed to be contacted or kept in a microphone cell, or to be so flat that the mirage effect could be applied (Boccaro and Fournier 1979).

A highly attractive technique was remote photothermal detection developed by Nordal and Kanstad (1979). It is based on the analysis of modulated infrared thermal emission caused by the thermal wave. It allows for point-like detection in a thermal wave field so that stereoscopic imaging for depth probing becomes feasible in a transmission arrangement.

Remote photothermal detection is applicable e.g. for wet surface coatings and to monitor drying or curing processes also on non-flat large surfaces. When we imaged a fingerprint underneath paint, the Munich police came up and said they had some cars for us to inspect. The turning point of our thermal wave work had come: The point-by-point raster scan imaging was too slow for real life NDE.

As mentioned above, a good solution fits to more than one problem. People who boil several eggs in the kitchen perform parallel processing. How to transfer this concept to photoacoustic or photothermal imaging? Part of the hardware solution is simple: A lamp instead of just one laser spot generates thermal waves on the whole inspected surface, and a thermography camera instead of an infrared point detector monitors the complete temperature field and generates a stack of images while modulation goes on. So, the bottleneck is the multichannel version of a hardware lock-in amplifier.

Such a device is a black box that extracts a given frequency component out of a noise that is by magnitudes higher. So, the lock-in amplifier performs signal processing in which Fourier transform is the major part. This needs to be done at every pixel of the image, but it can be performed after a whole sequence of images has been recorded during modulation. This idea has been suggested in 1976 by Carlomagno, demonstrated by Egee in Reims/France and used later also by Thomas. Thereafter we developed for this technique an algorithm to obtain phase angle images rapidly. The technique has been named “Lock-in thermography” according to the hardware device whose function is simulated by mathematical image stack analysis.

Of course all advantages of phase angle images stay the same as in single point detection though the duration of a measurement is not any more given by the number of pixels multiplied by the time spent for one measurement, but essentially only by the time for one measurement plus several cycles required until after a transient time a stationary situation has been achieved. Thus, sample areas of a square meter can be inspected within some minutes which makes the technique highly attractive for NDE under real life conditions. Typical applications are inspection of riveted or bonded structures e.g. in aerospace components consisting usually of light materials with high specific strength, e.g. carbon fibre reinforced polymers (CFRP).

It is essential to know which appearance of a boundary is normal and which is not. The hysteresis behaviour makes the difference because loading and unloading results in irreversible heat production which depends on the square of amplitude and on frequency. At high frequencies in the ultrasound range, heating e.g. due to cracks can be so efficient that it can be observed directly with thermography. This has been demonstrated in the pioneering work published by Henneke and Reifsnider in 1979 who were the first to perform pulsed ultrasound (or “sonic”) thermography. We applied ultrasound excitation in a modulated way for lock-in thermography and used this “Ultrasound lock-in thermography (ULT)” in a resonant and non-resonant arrangement for reliable defect-selective imaging: Only those defects are imaged that generate heat in the ultrasound field.

Though Lock-in thermography with optical or sonic excitation has become meanwhile a powerful tool for NDE, we were interested to see how well it compares when instead of monitoring the infrared thermal emission caused by the thermal wave one monitors the related modulated thermal expansion by using optical interferometric methods. It turned out that depth range is larger with interferometric thermal wave detection since a depth integral is involved and that such images display the mechanical effect of a defect.

ULT requires mechanical contact for injection of elastic energy while Lock-in thermography with optical excitation (OLT) has the advantage of being a remote technique. As it responds to all kinds of boundaries, we tried to separate intact from defective areas mathematically by feature extraction in a scatter plot to reveal defects by their dimensionality.

Another recent development relates to use not a lamp for OLT but rather a light source whose intensity can locally be tuned, e.g. a computer-controlled beamer. This way projection patterns can be generated that are related to defect patterns. This OLT feed-back-imaging allows eliminating modulated lateral heat flow in the surface thereby improving resolution.

A permanent challenge in NDE applications is to make ULT more efficient so that the mechanical load of input coupling can be reduced or even avoided so that remote ultrasound excitation becomes feasible.

It is obvious that much has been achieved, but much more is ahead of us to make NDE of safety relevant materials and structures better applicable and more reliable in future.

Chasing after propagating waves

Keith A NELSON

Department of Chemistry, MIT, Cambridge, MA 02139, USA

kanelson@mit.edu

My first measurements in the field of photoacoustics [1,2] happened accidentally. I was conducting transient grating (TG) measurements in graduate school with the aim of measuring exciton dynamics in organic molecular crystals, and the signals kept showing time-dependent oscillations! When I changed the angle between the crossed excitation laser pulses, thereby changing the spatial period of the interference pattern formed at the sample, the frequency changed proportionally. It didn't take long to figure out that the crossed pulses were generating coherent acoustic waves, with the wavelength given by the TG spatial period. This accidental discovery – really a re-discovery, since the effect had been demonstrated earlier [3] – kindled an obsession with optical generation, control, and measurement of coherent acoustic waves, and coherent waves and vibrational modes generally. This obsession has continued throughout my independent scientific career. It has included longitudinal and transverse acoustic waves and surface acoustic waves spanning the widest frequency and wavevector ranges that I can reach; I remain obsessed with extending the ranges farther still. It has extended to optical as well as acoustic phonons, to magnons, and to phonon-polaritons and magnon-polaritons that propagate at light-like rather than acoustic speeds. It has extended to large amplitudes at which nonlinear and far-from-equilibrium regimes can be reached. In this presentation I'll review some of the results, current efforts, and new possibilities that nurture my continuing obsession.

Using transient grating methods with optical excitation and probe pulses, acoustic waves in the micron and somewhat submicron wavelength range can be generated, with frequencies typically in the MHz to low GHz range. Both longitudinal and transverse waves in this range can be used to study crystals near structural phase transitions and supercooled glass-forming liquids. For the former, "soft" acoustic modes may be studied at temperatures arbitrarily close to phase transition temperatures, even though the modes may become critically damped or overdamped. Impulsive stimulated Brillouin scattering (ISBS) excitation of transverse acoustic waves is particularly useful for this purpose [4], as is its extension to impulsive stimulated Raman scattering (ISRS) excitation of soft optical phonon modes [5]. For the study of complex and highly temperature-dependent structural relaxation dynamics in glass-forming liquids, both shear and compressional waves provide valuable information [6-9]. An extremely wide range of frequencies is particularly important since relaxation dynamics range from picoseconds to many seconds as the temperature is varied. Picosecond photoacoustics provides access to acoustic frequencies up to hundreds of GHz. But measurement of frequency-dependent damping rates from a single-cycle acoustic wave demands extremely high signal/noise ratios, which are difficult to achieve when the damping rates are as high as they are in liquids at such frequencies. Instead, multiple-cycle GHz acoustic waves can be generated and their propagation lengths measured [10,11]. Combining this class of photoacoustic measurement with TG measurements can provide more than five decades of frequencies in the MHz-GHz range. An additional wide range at lower frequencies can be obtained through dynamic mechanical analysis measurements. In this manner the full range of dynamics from lightly viscous liquid to glass can be probed, allowing empirical models and fundamental theories of supercooled liquids to be tested [9]. Weakly nonlinear acoustic waves can reveal additional dynamical features [12], and strong shock waves can induce entirely new phenomena such as cavitation in liquids and gels [13] and fracture as well as phase transitions in solids [14]. Large-amplitude surface acoustic waves also can result in fracture or thin film delamination [15], far beyond the linear acoustic regime that is useful for characterization of thin film mechanical properties and rapid noncontact metrology of film thickness [16]. Real-time imaging and spectroscopy can provide detailed information about shock-induced far-from-equilibrium transformations. It has recently become possible to drive large-amplitude soft optical phonon responses as well, in some cases also inducing phase transitions that can be monitored on ultra-fast time scales [17]. Large-amplitude magnon responses, extending all the way to the flipping of macroscopic magnetic moments, have also been demonstrated [18]. Similar control over phonon-polariton and magnon-polariton [19] responses can be anticipated.

Finally, a new frontier has been opened through the recent development of x-ray free-electron lasers that can produce soft or hard x-ray pulses with nanometer or angstrom wavelengths respectively. Transient grating measurements have been conducted with soft x-rays [20], and hard x-ray TG measurements may not be far behind. Thus, excitation of coherent acoustic waves that span an ever-widening wavevector range covering much of the Brillouin zone is becoming possible.

Continued advances in optical generation and control of acoustic waves are assured through the continued efforts, and perhaps obsessions, of scientists in our field.

References

1. K.A. Nelson, M.D. Fayer, *Journal of Chemical Physics* 72, 5202 (1980) doi:10.1063/1.439756
2. K.A. Nelson, R.J.D. Miller, D.R. Lutz, M.D. Fayer, *Journal of Applied Physics* 53, 1144 (1982) doi:10.1063/1.329864
3. H. Eichler, *Optica Acta* 24, 431 (1977) doi:10.1080/713819604
4. L.-T. Cheng, K.A. Nelson, *Physical Review B* 37, 3603 (1988) doi:10.1103/PhysRevB.37.3603

5. T.P. Dougherty, G.P. Wiederrecht, K.A. Nelson, M.H. Garrett, H.P. Jenssen, C. Warde, *Science* 258, 770 (1992) doi:10.1126/science.258.5083.770
6. Y.-X. Yan, L.-T. Cheng, K.A. Nelson, *Journal of Chemical Physics* 88, 6477 (1988) doi:10.1063/1.454433
7. D.H. Torchinsky, J.A. Johnson, K.A. Nelson, *Journal of Chemical Physics* 136, 174509 (2012) doi:10.1063/1.3700756
8. D.H. Torchinsky, J.A. Johnson, and K.A. Nelson, *Journal of Chemical Physics* 130, 064502 (2009) doi:10.1063/1.3072476
9. T. Hecksher, D. H. Torchinsky, C. Klieber, J. A. Johnson, J. C. Dyre, and K. A. Nelson, *PNAS* 114, 8710 (2017) doi:10.1073/pnas.1707251114
10. T. Pezeril, C. Klieber, S. Andrieu, and K. A. Nelson, *Physical Review Letters* 102, 107402 (2009) doi:10.1103/PhysRevLett.102.107402
11. C. Klieber, E. Peronne, K. Katayama, J. Choi, M. Yamaguchi, T. Pezeril, and K.A. Nelson, *Applied Physics Letters* 98, 211908 (2011) doi:10.1063/1.3595275
12. C. Klieber, V.E. Gusev, T. Pezeril, K.A. Nelson, *Physical Review Letters* 114, 065701 (2015) doi:10.1103/PhysRevLett.114.065701
13. D. Veysset, U. Gutiérrez-Hernández, L. Dresselhaus-Cooper, F. De Colle, S. Kooi, K. A. Nelson, P. A. Quinto-Su, and T. Pezeril, *Physical Review E* 97, 053112 (2018) doi:10.1103/PhysRevE.97.053112
14. L. Dresselhaus-Cooper, J. E. Gorfain, C. T. Key, B. K. Ofori-Okai, S. J. Ali, D. J. Martynowych, A. Gleason, S. Kooi, K. A. Nelson, *Scientific Reports* 9, 3689 (2019) doi.org/10.1038/s41598-019-40037-3
15. D. Veysset, A.A. Maznev, I.A. Veres, T. Pezeril, S. Kooi, A. Lomonosov, K.A. Nelson, *Applied Physics Letters* 111, 031901 (2017) doi:10.1063/1.4993586
16. J.A. Rogers, A.A. Maznev, M.J. Banet, K.A. Nelson, *Annual Reviews of Materials Science* 30, 117 (2000) doi:10.1146/annurev.matsci.30.1.117
17. X. Li, T. Qiu, J. Zhang, E. Baldini, J. Lu, A. M. Rappe, K. A. Nelson, *Science* 364, 1079 (2019) doi:10.1126/science.aaw4913
18. S. Schlauderer, C. Lange, S. Baierl, T. Ebnet, C. P. Schmid, D. C. Valovcin, A. K. Zvezdin, A. V. Kimel, R. V. Mikhaylovskiy, R. Huber, *Nature* 569, 383 (2019) doi.org/10.1038/s41586-019-1174-7
19. P. Sivarajah, A. Steinbacher, B. Dastrup, J. Lu, M. Xiang, W. Ren, S. Kamba, S. Cao, and K. A. Nelson, *Journal of Applied Physics* 125, 213103 (2019) doi:10.1063/1.5083849
20. A. A. Maznev, F. Bencivenga, A. Cannizzo, F. Capotondi, R. Cucini, R. A. Duncan, T. Feurer, T. D. Frazer, L. Foglia, H.-M. Frey, H. Kapteyn, J. Knobloch, G. Knopp, C. Masciovecchio, R. Mincigrucci, G. Monaco, M. Murnane, I. Nikolov, E. Pedersoli, A. Simoncig, A. Vega-Flick, and K. A. Nelson, *Applied Physics Letters* 113, 221905 (2018) doi.org/10.1063/1.5048023

Solid state photoacoustics with extreme ultraviolet and x-ray radiation

A. A. MAZNEV

Department of Chemistry, Massachusetts Institute of Technology, Cambridge Massachusetts, USA

alexei.maznev@gmail.com

Historically, the development of photoacoustics was greatly stimulated by progress in laser physics. The invention of the laser resulted in the emergence of photoacoustics as a distinct field. The advent of femtosecond lasers enabled key developments – such as picosecond ultrasonics – that largely define our field today. Yet the developments stemming from new laser sources slowed down considerably in the past quarter century. The lasers we use now to study photoacoustic and photothermal phenomena have not changed much since early 1990ies. Likewise, many experimental techniques currently in use were originally developed back in 1980ies. For a long time now, the progress in the field is no longer associated with the sources of radiation. However, the rapid development of coherent short wavelength (extreme ultraviolet and x-ray) sources such as free electron lasers (FELs) in the past decade opens another opportunity for photoacoustics to make rapid progress by taking advantage of new radiation sources. In this talk, I will review the recent work and emerging opportunities in the use of time-resolved short-wavelength techniques for studying acoustic phonons and phonon-mediated thermal transport in solids. The principal limitation of studying phonons with traditional optical techniques lies in that the optical wavelength is typically much greater than the phonon wavelength and oftentimes greater than the phonon mean free path. This restricts one's ability to excite and probe phonons in the THz frequency range and to study thermal transport on the nanoscale. We will see that short-wavelength radiation can be harnessed either by extending the established optical techniques such as laser-induced transient gratings into EUV and x-ray ranges, or by applying techniques unique to short wavelength such as x-ray diffraction (XRD) to study photoacoustic and photothermal phenomena, or by developing entirely new techniques such as time-resolved diffuse x-ray scattering. These developments enable new classes of experiments yielding information not accessible with existing optical methods.

Time-resolved XRD combined with pulsed laser excitation is perhaps the most established ultrafast x-ray technique. While the initial experiments were conducted using synchrotron sources with picosecond time resolution, femtosecond resolution was achieved with plasma x-ray sources even before the introduction of FELs. This technique now allows to study nanoscale thermal transport by monitoring the lattice thermal expansion of layers as thin as 5 nm [1], as well as to detect coherent phonons at frequencies up to 3.5 THz [2]. Time-resolved EUV diffraction by fabricated nanostructures is also used to study both thermal transport and coherent phonons (primarily surface acoustic waves) [3]. Time-resolved diffuse x-ray scattering, on the other hand, is an entirely new development pioneered by D. Reis, M. Trigo and co-workers at SLAC [4]. It enables a new kind of phonon spectroscopy based on the parametric excitation of “squeezed” thermal phonon population via impulsive lattice softening by laser excitation, which makes the diffuse scattering intensity oscillate at twice the phonon frequency. On the other hand, this technique opens the (yet unexplored) prospect of studying thermal transport by making wavevector-resolved measurements of phonon population dynamics.

While the developments described in the previous paragraph employ short-wavelength probes to monitor acoustic and thermal dynamics excited by conventional optical laser pulses, femtosecond EUV and x-ray pulses can also be used to initiate acoustic and thermal phenomena. We will specifically discuss the laser-induced transient grating (TG) technique, in which two excitation pulses are crossed in the sample to create a spatially periodic material excitation, which is probed via diffraction of a probe pulse. The extension of this technique into EUV and x-ray ranges will enable coherent phonon excitation across the entire Brillouin zone and permit studying thermal transport on the deep nanometer scale. An EUV transient grating set-up has now come online at the FERMI free electron laser facility following a sustained effort by F. Bencivenga, C. Macchioreccio and co-workers [5]. We will discuss the initial photoacoustic and photothermal TG experiments conducted at FERMI with EUV excitation and optical probing [6] as well as preliminary results of more recent EUV pump / EUV probe experiments, with the TG period as short as 25 nm. The prospects of extending the TG technique further into the hard x-ray range will also be discussed.

References

1. J. Pudell, A. A. Maznev, M. Herzog, M. Kronseider, C. Back, G. Malinowski, A. von Reppert, and M. Bargheer, *Nature Commun.* 9, 3335 (2018) doi:10.1038/s41467-018-05693-5
2. T. Henighan et al., *Phys. Rev. B* 93, 220301 (2016) doi:10.1103/PhysRevB.93.220301
3. J. Hernandez-Charpak et al., *Nano Lett.* 17, 2178 (2017) doi:10.1021/acs.nanolett.6b04635
4. M. Trigo, *MRS Bulletin* 43, 520 (2018) doi: 10.1557/mrs.2018.151
5. F. Bencivenga et al., *Nature* 520, 205 (2015) doi: 10.1038/nature14341
6. A. A. Maznev et al., *Appl. Phys. Lett.* 113, 221905 (2018) doi:10.1063/1.5048023

Recent advances in ultrafast generation and detection of GHz-THz coherent acoustic phonons: fundamentals and applications

P. Ruello

Institut des Molécules et Matériaux du Mans, UMR CNRS 6238, Le Mans Université, 72085 Le Mans, France

pascal.ruello@univ-lemans.fr

In this presentation, I will review the last advances in the generation and detection of ultrafast strain pulses, i.e. the generation and detection of GHz-THz coherent acoustic phonons. Both fundamental phenomena and applications will be discussed. The main objective is to control very high frequency acoustic phonons with short light pulses to be able to envision in the future new sources of acoustic nanowaves that could be used for nanoscale imaging or for the manipulation by GHz-THz acoustic phonons of other degree of freedom of a solid (ultrafast acousto-optics, acousto-plasmonics, magneto-acoustics) for the information and telecommunication technologies. Since the birth of picosecond acoustics in the end of 80s [1,2], continuous efforts and progress have been done in these above directions [3].

In the first part, we will then discuss the physical mechanism of generation of GHz-THz coherent acoustic phonons in various materials such as piezoelectric semiconductors (GaAs), multiferroic BiFeO₃ (BFO), or topological insulator Bi₂Te₃ (BT). These studies are carried out within the time-domain methods thanks to a femtosecond laser setup following a traditional pump and probe scheme. In the case of visible light that permits efficient interband transitions, the ultrafast laser action provides the opportunity to control the hot electrons population and then offers the possibility to investigate how these electrons interact with acoustic phonons [1-3]. We will then discuss different mechanisms of coupling between electron and phonon such as the deformation potential [2-4], the inverse piezoelectricity effect [5-6] or the thermoelasticity. Alternative mechanisms involving non-linear and parametric amplification processes will be also mentioned [7-8]. Finally, while most of the coherent acoustic phonons have been generated/detected with visible light pulse, the recent development of new ultrashort light pulse with meV energy (THz, IR sources) offers new approaches of generation of coherent acoustic phonons and of manipulation of the strain in the matter, that I will also discuss.

In the second part, I will show you that with these GHz-THz acoustic phonons we can probe the elastic and photoelastic properties at the nanometric scale. In particular, we can now improve the in-depth imaging of nanomaterials with resolution down to around 50nm. This is achieved thanks to the time-domain Brillouin scattering methods [9]. I will show you that in transparent materials, scattering of the probe laser beam by the coherent acoustic phonons permits imaging of sample inhomogeneities [10-13]. This picosecond acoustic interferometry imaging is based on Brillouin scattering and has the potential to provide all the information that researchers in materials science, physics, chemistry, biology etc., get with classic frequency-domain Brillouin scattering of light. I will show applications of picosecond acoustic interferometry for imaging of nanoporous films [10,12], ion-implanted semiconductors [11] or dielectrics [14] and of texture in polycrystalline materials [15-16]. These GHz-THz acoustic phonons are also very useful to help chemist in the optimization of materials preparation and I will show you how picosecond acoustics transformation of Van der Waals bonds into covalent bonds in colloidal nanoparticle assemblies [17]. Finally, I will discuss some recent applications where GHz-THz acoustic phonons are used for the control of the light polarization [18] or the exciton levels [19]. Some current challenges and perspectives will then be discussed at the end of this presentation.

Acknowledgements

The authors acknowledge the projects Ferrotransducers (Lmac, Région Pays de la Loire France), ANR UP-DOWN project (18-CE09-0026-04) and the Internatinal Laboratory France-Japan LIA IM-LED.

References

1. C. Thomsen, H.T. Grahn, H.J. Maris, J. Tauc, Phys. Rev. B 34, 4129 (1986) doi.org/10.1103/PhysRevB.34.4129.
2. V. Gusev, A. Karabutov, Laser Optoacoustics, AIP, New York, 1993.
3. P. Ruello, V. Gusev, Ultrasonics, 56, 21-35 (2015). doi.org/10.1016/j.ultras.2014.06.004
4. M. Weis, K. Balin, R. Rapacz, A. Nowak, M. Lejman, J. Szade, and P. Ruello, Phys. Rev. B 92, 014301 (2015) doi.org/10.1103/PhysRevB.92.014301, M Weis, B Wilk, G Vaudel, K Balin, R Rapacz, A Boulou, B Arnaud, J Szade, P. Ruello Scientific reports 7 (1), 13782 (2017). doi.org/10.1038/s41598-017-12920-4
5. G Vaudel, T Pezeril, A Lomonosov, M Lejman, P Ruello, V Gusev, Phys. Rev. B 90 (1), 014302 (2014) doi.org/10.1103/PhysRevB.90.014302
6. M. Lejman, G. Vaudel, I.C. Infante, P. Gemeiner, V. Gusev, B. Dkhil, P. Ruello, Nature Comm. 5, 4301 (2014). doi.org/10.1038/ncomms5301
7. Thomas E. Wilson, Phys. Rev. B 98, 220304(R) (2018) doi.org/10.1103/PhysRevB.98.220304
8. Akimov, Andrey V.; Poyser, Caroline L.; Kent, Anthony J. Semiconductor science and technology 32, 1-35 (2017) 10.1088/1361-6641/aa52de
9. V.E. Gusev, P Ruello, Appl. Phys. Rev. 5 (3), 031101 (2018). doi.org/10.1063/1.5017241

Plenary Session D4

10. C Mechri, P Ruello, JM Breteau, MR Baklanov, P Verdonck, V Gusev, *Appl. Phys. Lett.* 95, 091907 (2009). doi.org/10.1063/1.3220063
11. A. Steigerwald, Y. Xu, J. Qi, J. Gregory, X. Liu, J. K. Furdyna, K. Varga, A. B. Hmelo, G. Lüpke, L. C. Feldman and N. Tolk, *Appl. Phys. Lett.* 94, 111910 (2009). doi.org/10.1063/1.4765647
12. Alexey M Lomonosov, Adil Ayouch, Pascal Ruello, Gwenaëlle Vaudel, Mikhail R Baklanov, Patrick Verdonck, Larry Zhao, Vitalyi E Gusev, *ACS Nano* 6, 1410 (2012). 10.1021/nn204210u
13. V Gusev, AM Lomonosov, P Ruello, A Ayouch, G Vaudel, *J. Appl. Phys.* 110, 124908 (2011).
14. D. Yarotski, E. Fu, L. Yan, Q. Jia, Y. Wang, A. J. Taylor, and B. P. Uberuaga, *Appl. Phys. Lett.* 100, 251603 (2012). doi.org/10.1063/1.4729621
15. S. M. Nikitin, N. Chigarev, V. Tournat, A. Bulou, D. Gasteau, B. Castagnede, A. Zerr, and V. E. Gusev, *Sci. Rep.* 5, 9352 (2015).16. M. Kuriakose, et al., *Phys. Rev. B* 96, 134122 (2017). doi.org/10.1038/srep09352
17. J Avice, C Boscher, G Vaudel, G Brotons, V Juve, M Edely, C Méthivier, Vitalyi E Gusev, Philippe Belleville, Herve Piombini, Pascal Ruello, *The Journal of Physical Chemistry C* 121 (42), 23769-23776 (2017). 10.1021/acs.jpcc.7b08404
18. M Lejman, G Vaudel, IC Infante, I Chaban, T Pezeril, M Edely, GF Nataf, M. Guennou, J. Kreisel, V. E. Gusev, B. Dkhil, P. Ruello, *Nat. comm.* 7, 12345, (2016). doi: 10.1038/ncomms12345.
19. E Baldini, T Palmieri, A Dominguez, P Ruello, A Rubio, M Chergui, *Nano letters* 18 (8), 5007-5014 (2018). 10.1021/acs.nanolett.8b01837.



ORAL CONTRIBUTIONS

KEYNOTE

Noninvasive Optoacoustic Diagnostics, Therapy, and Theranostics: From Ideas to Clinical Studies

Rinat Esenaliev

University of Texas Medical Branch, Galveston, Texas, USA

riesenal@utmb.edu

We proposed biomedical optoacoustics/photoacoustics more than 25 years ago and started optoacoustic imaging research followed by development and tests of this technology in pre-clinical and clinical studies [1-35]. We were first to demonstrate: 1) detection of optoacoustic signals from tissues at depths well beyond the optical diffusion limit (up to several centimeters); 2) detection and characterization of microscopic tissue volumes using high-resolution optoacoustic measurements; 3) optoacoustic imaging in large tissue phantoms and tissues with high-resolution; 4) monitoring of tissue hyperthermia, coagulation, and freezing; 5) optoacoustic probing of cerebral tissues noninvasively from the intracranial space in large animals and in humans (both neonates and adults); 6) optoacoustic technique capability for accurate oxygenation measurements in humans in tissues and in specific blood vessels; and 7) optoacoustic waves therapeutic effects that can be used for noninvasive optoacoustic therapy and theranostics.

We developed optoacoustic systems (including highly-compact, multi-wavelength, fiber-coupled, FDA-compliant laser diode systems) with ultra-sensitive, wide-band optoacoustic probes. We tested them in small and large animal studies and in clinical studies in healthy volunteers and patients with traumatic brain injury and circulatory shock as well as in neonatal and fetal patients. The obtained data indicated that the systems were capable of optoacoustic measurements and mapping of cerebral blood oxygenation in adults and in neonates, detection of intracranial hematomas, oxygenation measurements both from cerebral and central blood vessels and from cerebral tissues.

Optoacoustic therapy studies were performed in animals with traumatic brain injury (TBI). Transcranial optoacoustic therapy significantly reduced negative effects of TBI as assessed by vestibulomotor, cognitive, and immunofluorescence tests. The obtained data suggest that optoacoustic theranostics can be used for diagnostics, therapy, and real-time monitoring of therapeutic response as well as for follow-up after the therapy.

Dr. R.O. Esenaliev is a co-owner of Noninvasix, Inc., a UTMB-based startup that has licensed the rights to optoacoustic technology.

Acknowledgements

Grant support: NIH grants #R01EB00763 and #U54EB007954 from the National Institute of Biomedical Imaging and Bioengineering, #R01NS044345 and #R21NS40531 from the National Institute of Neurological Disorders and Stroke, #R41HD076568, #R43HD075551, and #R41HD094542 from the Eunice Kennedy Shriver National Institute of Child Health & Human Development, and #R41HL10309501 from the National Heart, Lung and Blood Institute, contracts from Noninvasix, Inc., the Texas Emerging Technology Fund, and the Moody Center for Brain and Spinal Cord Injury

Research/Mission Connect of UTMB. The content is solely the responsibility of the authors and does not necessarily represent the official views of the NIBIB or NIH.

References

1. Esenaliev R.O., Oraevsky A.A., Letokhov V.S., Karabutov A.A., Malinsky T.V., "Studies of acoustical and shock waves in the pulsed laser ablation of biotissue", *Lasers in Surgery and Medicine* 13, 470-484 (1993).
2. Esenaliev R.O., Golovlyova O.A., Golovlyov V.V., Letokhov V.S., "Effect on erythrocytes of acoustic waves generated upon absorption of laser radiation", *Lasers in the Life Sciences* 6(3), 153-161 (1994).
3. Esenaliev R.O., Oraevsky A.A., Jacques S.L., Tittel F.K., "Laser optoacoustic tomography for medical diagnostics: Experiments on biological tissues", *SPIE Proc.* 2676, 84-90 (1996).
4. Oraevsky A. A., S. L. Jacques, R. O. Esenaliev. "Optoacoustic imaging for medical diagnostics," US Patent #5,840,023.
5. Esenaliev R.O., Motamedi M., Karabutov A.A., Oraevsky A.A. "Real Time Optoacoustic Monitoring of Changes in Tissue Properties", US Patent #6,309,352.
6. Esenaliev R.O., Karabutov A.A., Oraevsky A.A., "Sensitivity of laser optoacoustic imaging in detection of small deeply embedded tumors", *IEEE J. of Selected Topics in Quantum Electronics: Lasers in Medicine and Biology* 5(4), 981-988 (1999).
7. Esenaliev R.O., Karabutov A.A., Tittel F.K., Fornage B.D., Thomsen S.L., Stelling C., Oraevsky A.A., "Laser optoacoustic imaging for breast cancer diagnostics: Limit of detection and comparison with X-ray and ultrasound imaging", *SPIE Proc.* 2979, 71-82 (1997).
8. Esenaliev R.O., Alma H., Tittel F.K., Oraevsky A.A., "Axial resolution of laser optoacoustic imaging: Influence of acoustic attenuation and diffraction", *SPIE Proc.* 3254, 294-301 (1998).
9. Larin K.V., Hartrumpf O., Larina I.V., Esenaliev R.O., "Comparison of optoacoustic tomography with ultrasound and X-ray imaging for breast cancer detection", *SPIE Proc.* 4256, 147-153 (2001).

Session A2: Cytometry and Imaging

10. Larin K.V., Larina I.V., Motamedi M., Esenaliev R.O., "Optoacoustic laser monitoring of cooling and freezing of tissues", *Quantum Electronics* 32(11), 953-958 (2002).
11. Larina I.V., Larin K.V., Esenaliev R.O., "Real-time optoacoustic monitoring of temperature in tissues", *Journal of Physics D: Applied Physics* 38(15), 2633-2639 (2005).
12. Larin K.V., Larina I.V., Esenaliev R.O., "Monitoring of tissue coagulation during thermotherapy using optoacoustic technique", *Journal of Physics D: Applied Physics* 38(15), 2645-2653 (2005).
13. Esenaliev R. O., Motamedi M., Prough D. S., Oraevsky A. A. Optoacoustic monitoring of blood oxygenation. Patent# 6,498,942.
14. Esenaliev R. O., Motamedi M., Prough D. S. Continuous optoacoustic monitoring of hemoglobin concentration and hematocrit. Patent# 6,751,490.
15. Esenaliev R.O., Larina I.V., Larin K.V., Deyo D.E., Motamedi M., Prough D.S., "Optoacoustic technique for noninvasive monitoring of blood oxygenation: A feasibility study", *Applied Optics* 41(22), 4722-4731 (2002).
16. Petrov Y.Y., Prough D.S., Deyo D.E., Klasing M., Motamedi M., Esenaliev R.O., "Optoacoustic, noninvasive, real-time, continuous monitoring of cerebral blood oxygenation: An in vivo study in sheep", *Anesthesiology* 102(1), 69-75 (2005) (The article is featured in "This Month in Anesthesiology").
17. Petrov Y.Y., Petrova I.Y., Patrikeev I.A., Esenaliev R.O., Prough D.S., "Multiwavelength optoacoustic system for noninvasive monitoring of cerebral venous oxygenation: a pilot clinical test in the internal jugular vein", *Optics Letters* 31(12) 1827-1829 (2006).
18. Brecht H. P., D. Prough, I. Patrikeev, D. Deyo, Y. Petrov, I. Cicenaitis and R. Esenaliev, "In vivo monitoring of blood oxygenation in large veins with a triple-wavelength optoacoustic system", *Optics Express* 15(24), 16261-16269 (2007).
19. Petrova I.Y., Y.Y. Petrov, R.O. Esenaliev, D.E. Deyo, I. Cicenaitis and D.S. Prough, "Noninvasive monitoring of cerebral blood oxygenation in ovine superior sagittal sinus with novel multi-wavelength optoacoustic system", *Optics Express* 17(9), 7285-7294 (2009).
20. Petrov, I. Y., Petrov, Y., Prough, D. S., Deyo, D. J., Cicenaitis, I., and Esenaliev R. O., "Optoacoustic monitoring of cerebral venous blood oxygenation through extracerebral blood." *Biomedical Optics Express* 3(1), 125-136 (2012).
21. Petrov, I. Y., Petrov, Y., Prough, D. S., Cicenaitis, I., Deyo, D. J., and Esenaliev R. O., "Optoacoustic monitoring of cerebral venous blood oxygenation through intact scalp in large animals." *Optics Express* 20(4), 4159-4167 (2012).
22. Petrov I.Y., Petrov Y., Prough D.S., Richardson C.J., Fonseca R.A., Robertson C.S., Asokan C.V., Agbor A., Esenaliev R.O. Transmission (forward) mode, transcranial, noninvasive optoacoustic measurements for brain monitoring, imaging, and sensing. *SPIE Proc.* 9708, (2016).
23. Herrmann S., Petrov I.Y., Petrov Y., Richardson C.J., Fonseca R.A., Prough D.S., Esenaliev R.O. "Cerebral blood oxygenation measurements in neonates with optoacoustic technique." *Proc. of SPIE*, vol.10064, pp.10064Q-1-10064Q-7, 2017.
24. Petrov Y., Prough D. S., Petrov I. Y., Richardson C. J., Fonseca R. A., Robertson C. S., Esenaliev R. O. "Optoacoustic mapping of cerebral blood oxygenation in humans." *Proc. of SPIE*, vol.10064, pp.10064A-1-10064A-7, 2017.
25. Esenaliev R.O., Prough D. S., Petrov Y., Petrov I. Y., Saade G., Olson G.L. "Systems and methods for measuring fetal cerebral oxygenation." Patent #9,380,967.
26. Esenaliev R.O., Prough D.S., Petrov Y., Petrov I., Richardson C.J. "Systems and Methods for Measuring Neonatal Cerebral Oxygenation." Patent #10,226,206.
27. Prough D.S., Kinsky M.P., Esenaliev R.O., Petrov Y., Petrov I.Y. "Ultrasound Guided Optoacoustic Monitoring of Oxygen Saturation." (Pending US and International Patents).
28. Petrov A., Wynne K.E., Parsley M.A., Petrov I.Y., Ruppert K.A., Prough D.S., DeWitt D.S., Esenaliev R.O. Optoacoustic detection of intra- and extracranial hematomas in rats after blast injury. *Photoacoustics* 2, 75-80 (2014).
29. Esenaliev R.O. Optoacoustic diagnostic modality: from idea to clinical studies with highly-compact laser diode-based systems. Invited review. *Journal of Biomedical Optics*, 2017, 22(9), 091512. doi:10.1117/1.JBO.22.9.091512.
30. Esenaliev R.O. Optoacoustic monitoring of physiologic variables. *Frontiers in Physiology*, 2017, 8:1030, 091512. doi: 10.3389/fphys.2017.01030
31. Esenaliev R.O., "Noninvasive therapies in the absence and presence of exogenous nanoparticles". US Patent #9,504,824.
32. Esenaliev R. O., Y. Y. Petrov, I. Cicenaitis, O. V. Chumakova, I. Y. Petrova, I. Patrikeev, A. Liopo, "Real-time noninvasive optoacoustic monitoring of nanoparticle-mediated photothermal therapy of tumors", *SPIE Proc.* # 6437-0Q (2007).
33. Esenaliev R.O., Petrov I.Y., Petrov Y., Guptarak J., Boone D.R., Mocciano E., Weisz H., Parsley M.O., Sell S.L., Hellmich H.L., Ford J.M., Pogue C., DeWitt D., Prough D.S., Micci M.A. Nano Pulsed Laser Therapy Is Neuroprotective In A Rat Model Of Blast-Induced Neurotrauma. *J Neurotrauma*. (2018); Apr 30. doi: 10.1089/neu.2017.5249
34. Esenaliev R.O., Micci M.A., Prough D.S. "Nanopulse Light Therapy." (Pending US and International Patents).
35. Esenaliev R.O. "25 years of biomedical optoacoustics: From idea to optoacoustic imaging and theranostics." *SPIE Proc.*, v.10878, *Photons Plus Ultrasound: Imaging and Sensing 2019*, pp. 108780U-1 – 108780U-8 (Published 18 March 2019); Invited Paper presented at the Photonics West Conference, Special Session "Celebrating 25 Years of Photoacoustic/Optoacoustic Imaging" doi:10.1117/12.2511785.

KEYNOTE

Application of nanostructured core/shell and shell particles in photoacoustic/fluorescence cytometry and imaging

Dmitry Gorin

Skolkovo Institute of Science and Technology, Moscow, Russia

d.gorin@skoltech.ru

Photoacoustics is the most promising direction of modern photonics. This method has a very good perspective for biomedical applications agree its deep tissue penetration, microscale spatial resolution and very high sensitivity to contrast agent [1]. At present time, photoacoustics is used both for in vivo flow cytometry and imaging. There is some combination of photoacoustic and other imaging modalities as fluorescent tomography, MRI, OCT, CT. It gives us opportunity for using of multimodal contrast agents. Nanostructured particles can be used not only as contrast agent for photoacoustic microscopy and photoacoustic tomography but also for cell labeling in photoacoustic flow cytometry and for contrast enhancing in imaging by photoacoustic probe. Appreciative examples of such carriers are core-shell nanoparticles, liposomes, polymer micelles, capsules produced by Layer by Layer assembly (LbL) method [2]. Every type of nanostructured carriers has its own advantages and disadvantages. Undoubted advantages of LbL capsules are high loading capacity for drugs, wide range of possible internal payloads and wide possibilities of controlling physical and chemical properties of nanostructured carriers by variation of shell structure, thickness and its chemical composition [2]. It is also very important for detection and killing of free circulating cancer cells required for early cancer diagnostics and decreasing the metastases probability [3]. Limitation of this method is connected with requirements to have endogenous chromophores in the detected objects therefore as example we have melanin in the melanoma cells and hemoglobin in the RBCs. Contrast agent or probes (labels) are used for cell detection without endogenous chromophores. For in vivo using contrast agent should be corresponded to some requirements. It can be divided on the six groups. There is sensitivity, specificity, selectivity, safety, multifunctionality, multimodality. The sensitivity includes the highest analytical signal for example photoacoustic (PA) signal of fluorescent signal (FS) in the transparent window for biological tissue, Low Lowest Level of Quantification (LLOQ) and linear concentration dependence. The other important issue is specificity that can be realized using chemical targeting or physical targeting. Chemical targeting was achieved by surface modification using targeted molecules [4]. Physical targeting is provided by magnetic field gradient [5] or laser tweezers [6]. Selectivity has achieved by ability to resolve spectrum in a background of endogenous absorbers and to multiplexing with endogenous and exogenous absorbers. Multimodality is important for verification and reliability. It can be obtained by combination of photoacoustic approach with fluorescent tomography, MRI, OCT, CT, US and other clinically relevant imaging tools. Multifunctionality is a modern trend that is realized the theranostic concept. It can be obtained by loading contrast agents and anti-tumor drugs and remote release encapsulated substances by external influences like ultrasound, alternative magnetic field, laser [2]. The most of important requirement to contrast agents is safety that including biodegradability and absence of toxicity [7]. Since the photoacoustic signal is proportional of adsorption coefficient of absorbed media. Agents can be classified based on type of light absorbers. There are gold or silver nanoparticles, magnetite nanoparticles, carbon nanotubes, dopamine, endogenous absorbers like melanine, exogenous absorbers for example indocyanine green. The second parameter for classification is a type of structured agents for example individual nanoparticles, spasers, liposomes, polymer micelles, layer by layer based composite structures (core-shells and shells) [7-10]. Unique combination of photoacoustic cytometry and nanostructured carriers prepared by LbL assembly approach gives clinicians and researchers significant advantages in the developing of new therapy method based on delivery of nanostructured carriers loaded by bioactive substances into lesion focus and also their visualization and remote-controlled release of encapsulated bioactive substances using PA approach. Visualization of two types of nanostructured carriers produced by LbL assembly method was demonstrated recently in diluted and undiluted blood [8]. It was established that hollow microcapsules exhibited greater photoacoustic signal comparing to core-shell type of microparticles with the same composition of polymeric shell [8]. Nevertheless, there are no known examples of in vivo photoacoustic detection of LbL nanostructured carriers, therefore the main goal of present study is formation of biocompatible nanostructured carriers (BNCs) that will exhibit giant photoacoustic signal allowing in vivo detection of such structures. It was demonstrated for the first time, the super (giant) PA contrast of BNCs both in vitro and in vivo [7]. It was verified the unique PA characteristics of these advanced contrast agents using PA flow cytometry diagnostic platform. The obtained data suggest the high PA contrast of BNCs that can be associated with synergistic plasmonic, thermal and acoustic effects, especially in nonlinear mode with nanobubble formation in overheated absorbing layers, in particular gold nanoclusters between two light transparent shells [7]. The other type based on composite indocyanine green/polymer have using self-quenching effect has been successfully prepared and characterized in vivo and in vitro by fluorescent and optoacoustic tomographies. The combination of LbL (Layer by Layer) [2,5-9] and FIL (Freezing-Induced Loading) methods [10] can be allow us to obtain the particles exhibited both PA and FL signals. This type of nanostructured carriers has a very good perspective for clinical applications agree high safety and the easiest scaling up for their preparation methods [10].

The analysis of published articles allows to make the following conclusions related to the most perspective contrast agents. It should be multimodal and multifunctional and using such type of physical phenomena as interaction of plasmonic nanoparticles and dye for quenching and enhancement of fluorescence [7], self-quenching [10], spaser effect and lasing [11]. This type of multimodal and multifunctional carriers can be combined with microstructured optical waveguide-based endoscopic probes [12] and has a good perspective for intraoperative applications.

Acknowledgements

This work was partly supported by the Russian Foundation for Basic Research (RFBR grant 18-29-08046) and by the Government of the Russian Federation (grant no.14.Z50.31.0044 to support scientific research projects implemented under the supervision of leading scientists at Russian institutions and Russian institutions of higher education) and Saratov State University.

References

1. A. S. Timin, M. M. Litvak, D. A. Gorin, E. N. Atochina-Vasserman, D. N. Atochin, and G. B. Sukhorukov, *Adv. Healthcare Mater.* 7(3), 1700818 (2017) DOI: 10.1002/adhm.201700818
2. A.S. Timin, H. Gao, D.V. Voronin, D.A. Gorin, G.B. Sukhorukov, *Adv. Mater. Interfaces* 4, 1600338(22) (2016) DOI: 10.1002/admi.201600338
3. E.I. Galanzha, E.V. Shashkov, P. Spring, J.Y. Suen, V.P. Zharov, *Cancer Res.* 69, 7926 (2009) DOI: 10.1158/0008-5472.CAN-08-4900
4. H. K. Zhang, Y. Chen, J. Kang, A. Lisok, I. Minn, M. G. Pomper and E. M. Boctor, *J. Biophotonics* 11, e201700246 (2018) DOI:10.1002/jbio.201700246
5. D.V. Voronin, O. A. Sindeeva, M. A. Kurochkin, O. Mayorova, I. V. Fedosov, O.B. Semyachkina-Glushkovskaya, D.A. Gorin, V.V. Tuchin, G. B. Sukhorukov, *ACS Applied Materials & Interfaces* 9, 6885 (2017) DOI: 10.1021/acsami.6b15811
6. Y. Stetciura, A. Yashchenok, A. Masic, E.V. Lyubin, O.A. Inozemtseva, M.G. Drozdova, E. A. Markvichova, B.N. Khlebtsov, A.A. Fedyanin, G.B. Sukhorukov, D.A. Gorin, D.Volodkin, *Analyst* 140, 4981(2015) DOI: 10.1039/C5AN00392J
7. M.V. Novoselova, D.N. Bratashov, M.Sarimollaoglu, D.A. Nedosekin, W. Harrington, J. A. Watts, M.Han, B.N. Khlebtsov, E.I. Galanzha, D.A. Gorin, V.P. Zharov, *J. Biophotonics* 12, e201800265 (2018) DOI: 10.1002/jbio.201800265
8. A. M. Yashchenok, J. Jose, P. Trochet, G. B. Sukhorukov, D. A. Gorin, *J. Biophotonics* 9(8), 792 (2016) DOI 10.1002/jbio.201500293
9. S.V. German, M.V. Novoselova, D.N. Bratashov, P. A. Demina, V.S. Atkin, B. N. Khlebtsov, B.V. Parakhonskiy, G.B. Sukhorukov, D.A. Gorin, *Scientific Reports* 8, 17763 (2018) DOI:10.1038/s41598-018-35846-x
10. M.D. Mokrousov, M.V. Novoselova, J. Nolan, W. Harrington, P. Rudakovskaya, D.N. Bratashov, E.I. Galanzha, V. P. Zharov, D. A. Gorin, *Biomedical Optical Express*, (2019) (under review, manuscript ID 364931)
11. E. I. Galanzha, R. Weingold, D. A. Nedosekin, M. Sarimollaoglu, J. Nolan, W. Harrington, A. S. Kuchyanov, R. G. Parkhomenko, F. Watanabe, Z. Nima, A. S. Biris, A. I. Plekhanov, M. I. Stockman and V. P. Zharov, *Nat. Commun.* 8, 15528 (2017) DOI: 10.1038/ncomms15528
12. T.Ermatov, Y.V. Petrov, S.V. German, A. A. Zanishevskaya, A. A. Shuvalov, V. Atkin, A. Zakharevich, B.N. Khlebtsov, J.S. Skibina, P. Ginzburg, R. E. Noskov, V. V. Tuchin, D. A. Gorin, *Materials*,12, 1424 (2019) DOI:10.3390/ma12091424

Photoacoustic signal generation in complex biological media

Elena V. Petrova ^{(1)*}, Ivan Pelivanov ⁽²⁾, Matthew O'Donnell ⁽²⁾

1. Department of Medicine and Gastroenterology, Baylor College of Medicine, Houston, TX, USA

2. Department of Bioengineering, University of Washington, Seattle, WA, USA

elena.petrova@bcm.edu

Biomedical photoacoustic (PA) imaging is a unique modality that can non-invasively visualize optically contrasted components in living tissue at clinically relevant depths. One key advantage of PA imaging is localized multispectral measurement of both targeted exogenous optical nanoabsorbers and endogenous contrast agents in biological systems. However, quantifying optical absorption spectra, and thus PA properties, of nanoabsorbers in complex biological processes producing significant optical scattering remains extremely challenging.

Here, we present results on measurement of absorption spectra of gold nanorods (GNRs) internalized by human umbilical vein endothelial cells (HUVEC) as evaluated using non-contact photoacoustic spectrophotometer.

Fig. 1. PA spectrophotometry for cellular uptake of non-targeted PEGylated GNRs ($L \sim 40$ nm) by HUVEC. (a,b) Schematic of GNRs' distribution in extracellular and intracellular matrix, correspondingly. (c,d) Comparison of optical absorption spectra measured with conventional UV-Vis and PA spectrophotometers for biological systems illustrated above. Pictures (c,d) are reproduced from open source publication [1].

A new approach for non-contact PA spectrophotometry instrumentation has been described in detail [1]. The tool can accurately assess optical absorption properties in scattering media even if light scattering is a few orders of magnitude higher than absorption.

We used commercially available non-targeted PEG coated GNRs of ~ 40 nm length and HUVEC as a model cell [1]. Nanoparticles were taken up by cells after incubation with GNRs at 37°C for 24 hours. Harvested cells with GNRs were washed 3 times to remove extracellular nanoparticles and fixed in 4% formaldehyde at room temperature for 20 min before PA and UV-Vis measurements.

Accurately quantifying absorption spectra for a variety of targeted nanoabsorbers is critical for the field of biomarker specific nanomedicine, diagnostic imaging, and laser therapy. For example, nanoabsorber-based photothermal ablation of pancreatic cancer malignancy and its quantification will be an important application of the proposed approach.

In summary, PA signal generation must be considered at the cellular level, accounting for potential changes in absorber spectral features due to cellular microstructure, to ensure optimal use of targeted nanoabsorbers for critical applications in molecular medicine.

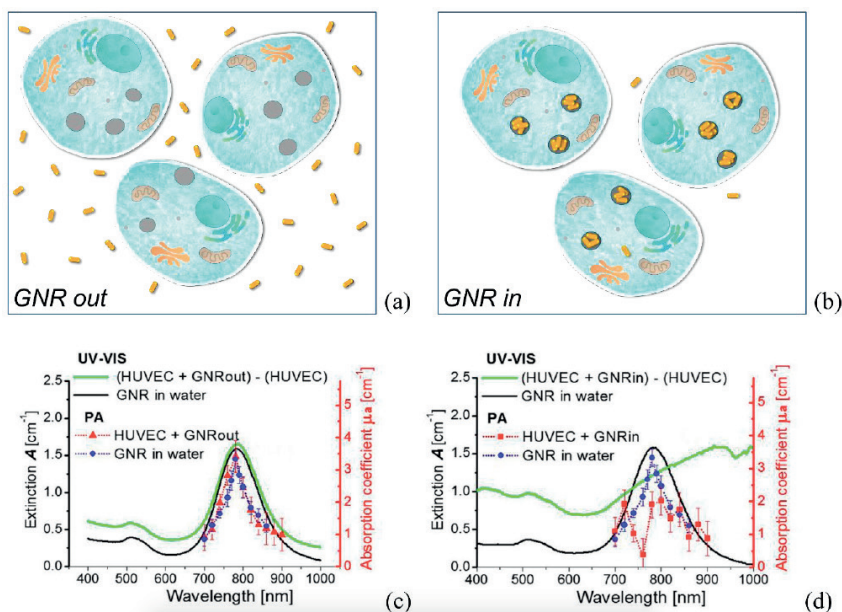


Fig.1(a,c) represents GNRs in extracellular medium. One can see that the absorption spectrum of GNRs mixed with HUVEC in physiological solution almost coincides with GNRs suspension diluted in water. Conversely, GNRs internalized into the intracellular matrix of HUVEC demonstrate a significantly reduced peak and a change in spectral shape (Fig.1b, d) compared to their spectrum in water. Such spectral changes are most likely related to subcellular compartmentalization of GNRs on cellular uptake routes [2], and further plasmonic coupling between clustered particles [3].

References

1. I. Pelivanov, E.V. Petrova, S.J. Yoon, Z. Qian, K. Guye, M. O'Donnell, Scientific Reports 8, 14425 (2018) doi:10.1038/s41598-018-32580-2
2. B. Yameen, W.I. Choi, C. Vilos, A. Swami, J. Shi, O.C. Farokhzad, Journal of Controlled Release 190, 485 (2014) doi:10.1016/j.jconrel.2014.06.038
3. P.K. Jain, S. Eustis, M.A. El-Sayed, Journal of Physical Chemistry B 110 (37), 18243 (2006) doi:10.1021/jp063879z

Statistics peculiarities of photoacoustic signals in flow cytometry of B16F10 cells

Daniil BRATASHOV ^{(1)*}, Oleg GRISHIN ⁽¹⁾, Anastasiia KOZLOVA ⁽¹⁾, Arkady ABDURASHITOV ⁽¹⁾, Roman VERKHOVSKII ⁽¹⁾, Eugene V SHASHKOV ⁽²⁾, Olga INOZEMTSEVA ⁽¹⁾, Vladimir P ZHAROV ⁽³⁾

1. Biomedical photoacoustics lab, Saratov State University, Saratov, Russia

2. Prokhorov General Physics Institute of RAS, Moscow, Russia

3. University of Arkansas for Medical Sciences, Arkansas, USA

Correspondence: dn2010@gmail.com

Anomaly high-skewed distribution of photoacoustic signals from the B16F10 cells was obtained during flow cytometry measurements. Generally, the main two characteristics used in biomedical diagnostics based on photoacoustic flow cytometry are the mean signal and the number of signals above some threshold (usually defined by background noise level). This fact makes both signals highly sensitive to the threshold choice and thus makes both characteristics less reliable to be used as some diagnostics criteria. There is also an essential problem of different photoacoustic devices testing and comparison by average signal and signal-to-noise ratio that is also affected by such an issue.

The photoacoustics flow cytometry has been used as a label-free method for detection of different blood problems for quite a long time [1, 2]. It has a good correlation with other in vivo cytometry methods [3], allowing to detect circulating tumor cells, blood clotting, and some other blood diseases.

In our experiments, the B16F10 melanoma cell culture in the Ca²⁺ and Mg²⁺-free DPBS media was used as the test sample. The average number of cells was 1.2 million per 1 mL of sample media. The pulsed laser with the wavelength 1064 nm, pulse energy 50 μJ, pulse repetition rate of 2 kHz and pulse duration 2 ns was used in the experiment and the light was focused on the sample through 8x/0.2 n.a. objective lens. The acoustic signal was detected by the unfocused ultrasound transducer in the 0.3 mm soft capillary tube with the media flow speed 0.25 mL/min.

The photoacoustic signal amplitude was calculated as the root mean square of the overall waveform. The dependence of signal amplitude versus time is shown in Fig 1a, representing the well-known short impulses when the cell with a high amount of melanin passed the laser line. Histogram for all signals higher than +3σ of background signal for 3 min of cell flow is shown in Fig 1b. There is a very low amount of high amplitude signals, and the significant number of signals with amplitude slightly higher than +3σ, resulting in the overall tendency of decreasing the number of signals with the increasing of amplitude. However, the major number of signals has an amplitude higher than any background signal from the flow without the cells. Such signal statistic imposes the large problem on the determination of any signal average characteristics: the mean, median values for such skewed distribution will not correspond to the most frequently appearing signals and the majority of cells.

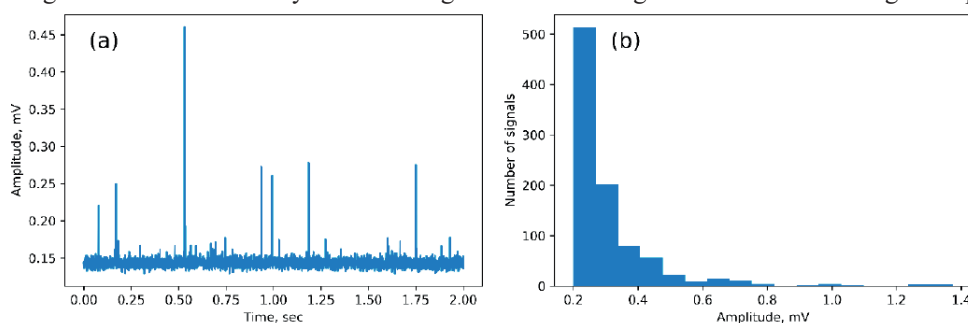


Fig. 1. Time trace of signal amplitude (2 sec) (a) and histogram of overall signals (3 min) over the 3σ of background signal (b).

Acknowledgments

This work was supported by the Government of the Russian Federation (grant no. 14.Z50.31.0044 to support scientific research projects implemented under the supervision of leading scientists at Russian institutions and Russian institutions of higher education)

References

1. V.P. Zharov, E.I. Galanzha, E.V. Shashkov, N.G. Khlebtsov, V.V. Tuchin, "In vivo photoacoustic flow cytometry for monitoring of circulating single cancer cells and contrast agents," *Opt. Lett.* 31, 3623-3625 (2006) doi: 10.1364/OL.31.003623
2. D.A. Nedosekin, M. Sarimollaoglu, J. Ye, E.I. Galanzha and V.P. Zharov, "In vivo ultra-fast photoacoustic flow cytometry of circulating human melanoma cells using near-infrared high-pulse rate lasers," *Cytometry*, 79A: 825-833. (2011) doi:10.1002/cyto.a.21102
3. D.A. Nedosekin, M. Sarimollaoglu, E.I. Galanzha, R. Sawant, V.P. Torchilin, V.V. Verkhusha, J. Ma, M.H. Frank, A.S. Biris, V.P.Zharov "Synergy of photoacoustic and fluorescence flow cytometry of circulating cells with negative and positive contrasts," *Journal of biophotonics*, 6 (5), 425-434. (2012) doi:10.1002/jbio.201200047

High-intensity, high-frequency photoacoustic waves in gene transfection

Luis Guilherme ARNAUT ^{(1)*}, Alexandre Duarte SILVA ⁽¹⁾, Diogo António PEREIRA ⁽¹⁾, Joana CUNHA ⁽¹⁾, Patrícia MARTINS ⁽¹⁾, Luisa CORTES ⁽²⁾, Maria João MORENO ⁽¹⁾, Carlos SERPA ⁽¹⁾

1. Chemistry Department, University of Coimbra, 3004-535 Coimbra, Portugal

2. CNC - Center for Neuroscience and Cell Biology, University of Coimbra, 3004-504 Coimbra, Portugal

lgarnaut@ci.uc.pt

The ability to generate high-intensity (>10 bar) high-frequency (>50 MHz) ultrasound pulses using short (<10 ns) laser pulses and piezophotonic materials [1] offers intriguing possibilities for ultrasound to interact with biological materials. A recent face-split study with 15 volunteers showed that such ultrasound pulses are safe and effective in permeabilizing the stratum corneum and facilitating the dermal delivery of large molecules such as hyaluronic acid [2]. Visual facial rejuvenation was achieved in 5 treatment sessions of *ca.* 20 min each. In this work, we report the use of picosecond lasers to produce more intense and higher frequency ultrasounds and their interaction with models of cell membranes and with eukaryotic cells.

The wavelength associated to a 100 MHz ultrasonic pulse traveling in biological medium is 15 μm . This means that a structure of this size is subject to push-pull forces operating simultaneously in opposed sides when traversed by such ultrasound pulses. The permeabilization of the stratum corneum was associated with this effect. Interestingly, giant unilamellar vesicles (GUVs), often used as biomimetic models of cellular membranes, have diameters of 10-20 μm and should also respond to such push-pull forces. We produced GUVs with encapsulated fluorescein dye and exposed them to ultrasound pulses to assess their stability and the possible release of the dye. Under the conditions employed in our experiments (10 min exposure to ultrasound pulses generated by piezophotonic materials absorbing laser pulses), the number and morphology of GUVs observed by confocal microscopy did not significantly change. Figure 1 shows images of GUVs before and after exposure to the ultrasound pulses. Although the GUVs were not destroyed, loss of interior fluorescence was observed in some experimental conditions, suggesting temporary destabilization and leakage of the dye.

The thickness of cells grown in monolayers is typically less than 5 μm . Although this is a challenging size to exert push-pull forces with ultrasound pulses, we investigated the cytotoxicity of ultrasound pulses with frequency components extending to 100 MHz together with the ability of such pulses to permeabilize the cell membrane and enable gene transfection. Using a picosecond laser with a fluence of 100 mJ/cm^2 and piezophotonic materials to produce high-intensity high-frequency ultrasound, we succeeded in transfecting a plasmid DNA encoding Green Fluorescent Protein (gWizGFP, 3.74 MDa) in COS-7 monkey fibroblast cells with an efficiency of 5% at 20 $^{\circ}\text{C}$, in 10 minutes, measured 24 h post-exposure [3]. We did not observe significant cytotoxicity under these conditions. Figure 2 shows the GFP fluorescence from transfected cells.

The 5% transfection efficiency is an encouraging result considering that the absence of cytotoxicity shows that it should be possible to generation still higher intensity and higher frequency ultrasound pulses to increase the transfection efficiency. This work shows that transfection with ultrasound pulses generated by photoacoustic methods is scalable, affordable, enables nuclear localization and the dosage is easily controlled by the laser parameters.

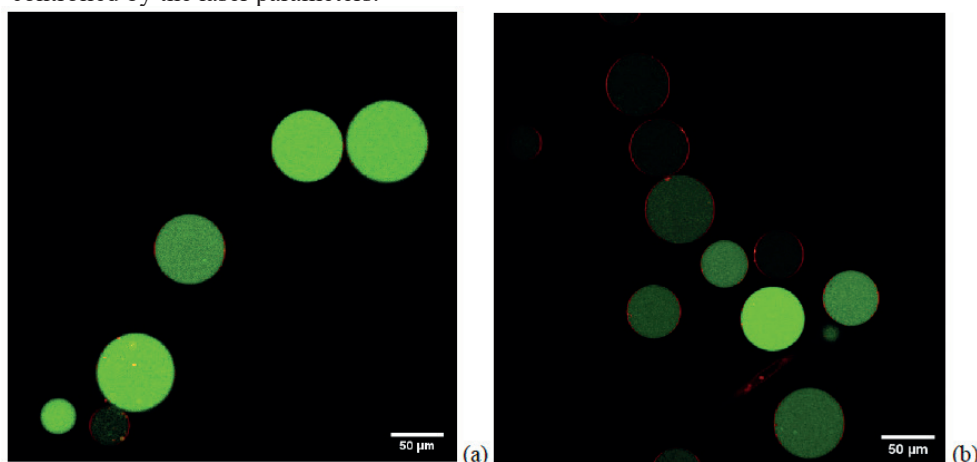
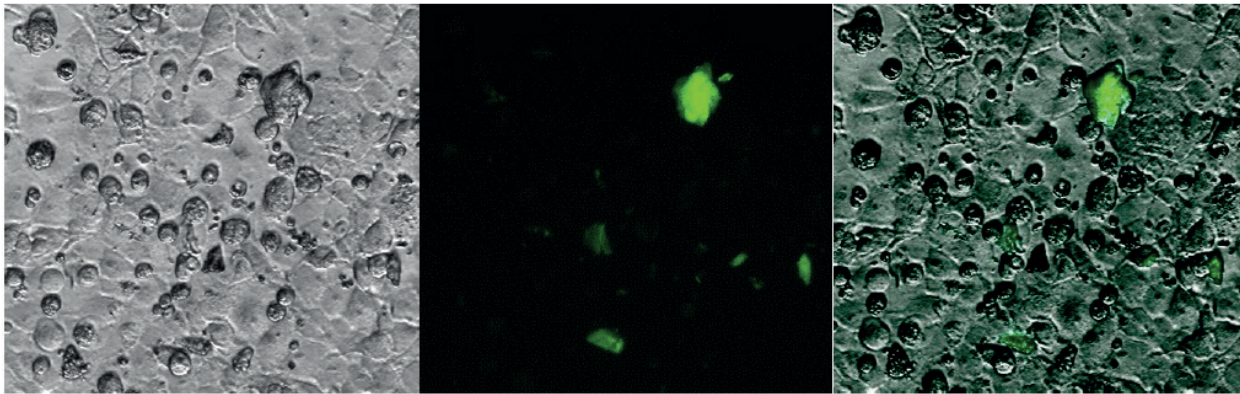


Fig. 1. Confocal microscopy of GUVs containing fluorescein compounds. (a) High contrast of fluorescein emission from inside the GUVs before exposure to ultrasound pulses. (b) GUVs after 10 min exposure to ultrasound pulses using a picosecond laser and a laser fluence of 100 mJ/cm^2 .



(a) (b) (c)

Fig. 2. GFP fluorescence in COS-7 cells 24 h after 3 min transfection of gWizGFP plasmid [100 $\mu\text{g}/\text{mL}$] with PA waves generated by 8 ns laser pulses. (a) Bright field. (b) Fluorescence microscopy. (c) Superposition of the two previous images

Acknowledgements

This research was supported by the Portuguese Science Foundation and FEDER (Projects no. UID/QUI/00313/2019, Roteiro/0152/2013/022124 and PTDC/QEQ-MED/3521/2014)

References

1. G. F. F. Sa, C. Serpa, L. G. Arnaut, *J. Control. Release*, 167, 290 (2013) doi: 10.1016/j.jconrel.2013.02.005
2. M. J. Freire-dos-Santos, R. Carvalho, L. G. Arnaut, *Aesth. Plast. Surg.*, 42, 1655 (2018) doi: 10.1007/s00266-018-1208-9
3. A. D. Silva, C. Serpa, L. G. Arnaut, *Sci. Rep.*, in press (2019) doi: not yet available

Raster-scan optoacoustic imaging of cerebral vasculature of rodents in vivo

Pavel Subochev*, Ekaterina Smolina, Anna Orlova, Daniil Emyanov,
Maxim Prudnikov, Vladimir Vorobyev

Institute of Applied Physics RAS, Nizhny Novgorod, Russia
Pavel.Subochev@gmail.com

The recent studies of our group are being devoted optoacoustic (OA) imaging of cerebral vasculature of small laboratory animals [1-2]. The first, theoretical part of this work, is devoted to finding optimal optical and acoustical wavelengths for OA imaging of whole-brain vasculature using wideband PVDF detectors (10 Pa noise equivalent pressure in 1-100 MHz bandwidth) being gradually developed by our group. The second, experimental part, is devoted to *in vivo* evaluation of the opportunities of OA imaging of rodent's brains with intact skull and scalp employing raster-scan OA technique [3-4]. The preliminary results of *in vivo* OA experiments are presented at figure 1.

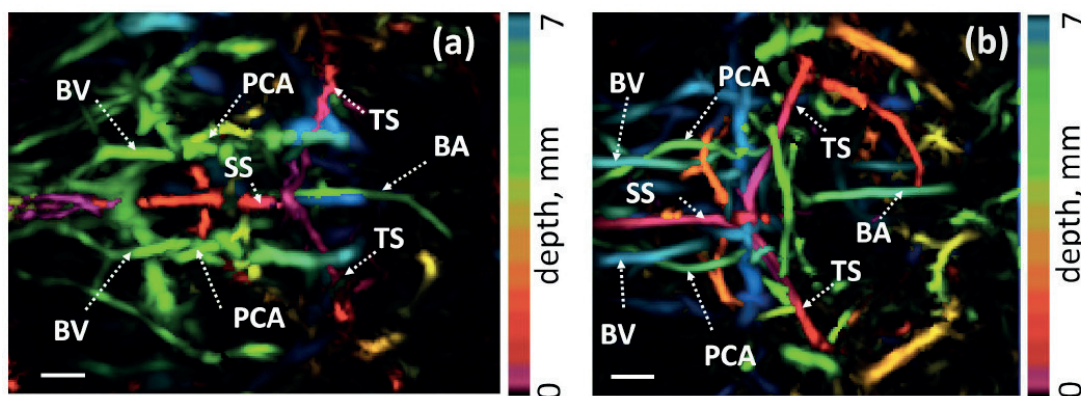


Fig. 1. Revealing deep brain vasculature of rodents: (a) – adult mouse; (b) – newborn rat. BV- basal vein, SS- sagittal sinus, PCA - posterior communicating artery, TS - transverse sinus, BA - basilar artery. Scanning steps $dX=dY=100\ \mu\text{m}$. Bars are 1 mm.

Acknowledgements

This work was supported financially by the Russian Science Foundation (project #18-45-06006).

References

1. J.Yao, & L.V.Wang (2014). Photoacoustic brain imaging: from microscopic to macroscopic scales. *Neurophotonics*, 1(1), 011003.
2. H.Estrada, X.Huang, J.Rebling, M.Zwack, S.Gottschalk, & Razansky, D. (2018). Virtual craniotomy for high-resolution optoacoustic brain microscopy. *Scientific reports*, 8(1), 1459.
3. M.Omar, J.Gateau, & V.Ntziachristos (2013). Raster-scan optoacoustic mesoscopy in the 25–125 MHz range. *Optics letters*, 38(14), 2472-2474.
4. P. Subochev "Cost-effective imaging of optoacoustic pressure, ultrasonic scattering, and optical diffuse reflectance with improved resolution and speed" *Optics letters*, 41(5), 1006-1009, (2016).

KEYNOTE

Characterization of submicrometric abnormal accumulations in kidney biopsy using infrared nanospectroscopy AFMIR

Ariane Deniset-Besseau⁽¹⁾, Emmanuel Esteve^(2,3), Yosu Luque^(2,4), Jehan Waeytens^(1,5), Dominique Bazin⁽¹⁾, Chantal Jouanneau⁽²⁾, Pierre Ronco^(2,3), Alexandre Dazzi⁽¹⁾, Michel Daudon^(2,6)

1. Laboratoire de Chimie Physique (LCP), CNRS UMR 8000, Univ. of ParisSud, Université ParisSaclay, Orsay, France

2. Sorbonne Université, UPMC Paris 06, Institut National de la Santé et de la Recherche Médicale, Unité Mixte de Recherche S 1155, F-75020 Paris, France

3. Nephrology and dialysis department, Hôpital Tenon, Assistance Publique – Hôpitaux de Paris, Paris, France

4. Urgences Néphrologiques et Transplantation rénale, Hôpital Tenon, Assistance Publique – Hôpitaux de Paris, Paris, France

5. Structure et Fonction des Membranes Biologiques, Faculté des sciences, Université libre de Bruxelles (ULB), CP 206/02, Boulevard du Triomphe, B-1050 Bruxelles, Belgium.

6. Explorations fonctionnelles multidisciplinaires, Hôpital Tenon, Assistance Publique – Hôpitaux de Paris, Paris, France;

ariane.deniset@u-psud.fr

InfraRed (IR) spectromicroscopy allows chemical mapping of kidney biopsy. It is particularly interesting for chemical speciation of abnormal tubular deposits and calcification. In 2017 using IR spectromicroscopy, it was possible to describe a new entity called vancomycin cast nephropathy [1]. However, despite recent progresses IR microspectrometer spatial resolution is intrinsically limited by diffraction (few micrometers). Combining atomic force microscopy and IR lasers (AFMIR) allows acquisition of infrared absorption spectra with a resolution and sensitivity in between 10 and 100 nm [2,3]. Here we show that AFMIR can be used on standard paraffin embedded kidney biopsies. Vancomycin cast could be identified in a damaged tubule. Interestingly unlike standard IR spectromicroscopy, AFMIR revealed heterogeneity of the deposits and established proving that vancomycin co-precipitated with phosphate containing molecule. These findings highlight the high potential of this approach with nanometric spatial resolution that opens new perspectives for studies on drug-induced nephritis, nanocrystals and local lipid or glucid alterations.

References

1. Y. Luque, K. Louis, C. Jouanneau, S. Placier, E. Esteve, D. Bazin, E. Rondeau, E. Letavernier, A. Wolfrohm, C. Gosset, A. Boueilh, M. Burbach, P. Frère, M.-C. Verpont, S. Vandermeersch, D. Langui, M. Daudon, V. Frochot, and L. Mesnard, *J. Am. Soc. Nephrol.* 28, 1723 (2017).
2. A. Dazzi, F. Glotin, and R. Carminati, *J. Appl. Phys.* 107, 1 (2010).
3. A. Dazzi and C. B. Prater, *Chem. Rev.* 117, 5146 (2017).

KEYNOTE

Wavelength-Modulated Differential Photothermal Radiometry (WM-DPTR) biosensor and applications to in-vivo blood glucose, alcohol and cannabis detection

Xinxin GUO*, Andreas MANDELIS

Center for Advanced Diffusion-Wave and Photoacoustic Technologies (CADIPT), Department of Mechanical and Industrial Engineering, University of Toronto, 5 King's College Road, Toronto, ON M5S 3G8, Canada

guox@mie.utoronto.ca, mandelis@mie.utoronto.ca ≈

Wavelength-Modulated Differential Photothermal Radiometry (WM-DPTR) [1] has been used for noninvasive in-vivo blood glucose, alcohol and cannabis detection. The measurement results have demonstrated that WM-DPTR has excellent potential to be developed as a biosensor to improve diabetes management and prevent alcohol/drug impaired driving.

Materials and Methods

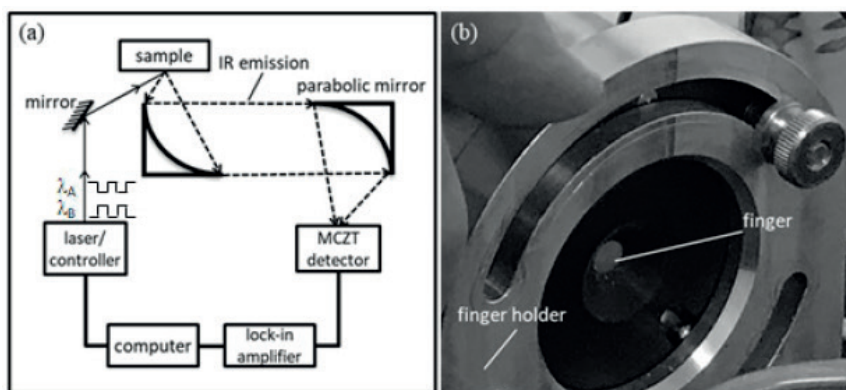


Fig. 1. WM-DPTR system. (a) schematic diagram of system setup: The modulated laser beams from two Quantum Cascade Lasers (QCLs) are steered to sample surface; the generated IR emission is collected by a MCZT detector through a pair of off-axis paraboloidal mirrors and then sent to a lock-in amplifier for demodulation; the amplitude and phase of the PTR signal are sent to a computer for further processing; (b) finger holder used for *in-vivo* measurements: a flat region of the finger back is exposed to the laser beam through a measurement window

WM-DPTR is a noninvasive and non-contacting technique for measuring minute absorptions of low-concentration solutes in strongly absorbing fluids like water and blood [1-4] in the mid-infrared (MIR) spectral range. Advantages of WM-DPTR over other blood analyte biosensors are: 1) wide signal dynamic range featuring baseline suppression results for high sensitivity in the presence of background noise and the ability to detect signal changes, e.g. due to early appearance of dissolved substances in the blood and the interstitial fluid (ISF); 2) high specificity based on spectroscopic detection of tissue subsurface absorptions associated with the presence in blood of specific biomolecules such as glucose, alcohol and delta-9-tetrahydrocannabinol (Δ^9 -THC, or, simply, THC), the main psychoactive ingredient in cannabis; and 3) high diagnostic reliability due to simultaneous availability of amplitude and phase channels.

In the current CADIPT WM-DPTR system, the two laser beams emitting at two wavelengths (peak and baseline of an absorption band of a probed analyte) irradiate the sample (finger here) using 180° (out-of-phase) square-wave modulation, Fig. 1. The generated infrared (blackbody) emission from the sample is collected and focused onto the MIR detector using the pair of paraboloidal mirrors. The photothermal signal is then sent to the lock-in amplifier for demodulation. The computer controls laser modulation, data acquisition and data processing.

In-vivo Blood Glucose Detection

In-vivo WM-DPTR measurements and simultaneous finger pricking blood glucose concentration (BGC) reference measurements were performed on diabetic and nondiabetic volunteers during oral glucose tolerance testing (OGTT) at the peak/base wavelength pair, Fig. 2(a). The measurement results demonstrated high resolution and large phase dynamic range (~80 degrees) in the normal-to-hyperglycemia BGC range (5 mmol/L – higher than 33.2 mmol/L), which were supported by negative control measurements Figs. 2(b) and 2(c).

In-vivo Blood Alcohol Detection

In-vivo alcohol consumption WM-DPTR measurements and simultaneous breath alcohol concentration (BrAC) measurements were performed in the blood alcohol (ethanol) concentration (BAC) range 0-80 mg/dl with an optimal wavelength pair for ethanol, Fig. 3(a). The results demonstrated the alcohol detection capability of WM-DPTR with high resolution (~5 mg/dl) and low detection limit (~10 mg/dl), Figs. 3(b) and 3(c). The immunity of WM-DPTR to temperature and glucose variations makes the differential signals alcohol sensitive and specific, yielding precise and accurate noninvasive alcohol concentration measurements in the interstitial fluid.

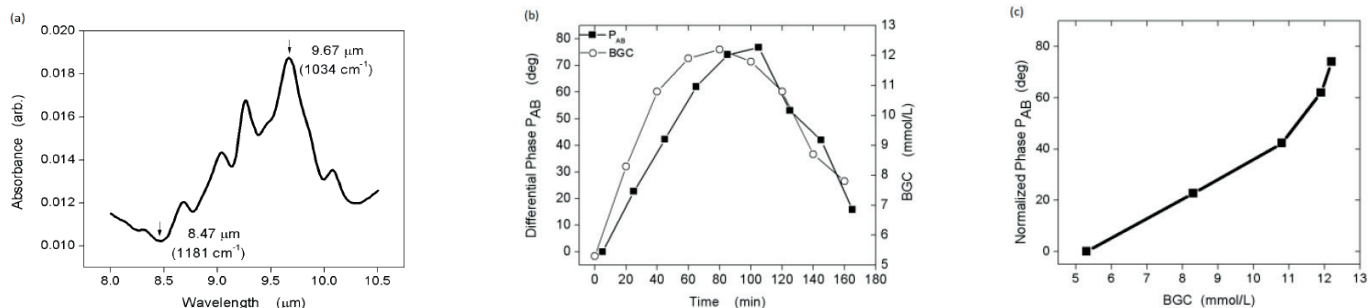


Fig 2. Correlation between WM-DPTR signal and simultaneously measured blood glucose concentration (BGC) with a glucometer in an in vivo oral glucose tolerance test (OGTT) [3]. (a) FTIR glucose absorption band in MIR range and the selected wavelength pair $1034\text{ cm}^{-1}/1181\text{ cm}^{-1}$; (b) time profile comparison between WM-DPTR phase P_{AB} (solid squares + line) and the BGC reference (open circles + line); (c) normalized WM-DPTR phase P_{AB} vs. BGC.

In-vivo Blood Cannabis Detection

Driving while impaired by drugs is a major contributor to fatal road crashes and cannabis is the most commonly consumed drug. Cannabis sensing is based on the detection of THC concentration for law enforcement and workplace compliance applications. Preliminary WM-DPTR cannabis smoking measurements were performed on a volunteer cannabis smoker and a nonsmoker at a THC optimal wavelength pair λ_A/λ_B , Fig. 4(a). The results, Fig. 4(b), show the phase of the smoker steeply rises immediately after smoking, peaking after 15 min, and then gradually dropping back to the baseline after 60 min, whereas the phase of the nonsmoker remains flat during the entire measurement, as expected from the absence of THC in the ISF.

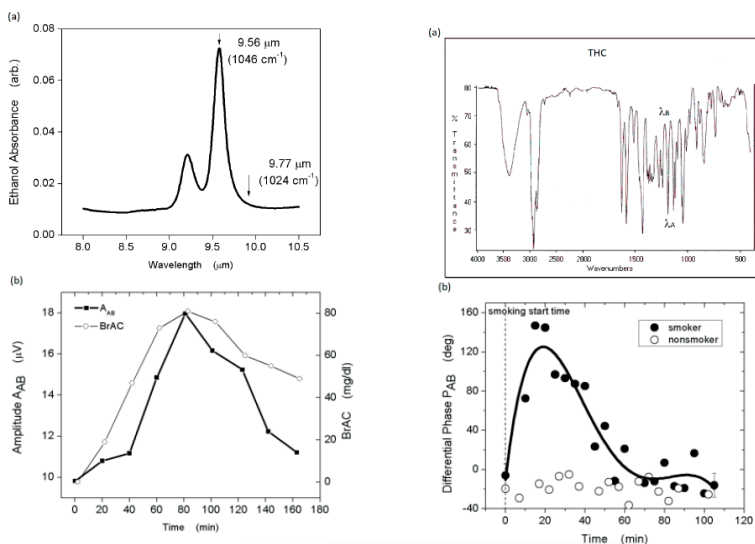


Fig 4. WM-DPTR in-vivo cannabis smoking measurements. (a) THC absorption bands and the selected wavelength pair $1046\text{ cm}^{-1}/1024\text{ cm}^{-1}$ [5]; (b) WM-DPTR phase P_{AB} time profile comparison between cannabis smoker (solid circles) and nonsmoker (open circles).

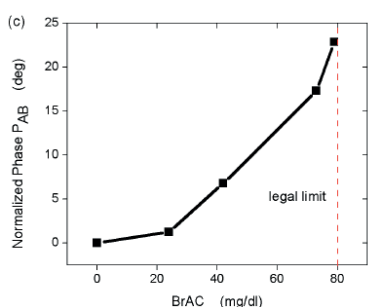


Fig 3. Correlation between WM-DPTR signal and simultaneously measured breath alcohol concentration (BrAC) with a breath analyzer in in vivo alcohol consumption measurements [4]. (a) ethanol absorption band and the selected wavelength pair $1046\text{ cm}^{-1}/1024\text{ cm}^{-1}$; (b) time profile comparison between WM-DPTR amplitude A_{AB} (solid squares + solid lines) and BrAC (open circles + dashed lines); (c) normalized WM-DPTR phase P_{AB} vs. BrAC.

Acknowledgements

The authors wish to thank K. Shojaei-Asanjan, D. Zhang, K. Sivagurunathan, Q. Sun, P. Song and A. Melnikov from the University of Toronto for their contributions to the WM-DPTR biosensor research program. The authors are grateful to the Natural Sciences and Engineering Research Council of Canada (NSERC) (DG, CR, DCR programs), Ontario Centers of Excellence (OCE) (VIP II program); Alcohol Countermeasure Systems Inc. (ACS) and Cannabix Technologies Inc. (Cannabix) for their support to the research.

References

1. A. Mandelis and X. Guo, "Method of performing wavelength modulated differential photothermal radiometry with high sensitivity", US Patent No. 08649835 Cl. 600-316, issued on Feb. 11, 2014.
2. A. Mandelis and X. Guo, Phys. Rev. E 84 (4), 041917 (2011).
3. X. Guo et al., J. Biophotonics, doi: 10.1002/jbio.201800441 (2019).
4. X. Guo et al. Biomed. Opt. Express 9 (10), 4638 (2018).
5. Scientific Working Group for the Analysis of Seized Drugs (SWGDRUG)-Marijuana, May 13, 2005, <http://www.swgdrug.org/monographs/marijuana.pdf>.

Remote measurement of single cell 3D morphology

Bertrand AUDOIN^{(1)*}, Liwang LIU⁽¹⁾, Alexis VIEL⁽¹⁾, Guillaume LE SAUX⁽²⁾, Laurent PLAWINSKI⁽²⁾,
Giovanna MUGGIOLU⁽³⁾, Philippe BARBERET⁽³⁾, Marco PEREIRA⁽⁴⁾, Cédric AYELA⁽⁴⁾,
Hervé SEZNEC⁽³⁾, Marie-Christine DURRIEU⁽²⁾, Jean-Marc OLIVE⁽¹⁾

1. University of Bordeaux, CNRS UMR 5295, I2M, F-33400 Talence, France

2. University of Bordeaux, CNRS UMR 5248, Bordeaux INP, CBMN, F-33600 Pessac, France

3. University of Bordeaux, CNRS UMR 5797, CENBG, F-33170 Gradignan, France

4. University of Bordeaux, CNRS UMR 5218, IMS, F-33400 Talence, France

bertrand.audoin@u-bordeaux.fr

Cell morphological analysis^{1,2} has long been used in cell biology and physiology for abnormality identification,^{3,4} early cancer detection,^{5,6} and dynamic change analysis under specific environmental stresses.^{7,8} In such investigations, cell biologists usually use planar 2D cell images provided by optical microscopy to examine cell shape by locating edges, spreading area and so forth. However, the pathway to the third dimension, i.e. to the cell thickness imaging, is essential since cell morphology is virtually a result of the mechanical balance^{9,10} between the intracellular components and the outside 3D extracellular microenvironment.¹¹

The picosecond ultrasonics (PU) technique allows the optical generation and detection of ultrafast acoustic waves, up to THz frequencies,⁴⁴ using femtosecond lasers. After decades of being used to study thin solid films, PU has attracted increasing attention for cell probing and imaging, owing to its two superior features beyond all-optical and non-invasive.¹² One is its direct access to sound velocities in the penetrated volume.¹³⁻¹⁶ The other is its high resolution in time and space.^{17,18}

In this talk, we report on the remote mapping of cell 3D morphology with an in-plane resolution limited by optics and an in-depth resolution down to a tenth of the optical wavelength. For this, we tracked GHz coherent acoustic phonons (CAPs) and their resonance harmonics by means of an ultrafast opto-acoustic technique, and we analysed both the homogenous propagation of CAPs in cells and of their interaction with the cell outer interfaces.

After illustrating the measurement accuracy with cell-mimetic polymer films we map the 3D morphology of an entire osteosarcoma cell. The entire 3D morphology of the same cell was also obtained using AFM as a reference mean for contact thickness measurement. The good agreements of the measured profiles and mean thicknesses confirm accuracy of the remote technique for measuring cell thicknesses as small as $\lambda/7$. In addition, we show that the in-plane definition of 1 μm , as limited by optical diffraction, is convenient for performing relevant roughness analysis. A sensitivity to cell roughness of the order of $\lambda/10$ is demonstrated.

In addition, while mapping macrophages and monocytes, we demonstrate an enhanced contrast of thickness inhomogeneity by taking advantage of the detection of high-frequency resonance harmonics. Illustrations are given with the remote quantitative mapping of the nucleus thickness inhomogeneity of migrating monocyte cells.

The 3D PU morphology is thus a new imaging modality that could be used as an alternative method to AFM for such studies. This modality was inserted on a regular upright microscope, making it handy to cooperate with bright field and fluorescence microscopies, so that complementary images could be obtained simultaneously. These results open the path for wide applications in biology and medicine where remote measurement of the cell 3D-morphology is required.

Acknowledgements

L. L., A. V., and B.A. acknowledge financial support from the Agence Nationale de la Recherche (grant ANR-17-CE11-0020-01), from the Region Nouvelle-Aquitaine (grant 2016-1R-60301) and from Université de Bordeaux.

References

1. Z. Pincus and J. A. Theriot, *J. Microsc.* 227, 140 (2007).
2. S. Chen, M. Zhao, G. Wu, C. Yao, and J. Zhang, *Comput. Math. Methods Med.* 2012, e101536 (2012).
3. K. Tripathi, N. Matmati, W. J. Zheng, Y. A. Hannun, and B. K. Mohanty, *Genetics* 189, 533 (2011).
4. S. W. K. Chan, K. S. Leung, and W. S. Felix Wong, *Artif. Intell. Med.* 8, 67 (1996).
5. C. Ortiz De Solórzano, S. Costes, D. E. Callahan, B. Parvin, and M. H. Barcellos-Hoff, *Microsc. Res. Tech.* 59, 119 (2002).
6. G. A. Losa and C. Castelli, *Cell Tissue Res.* 322, 257 (2005).
7. M. Théry, *J Cell Sci* 123, 4201 (2010).
8. S. P. Arnoczky, M. Lavagnino, J. H. Whallon, and A. Hoonjan, *J. Orthop. Res.* 20, 29 (2002).
9. E. Paluch and C.-P. Heisenberg, *Curr. Biol.* 19, R790 (2009).
10. K. M. Yamada and E. Cukierman, *Cell* 130, 601 (2007).

11. E. Cukierman, R. Pankov, D. R. Stevens, and K. M. Yamada, *Science* 294, 1708 (2001).
12. V. Gusev and P. Ruello, *Appl. Phys. Rev.* 5, 031101 (2018).
13. C. Rossignol, C. Nikolay, M.-C. Durrieu, B. Audoin, F. Guillaume, and M.-C. Durrieu, *Appl. Phys. Lett.* 93, 123901 (2008).
14. O. F. Zouani, T. Dehoux, M.-C. Durrieu, and B. Audoin, *Soft Matter* 10, 8737 (2014).
15. M. Abi Ghanem, T. Dehoux, O. F. Zouani, A. Gadalla, M.-C. Durrieu, and B. Audoin, *J. Biophotonics* 7, 453 (2014).
16. T. Dehoux, M. A. Ghanem, O. F. Zouani, J.-M. Rampnoux, Y. Guillet, S. Dilhaire, M.-C. Durrieu, and B. Audoin, *Sci. Rep.* 5, 8650 (2015).
17. S. Danworaphong, M. Tomoda, Y. Matsumoto, O. Matsuda, T. Ohashi, H. Watanabe, M. Nagayama, K. Gohara, P. H. Otsuka, and O. B. Wright, *Appl. Phys. Lett.* 106, 163701 (2015).
18. F. Pérez-Cota, R. J. Smith, E. Moradi, L. Marques, K. F. Webb, and M. Clark, *Sci. Rep.* 6, 39326 (2016).

Shock wave focusing in human eyes following laser medical procedures

Tomaž POŽAR *, Darja HORVAT, Vid AGREŽ, Bojan STARMAN,
Mirko HALILOVIČ, Rok PETKOVŠEK

Faculty of Mechanical Engineering, University of Ljubljana, Ljubljana 1000, Slovenia

tomaz.pozar@fs.uni-lj.si

About 43% of those who suffer from vision loss that interferes with daily activities have refractive errors and 33% suffer from cataracts. Some 80% of cases are preventable or treatable, often using lasers. Refraction-correcting, photoablation-based eye laser procedures as well as photoionization-based therapeutic laser eye surgery such as iridotomy, capsulotomy and vitreolysis have become standard methods of treatment. Although it is commonly believed that such laser medical procedures have negligible side effects, our research puts the conviction of minimal invasiveness under question.

We found that shock/pressure waves accompanying photoablation or photoionization of water-rich eye tissues [1] reach sufficient negative peak pressure values that exceed some of the reported threshold values (see Figure 1 for photoablation) [2]. In photoablation, the shock waves launched from the curved surface of the cornea focus along the optical axis near the posterior surface of the eye lens. In photoionization of the capsule (capsulotomy) or of the eye floaters (vitreolysis) within the vitreous, the spherical shock wave emitted from the breakdown reflects from the retina, switches polarity and is focused back within the eye. Large negative peak amplitudes, for example, generate acoustic (inertial) cavitation capable of inducing lesions and cutting of the tissue in the refocusing volume which is located at a different position relatively far away from the original light-tissue interaction site (see the experiments in Figure 2)

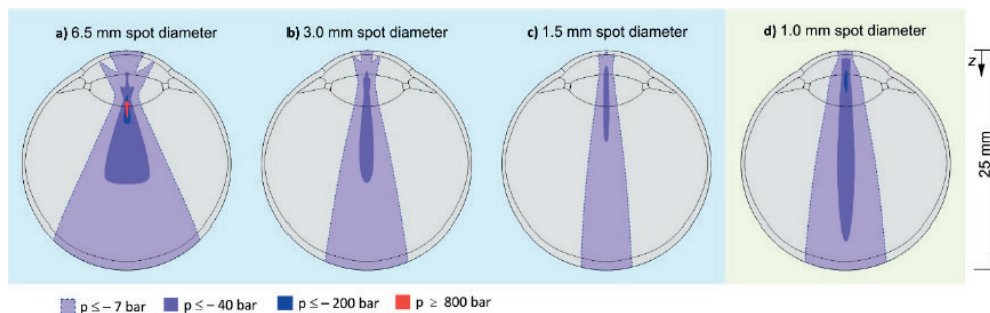
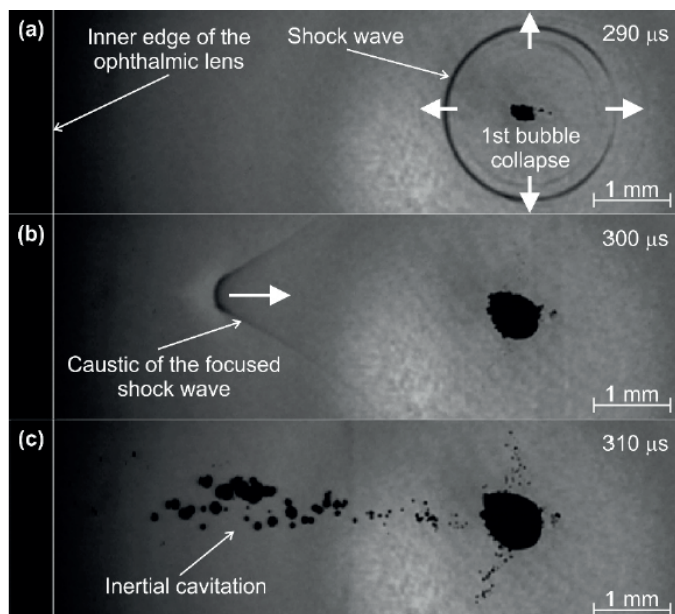


Fig. 1. Photoablation - modeling. Cross section of the eye showing the critical volume inside which the thresholds (see legend) for negative and positive pressure peaks are exceeded. Fig. 4 Pressure field at selected times, source at S2, near the eye lens.



The dynamics of the photoablation- or photoionization-induced pressure waves within the eye is first validated against the existing, but scarce measurements [3], followed by a description of intricate physical effects accompanying the temporal evolution of the pressure field (see Figure 3 for photoionization). Finally, we discuss the implications of the acoustic focusing related to keratorefractive surgery by comparing the simulated pressure contour maps with the recommended values and threshold values for the inception of secondary physical effects such as the potentially harmful inertial cavitation.

Fig. 2. Photoionization in water - experiments. Shadowgraphs at 290 μ s (a), 300 μ s (b) and 310 μ s (c) after laser photoionization event (wavelength: 1064 nm, pulse duration: 6 ns, pulse energy: 15 mJ) in water. (a) The emission of the shock wave after the first collapse of the cavitation bubble. (b) The shock wave is reflected from the concave surface of the ophthalmic lens (same as the surface of the cornea) forming a caustic in the focusing volume. (c) Secondary (inertial) cavitation takes place in the path of the focused shock wave and the light cone of the initial laser pulse.

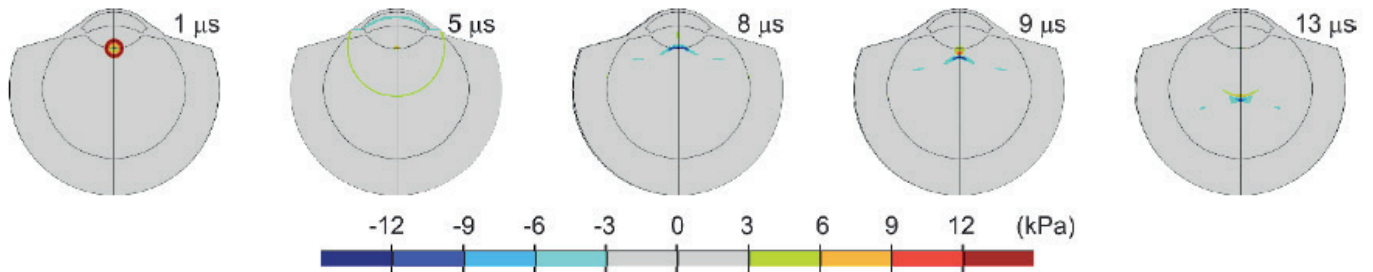


Fig. 3. Photoionization - modeling. Pressure field at selected times after photoionization event during capsulotomy.

Acknowledgements

The authors acknowledge the financial support from the Slovenian Research Agency (research core Funding No. P2-0270, No. P2-0392 and No. P2-0263, and Projects No. L2-6780, No. L2-8183, No. L2-9240 and No. L2-9254). The article is in part the result of work in the implementation of the SPS Operation entitled Building blocks, tools and systems for future factories—GOSTOP. The work is co-financed by the Republic of Slovenia and the European Union from the European Regional Development Fund.

References

1. R.O. Esenaliev, A.A. Oraevsky, V.S. Letokhov, A.A. Karabutov, T.V. Malinsky, *Lasers in Surgery and Medicine* 13 (4), 470 (1993) doi:10.1002/lsm.1900130412
2. T. Požar, M. Halilovič, D. Horvat, R. Petkovšek, *Applied Physics A: Materials Science and Processing* 124 (2), 112 (2018) doi:10.1007/s00339-018-1552-2
3. S. Siano, R. Pini, F. Rossi, R. Salimbeni, P.G. Gobbi, *Applied Physics Letters* 72 (6), 647 (1998) doi:10.1063/1.120834

Characterization of photothermal signatures of cancerous breast tissue ex vivo

R. Quispe Siccha ^{(1)*}, A. Pérez Pacheco ⁽¹⁾, R. Mosiñoz Montes ⁽²⁾, G. Quintero Beuló ⁽²⁾,
A. Ramírez Morales ⁽³⁾, E. Alvarado Espinosa ⁽³⁾, A. Serrano Aguilar ⁽³⁾, J. Hernández Ruíz ⁽⁴⁾,
J.C. López Alvarenga ⁽⁴⁾

1. Unidad de Investigación y Desarrollo Tecnológico, Hospital General de México DEL, Dr. Balmis 148, Doctores, 06726 Ciudad de México, México.

2. Servicio de Oncología, Hospital General de México DEL, Dr. Balmis 148, Doctores, 06726, Ciudad de México, México,

3. Unidad Profesional Interdisciplinaria de Biotecnología, Instituto Politécnico Nacional, La Laguna Ticoman, 07340, Ciudad de México, México.

4. South Texas Diabetes & Obesity Institute/School of Medicine, The University of Texas Rio Grande Valley, ERAHC 2.212, Edinburg TX

rosa.quispe@gmail.com

The detection of breast cancer in early stages is still limited although there are several diagnostic methods; some of them are invasive and expensive. It is for this reason that we seek to obtain new diagnostic methods that are complementary to existing ones. Currently, there are several investigations on breast cancer images obtained by photoacoustic tomography (PAT) based on the photoacoustic effect (PA), either using phantoms or nanoparticles as a representation of healthy tissue and mammary lesions [1]. In some cases, it has been studied directly in patients using PAT [2], however, it is necessary to find a characteristic pattern that differentiates healthy tissue from cancer. Therefore, it is important to identify a characteristic pattern of the PA signal (photothermal signature) that represents the cancerous breast tissue and differentiates it from healthy tissue. So, in this work we characterize the PA signals of cancerous and healthy tissue, using ex vivo breasts (mastectomies) with mammary lesions (tumors) and healthy tissue (breast periphery indicated by the surgeon). Although in this research work, we do not offer images by PAT we do offer a characteristic pattern of the PA signature and its frequency spectrum, which represents healthy tissue and cancer tissue obtained by a considerable sample size to obtain a representative and reliable characteristic pattern.

Materials and Methods

Twenty-five breasts of the patients of the Oncology Service of the General Hospital of Mexico DEL were used, who signed the informed consent letter. The photoacoustic experimental setup was using piezoelectric sensors in direct contact with the sample, as seen in fig. 1.

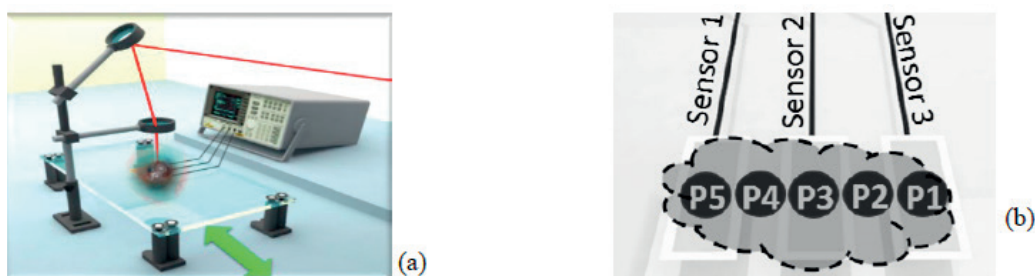


Fig. 1. PA experimental setup (a) and the representative scheme of scanning the sample with the laser light at 5 points (b).

Experimental setup consists of an Nd:YAG laser ($\lambda = 1064$ nm, $F = 10$ Hz, $\tau = 5$ ns, fluence = 200 mJ/cm²), 3 sensors of polyvinylidene difluoride (PVDF), a 2.5 GHz oscilloscope, optical arrays and a sliding glass base to scan the sample on both sides. This method consists of irradiating the sample with near-infrared light at several points on the sample; where part of the energy is absorbed by the sample and the other part is lost by optical scattering. The energy absorbed by the tumor (due to vascularization) generates a thermoelastic effect that produces mechanical waves that travel at the sound speed and that are detected by the piezoelectric sensors (fig. 1b). These waves carry information about the mammary lesion and are recorded by the oscilloscope for analysis.

Results

A characteristic pattern of 25 samples was obtained that differentiates healthy tissue from cancer. To do this, two mathematical methods were used: 1) PA signal in time and frequency (FFT) and 2) Principal Component Analysis (PCA) in the frequency space. As a preliminary result, in fig. 2 we show a characteristic pattern of 5 samples using the first method, because the location of the tumor in the 5 samples is approximately similar.

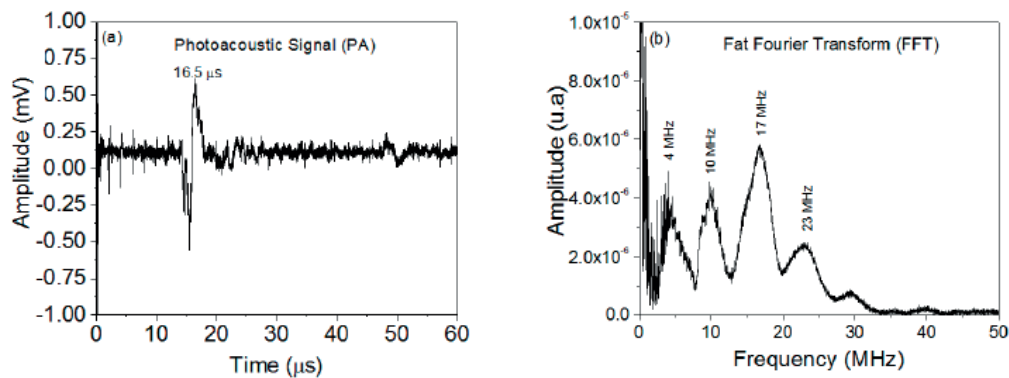


Fig. 2. Representative PA signature of the tumors in 5 samples (a) and characteristic pattern of the vibration modes obtained by FFT (b).

Fig. 2 represents a characteristic pattern of five tumors since the PA signature and the vibrational modes of the frequency spectrum always tend to do the same. Using the delay time of the PA signal (fig. 2a) and the propagation velocity equation ($v = d/t$), we find the depth of the tumor at 2.5 cm from the surface of the breast, these data coincide approximately with the actual depth of the tumors in the five breasts used (with a standard error of ± 0.2 cm).

The 25 analyzed samples maintain the same characteristic pattern by the two mathematical methods, what varies is the delay time (this depends on the depth in which the tumor is located inside the breast). For the PCA two clusters were identified, one of them represents the tumor and the cluster with dispersed points represents the healthy tissue. The dispersed points are due to the variation of mammary density (glandular tissue and fat) according to the age of the patient.

References

1. A. Oraevsky, R. Su, H. Nguyen, J. Moore, Y. Lou, S. Bhadra, L. Forte, M. Anastasio, W. Yang, Proc. of SPIE Vol. 10494, 104942Y (2018) doi: 10.1117/12.2318802
2. M. Klosner, G. Chan, C. Wu, D. Heller, R. Su, S. Ermilov, H. Brecht, V. Ivanov, P. Talole, Y. Lou, M. Anastasio, A. Oraevsky. Proc. of SPIE Vol. 9708, 97085B (2016) doi: 10.1117/12.2209398

3D Dental Subsurface Imaging Using Enhanced Truncated-Correlation Photothermal Coherence Tomography

Sohrab Roointan*, Pantea Tavakolian, Koneswaran Sivagurunathan, Andreas Mandelis

Center for Advanced Diffusion-Wave and Photoacoustic Technologies (CADIPT), Department of Mechanical and Industrial Engineering, University of Toronto, Toronto, Ontario, M5S3G8, Canada

s.roointan@mail.utoronto.ca

Dental decay is the most common human oral disease [1], leading to the destruction of the crystalline structure of teeth. However, while accurate decay characterization and routine monitoring of treatment progress are crucial for effective long-term results, current radiographic technologies fall short of this objective due to low sensitivity [2] and use of ionizing radiation which is unsuitable for frequent monitoring due to potential hazardous side effects. As such, there exists the need for a suitable dental monitoring technology to combine high sensitivity and safety for routine exposure, to promptly address these limitations. To tackle this need, there has been an effort to develop optical and thermal techniques as alternatives for early detection and imaging of dental decay. Developed by Mandelis et al.[3] [4], enhanced truncated-correlation photothermal coherence tomography (eTC-PCT), is a novel thermophotonic imaging modality proven to achieve higher depth-profiling capabilities over conventional photothermal methods (e.g. lock-in thermography) in industrial materials. Recently, we showed that eTC-PCT can be applied to dental imaging [5] as a viable non-ionizing alternative to existing technologies. Dental eTC-PCT is the first 3-dimensional tomographic thermophotonic dental imaging modality, capable of monitoring and characterizing dental decay with high sensitivity. eTC-PCT can provide the dentist with information regarding the extent and severity of demineralized or eroded regions on teeth through detailed 3D imaging with operator controlled axial resolution. Further studies on controlled dental caries and erosion are currently in progress to optimize dental eTC-PCT for the characterization of different clinical conditions. This modality is non-ionizing, compatible with the maximum permissible exposure (MPE) guidelines for use on human tissue, and currently achieves a subsurface depth profilometric capability of ~ 3.8 mm in teeth.

References

1. Examination, Report on the National Health and Nutrition Survey, U.S. National Institute of Dental and Craniofacial Research (2004). Available at: <http://www.nidcr.nih.gov/DataStatistics/FindDataByTopic/DentalCaries/DentalCariesAdults20to64.htm>.
2. Diagnosis and management of dental caries throughout life. National Institutes of Health Consensus Development Conference statement, March 26-28, 2001. J. Dent. Educ. 65, 1162-8 (2001).
3. Kaipilavil, S. and Mandelis, A. Truncated-correlation photothermal coherence tomography for deep subsurface analysis, Nature Photonics 8, 635 - 642 (2014).
4. Tavakolian, P., Sivagurunathan, K. & Mandelis, A. Enhanced truncated-correlation photothermal coherence tomography with application to deep subsurface defect imaging and 3-dimensional reconstructions. J. Appl. Phys. 122, 23103 (2017).
5. Roointan S, Tavakolian P, Floryian M, Sivagurunathan K, Mandelis A. Three-Dimensional Imaging of Healthy and Carious Human Teeth using Enhanced Truncated-Correlation Photothermal Coherence Tomography (Submitted to Scientific Reports-SREP-19-12121).

Enhanced Truncated-Correlation Photothermal Coherence Tomography

Pantea Tavakolian^{(1)*}, Koneswaran Sivagurunathan⁽¹⁾, Wei Shi⁽²⁾, Andreas Mandelis⁽¹⁾

1. Center for Advanced Diffusion-Wave and Photoacoustic Technologies (CADIPT), Department of Mechanical and Industrial Engineering, University of Toronto, Toronto, Ontario, M5S3G8, Canada
2. Princess Margaret Cancer Center, University Health Network, Toronto, M5G 2M9, Canada

Photothermal diffusion-wave imaging is a promising technique for non-destructive evaluation (NDE) 1,2 and medical applications. Several diffusion-wave techniques have been developed to produce depth-resolved planar images of solids and to overcome imaging depth and image blurring limitations imposed by the physics of parabolic diffusion waves. Truncated-Correlation Photothermal Coherence Tomography (TC-PCT) is the most successful class of these methodologies to-date providing 3-D subsurface visualization with maximum depth penetration and high axial and lateral resolution. To extend depth range and axial and lateral resolution, an in-depth analysis of TC-PCT, an enhanced imaging system (eTC-PCT) with improved instrumentation, and an optimized reconstruction algorithm over the original TC-PCT technique was developed. eTC-PCT was then used for small animal imaging. First, eTC-PCT was applied successfully for in-vivo brain structural imaging non-invasively. The intrinsic optical contrast revealed not only blood vessels but also other brain structures, such as the cerebellum, and olfactory lobes. Second, the feasibility of the technique was studied for early detection of cancer in mice. Since chances of survival increase considerably when detected and treated early, developing a simple reliable technique for early detection of tumors is crucial. The eTC-PCT modality was able to detect a tumor size $1.6 \text{ mm} \times 2.8 \text{ mm}$ at the depth of 1.5 mm under the skin 3 days after injecting $20 \mu\text{L}$ cancer cells into a mouse thigh. The early appearance of the tumor in the eTC-PCT was validated by immunohistochemistry. A histological image of the excised tumor and the eTC-PCT phase image of the mouse thigh are shown in Fig 1.

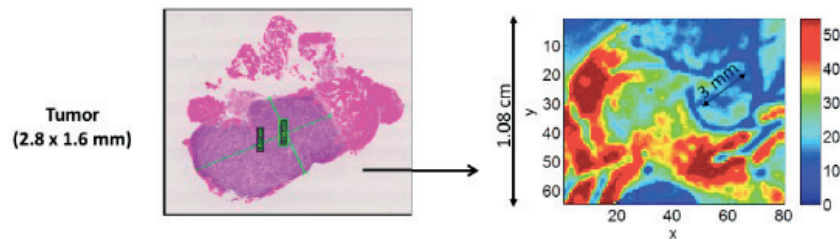


Fig 1. Immunohistochemistry stain of tumor cells surrounded by normal muscle cells and eTC-PCT phase image of the mouse thigh which shows the tumor with size of 2.8 mm and the vascular network around the tumor in dark blue

References

1. Tavakolian P, Sivagurunathan K, Mandelis A. Enhanced truncated-correlation photothermal coherence tomography with application to deep subsurface defect imaging and 3-dimensional reconstructions. *J Appl Phys.* 2017;122:023103.
2. Tavakolian P, Sfarra S, Gargiulo G, Sivagurunathan K, Mandelis A. Photothermal coherence tomography for 3-D visualization and structural non-destructive imaging of a wood inlay. *Infrared Phys.* 2018;91:206-213.

KEYNOTE

Breath air analysis using laser photo-acoustic spectroscopy and machine learning

Yury V. Kistenev^{*(1,2,3)}, A.V.Borisov^(1,2), V.V.Nikolaev^(1,3), D.A.Vrazhnov^(1,3), A.A.Karapuzikov⁽⁴⁾,
D.B.Kolker⁽⁵⁾, N.Yu.Kostyukova^(4,5), A. A. Boyko^(4,5), A.A.Markelov^(3,4,6), K.G.Zenov⁽⁴⁾

1. Tomsk State University, Tomsk, Russia,

2. Siberian State Medical University, Tomsk, Russia,

3. Institute of Strength Physics and Materials Science of SB RAS, Tomsk, Russia

4. Special technologies, Ltd., Novosibirsk, Russia

5. Novosibirsk State University, Novosibirsk, Russia

6. Insitute of Laser Physics of SB RAS, Novosibirsk, Russia

yuk@iao.ru

Control of metabolites in breath being called as “breathomics” is very attractive for express and noninvasive medical screening. Most important metabolites, being associated with pathological processes in the body, are nitric oxide, hydrogen peroxide, volatile organic compounds (VOCs), which include saturated hydrocarbons (ethane, pentane, aldehydes), unsaturated hydrocarbons (isoprene), oxygen containing (acetone), sulphur containing (ethyl mercaptane, dimethylsulfide) and nitrogen containing (dimethylamine, ammonia) [1].

IR laser absorption spectroscopy (LAS) has high sensitivity of molecular species control on the level of ppb and below, as they frequently occur in environmental, medical or biological applications [2]. Laser photoacoustic spectroscopy (LPAS) is based on registration of pressure wave which is generated in an analyzed gas sample due to absorption of amplitude modulated laser beam tuned on a frequency of resonant absorption of a specific substance of the sample.

The problem is that typical for a disease VOCs are not highly specific. To solve this problem, molecular biomarker ‘profile’ approach can be used. In this case, pattern-recognition-based techniques can be used. The aim of the work is to show abilities of laser photoacoustic spectroscopy and machine learning to extract diagnostically significant biomarker profiles.

Materials and Methods

The study involved patients with lung cancer (LC) patients (N=9); patients with chronic obstructive pulmonary disease (COPD) (N= 12); patients with pneumonia (n=11) and a control group of healthy volunteers (N=29). All patients had been treated in medical organizations, so the diagnosis has been verified by clinical methods.

We used developed by Special Technologies Ltd. laser photoacoustic gas analyzer LaserBreeze *based on the dual OPO* with tuning range 2.5 – 10.7 μm [3]. Two types of nonlinear elements are used in this OPO: periodically poled lithium niobate structure (PPLN) and mercury thiogallate crystal HgGa_2S_4 (HGS). Nd:YLF laser (10 ns, 0.5–1.5 kHz, 1.5 mJ) was used as a pump source. The double channel resonant photo-acoustic cell was used for recording absorption spectra of gaseous samples.

Exhaled breath samples were collected in 150 ml disposable plastic containers (syringe) and were analyzed using the LaserBreeze gas analyzer. All measurements were carried out at room temperature (20-25 Co) and humidity (50-60%). We repeat measurements of a EAS absorption spectrum 5 times.

"Pattern" approach requires the selection of the informative features allowing to separate one group of objects from another. The problem of weak distinguishability of features vectors in high dimension features space is known (see, for example [23]). Dimensional reduction of features space simplifies the classification, visualization and compression of multidimensional data [4]. The principal component analysis is one of the most effective methods in this field.

Classification is as a tool for computer-aided diagnostic decision support. There are supervised and non supervised learning classification methods. Supervised learning means training the classifier when the certain set of vectors is available for which belonging to one of the classes is known. When classifiers are trained, there is a danger that the classifier will be too well adjusted for training data, which will lead to the impossibility of correctly classifying new (unseen) data. This problem is called "overtraining" or "overfitting" of the classifier.

We plan to discuss various supervised learning methods, including Support Vector Machine, Artificial Neural Networks with various ways to split data for learning and testing stages, to create predictive models, which allow to distinguish groups under study on a base absorption characteristics of breath air, measured by laser optical-acoustic spectroscopy.

Acknowledgements

This work has been supported by Russian Foundation for Basic Research (project 17-00-00186).

References

1. A.G. Dent, T.G. Sutedja, P.V., J. Thorac. Dis. 5, 540-550 (2013).
2. F. Kühnemann, F.Müller, G. von Basum, D. Halmer, A. Popp, S. Schiller, P. Hering, M. Mürtz. Proceedings of SPIE. 5337, 117-127 (2004), doi: 10.1117/12.532580.117-127
3. A.A. Karapuzikov, et al. Physics of Wave Phenomena. 22 (3), 189-196 (2014).
4. M.B. Shapiro, R.B. Marimont IMA Journal of Applied Mathematics. №24, 59-70 (1979)

KEYNOTE

Noninvasive characterization of human skin by combining photothermal radiometry and optical spectroscopy

Boris MAJARON ^{(1,2)*}, Nina VERDEL ⁽¹⁾

1. Jožef Stefan Institute, Ljubljana, Slovenia

2. Faculty of Mathematics and Physics, University of Ljubljana, Slovenia

boris.majaron@ijs.si

We have recently developed a novel methodology for noninvasive assessment of structure and composition of human skin *in vivo* [1-2]. The approach combines pulsed photothermal radiometry (PPTR), involving time-resolved measurements of mid-infrared emission after irradiation with a millisecond laser pulse ($\lambda = 532$ nm, $H_0 \sim 0.3$ J/cm²), and diffuse reflectance spectroscopy (DRS) in visible part of the spectrum ($\lambda = 400$ –600 nm) measured using an integrating sphere.

The data acquired from human volunteers are fitted simultaneously with the corresponding predictions of a dedicated numerical model of light transport in human skin, utilizing the Monte Carlo technique (MC). A very good match between the experimental and model data is obtained by applying a four-layer optical model of human skin, accounting for the epidermis, papillary and reticular dermis, and fatty subcutis.

The described approach allows quantitative assessment of the contents of the specific chromophores (melanin, oxy- and deoxy-hemoglobin) as well as thicknesses and scattering properties of the epidermis and dermis. Relevant physiological information, such as fractional blood content and oxygen saturation are thus obtained in a noninvasive manner, which was not possible by applying each of the two techniques individually [3].

The assessed values correlate nicely with the corresponding ranges from literature and demonstrate the expected trends in controlled tests involving temporary obstruction of peripheral blood circulation using a pressurized arm cuff, as well as acute and seasonal sun tanning. In addition, our coregistration test involving multi-photon microscopy showed that the obtained values for epidermal thickness correspond to the maximal thickness within the investigated area.

The example in Fig. 1 presents a comparison of the PPTR signals and DRS as measured on the forearm of a healthy volunteer before (orange solid lines) and after application of a blood-pressure cuff inflated to 100 mm Hg, thus causing obstruction of the peripheral blood circulation (red). The dashed lines indicate the predictions of our numerical forward model after objective optimization of its 14 free parameters: epidermal and dermal thickness, epidermal melanin content, epidermal blood content, papillary and reticular dermal blood contents, papillary and reticular blood oxygenation levels, subcutis scattering amplitude, scattering amplitude and power, which can differ between the epidermis and dermis, and the applied radiant exposure [2].

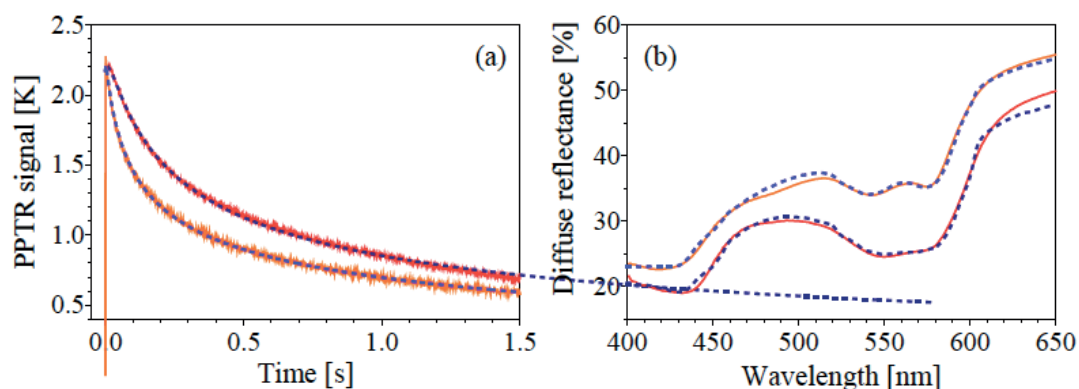


Fig. 1. PPTR signals (a) and DRS spectra as measured in intact human skin (orange solid lines) and during an obstruction of the peripheral blood circulation (red solid lines). Dashed lines present the best fitting predictions of our numerical model.

Figure 2 illustrates the most prominent changes of the skin properties upon application of the pressure cuff (blue), as assessed from data in Fig. 1 using our inverse analysis. These include a substantial rise of the blood content in the papillary dermis and significant decrease of blood oxygenation in both dermal layers. This is consistent with the fact that the applied cuff pressure of 100 mm Hg completely obstructed blood flow through the veins but not also through the arteries (i.e., venous occlusion).

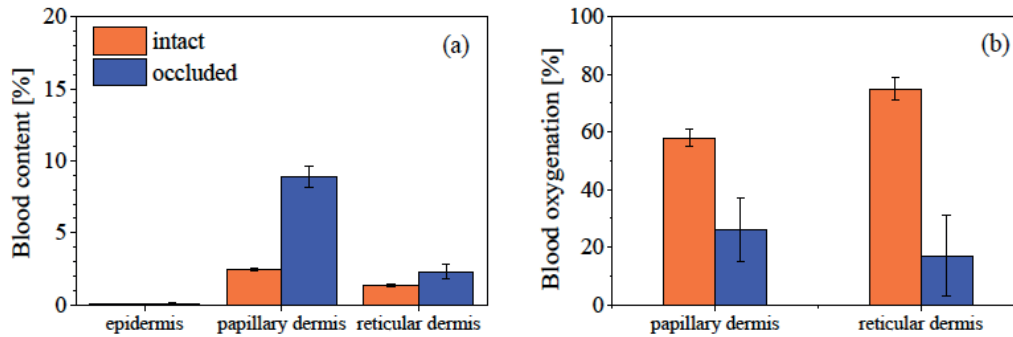


Fig. 2. Changes in blood contents (a) and oxygenation levels (b) in different skin layers upon obstruction of peripheral blood circulation in a human volunteer, as extracted from data in Fig. 1.

One important limitation of the described approach is that the involved high-dimensional optimization utilizing a numerical forward model (i.e., inverse MC) is computationally very expensive, thus leading to impractical durations of analyses despite massive parallelization of the MC procedure. In response to this challenge we have recently initiated the development of a predictive model (PM) based on machine learning. Our PM employs the technology of random forests and is trained by several thousand combinations of various skin parameter values and the corresponding PPTR signals and DRS spectra, computed using the forward MC model [4].

References

1. N. Verdel, G. Lentsch, M. Balu, B.J. Tromberg, B. Majaron, *Applied Optics* 57 (18), D117 (2018) doi: 10.1364/AO.57.00D117
2. N. Verdel, A. Marin, M. Milanič, B. Majaron, *Biomedical Optics Express* 10 (2) 944 (2019) doi: 10.1364/BOE.10.000944
3. L. Vidovič, M. Milanič, L.L. Randeberg, B. Majaron, *Proceedings of SPIE* 9303, 930307 (2015) doi: 10.1117/12.2077188
4. N. Verdel, J. Tanevski, S. Džeroski, B. Majaron, *Proceedings of SPIE*, 10851 1085107 (2019) doi: 10.1117/12.2509691.

Influence of signal binning on characterization of skin using photothermal radiometry and optical spectroscopy

Nina VERDEL ^{(1)*}, Boris MAJARON ^(1,2)

1. Jozef Stefan Institute, Jamova 39, 1000 Ljubljana, Slovenia
2. Faculty of Mathematics and Physics, University of Ljubljana, 1000 Ljubljana, Slovenia

nina.verdel@ijs.si

We have recently introduced a novel methodology for noninvasive assessment of structure and composition of human skin in vivo [1]. The approach combines pulsed photothermal radiometry (PPTR), involving time-resolved measurements of mid-infrared emission after irradiation with a millisecond light pulse, and diffuse reflectance spectroscopy (DRS) in visible part of the spectrum (400–600 nm). The experimental data are fitted simultaneously with respective predictions from a four-layer Monte Carlo (MC) model of light transport in human skin.

The described approach allows assessment of the contents of specific chromophores (melanin, oxy-, and deoxy-hemoglobin), as well as scattering properties and thicknesses of the epidermis and dermis. However, the involved multi-dimensional optimization using the numerical forward model (i.e., inverse MC) is computationally very expensive. We have therefore developed a predictive model (PM) based on machine learning [2]. The PM involves random forests trained using several thousand pairs of skin parameter combinations and the corresponding PPTR signals and DRS spectra, computed by our forward MC model.

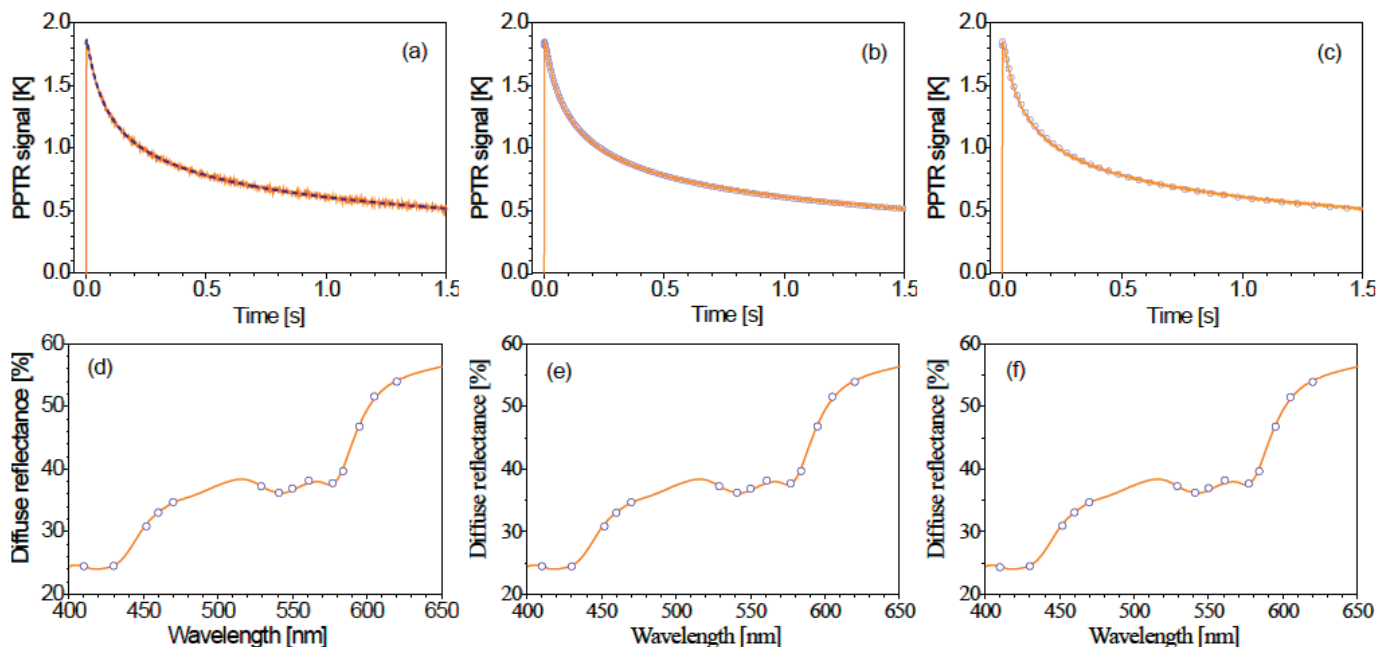


Fig. 1. Comparison of the PPTR signals and DRS spectra as measured in vivo (orange lines) and the best-fitting model predictions (dashed) when using the entire PPTR signal (a,d) and compressed to a subset of 162 (b,e) or 41 data points (c,f) by quadratic binning.

In order to reduce the computational load of the PM training procedure, PPTR signals (which in experimental setting consist of 1500 uniformly distributed data points) must be compressed to a smaller set of characteristic features. For this purpose we apply non-uniform (quadratic) binning as presented earlier [3]. In this study we analyze the effect of such signal compression on the accuracy and stability of skin characterization using the inverse MC procedure.

Fig. 1 presents a comparison between the PPTR signals and DRS spectra as acquired in healthy skin (orange solid curves) with the best fitting model predictions (blue circles) when using the entire PPTR signal (a,c), and using a subset of 162 (b,e) or 41 data points (c,f) obtained by application of quadratic binning. Meanwhile, the DRS spectra are always analyzed at only 14 wavelengths, selected by considering the absorption characteristics of skin chromophores.

Table 1. The assessed model parameters values and residual norms with the entire PPTR signal (first column), or compressed to a subset of 162 (second column), and 41 (third column) data points obtained by application of quadratic binning.

	all points	162 points	41 points
d_{epi} [μm]	110 ± 8	114 ± 4	117 ± 7
mel [%]	1.1	1.1	1.1
b_{epi} [%]	0.4 ± 0.1	0.4 ± 0.1	0.5 ± 0.1
b_{pap} [%]	1.9 ± 0.2	1.9 ± 0.2	2.1 ± 0.2
b_{ret} [%]	1.3	1.3 ± 0.1	1.3 ± 0.2
S_{pap} [%]	56 ± 2	57 ± 3	59 ± 1
S_{ret} [%]	88 ± 4	88 ± 3	88 ± 1
d_{der} [mm]	0.71 ± 0.11	0.67 ± 0.14	0.73 ± 0.19
a_{epi} [cm^{-1}]	129 ± 1	129 ± 5	135 ± 5
p_{epi}	1.3 ± 0.1	1.3 ± 0.2	1.2 ± 0.2
a_{der} [cm^{-1}]	59 ± 3	58 ± 2	60 ± 2
p_{der}	0.6 ± 0.1	0.7 ± 0.1	0.6 ± 0.1
A_{sub}	0.8 ± 0.2	0.9 ± 0.1	0.8 ± 0.2
F [J/cm^2]	0.27	0.26	0.26
resnorm, DRS	0.94 ± 0.11	0.95 ± 0.16	0.93 ± 0.06
resnorm, PPT R	0.0097 ± 0.0016	0.0034 ± 0.0007	0.0029 ± 0.0015

As can be seen in Fig. 1, quadratic binning of the PPTR signals doesn't affect the quality of the fits. Moreover, the assessed values of all model parameters remain the same within the respective error margins (Table 1). Therefore, data compression by quadratic binning can be applied in inverse MC analysis and consequently also for training of the predictive model.

References

1. N. Verdel, A. Marin, M. Milanič, B. Majaron, Biomedical Optics Express 10(2) 944-960 (2019) doi: 10.1364/BOE.10.000944.
2. N. Verdel, J. Tanevski, S. Džeroski, and B. Majaron, Proceedings of SPIE, 10851 1085107 (2019) doi:10.1117/12.2509691.
3. M. Milanič and B. Majaron, Proceeding of SPIE, 7371 737100 (2009), doi:10.1117/12.831734.

Laser Excitation of Coherent Gigahertz Acoustic Vibrations in Albumin

Anna Kudryavtseva ^{(1)*}, Maxim Karpov ⁽²⁾, Vladimir Savichev ^(1,3),
Mikhail Shevchenko ⁽¹⁾, Nikolay Tcherniega ⁽¹⁾

1. P.N. Lebedev Physical Institute of the RAS, Leninsky pr, 53, Moscow, 119991, Russia

2. FSUE VNIIA, ul.Sushchevskaya, 22, Moscow, 127055, Russia

3. Bauman Moscow State Technical University, ul. Baumanskaya 2-ya, 5, Moscow, 105005, Russia

e-mail: akudr@sci.lebedev.ru

Photoacoustic methods are now increasingly used for the study of nanomaterials, for instance, nanosized biological systems. One of such methods is low-frequency Raman scattering (LFRS), caused by light interaction with eigen vibrations of nanoparticles [1]. LFRS was applied for theoretical [2] and experimental [3] study of biological nanoobjects. In [2] lowest vibrational modes of rod-shaped viruses (M13 bacteriophage and tobacco mosaic virus TMV) in water and air were calculated. First experimental results on the SLFRS in biological nanoparticles (M13 phage protein coat) have been obtained in [3].

Stimulated analogue of LFRS – stimulated low-frequency Raman scattering (SLFRS) has very important advantages compare to LFRS, namely, essentially higher conversion efficiency and much lower threshold. We observed SLFRS in many nanoparticles systems: metal, dielectric, semiconductors, both high-ordered and random materials [4-6].

We for the first time applied SLFRS for the study of biological objects: tobacco mosaic viruses (TMV) [7]. Later we registered SLFRS in two types of potato viruses (PVA and PVX) and in cauliflower mosaic viruses (CaMV). In the cases of simple virus form (spherical or cylindrical) it is possible to compare experimental results with theoretical calculations. For TMV, having a form of a rigid cylinder, LFRS radial breathing mode frequency calculated in [2] is 2.1 cm^{-1} (63 GHz), which is near to our experimental value 60 GHz.

In this work, we present our experimental results on the SLFRS investigations in human and bovine serum albumin (HSA and BSA) in water. Albumin is a polypeptide chain which can form a globule with a size of $\sim 8 \text{ nm}$. It plays an important role in blood plasma, having a wide variety of functions. Both albumins are known to form associates with a size of a few hundred nanometers. In our experiments, we used HSA and BSA water solutions with the pH value equal to 7. The mass concentration of serum albumin in the solution was 10%. Radius distribution of HSA and BSA nanoparticles was measured with the help of the dynamic light scattering method (DLS). In HAS besides monomers with size 8 nm, aggregates with radius 50 nm were present in the solution. In BSA DLS showed globules with radius 1 nm and aggregates with radius 46 nm.

SLFRS was excited by single 20 ns pulses of a ruby laser with wavelength 694.3 nm, maximum energy 0.3 J, line width 0.015 cm^{-1} and divergence $3.5 \cdot 10^{-4} \text{ rad}$. Laser light was focused at the centre of the 1 cm quartz cell with the sample by the lens with focal length 5 cm. SLFRS spectra have been registered with Fabri–Perot interferometers with different base and consequently different ranges of dispersion from 0.3 cm^{-1} to 8.3 cm^{-1} (9 - 250 GHz). In HSA SLFRS was observed both in a forward and backward direction at the exciting intensity more than 0.1 GWcm^{-2} . For BSA the threshold was reached only at liquid nitrogen temperature (77K). The maximum conversion efficiency of pumping light into SLFRS for HSA and was 55 %, for BSA 25 %.

SLFRS interferograms and spectra in HSA and BSA are shown in Figure 1.

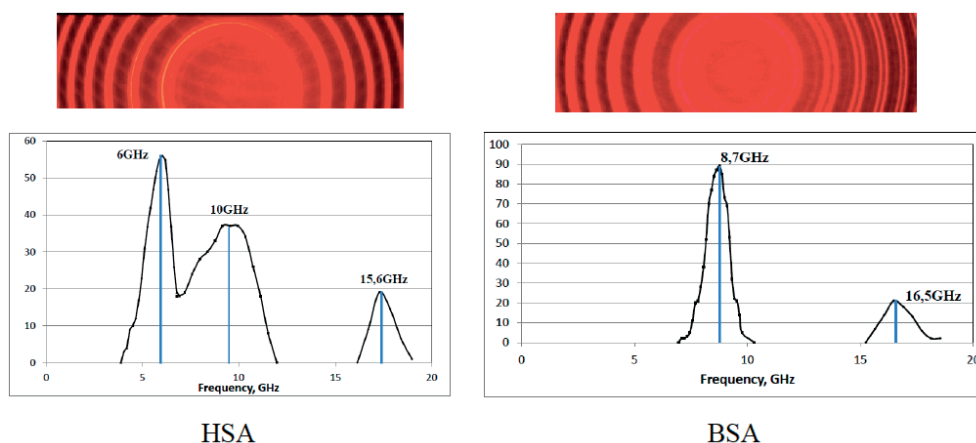


Fig. 1. SLFRS interferograms and spectra in HSA and BSA.

SLFRS in biological nanosized objects can be used for their identification and for the creation of biharmonic pumping, which is an effective method of nanoscale systems study and impact on them. Dependence of SLFRS frequency shift on the excitation conditions gives the possibility to change the frequency shift between biharmonic pumping components.

Acknowledgements

The reported study was funded by RFBR according to the research project № 19-02-00750-a.

References

1. E. Duval, A. Boukenter and B. Champagnon, Phys. Rev. Lett. 56, 2052 (1986) doi: 10.1103/PhysRevLett.56.2052
2. A. Balandin and V. Fonoberov, Journal of Biomedical Nanotechnology 1, 90 (2005) doi:10.1166/jbn.2005.005
3. E.C. Dykeman, O.F. Sankey and Kong-Thong Tsen, Phys. Rev. E 76, 011906 (2007) doi: 10.1103/PhysRevE.76.011906
4. A. Kudryavtseva, N. Tcherniega, M. Samoylovich and A. Shevchuk, Int. Journ. of Thermophys. 33, 2194 (2012) doi: 10.1007/s10765-012-1259-0
5. N. Tcherniega, M. Samoylovich, A.Kudryavtseva et al, Op. Lett. 35, 300 (2010) doi: 10.1364/OL.35.000300
6. N. Tcherniega, K. Zemskov, V. Savranskii et al, Opt. Lett. 38, 824 (2013) doi: 10.1364/OL.38.000824
7. O.V. Karpova, A.D. Kudryavtseva, V.N. Lednev et al, Laser Physics Letters 13, 085701 (2016) doi:10.1088/1612-2011/13/8/085701

Speckle-contrast and OCT-elastography-based visualization of interplay of temperature, thermal-stress and strain fields in laser-assisted modification of collagenous tissues

Vladimir Y. ZAITSEV^{(1)*}, Olga I. BAUM⁽²⁾, Alexey V. YUZHAVKOV⁽²⁾, Aleksander P. Sviridov⁽²⁾, Aleksandr A. SOVETSKY⁽¹⁾, Aleksander L. MATVEYEV⁽¹⁾, Maria L. NOVIKOVA⁽²⁾, Lev A. MATVEEV⁽¹⁾, Emil N. SOBOL⁽²⁾

1. Institute of Applied Physics, Russian Academy of Sciences, Nizhny Novgorod, Russia

2. Institute of Photon Technologies, Russian Academy of Sciences, Moscow, Russia

*vyuzai@ipfran.ru

Moderate short-time heating (~50-70°C) of collagenous tissues such as cartilage and cornea under IR-laser irradiation can produce nonablative structural rearrangements, possibility to perform biologically non-destructive reshaping with fairly stable conservation of the remodeled form due to relaxation of internal stresses. The results of such reshaping and eventual changes in optical and biological properties strongly depend on the laser-irradiation regime, so that development of methods and means allowing for sufficiently precise control of such thermo-mechanical tissue modification is of high interest. Here, we report the results of application of a speckle-contrast technique based on monochromatic illumination of the tissue in combination with strain-evolution mapping by means of Optical Coherence Elastography (OCE) to reveal the interplay between the temperature-, thermal-stress producing tissue modifications during laser heating. The speckle-based technique ensured *en face*-visualization of the interplay among cross-correlation of speckle images, their contrast, temperature field and thermal-stress field under various heating-laser settings (see an example in Fig. 1).

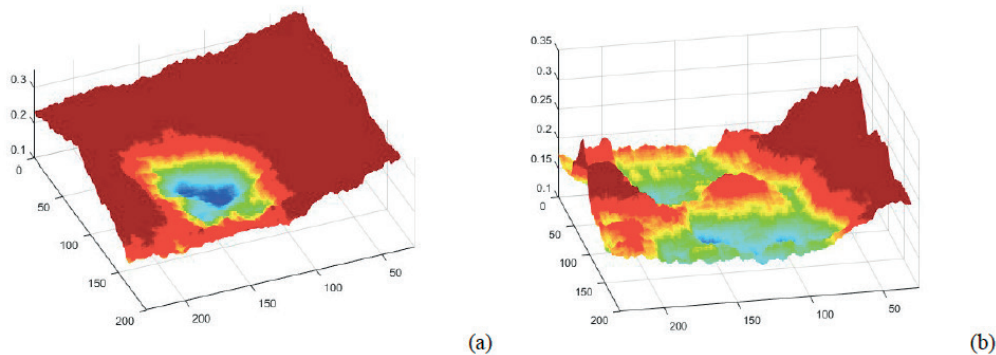


Fig. 1. Examples of speckle contrast *en face* visualization of a cartilaginous sample (4mm x5mm in size) heated by a Gaussian beam. (a) is the very beginning of the heating when the maximal intensity of structural rearrangement coincides with the the axis of the heating beam, where the temperature is maximal, but thermal stresses are zero; (b) speckle contrast distribution ~ 5 s after beginning of the heating, when a ring-shape zone of maximal-intensity of modifications gradually shifts to the slopes of the temperature distribution, where thermal stresses are maximal

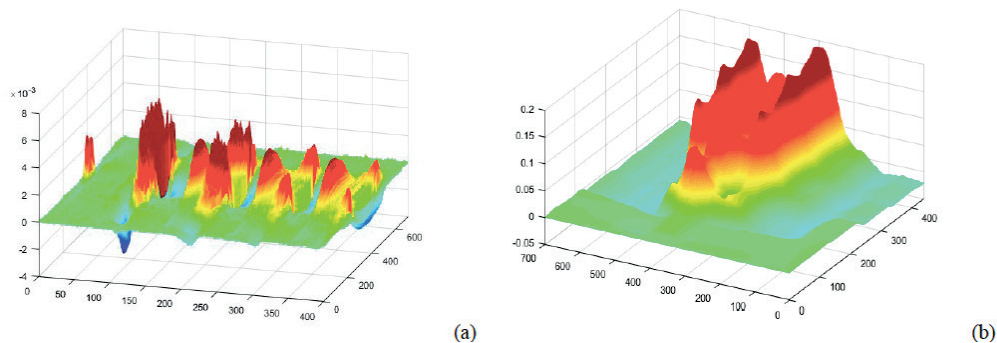


Fig. 1. OCE-based "waterfall" sequences of depth-resolved quantitative strain maps over a vertical cross section of the heating beam for 5 laser pulses. Vertical axis in (a) shows interframe strains (i.e., strain rate) with initial maximal strain at the beam axis (where the temperature is maximal) and gradual progression of the zone of maximal strains towards the region of maximal thermal strains located at the temperature-distribution slopes; (b) is a similar waterfall sequence for cumulative-strain profiles corresponding to interframe strains in panel (a). This example is obtained for an excised rabbit cornea demonstrating striking similarity with the behavior of cartilaginous samples. Lateral size is 4 mm, record duration is 20 s (400 frames with 50 ms time step).

The speckle-contrast findings are supported by quantitative visualization of depth-resolved strains in the heated tissue sample by means of phase-sensitive Optical Coherence Elastography (OCE) in a recently developed advanced variant [1,2]. This method readily allows one to perform high-sensitivity quantitative, temporally and spatially (in-depth and laterally) resolved visualization of aperiodic and rapidly evolving thermally-produced strains, although en face visualization based on of scanning optical coherence tomography is problematic. Thus, each of the two used approaches (speckle contrast and OCE-based) has its own advantages.

The performed study allowed for analyzing different stages of laser modification of collagenous tissues. Spatially-resolved analysis of speckle dynamics in the horizontal plane (en face view) and quantitative OCE-based strain mapping in the vertical plane combined with theoretical modeling of thermal stresses confirmed the hypothesis that intense modification of collagenous tissues can be obtained not only by straightforward temperature increase, but also promoted by elevated thermal-stresses created by the temperature gradients. These findings can be used for optimization of the heating-beam profile and temporal pattern of irradiation to obtain the desirable tissue reshaping with minimal heating

The revealed relationships can be used as a basis for controlling tissue irradiation regimes in real time during laser modification/shaping of cartilaginous implants in otolaryngology, maxillofacial surgery and novel methods of corneal-shape correction.

Acknowledgements

This study was supported by the RSF grant 16-15-10274.

References

1. A. L. Matveyev, L. A. Matveev, A. A. Sovetsky, G. V. Gelikonov, A. A. Moiseev, and V. Y. Zaitsev, *Laser Physics Letters* 15 (6), 065603 (2018) doi: 10.1088/1612-202X/aab5e9
2. V. Y. Zaitsev, A. L. Matveyev, L. A. Matveev, G. V. Gelikonov, O. I. Baum, A. I. Omelchenko, D. V. Shabanov, A. A. Sovetsky, A. V. Yuzhakov, A. A. Fedorov, V. I. Siplivy, A. V. Bolshunov, and E. N. Sobol, *Journal of Biophotonics* 12 (3), e201800250 (2019) doi: 10.1002/jbio.201800250

Imaging of wrinkles in CFRP composites using laser-ultrasonics with a fiber-optic Sagnac interferometer on receive

Lukasz AMBROZINSKI ^{(1)*}, Jakub MRÓWKA ⁽¹⁾, Kamil Szpila ⁽¹⁾,
Matthew O'DONNELL ⁽²⁾, Ivan PELIVANOV ^{(2)*}

1. Institute of Applied Physics, Russian Academy of Sciences, Nizhny Novgorod, Russia

2. Institute of Photon Technologies, Russian Academy of Sciences, Moscow, Russia

*vyuzai@ipfran.ru

The increased use of carbon-fiber reinforced plastics (CFRP) for load-bearing aircraft structures has heightened demand for highly automated manufacturing and fast, robust non-destructive testing (NDT) techniques.

Despite significant effort, CFRP inspection remains challenging since a number of failure modes do not exhibit large material discontinuities. A good example is wrinkling of composite plies that can significantly reduce the strength of a component and can occur even when automated fibre placement (AFP) manufacturing is used [1]. Recent developments in laser-ultrasound (LU) enable sub-ply resolution imaging of composites in a fully non-contact manner [2,3]; therefore, the technique seems feasible for wrinkle detection.

In this paper, we present results of non-contact experiments, performed with a recently developed LU scanner [2] to study wrinkle orientation in CFRPs. Key scanner components include a diode-pumped laser generating impulses of 2 mJ energy at a repetition rate up to 1 kHz, a high-sensitivity double-differential fiber-optic Sagnac interferometer, an XY translation stage with position synchronized output to trigger the laser, and a data acquisition system.

A composite sample, with out-of-plane ply wrinkling introduced during manufacturing, was fixed to the translation platform and scanned with 0.05 mm lateral XY resolution. Incident pump laser pulses, delivered along an axis inclined approximately 40° from the sample normal (Z axis), were focused to a spot size of about 2 mm (resulting in a laser fluence of about 60 mJ/cm², well below any damage thresholds for composite material illumination). Non-contact detection of US signals was performed at the same point on the surface with the fiber-optic Sagnac interferometer. Signal processing was applied to recorded signals as described in Ref. [2]. Next, signals were time-gain corrected (TGC) to compensate for exponential loss assuming an attenuation coefficient of about 2.7 cm⁻¹, yielding the B-scan presented in Fig. 1a.

Next, data were subject to tilt filtering (TF) [4] – a method averaging A-scans along local ply orientations. As can be seen from the filtered image, presented in Fig. 1b, noise was significantly reduced compared to the initial B-scan. Additionally, the delay resulting from the TF was used to calculate ply rotation angle superimposed in color on Fig. 1b. The angle information was threshold to mark the most significant angles exceeding ±2°.

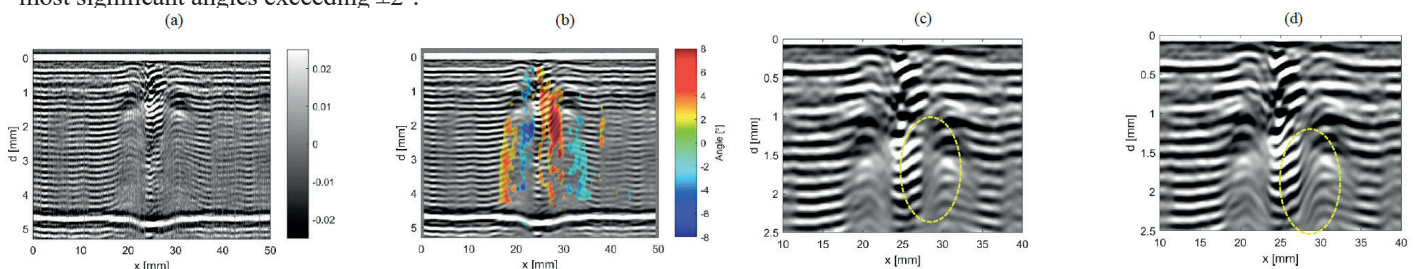


Fig. 1: LU imaging of wrinkles in composite plates. Initial B-scan processed according to Ref. [2] (a); B-mode image after tilt filtration with local ply orientation information superimposed in color (b). Zoomed area of moving average (c) and tilt-filter result (d).

For better visualization of the results in Fig. 1b, an area of most significant wrinkling is zoomed and presented in Fig. 1d. The image can be compared to a corresponding one (Fig. 1c) processed using a conventional spatial moving average (MA). Clearly, MA results in amplitude reduction in the wrinkled areas due to incoherent summation. In contrast, TF, averages time-delayed signals coherently enhancing ply waviness visualization.

As presented in this paper, laser-ultrasonics represents a feasible tool for ply wrinkle detection and visualization. TF processing not only improves SNR preserving wrinkled structure, but also provides information on local ply orientation, which can be used as a measure of wrinkle severity. The proposed method is limited in depth due to strong US attenuation in composites, destroying the structural signal at large depths. For the current setup, the maximum depth where wrinkles can still be quantified is estimated to be about 8 mm for aircraft CFRP composites.

References

1. J. P. H. Belnoue, J. Kratz, O. J. Nixon-Pearson, T. Mesogitis, D. S. Ivanov, and S. R. Hallett, in ECCM17 -17th European Conference Compos. Mater. (Munich, 2016), pp. 26–30.
2. I. Pelivanov, T. Buma, J. Xia, C. W. Wei, and M. O'Donnell, *J. Appl. Phys.* 115, (2014). doi.org/10.1063/1.4959827
3. I. Pelivanov, L. Ambrozinski, A. Khomenko, E. G. Koricho, G. L. Cloud, M. Haq, and M. O'Donnell, *Photoacoustics* 4, 55 (2016). doi: 10.1016/j.pacs.2016.05.002
4. L. Huang, Y. Petrank, S. W. Huang, C. Jia, and M. O'Donnell, *IEEE Trans. Ultrason. Ferroelectr. Freq. Control* 56, 1368 (2009). DOI: 10.1109/TUFFC.2009.1193

Pulsed excitation of ultrasound by Gaussian and Bessel laser beams in specimens of rock

George S. MITYURICH^{(1)*}, Victor V. KOZHUSHKO⁽²⁾, Victor N. MYSHKOVETS⁽¹⁾,
Denis G. MITYURICH⁽³⁾

1. Gomel State University named after F. Skoriny, Gomel, Belarus

2. V.A. Belyi metal-polymer research institute of National Academy of Sciences of Belarus, Gomel, Belarus

3. State Production Association Belorusneft, BelNIPIneft, Gomel, Belarus

george_mityurich@mail.ru

It is known that the core analysis is required to assess porosity, permeability, fluid saturation, density of the mineral skeleton (grains), lithological composition and rock structure [1]. However, the existing methods for studying the capacitive and strength properties of geomaterials are rather laborious and are associated with considerable time costs. The impact of laser pulsed radiation on absorbing media can lead to the excitation of acoustic surface, longitudinal and transverse waves for properties evaluation [2]. The efficiency of optoacoustic transformation depends on optical, thermophysical and elastic properties of materials and also polarization and energetic parameters of laser radiation [3].

The objective of paper is study of pulsed laser excitation of elastic waves, measurement of longitudinal and shear velocities in core specimens illuminated by Gaussian and Bessel laser beams [4,5] and calculation in the frame of two component model of the medium capacitive and strength properties of the rock specimens on the base of experimental measurement of optoacoustic signals.

Materials and Methods

The radiation of Q-switched Nd:YAG laser Lotis Tii LS-2134 was used. The operating wavelength was 532 nm with pulse energy of 15-20 mJ and pulse duration of 10 ns. The pulse repetition rate was 15 Hz. The detection of laser-induced ultrasonic pulses was carried out by transducer based on polarized PZT ceramics 0.2 mm thick. The electrical signal was amplified by preamplifier with high frequency at about 15 MHz. The signals were averaged by oscilloscope with analog bandwidth 60 MHz. The oscilloscope was triggered by signal of PIN photodiode. It was assumed that unfocused laser radiation has Gaussian profile, while Bessel beams were formed by axicon lens with conicity angle of 1°. Cores of different rock specimens such as limestone, dolomite, siltstone, clay, marl, sandstone of cylindrical form with thickness from 8 mm up to 16 mm were studied. The specimens with physical and technical parameters were provided by Center of study, treatment and store of core at RUP "PA "Belorusneft". The laser radiation illuminated specimen surface and ultrasonic pulses were measured from the opposite side by piezoelectric transducer.

It is noteworthy that the efficiency and diagram of excited longitudinal and shear pulses depend on the laser beam profile. In the case of Gaussian beam the time profile of longitudinal ultrasonic pulses corresponded to typical laser-induced forms. In the case of Bessel beam the ring shape distribution of intensity on the surface of the specimen increases the efficiency of shear pulses. The velocity of longitudinal and shear pulses were measured from the ratio of specimen thickness and arrival time. The values of longitudinal and shear velocities yield Young's modulus and Poisson's ratio. The calculations of the porosity were implemented in MathCAD software package.

Table 1. Results of determination of core specimen porosity

Sample number	Horizon	Lithology	Coefficient of open porosity, %, obtained by means of	
			Hydrostatic weighing	Laser optoacoustics
5768	D3ln	Sandstone	13,5	14,5
5712	D3ln	Clay	11,3	8,7
1358	D3zd(ton)	Dolomite	6,4	5,3
8465	D3sr	Limestone	4,6	4,3
6016	D3vr(pch)	Limestone	4,1	5,4
3493	D3lb	Limestone poor clayey	1,8	1,0
3814	D3ln	Clay	7,4	6,0

Conclusions

Thus, the presented paper shows the results of measurements of longitudinal and shear velocities, which were obtained in specimens of rock (cores) by means of laser pulses with Gaussian and Bessel beam profiles. In the frame of two component medium the possibilities of porosity calculation as well as calculation of elastic moduli of specimens which are required for characteristics of their strength are demonstrated. The estimated error for porosity calculation is about 5%.

References

1. M. A. Anderson, B. Duncan, R. McLin, *Oilfield Review* 25(2), 16 (2013)
2. V.É. Gusev, A.A. Karabutov, *Laser Optoacoustics* (American Institute of Physics, New York, 1993) p. 304
3. L.N. Pyatnitskiy, *Wave Bessel beams* (Fizmatlit, Moscow, 2012) p. 406 [in Russian]
4. G.S. Mityurich, M. Aleksiejuk, P. V. Astakhov, P. A. Khilo, A. N. Serdyukov, *International Journal of Thermophysics* 32 (4), 844 (2011) doi: 10.1007/s10765-010-0749-1
5. Mityurich, G.S. Photoacoustic transformation of Bessel light beams in magnetoactive superlattices / G.S. Mityurich, E.V. Chernenok, V.V. Sviridova, A.N. Serdyukov // *Crystallography Reports*. – 2015. – Vol. 60, № 2. – P. 273–279.

Contact Laser-Ultrasonic Evaluation for the Cast Turbine Blades

Alexey ZHARINOV^{(1)*}, Alexander KARABUTOV^(2,3,4), Varvara SIMONOVA^(3,4), Valeriy PIYANKOV⁽⁵⁾

1. Faculty of Physics M.V.Lomonosov Moscow State University, Moscow, Russia
2. NUST MISiS – The National University of Science and Technology MISiS, Moscow, Russia
3. ILIT RAS Branch of the FCRS “Crystallography and Photonics” RAS, Moscow region, Russia
4. ILC MSU – International Laser Center M.V.Lomonosov Moscow State University, Moscow, Russia
5. JSC “UEC-Perm Engines”, Perm, Russia

zharinov@optoacoustic.ru

High Pressure Turbine (HPT) blades operate at extremely high temperatures, high centrifugal loads and thermal cycling. The use of conventional alloys is not feasible for turbine engine operation, as they do not provide desired properties and usually have their melting point below the operating temperature. Thus, heavier Nickel base superalloys are used. Moreover, the material of HPT blades must be resistant to the property of stresses to accelerate the growth of any flaws or defects present in the alloy. The special single crystal process is used for these purposes to harden superalloy during the investment casting. Unfortunately, even in this case defects called as high temperature crystallization (HTC) cracks can appear on grain boundaries within manufacturing. There are several conventional techniques used to detect such defects but their disadvantages impose complications to their application manufacturing conditions.

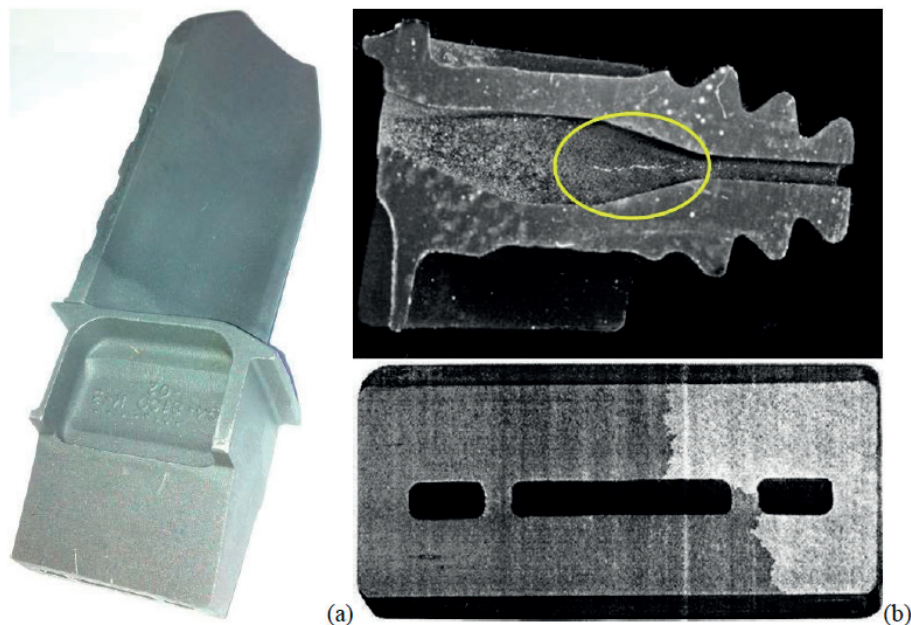


Fig.1 Blade blank (a) High temperature crystallization crack at the blade root cooling channel wall and the grain boundaries at the blade root part.

The possibility of macrostructure control in thin walls of the blade root section using laser ultrasound to solve conventional techniques limitations was experimentally investigated. Testing system design was described. Laser-ultrasonic evaluation results of the blade samples with artificial defects and HTC cracks was presented. Nickel based superalloy acoustoelasticity properties for the grain boundaries to detect were analyzed.

Combined laser ultrasonics and laser heating in high pressure cell

Pavel V. Zinin^{(1,2)*}, Vitali Prakapenka⁽³⁾, Katherine Burgess⁽²⁾, Shoko Odake⁽²⁾, Nikolay Chigarev⁽⁴⁾, Sergei Titov⁽¹⁾, Shiv K. Sharma⁽²⁾

1. Scientific-Technological Center of Unique Instrumentation, Russian Academy of Sciences, Moscow, Russia
2. Hawaii Institute of Geophysics and Planetology, University of Hawaii, Honolulu, HI, USA
3. Center for Advanced Radiation Sources, University of Chicago, IL, USA
4. Laboratoire d'Acoustique de l'Université du Maine, UMR-CNRS 6613, Université du Maine, Le Mans, France

zosimpvz@mail.ru

Understanding of the elastic behavior of minerals under high pressure is a crucial factor for developing a model of the Earth's structure because most information about the Earth's interior comes from seismological data. Therefore, direct measurements of velocities and other elastic properties of minerals at elevated pressures and temperatures are keys to understand the seismic information, allowing us to translate it into chemical composition, mineralogy, and temperature of the minerals inside the Earth.

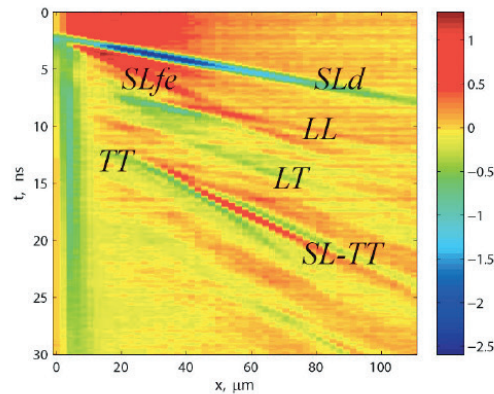
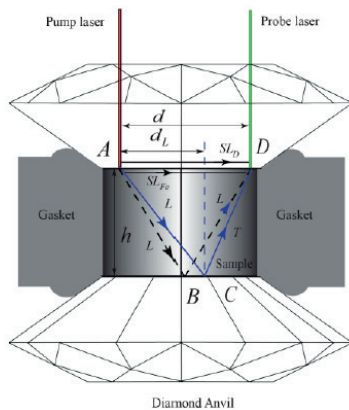


Fig. 1. Sketch of the sound waves propagation in the DAC: Fig. 2 Signal at 47 GPa with diamond and iron skimming waves SL_D , SL_{FE} , LL , LT , TT and head wave $SL-TT$ waves. Each signal is the sum of 50k-100k laser pulses at a specific pump-probe distance.

Iron is thought to be the main constituent of the Earth's core and considerable efforts have been made to understand its properties at high pressure and high temperature. However, there are discrepancies between experimental data and theory on the elastic behavior of iron under high pressure and high temperature conditions. To understand the reason for this, the shear and longitudinal wave velocities of iron and iron alloys at high pressure and high temperature should be measured directly.

The advantage of the laser ultrasonic (LU) or laser opto-acoustic technique is that it allows remote measurements of time of flight of the acoustic waves inside a specimen. When an ultra-short light pulse, known as a "pump pulse", is focused onto an opaque surface the optical absorption results

in a thermal expansion that launches an elastic strain pulse. This strain pulse consists of acoustic phonons that propagate directly into the bulk as a coherent pulse. After acoustic reflection from the sample-substrate interface, the strain pulse returns to the sample surface, where it is detected by a delayed optical probe pulse through optical reflectance [1].

Recent experiments conducted at 22 GPa revealed that numerous acoustic waves (bulk, surface, interfacial, and head waves) are generated by probe laser inside acoustically multi-layered media inside high pressure cell [1,2]. Further progress in studies of the elastic properties of materials (such as iron, iron rich materials, etc.) at pressures near mantle - core interface (130 GPa) or deeper require (a) full understanding of the physics of laser excitation of acoustical waves, (b) development of theory a short acoustical pulse propagation in a thin elastic layer, (c) identification of different types of bulk, surface and interfacial waves propagating in multilayered elastic media in a high pressure cell under extremely high pressure (100 - 150 GPa). The aim of this report is to demonstrate that the shear velocity in iron can be measured at high pressures at least up to 55 GPa. We present experiments showing the

Session B1: ND&E I / Ultrasonics I

detection of direct, reflected and head waves in a steel gasket up to 55 GPa using laser ultrasonics techniques. In this report we also demonstrate that the laser ultrasonics technique combined with laser heating allows measurements of velocities of the skimming waves in iron at 2580 K and 22 GPa [3].

To illustrate the operation of the LU system in reflection mode at ambient conditions, laser-ultrasonic measurements were conducted on a steel plate. The schematic of the measurements of velocities of acoustic waves by LU in a DAC (LU-DAC) is shown in Fig. 1. In the reflection configuration the pulse laser, which causes the excitation, and the probe laser is measuring different kinds of acoustic waves including bulk longitudinal (L) and shear (T) waves. A pattern of waves observed on the surface of the steel is shown in Fig. 2. Two peaks can be assigned as the longitudinal skimming (SL) bulk waves in diamond and steel, and one to the head wave $SL-TT$.

References

- 1 N. Chigarev, P. Zinin, L.C. Ming, G Amulele, A. Bulou, V. Gusev, Applid Physics Letters 93 (18), 181905 (2008) doi: 10.1080/08957950903549519.
- 2 N. Chigarev, P. Zinin, D. Mounier, A. Bulou, L. C. Ming, T. Acosta and V. Gusev, High Pressure Research 30 (1), 78 (2010) doi: 10.1080/08957950903549519.
- 3 P. Zinin, V. Prakapenka, K. Burgess, S. Odake, N. Chigarev, S. Sharma, Review Sci. Instrum. 87 123908 (2016) doi: 10.1063/1.4972588.

Contact laser ultrasonic evaluation of residual stresses in steel pipes

E.V. Savateeva ^{1*}, E.A. Mironova ⁽²⁾, A.N. Zharinov ⁽³⁾, V.A. Simonova ⁽¹⁾, A.A. Karabutov ^(1,2,4)

*1. Institute on Laser and Information Technologies —
Branch of the Federal Scientific Research Center «Crystallography and Photonics» of Russian Academy of Sciences*

2. National University of Science and Technology MISIS

3. M.V. Lomonosov Moscow State University Faculty of Physics

4. ILC M.V. Lomonosov Moscow State University

Residual stresses in stainless steel pipes were investigated with contact laser ultrasonic evaluation. Steel pipes were subjected to non-stationary thermal loading. Studies of the residual stresses and the internal structure heterogeneity of the samples were carried out before the heat load and after it. The ultrasonic wave velocity was measured with high precision and relative variation of the velocity enables us to calculate the distribution of residual stress. The maps of the residual stress over pipes surface correspond to the distribution of the thermal load. A comparison of the internal structure of the samples and stress state maps was analyzed. The failure of the internal structure and possible estimation of the residual life is discussed.

Laser ultrasonics for non-destructive evaluation of adhesively bonded joints

Romain HODÉ^{(1,2)*}, Samuel RAETZ⁽¹⁾, Vitalyi GUSEV⁽¹⁾, Frédéric JENSON⁽²⁾,
Nicolas CUVILLIER⁽²⁾, Mathieu DUCOUSSO⁽²⁾, Vincent TOURNAT⁽¹⁾

1. Laboratoire d'Acoustique de l'Université du Mans, LAUM-UMR 6613 CNRS, Le Mans Université,
Avenue O. Messiaen, 72085 Le Mans Cedex 9, France

2. Safran Tech, Rue des Jeunes Bois – Châteaufort, 78772 Magny les Hameaux, France

*romain.hode@safrangroup.com, samuel.raetz@univ-lemans.fr,
vitali.goussev@univ-lemans.fr, frederic.jenson@safrangroup.com,
nicolas.cuvillier@safrangroup.com, mathieu.ducoussou@safrangroup.com, vincent.tournat@univ-lemans.fr*

The non-destructive evaluation of adhesively bonded joints is a major issue in the aeronautical industry. Indeed, this assembly technique has got a lot of advantages compared to more conventional ones (riveting...): it allows lighter aircraft structures and therefore reduced fuel consumption and emissions. Furthermore, a better stress distribution can be achieved between assembled parts. Nevertheless, the significant deployment of this assembly technique is currently limited by the nonexistence of a method to quantify the practical adhesion without damaging the structure. In the past 50 years, a large number of non-destructive methods have been investigated to measure bond strength quantitatively [1]. Concerning ultrasonic techniques, various approaches based on the reflection or the transmission of bulk waves at an imperfect interphase have been studied [2-3]. Other methods based on guided waves have been proposed: shear horizontal modes [4], Lamb modes [5] (especially Zero-Group Velocity modes [6]). However, up to now, none of these methods allows to quantify the mechanical strength of an industrial bonded joint. Thus, the goal of this work is to propose a new non-destructive technique to face this issue.

In order to evaluate the practical adhesion of an adhesively bonded joint, a laser ultrasonic method can be considered as a good candidate. Two main reasons can explain this choice. First, the propagation of ultrasounds in a bonded assembly may give relevant information concerning the practical adhesion. Indeed, these elastic waves interact mechanically with the bonded joint and therefore the presence of an adhesive defect should lead to a signature in the received ultrasonic signals. Secondly, a contactless method for the non-destructive evaluation of bonded joints is really interesting in an industrial context. For these reasons, lasers are used to generate and to detect ultrasonic waves on the same free surface of the assembly. The laser generation remains in the thermo-elastic regime in order to stay non-destructive.

The aim of this research project is to quantify the practical adhesion of a bonded assembly: aluminum/epoxy/aluminum. To investigate this issue, samples with different conditions of interface have been prepared. The experimental set-up (Figure 1) is composed of a first pulsed laser (Nd:YAG, Q-switched) which is used to generate the ultrasonic waves in the sample. The pulse duration is several nanoseconds. To detect the propagation of these waves, a second laser beam is focused on the free surface of the aluminum substrate. An interferometric method is employed to measure the normal displacement as a function of time. The reflection of bulk waves at an imperfect interphase or the propagation of guided waves in the bonded assembly may contain information concerning the practical adhesion because these elastic waves will interact mechanically with the bonded joint.

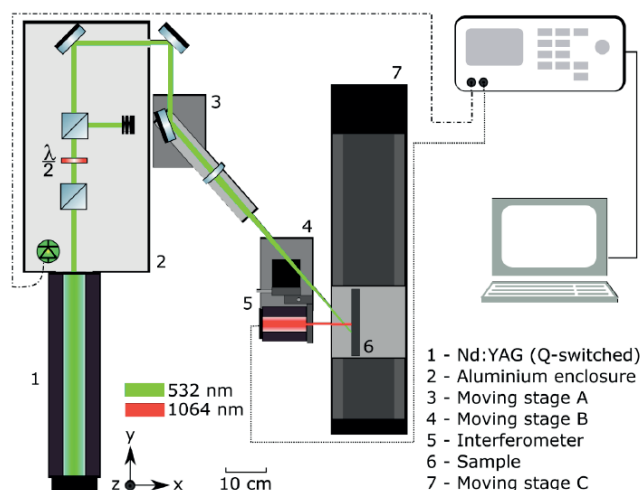


Fig. 1. Schema of the experimental set-up

The experimental data are then compared with numerical simulations. The propagation of elastic waves and their reflections at the bonding interface between two solid media are simulated with a semi-analytical method [7]. A uniform distribution of normal and transversal springs (K_N , K_T) is used to model the bonding interface [8]. These numerical simulations allow understanding and analyzing the experimental signals in order to identify the key parameters which characterize the practical adhesion of a bonded joint.

References

1. M.D. Bode, M.J. Holle, and D. Westlund, Literature review of weak adhesive bond fabrication and nondestructive inspection for strength measurement (U.S. Department of Transportation, Washington, DC, 2015).
2. A. Baltazar, L. Wang, B. Xie, and S.I. Rokhlin, *J. Acoust. Soc. Am.* 114 (3), 1424 (2003) doi:10.1121/1.1600723.
3. E. Syriabe, M. Rénier, A. Meziane, J. Galy, and M. Castaings, *Ultrasonics* 79, 34 (2017) doi:10.1016/j.ultras.2017.02.020.
4. B. Le Crom and M. Castaings, *J. Acoust. Soc. Am.* 127 (4), 2220 (2010) doi:10.1121/1.3309441.
5. M.J.S. Lowe, R.E. Challis, C.W. Chan, *J. Acoust. Soc. Am.* 107 (3), 1333 (2000) doi:10.1121/1.428420.
6. S. Mezil, F. Bruno, S. Raetz, J. Laurent, D. Royer, and C. Prada, *J. Acoust. Soc. Am.* 138 (5), 3202 (2015) doi:10.1121/1.4934958.
7. H. Meri, Ultrasonic radiation generated by laser in an anisotropic medium; effects of the optical penetration, the thermal diffusion and the electronic density diffusion, Doctoral dissertation, Université Bordeaux I, 2004.
8. J.P. Jones and J.S. Whittier, *J. Appl. Mech.* 34 (4), 905 (1967) doi:10.1115/1.3607854.

Non-contact measurements of Young's modulus in steel wires

Viktor V. KOZHUSHKO ^{(1)*}, George S. MITYURICH ⁽²⁾,
Vladimir P. SERGIENKO ⁽¹⁾, Victor N. MYSHKOVETS ⁽²⁾

1. V.A. Belyi metal-polymer research institute of National Academy of Sciences of Belarus, Gomel, Belarus

2. Gomel State University named after F. Skoriny, Gomel, Belarus

vkozhushko@mpri.org.by

The elastic properties of the wire depend on the microstructure, which changes significantly during metalwork of metal cord production. Ultrasound can be applied for evaluation of elastic properties. The dispersion is a feature of ultrasonic waves propagating in wires [1]. The velocity of high frequency part of the spectrum approaches the value of Rayleigh waves while the velocity of low frequency spectrum can be expressed as square root from the ratio of Young's modulus and density [2]. The problem of testing concerns acoustic contact both for excitation and detection of elastic disturbances in the steel wires. The combination of two non-contact technique such as laser-induced ultrasound and electromagnetic acoustic transducers (EMATs) possesses some advantages that will be considered in this paper.

Materials and Methods

The steel wires of different diameters from 0.225 mm up to 1.83 mm, were cut to parts of length more then 100 mm. The wires were magnetized by permanent NdFeB magnet of ring shape with the field of 0,25 T before measurements. The external radius of the ring magnet is 25 mm, the internal radius is 13 mm and the thickness is 3 mm. The experimental setup is presented in Fig.1. The radiation of the Q-switched Nd:YAG laser illuminated free part of steel wire. The operating wavelength was 532 nm the energy per pulse was less then 5 mJ. The laser beam was unfocused with a diameter of about 6 mm. The pulse repetition rate was 15 Hz. The signal front of PIN photodiode triggered the oscilloscope with analog bandwidth of 60 MHz. The measured signals were averaged by 16 realizations. Two EMATs were located touching wire on the distance 23 mm in between. The sensitive coils were industrial inductive elements with ferrite core. The dimension of the coil is 2.5x2.5x2 mm³. The coil included in electrical circuit of differential amplifier based on the single operational amplifier.

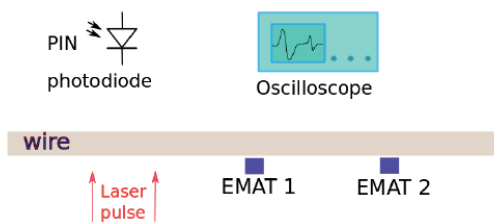


Fig. 1. Experimental setup.

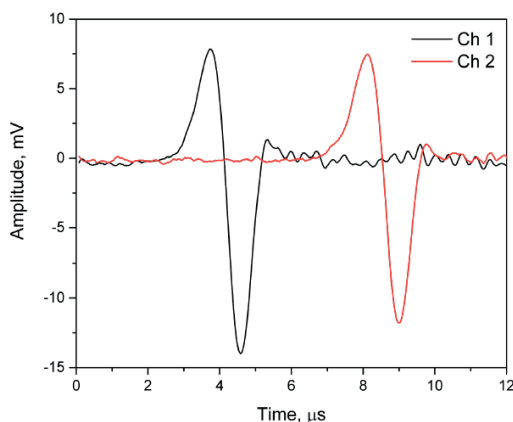


Fig.2. Signals measured in the wire with 1.6 mm diameter

Results

The optoacoustic signals measured by two EMATs are presented in Fig. 2. The spectra of the pulses are limited by high frequency at about 1.5 MHz. The time interval of 4.4 μ s was measured between points crossing base lines. The group velocity of low frequency ultrasonic waves was around 5.2 \pm 0.2 km/s. The density of the steel wires is 7.8 g/cm³ that defines Young's modulus 210 \pm 4 GPa.

The laser-induced ultrasound is well promising technique for materials evaluation [3,4]. The feature of the considered experiment is low frequency excitation of ultrasound by unfocused laser spot. The EMATs are sensitive to the transient magnetic field caused by variation of magnetization vector due to magnetostrictive effect. The laser-induced low frequency pulses demonstrated insignificant distortion during propagation that allowed detection of numerous reverberations of the probe pulses reflected at the ends of wires with changing of the phase to the opposite. The relative error of 0.75% of velocity measurement is the sum of the relative errors of time interval and distance measurements. The estimation of relative modulus error yields 2% as the sum of relative error of density and double relative error of the velocity. The suggested method of laser excitation and detection of ultrasound can be applied for on-line monitoring of manufacture of steel wires.

References

1. R.N. Thurston J. Acoust. Soc. Am. 64(1), 1 (1978) doi:10.1121/1.381962
2. H. Kolsky, Stress Waves in Solids (Dover Publications, 2003)
3. V. V. Kozhushko, G. Paltauf, H. Krenn, Acoust. Phys. 59(2), 250 (2013) doi:10.1134/S1063771013020085
4. V.É. Gusev, A.A. Karabutov, Laser Optoacoustics (American Institute of Physics, New York, 1993)

Analysis of photoinduced phase transitions in photochromic liquid crystals by means of the photopyroelectric (PPE) calorimetric technique

Stefano PAOLONI, Fulvio MERCURI, Ugo ZAMMIT*

Dipartimento di Ingegneria Industriale, Università di Roma "TorVergata", Via del Politecnico 1, 00133 Rome, Italy

stefano.paoloni@uniroma2.it

Liquid crystals (LCs) are characterized by a rich a variety of phase transitions between their different mesophases. In this respect, LCs are traditionally classified as thermotropics or lyotropics depending on whether the phase transitions are stimulated by, respectively, a change in the temperature or in the concentration. Recently, there has been increasing interest in a new class of LC, named phototropics, in which phase transitions are induced using light. Phototropic LCs typically consist of photoactive molecules dispersed into a LC host. Among others, photoinduced phase transitions have been recently observed in mixtures comprising LCs and naphthopyran (NP) [1] guest molecules. In fact, upon UV irradiation the NP molecules undergo a conformational change from a *closed* form to an *open* form which results in a significant modification of the NP molecular shape being the *open* form more elongated and planar than the *closed* form. While the bent shape of the equilibrium *closed* form does not conform with the "rod-like" shaped molecules of most conventional LCs, the similarity between the *open* form and the LC molecules can improve the order of the LC mesophase even to the point of inducing an isothermal phase transition to a more ordered mesophase.

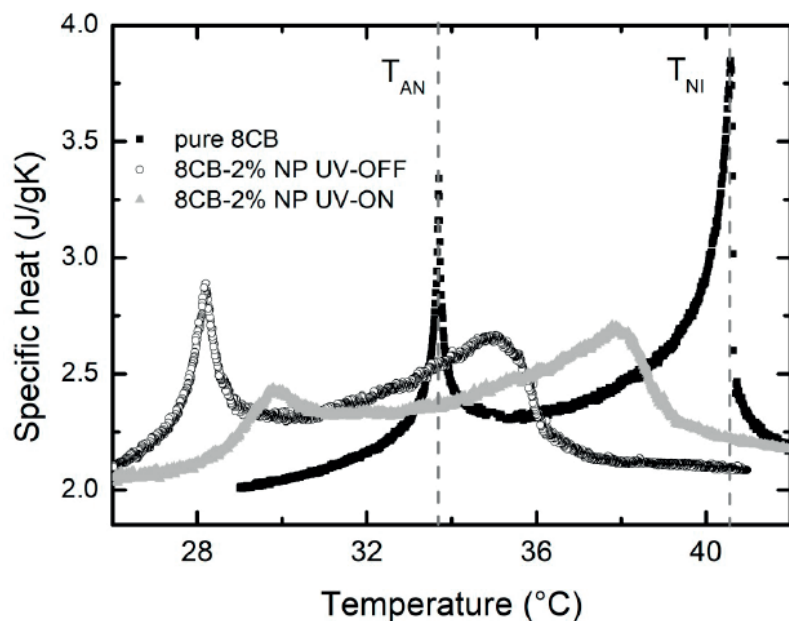
Among others, calorimetric techniques are typically employed for the experimental characterizations of phase transitions. However, such techniques have not yet been applied to study of light induced phase transitions in phototropic LCs mainly because of the difficulty of introducing the light beam onto the sample during the calorimetric evaluations. In this respect, thanks to the optical transparency of both the pyroelectric transducer and the respective ITO electrodes, the photopyroelectric (PPE) calorimetry [2] technique has been demonstrated a valuable tool thanks to the unique capability of measuring the thermal parameters of the sample even during its illumination by the light inducing the photoisomerization of the photoactive molecules.

In the present study, a PPE setup has been employed for the thermal parameters measurement in 4-(n-octyl)-4'-cyanobiphenyl (8CB) and in 4-n-pentylphenylthiol-4'-octyloxybenzoate (8S5) LC-NP mixtures before, during, and after the photo-activation of

the dispersed NP photochromic molecules over a temperature range including both the smectic A-Nematic and Nematic-Isotropic phase transition temperatures.

As shown in Fig. 1, the evaluation of the temperature dependence of the specific heat enabled the determination of the photoinduced upward shift of the phase transition temperature values. In addition, the analysis of the specific heat profiles over the smectic A-Nematic transition temperature allowed to get some insights about the changes of the phase transition critical behaviour induced by the NP molecules photoisomerization.

Fig. 1. Specific heat temperature dependence for: (■) pure 8CB; (○) 8CB-2% NP mixtures before UV irradiation; (▲) 8CB-2% NP mixtures during UV irradiation. For a clearer presentation, two vertical lines have been inserted to put into evidence the Smectic A-Nematic (AN) and Nematic-Isotropic (NI) transition temperature in pure 8CB.



References

1. T.Kosa, L. Sukhomilina, L. Su, B. Taheri, T.J. White and T.J. Bunning, Nature 485, 347 (2012) doi:10.1038/nature11122
2. U. Zammit, M. Marinelli, F. Mercuri, S.Paoloni and F. Scudieri, Rev. Sci. Instrum. 82, 121101 (2011) doi:10.1063/1.3663970

Photothermal heterodyne imaging (PHI) of gold nanoparticles: simulation and experiments

Yonghui Wang^{(1,2)*}, Junyan Liu^{(1,2)*}, Fei Wang^(1,2), Yang Wang^(1,2)

1. School of Mechatronics Engineering, Harbin Institute of Technology, Harbin, 150001, China

2. State Key Laboratory of Robotics and System, Harbin Institute of Technology, Harbin, 150001, China

ljywlj@hit.edu.cn

The photothermal heterodyne imaging (PHI) has been as a far field optical superresolution imaging technique with application of gold nanoparticles (NPs), protein, DNA and cell structure. The simulations and experiments of gold NPs (~100 nm) by PHI are reported. A modulated pump laser beam (532 nm) is employed to heat gold NPs, and it induces a continuous thermal wave field in the medium of gold NPs. The thermal wave field furthermore results in a modulated scattering field of probe laser (638 nm) as PHI signal. The thermal wave field and scattering field were calculated through solving heat conduction model and Maxwell equations by finite element method (FEM). The effects of probe laser power, the pump laser power and modulated frequency on PHI signals were deeply analyzed by FEM simulation. The PHI experiments of gold nanoparticles were performed on a homemade PHI system. The results show a good agreement with simulation analysis and indicates that PHI method is available for gold NPs microscopic imaging. Simultaneously, PHI provides a powerful tool for gold NPs imaging compare to traditional optical imaging. The simulation far field scattering intensities of line polarized probe beam with changes of pump beam power are shown in Fig. 1. The CCD and PHI imaging of gold NPs are presented in Fig. 2.

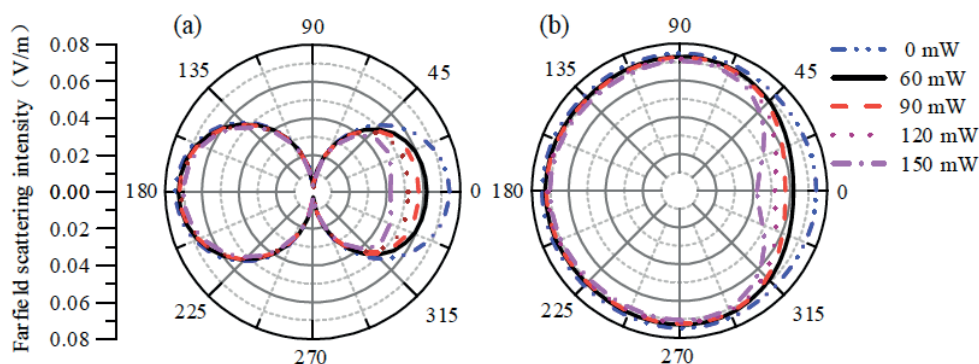


Fig. 1. The far field scattering intensity, (a) Perpendicular to the polarization direction, (b) Parallel to the polarization direction

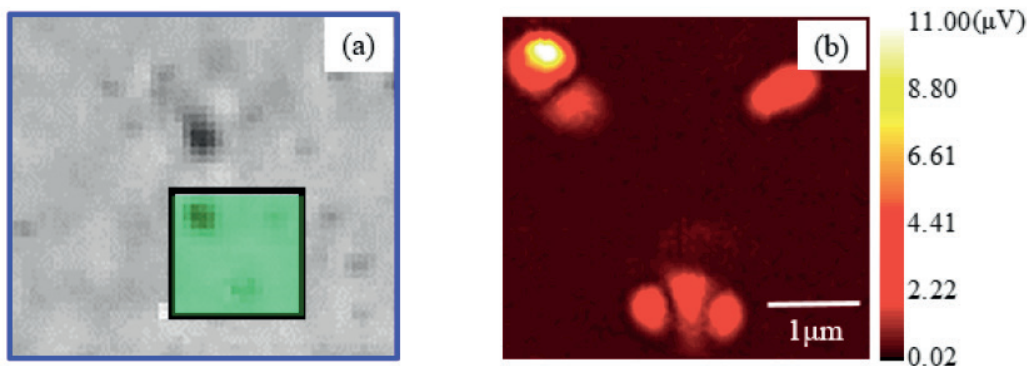


Fig. 2. The image of gold nanoparticles, (a) The CCD image and (b) The PHI image

References

1. Berciaud S, Cognet L, Blab G A, Lounis B, Physical Review Letters, 93, 257402(2004) doi: 10.1103/PhysRevB.73.045424
2. Gaiduk A, Ruijgrok P V, Yorulmaz M, Orrit M, Chemical Science, 1, 343(2010) doi: 10.1039/C0SC00210K
3. Selmke M, Braun M, Cichos F, ACS Nano, 6, 2741(2012) doi: 10.1021/nn300181h

ac photopyroelectric calorimetry applied to the study of the critical behavior of magnetic transitions in intermetallic materials

A. Herrero ^{(1)*}, A. Oleaga ⁽¹⁾, P. Manfrinetti ^(2,3), A. Provino ^(2,3), and A. Salazar ⁽¹⁾

1. Departamento de Física Aplicada I, Escuela de Ingeniería de Bilbao, Universidad del País Vasco UPV/EHU, Bilbao, Spain

2. Department of Chemistry, University of Genova, Genova, Italy

3. Institute SPIN-CNR, Genova, Italy

aritz.herrero@ehu.es

Intermetallic materials showing a large magnetocaloric effect and giant magnetoresistance are interesting due to their technological application as cryocoolers. In order to evaluate the potential of different candidates, a thorough understanding of their physical properties is needed. One of the most promising intermetallic families is the ternary RTX family (R=rare earths, T= 3d/4d/5d transition metals and X=p-block elements). In this work our attention is focused on RSc(Si,Ge) (R=Nd, Gd, Pr, Sm) samples, for which thermal diffusivity has been obtained (Fig. 1) by an ac photopyroelectric calorimeter in the standard back detection configuration.

All of the materials presented here show a second order magnetic phase transition; however, these transitions are found at different temperatures and while NdSc(Si,Ge), GdSc(Si,Ge), and SmSc(Si,Ge) families order ferromagnetically below their respective critical temperatures, PrSc(Si,Ge) family orders antiferromagnetically. Due to its high resolution and sensitivity, ac photopyroelectric calorimetry is a well-known technique in order to study the critical behavior of second order phase transitions. According to the renormalization group theory, the critical behavior of these transitions in the near vicinity of the critical temperature is characterized by a set of critical exponents (α , β , γ , δ) corresponding to different universality classes. The magnetic interaction range, as well as the ordering of the spins, have been studied for the RSc(Si,Ge) family by fitting the thermal diffusivity (or its inverse) (Fig. 2) to the expressions coming from critical behavior theory, from where α is extracted. The study has been completed with magnetic measurements to obtain the rest of the parameters β , γ , δ .

It has been found that a change of the rare earth element modifies the universality class of the phase transitions in these materials: while the R=Gd family agrees with the 3D-Heisenberg class (isotropic distribution of spins), PrScSi and NdScGe are close to the mean field model (implying long-range order interactions) and NdScSi belongs to the 3D-XY model (planar ordering of the spins).

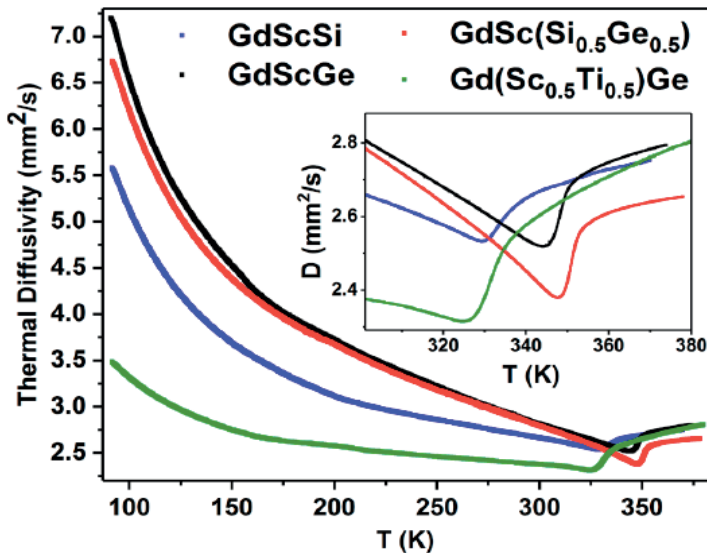


Fig. 1. Thermal diffusivity as a function of temperature for GdSc(Si,Ge) family. The inset shows a zoom-in around the second order phase transitions.

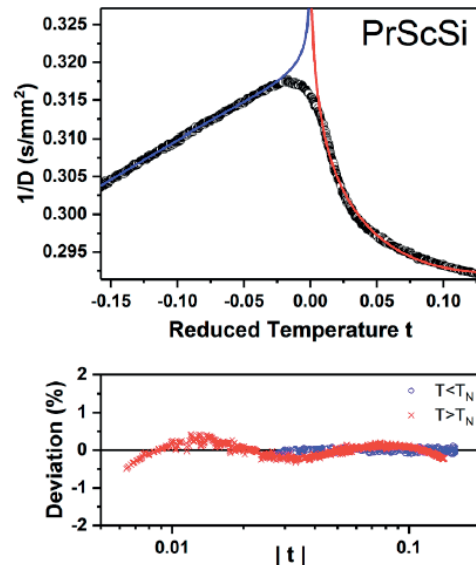


Fig. 2. Experimental (dots) and fitted curves (continuous lines) of the inverse of the thermal diffusivity as a function of the reduced temperature for PrScSi in the near vicinity of T_N (top); deviation plot for the fitting (bottom). Open circles are for $T < T_N$, crosses for $T > T_N$.

Acknowledgements

This work has been supported by Universidad del País Vasco UPV/EHU (GIU16/93). A. Herrero thanks the Department of Education of the Basque Government as grantee of the programme “Programa Predoctoral de Formación de Personal Investigador No Doctor”.

Photothermal Spectroscopy of Semiconducting Heterostructures

Jacek ZAKRZEWSKI^{(1,3)*}, Mirosław MALIŃSKI⁽²⁾, Michał PAWLAK⁽¹⁾

1. Institute of Physics, Nicolaus Copernicus University, ul. Grudziądzka 5/7, 87-100 Toruń, Poland

2. Faculty of Electronics and Computer Science, Technical University of Koszalin,
ul. Śniadeckich 2, 75-453, Koszalin, Poland

jzakrzew@fizyka.umk.pl

Piezoelectric photothermal spectroscopy (PPS) was used to characterize AlGaAs/GaAs heterostructures. PPS has been found to be very attractive method for monitoring of nonradiative states generated by optical absorption in semiconductors. In PPS, the stress and strain of a sample due to the absorption of electromagnetic radiation are detected by a piezoelectric transducer. The new procedure of measurements is applied. It involves the detection of the PPS signal in front and rear configurations and measurements with illumination of different surfaces of the samples. These configurations are associated with the geometry of sample and detector position. At rear mode, the sample is irradiated from one side and the detector is located on the other (non illuminated), at front mode detector is located at the illuminated surface. Four pairs of amplitude and phase spectra are obtained for each sample.

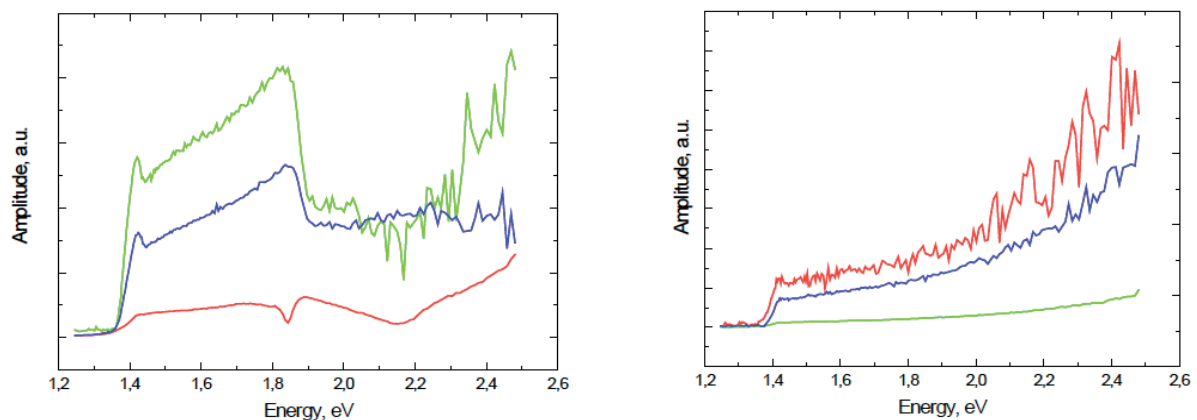


Fig. 1 Amplitude spectra of AlGaAs/GaAs for the illumination of the side of AlGaAs (left) and GaAs (right)

Due the theoretical models the waveform is different for each of configuration. The two layer model proposed by Fernelius [1] and interference model of Malinski [2] were chosen to analyze the phase and amplitude of PPS spectra. For each type of configuration, the theoretical models were fitted to experimental data in order to obtain the thermal and optical parameters of investigated material. The PPS method turned out to be especially useful for determination of the values of the energy gaps of thin layers on the substrate and the spectrum of surface states of such a structure.

References

1. N. Fernelius, J. Appl. Phys. 51 (1), 650 (1980)
2. M. Maliński, Archives of Acoustics, 27, 3, 217 (2002).

KEYNOTE

Advances in Hardness Depth Profiling by Photothermal Radiometry of Steel Mechanical Components in Vehicles

R. LI VOTI ^{(1)*}, G. LEAHU ⁽¹⁾, M. DENI ⁽²⁾, G. GUERRINI ⁽²⁾, R. BIASION ⁽³⁾, P. MORO ⁽³⁾

1. Department of Basic and Applied Sciences for Engineering, Sapienza University of Rome,
Via Antonio Scarpa 16, 00161 Rome, Italy

2. MDM Metrosoft Laboratorio Metrologico, Via IV Novembre 22 - 40061 Minerbio, Italy

3. Bifrangì, Via A. Manzoni 14 - 36065 Mussolente, Vicenza, Italy

roberto.livoti@uniroma1.it

Quality control of the performance of mechanical components subjected to hardness processing is a topic of fundamental importance in the field of automotive. The lack of hardening may cause failures with serious repercussions. The industry and the companies responsible for the hardening processes as well as for the quality control of the mechanical components are continuously seeking for improvements in the standard destructive tests performed by Vicker or Brinell durometers.

In this paper a new methodology based on photothermal radiometry (PTR) is introduced for NDT of steel mechanical components for vehicles [1-4]. Such a methodology is useful for a fast nondestructive and noninvasive inspection of the hardness depth profiles, of the effective hardening depth, of possible lack of hardening. We describe here a PTR compact system, fully automatized with robotic arms to measure the hardness depth profile of S53CG steel samples.

For the calibration of the system we have applied photothermal deflection technique to measure the thermal diffusivity of the S53CG steel, so to determine the hardness/thermal diffusivity anticorrelation curve. A thermal diffusivity changes from $13 \times 10^{-6} \text{ m}^2/\text{s}$ (unhardened) to $9 \times 10^{-6} \text{ m}^2/\text{s}$ (at 300 HV) has been found. Experimental results show accurate hardness profile reconstructions in comparison with the hardness measurements by standard Vicker test.

References

1. H. G. Walther, D. Fournier, J. C. Krapez, M. Luukkala, B. Schmitz, C. Sibilìa, H. Stamm, and J. Thoen, *Analytical Sciences*. 17, s165–s168 (2001). Quintiliani, M. et al. *J. Mater. Chem. C*, 2014, 2, 2517
2. M. Munidasa, F. Funak, and A. Mandelis, *J. Appl. Phys.* 83, 3495–3498 (1998).
3. C. Wang, A. Mandelis, H. Qu, and Z. Chen, *J. Appl. Phys.* 103, 043510 (2008).
4. R. Li Voti, G. Leahu and C. Sibilìa, "A New Device for High-Accuracy Measurements of the Hardness Depth Profile in Steels" in Proc. of 4th Int. Conference in Software Engineering for Defence Applications SEDA 2015 in *Advances in Intelligent Systems and Computing* ISBN 978-3-319-27896-4, pp.239-242 Vol. 422 (2016)

KEYNOTE

Listening to light reflections from liquids and solids: detection of elastic waves driven by the momentum of light

Nelson Guilherme Castelli ASTRATH ^{(1)*}, Luis Carlos MALACARNE ⁽¹⁾, Mauro Luciano BAESSO ⁽¹⁾, Gustavo Vinicius Bassi LUKASIEVICZ ⁽²⁾, Max BETHUNE-WADDELL ⁽³⁾, Kenneth J. CHAU ⁽³⁾, Stephen Edward BIALKOWSKI ⁽⁴⁾, Jernej LALOŠ ⁽⁵⁾, Aleš BABNIK ⁽⁵⁾, Rok PETKOVŠEK ⁽⁵⁾, Tomaž POŽAR ⁽⁵⁾

1. Department of Physics, Universidade Estadual de Maringá, Maringá, PR 87020-900, Brazil

2. Department of Physics, Universidade Tecnológica Federal do Paraná, Medianeira, PR 85884-000, Brazil

3. School of Engineering, The University of British Columbia, Kelowna, BC V1V-1V7, Canada

4. Department of Chemistry and Biochemistry, Utah State University, Logan, UT 84322-0300, USA

5. Faculty of Mechanical Engineering, University of Ljubljana, Ljubljana 1000, Slovenia

ngcastrath@uem.br

The effect of radiation forces at the interface between dielectric materials has been a long-standing debate for over a century. Yet there has been so far only limited experimental verification in complete accordance with the concurrent electrodynamic theories. Here we present measurements of the surface deformation at the air-liquid interface induced by a continuous and pulsed laser excitation and at the air-solid interface by a pulsed laser excitation. The experimental measurements are compared to the rigorous theory of radiation forces [1-3] and the results are quantitatively described by the numerical calculations of radiation forces.

The effects of radiation pressure exerted on a dielectric surface parallel to the propagation of the incident electromagnetic radiation can be interpreted as the transfer of momentum from the photons at the surface. Radiation pressure effects were predicted by Maxwell in 1871 and experimentally observed by Lebedev in 1900. In 1905, Poynting presented a detailed geometrical calculation of the force by radiation pressure of light incident from free space on a transparent and non-dispersive dielectric medium, which predicted an outward force normal to the surface of the dielectric, opposite to the direction of propagation of the incident electromagnetic field. Conflicting theories for the energy-momentum tensor were proposed by Minkowski in 1908 and Abraham in 1909 to explain this effect. These have subsequently been extensively debated in the literature over the past century. The most-used electrodynamic theories are the Abraham, Minkowski, Einstein-Laub, Chu, and Amperian formulations [2,4]. These theories can be used in conjunction with the elastodynamic theory to simulate the shape, amplitude, and speed of momentum-driven elastic waves using the elastic properties of the medium and the properties of the incident light. The absolute surface displacement measurements and the simulated displacements, based on first principles, would provide a highly rigorous method to correlate the elastic waves in an illuminated object to the electromagnetic momentum delivered by the incident light.

The measurements of the surface deformation at the air-liquid interface are performed using the photomechanical mirror technique [1,2]. In this method, the probe laser is reflected off the water surface and the cylindrically symmetric surface deformation generated by the laser excitation causes focusing or defocusing of the central portion of the probe laser beam. A convex deformation is similar to a convex mirror in turn causing the intensity of the probe laser to decrease in the far field while a concave deformation focuses the probe and thereby increases the power that passes through the pinhole placed in front of the detector (Fig. 1a). In the continuous irradiation experiment, the calculated surface distortion is always convex and the corresponding signal shows a decrease in the probe power past the pinhole at all times. As illustrated in Fig. 1b, during pulsed irradiation, the surface first produces a convex column. The column subsequently collapses after irradiation causing a concave surface perturbation. This behavior corresponds to the probe laser power initially decreasing then increasing past the pinhole. The numerical calculations are in excellent agreement with our experimental results, in a test that is significantly more discerning than the earlier experiments by Ashkin and Dziedzic [5]. This demonstrates that this light-matter system is well modeled by our present understanding of radiation forces that lead to the momentum transfer. The Helmholtz force density is used to describe the imparted pressure on the surface of the liquid.

At the air-solid interface, momentum transfer from the electromagnetic field to matter launches elastic waves within the solid [2,6,7]. This transfer is caused by a string of electrodynamic and elastodynamic phenomena, collectively bound by momentum and energy continuity. The details of this conversion, as predicted by different theories, have yet to be validated by experiments, as it is difficult to distinguish transients driven by different light-induced mechanisms [1-7]. The experiments were performed in a dielectric mirror illuminated by short laser pulses from air, generating transient elastic waves. These waves were detected by a piezoelectric sensor as transient ripples on the top (Fig. 2a) and bottom surfaces of the mirror. *Ab initio* modelling of the momentum deposition and material deformation is used to describe the creation and propagation of multicomponent elastic waves within the mirror

Session B2: Spectroscopy II / Radiometry II

(Fig. 2b). The numerical predictions were found to be in complete agreement with the measurements of surface displacements. The results offer compelling evidence that the momentum of light, transferred by radiation pressure, is responsible for the generation of the elastic transients.

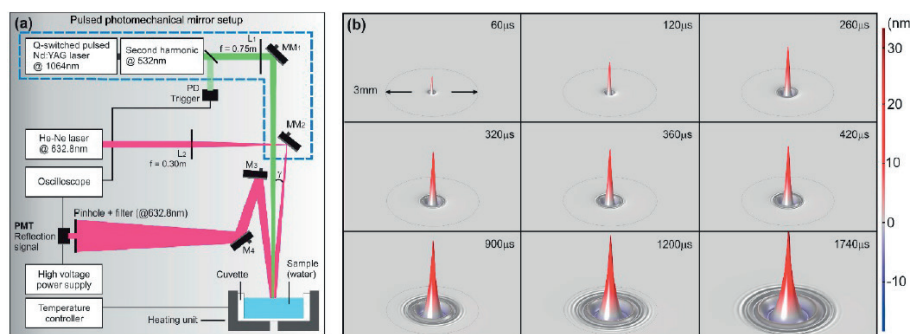


Fig. 1. (a) Schematic diagram of the apparatuses for the time-resolved photomechanical mirror used for pulsed excitation. A Q-switched pulsed Nd:YAG with second harmonic TEM00 laser beam with a pulse width of 15 ns was used to excite the sample. A continuous TEM00 He-Ne laser, almost collinear to the excitation beam, was used to probe the deformation of the sample surface. The intensity variation of the probe beam center after reflection was detected by a pinhole-laser line filter-photomultiplier assembly in the far field. (b) The numerical simulation of the time evolution of the water surface deformation under pulsed excitation. A sharp peak appears a few ms after irradiation and is subsequently dispersed on the surface. The probe beam senses the entire region affected by the excitation laser. The complex reflection pattern of the probe beam just out of the sample propagates to the detector plane. The intensity variation measured at the center of the probe beam in the far field consists of complex contributions originating from all the surface waves created on the water.

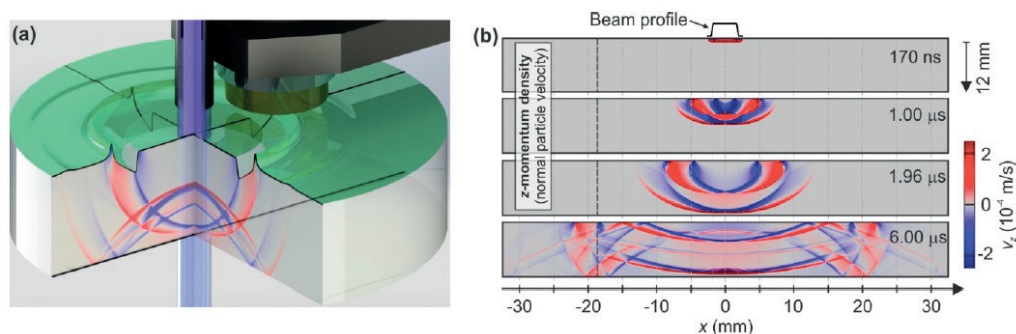


Fig. 2. (a) Perspective view of the experimental setup used for the detection of elastic waves driven by the momentum of light with the sensor deployed on the highly reflective impact surface. The laser pulse from the Nd:YAG laser impinges on the highly reflective surface of the cylindrical sample to which the sensor head is coupled. The radiation pressure launches elastic waves that propagate from the source and carry the momentum and energy transferred from the laser pulse. (b) Simulated propagation of radiation-pressure-driven elastic waves within the mirror. The frames reveal the temporal evolution of the normal component of particle velocity field, which is directly proportional to the normal component of momentum density. The elastodynamic picture describes how z-momentum is localized in various wave-types, each propagating with a different velocity.

This work presents experimental methods to quantitatively measure the momentum coupling between the electromagnetic field and matter [1-3]. These methods can be applied to characterize materials, to further advance optical manipulation technology of deformable matter, and to provide the means to empirically validate differing electrodynamic formalisms, commonly known as the Abraham–Minkowski controversy.

Acknowledgements

The authors acknowledge the financial support from the Brazilian agencies CAPES, CNPq, and Fundação Araucária, Slovenian Research Agency, NSERC Discovery Grants program, and Fulbright.

References

1. N.G.C. Astrath, L.C. Malacarne, M.L. Baesso, G.V.B. Lukasiewicz, S.E. Bialkowski, *Nature Communications* 5, 4363 (2014) doi:10.1038/ncomms5363
2. O.A. Capeloto, V.S. Zanuto, L.C. Malacarne, M.L. Baesso, G.V.B. Lukasiewicz, S.E. Bialkowski, N.G.C. Astrath, *Scientific Reports* 6, 20515 (2016) doi.org/10.1038/srep20515
3. T. Požar, J. Laloš, A. Babnik, R. Petkovšek, M. Bethune-Waddell, K.J. Chau, G.V.B. Lukasiewicz, N.G.C. Astrath, *Nature Communications* 9, 3340 (2018) doi:10.1038/s41467-018-05706-3
4. M. Bethune-Waddell, K.J. Chau, *Reports on Progress in Physics* 78 (12), 122401 (2015) doi:10.1088/0034-4885/78/12/122401
5. A. Ashkin, J.M. Dziedzic, *Physical Review Letters* 30, 139 (1973) doi.org/10.1103/PhysRevLett.30.139
6. T. Požar, J. Možina, *Physical Review Letters* 111 (18), 185501 (2013) doi:10.1103/PhysRevLett.111.185501
7. J. Laloš, M. Jezeršek, R. Petkovšek, T. Požar, *Ultrasonics* 81, 158 (2017) doi:10.1016/j.ultras.2017.06.018

Session B3: Thermography II

Sizing the width of infinite vertical cracks on moving samples using infrared thermography

Jorge GONZÁLEZ^{(1),(2)}, Arantza MENDIOROZ⁽¹⁾, Agustín SALAZAR⁽¹⁾

1. Departamento de Física Aplicada I, Escuela de Ingeniería de Bilbao, Universidad del País Vasco UPV/EHU, Plaza Ingeniero Torres Quevedo 1, 48013 Bilbao, Spain

2. Department of Applied Physics, CINVESTAV Unidad Mérida, carretera Antigua a Progreso km 6, A.P. 73 Cordemex, Mérida Yucatán 97310, Mexico.

agustin.salazar@ehu.es

The aim of this work is to size accurately the width of infinite vertical cracks on samples that are moving at constant velocity, as it is the case of in-line production or in-line quality control processes in factories, where cracks must be detected in real time, without stopping the production chain. First, we have found an analytical expression for the surface temperature of a sample containing an infinite vertical crack when it is moving at constant speed and its surface is illuminated by a focused CW-laser spot, which remains at rest. The signature of the crack is a temperature discontinuity at the crack position. We analyze the dependence of this temperature jump on the experimental parameters: laser speed, laser radius, crack width and sample thermal properties. We propose a method to size the width of vertical cracks by fitting the temperature profile along the line that contains the center of the laser spot and is perpendicular to the crack to the analytical model.

To verify the ability of this method to size infinite vertical cracks we have prepared AISI-304 stainless steel samples with calibrated vertical cracks by putting in contact two parallelepiped steel blocks. In order to calibrate the air gap between the two blocks we place nickel tapes of equal thickness between them (10, 5 and 2.5 mm) and keep the blocks under pressure. In this way, the width of the air gap is approximately equal to the thickness of the tapes. On the other hand, the surface of the blocks facing the IR camera is covered by a thin graphite layer (≈ 3 mm thick) to enhance both the absorption to the laser and the emissivity at infrared wavelengths.

We start measuring the case of two AISI-304 blocks put directly in contact without any nickel tape in between. Although the surfaces in contact are polished, the width of that crack is not zero due to the remaining slight roughness. In fact we measured the width using a lock-in thermography setup and we found $L_{ref} = 0.56$ mm. Figure 1 shows a sequence of thermograms corresponding to this sample when it is moving to the left. The white arrow indicates the position of the crack. Note that even for such a narrow fissure the temperature discontinuity is clearly marked.

In order to size the crack width we take the temperature profile along the horizontal line across the center of the laser spot and perpendicular to the crack. Figure 2 shows those profiles for two crack widths (0.56 and 2.72 mm) and for two sample speeds (3.56 and 7.53 mm/s). Dots are the experimental data and the continuous lines the fits to the model. The values in red in Fig. 2 correspond to the retrieved crack widths. As can be observed the values are consistent and in good agreement with the lock-in thermography values that used as a reference, within the experimental uncertainty, indicating the reliability of the method. The fitting of each profile is performed in less than one minute in a laptop.

It is worth mentioning that this method can be directly applied, just by performing a Galilean transformation of coordinates, when the sample remains at rest and its surface is scanned by a laser spot moving at constant speed, i.e. the so-called Flying Spot Thermography.

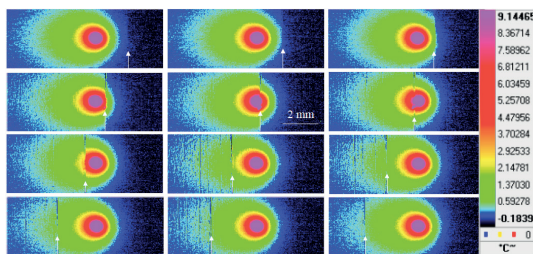


Fig. 1.

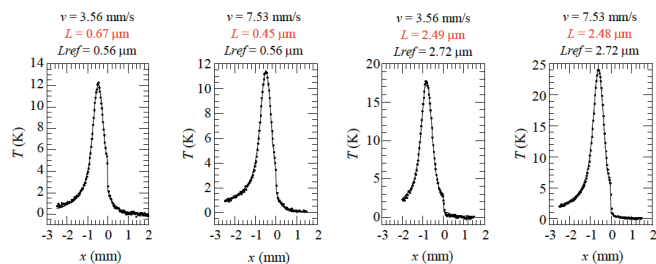


Fig. 2.

Fig. 1. Sequence of thermograms corresponding to a crack with $L_{ref} = 0.56$ mm in AISI-304. The laser is at rest while the sample is moving to the left at $v = 3.56$ mm/s. The arrow indicates the position of the crack.

Fig. 2. Temperature profiles corresponding to two cracks 0.56 mm and 2.72 mm wide, before reaching the laser. For each crack two sample speeds are used. Dots are the experimental data and the continuous lines the fit to the model. The retrieved crack width is indicated in red.

Acknowledgements

This work has been supported by Ministerio de Economía y Competitividad (DPI2016-77719-R, AEI/FEDER, UE), by Gobierno Vasco (PIBA2018/15) and by Universidad del País Vasco UPV/EHU (GIU16/33).

Measuring the width and angle of slanted cracks by lock-in thermography and discontinuous finite elements

Jorge GÓNZALEZ ^{(1),(2)}, Javier RODRÍGUEZ-ASEGUINOLAZA ⁽¹⁾, Arantza MENDIOROZ ⁽¹⁾,
 Alberto Oleaga ^{(1)*}, Agustín SALAZAR ⁽¹⁾

1. Departamento de Física Aplicada I, Escuela de Ingeniería de Bilbao, Universidad del País Vasco UPV/EHU, Plaza Ingeniero Torres Quevedo 1, 48013 Bilbao, Spain

2. Department of Applied Physics, CINVESTAV Unidad Mérida, carretera Antigua a Progreso km 6, A.P. 73 Cordemex, Mérida Yucatán 97310, Mexico.

alberto.oleaga@ehu.es

The detection and characterization of surface breaking cracks is a key aspect concerning the inspection of industrial parts. Optically excited lock-in thermography is a promising tool to detect cracks in a non-contact manner. When a modulated laser beam impinges on the sample surface close to a crack, the surface temperature shows a clear discontinuity at the crack position. The characterization of the crack in terms of its width, dimension and inclination requires solving the heat diffusion equation in order to find the perturbation of the surface temperature produced by the fissure. Unfortunately, only in the case of infinite and vertical cracks an analytical solution of the surface temperature can be found [1].

In this work, we address the challenge of determining the width and angle of slanted cracks from lock-in thermography data. With this objective, we have developed finite element methods (FEM) to describe the heat diffusion from a modulated source over a cracked sample. Usually, conventional space conformal discretization methods (Fig. 1a) have been deployed on the modeling of equivalent heat transfer phenomena, producing a continuous solution for the temperature distribution. This strategy turns out to be very complex when thin cracks are to be modeled, since high spatial node density grids are required in order to accurately reproduce the heat transfer perturbation derived from the crack. As a consequence, a highly inefficient computation is found.

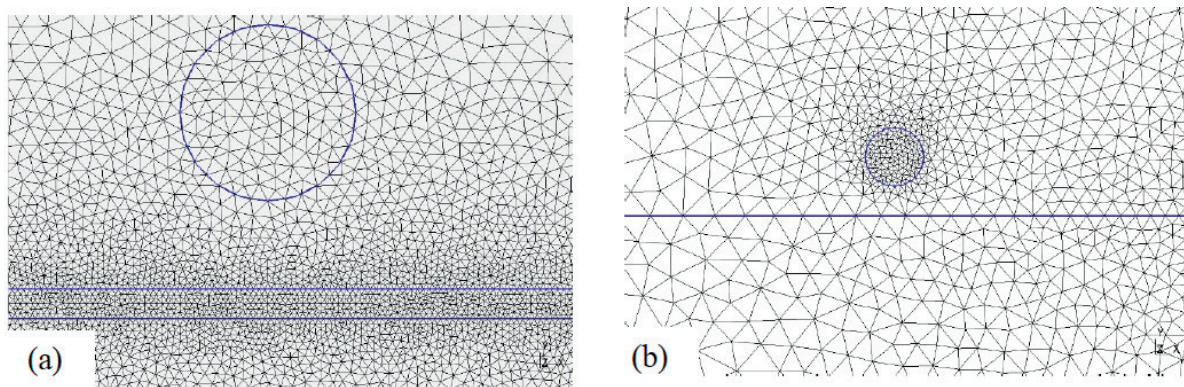


Fig. 1. (a) Surface representation of continuous FEM spatial discretization. The blue circle represents the laser spot and the region between the two blue straight lines the crack. (b) Surface representation of Discontinuous Galerkin FEM spatial discretization. The crack is a conformally meshed single interface.

To overcome this problem, a new numerical method has been developed in this work, based on a Discontinuous Galerkin FEM approach [2]. This allows a weak formulation of the heat transport phenomena, enabling a non-continuous thermal distribution over the crack, which is modeled as a single interface characterized by a thermal resistance (R_{th}) value (see Fig. 1b).

Figure 2a shows the cross-section of an opaque sample containing a slanted crack, making an angle α with respect to the surface. A modulated laser beam impinges on the sample surface at a given distance with respect to the crack position. To experimentally validate the proposed numerical approach, several stainless-steel samples with calibrated artificial slanted cracks have been prepared by means of two AISI 304 steel blocks separated by thin metallic tapes. This design strategy guarantees the controlled width of the emulated crack. Figure 2b shows the experimental profiles of the natural logarithm of the temperature amplitude along the y-axis, perpendicular to the crack, through the center of the laser spot, on three samples with the same nominal crack width ($L = 5 \mu\text{m}$) and different angles: $\alpha = 30^\circ, 45^\circ$ and 60° . Measurements were at $f = 1.5 \text{ Hz}$. The continuous line is the fit to the model assuming knowledge of the angle. The retrieved crack widths (given on the figure) are in excellent agreement with the nominal value and confirm the validity of the numerical model based on Discontinuous Galerkin FEM.

We are now developing a method to retrieve both width and angle simultaneously.

Session B3: Thermography II

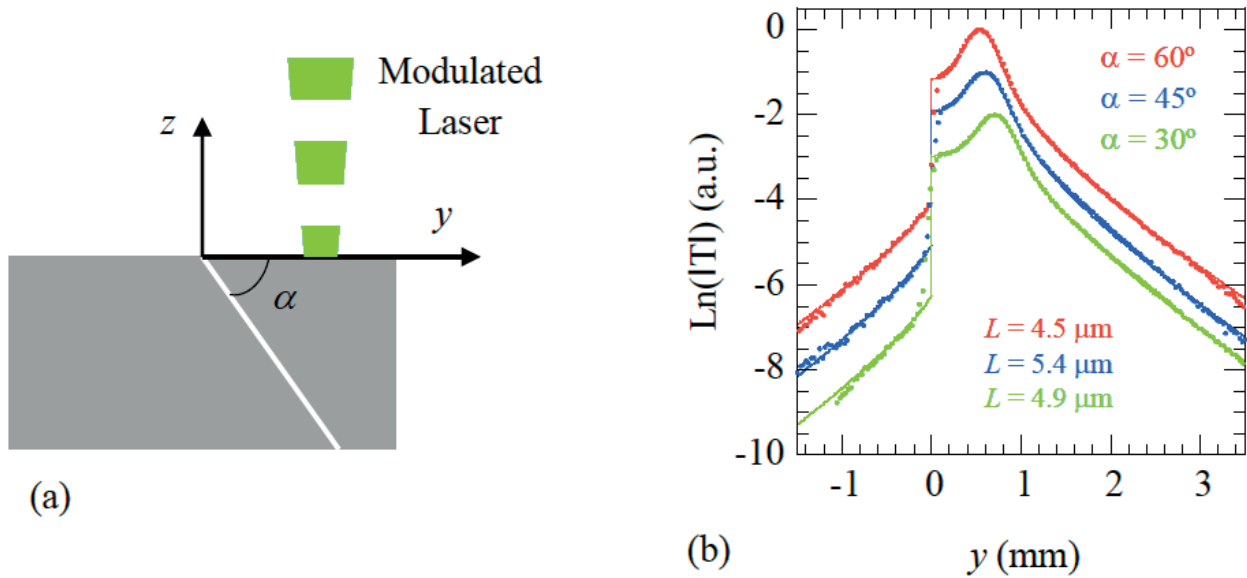


Fig. 2. (a) Cross-section of the slanted crack illuminated by a modulated laser beam. (b) Temperature profile along the y -axis for three calibrated slanted cracks of nominal width $L = 5$ mm in AISI-304 stainless steel (modulation frequency 1.5 Hz). Dots are the experimental data and the continuous line is the fit to the numerical model.

Acknowledgements

This work has been supported by Ministerio de Economía y Competitividad (DPI2016-77719-R, AEI/FEDER, UE), by Gobierno Vasco (PIBA2018/15) and by Universidad del País Vasco UPV/EHU (GIU16/33).

References

1. N.W. Pech-May, A. Oleaga, A. Mendioroz, A.J. Omella, R. Celorrio, A. Salazar, *Meas. Sci. Technol.* 25, 115601 (2014).
2. R. Celorrio, A.J. Omella, N.W. Pech-May, A. Oleaga, A. Mendioroz, A. Salazar, *Meas. Sci. Technol.* 25, 115602 (2014).

Low-Cost and Portable Active Thermography Using Cellphone Attachment Infrared Cameras

Nima Tabatabaei*, Nakisa Samadi, Artur Parkhimchyk, Marjan Razani

Department of Mechanical Engineering, Lassonde School of Engineering, York University, Toronto, Canada

Nima.Tabatabaei@Lassonde.Yorku.ca

Lock-in thermography (LIT) is a non-destructive testing technique which offers key advantages of enhanced signal-to-noise ratio and depth profilometry compared to the conventional passive thermography approach. Applications of LIT covers a broad spectrum, spanning from interrogation of industrial samples (e.g., nondestructive evaluation of materials[1]) to early diagnosis of diseases in hard and soft tissues (e.g., early detection of dental caries [2] or cutaneous melanoma[3]). However, despite these promising range of applications, commercialization and wide-spread adaption of LIT has long been impeded by the cost (usually \$10k-\$100k) and size of infrared cameras. In this paper, we demonstrate that this cost and size limitation can be overcome using cell-phone attachment infrared cameras. While the cost (~\$250) and size of such cameras are significantly less than the research-grade infrared cameras, our most recent research results [4] indicate that acceptable performance can be achieved through implementation of better and more optimized instrumentation and signal processing; thus, paving the way for commercialization of TPI technology as end-user affordable and portable products. To demonstrate efficacy of developed system, we have carried out experiments on dental samples for early detection of caries as well as on lateral flow immunoassays (LFIAs) for detection of Cannabis consumption from oral fluid.

Materials and Methods

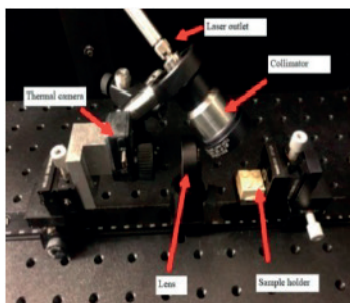


Fig 1. Developed low cost LIT system

Experimental setup includes a conventional LIT illumination sub-system in which intensity-modulated near infrared light (808 nm; Jenoptik, Jena, Germany) is collimated and intensity-homogenized before illuminating the sample. Detection sub system includes a low-cost cellphone attachment infrared camera (Seek thermal compact; Android) in conjunction with a 1" Zinc selenide objective lens offering 209x156 pixel² images. While the nominal frame rate of camera through its standard applet is less than 9fps, we have deciphered the communication protocol and frame information structure of the camera and managed to utilize USB 2.0 documentation and Microsoft Windows native application programming interfaces (APIs such as WinUSB and SetupAPI) in order to set up packets of information and send them to the camera's default endpoint address and, subsequently, acquire frame data from camera through a corresponding pipe. As such, the developed platform has not only the ability to control camera attributes (e.g., calibrate camera, acquire frame, etc) through a simple USB interface but also can achieve a stable high frame rate of

33fps through a circular buffer hierarchy and multi-threading. To demonstrate performance of developed low-cost and portable system, two series LIT experiments were conducted: (i) in response to the recent legalizations of marijuana in North America, we interrogated the photothermal responses of commercially available oral fluid LFIAs with the developed system. The interrogated LFIAs were spiked with different concentrations of THC (Δ^9 -tetrahydrocannabinol; the psychoactive substance of cannabis) while LFIAs spiked with pure saliva were used as control. (ii) To demonstrate ability of the system in early detection of dental caries, artificially induced caries were created on healthy enamel surfaces and imaged with the low cost and portable system.

Results

Figs. 2(a) and 2(b) depict LIT amplitude images from LFIAs spiked with THC concentrations of 25 and 5 ng/ml, respectively, and corresponding pure saliva controls. The study reproducibility of results 3 LFIAs were studied at each concentration. The bar plots of Fig. 2(c) demonstrate that, despite the variability in manufacturing of LFIAs, the developed low-cost system can reliably detect THC concentrations as low as 5 ng/ml in oral fluid. The results obtained from early dental caries sample (Fig. 3) also clearly demonstrates the promise of the developed low-cost and portable system in detection early stages of tooth demineralization, otherwise hidden to human eye and x-ray.

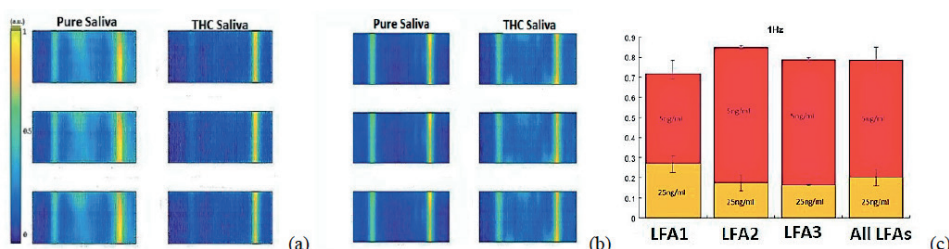


Fig. 2. Image of LFA with 25 ng/ml (a), and 5 ng/ml (b), it can be seen that as the concentration increases, the test line becomes dimmer. (c) Bar plot of 3 LFIAs with 5 and 25 ng/ml concentrations. It is obvious that as the THC concentration increases, the amplitude of test line decreases.

Session B3: Thermography II

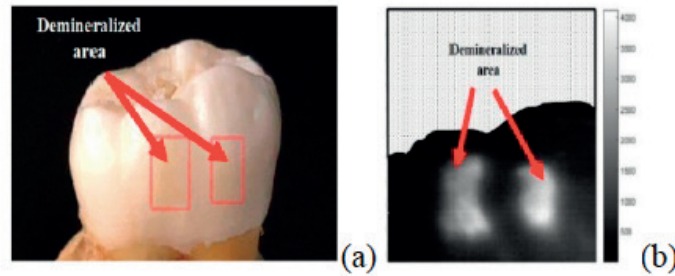


Fig. 3. Dental sample (a), amplitude image of demineralized area in enamel (b) Based on the Lock-in thermography theory; there is inverse relationship between the intensity of reflection and density of sample.

References

1. Wu, D. and G. Busse, Lock-in thermography for nondestructive evaluation of materials. *Revue générale de thermique*, 1998. 37(8): p. 693-703.
2. Tabatabaei, N., et al., On the sensitivity of thermophotonic lock-in imaging and polarized Raman spectroscopy to early dental caries diagnosis. Vol. 17. 2012: SPIE. 1-5, 5.
3. Bonmarin, M. and F.-A. Le Gal, Lock-in thermal imaging for the early-stage detection of cutaneous melanoma: a feasibility study. *Computers in biology and medicine*, 2014. 47: p. 36-43.
4. Razani, M., A. Parkhimchyk, and N. Tabatabaei, Lock-in thermography using a cellphone attachment infrared camera. *AIP Advances*, 2018. 8(3): p. 035305.

The inspection of CFRP laminate with subsurface defects by laser arrays scanning thermography (LAsST)

Fei Wang ^(1,2), Junyan LIU ^{(1,2)*}, Jiacheng Wei ⁽³⁾, Yang Wang ^{(1,2)*}

1. School of Mechatronics Engineering, Harbin Institute of Technology, Harbin, 150001, P. R. China
2. State Key Laboratory of Robotics and System, Harbin Institute of Technology, Harbin, 150001, P. R. China
3. School of Mechanical Engineering, Guizhou university, Guiyang, 550025, P. R. China

ljywj@hit.edu.cn, wyyh@hit.edu.cn

Laser arrays scanning thermography (LAsST) as a nondestructive testing and evaluation (NDT&E) tool, is presented to detect the subsurface delamination or abnormally of carbon fiber reinforced polymer (CFRP) laminate composite. A series of woven CFRP specimens with artificial bottom flat holes (BFHs) were inspected by laser arrays scanning thermography (LAsST). The thermal behavior of CFRP laminate with laser arrays scanning as local moving heat source was simulated and analyzed by finite element method (FEM), and the thermal response signal was reconstructed and in turn appeared as the analogous thermal responsible characteristic of pulsed thermography (PT). The thermal response signal was processed by using of Fourier transform (FT), Principal component analysis (PCA), cross-correlation, and partial linear square regression (PLSR). The experiments were performed on CFRP specimens, and the signal noise ratios (SNRs) of defects were calculated and employed to evaluate the defect detectability of different post processing algorithms. An optical flow approach was proposed to eliminate the effects of lateral thermal diffusion and to improve the identification of defect during LAsST inspection. The results indicate that FFT phase and PLSR based image show higher SNRs, and optical flow approach powerfully enhanced the SNRs and reduced the lateral thermal diffusion interruption.

The reconstructed thermal response signal is presented in Fig. 1, the SNRs comparisons are shown in Fig. 2, and the thermal characteristic images are illustrated in Fig. 3, respectively.

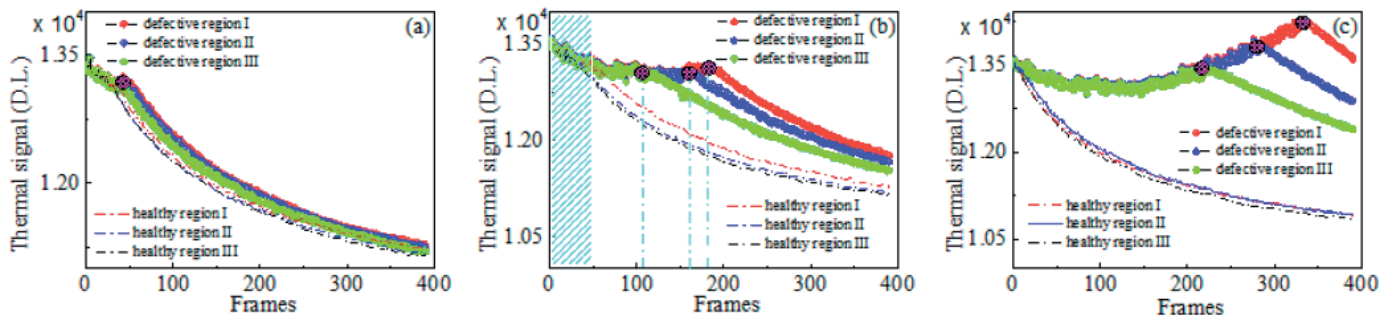


Fig. 1. The reconstructed thermal response signal, (a) defect diameter of 2.0 mm, (b) defect diameter of 5.0 mm, and (c) defect diameter of 9.0 mm

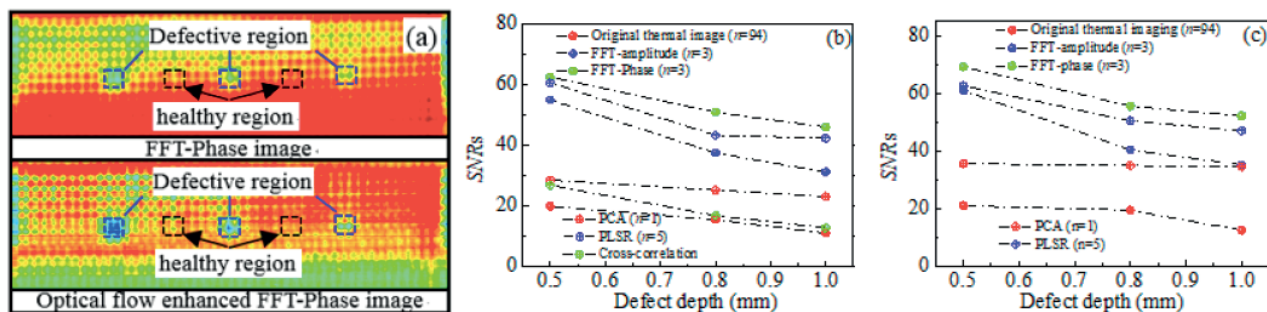


Fig. 2. The SNRs comparisons, (a) defective and healthy region (defect diameter of 2.0mm), (b) SNRs, and (c) optical flow enhanced SNRs.

Session B3: Thermography II

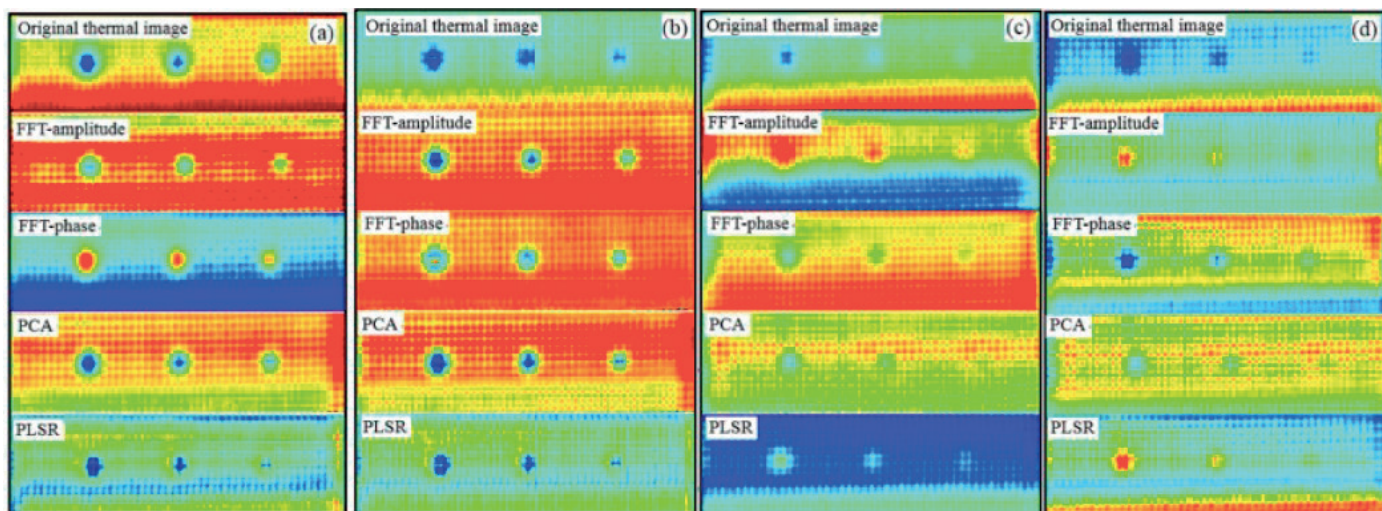


Fig. 3. (a),(b) thermal characteristic images and optical flow enhanced (defect diameter of 3.0 mm/depth of 0.5 mm, 0.8 mm, and 1.0 mm), and (c), (d) thermal characteristic images and optical flow enhanced (defect diameter of 3.0 mm/depth of 1.2 mm, 1.4 mm, and 1.6 mm).

References

1. F. Khodayar, F. Lopez, C. Ibarra-Castanedo, X. Maldague, *J. Nondestruct Eval*, 36:32 (2017)
2. D.Q. Sun, S. Roth, M. J. Black, *Int. J. Comput. Vis.*, 106:115–137 (2014)

KEYNOTE

Non-destructive investigations of Cultural Heritage by Infrared Thermography

Fulvio MERCURI ^{(1)*}, Stefano PAOLONI ⁽¹⁾, Ugo ZAMMIT ⁽¹⁾, Cristina CICERO ⁽¹⁾,
Sofia CECCARELLI ⁽¹⁾, Noemi ORAZI ⁽¹⁾, Giovanni CARUSO ⁽²⁾

1. Department of Industrial Engineering Università di Roma "Tor Vergata", Rome, Italy

2. CNR-ITABC, AdR RM1, Monterotondo (Roma), Italy

* mercuri@uniroma2.it

In the investigation of cultural heritage artworks, most of the valuable information is often not accessible by means of ordinary techniques. To this aim, over the recent years, non-destructive techniques for the inspection of artworks have been developed. Among others, infrared thermography (IRT) is nowadays established as a very effective tool and it has been extensively applied to the investigation of many kinds of cultural heritage items [1,2]. Although several of these studies have been carried out in a qualitative way by simple image analysis, recently a number of artefacts has been investigated also quantitatively by means of the IRT. That is the case of the ancient bronzes and historical books whose analysis is the subject of this work. Their study, due to the very different opto-thermal properties of the respective materials, required different thermographic approaches, both in terms of experimental configuration and of signal modeling.

In the case of the bronzes, the stratigraphic study of the assembled structures could be performed by analyzing the thermal properties of the constituent copper alloys and of the interface between the various layered elements. In particular, the analysis of the interface thermal conductance, has allowed the characterization of the manufacturing process of ancient bronzes which, in the past, were largely produced by means of the lost wax method. According to this method, after the main casting process, several kind workings like the repairing of casting faults and the surface finishing, were undertaken in order to obtain the final appearance of the statue. These workings often required the insertion of different kind of plugs and fillings producing specific inhomogeneities in the structure of the bronze. Such features can be identified and characterize by IRT thus providing important information on the *modus operandi* typical of the artist.

Fig.1, for example, concerns a result obtained on the bronze "Boxer at rest", a masterpiece of the Greek statuary preserved at the Roman National Museum of Rome [3]. The thermogram refers to a nipple which presented a different color with respect to the bronze statue while the graph shows the time dependence of the pulsed IRT signal recorded over the red dot. The experimental data have been compared with the curve obtained by a numerical analysis, based on Finite Element Method, which led to the determination of the thermal diffusivity of the materials constituting the double layer element (nipple-underlying bronze), the thermal conductance of the interface between the layers and the thickness of the nipple structure. The obtained experimental results were consistent with the theoretical results where the nipple is composed by copper about 5.5mm thick in the measured point, where bronze consisted of a copper-tin alloy characterized by a thermal diffusivity ten time lower than the one of the pure copper, and with a significant value of the interface thermal conductance, G . Such a large G value is typical of a situation where the contact between the two layers is non-ideal like that of a mechanical insertion of the nipple into the body of the statue.

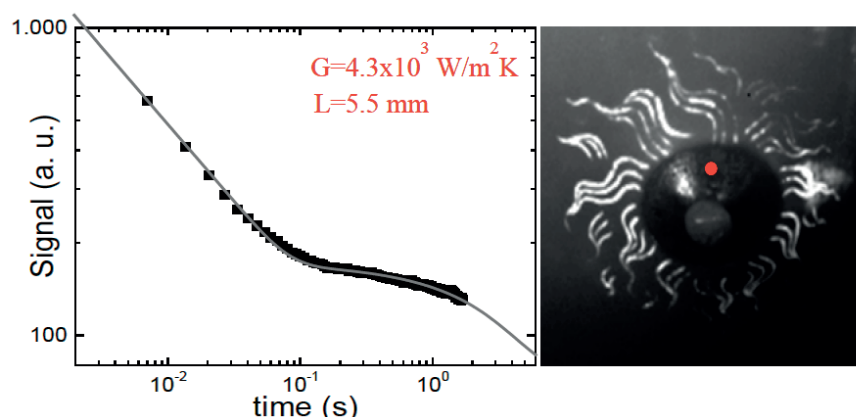


Fig. 1. Time dependence the thermographic signal and thermogram obtained over the nipple of the Boxer at Rest.

Session B3: Thermography II

As for the library material, the IRT has been successfully applied for the detection of subsurface graphical features, such as texts buried inside the bookbinding structure of ancient books [4] or drawings laying beneath painted decorations of ancient manuscripts [5]

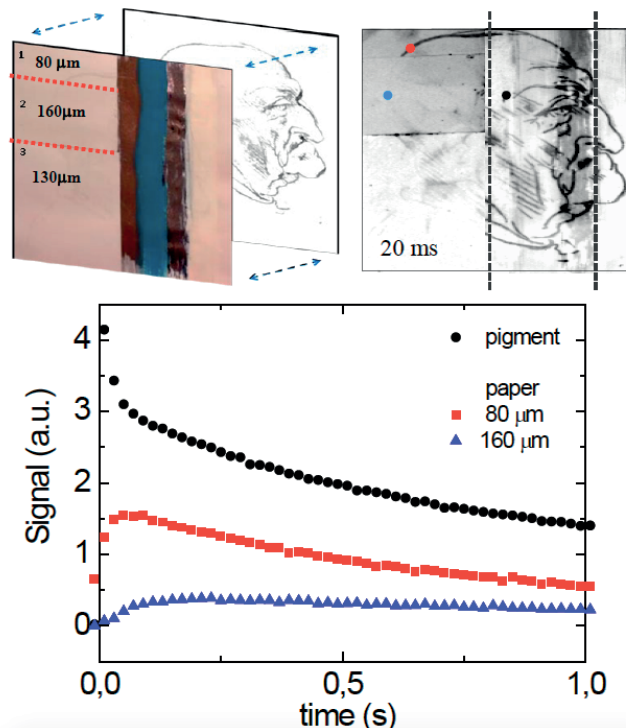


Fig. 2. Drawing covered by paper and pigment layers of different thickness. The curves describes the behavior of the IRT signal in correspondence of graphic element burier at different depth.

In this kind of investigations, the thermographic contrast is likely to be associated mostly with local differences in both the visible light absorption and infrared emission properties of the drawings with respect to the surrounding material. Even in this case, a specific theoretical model for the description of the thermographic signal generated in a semitransparent medium was developed, leading to quantitative evaluations concerning the detected features buried beneath paper and pigment layers [6].

Fig. 2 concerns the case of a drawing covered by paper leaves and pigment layers of different thicknesses. The thermogram, obtained by the pulse IRT, shows that, at 20 ms after the light heating pulse, the graphic features buried at different depths beneath paper and pigments appear with a different contrast. The time dependence of the IRT signal, recorded in the areas covered by paper layers of different depths is also shown in Fig. 2. The analysis of such profiles performed thanks to the above mentioned model, provided information on the optical and thermal parameters of the paper.

Acknowledgements

With reference to the measurement campaigns conducted at the various Cultural Institutions of Rome, the authors would like to thank M. Fidomanzo and F. Terlizzi (Biblioteca Angelica), O. Verdi and P. Buonaora (Archivio di Stato of Rome), C. Parisi Presicce and E. Di Gioia (Capitoline Museums), O. Colacicchi Alessandri, M. Ferretti, M. Serlorenzi and D. Porro (Museo Nazionale Romano).

References

1. D. Grivilov, R.G. Maev, D.P. Almond, *Can. J. Phys.* 92, 341 (2014)
2. F. Mercuri, U. Zammit, N. Orazi, S. Paoloni, M. Marinelli, F. Scudieri, *J. Therm. Anal. Calorim.* 104, 475 (2011)
3. N. Orazi, F. Mercuri, U. Zammit, C. Cicero, O. Colacicchi Alessandri, V. Brinkmann, G. Caruso, M. Ferretti, S. Paoloni, *J. Archaeol. Sci. Rep.* 24, 115 (2019)
4. F. Mercuri, R. Gnoli, S. Paoloni, N. Orazi, U. Zammit, C. Cicero, M. Marinelli and F. Scudieri, *Restaurator* 34, 195 (2013)
5. F. Mercuri, F. Mercuri, P. Buonora, C. Cicero, P. Helas, F. Manzari, M. Marinelli, S. Paoloni, A. Pasqualucci, F. Pinzari, M. Romani, A. Terrei, O. Verdi, G. Verona Rinati, U. Zammit, N. Orazi, *J. Cult. Herit.* 31, 53 (2018)
6. F. Mercuri, S. Paoloni, C. Cicero, U. Zammit, N. Orazi, *Infrared. Phys. Technol.* 89, 223 (2018)

KEYNOTE

Lock-in Thermography Imaging Characterization of Non-Flat Structures

Mingfeng Wang^{1,2,3}, Andreas Mandelis³, Alexander Melnikov³, Chinhua Wang^{1,2}

1. School of Optoelectronic Science and Engineering and Collaborative Innovation Center of Suzhou Nano Science and Technology, Soochow University, Suzhou 215006, China

2. Key Lab of Advanced Optical Manufacturing Technologies of Jiangsu Province & Key Lab of Modern Optical Technologies of Education Ministry of China, Soochow University, Suzhou 215006, China

3. Center for Advanced Diffusion-Wave and Photoacoustic Technologies (CADIPT), Department of Mechanical and Industrial Engineering, University of Toronto, Toronto, Ontario M5S 3G8, Canada

chinhua.wang@suda.edu.cn

Lock-in thermography (LIT) imaging characterization for solid materials of non-flat structures is presented. Particularly, we established a theoretical photothermal model and its experimental validation for an infinitely long solid with an inner corner of arbitrary opening angle, with the solid being irradiated photothermally by a modulated laser beam of arbitrary spatial intensity distribution directed to the corner. The thermal-wave field distribution on the flat surfaces of the solid centered at the corner was obtained using the Green function method. Experimental results based on quantitative LIT imaging were obtained and used to validate the theoretical model in which the thermal diffusivity of a stainless steel sample with an inner corner was measured and the thermal-wave field spatial distribution in the neighborhood of the inner corner was explored (Fig. 1).

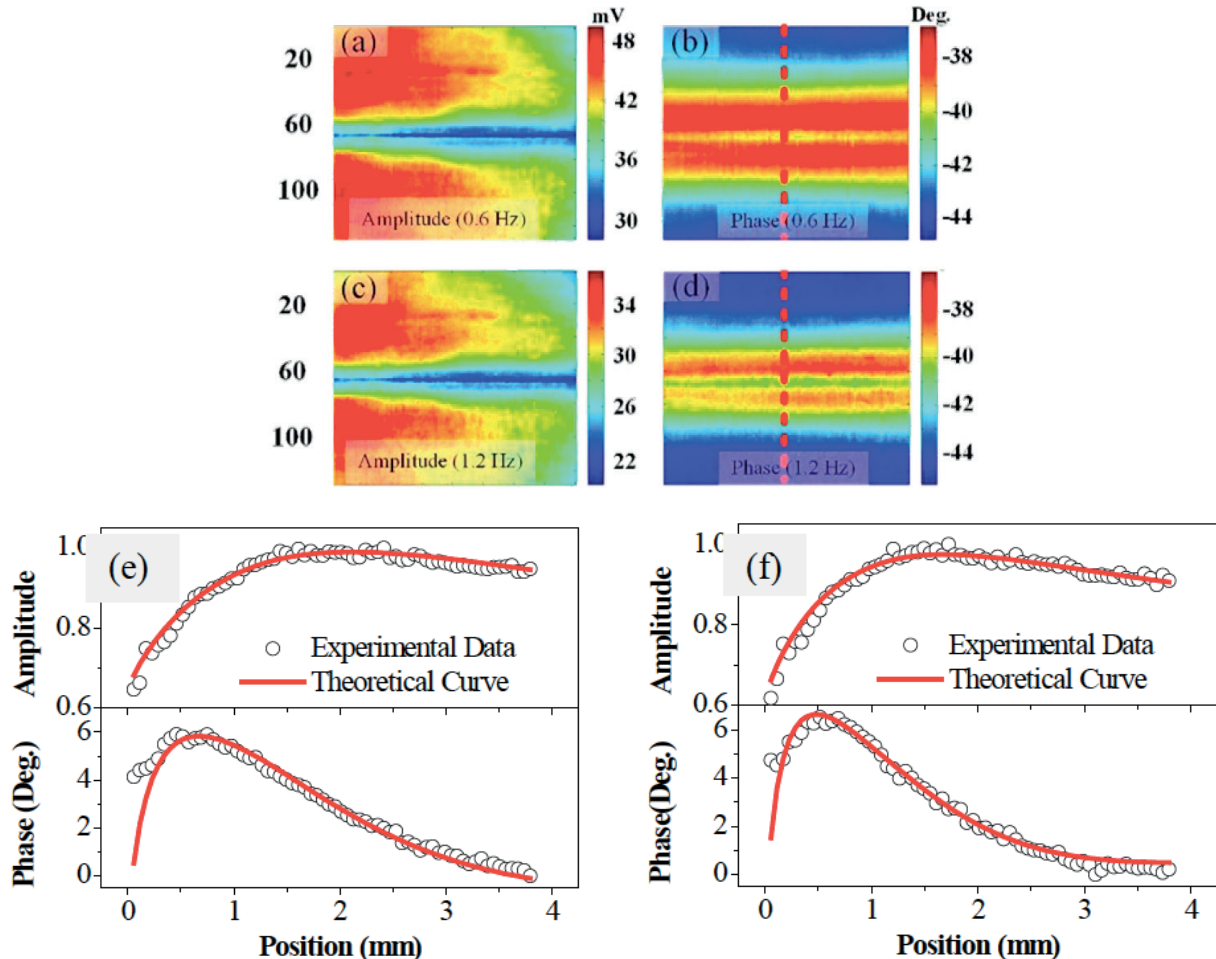


FIG. 1. LIT amplitude [(a), (c)] and phase [(b), (d)] images of the inner corner at 0.6 Hz, 1.2 Hz. Experimental results and the corresponding generalized theoretical model fits for the AISI 304 steel sample at (e): 0.6 Hz, and (f): 1.2 Hz. Data of amplitude and phase at the pixel row # 80 were used.

Session B3: Thermography II

The thermal-wave theory-based LIT imaging technique provides a fast quantitative tool for thermal property measurements and/ or non-destructive evaluation of non-flat structures in industrial applications. It also generates valuable physical insights into the spatial distribution of the thermal-wave field in the neighborhood of geometric discontinuities such as inner corners in solids.

References

1. G. Busse, D. Wu, and W. Karpen, "Thermal wave imaging with phase sensitive modulated thermography," *J. Appl. Phys.* 71(8), 3962 (1992).
2. C. Wang, A. Mandelis, and Y. Liu, "Photothermal radiometry with solid cylindrical samples," *J. Appl. Phys.* 96(7), 3756 (2004).
3. R. Tai, J. Zhang, C. Wang, and A. Mandelis, "Thermal-wave fields in solid wedges using the Green function method: Theory and experiment," *J. Appl. Phys.* 113(13), 133501 (2013).
4. A. Mandelis, *Diffusion-Wave Fields: Mathematical Methods and Green Functions* (Springer, New York, 2001).

Thermographic porosity estimation in composite structures using virtual A-scans

Holger PLASSER ^{(1)*}, Günther MAYR ⁽¹⁾, Gregor THUMMERER ⁽¹⁾, Günther HENDORFER ⁽¹⁾, Peter BURGHOLZER ⁽²⁾

1. Josef Ressel Centre for Thermal NDE of Composites, University of Applied Sciences Upper Austria, Wels, Austria
 2. RECENTD - Research Centre for Nondestructive Testing, Linz, Austria

holger.plasser@fh-wels.at

In this work, the quantitative evaluation of porosity in carbon fiber reinforced plastics (CFRP) with pulsed thermography data is shown by applying the Virtual Wave Concept (VWC) [1]. Therefore, a virtual temperature signal T_{virt} is calculated by applying a local transformation at the point r to the measured surface temperature data T . This transformation is a linear inverse problem and can be formulated as a Fredholm integral of the first kind

$$\int_{-\infty}^{\infty} K(t, t') T_{\text{virt}}(\mathbf{r}, t') dt' = T(\mathbf{r}, t), \quad (1)$$

where the right-hand side T and the kernel K are in principal known functions, while T_{virt} is the unknown solution. The aim is to find the virtual wave field T_{virt} from the measured temperature field T and the corresponding model K . The kernel K allows a transformation between the heat conduction equation and the wave equation

$$\int_{-\infty}^{\infty} K(t, t') T_{\text{virt}}(\mathbf{r}, t') dt' = T(\mathbf{r}, t), \quad (1)$$

where α is the thermal diffusivity and c the virtual speed of sound. It can be discretized to produce a matrix equation

$$\mathbf{T} = \mathbf{K} \mathbf{T}_{\text{virt}}, \quad (3)$$

where \mathbf{T} and \mathbf{T}_{virt} are the vectors of the measured temperature signal and the virtual wave signal. Since the problem is severely ill-posed, the alternating direction method of multipliers (ADMM) [2] is used as regularization technique. Prior information, such as positivity and sparsity of the virtual wave field, is included in the ADMM procedure to improve the reconstruction quality (Fig. 1(a)).

The propagation of the virtual temperature can be described by the wave equation, whereby for parameter estimation well-established ultrasonic methods can be used, e.g. pulse-echo method for time-of-flight measurements [3]. In Fig. 1(b) the A-Scan representation of the analytical virtual wave and the regularized solution with the classical truncated singular value decomposition (SVD) and ADMM is shown. The time-of-flight determined from the back-wall echo of the virtual temperature signal is directly related to the thermal diffusion time $t_D = L^2 / \alpha$. Therefore, if the specimen thickness L is known the effective thermal diffusivity can be calculated and vice versa.

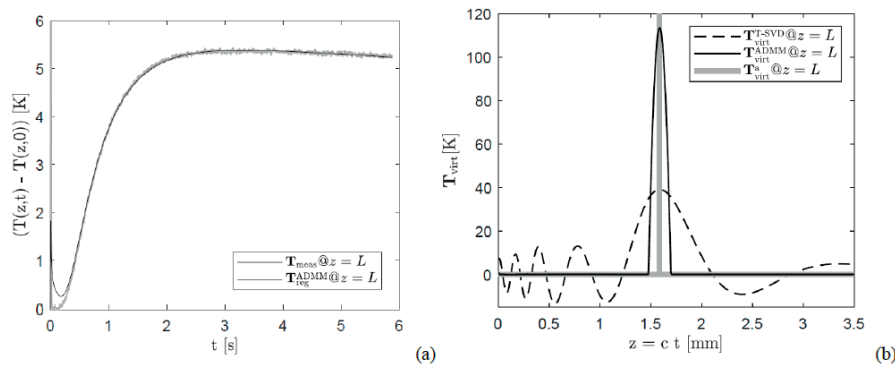


Fig. 1: Comparison between measured and regularized transmission mode temperature signal (a), virtual A-Scan comparison between ideal virtual wave and different regularization techniques (b)

The measurement of the thermal diffusion time with the VWC allows a thickness estimation of a CFRP step wedge sample as well as a porosity estimation of different CFRP test coupons. The measurement uncertainty of the VWC method was determined from

Session B3: Thermography II

the measurement data of the step wedge. Furthermore, effective medium theories are used to derive the porosity from the estimated thermal diffusivity on a range of different calibrated CFRP specimens. All thermography results are validated with X-ray computed tomography. The main advantage of the VWC is the possibility to use the same data algorithm for pulsed thermography measurements in reflection as well as in transmission configuration for parameter estimation.

Acknowledgements

The financial support by the Austrian Federal Ministry of Science, Research and Economy and the National Foundation for Research, Technology and Development is gratefully acknowledged.

References

1. P. Burgholzer, M. Thor, J. Gruber, G. Mayr, *Journal of Applied Physics* (2017) doi:10.1063/1.4978010
2. R.C. Aster, B. Borchers, C.H. Thurber, *Parameter estimation and inverse problems* (Elsevier, Amsterdam, Netherlands, 2019)
3. J. Krautkrämer, H. Krautkrämer, *Ultrasonic Testing of Materials* (Springer Berlin Heidelberg, Berlin, Heidelberg, 1990)

Super-Resolution Imaging by Sub-Diffraction Localization of Laser-Primed Temperature Variations

Maddalena COLLINI ^{(1)*}, Margaux BOUZIN ⁽¹⁾, Mario MARINI ⁽¹⁾, Amirbahador ZEYNALI ⁽¹⁾, Laura SIRONI ⁽¹⁾, Laura D'ALFONSO ⁽¹⁾, Francesca MINGOZZI ⁽²⁾, Francesca GRANUCCI ⁽²⁾, Piersandro PALLAVICINI ⁽³⁾, Giuseppe CHIRICO ⁽¹⁾

1. Physics Department, Università degli Studi di Milano-Bicocca, Piazza della Scienza 3, 20126, Milano, Italy

2. Biotechnology and Biosciences Department, Università degli Studi di Milano-Bicocca, Piazza della Scienza 2, 20126, Milano, Italy

3. Chemistry Department, Università degli Studi di Pavia, Viale Taramelli 12, 27100, Pavia, Italy

*maddalena.collini@unimib.it

Conventional thermal imaging provides temperature spatial maps based on the intensity of infrared radiation emitted by the sample and detected by a microbolometer-based thermal camera under the assumption of grey body radiance. The typically low numerical aperture of collecting Germanium lenses sets a diffraction-limited spatial resolution of ~ 0.1 - 0.5 mm. However, the nominal limit is effectively worsened to ~ 1 mm by the thermal wave diffusion in the sample, so that high sensitivity ($\sim 0.1^\circ\text{C}$) temperature mapping with tens-of-microns resolution across extended (mm-/cm- sized) fields of view is not routinely achieved.

We describe and validate here a photo-thermal super-resolution image acquisition approach based on a time modulated and spatially sparse laser-light scanning of the sample, and on the automated a posteriori localization of the resulting laser-induced temperature variations. By the non-linear surface fit of the isolated temperature peaks in the acquired thermal camera frames, light-absorbing and heat-releasing centers get localized and rendered in the final super-resolution image. While best-fit amplitudes color-code for local temperature values, peak coordinates provide morphological information on the absorbing sample. Provided the uncertainty in the peaks localization can be reduced by increasing the signal-to-noise ratio of the acquired thermal camera frames, the spatial resolution of the rendered image is ultimately determined by the excitation laser spot size, which can be tuned at will down to the $\sim \mu\text{m}$ range by adjustment of the optical path.

Photo-activated super-resolution thermal imaging is demonstrated at first with proof-of-principle experiments on synthetic ink samples (Fig.1). Comparison of our results with conventional transmitted-light images of the same samples confirms accurate imaging capability and quantifies the $60\text{-}\mu\text{m}$ attainable resolution on the adopted setup configuration. This proves resolution enhancements of a factor of ~ 6 and ~ 20 with respect to the diffraction-limited prediction and the effective $(1200\pm 180)\text{-}\mu\text{m}$ resolution of our thermal camera in conventional operation. We further demonstrate the applicability of the proposed approach to complex biological samples, and image explanted murine skin biopsies treated with Prussian blue 30-nm nanocubes. With photo-activated temperature increases as low as 0.1 - 2°C , we provide temperature-based super-resolution maps of the distribution of the absorbing nanostructures inside the tissue across mm-sized areas. This is a necessary step to develop effective in-vivo imaging tools based on the localization of photo-thermal nanoparticle tracers and for the subsequent nanoparticle-mediated photo-thermal therapy of the tissue in pathological conditions. We envision therefore potential applications and future impact of photo-activated super-resolved thermal imaging in both the biotechnological and nano-medical fields.

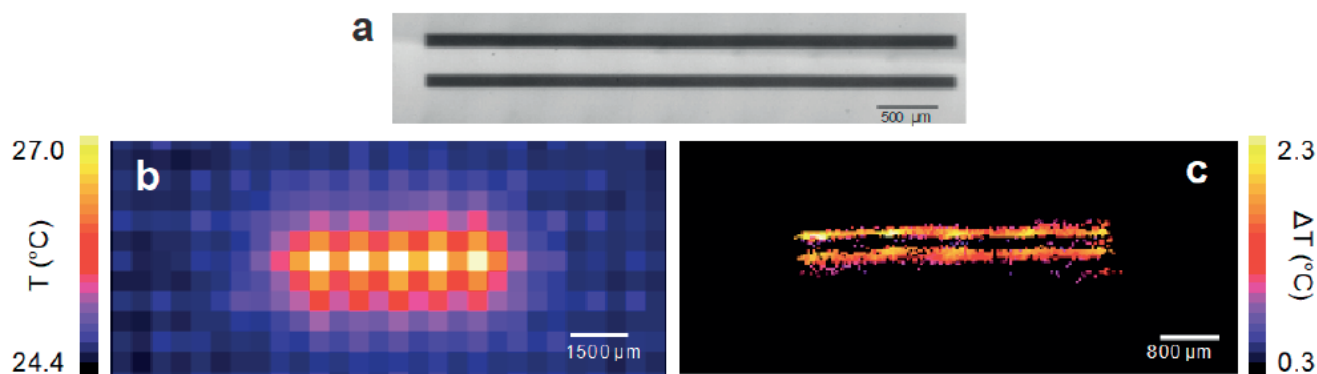


Fig. 1. Representative application of super-resolution thermal imaging. (a) Transmitted-light image of a synthetic ink sample employed for exemplary proof-of-concept demonstration of super-resolution thermography. Ink stripes are $90\text{-}\mu\text{m}$ thick at $200\text{-}\mu\text{m}$ distance. (b) Conventional thermal image of the sample in (a); note the $490\text{-}\mu\text{m}$ pixel size on the sample plane entirely contains the width of the ink-stripes pair. (c) Super-resolution image of the sample in (a) recovered by localization of sparse laser-induced temperature variations (laser excitation wavelength, 633 nm for both (b) and (c)).

Non-contact imaging of disbonds in adhesively bonded aluminum plates with photoacoustically generated shear waves

Lukasz AMBROZINSKI ^{(1)*}, Patrycja PYZIK ⁽¹⁾, Aleksandra ZIAJA-SUJDAK ⁽¹⁾,
Kajetan DZIEDZIECH ⁽¹⁾, Jakub MROWKA ⁽¹⁾, Matthew O'DONNELL ⁽²⁾, Ivan PELIVANOV ⁽²⁾

1. AGH University of Science and Technology, Krakow, Poland
2. Department of Bioengineering, University of Washington, Seattle, WA, USA

*ambrozin@agh.edu.pl

Aircraft components are carefully designed to maximize load-bearing capability and reduce mass. These demands can be met using adhesively bonded stiffeners in highly loaded zones. To satisfy safety requirements, the bonds must be inspected for various possible failure modes [1]. For typical aircraft components, two to four 0.5-4 mm thick plates are joined together. Multiple ultrasonic (US) wave reflections and mode-conversions at subsequent metal-epoxy layers make pulse-echo signal interpretation extremely difficult. Therefore, through-transmission measurements are standard practice, even though they cannot provide in-depth resolution.

Recently, laser ultrasound (LU) has overcome many limitations of conventional US testing, providing broadband signals with resolution much better than contact US probes [2-4]. For metals, however, LU is rather limited because photoacoustic generation of longitudinal waves in the normal direction is inefficient without surface ablation. Therefore, other wave modes must be used for metallic plate inspection.

In this work, LU-based damage detection in adhesively bonded aluminum plates is presented. Photoacoustically-generated shear waves propagate at an oblique angle into the inspected structure. If a discontinuity lies along their propagation path, a reflected wave travels to the surface where it can be detected. To optimize the source-receiver distance for maximal sensitivity, a two-dimensional, finite-difference simulation of a two-layered metal plate structure with plate characteristics equivalent to those of aluminum ($\rho=2700 \text{ kg/m}^3$, $E=68.9 \text{ MPa}$, $\nu=0.33$) was developed [5].

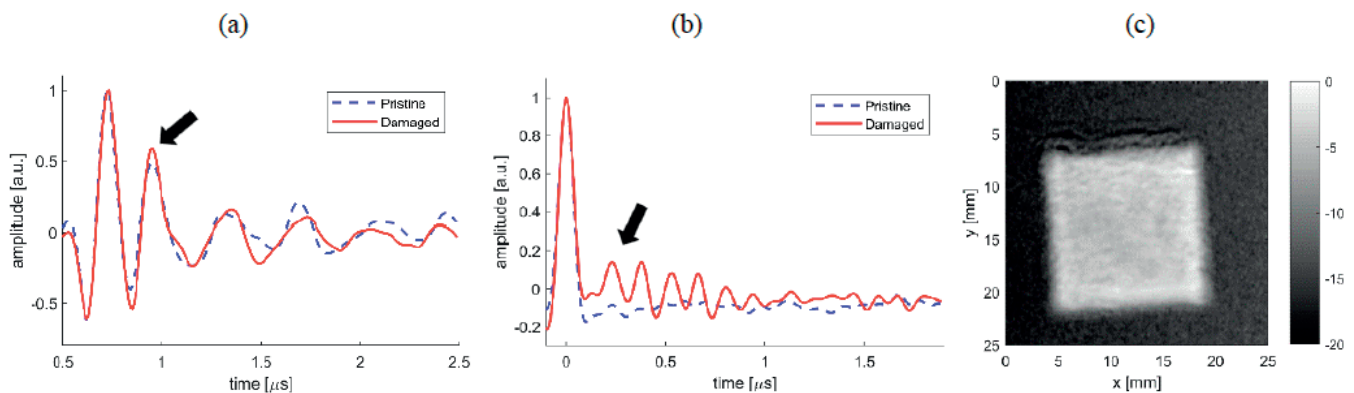


Fig. 1. Comparison of signals acquired over damaged and undamaged area. Normalized raw waveforms (a) result of inverse filtration (b); C-scan image using deconvolved signal amplitude expressed in dB for $t = 0.24 \mu\text{s}$ (c).

The inspected sample contained 3 aluminum plates (1, 1.5, and 3.5 mm thick) bonded using epoxy film. A 15x15 mm Teflon insert was placed between the first and second layers. The sample was fixed to a mechanical scanner and inspected over the defect area with 0.02 mm lateral resolution.

Experiments were performed using a LU scanner with fiber-optic Sagnac interferometer on receive (see Ref [3] for details). The excitation laser beam was focused using a cylindrical lens to form a thin line on the sample surface. Based on the numerical simulation, the source-receiver distance was set to 2 mm.

An example of A-scans acquired over bonded versus disbonded areas is presented in Fig.1a. They were normalized to the peak amplitude. These signals are very similar since not all modes were sensitive to the defect. Indeed, the largest peak at $t = 0.72 \mu\text{s}$ corresponds to the surface wave, which is expected to remain undisturbed over the inspected area. For time-of-flight equal to approx. $0.95 \mu\text{s}$, the signal acquired over the defect has a significantly larger amplitude.

To focus on differences related to the defect, signals were inverse filtered (i.e., deconvolved). First, a reference was obtained by averaging over the undamaged area. Next, spectra from each scan position were divided by the reference spectrum and multiplied by the

Session B4: ND&E II / PA/OA and Imaging II

frequency response of a Gaussian-window low-pass filter to prevent noise amplification above 10 MHz. The resultant was inverse Fourier transformed to produce deconvolved signals, such as those in Fig. 1b. Near time $t=0$, all signals contain a large impulse, as expected. For signals in the damage zone, however, more significant differences can be seen for larger delays, peaking at 0.23 μs . This value corresponds to the difference between the time of flight of surface and shear waves. Finally, the deconvolved signal amplitude at time-of-flight equal to 0.23 μs was imaged in the form of a C-scan (Fig. 1c). Clearly, the Teflon insert was successfully detected and imaged.

We demonstrated that damage in adhesively bonded aluminum plates can be detected using photoacoustically excited oblique shear waves. Because the layer geometry is usually known, the optical detection beam can be precisely positioned to receive reflected shear waves with maximum efficiency. We believe that this method can also be used in bonding control when porosity presents in the adhesive or it is not fully cured. The proposed method is non-contact and, thus, has high potential for translation into the field.

References

1. C. C. H. Guyott, P. Cawley, and R. D. Adams, *J. Adhes.* 20, 129 (1986). <https://doi.org/10.1080/00218468608074943>
2. I. Pelivanov, Ł. Ambroziński, A. Khomenko, E. G. Koricho, G. L. Cloud, M. Haq, and M. O'Donnell, *Photoacoustics* 4, 55 (2016). <https://doi.org/10.1016/j.pacs.2016.05.002>
3. I. Pelivanov, A. Shtokolov, C. W. Wei, and M. O'Donnell, *IEEE Trans. Ultrason. Ferroelectr. Freq. Control* 62, 1696 (2015). <https://doi.org/10.1109/TUFFC.2015.007110>
4. I. Pelivanov, T. Buma, J. Xia, C.-W. Wei, and M. O'Donnell, *J. Appl. Phys.* 115, (2014). <https://doi.org/10.1063/1.4868463>
5. P. P. Delsanto, R. S. Schechter, and R. B. Mignogna, *Wave Motion* 26, 329 (1997). [https://doi.org/10.1016/S0165-2125\(97\)00013-9](https://doi.org/10.1016/S0165-2125(97)00013-9)

KEYNOTE

Contact Laser-Ultrasonic Evaluation of Construction Materials

Alexander Alexeevich Karabutov^{(1,2,3)*}, Elena Borisovna Cherepetskaya⁽³⁾,
Elena Alexandrovna Mironova⁽³⁾, Elena Vasil'evna Savateeva⁽²⁾, Varvara Arkadieva Simonova⁽²⁾,
Alexey Nikolaevich ZHARINOV⁽¹⁾

1. ILC MSU – International Laser Center of Lomonosov Moscow State University, Moscow, Russia

2. ILIT RAS – Institute on Laser and Information Technologies Branch
of FSRC “Crystallography and Photonics” RAS, Shatura, Russia

3. NUST MISiS - The National University of Science and Technology MISiS, Moscow, Russia

aak@optoacoustic.ru

Basics of CLUE

Contact Laser-Ultrasonic Evaluation is a branch of non-destructive ultrasonic testing exploring laser excitation of a probe ultrasonic pulse and wideband piezodetection of reflected, transmitted or scattered pulse with high temporal resolution [1-2].

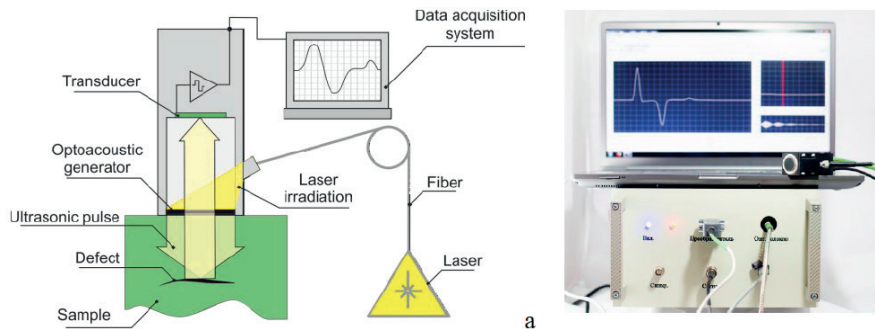


Fig. 1. The schematics of basic CLUE system (a) and its picture (b).

Typical duration of the probe pulse is ~ 70 ns. It has sharp and well repetitive shape. This makes it possible to measure the delay time between the ultrasonic pulses with the accuracy of ~ 1 ns. This corresponds ~ 3 mm path difference in metal. The prolongation of probe ultrasonic pulse in metal is ~ 0.4 mm. This provides high in-depth resolution of testing and thin “dead zone” ~ 0.2 mm. Probe ultrasonic beam has smooth phase front and no side lobes. Small diameter of ultrasonic beam ~ 3 mm provides enhanced sensitivity of defect detection. The laser-ultrasonic transducer can be mounted on the robotic stage and CLUE can be produced in automated manner [1]. In this case capabilities of CLUE can be realized with the best success.

Experimental cases

High accuracy of time-of-flight measurement makes it possible to measure the ultrasonic wave velocity with high precision. This makes relevant measurement of stress in metal by acousto-elastic effect. Commonly the dependence of ultrasonic wave variation vs stress is linear up to the limit of plasticity. Coefficients of regression should to be measured experimentally. The variation of ultrasonic wave velocity is of the order of 1% at the limit of plasticity. So, the precise measurement of the velocity at relatively short path is needed.

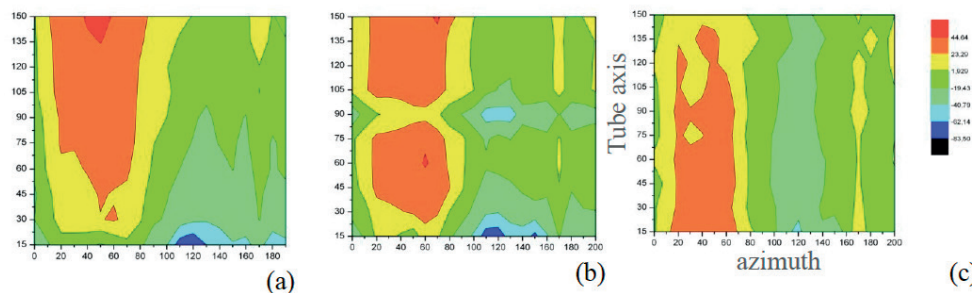


Fig. 2. The distribution of relative variation of the velocity of the wave, propagated along the axis of stainless steel tube at successive exposure to turbulent inner hot water flow (a) – 20 hours, (b) – 50 hours, (c) – 150 hours.

Session B4: ND&E II / PA/OA and Imaging II

The transformation of stress in a stainless steel ANSI321 pipe (60 mm in diameter, 5 mm wall thickness) with the exposure to turbulent flow of hot (690K, 26 MPa) water is presented in Fig.2. The injection of stream of cold water produces inhomogeneous heat flow through the tube wall and corresponding thermal stress. Color palette of the velocity variations are depicted in Fig.2c.

CLUE can be effectively used for non-uniform stress distribution investigation at a value greater 3 MPa and up to plasticity for steel [1-3].

Short duration of probe ultrasonic pulse makes CLUE effective for the investigation of composites as well. The 3-D pattern of CFRC texture get with CLUE in automated scanning is presented in Fig.3.

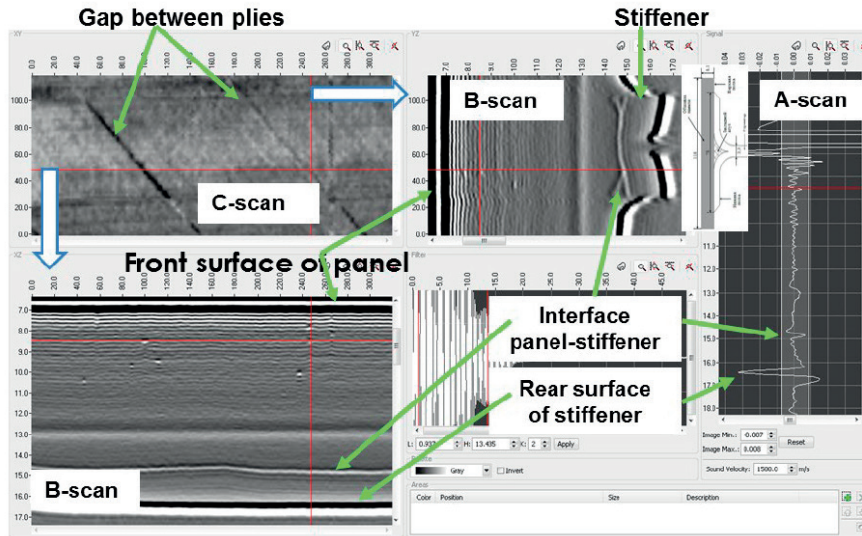


Fig. 3. The image of stiffener part texture obtained with CLUE.

The interface of automated CLUE system contains one panel of C-scan, two panels of B-scans and single panel of A-scan (Fig.3) [3]. Red cursors show the coordinates at which corresponding scans are presented. If the ultrasonic pulse propagates from softer to harder medium, the reflection at their interface takes place in phase and its image is a bright light. In an opposite case the reflection takes place out of phase and image of interface is gray line. In-depth resolution of CLUE (~0.05 mm) enables investigation the texture layer by layer – bright lines are the image of fibers, gray lines – of adhesive.

In Fig. 3 periodic structure of composite panel is evident; the structure of stiffener is seen too. C-scan shows the structure of the gap between the fiber plies. The delamination with the size of 10 mm are discriminates in any position of the part (even at curved zones). So, the presented technology seems to be very useful for the investigation of real texture of composite.

Acknowledgements

This study was supported by the Federal Agency of Scientific Organizations according to the state assignment of the ILIT RAS — Institute on Laser and Information Technologies Branch of FSRC “Crystallography and Photonics” RAS.

References

1. A. Bychkov, V. Simonova, V. Zarubin, E. Cherepetskaya, A. Karabutov, Applied Sciences-Basel 8 (10), 1931 (2018).
2. A.N. Zharinov, A.A. Karabutov, E.A. Mironova, S.N. Pichkov et al., Acoust. Journ. 65 (3), 372-381 (2019).
3. V.A. Simonova, E.V. Savateeva, A.A. Karabutov jr., A.A. Karabutov et al., RFFI Bulletin 3 (83), 10-20 (2014).

Photothermal properties of silicone polymer coatings of active laser fibers

Renat SHAIDULLIN ^{(1),(2)*}, Renata ISMAGILOVA ⁽²⁾, Oleg RYABUSHKIN ^{(1),(2)}

1. Moscow Institute of Physics and Technology, Institutskii per. 9, Dolgoprudny, Moscow region, 141700, Russia

2. Kotelnikov Institute of Radio Engineering and Electronics of RAS, Fryazino branch, Vvedensky Sq.1, Fryazino, Moscow region, 141190, Russia

r.shaidullin@phystech.edu

Output optical power of continuous wave single-mode fiber lasers achieved a 10 kW level. Some part of optical power inevitably converts into heat due to the energy difference between pump and generated photons leading to considerable heating of the active medium. High temperatures lead to deterioration of laser radiation properties and eventually to the thermal degradation of active fibers. Typical optical fiber consists of quartz silica waveguide coated with different silicone polymer layers. Due to low thermal stability of polymers degradation of polymer coatings is one of the main limiting factors of fiber lasers power scaling [1]. Earlier it was shown [2] that polymers can be additionally heated due to absorption of pump, luminescence and scattered laser radiation, leading to the faster failure of fiber laser. Therefore, we have performed measurements of absorption of silicone polymers at the most important wavelengths: optical pumping (960 nm) and laser generation of Yb (1064 nm) and Er (1550 nm) doped fiber lasers. Temperature dependences of the polymer absorption coefficients were also investigated.

Several polymers conventionally used in fiber optics were studied: Dow Corning Sylgard polymer used for protective coating of active fibers, Wacker Silgel polymer used for filling of commercial fiber laser units, and special FSX polymer with low refractive index used as a wave guiding material. Polymer samples were prepared inside the glass cuvette with internal volume $3.4 \times 1.8 \times 1 \text{ cm}^3$. Transmission spectra of the polymer samples were measured using Perkin Elmer Lambda 950 spectrometer in the 800-1100 nm and 1000-2300 wavelength ranges. The spectral pattern of all polymer samples turned out to be similar. Typical transmission spectrum of polymer (on the example of Silgel) measured at room temperature is shown in Fig. 1. As can be seen, the absorption of PS polymers in the emission wavelength ranges of Er and Tm-doped fiber lasers are significantly higher compared to that of Yb-doped laser and pump laser diodes.

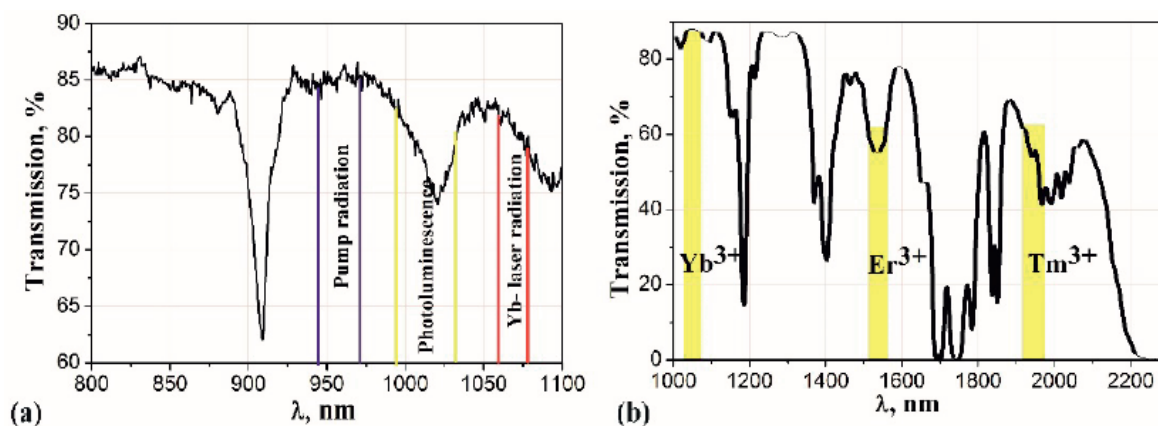


Fig. 1. Transmission spectra of Silgel polymer at room temperature in the ranges of 800-1100 nm (a) and 1-2.3 μm (b). Yellow stripes denote typical operating wavelength ranges of fiber lasers with different dopants.

It is impossible to determine optical absorption coefficient from the transmission spectra, because bulk polymers have a significant radiation scattering. Therefore, we used the laser calorimetry

method, i.e. measuring the polymer heating depending on absorbed optical power. The following radiation sources were used: GaAs pump laser diode (960 nm), Yb (1064 nm) and Er (1550 nm) doped fiber lasers. Collimated laser beam was transmitted through the polymer sample inside the cuvette. Polymer temperature was measured using a thermocouple sensor that was submerged into the polymer. In order to determine optical absorption coefficient we have developed a mathematical model of the polymer sample heating, based on the solution of the stationary heat conduction equation. Using the developed model, we calculated the absorption coefficients of all polymers at the wavelengths 960 nm, 1064 nm and 1550 nm. Temperature dependences of the absorption coefficients of polymers are shown in Fig. 2.

Session B4: ND&E II / PA/OA and Imaging II

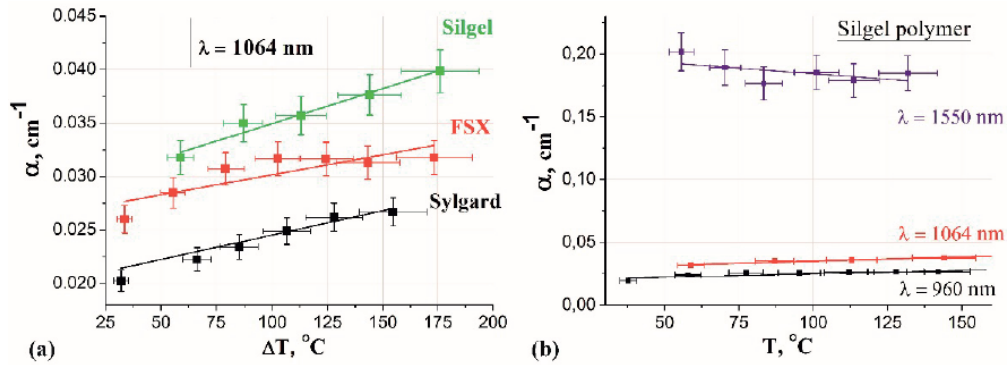


Fig. 2. Temperature dependences of the absorption coefficients of (a) all polymers at 1064 nm, (b) Silgel polymer at all wavelengths.

The averaged values of the absorption coefficients of investigated polymers are listed in Table 1. The absorption at 1550 nm wavelength is several times higher compared to other two wavelengths, what is in a good agreement with the measured transmission spectra (Fig. 1(b)).

Table 1. Temperature-averaged values of the absorption coefficients α of the studied polymers at different wavelengths (cm⁻¹)

Polymer	α ($\lambda_1 = 960$ nm)	α ($\lambda_2 = 1064$ nm)	α ($\lambda_3 = 1550$ nm)
FSX	0.019	0.030	0.11
Sylgard	0.020	0.024	0.16
Silgel	0.025	0.035	0.18

Thus, photothermal properties of silicone polymers conventionally used in fiber optics were investigated. Measured optical transmission spectra of polymers revealed the presence of absorption bands in the operational wavelength ranges of fiber lasers. Absorption coefficients of these polymers were measured using laser calorimetry technique. Its values varied from 0.02 to 0.2 cm⁻¹ depending on the polymer type, radiation wavelength and temperature.

References

1. M.-A. Lapointe, S. Chatigny, M. Piche, M. Cain-Skaff, J.-N. Maran, Proceedings of SPIE 7195, 71951U (2009) doi: 10.1117/12.809021
2. O. A. Ryabushkin, R. I. Shaidullin, I. A. Zaytsev, Optics Letters 40 (9), 1972-1975 (2015) doi: 10.1364/OL.40.001972

Influence of protection layer on photoacoustic response of polymer samples — theory and experiment

Marica N. POPOVIC⁽¹⁾, Dragan D. MARKUSHEV⁽²⁾, Miroslava I. JORDOVIC-PAVLOVIC⁽³⁾,
Katarina Lj. DJORDJEVIC⁽⁴⁾, Vesna V. MILETIC⁽⁵⁾, Mioljub V. NESIC⁽¹⁾, Slobodanka P. GALOVIC⁽¹⁾

1. Vinča Institute of Nuclear Sciences, P.O. Box 522, 11001 Belgrade, Serbia

2. Institute of Physics, University of Belgrade, Pregrevica 118, 11080 Belgrade-Zemun, Serbia

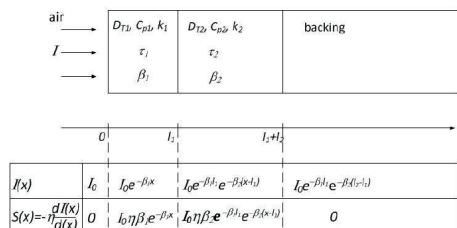
3. College of Applied Sciences Uzice, Trg Svetog Save 34, Uzice

4. Faculty of Physics, University of Belgrade, Studentski Trg 12, 11000 Belgrade, Serbia

5. The Faculty of Philosophy, University of East Sarajevo, Vuka Karadžića 30, 71126 Lukavica, East Sarajevo

maricap@vin.bg.ac.rs

Photoacoustic techniques are useful techniques for determination thermal characteristics of individual layers of multilayered structures. Many papers that observe this problem are based on the assumption that the optically excited layer of a two-layer (or multilayered) structure is surface absorber, so that optical properties of the examined layer do not affect the measured signal.



In this work, theoretical-mathematical model of transmission photoacoustic response for two-layer samples with volumetric absorption of incident radiation is obtained. This model is derived based on the generalized theory of heat conduction and equations for temperature variations given in [1]. The geometry of the problem is presented on the figure 1. The difference from the existing models is discussed.

Fig. 1. Geometry of the problem

It is analyzed case when the examined sample is covered with a thin protection layer. The influence of the investigated sample thickness upon the selection criterion for the theoretical-mathematical model (double-layer vs. surface absorbent [2,3,4]) is analyzed. Experimental results obtained on laser-sintered polyamide samples (PA12) of different thickness, uniformly covered with the layer of ink, are presented.

Theoretical predictions are compared to experimental results. It is demonstrated that, in case of thinnest samples, the influence of protection layer cannot be neglected, which is in accordance with theoretical predictions.

Acknowledgements

Authors wish to acknowledge the support of the Ministry of Education and Science of the Republic of Serbia for their support throughout the research projects III 45005 and OI 171016.

References

1. M. Popovic, M. Nestic, M. Zivanov, D. Markushev, S. Galovic, Optical and Quantum Electronics 50(9):330 (2018) doi: 10.1007/s11082-018-1586-x
2. S. Galović, Z. Šoškić, M. Popović, D. Čevizović and Z. Stojanović, Journal of Applied Physics, 116, 024901(2014), doi: 10.1063/1.4885458
3. M. Nestic, S. Galovic, Z. Soskic, M. Popovic, D. M. Todorovic, International Journal of Thermophysics 33:2203–2209 (2012), doi: 10.1007/s10765-012-1237-6
4. D. D. Markushev, M. D. Rabasovic, M. Nestic, M. Popovic, S. Galovic, International Journal of Thermophysics, 33, pp. 2210–2216 (2012), doi: 10.1007/s10765-012-1229-6

Super-Resolution Photoacoustic Imaging Using Multiple-Angle Illumination

Mohammadreza Amjadian, Zahra Kavehvash*, Rahim Faez

Sharif University of Technology, Tehran, Iran mohammadreza

amjadian@ee.sharif.edu, kavehvash@sharif.edu, faez@sharif.edu

A novel multi-illumination photoacoustic imaging structure based on synthetic-aperture-radar (SAR) approach is proposed in this paper. In conventional photoacoustic imaging systems, due to the single illumination direction of the laser source, the obtained image lacks resolution and resolution consistency in the whole image. Using multiple plane-wave illuminations from different directions help to improve field-of-view and resolution of the system based on the structured illumination concept. The multi-view illumination helps in more complete capture of spatial frequency components which could be approved through a mathematical model of the system. Capturing more frequency components, in turn, results in the improved frequency bandwidth and thus resolution of the system. Simulation results shows 1.54 dB in image quality, based on peak signal-to-noise ratio (PSNR) metric compared to a conventional structure.

Theory

Photoacoustic imaging modality experiences three physical modes in photon, thermal and acoustic pressure phases. The first step in a photoacoustic imaging process includes light illumination which makes a spatial photon distribution in the tissues. The equation that relates the photon density distribution in tissue, Ψ_{dB} , to the incident wave function, Ψ_{d0} , in Cartesian coordinate, considering the first Born approximation, can be written as [1]:

$$\Psi_{dB}(k_x, k_y, k_z, \omega) = -\frac{1}{2Dk_p} \left(O_a(k_x, k_y, k_z, \omega) * \Psi_0(k_x, k_y, k_z, \omega) \right) \frac{1}{k_x^2 + k_y^2 + k_z^2 - k_p^2} \quad (1)$$

Where O_a is the object function, and k_p and D are photon wave-number and optical diffusion coefficient, respectively. Ψ_{d0} is the incident optical wave function. Also, k_x , k_y and k_z are the wave-number components in x, y and z directions, respectively. Like the procedure followed for obtaining photon distribution, Ψ_{dB} , from the input optical function, the thermal and acoustic pressure waves could be calculated from their respective inputs, i.e. photon distribution and thermal wave, as follows:

$$T(k_x, k_y, k_z, \omega) = -\frac{\mu_a}{2\kappa_s k_t} \Psi_{dB}(k_x, k_y, k_z, \omega) \frac{1}{k_x^2 + k_y^2 + k_z^2 - k_t^2} \quad (2)$$

$$P(k_x, k_y, k_z, \omega) = -\frac{\kappa_s \beta_s \omega^2}{2c_s^2 \kappa_s} T(k_x, k_y, k_z, \omega) \frac{1}{k_x^2 + k_y^2 + k_z^2 - k_s^2} \quad (3)$$

Where μ_a , κ_s , β_s and c_s are optical absorption coefficient, thermal conductivity, thermal expansion coefficient and speed of sound in tissue, respectively. Each three phases could be represented by a frequency response in the form of

$$1/(k_x^2 + k_y^2 + k_z^2 - k_i^2)$$

where $i = s, p, t$. The squared acoustic wave-number, k_s^2 , is equal to $\frac{\omega^2}{c_s^2}$. In contrast, k_p^2 and k_t^2 are complex values where $k_p^2 = -\frac{\mu_a}{D} - \frac{\omega^2}{c_p^2}$ and $k_t^2 = i\frac{\omega}{\alpha}$ that $i = \sqrt{-1}$. Consequently, according to Eqs. (1)-(3), the first two phases, have low-pass frequency responses while the third phase, has a band-pass frequency response. These different filters in each phase of imaging cause information loss and hence the final reconstructed image would be of low resolution and contrast. Multi-angle illumination is a solution for compensating the limited bandwidth of imaging systems through the idea of SAR imaging and structured illumination. Therefore, here, for the first time, a novel photoacoustic super-resolution technique based on structured illumination concept is proposed in order to overcome this limitation.

In the proposed super-resolved structure, the configuration of Fig. 1 is suggested where illuminations are performed with sinusoidal fringes of different spatial frequencies in sequential time steps. These sinusoidal fringes are produced via interference of tilted plane-wave pairs of verifying inclination angles produced via switching a DMD [2]:

$$\Psi_0(x, y, z, \omega) = \cos(k_{px}x + k_{py}y + k_{pz}z) \quad (4)$$

In this case, the object's spectrum would become shifted with (k_{px}, k_{py}, k_{pz}) along (k_x, k_y, k_z) frequency axis before passing through the frequency response of the system. By changing the value of the interfering plane-wave angles and thus the input sinusoidal fringe,

Session B4: ND&E II / PA/OA and Imaging II

each time, a different part of the object's frequency spectrum would be passed through the limited frequency response of the system. By combining the resultant images in the spatial frequency domain like [3], a wider frequency spectrum of the object could be recovered in the output.

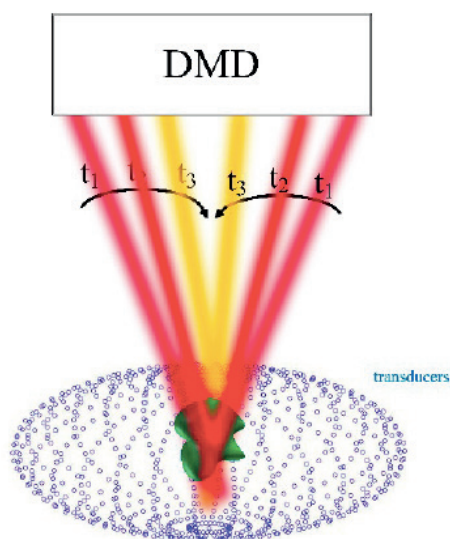


Fig. 1. The suggested experimental set-up for multi-view illumination.

References

1. N. Baddour, The Journal of the Acoustical Society of America 123, no. 5, 2577-2590, (2008)
2. Y. Jiamiao, L. Gong, X. Xu, P. Hai, Y. Shen, Y. Suzuki, and L.V. Wang., Nature communications 8, no. 1 (2017): 780., doi: 10.1038/s41467-017-00856-2
3. A. Shayei, Z. Kavehvash, and M. Shabany, Appl. Opt. 56, 4454-4465 (2017)

Effect of Graphene Nanoplatelet Size in Thermal Properties of Heat Sink Compound

Caridad VALES PINZON*, Rubén Arturo MEDINA ESQUIVEL, Jorge Alejandro TAPIA GONZÁLEZ,
José Rodrigo OROZCO CHAC

*Facultad de Ingeniería-UADY, Av. Industrias no Contaminantes por Periférico Norte,
Apdo. Postal 150 Cordemex, 97310 Mérida, Yucatán, Mexico*

*caridad.vales@correo.uady.mx, ruben.medina@correo.uady.mx,
jorge.tapia@correo.uady.mx, ro.dri.go.123@hotmail.com*

Electronics, computing, and systems for energy saving and generation are amongst the most demanding developments of flexible and versatile materials which command the challenges of controlling the dissipation of heat. This is difficult to obtain with homogeneous materials, even so, is possible with compounds based in nanostructures. In recent years, several studies have reported how the inclusion of carbonaceous materials into different matrix changes its physical properties. Graphene nanoplatelets (GNPs), a recently developed and lower cost material, have high achievement in this area, such as can improve mechanical, electric and thermal properties of compounds. This is due to the outstanding physical properties attributed to the structural configuration, a non-oxidizing manufacturing process that provide a pristine graphitic surface that makes it especially suitable for applications requiring high electrical or thermal conductivity.

This work shows the study of the thermal properties enhancement of heat sinks due to loads of different kinds of GNPs. A photopyroelectrical technique with a sample thickness scan was employed in order to measure the thermal diffusivity of the samples. The thermal properties analysis was carried out as a function of particle size of the GNPs and its volume concentration in the sample. The results show that heat transport on these compounds strongly depends on the GNPs volume fraction, thus even with a low loading percentage of them produce a meaningful increase in the thermal diffusivity of the composite. This is related to their pure graphitic composition of these 2D carbon nanostructures, these are excellent thermal conductors compared to the matrix. The thermal conductivity of the samples was calculated, and it was analyzed using Lewis–Nielsen model, taking into account the dependence of the maximum packing fraction and the form factor with the agglomeration, geometry and particle size of the GNPs.

Acknowledgements

This work was supported by SEP- CONACYT-CB-2015-256497

Session B5: Thermal Properties I

Thermal and electric percolation in random microparticles composites

Juan José ALVARADO-GIL⁽¹⁾, Ivan Yecid FORERO-SANDOVAL⁽¹⁾, Fernando CERVANTEZ-ALVAREZ⁽¹⁾, Jorge Andrés RAMIREZ-RINCON⁽¹⁾, Juan Daniel MACIAS⁽¹⁾, Nelson Wilbur PECH-MAY⁽²⁾, José ORDONEZ-MIRANDA^{(3)*}

1. Applied Physics Department, CINVESTAV-IPN Mérida, Mexico.

2. Department of Chemistry, University of Bayreuth, Universitätsstrasse 30, 95447 Bayreuth, Germany

3. Institut Pprime, CNRS, Universit de Poitiers, ISAE-ENSMA, F-86962, Futuroscope

Chasseneuil, France. jjag09@yahoo.com The present study discusses the thermal diffusivity, thermal effusivity, volumetric heat capacity, thermal conductivity and electrical conductivity of iron/polyester composites in the range of filler content 0 to 0.55 volume fraction (vf). The well-known flash method in the front-face configuration is used to retrieve the thermal diffusivity and thermal effusivity of polymers [1-2]. The volumetric heat capacity and the thermal conductivity is determined from these measured properties. The electrical conductivity was derived by the I-Vs measurements, by means of a DC voltage applied between two terminals. It was found that the addition of iron particles increases the thermal diffusivity, the thermal effusivity, the volumetric heat capacity, the thermal conductivity and the electrical conductivity of the composites. The experimental data were analyzed to find the percolation threshold v_p [3-5], which was found in 0.38 vf for the thermal conductivity and 0.30 vf for the electrical conductivity.

References

1. N. W. Pech-May, C. Vales-Pinzón, A. Vega-Flick, A. Cifuentes, A. Oleaga, A. Salazar, J. J. Alvarado-Gil, *Polymer Testing* 50, 255–261 (2016) doi:10.1016/j.polymertesting.2015.12.011
2. N. W. Pech-May, A. Cifuentes, A. Mendioroz, A. Oleaga, A. Salazar, *Measurement Science and Technology* 26 (8), 085017 (2015) doi:10.1088/0957-0233/26/8/085017
3. Y. P. Mamunya, V. V. Davydenko, P. Pissis, E. V. Lebedev, *European Polymer Journal* 38 (9), 1887–1897 (2002) doi:10.1016/S0014-3057(02)00064-2
4. F. Kargar, Z. Barani, R. Salgado, B. Debnath, J. S. Lewis, E. Aytan, A. A. Balandin, *ACS Applied Materials & Interfaces* 10 (43), 37555–37565 (2018) doi:10.1021/acsami.8b16616
5. G. Zhang, Y. Xia, H. Wang, Y. Tao, G. Tao, S. Tu, H. Wu, *Journal of Composite Materials* 44 (8), 963–970 (2010) doi:10.1177/0021998309349690

Photon momentum transfer at water/air interfaces under total internal reflection

Fabio A. SCHABERLE*, Luís A. REIS, Carlos SERPA, Luís G. ARNAUT

Centre of Chemistry, University of Coimbra, 3004-535 Coimbra, Portugal

fschaberle@qui.uc.pt

The transfer of photon momentum at the water/air interface is important for optical manipulation of minute particles and is at the heart of the Minkowski–Abraham controversy. We use photoacoustic (PA) detection of ultrasound waves generated when pulsed laser light meets the water/air interface at 3.9°C (zero thermal expansion), to distinguish momentum transfer from thermoelastic effects. Momentum transfer is most efficient when the photons travel in water and remain in water after total reflection at the interface, rather than when they cross the interface between dielectric media.

The experimental configuration is schematically presented in fig. 1.

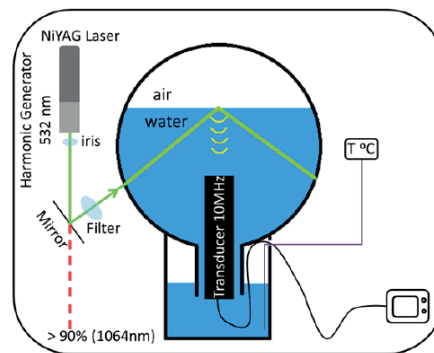


Figure 1: Experimental scheme for photoacoustic detection of waves generated at the interface air/water.

The laser pulse reaches the water/air interface from below (water), with an angle of incidence θ_i relative to the normal. According to Snell's law, using $n = 1.33$ for water at 20°C, the critical angle is $\theta_c = 48.75^\circ$. Water was initially cooled below 3.9°C and its temperature was allowed to slowly increase to room temperature (measured with a thermocouple thermometer Delta OHM model HD 2108.1). Laser pulses were directed at the selected angle to the water/air interface and the PA waves generated were detected with an A311S Panametrics (Olympus) immersion piezoelectric transducer (10MHz), pre-amplified (Panametrics ultrasonic preamp) and connected to a Tektronix digital oscilloscope (model DPO7254, 2.5 GHz, 40 GS s⁻¹). The laser pulses were generated with a Quantel Big Sky Ultra50 Nd:YAG laser (pulse width $\tau = 8$ ns, TM polarization). We used a dielectric mirror (Unaxis BD10307805) ca. 90% transparent at 1064nm, to reflect mostly the 532 nm to our setup. Additionally, we used Newport filters 10LWF-650-B and 10SWF-900-B to cutoff either 532 nm or 1064 nm laser pulses, respectively. The spectral purity of the beam was checked with an Avantis spectrophotometer. The laser pulse energies entering the setup were either 1.65mJ at 532 nm or 0.165 mJ at 1064 nm, perfectly separated.

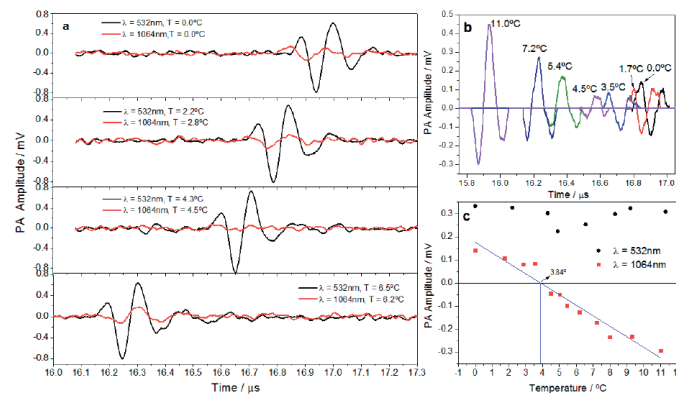


Figure 2: Photoacoustic (PA) waves for an angle of incidence $\theta_i = 69.8^\circ$ measured with a 10 MHz transducer. (a) Temperature dependence of PA waves generated with 532 nm (black) and 1064 nm (red) laser pulses at fluence rates of 52.5 and 4.5 mJ cm⁻², respectively. (b) PA waves generated with 1064 nm laser pulses at different temperatures. (c) First maximum amplitudes of PA waves generated with 532 and 1064 nm laser pulses as a function of the temperature.

Session B5: Thermal Properties I

Figure 2(a) shows PA waves collected at different temperatures using either 532 or 1064 nm pulses. The PA waves gen photothermal processes: as the temperature is allowed to increase from near 0 °C to room temperature, the amplitudes change sign at *ca.* $T = 3.9$ °C, from a thermoelastic contraction to a thermoelastic expansion (figure 2(b)). The amplitudes of the PA waves generated by 532 nm laser pulses are rather insensitive to the temperature (figure 2(c)) and must be assigned to transfer of momentum at the interface.

The thermoelastic properties of water and the sensitivity of the photoacoustic technique provided the conditions necessary to measure the transfer of photon momentum at the water/air interface. The thermoelastic component due to concurrent light absorption by water was suppressed by proper control of water temperature or selection of the wavelength. Our measurements show that when light is reflected at the water/air interface and remains in water, a larger change in photon momentum occurs.

Acknowledgements

This research was supported by the Portuguese Science Foundation and FEDER (Projects no. UID/QUI/00313/2019, Roteiro/0152/2013/022124 and PTDC/QEQ-MED/3521/2014), and by H2020 Research Infrastructures (LaserLab Europe 654148).

References

1. F.A. Schaberle, L.A. Reis, C. Serpa and L.G Arnaut, New Journal of Physics 21, 033013 (2019) doi: <https://doi.org/10.1088/1367-2630/ab098a>

Thermophysical properties of nanodiamond aqueous dispersions by thermal lensing and heat-flow techniques

Liliya O. USOLTSEVA*, Dmitry S. VOLKOV, Natalya V. AVRAMENKO,
Mikhail V. KOROBV, Mikhail A. PROSKURNIN

Department of Chemistry, M.V. Lomonosov Moscow State University, Moscow, Russia

usoltsevalilya@gmail.com

Thermal conductivity enhancement has appeared as the main target in many recent studies on heat transfer applications. A great part of novel solutions trying to enhance thermal performance deals with nanofluids. These two-phased systems have been widely used to take advantage of the high thermal conductivity of their solid particles in a fluid with lower thermal properties (conventional heat transfer fluids—water, lubricant oils, or glycols) [1, 2]. The possibilities of improving thermal conductivity in such systems relative to thermal conductivity of pure fluids have not been studied to date in full. Partially this is due to the lack of adequate experimental techniques to provide the accurate data on thermal conductivity in dispersions. The accuracy of existing data often suffers from convective effects. This makes some reports on the achieved increase in thermal conductivity in nanofluids doubtful.

We present the results of extensive study of thermal properties of carbon nanofluids using thermal-lens spectrometry (TLS) i.e. a remote optical approach to the detection of thermophysical parameters. TLS may provide data for both the dispersed phase and the dispersion medium. Thermal diffusivity was derived from TLS transient curves and converted then into thermal conductivity with volume specific heat measured by DSC and densitometry.

Nanodiamond (ND) aqueous dispersions are environment-friendly and chemically inert systems stable over time. In this study, aqueous dispersions of NDs of various types with high concentrations (up to 20%) were produced and examined by TLS. Thermal conductivities were obtained from TLS and independently measured by conventional heat flow steady-state technique. An increase (up to 3%) in thermal conductivity of ND-based nanofluids was observed. Comparison analysis of the results obtained from two methods was carried out. Advantages of simultaneous use of photothermal and heat-flow techniques along with possible sources of disagreement between results of two methods will be discussed in detail.

Acknowledgements

This work was supported by the RFBR grant 18-33-00586 mol_a.

References

1. N. Sezer, M.A. Atieh, M. Koc, Powder Technology, (2018)
2. F. Mashali, E.M. Languri, J. Davidson, D. Kerns, W. Johnson, K. Nawaz, G. Cunningham, International Journal of Heat and Mass Transfer 129, 1123 (2019)

KEYNOTE

Scanning thermal microscopy — the tool for thermal measurements in nanoscale

Jerzy BODZENTA

Silesian University of Technology, Institute of Physics, Gliwice, Poland

jerzy.bodzenta@polsl.pl

Development in material science and engineering allows manufacturing of devices with unprecedented performance. It is especially noticeable in electronics where a miniaturization is accompanying by continuous improvement of functionality. However, this process causes growth of the density of heat sources in active devices and leads to problems with heat extraction. Nowadays this is a limiting factor for further improvement of processing units used in computers. Similar problems occur in high power electronic and optoelectronic devices [1]. A possible solution is an improvement of thermal design of devices. To do this the thermal properties of materials used in devices must be known. Advanced integrated circuits are fabricated in 12 nm technology which means that the structure is built of few nm thick layers. It is well known that the thermal conductivity of submicrometer dielectric layers is lower than the one of bulk material and strongly depends on layer thickness or inner structure, e.g. mean grain size [2]. Theoretical prediction of the thermal conductivity of thin layer is difficult, so its value must be determined experimentally. The scanning thermal microscopy (SThM) is one of a few methods allowing thermal measurements in the nanoscale. SThM based on equipment same as for atomic force microscopy (AFM), and in practice AFM and SThM measurements run in parallel. To obtain information about thermal properties special AFM probes with temperature sensor near the apex are used. Additionally, the microscope must be fitted with a module collecting signal from this sensor and controlling its current [3].

Scanning thermal microscope can operate in two modes – temperature contrast (or passive) mode (TCM) and conductivity contrast (or active) mode (CCM). In the TCM the temperature sensor measures temperature distribution on sample surface. In the CCM the probe is heated, usually by Joule heating. The probe temperature depends on an efficiency of heat extraction, which is sensitive to the thermal conductivity of sample. So, thermal conductivity maps can be obtained.

The most demanding experiments using SThM equipment are quantitative thermal measurements - measurements of local thermal conductivity. It is proved experimentally that determination of the thermal conductivity of films with thicknesses of about 15 nm is possible by this technique. However, such measurements require quite sophisticated measuring procedure and advanced analysis of experimental data [4, 5]. The main difficulty of quantitative SThM measurements is that the influence of the sample thermal conductivity on measured signal is relatively weak. In addition, this signal depends on many factors, which are difficult to control during measurements (e.g. sample roughness, the temperature and the humidity of ambient air, the hydrophilicity/hydrophobicity of sample surface). Fig. 1 shows topographic and thermal images of through silicon via (TSV) structure, a cylinder made of Cu based conductive paste getting the body of chip. It can be seen that every irregularity in the sample surface (light spot) is visible as a low conductivity spot in the thermal image. The reason is simple, irregularities cause reduction of contact area between the probe and the sample, so the heat flux to the sample is also reduced. The dark spots in the thermal image shown in Fig. 1(b) are artefacts, which source is easy to interpret. However in general case proper interpretation of thermal images could not be so obvious.

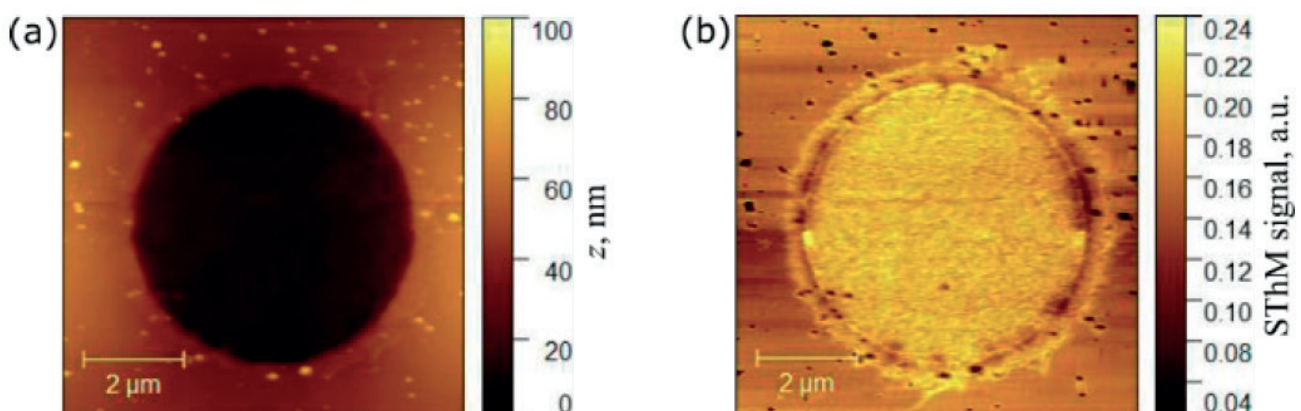


Fig. 1. Topographic (a) and thermal (b) images of TSV structure

The SThM measurement of the thermal conductivity is based on comparison of signal measured for investigated sample with a reference curve obtained from measurements for samples with known thermal conductivities. Determination of the reference curve must be carried out with care. Firstly, reference samples must be thermally isotropic and must have optically flat surfaces to avoid an influence of surface roughness on measured signal. In a case of the most popular resistive probes an influence of the electrical conductivity of sample on the signal should be considered. Therefore, electrically non-conducting samples would be preferable. It should be also taken into account that the effectiveness of heat transport from the thermal probe to the sample can be influenced by water meniscus which can appear near the probe apex [6]. The meniscus enlarges the effective contact area so the measured signal corresponds to the sample of higher thermal conductivity.

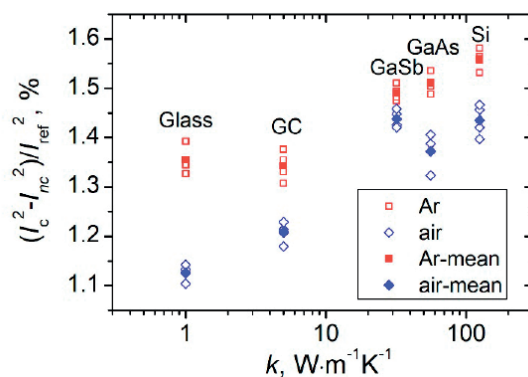


Fig. 2. Change of square of probe current normalized to the current for 5 μm over the sample vs. the thermal conductivity. Experiments were carried out for five reference samples in Ar and air atmospheres. For each sample measurements were repeated at four points on the surface. Mean values are also shown.

Experiments were carried out for five reference samples (glass, glassy carbon GC, GaSb, GaAs, and Si) in argon and air atmospheres. The probe temperature was kept constant and a square of probe current square was measured. Heights of signal jumps caused by reaching the contact to the sample, normalized to the signal at a 5 μm distance from the sample, are shown in Fig. 2. An analysis of this graph allows following conclusions. The normalized jumps are higher for measurements in Ar. Mean values of signals calculated from four measurements at different positions on the surface can be fitted with smooth curve only for data obtained in Ar. Moreover, signal behavior in Ar is in good agreement with results of analysis based on finite element modelling. The sensitivity of SThM signal to the sample thermal conductivity should be relatively high near 100 $\text{W}\cdot\text{m}^{-1}\cdot\text{K}^{-1}$, and diminishes for higher (>1000 $\text{W}\cdot\text{m}^{-1}\cdot\text{K}^{-1}$) and lower (<10 $\text{W}\cdot\text{m}^{-1}\cdot\text{K}^{-1}$) conductivities [4]. Measurements in the air gave unexpectedly high signal changes for samples with low thermal conductivities (glass and GC), and unexpectedly high signal for GaSb. Possible explanation of these facts is the influence of water condensed on the surface. However, this hypothesis needs further verification.

It should be also noticed that parameters of SThM probes differ, even if we use probes from the same batch, so the reference curve must be built for each probe separately. Moreover, correctness of this curve should be checked regularly as the probe parameters can change because of wear.

To summarize, SThM is a valuable tool for qualitative and quantitative thermal measurements in the nanoscale. However, this technique is still in a development stage. There are two main problems which should be solve before SThM could be recognize as well-established method providing reliable, reproducible results. The first one is connected with the low sensitivity of measured signal to the thermal conductivity of sample. This is caused by the fact that the heat flux through the contact to the sample is only a small share of the whole heat flux from heated zone. The situation can be improved by such a design of probes which will restrict the heat flux along probe cantilever to a mounting. The second problem is complex dependence of SThM signal on thermal, electrical, and topographical properties of the sample, and ambient conditions. The influence of ambient conditions can be minimized by measurements in protective gas atmosphere or, preferably, in vacuum. The influence of electrical properties can be excluded by electrical insulation of conducting elements of the probe from the sample.

References

1. R. Heiderhoff, A. Makris, T. Riedl, Thermal microscopy of electronic materials, *Mat. Sci. Semicon. Proc.* 43, 163 (2016) doi: 10.1016/j.mssp.2015.12.014
2. J. Bodzenta, Thermal properties of thin films and problems with their determination, *Ann. Chim. Sci. Mat.* 32, 401 (2007) doi: 10.3166/acsm.32.401-420
3. J. Bodzenta, Scanning thermal microscopy – a tool for thermal measurement in the nanoscale, in *Nanostructured Thin Films: Fundamentals and Applications* (M. Benelmekki, A. Erbe Eds.), Elsevier 2019 (in production).
4. J. Bodzenta, J. Juszczyk, A. Kaźmierczak-Bałata, P. Firek, A. Fleming, M. Chirtoc, Quantitative thermal microscopy measurement with thermal probe driven by dc+ac current, *Int. J. Thermophys.* 37, 73 (2016) doi: 10.1007/s10765-016-2080-y
5. J. Juszczyk, A. Kaźmierczak-Bałata, P. Firek, J. Bodzenta, Measuring thermal conductivity of thin films by Scanning Thermal Microscopy combined with thermal spreading resistance analysis, *Ultramicroscopy* 175, 81 (2017) doi: 10.1016/j.ultramic.2017.01.012
6. A. Assy, S. Lefèvre, P.-O. Chapuis, S. Gomès, Analysis of heat transfer in the water meniscus at the tip-sample contact in scanning thermal microscopy, *J. Phys. D: Appl. Phys.* 47, 442001 (2014) doi: 10.1088/0022-3727/47/44/442001

KEYNOTE

Time-Domain Thermoreflectance for Thermal Characterization of Nanostructures

Roman Anufriev^{(1)*}, Masahiro Nomura^(1,2)

1. Institute of Industrial Science, The University of Tokyo, Tokyo 153–8505, Japan

2. CREST, Japan Science and Technology Agency, Saitama 332–0012, Japan

*anufriev@iis.u-tokyo.ac.jp

Measurements of thermal properties of nanostructures is a challenging task because the experimental techniques inevitably struggle with instrumental uncertainties, parasitic contact effects, and often non-trivial data analysis. Whereas popular electrical measurement methods offer low instrumental uncertainties, they allow studying only a few samples at a time in a limited temperature range, which is limiting for studies requiring multiple samples and high statistical significance.

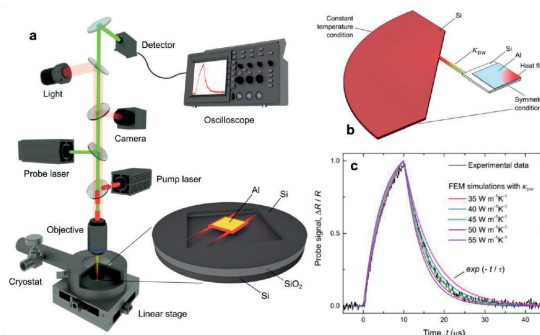


Fig. 1. (a) Schematic of μ TDTR setup and a typical sample. (b) FEM model used to analyze the experimental data. (c) Fitting of the experimental thermal decay curves by the curves from the model.

Here, we present an optical micro time-domain thermoreflectance (μ TDTR) method [1], which allows to measure large quantities of samples and achieve high statistical significance and often straightforward data analysis. The method uses a classical TDTR principle: since the temperature of the material is proportional to its reflectance coefficient, the temperature at a given spot can be monitored in time measuring the intensity of reflected probe laser beam. If at the same time the spot is heated by the pulses of a pump laser, as shown in Fig. 1(a), we can study the heat dissipation process and measure how temperature gradually drops in time.

Comparing the experimental results to the FEM modelling (Fig. 1(b-c)), we can obtain commonly used thermal properties, such as the thermal conductivity and thermal resistance. However, even without the modeling we can conduct comparative studies and compare heat conduction in similar samples.

To illustrate the power of this method, we present the measurements of the heat guiding and heat focusing phenomena in silicon thin membrane [2]. In this work, we use only the directly obtained signals measured on hundreds of samples fabricated on the same wafer, to show that the method allows to avoid complicated fabrication and analysis. Next, we present measurements on silicon nanowires in the 4 - 300 K range [3]. These experiments show that using additional FEM modelling, we can extract the thermal conductivity of the nanowires and thus gain a deep insight into the phenomenon of ballistic heat conduction in silicon.

To conclude, our optical μ TDTR method is an excellent tool for contactless studies of the thermal properties of nanostructures. This method allows to study large quantities of samples on the same wafer and achieve high statistical reliability of the study at a low fabrication cost.

Acknowledgements

This work was supported by CREST JST (JPMJCR19Q3), Kakenhi (15H05869 and 17H02729) and Postdoctoral Fellowship program of Japan Society for the Promotion of Science.

References

1. J. Maire and M. Nomura, *Jpn. J. of Appl. Phys.*, 53, 06JE09 (2014).
2. R. Anufriev, A. Ramiere, J. Maire, and M. Nomura, *Nat. Commun.* 8, 15505 (2017).
3. R. Anufriev, S. Gluchko, S. Volz, and M. Nomura, *ACS Nano* 12, 11928 (2018).

Thermoreflectance microscopy as a method for accurate determination of thermal properties of layered samples

C. Fretigny¹, D. Fournier^{2*}

1. Laboratoire SIMM, Sorbonne Université, PSL Research University, UMR 7615, CNRS, UPMC, ESPCI, 10 rue Vauquelin, Paris, 75005, France

2. Sorbonne Université, UPMC, Univ. Paris 06, CNRS, UMR 7588, Institut des NanoSciences de Paris, 75005, Paris, France

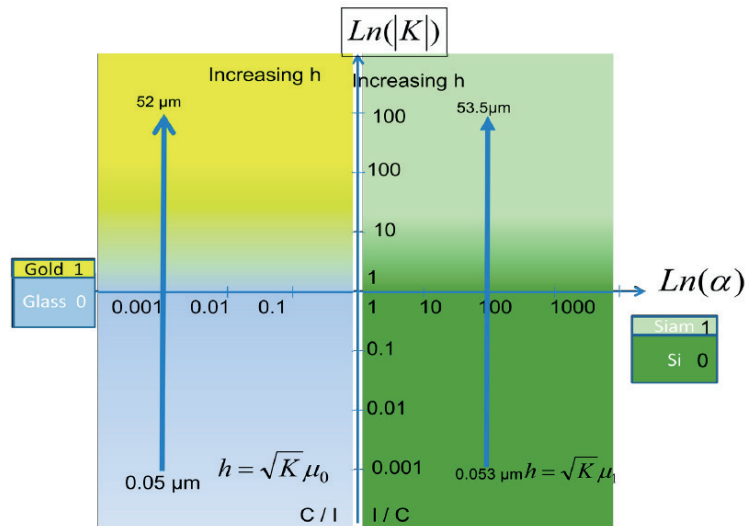
We report on thermal properties determination when the sample is a layer deposited on a substrate with known properties (layered sample) or is inserted between a known substrate and a known surface layer. The experimental setup is a thermoreflectance microscope in which the 1 μm diameter intensity modulated pump beam creates a thermal wave in the sample. The spatio-temporal heat diffusion is detected through the variation of the reflectivity of the probe beam which is scan on the sample surface. Experimental amplitude and phase are recorded versus the distance of the two beams. It is well known that a multiparameter best fit can find the thermal values required. Instead of a numerical approach, we show here that asymptotic behaviour of the heat diffusion in layered structures can be calculated and used to recover thermal properties. To do that the integral

$$T(r,0,\omega) = \Phi \int_0^\infty \frac{1}{k_1 \sigma_1} \frac{k_1 \sigma_1 + k_0 \sigma_0 \tanh(\sigma_1 h)}{k_0 \sigma_0 + k_1 \sigma_1 \tanh(\sigma_1 h)} J_0(\lambda r) \lambda d\lambda$$

can be evaluated with incomplete Bessel function

$$T(\rho,0,\omega) = \frac{\Phi}{k_1 h} \left[\frac{e^{-\rho \varepsilon \theta_0}}{\rho} + \sum_0^\infty R_n K_0(\rho y_n, w_n) \right] \text{ with } \rho = \frac{r}{h}$$

Domains of applicability of these different regimes will be discussed and illustrated with examples in the plane of Figure 1



Where $\alpha = \frac{k_{\text{substrate}}}{k_{\text{layer}}}$ and $K = h^2 \left(\frac{1}{\mu_0^2} - \frac{1}{\mu_1^2} \right)$ where 0 is the substrate and 1 is the layer

References

- [1] Fretigny C, Duquesne J-Y, Fournier D et al. Jour. Appl. Phys 111 , 084313 (2012)
- [2] Fretigny C, Roger JP, Reita V, et al. Jour. Appl. Phys 102 , 116104 (2007)

Photothermal radiometry method development and application for nuclear technologies

Alexandre SEMEROK ^{(1)*}, Sergey Venediktovich FOMICHEV ^(2,3), Christian GRISOLIA ⁽⁴⁾, Sang PHAM TU QUOC ⁽¹⁾, Antonin POISSON ⁽¹⁾, Guy CHEYMOL ⁽¹⁾, Fernando LOMELLO ⁽¹⁾, Alexandre MICHAU ⁽⁶⁾, Frederic SCHUSTER ⁽⁵⁾, George HAMAOU ⁽⁶⁾, Nicolas HORNY ⁽⁶⁾, Mihai CHIRTOC ⁽⁶⁾, Hicham MASKROT ⁽¹⁾

1. Den-Service d'Etudes Analytiques et de Réactivité des Surfaces (SEARS), CEA, Université Paris-Saclay, F-91191, Gif sur Yvette, France

2. National Research Center "Kurchatov Institute", 123182 Moscow, Russia

3. Moscow Institute of Physics and Technology, 141700 Dolgoprudny, Moscow region, Russia

4. CEA, IRFM, F-13108, Saint Paul Lez Durance, France

5. CEA Cross-Cutting Program on Materials and Processes Skills, F-91191, Gif sur Yvette, France

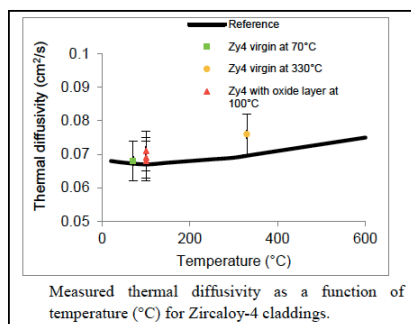
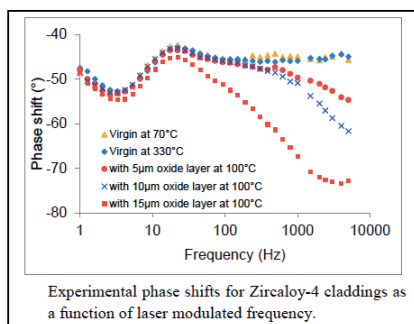
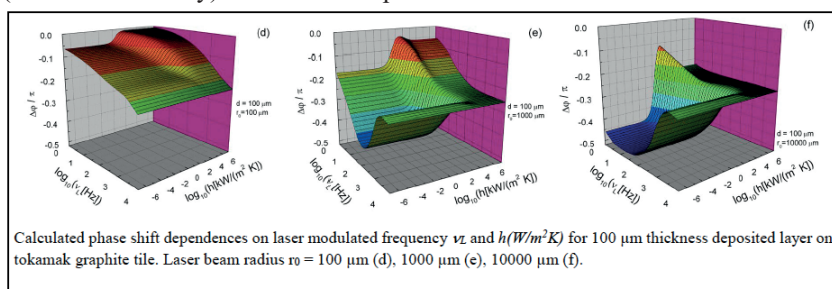
6. Multiscale Thermophysics Lab, GRESPI, Université de Reims Champagne Ardenne, URCA, Moulin de la Housse, BP 1039, Reims, 51687, France

alexandre.semerok@cea.fr

In the search for new materials for nuclear industry and reliable nuclear safe technologies, much attention is given to methods for non-destructive remote testing and control of materials in severe environment of nuclear installations. Photothermal radiometry, as one of these possible methods, is under development in the CEA (French Atomic Energy Commission). In our studies, it was used with repetition rate laser heating of a sample by either a pulsed (100 ns-1 ms, 1-10000 Hz) [1, 2] or a sinusoidal modulated laser power (1 Hz - 1 MHz) [2,3] followed by measurements of the thermal radiation emitted by the sample under study. Thermal radiation time-dependence or phase shifts between the laser power and the thermal radiation measured at different modulated frequencies (lock-in radiometry) were then compared with those obtained with a model of laser heating to characterize some sample properties

(thermal diffusivity, thickness, layer adhesion, under-surface defects and their changes in time).

Samples from European TOKAMAKS (graphite or carbon fibre composite protective tiles with 1 - 100 μm deposits) and nuclear installations (metal pieces, Zircaloy cladding, micrometric oxide layers or PVD thin films, 3D-printed metal objects) were tested and characterized with the home-made experimental setups and the developed analytical (3D+t) models of laser heating [4-6]. The numerical simulation of laser heating was used to fit the calculated thermal radiation or phase shifts with the experimental ones by adjusting the material properties. This method of characterization was validated with a set of etalon samples. The applied methods will be presented along with the obtained results. The possible ways to improve the method to widen the scope of its application in the nuclear industry will be discussed as well.



References

1. A. Semerok, S. V. Fomichev, J.-M. Weulersse, F. Brygo and P.-Y. Thro, Journal of Applied Physics 101, 084916 (2007)
2. A. Semerok, F. Jaubert, S.V. Fomichev, P.-Y.Thro, X. Courtois, C. Grisolia, Nuclear Instruments and Methods in Physics Research Section A: Accelerators, Spectrometers, Detectors and Associated Equipment A693, 98 (2012)
3. N. Horny, M. Chirtoc, A. Fleming, G. Hamaoui and H. Ban, Applied Physics Letters 109, 033103 (2016)
4. A. Semerok, S.V. Fomichev, F. Jaubert, C. Grisolia, Nuclear Instruments and Methods in Physics Research Section A: Accelerators, Spectrometers, Detectors and Associated Equipment A738, 25 (2014)
5. S. Pham Tu Quoc, G. Cheymol, A. Semerok, Review of Scientific Instruments 85, 054903 (2014)
6. A. Semerok, S. Pham Tu Quoc, G. Cheymol, C. Gallou, H. Maskrot and G. Moutiers, European Journal of Physics, Nuclear Sciences & Technology 2, 20 (2016) doi: <https://doi.org/10.1051/epjn/2016015>

Thermophysical Characterization of W-Doped and Undoped Nanocrystalline Powders of VO₂

Cindy Lorena GÓMEZ HEREDIA⁽¹⁾, Jorge Andrés RAMIREZ RINCÓN⁽¹⁾,
Parasuraman RAJASEKAR⁽²⁾, Jose Luis CERVANTES LOPEZ⁽¹⁾, Jose ORDOÑEZ MIRANDA^{(3)*},
Oscar ARES⁽¹⁾, Arun UMARJI⁽²⁾, Karl JOULAIN⁽³⁾, Younes EZZAHRI⁽³⁾, Jeremy DREVILLON⁽³⁾,
Juan José ALVARADO GIL⁽¹⁾

1. Departamento de Física Aplicada, Cinvestav-Unidad Mérida, C
arretera Antigua a Progreso km. 6, 97310, Mérida, Yucatán, México.

2. Materials Research Centre, Indian Institute of Science, 560012, Bengaluru, India.

3. Institut Pprime, CNRS, Université de Poitiers, ISAE-ENSMA, F-86962 Futuroscope Chasseneuil, France.

Authors' e-mail cindy.gomez@cinvestav.mx

Vanadium dioxide (VO₂) has become a subject of great interest because of their impressive ability to reversibly change its electrical and optical properties with temperature due to its metal-to-insulator transition (MIT) around 68 °C [1-2]. To enlarge its application range, VO₂ powders doped with tungsten have been used to reduce this transition temperature nearly to room temperature [3-4]. This tailoring of the MIT of VO₂ is also expected to be possible on its thermal properties, which have received much less attention, though they can provide routes for controlling heat transfer.

In this study, the hysteresis loops exhibited by the thermal properties of undoped and 8 at% W-doped nanocrystalline powders of VO₂ synthesized by means of the solution combustion method and compacted in pellets we measure around the MIT. This is done through the photothermal radiometry (PTR) technique in the transmission mode using also the well-established self-normalization and thermal contrast methods. Remarkable variations in the critical temperature up to 15°C have been observed among the VO₂ undoped and VO₂ W-doped sample, as well as significantly narrower hysteresis loops for this latter. It was shown that the thermal properties of VO₂ nanocrystalline in its dielectric phase are much more influenced by the W substitution doping than in its metallic state. Moreover, we find that thermal diffusivity decreases (increases) until (after) the metallic domains become dominant in the VO₂ insulating matrix, and as a consequence, the change of this property across the MIT can be raised in around 23% with tungsten doping. In contrast, the thermal conductivity and thermal effusivity during the entire transition grows (falls) in heating (cooling) cycle of both samples, exhibiting in the dielectric state higher values for the W-doped pellet respect to the undoped one. In addition, these properties exhibit an improvement up to 1.44 and 1.13 respectively, among their pure insulating-metallic states. However, we found that their change determined from the extreme insulating and metallic states is diminished by doping. Furthermore, the characteristic peak of the specific heat capacity within the MIT has been observed in both heating and cooling cycles for two samples. At our doping level, we found that W-doped sample requires about 24% less thermal energy than the undoped one to carry out the phase transition. Based upon these significant findings, we conclude that W doping promotes a VO₂ material with better abilities to generate and propagate heat through the nanocrystals, but with low thermal switching efficiency.

References

1. Z. Peng, W. Jiang and H. Liu, J. Phys. Chem. C. 111, 1119 (2007).
2. H. Ji, D. Liu, H. Cheng, C. Zhang, L. Yang and D. Ren, RSC Adv, 7, 5189 (2017).
3. Peng, Z., Wang, Y., Du, Y., Lu, D., & Sun, D. J Alloy Compd, 480, 537 (2009).
4. A. Hendaoui, N. Émond, S. Dorval, M. Chaker and E. Haddad, Sol. Energy Mater Sol. Cells, 117, 494 (2013).

Photocarrier radiometry of silicon wafers: Linear versus nonlinear theoretical models

Bincheng LI ⁽¹⁾, Xiaoke LEI ⁽¹⁾, Qiming SUN ⁽¹⁾, Jing WANG* ⁽¹⁾, Qian WANG ^{(2)*}, Chunming GAO ⁽¹⁾

1. School of Optoelectronic Science and Engineering,
University of Electronic Science and Technology of China, Chengdu 610054, China
2. School of Optoelectronic Engineering, Xi'an Technological University, Xi'an 710021

China bcli@uestc.edu.cn

Since first developed by Mandelis, *et al* in 2003 [1], photocarrier radiometry (PCR) has been widely used to characterize the electronic transport properties of semiconductor materials, especially silicon wafers with or without ion implantation [2, 3]. In modulated PCR, the determination of electronic transport parameters, such as carrier lifetime, carrier diffusivity, and surface recombination velocities is performed by fitting the measured modulation frequency dependences of PCR amplitude and phase to an appropriate theoretical model [4]. Conventionally, linear PCR models, either one-layer [1] model for non-implanted wafers or two- [5] or three-layer [6] model for ion-implanted wafers, are employed in the multi-parameter fitting. In these linear models, the PCR signal is assumed to be linearly proportional to the photo-generated carrier density that is linearly proportional to the excitation laser power. Unfortunately it is experimentally observed that the PCR amplitude is either linearly or nonlinearly dependent on the photo-generated carrier density (or excitation power), depending on the resistivity of the silicon wafers. And a nonlinearity coefficient, which describes the dependence of the PCR amplitude on the photo-generated carrier density (or excitation power), is experimentally measured to be between 1 and 2, as shown in Fig. 1(a). Following these experimental observations, nonlinear PCR models are developed to describe the PCR signals and to determine the transport parameters [7, 8].

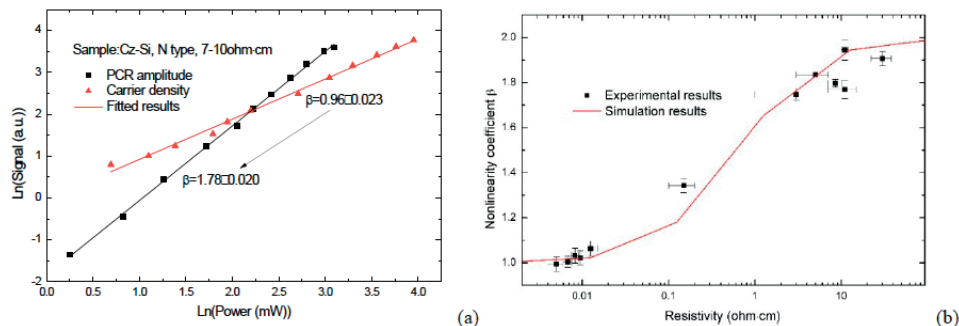


Fig. 1. Nonlinear dependence of PCR amplitude on the excitation power. (a) The dependences of photo-generated carrier density (measured by modulated free carrier absorption) and PCR amplitude on excitation power for a Cz-Si wafer with a nominal resistivity 7-10 ohm·cm. (b) The nonlinearity coefficient versus resistivity of Si wafers.

In this presentation, the development of linear and nonlinear PCR models is reviewed. The comparison between the linear and nonlinear models for the simultaneous determination of electronic transport properties via multi-parameter fitting is presented in detail. Theoretical simulations are performed to analyze the errors when linear models are employed to fit the experimental data with nonlinear behaviors for both non-implanted and ion-implanted silicon wafers. The transport parameter determination of non-implanted and ion-implanted silicon wafers with appropriate nonlinear PCR models is presented with silicon wafers with different resistivities.

Acknowledgements

The authors thank the financial support by the Natural Science Foundation of China (Grant Nos. 61601092, 61771103, and 61771103).

References

- [1] A. Mandelis, J. Batista, and D. Shaughnessy, Phys. Rev. B 67, 205208 (2003) doi: 10.1103/PhysRevB.67.205208
- [2] B. Li, D. Shaughnessy, A. Mandelis, J. Batista, and J. Garcia, J. Appl. Phys. 96, 186 (2004) doi: 10.1063/1.1755847
- [3] D. Shaughnessy, B. Li, A. Mandelis, and J. Batista, Appl. Phys. Lett. 84, 5219(2004) doi: 10.1063/1.1765737
- [4] B. Li, D. Shaughnessy, and A. Mandelis, J. Appl. Phys. 97, 023701 (2005) doi: 10.1063/1.1836854
- [5] C. Wang, A. Mandelis, J. Tolev, B. Burchard, and J. Meijer, J. Appl. Phys. 101, 123109 (2007) doi: 10.1063/1.2748868
- [6] B. Li, D. Shaughnessy, A. Mandelis, J. Batista, and J. Garcia, J. Appl. Phys. 95, 7832 (2004) doi: 10.1063/1.1748862
- [7] Q. Wang and B. Li, J. Appl. Phys. 118, 215707 (2015) doi: 10.1063/1.4936958
- [8] X. Lei, B. Li, Q. Sun, J. Wang, and C. Gao, AIP Advances 9, 035125 (2019) doi: 10.1063/1.5092621

Photopyroelectric determination of the thermal conductivity tensor of magnetoactive fluids

Rubén Arturo MEDINA ESQUIVEL*, Caridad Guadalupe VALES PINZÓN, Diego GONZÁLEZ MEDINA, David José CASTILLO DORBECKER, Dekar Andrés LUIS LÓPEZ

*Facultad de Ingeniería-UADY, Av. Industrias no Contaminantes por Periférico Norte,
Apdo. Postal 150 Cordemex, 97310 Mérida, Yucatán, Mexico*

*ruben.medina@correo.uady.mx, caridad.vales@correo.uady.mx,
diego.gonz91@gmail.com, davidjosecastillodorbecker@hotmail.com, dekar.luis@gmail.com*

Magnetoactive fluids are composite liquid materials, that usually consist of dielectric liquids with embedded ferromagnetic particles that quickly response to magnetic field. These materials are the subject of raising interest due to the rich diversity of physical phenomena observed under the effect of magnetic fields and their technological applications.

In this work, by means of a sample thickness scan photopyroelectric technique, we measured the thermal diffusivity of magnetoactive fluids, as a function of direction and intensity of an external uniform magnetic field. Three types of samples are studied: magnetorheological fluids (MRF), ferrofluids (FF), and magnetic carbon nanofibers suspended in a highly viscous carrier fluid (CNF-F). Additionally, the magnetic particles volume concentration in the thermal behavior is examined. Once the thermal diffusivity is obtained, the thermal conductivity is calculated using the density and specific heat capacity of the fluid.

As expected, the experimental results show that filler concentration monotonously increase the effective thermal conductivity of samples. When magnetic field is not applied, the magnetoactive fluids behaves as a homogeneous material, once the uniform magnetic field is applied, an important effective thermal conductivity anisotropy is observed for the case of MRF and CNF-F. For FF no thermal anisotropy is observed, mainly due to the high thermal resistance between magnetic nanoparticles that constitute the FF. The high thermal anisotropy observed for MRF and CNF-F is a result of a chain-like micro-structuring along the magnetic field lines, of the magnetic particles fillers.

We demonstrate that using a sample thickness scan photopyroelectric technique it is possible to measure the thermal diffusivity of magnetoactive fluids under the effect of externally applied uniform magnetic fields as a function of its direction and intensity. The highly effective thermal conductivity anisotropy of this magnetoactive fluids is properly presented in the form of thermal conductivity tensors.

Acknowledgements

This work was supported by SEP- CONACYT-CB-2015-256497 and Project CONACYT-SENER 254667.

Quantitative assessment of surface electronic quality of HF-etched Si wafers using heterodyne lock-in carrierography

Qiming SUN ^{(1,2)*}, Alexander MELNIKOV ⁽²⁾, Peng SONG⁽²⁾, Robert H. PAGLIARO ⁽³⁾,
Jing WANG ⁽¹⁾, Chunming GAO ⁽¹⁾, Andreas MANDELIS ^(1,2)

1. School of Optoelectronic Science and Engineering,

University of Electronic Science and Technology of China, Chengdu, 610054, China

2. Center for Advanced Diffusion-Wave and Photoacoustic Technologies (CADIPT), University of Toronto, Toronto, M5S 3G8, Canada

3. Advanced Processing Equipment Technology (APET) Co., Ltd, 20-15, Sukwoo-Dong, Hwaseong-City, Gyunggi-Do, 463-802, Korea

Corresponding Author's e-mail: mandelis@mie.utoronto.ca

Surface preparation has become amongst the most important fabrication steps in the electronic device manufacturing industry. Leading edge semiconductor devices require methods to provide stable, pristine, “oxide free”, and hydrogen passivated Si surfaces. This can be achieved using wet cleaning process chemistries such as diluted hydrofluoric (HF) acid to maximize the hydrogen termination efficiency and to minimize surface contaminants and micro-roughness. One of the key issues surface preparation experts are facing has been the ability to *quantify* the integrity of dynamically changing surface conditions that come with creating bare Si surfaces.

Heterodyne lock-in carrierography (HeLIC) [1,2], a camera-based dynamic photoluminescence imaging methodology, has been demonstrated to be capable of all-optical and noncontact evaluation of carrier recombination and transport properties of various electronic materials and devices. In this work we illustrate the LIC capability to quantitatively evaluate bare Si wafers that have undergone different HF-etching conditions, shown in Table 1. The samples under test were 11 p-type FZ wafers with resistivity > 10 kΩ.cm, 150-mm in diameter, and 675-μm thick.

Table 1. Samples under test with the information of processor, HF concentration, and dissolved-oxygen (DO) level.

Sample	Processor	[HF]	DO level
Nos. 1 & 2	APET	0.5%	400 ppb
Nos. 3 & 4	TPW	0.5%	> 2 ppm
No. 5	APET	0.5%	40 ppt
No. 6	R&D	2%	> 2 ppm
No. 7	None	N/A	N/A
Nos. 8 & 9	APET	0.5%	100 ppt
Nos. 10 & 11	TPW	0.5%	> 2 ppm

*APET: Advanced Processing Equipment Technology Co.; TPW: typical production wet bench.

Surface recombination velocity (SRV) is an ideal parameter for in-line quantitative assessment of surface quality of wet-cleaned semiconductor wafers, as it captures everything that can produce a negative impact such as the “oxide free” degree, defects, impurities, roughness etc. As today’s IC wafer size increases, quantitative *imaging* characterization techniques instead of local diagnostics are in demand, as imaging can provide both spatially resolved and globally integrated information, as shown in Fig. 1.

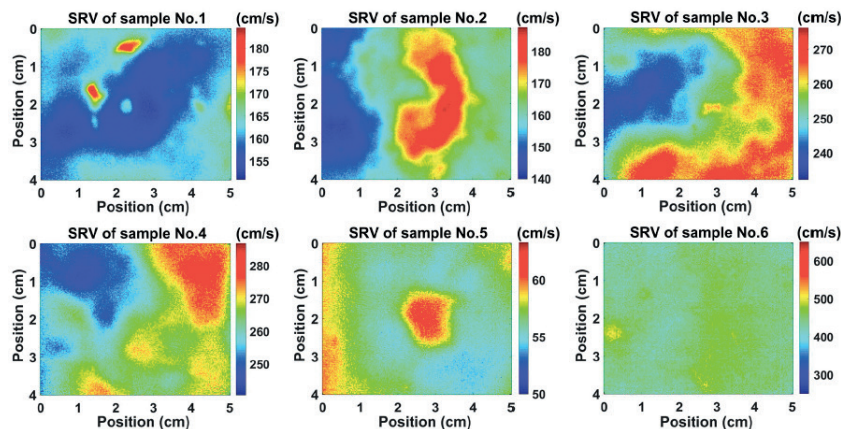


Fig. 1. SRV images of sample Nos. 1-6 with colormap indicating the quantitative values

Session B6: Radiometry III / Thermal Properties II

The surface electronic quality of bare silicon wafers changes in air with exposure time (Q-time) due to native oxide growth. The ability to suppress this naturally occurring phenomenon is also a key goal of the surface preparation process. Fig. 2 shows the evolution behavior of SRV versus Q-time. In summary, HeLIC has been demonstrated to be able to provide quantitative imaging characterization of surface quality of bare “oxide-free” hydrogen passivated Si wafers.

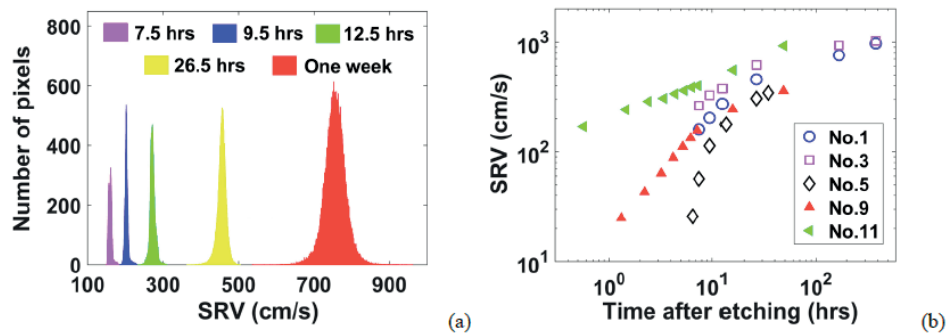


Fig. 2. (a) SRV-image pixel-value statistical distributions of sample No. 1 at various Q-times; (b) comparison of image-averaged SRV values among samples.

Acknowledgements

The authors are grateful to NSERC for a Discovery grant, to the University of Toronto Connaught Innovation Award for an operating grant, to the Canada Research Chairs Program, to the Lawrence Semiconductor Research Laboratory for their wafer donation, and to NNSFC (Grant Nos. 61601092, 61771103, & 61704023).

References

1. A. Melnikov, A. Mandelis, J. Tolev, P. Chen, and S. Huq, *J. Appl. Phys.* 107, 114513 (2010)
2. Q. M. Sun, A. Melnikov, A. Mandelis, and R. H. Pagliaro, *Appl. Phys. Lett.* 112, 012105 (2018)

Session B6: Radiometry III / Thermal Properties II

Ultra-Wideband Electromagnetic Characteristics for CVD Graphene

Yunqiu Wu*, Yuehang Xu, Zijun Wang, Kai Kang

University of Electronic Science and Technology of China

yqw@uestc.edu.cn

Since the graphene has been fabricated at 2004, it has brought great opportunities for the development of high-speed electronic devices [1, 2]. Electromagnetic characteristic is the intrinsic characteristic of graphene. In the previous work, the permittivity and conductivity are already determined in the micro-/millimeter wave frequency [3]. However, as the application of graphene is up to terahertz, infrared, and even higher, the ultra-wideband electromagnetic characteristics of graphene becomes more and more important. In this paper, the complex relative permittivity and the refraction index is investigated and discussed from 1 GHz to 1000 THz.

From the Drude model [4] the complex relative permittivity can be expressed as

$$\varepsilon_r(\omega) = 1 + \frac{\omega_p^2}{\omega(j \cdot \frac{1}{\tau} - \omega)} = \left(1 - \frac{\omega_p^2}{\omega^2 + \frac{1}{\tau^2}} \right) - j \cdot \left(\frac{\omega_p^2}{\omega \tau (\omega^2 + \frac{1}{\tau^2})} \right) = \varepsilon_r' - j \cdot \varepsilon_r'' \quad (1)$$

Where ε_r is the complex relative permittivity, ω_p is the plasma frequency, and τ is the collision rate. ε_r' and ε_r'' are the real part and imaginary part of the permittivity, respectively. Furthermore, the plasma frequency ω_p and the collision rate τ can be expressed as

$$\tau = \frac{\partial \left(\frac{1 - \varepsilon_r'}{\varepsilon_r''} \right)}{\partial \omega} \quad (2)$$

$$\omega_p = \frac{\sqrt{1 - \varepsilon_r'}}{\tau} \Bigg|_{\omega=0} \quad (3)$$

Based on the reported permittivity [3], the values of ω_p and τ can be obtained from equation (2) and (3) as $\omega_p = 2\pi \times 16.3$ THz and $\tau = 0.077$ ns. Then induce the value of ω_p and τ into equation (1), the relative permittivity of graphene from 1 GHz to 1000 THz can be determined (as shown in Fig 1 (a) and (b)). Moreover, the refraction index, n , can be deduced from the permittivity [5] as follows and the result is shown in Fig. 2.

$$n = \left(\frac{\sqrt{\varepsilon_r'^2 + \varepsilon_r''^2} + \varepsilon_r'}{2} \right)^{\frac{1}{2}} \quad (4)$$

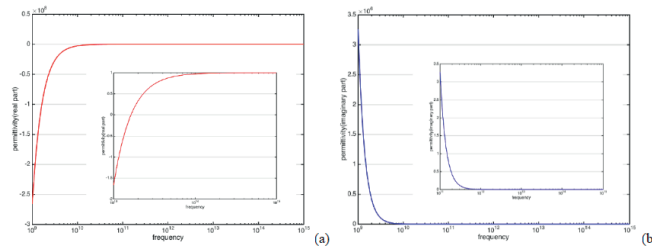


Fig. 1. The complex relative permittivity of graphene up to 1000 THz. (a) is the real part, (b) is the imaginary part

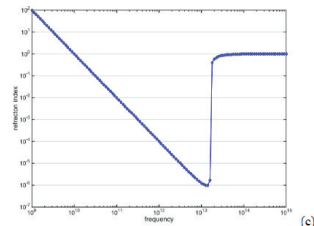


Fig. 2. The refraction index of graphene up to 1000 THz.

Session B6: Radiometry III / Thermal Properties II

As shown in Fig.1 (a) and (b), both the real part and the imaginary part of the permittivity of graphene are quite large in the micro-/millimeter frequency range. However, as the frequency increasing, the values decreased dramatically. Beyond the plasma frequency, the permittivity is converged to 1. Furthermore, as shown in Fig.2, in the frequency range lower than ω_p , the refraction index changing with the frequency increasing remarkably, which demonstrate the dispersion effect is obviously in this frequency range. Nevertheless, in the frequency beyond ω_p , the refraction tends to be 1. In other words, the dispersion effect reduced to be ignorable in this frequency range. The results of this paper will be helpful for the electronic and optical applications of graphene.

Acknowledgements

This work is supported by National Natural Science Foundation of China (Grant No. 61874020, 61771115, 61804024), and National Science and Technology Major Project of the Ministry of Science and Technology of China (Grand No. 2018ZX03001008).

References

1. F. Schwierz, Nature 472, 41 (2011). doi: 10.1038/472041a
2. Shu-Jen Han, Alberto Valdes Garcia, Satoshi Oida, Keith A. Jenkins, and Wilfried Haensch, Nature Communications 5, 3086(2014) doi:10.1038/ncomms4086
3. Y. Wu, Y. Wu, K. Kang, Y. Chen, Y. Li, T. Chen, Y. Xu, AIP Advances 6 (9), 095014 (2016) doi: 10.1063/1.4963140
4. H. Gai, J. Wang, Q. Tian, applied optics 46 (12), 2229 (2007) doi:10.1007/bf00035379
5. K. Patel, P. K. Tyagi, Carbon 121, 56 (2017) doi: 10.1016/j.carbon.2017.05.057.

KEYNOTE

Novel Methods and Applications of Photothermal Techniques for Speciation Studies in Environmental Samples

Leja GOLJAT⁽¹⁾, Hanna BUDASHEVA⁽¹⁾, Arne BRATKIČ^(2,3), Virginie VINATIER⁽⁴⁾,
Anne Marie DELORT⁽⁴⁾, Dorota KORTE⁽¹⁾, Mladen FRANKO^{(1)*}

1. Laboratory for Environmental and Life Sciences, University of Nova Gorica, Nova Gorica, Slovenia

2. Department of Astrophysics Geophysics and Oceanography, University of Liège, Liège, Belgium

3. Analytical, Environmental and Geo- Chemistry, Vrije Universiteit Brussel, Brussels, Belgium

4. Institute of Chemistry of Clermont-Ferrand, University of Clermont Auvergne, Clermont-Ferrand, France

mladen.franko@ung.si

Speciation of elements is critical for numerous processes at molecular and cellular level as well as at the level of organisms. Furthermore, speciation of certain elements governs their essentiality and/or toxicity, their mobility in the environment as well as their role in environmental processes on ecosystem level. A typical example is speciation of iron which in general occurs in Fe(II) and Fe(III) redox forms. Several ligands, however form complexes of different stability with Fe(II) or Fe(III), which determines the prevalence of a particular Fe form in various biological and environmental systems. Iron, for example, may limit the growth of marine phytoplankton [1] and thus the process of CO₂ fixation in oceans, which is crucial from the point of global warming and ocean acidification. On the other hand, the concentrations of iron in oceans are governed among other factors by the redox state of iron, since Fe(III) is much less soluble due to particle adsorption or precipitation as hydroxide [2]. Similarly, the iron redox species and their complexes govern the photochemical processes through the Fenton processes [3]. In cloud-water, such processes are suspected to be affected by organic ligands released by metabolically active bacteria, including siderophores such as pyoverdine [4].

Studies of biogeochemical processes involving iron species in samples from remote environments such as oceans and clouds impose additional demands on the applied analytical methods. Low concentrations of iron species demand high sensitivity, while presence of various iron species in complex sample mixtures requires adequate selectivity of the analytical method. In addition, sampling at remote locations requires compatibility of analytical methods with advanced sampling strategies, while demands of multiparameter analysis in limited amounts of samples, like in case of cloud-water, makes the capability of analysing small volume samples an important criterion in selection of most suitable analytical method.

It is therefore the objective of this contribution to present the most recent and novel approaches to speciation of iron in environmental samples by exploiting the advantages of photothermal techniques such as thermal lens spectrometry (TLS) and beam deflection spectrometry (BDS). This includes determination of iron redox species by coupling of TLS to flow injection analysis (FIA) and TLS microscopy to microfluidic systems (μ FIA-TLM) which was recently shown to provide limits of detection at ng/mL level in sub μ L samples [5]. TLS was also applied for detection in liquid chromatography for determination of fluorescing pyoverdines as well as nonfluorescing Fe(III)-pyoverdine complexes in a single chromatographic run. Application of BDS was related to analysis of passive samplers based on diffusive gradients in thin-technique, which is increasingly used for monitoring of environmental pollution due to its robustness, versatility, precision and capacity of pre-concentrating bioavailable trace-level metal pollutants [6].

Materials and Methods

TLS, TLM and BDS instruments used in this work were described in literature previously [5, 7, 8]. Detection of Fe(II) and Fe(III) was based on colorimetric reaction using 1,10-phenanthroline and excitation by Ar-laser 514.5 nm line in case of TLS or by a solid state laser emission at 532 nm for BDS measurements.

Pyoverdines and Fe(III)-pyoverdines were determined following a HPLC separation on a reverse-phase C18 chromatographic column (Hypersil Gold, 150 mm x 3 mm I.D., Thermo Fisher Scientific) with 20 mM ammonium acetate: MeOH (95:5, v/v) as mobile phase at 0.6 mL/min flow rate. A Kr-laser 407-413 nm multiline emission was used for TLS detection in this case.

DGT gels were provided by the Analytical, Environmental and Geo-Chemistry department at the Vrije Universiteit Brussel (Brussels, Belgium) and were prepared according to previously described procedure [9].

Pyoverdine standard, produced by the bacterial strain *Pseudomonas fluorescens 36b5*, was obtained from the Université Clermont Auvergne, Institut de Chimie de Clermont-Ferrand (Clermont-Ferrand, France), where it was isolated and purified [10].

Results and Discussion

Validation of FIA-TLS and μ FIA-TLM techniques for Fe determination in comparison to UV-Vis spectrometry (Table 1) show that despite 100 times shorter optical path length (comparing to UV-Vis spectrophotometry), μ FIA-TLM offers LODs of 0.10 and 0.07 $\mu\text{mol/L}$ for Fe(II) and Fe(total), respectively, and analysis of only 3 $\mu\text{mol/L}$ samples. This is sufficiently low for cloudwater analysis, since concentrations, lower than 0.1 $\mu\text{mol/L}$ (5 ng/mL) are not expected [11]. Analysis of spiked synthetic cloud water has shown recoveries in the 102-105% range for Fe(total), which confirms good specificity of the method.

In case of pyoverdines and Fe(III)-pyoverdine complexes, LODs were estimated to be 0.05- 0.06 $\mu\text{g/mL}$ for HPLC-DAD while TLS detection offered about 10 times lower detection limits (0.004 - 0.007 $\mu\text{g/mL}$) for determination of all pyoverdine species in a single run. Still, about 10 times lowest LODs of fluorescent pyoverdines (not complexed with Fe) were achieved by spectrofluorimetric (SF) detection. However, SF does not offer a possibility of measuring nonfluorescent Fe(III)-pyoverdines.

Combined DGT-BDS has provided LODs between 40-80 nmol/L (2.2 – 4.4 $\mu\text{g/L}$) Fe(II), which depends strongly on the type of the resin used in the DGT sampler. These values correspond to about 30 ng of total Fe amount diffused into the DGT gel and compare favorably to the LODs obtained by UV-Vis spectrometry which were between 200 and 400 nmol/L, respectively.

Table 1. Comparison of analytical performances of FIA/TLS, μ FIA-TLM, and UV/Vis for determination of Fe(II) and Fe(total).
Fe(total) = Fe(II)+Fe(III).

Technique	μ FIA-TLM		FIA-TLS		UV-Vis	
	Fe(II)	Fe(total)	Fe(II)	Fe(total)	Fe(II)	Fe(total)
Linear range ($\mu\text{mol/L}$)	0.1 – 70	0.1 – 70	0.04 – 0.2	0.04 – 0.2	0.8 – 4.8	0.8 – 4.8
LOD ($\mu\text{mol/L}$)	0.1	0.07	0.001	0.0008	0.01	0.01
Within day precision-RSD (%)	8	4	2.6	3.2	0.9	0.2
Optical path	100 μm		1 cm		10 cm	
Sample volume	3 μL		50 μL		25 mL	

Acknowledgements

This work was supported by the ARRS - Slovenian Research Agency within the research program P2-0393: Advanced materials for low-carbon and sustainable society, and by the French ANR program BIOCAP. L.G. and H.B. acknowledge the Young Researchers' grants by the ARRS. A.B. acknowledges grant No11013-18/2018-5 by AD FUTURA - The Public Scholarship, Development, Disability and Maintenance Fund of the Republic of Slovenia.

References

1. D. Lannuzel, M. Vancoppenolle, P. van der Merwe, J. de Jong, K.M. Meiners, M. Grotti, J. Nishioka, V. Schoemann, *Elementa: Science of the Anthropocene*, 4(0):000130, 1 (2016) doi.org/10.12952/journal.elementa.000130
2. J.K. Moore, O. Braucher, *Biogeosciences Discussions*, 4, 1241 (2007)
3. W. Huang, M. Brigante, F. Wu, C. Mousty, K. Hanna, G. Mailhot, *Environmental Science and Technology*, 47, 1952 (2013)
4. V. Vinatier, N. Wirgor, M. Joly, M. Sancelme, M. Abrantes, L. Deguillaume, A.M. Delort, *Environmental Science and Technology*, 50, 9315 (2016)
5. M. Liu, S. Malovrh, M. Franko, *Analytical Methods*, 8, 5053 (2016) doi: 10.1039/C6AY00932H
6. W. Bennett, M. Arsic, J.G. Panther, D.T. Welsh, P.R. Teasdale, in: W. Davison (Ed.): *Diffusive Gradients in Thin-Films for Environmental Measurements*. 1.ed. Cambridge University Press, Cambridge, UK, 2016, pp. 66–92. DOI:10.1017/CBO9781316442654.005
7. M. Martelanc, L. Žiberna, S. Passamonti, M. Franko, *Talanta*, 154, 92 (2016) doi: 10.1016/j.talanta.2016.03.053.
8. H. Budasheva, A. Kravos, D. Korte, A. Bratkič, Y. Gao, M. Franko, *Acta Chimica Slovenica*, 66, 239 (2019)
9. Y. Gao, S. van de Velde, P.N. Williams, W. Baeyens, H. Zhang, *Trends in Analytical Chemistry*, 66, 63 (2015)
10. M. Passananti, V. Vinatier, A.M. Delort, G. Mailhot, M. Brigante, *Environmental Science and Technology* 50, 9324 (2016)
11. L. Deguillaume, T. Charboullot, M. Joly, M. Väitingom, M. Parazols, A. Marinoni, P. Amato, A.M. Delort, V. Vinatier, A. Flossmann, N. Chaumerliac, J.M. Pichon, S. Houdier, P. Laj, K. Sellegri, A. Colomb, M. Brigante, G. Mailhot, *Atmospheric Chemistry and Physics*. 12, 1485 (2014).

KEYNOTE

Opto-thermal Radiometry for Detection of Surface Contamination

XU ZHANG ^(1, 2), CHRISTOS BONTOZOGLOU ⁽¹⁾, PERRY XIAO ^{(1) *}

1. School of Engineering, London South Bank University, 103 Borough Road, London SE1 0AA, UK

2. Auckland Tongji Medical & Rehabilitation Equipment Research Centre, Tongji Zhejiang College, Jiaxing, China

xiaop@lsbu.ac.uk

The aim of this work is to conduct a proof-of-concept study on detection of surface contamination by biological and chemical agents using opto-thermal transient emission radiometry (OTTER). OTTER is an infrared remote sensing technology that has been developed in our research group for skin measurements. It is based on the measurement of laser-induced transient thermal emission spectra in the infrared fingerprint region, and has advantages of non-contact, non-invasive, spectroscopic in nature, and can work on arbitrary surfaces of any materials [1-4]. In this paper, two types of experiments were conducted, different ingredients on the surface of a sample material and different ingredients on the skin surface. Figure 1 shows the OTTER raw signal data of finger skin only, finger skin and MS Neat (methyl salicylate), finger skin and olive oil, as well as finger skin plus MS Neat (methyl salicylate) and olive oil. The results show that by measuring the OTTER signal at different detection wavelengths, e.g. 13.1 μm , 11.5 μm , 9.5 μm , 8.5 μm , 7.79 μm , 6.48 μm , 6.05 μm , it is possible to differentiate from skin and skin with different ingredients on the surface. The next step is to develop mathematical models and analytical algorithms to quantify the ingredients concentration on the surface.

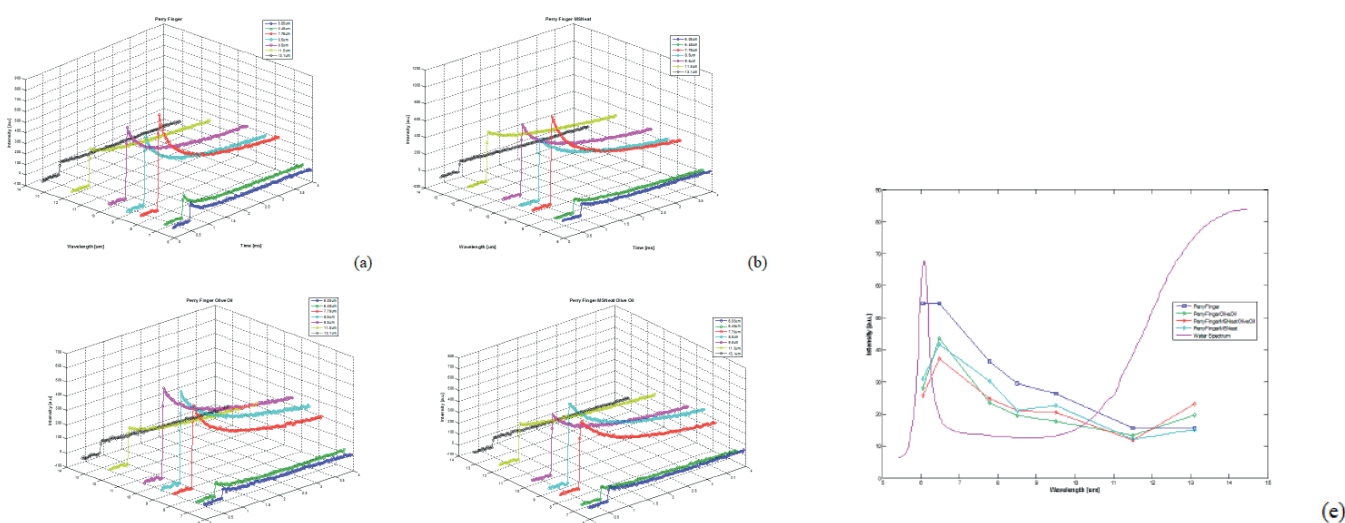


Fig. 1. The OTTER raw signal data of (a) finger skin only, (b) finger skin and MS Neat (methyl salicylate), (c) finger skin and Olive Oil, (d) finger skin, MS Neat (methyl salicylate) and Olive Oil at different detection wavelengths, e.g. 13.1 μm , 11.5 μm , 9.5 μm , 8.5 μm , 7.79 μm , 6.48 μm , 6.05 μm , whilst (e) shows the corresponding analyzed results of the raw OTTER signal data at different wavelengths.

Acknowledgements

We thank London South Bank University for the financial support and Biox Systems Ltd for the studentship support for C. Bontozoglou. We also thank University of Hertfordshire for providing the ideas, the samples and useful discussions.

References

1. R.E. Imhof, A.D. McKendrick and P. Xiao, "Thermal emission decay Fourier transform infrared spectroscopy", *Rev. Sci. Instrum.*, Vol. 66, No. 11, 5203-5213, 1995.
2. P. Xiao, J.A. Cowen and R.E. Imhof, "In-Vivo Transdermal Drug Diffusion Depth Profiling - A New Approach to Opto-Thermal Signal Analysis", *Analytical Sciences*, Vol 17 Special Issue, pp s349-s352, 2001. <https://doi.org/10.14891/analscisp.17icpp.0.s349.0>
3. P. Xiao, X. Ou, L.I. Ciortea, E.P. Berg and R.E. Imhof, "In-vivo Skin Solvent Penetration Measurements Using Opto-thermal Radiometry and Fingerprint Sensor", *International Journal of Thermophysics*, 33:1787-1794, DOI 10.1007/s10765-012-1318-6, 2012.
4. P. Xiao, "Photothermal Radiometry for Skin Research", *Cosmetics*, 3(1), 10, doi:10.3390/cosmetics3010010, 29 Feb 2016.

Chemical composition with photo-thermal optical coherence tomography

Nima Tabatabaei ^{(1)*}, Mohammad Hossein Salimi ⁽¹⁾, Marjan Razani ⁽¹⁾, Martin Villiger ⁽²⁾

1. Mechanical Engineering Department, Lassonde School of Engineering, York University, Toronto, Canada

2. Harvard Medical School and Massachusetts General Hospital, Wellman Center for Photomedicine, Boston, MA, USA

*nima.tabatabaei@lassonde.yorku.ca

Optical coherence tomography (OCT) is an interferometric optical imaging method which utilizes low-coherence light to capture micrometer-resolution images from optical scattering media (e.g., biological tissue) in two and three dimensions. Since the first demonstration of OCT imaging in human eye in 1990, the technology has undergone significant transformations and has become the gold standard for retinal imaging and is also routinely used in dermatology and for endoscopic imaging of the coronary arteries and the esophagus. Despite its widespread use, OCT, similar to ultrasound, forms images based on structure of tissue rather than its composition (i.e., scattering vs absorption of light), which limits its diagnostic performance. A case in point is identification of atherosclerotic plaques in the coronary arteries of patients with coronary artery disease. In OCT, a significant number of lesions frequently bear structural features of high risk of rupture, while only a subset of these plaques present the chemical composition associated with likelihood of rupture. To overcome this limitation, photothermal OCT (PT-OCT) has been developed as a molecular-contrast extension of OCT to complement the high-resolution structural images with depth-resolved and co-registered molecular information. In PT-OCT, a secondary intensity-modulated photothermal laser is integrated into the OCT system to locally modulate the optical path length (OPL) measured by OCT in the proximity of an absorbing molecule. The phase signal of OCT has excellent sensitivity to even minute changes in the OPL. Therefore, by tuning the wavelength of the photothermal laser to the absorption band of molecule(s) of interest (e.g., lipid), one can obtain an image in which the high-resolution structural information comes from scattering of light at subsurface microstructures through the OCT amplitude signal while, simultaneously, depth-resolved information with molecular specificity is detected through the OCT phase signal. In this paper we report on proof of principle PT-OCT experiments to gain insight into the chemical composition of a sample by scanning the intensity modulation frequency of the photothermal laser and studying the subsequent photothermal frequency responses of the OCT phase signals.

A schematic of the developed spectral-domain PT-OCT system is depicted in Fig. 1. The system uses broadband light of a superluminescent diode centered at 1310 nm (± 75 nm at 10 dB), a 2048-pixel line scan camera spectrometer with a maximum acquisition rate of 147 kHz, and a 808 nm intensity-modulated photothermal laser. The experimental axial and lateral resolutions are 11 μm and 10 μm , respectively. Through careful instrumentation and numerical dispersion compensation we have managed to achieve performance close to the shot-noise with a relative displacement error of 3 nm at a SNR of 35 dB and system sensitivity of >100 dB.

In order to study the concentration-dependence of the PT-OCT frequency response, methanol solutions with different concentrations of IR-806 dye (sigma Aldrich) were prepared. To avoid evaporation of methanol, solutions were injected into capillary glass tubes and imaged while the intensity of photothermal laser was modulated at frequencies of 40, 80, 120, 160 and 200 Hz.

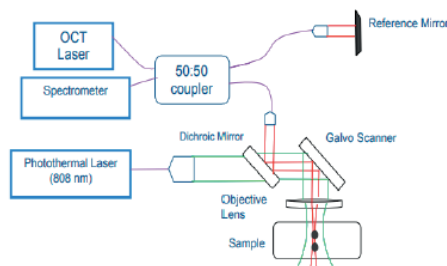


Fig. 1. Schematic of developed PT-OCT system [1].

After data acquisition, the time-lapse datasets were processed and the relative OCT phase in the tomograms was used for constructing PT-OCT photothermal frequency responses, Fig 2(a). Figure 2(b) depicts the normalized amplitude photothermal frequency response of different concentrations of IR-806 dye measured through the phase channel of PT-OCT system, demonstrating the characteristic photothermal frequency response ($\propto \sqrt{1/f_m}$) as the photothermal laser modulation frequency is scanned from 40 Hz to 200 Hz. Moreover, this preliminary data suggests that the amplitude ratio of obtained responses at 40 Hz and 80 Hz is closely correlated with concentration of targeted IR-806 molecules, Fig 2(b) inset.

Session C2: Applied Chemistry

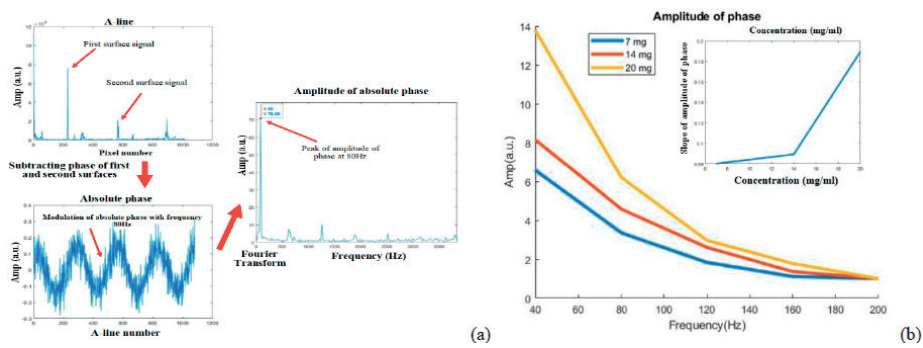


Fig. 3. Processing steps of signals: 1. acquiring A-line 2. Calculating absolute phase 3. Applying FFT(a) amplitude of phase in various concentrations(b) diagram for predicting concentration (b) inset

References

1. Ashish Gupta, Martin Villiger, Nima Tabatabaei, "Optimal selection of laser modulation parameters in photothermal optical coherence tomography," Proc. SPIE 10067, Optical Elastography and Tissue Biomechanics IV, 1006718 (21 February 2017); doi: 10.1117/12.2252779

Implementation of liquid chromatography coupled to thermal lens spectrometry (HPLC-TLS) in studies of yeasts' role in formation of stable pigments in Pinot Noir wines

Branka Mozetič Vodopivec ^{(2)*}, Jelena Topić Božič ⁽¹⁾, Lorena Butinar ⁽²⁾, Natka Ćurko ⁽³⁾, Karin Kovačević Ganić ⁽³⁾, Dorota Korte ⁽¹⁾, Mladen Franko ⁽¹⁾

1. Laboratory for Environmental and Life Sciences, Nova Gorica, Slovenia

2. Wine Research Centre, Vipava Slovenia

3. Laboratory for Wine Technology and Analysis, Faculty for Food technology and Biotechnology, University of Zagreb, Zagreb, Croatia

branka.mozetic@ung.si

Sensory properties of wines are crucially affected by the production process. The color of wine is one of the first characteristics that consumers assess in this type of alcoholic beverages. In red wines the color is associated with phenolic pigments called anthocyanins, which are present in wine mostly as anthocyanins mono-glucosides. They are most abundant in the young wine and during ageing and storage such pigments are replaced by anthocyanin-derived pigments pyranoanthocyanins [1]. The color of the wine can be influenced by the use of yeast strains that enhance the formation of pyranoanthocyanins [2]. Reversed phase high performance liquid chromatography (HPLC) in combination with DAD detector is most often used for analysis of anthocyanins and pyranoanthocyanins, and for structural information LC-MS and LC-MS/MS techniques are used [3]. From quantification point of view, significant improvement in lowering the limits of detection (LOD) and quantitation (LOQ) in comparison to DAD detectors can be achieved by coupling HPLC to thermal lens spectrometry (TLS) [4].

The aim of this study was to implement HPLC-TLS in investigation of yeasts' impact on the formation of stable vinylphenolic pyranoanthocyanins (VP-Pyr) in Pinot Noir wine. The investigations were initially performed in the synthetic wine supplemented with Pinot Noir skin extract. Yeast strains were selected for further lab-scale wine fermentations during which the start of VP-Pyr formation was monitored with the help of HPLC-TLC. This is of great importance in optimization of wine fermentation conditions.

Materials and methods

Table 1: Chromatographic conditions for HPLC-DAD and HPLC-TLS method.

Parameter	HPLC-DAD	HPLC-TLS
Column	Luna Phenomenx C18 PFP(2) 250x4.6 mm, 5 µm i.d.	
Detection wavelength [nm]	520	513
Injection volume [µL]	40	20
Elution	Gradient	Isocratic (calibration curve) Step gradient (sample analysis)
Standard	Malvidin-3-O-glucoside (Mvd3glc)	
Mobile Phase	A: 0.2% trifluoroacetic acid in water B: 0.2% trifluoroacetic acid in methanol	
Mobile phase	80/20 A/B up to 55/45 A/B	70/30 A/B to 60/40 A/B

Standards of vinylphenolic pyranoanthocyanins (VP-Pyr) were synthesized and isolated in collaboration with Laboratory for Wine Technology and Analysis (Faculty for Food technology and Biotechnology, University of Zagreb) and were used to confirm the identity of VP-Pyrs appearing in HPLC chromatograms. Samples from lab-scale wine fermentations were analyzed at days 2, 7 and 12 of fermentation process and the day of wine bottling.

Results and discussion

Four different mobile phases were assessed for obtaining the optimal thermal lens enhancement factor. The results in Table 2 show increase in the peak area of Mvd3glc with increase of methanol content in the used mobile phase. In the mobile phases with 80/20

Session C2: Applied Chemistry

and 70/30 water/methanol ratio, theoretically calculated enhancement factors are in good agreement with experimental results. Increase in methanol content shortens the retention time of Mvd3glc, which ultimately lead to elution of Mvd3glc with the solvent front. Because of this, discrepancies have been observed between experimental and calculated enhancement factors when using 65/35 and 60/40 water/methanol ratio in mobile phase, which also made expression of VP-Pyrs in terms of Mvd3glc equivalents impossible. The 70/30 water/methanol mobile phase was chosen because of increase in signal for Mvd3glc and samples of synthetic wine with Pinot Noir skin extract were analyzed. However, such composition of mobile phase did not enable separation of pyrano-anthocyanins in an isocratic mode. Thus, the step gradient was applied with mobile phase composition change from 70/30 to 60/40 water/methanol ratio after the elution of Mvd3glc standard (320 s). The same method was successfully applied for analysis of Pinot Noir wine samples during lab-scale fermentations.

Table 2: Enhancement factors for different mobile phase composition calculated from the peak area of 1 ppm malvidin-3-*O*-glucoside, relative to 80/20 water/methanol.

%water/%methanol	80/20	70/30	65/35	60/40
Experimental	1 ± 0.03	1.26 ± 0.02	1.59 ± 0.01	1.72 ± 0.06
Theoretical	1	1.30	1.47	1.65

HPLC-TLS provided LODs and LOQs at the level of 7 and 25 ppb Mvd3glc equivalents, respectively, while the LODs and LOQs for HPLC-DAD were 45 and 140 ppb Mvd3glc equivalents, respectively. Due to superior sensitivity of HPLC-TLS three VP-Pyrs could be detected, while with HPLC-DAD only detection of up to two VP-Pyrs was possible. By using HPLC-TLS method, formation of VP-Pyr was observed at day 12.

Conclusions

HPLC-TLS, which was used for the first time in the assessment of VP-Pyrs formed in Pinot Noir wines, offers 5-times lower LODs and two-times lower injection volume in comparison to HPLC-DAD. Furthermore, with HPLC-TLS more VP-Pyrs were detected and their formation was observed earlier during fermentation process, which enabled identification of most effective yeast strains for the formation of PV-Pyrs, which is important for wine color stability.

References

1. V. De Freitas and N. Mateus, *Anal. Bioanal. Chem.* 401, 1467 (2011) doi: 10.1007/s00216-010-4479-9.
2. S. Benito, A. Morata, F. Palomero, M. C. C. González, and J. A. A. Suárez-Lepe, *Food Chem.* 124, 15 (2011) doi:10.1016/j.foodchem.2010.05.096
3. P. Arapitsas, D. Perenzoni, G. Nicolini, and F. Mattivi, *J. Agric. Food Chem.* 60, 10461 (2012) doi:10.1021/jf302617e.
4. M. Martelanc, L. Žibera, S. Passamonti, and M. Franko, *Talanta* 154, 92 (2016) doi:10.1016/j.talanta.2016.03.053.

Rotator phase transitions in alkanes studied by Photopyroelectric and Adiabatic Scanning Calorimetry

Ugo ZAMMIT ^{(1)*}, Stefano PAOLONI ⁽¹⁾, Fulvio MERCURI ⁽¹⁾, Christ GLORIEUX ⁽²⁾,
Jan LEYS ⁽²⁾, Jan THOEN ⁽²⁾

1. Dipartimento di Ingegneria Industriale, Università di Roma "Tor Vergata", Rome, Italy
2. Soft Matter and Biophysics, Department of Physics and Astronomy, KU Leuven, Belgium

* zammit@uniroma2.it

Rotator phases are solid phases where there is three-dimensional crystalline order for the positions of the molecules, but no long-range rotational order about the molecular long axis [2]. We have studied the nature of the R_{III} - R_V , R_{IV} - R_{III} , R_{II} - R_V , and R_{IV} - R_{II} , rotator phase transitions in several linear alkanes (C26 to C30) by analyzing the hysteretic behavior of the specific heat between heating and cooling measurements. The investigations have been carried out by both Adiabatic Scanning Calorimetry (ASC) and Photopyroelectric Calorimetry (PPE) techniques, whose combined use has provided complementary information concerning the changes occurring in the samples structure during their temperature change to associate them with the changes in values of the thermal conductivity and of the thermal diffusivity.

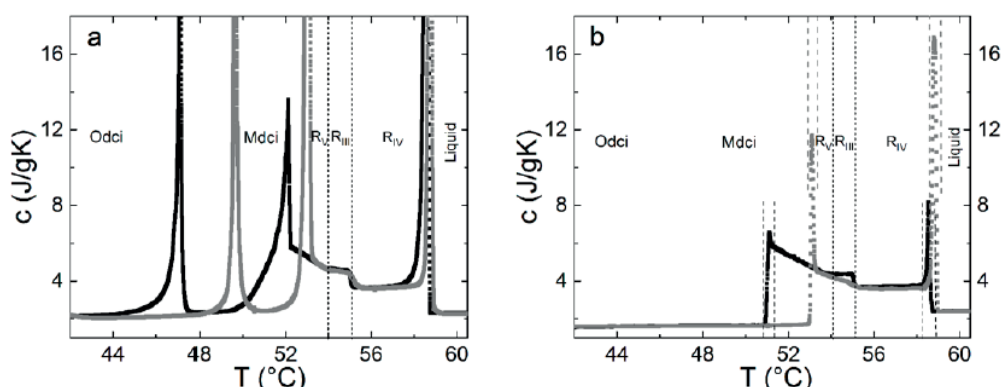


Fig. 1. Specific heat profile for C27 in the range crystal phase to liquid phase obtained by: a) ASC and b) PPE measurements. Black symbols correspond to the cooling runs and grey symbols to the heating runs. Double vertical long-dashed lines in b) delimit the two-phase coexistence regions.

For example, Fig. 2a and 2b show the sequence of phases obtained in C27 by ASC and PPE calorimetries, with the former being more sensitive to the presence of latent heat by the manifestation of sharp peaks. Hysteresis also denotes the presence of first order phase transitions. The phase transitions are also detected in the jumps observed in the thermal conductivity and diffusivity profiles displayed in Fig. 3a and 3b, with larger values in the more ordered phases. As for the textures, Fig. 4a displays that obtained when the sample was at 56°C in the R_{IV} phase during the cooling run from the liquid phase, while Fig. 4b shows the corresponding texture pattern obtained when the sample was in the Mdci crystalline phase at

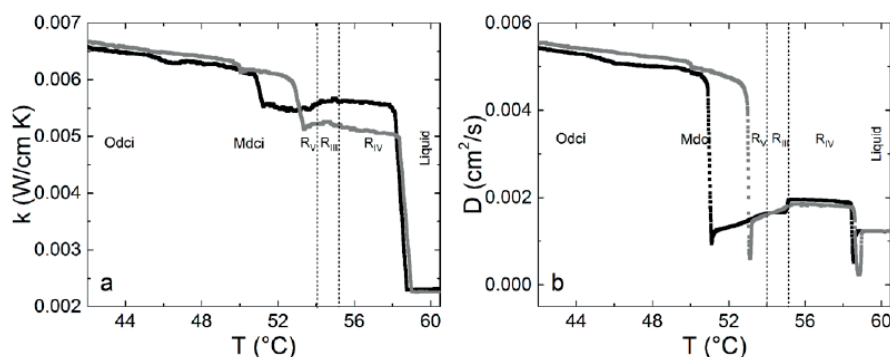


Fig. 2. a) Thermal conductivity and b) thermal diffusivity profiles for C27 in the range crystal phase to liquid phase obtained by PPE measurements. Black symbols correspond to the cooling runs and grey symbols to the heating runs.

47 °C. Fig. 4c reports the pattern obtained after taking the sample back in the R_{IV} phase at 56°C following its heating from the crystalline phase. The texture of the R_{IV} phase when heating the sample from the crystalline phase displays elements resembles that observed in the the crystalline phase. Thus, it appears that the R_{IV}, and also the R_{III} and R_{IV} phases, obtained following the heating

Session C2: Applied Chemistry

from the crystal phase maintained memory of the grain structure of the crystalline phase and possibly contained distortions imposed by such grain constrains. This is reflected in the smaller thermal conductivity values obtained in the temperature range of the R_V to R_{IV} phases during the heating of the sample than during the cooling. During the cooling and heating cycles to check for hysteresis, the inversion was performed before reaching the crystalline phase.

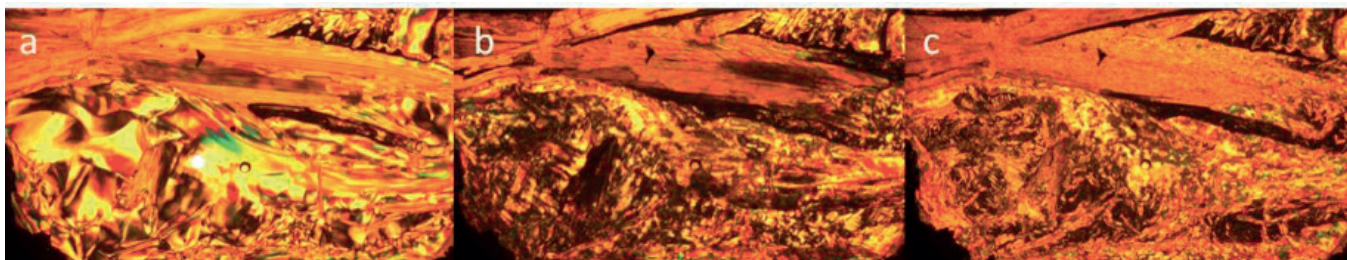


Fig. 3. Polarization microscopy images performed in C27 obtained: a) in the RIII phase during the first cooling run; b) in the MdcI crystalline phase during the first cooling run; c) in the RIII phase during the subsequent heating run.

References

1. G. R. Strobl, B. Ewen, E. W. Fisher and W. J. Pieszczek, *J. Chem. Phys.*, 61, 5257 (1974).

Optoacoustics of Oil-Water Mixtures. Control of Small-Volume Samples

Sergey EGEREV

Andreyev Acoustics Institute, 4 Shvernika street, Moscow 117036 Russia

E-mail: segerev@gmail.com

The content of oil products in the discharged reservoir waters during offshore oil and gas production is regulated by international conventions and slightly varies. Normally, the legislation (OSPAR, HELCOM, Kuwait Convention, Barcelona Convention) restricts average concentration of dispersed oil to exceed 40 mg/L of discharged water. These requirements are 1-2 orders of magnitude "softer" than the oil-content requirements applied to drinking water reservoirs. Such permissive requirements allow us to offer a compact optoacoustic device for detecting hydrocarbons in the sea water samples check near the mining platforms.

Optoacoustic calorimetric measurement method is actively used in environmental studies as a very sensitive spectroscopy technique. Optoacoustic technique is promising for detecting hydrocarbons in water [1-3]. Optoacoustic response of crude oil is defined by the features of the constituents, such as benzene, pentane and methanol.

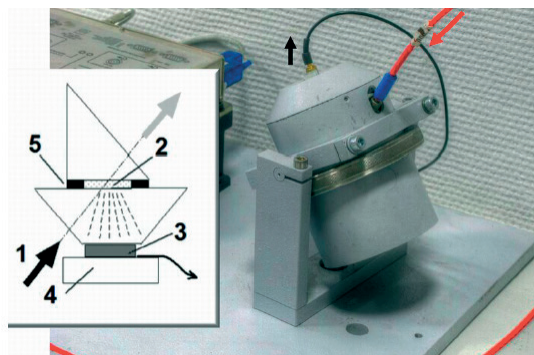


Fig. 1. Optoacoustic measurement cell based on a layered prism concept. Here inlet shows a simplified scheme of the device. 1 – incoming light pulse; 2 – sample; 3 – transducer; 4 – backing dumper; 5-shim. Red arrow - laser beam delivery; black arrow - optoacoustic response output.

A portable optoacoustic device utilizing commercially available laser source is presented as a tool for the detection of oil contamination. The peculiarity of the present work is that we deal with optoacoustic signal occurring due to the absorption of surprisingly small laser energy deposit 1 mJ in small liquid samples. In the present prototype, good optoacoustic contrast between water and hydrocarbons was achieved at the wavelength 527 nm. The corresponding Q-switched diode pumped solid state pulsed laser was used having pulse train frequency 1 kHz. Fiber-optic delivery of a laser beam to a sample was used.

Water samples with dissolved and emulsified oil components were prepared by means of ultrasonic dispersion of oil in 100 mL of distilled water. A broad range of concentrations was provided. The sample 2 has a layer thickness 260 μm , which corresponds to the duration of the outgoing acoustic pulse 700 nS. The thickness of the sample layer is controlled by thin wafers glued to the top prism. The pick-up of the acoustic response was provided with a thickness-mode piezoceramic transducer having thickness 200 μm . The transducer output signal was processed within a frequency band up to 100 MHz. Sets of 1000 successive output signals were acquired and averaged with the help of software. Thus, the noticeable optoacoustic response from the sample was obtained having a good noise immunity.

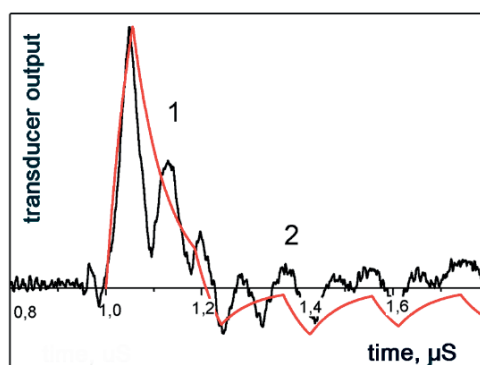


Fig. 2. Output signal profiles. Curve 1 - model (theory); curve 2 - averaged signal for oil concentration 1000 mg/L.

Session C2: Applied Chemistry

Optoacoustic measurement process with the use of the layered prism cell (Fig.1, inlet) was modeled theoretically within a step-by-step approach based on the transfer functions method. Our results indicate that such a cell provides sufficient figures of merit of determination of the low-concentration impurities in small-volume liquid samples. The calculated model curve 1 (Fig. 2) takes into account the optoacoustic conversion of the laser pulse in the contaminated sample. Then, the diffraction propagation of the acoustic response towards the receiver through the lower prism (dotted lines in Fig. 1). Finally, the model curve reflects the reaction of the piezoceramic receiver loaded on the resistance of the preamplifier. Test curve 2 represents accumulation of 2000 output transducer pulses.

The dependence of response pulse energy vs oil concentration remains linear within the broad range of concentrations. The detection limit of the contaminating objects' concentration proved to be (2-5) mg/L. This is much less than the admissible concentration level. The results contribute to further development of optoacoustic methods and equipment to be applied for environmental analysis.

References

1. L.M. He, L.L. Kear-Padilla, S.H. Lieberman, J.M. Andrews, *Analytica Chimica Acta*, 478 (2), 245 (2003) doi: doi.org/10.1016/S0003-2670(02)01471-X
2. P. Hodgson, K.M. Quan, H.A. MacKenzie, S.S. Freeborn, J. Hannigan, E.M. Johnston, F. Greig, T.D. Binnie, *Sensors and Actuators B*, 29 (1-3), 339 (1995) doi: doi.org/10.1016/0925-4005(95)01704-6
3. S.S. Freeborn, J. Hannigan, F. Greig, R.A. Suttie, H.A. MacKenzie, *Review of Scientific Instruments*, 69 (11), 3948 (1998) doi: doi.org/10.1063/1.1149204

KEYNOTE

Optical tension measurement of single aerosol droplet measurement based on surface thermal fluctuation

Akihide HIBARA*

Institute of Interdisciplinary Research for Advance Materials, Tohoku University, Sendai, Japan
hibara@tohoku.ac.jp

In recent years, the interfacial mechanism for aerosol chemistry and cloud droplet formation has been considered an essential problem in geochemistry.^{1,2} In particular, organic compounds in atmospheric environments can be dissolved in aerosols, and they sometimes exhibit surface activity; thus, organic aerosols have attracted considerable attention. However, despite such interest, experimental verification of the mechanism based on direct aerosol tension measurements has not been established due to lack of a suitable measurement method.

We have studied a quasi-elastic light scattering (QELS) method which measures optical frequency shift on a free surface during laser light scattering by capillary waves.³ Recently, we found spontaneous resonance of thermally induced capillary waves on liquid surfaces with spatial confinement in microchannels⁴ and 2D-confined apertures.⁵ In these experiments, capillary-wave modes satisfying the resonant conditions continue oscillating, and those under non-resonant conditions soon disappear. Therefore, the characteristic peaks corresponding to the resonant modes appear in the QELS power spectrum. Subsequently, surface tension has been successfully measured from the peak frequencies. The principle is promising for optical surface tension measurements. In this presentation, I will introduce the optical surface tension measurement of a single aerosol droplet for discussing environmental issues.

Principle

The interface between a gas/liquid is perturbed by thermal fluctuations with an amplitude of a few Ångströms. In the absence of spatial confinement, thermally induced capillary waves with random wavenumbers exist at the interface. For a certain wavelength λ , the corresponding wavenumber q is defined as $q=2\pi/\lambda$.

The optical configuration around the optically trapped aerosol droplet is illustrated in Figure 1.³⁻⁶ When divergent laser light with a frequency of F and wavenumber of K is incident on the liquid surface, the beam irradiates the liquid surface (travelling from liquid to gas) over a range of incident angles. For simplicity, three angles, θ_1 , θ_2 , and θ_3 ($\theta_1 > \theta_2 > \theta_3$) are selected for explanation.

For light scattering along the normal direction, the momentum conservation, expressed as $q_i=K\sin\theta_i$, is maintained for each incident angle. During scattering by the capillary wave (with wavenumber q_i), light frequency F is shifted as $F \pm f_i$. Therefore, the frequency shifts vary depending on the angle. Consequently, the optical beats between the non-scattered transmitted and scattered light signals can be considered as the convolution of the frequency shifts, and a broad peak is obtained in the resulting spectrum.

A spherical droplet does not have wall boundaries, but a periodic boundary condition may be applied to consider the resonant modes. Lamb derived the characteristic resonant frequency, f_l , as

$$f_l = \frac{1}{2\pi} \sqrt{\frac{l(l-1)(l+2)\gamma}{\rho a^3}}, \quad (1)$$

where γ , a , ρ , and l represent the droplet surface tension, radius of the sphere, density, and an integer representing oscillation mode $l=2,3,4,\dots$, respectively. These spontaneously resonating modes are reflected in the QELS power spectrum of an optically trapped aerosol droplet.

Results and Discussion

Figure 2 shows the QELS spectrum of the 5.5- μm -radius droplet of 5 mM aqueous solution of sodium dodecylsulfate). Upon fitting the multi-Lorentzian functions, we obtained 3 clear peaks (204, 392, and 808 kHz) along with a weak one (613 kHz).

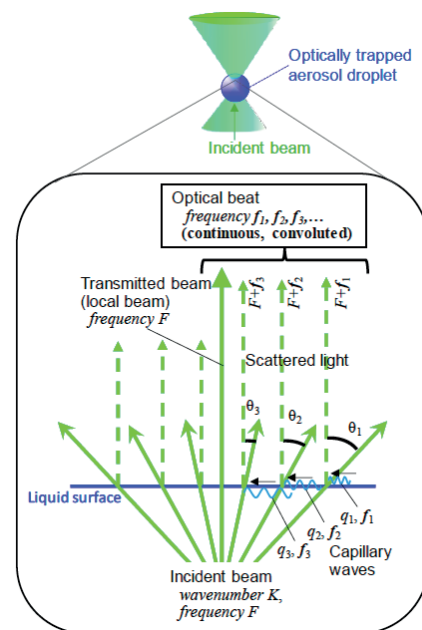


Fig. 1. Principle of quasi-elastic laser scattering (QELS) method with a single diverging beam configuration. "Reprinted with permission from Ref. 6. Copyright (2018) American Chemical Society."

Session C3: Applied / Gas Analysis

The inset of Figure 2 shows the dependence of the fitted frequencies on parameter l . Upon fitting the data with Eq. (1), we obtained the surface tension as 32.0 ± 1.0 mN/m. Thus, we were able to perform measurements reflecting the effect of organic compounds on the surface tension of a single aerosol droplet.

The simplicity of our optical setup is noteworthy; we only added certain optical components to the classical single-beam optical trapping system. Therefore, the method can potentially easily be used by even non-expert researchers. We believe that our method will significantly contribute to the field of aerosol laboratory experiments, particularly to the long-standing discussion of cloud nucleation.

Acknowledgements

We appreciate Prof. Ishizaka of Hiroshima University for his contribution. This work was partially supported by JSPS KAKENHI Grant Number 18H03912 and by the Research Program of the "Dynamic Alliance for Open Innovation Bridging Human, Environment and Materials" in the "Network Joint Research Center for Materials and Devices."

References

1. U. Pöschl, M. Shiraiwa, *Chem. Rev.* 115 (10), 4440 (2015) doi:10.1021/cr500487s
2. C.R. Ruehl, J.F. Davies, K.R. Wilson, *Science* 351 (6280), 1447 (2016) doi:10.1126/science.aad4889
3. A. Hibara, M. Nonaka, M. Tokeshi, T. Kitamori, *J. Am. Chem. Soc.* 125 (49), 14954 (2003) doi:10.1021/ja037308l
4. C. Pigot, A. Hibara, *Anal. Chem.* 84 (5), 2557 (2012) doi:10.1021/Ac3000804
5. M. Chung, C. Pigot, S. Volz, A. Hibara, *Anal. Chem.* 89 (15), 8092 (2017) doi:10.1021/acs.analchem.7b01611
6. T. Endo, K. Ishikawa, M. Fukuyama, M. Uraoka, S. Ishizaka, A. Hibara, *J. Phys. Chem. C* 122 (36), 20684 (2018) doi:10.1021/acs.jpcc.8b03784

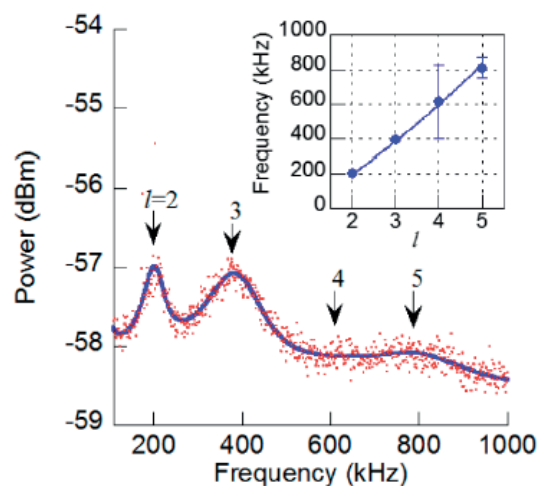


Fig. 2. Quasi-elastic light scattering (QELS) spectrum of 5.5- μm -radius droplet containing sodium dodecyl sulfate (SDS) and ammonium sulfate. The blue line indicates the fitting results obtained with multi-Lorentzian functions. (Inset) Equation (1) is fitted to the obtained frequencies to obtain a surface tension of 32.0 ± 1.0 mN/m. "Reprinted with permission from Ref. 6. Copyright (2018) American Chemical Society."

KEYNOTE

Combined laser heating and acousto-optical tunable filter in high pressure cell for synthesis of novel materials and phase transitions observation

PAVEL V. ZININ*, KAMIL BULATOV, ALEXEI BYKOV, SERGEI TITOV, IGOR KUTUZA

Scientific-Technological Center of Unique Instrumentation, Russian Academy of Sciences, Moscow, Russia

zosimpvz@mail.ru

Laser-based techniques are widely used for thin film deposition, crystallization of amorphous materials, surface treatment, alloying and the modification of material properties [1]. Laser heating (LH) is one of the main tools in the study of minerals and synthesis of new materials under high pressure and high temperature in a diamond anvil cell. The conventional way to determine the temperature of a laser-heated specimen is by measuring the thermal radiation emitted from the heated specimen using a diffraction spectrometer. However, those measurements only provide the temperature of the heated spot averaged over its area.

In this presentation a novel technique - acousto-optical multispectral imaging system for in situ measurements of the high temperature and emissivity distributions of a laser heated solids under high pressure will be discussed [2,3]. The main component of the system is an imaging tandem acousto-optical tunable filter (TAOTF) synchronized with a video camera.

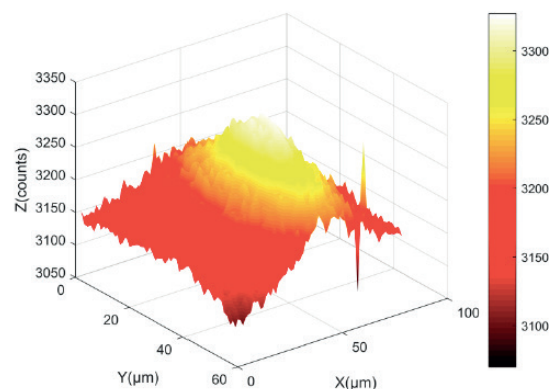


Fig. 1. The 2-D temperature distribution on the surface of a W plate near melting point heated with 24 W laser power, 620-740 nm, and 0.6 s exposure time.

A set of TAOTF spectroscopic images (up to a few hundreds) is taken by the TAOTF imaging system in order to fit the measured spectral curves in each pixel to the Planck radiation function and determine the temperature and emissivity of the sample using the gray body approximation. It was experimentally shown that this technique provides aberration-free spectral imaging suitable for precise multispectral imaging radiometry (MIR). Application of the LH-TAOTF method for studying different physical phenomena such as (a) phase transitions in boron rich carbon material, and (b) melting under high pressure and high temperature will be presented [4].

One of such applications is shown below. The temperature distribution on the tungsten plate heated by a high power laser is shown in Fig. 1. The number of the TAOTF spectroscopic images was ten with a 12 nm spectral step from 620 to 740 nm. The highest temperature in the hot spot is 3278 K and the lowest is 3056 K.

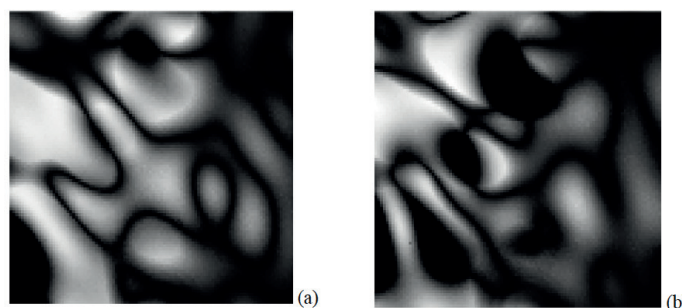


Fig. 2. Variation of the speckles images of the selected area, as a function of time: (a) the first image; and (b) the image taken in 1 s. The wavelength was 1040 nm and the laser power was 24 W.

Session C3: Applied / Gas Analysis

We expected to observe the phenomena similar to critical opalescence near the melting point. The speckle behavior can be associated with dynamic processes both on the surface and in the near-surface layer. As we can see from Fig. 2 the determination of the beginning of the increase of the fluctuations and melting point becomes unambiguous.

Acknowledgements

This work was supported by the program “Fundamental scientific research of the National academy of sciences for 2013-2020” (№0069-2016-0004). This work was performed using the Unique Scientific Instrument “Laser heating at diamond anvil cell” [<http://ckp-rf.ru/usu/507563/>].

References

1. R.I. Romanov, V.Yu. Fominski, I.S. Vasil'evskii, D.A. Safonov, A.A. Soloviev, P.V. Zinin, K.M. Bulatov, V.P. Filonenko, S.M. Novikov, *Diamond and Related Materials* (2019) doi: 10.1016/j.diamond.2018.12.026
2. S. Machikhin, P. V. Zinin, A. V. Shurygin, D. D. Khokhlov, *Optics Letters* 41(5), 901 (2016) doi: 10.1364/OL.41.000901.
3. P.V. Zinin, A.S. Machikhin, I.A. Troyan, K.M. Bulatov, A. A. Bykov, Y.V. Mantrova, V.I. Batshev, M.I. Gaponov, I.B. Kutuza, S.V. Rashchenko, V.B. Prakapenka, S.K. Sharma, *High Pressure Research* . (2019) doi:10.1080/08957959.2018.1564748
4. P. V. Zinin, A. V. Nozhkina, R. I. Romanov, V. P. Filonenko, S. Titov, I. Trojan, V. Y. Fominski, K. M. Bulatov, A. A. Bykov, I. B. Kutuza, A. Anohin, A. M. Lomonosov, *MRS Advances* 3(1-2), 45 (2018) doi:10.1557/adv.2018.5

KEYNOTE

From fundamental research to commercialization: the photoacoustic analyzer for the oil and natural gas industry

Zoltán Bozóki^(1,2,3)

1. Department of Optics and Quantum Electronics, University of Szeged, Hungary

2. Hilase Ltd., Székesfehérvár, Hungary

3. Hobre Laser Technology Ltd. Algyő, Hungary

zbozoki@physx.u-szeged.hu

In this presentation I give an overview of our efforts (focusing primary on their scientific components) started back in 1994, which led to a commercially available photoacoustic instrument family for measuring H₂S, H₂O and CO₂ concentration in natural gas, which already deployed worldwide for more than 100 installations at various offshore platforms and gas plants.

During the course of development, we had to face several scientific challenges such as:

- Due to the variation of the gas composition, the resonance frequency of the photoacoustic detection cell often varies rapidly over a considerable frequency range, which required the development of a fast and accurate resonance tracking method based on “chirp” excitation [1],
- The required stability of the laser wavelength is much higher than the actual “passive” stability of the applied lasers. Therefore, various wavelength stabilization methods were developed yielding a constantly improving stability (see Figure 1),
- There are several overlapping absorption lines in the vicinity of the measurement wavelength (especially in case of H₂S detection), which make it necessary to apply a multi-component type calculation method. Furthermore, we have developed a dual cell operation mode with zero gas generation, which improves further the selectivity of the photoacoustic measurements [2].

An additional issue is the necessary ruggedness of our photoacoustic analyzers, which is achieved by using carefully selected components such as:

- telecommunication type, fiber-coupled DFB diode laser light sources with extremely long lifetime and stable operation,
- miniature MEMS microphones with remarkable stability, resistance to high operational temperature (up to 80 °C) and to aggressive chemicals,
- longitudinal differential photoacoustic cells with high cell constant and low noise operation under continuous gas flow,
- compact electronics for laser driving, temperature stabilization, signal processing and concentration calculation. All the critical elements of the electronics is built from highly temperature insensitive components,
- the software of the instrument performs all the necessary self-checking and self-correction algorithms.

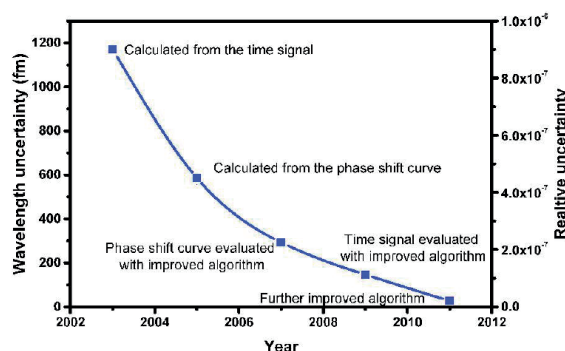


Fig. 1. Improvement of the wavelength stability of the diode laser in our photoacoustic systems over the years.

There are other issues, such as the importance and challenge of producing instrument with similar analytical parameters and the competition of the photoacoustic method with other concentration measuring methods, which are discussed as well.

Acknowledgement

Ministry of Human Capacities, Hungary grant 20391-3/2018/FEKUSTRAT is acknowledged.

References

1. M. Szakáll, A. Varga, A. Pogány, Z. Bozóki, G. Szabó, Applied Physics B. 94 691-698 (2009).
2. A. Varga, Z. Bozóki, M. Szakáll, G. Szabó, Applied Physics B. 85, 315-321 (2006).

Miniaturization and Integration on Silicon of Photoacoustic Gas Sensors

Alain GLIÈRE*, Jean-Guillaume COUTARD, Jean-Marc FEDELI, H el ene LHERMET, Justin ROUXEL, Alexandre TEULLE, Thierry VERDOT, Sergio NICOLETTI

Univ. Grenoble Alpes, CEA, LETI, Grenoble, France

alain.gliere@cea.fr

Integration on silicon platform led in the recent years to major successes in the domain of micro-electromechanical systems (MEMS). The cost reduction reached through mass production in silicon foundries has for instance enabled large-scale deployment of accelerometers in the automotive industry or capacitive microphones in cellular phones. The transposition of this strategy to photoacoustic (PA) based trace gas sensors, aiming at a widespread usage in indoor and outdoor air quality measurement, has been the object of a noteworthy design, fabrication and characterization effort at CEA-LETI.

In this paper, we present a half a dozen years downscaling process, marked by three generations of miniature PA sensors, namely a 40 mm³ 3D-printed metal cell [1], a 3.7 mm³ silicon cell [2], and a 2.3 mm³ silicon cell integrating a dedicated microphone and its expansion volume [3].

The first-generation PA sensor [1] relies on the differential Helmholtz resonator architecture, composed of two chambers linked by two capillaries. Gas excitation is ensured by lighting one of the chambers with a laser source and a differential pressure measurement provides a partial immunity to external acoustic noise. The cell, made of stainless steel, is 3D-printed by direct metal laser sintering, and hosts a pair of commercial capacitive MEMS microphones measuring the differential signal (Fig. 1(a)). The same architecture, still using commercial microphones, has then been harnessed to create the second-generation device (Fig. 1 (b)). Ten times smaller in volume, it is built with two bonded silicon wafers processed in our MEMS production facility [2]. A specialized electronic board including a digital lock-in amplifier and signal processing functions has been developed at this occasion to guarantee the consistency of the miniaturization of the sensor and its associated electronics. In both cases, the normalized noise equivalent absorption is in the order of 10⁻⁸ cm⁻¹ W Hz^{-1/2} and thus, depending on the addressed gas, optical power and integration time the detection limit reaches sub-ppm values (Fig. 2).

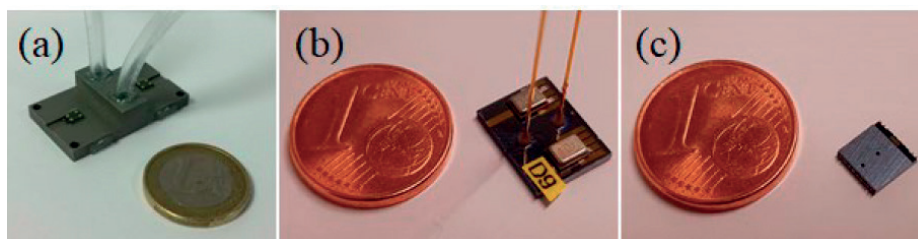


Fig. 1. Three generations of PA cells: (a) metal cell and (b) silicon cell, both equipped with capacitive commercial microphones and (c) integrated silicon cell including piezoresistive microphone.

A completely different architecture has been developed in the third generation device that includes the dynamic pressure sensor (Fig. 1(c)). The cell consists in an illuminated chamber, separated of a closed expansion volume by a channel where a beam-shaped diaphragm flexible hinge, is placed [3]. The stress induced by the motion of the diaphragm within doped silicon nanogauges causes resistance variations, related to the gas concentration. The laser modulation is set on the mechanical resonance of the diaphragm and not, as usually, on the acoustic resonance of the cell. The device is built by bonding a sensor wafer (mechanical diaphragm and piezoresistive nanogauges) and a cap wafer (chamber and expansion volume, electric circuitry and optical waveguide). Preliminary measurements performed on ambient CO₂ allow estimating the detection limit to ≈ 900 ppb for 1 s integration time [3,4].

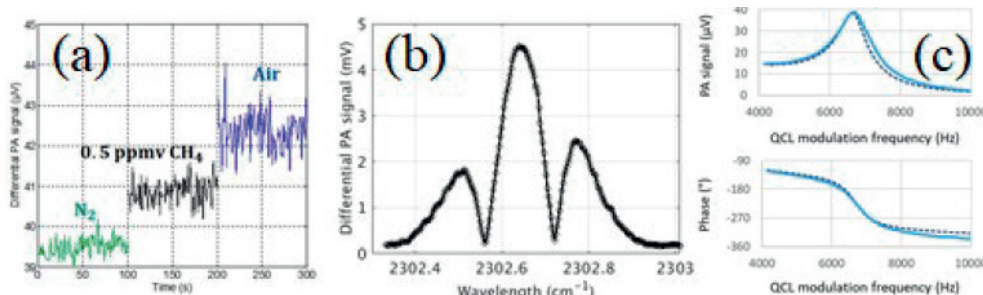


Fig. 2. Experimental data (a) diluted CH₄ with the metal cell, (b) 2-f measurement of ambient CO₂ with the silicon cell, (c) comparison of simulated (dashed line) and measured (solid line) amplitude and phase response of the integrated silicon cell.

In summary, three small-scale PA cells (40 mm^3 to 2.3 mm^3), made of steel or silicon, based on different architectures have been designed, fabricated and tested. All three versions reach a similar sub-ppm resolution, but each has its own benefits and drawbacks, regarding for instance fabrication, implementation and ease of use.

In parallel, significant progress has also been made in our institute towards the wafer scale fabrication of quantum cascade lasers. It thus seems that the goal initially stated, namely, to combine on the same chip a mid-infrared laser, a light injection circuit and a PA sensor including an integrated microphone is now within reach [5].

Acknowledgements

The authors acknowledge the capital contribution across the years by many colleagues at CEA – LETI and researchers at GSMA (Univ. of Reims Champagne Ardenne, France). Contributions to the funding of this work has been provided by several industrial (e.g. mirSense in the framework of our joint laboratory), national or European projects (currently H2020 REDFINCH, grant 780240).

References

1. J. Rouxel, J.-G. Coutard, S. Gidon, O. Lartigue, S. Nicoletti, B. Parvitte, R. Vallon, V. Zéninari, and A. Glière, *Sensors and Actuators B: Chemical* 236, 1104 (2016).
2. J.-G. Coutard, A. Glière, J.-M. Fedeli, O. Lartigue, J. Skubich, G. Aoust, A. Teulle, T. Strahl, S. Nicoletti, M. Carras, and L. Duraffourg, in *MOEMS and Miniaturized Systems XVIII* (International Society for Optics and Photonics, San Francisco, USA, Feb. 02-07, 2019), p. 109310V.
3. H. Lhermet, T. Verdot, A. Teulle, A. Berthelot, A. Glière, B. Desloges, F. Souchon, M. Fournier, J.-M. Fedeli, and J.-G. Coutard, to be presented at *Transducers 2019* (Berlin, Germany, Jun. 23-27, 2019).
4. A. Teulle, J.-G. Coutard, A. Glière, H. Lhermet, and T. Verdot, submitted to *20th International Conference on Photoacoustic and Photothermal Phenomena (ICPPP20)* (Moscow, Russia, Jul. 7-12, 2019).
5. S. Nicoletti, J.-M. Fédéli, M. Fournier, P. Labeye, P. Barritault, A. Marchant, A. Glière, A. Teulle, J.-G. Coutard, and L. Duraffourg, in *Silicon Photonics XIV* (International Society for Optics and Photonics, San Francisco, USA, Feb. 02-07, 2019), p. 109230H.

Trace Gas Detection with a Miniaturized Silicon Photoacoustic Cell

Alexandre TEULLE*, Jean-Guillaume COUTARD, Alain GLIÈRE, Audrey BERTHELOT, Brigitte DESLOGES, Hélène LHERMET, Thierry VERDOT

Univ. Grenoble Alpes, CEA, LETI, Grenoble, France

alexandre.teulle@cea.fr Photoacoustic spectroscopy (PAS) in the mid-infrared (mid-IR) range is a widely used technique to detect and quantify trace gases. Its principle lies in the measurement of the pressure wave generated by successive thermal expansions induced by the absorption of a modulated mid-IR light source impinging on the sample. Gas detection encompasses application domains as various as industrial process monitoring, food industry, leak and explosives detection and indoor and outdoor air quality analysis [1]. However, commercially available PAS sensors are usually cumbersome, expensive and resort to microphones that have not been optimized for the intended use. Integration on silicon would allow drastic cost reduction and open the way to new markets such as cell phones and smart homes.

Here, we present a miniaturized photoacoustic cell integrated on silicon with a novel MEMS pressure sensor nested within the device (Fig. 1(a)). This sensor is fabricated by bonding two 200 mm silicon wafers designed according to a 150 steps CMOS-compatible process flow.

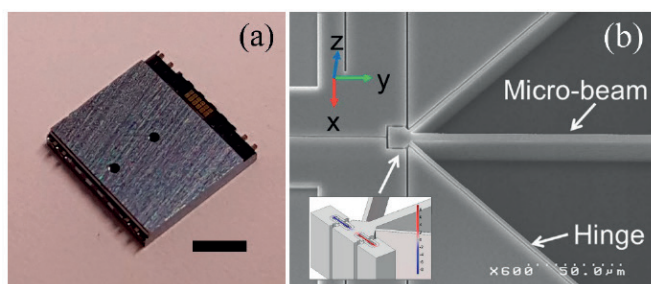


Fig. 1. (a) Miniaturized silicon photoacoustic cell. Scale bar represents 2 mm. (b) Scanning electron micrograph of the MEMS pressure sensor. Inset: Axial stress calculation (units: MPa) in the two nanogauges for a 1 Pa pressure differential on the beam.

This level of integration is the result of a six years development carried out at CEA-LETI [2]. In particular, a strong effort has been put on the careful modelling of the transduction chain from the heat generation to the measured signal [3]. It led to the innovative design of a PA cell made of two chambers partitioned by a beam-shaped diaphragm (Fig. 1(b)) anchored at one extremity but free to move according to the pressure differential between the two chambers at the other end. This displacement induces a stress in two piezoresistive nanogauges and results in resistance variations that are related to the gas concentration.

Results

In order to evaluate the performances of our micro-PA cell, a thorough characterization has been performed with the experimental setup schematized in Fig. 2(a).

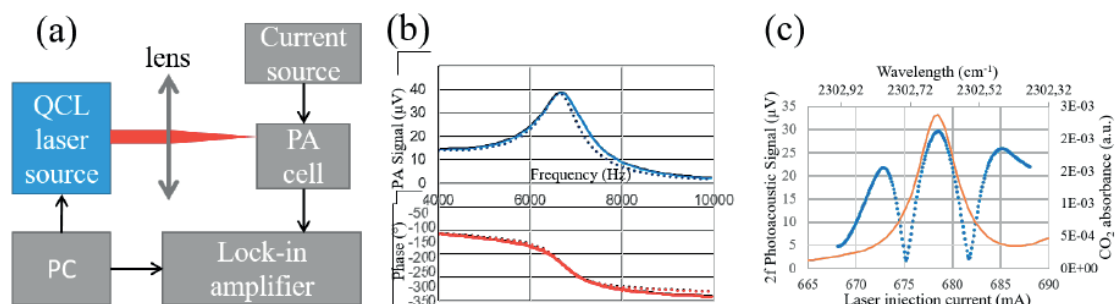


Fig. 2. (a) Schematic of the experimental setup. (b) Simulated (solid line) and measured (dashed line) frequency response of the photoacoustic cell. (c) $2f$ measurement of CO_2 in ambient air (dashed line) and CO_2 absorption line (solid line).

A quantum cascade laser (QCL) source tuned at the $4.34 \mu\text{m}$ CO_2 absorption line is focused by a lens into one of the two PA chambers. Light is wavelength-modulated by a lock-in amplifier which retrieves the voltage across the two current-polarized nanogauges. The interface between the elements is ensured by a home-made Labview program running on a computer.

We have measured the frequency response of the sensor (Fig. 2(b)). The simulated PA signal lies very close to the experimental response. The peak at 6600 Hz corresponds to the mechanical resonance of the MEMS acoustic transducer, with a quality factor estimated at 10. It is worth noticing that, contrary to an acoustic resonance on which rely conventional PA sensors, this mechanical resonance is independent of the speed of sound in the sample and therefore allows to work with various gas matrices with the same design.

For actual CO₂ detection, we adopt a 2f modulation scheme (Fig. 2(c)) because it reduces non-specific signal and links straightforwardly the PA signal to the gas concentration. With our miniaturized cell, we estimate the limit of detection at 900 ppb for a 1 s integration time. The corresponding normalized-noise equivalent absorption is equal to $3 \cdot 10^{-7} \text{ W} \cdot \text{cm}^{-1} \cdot \text{Hz}^{-1/2}$, at the state-of-the-art level of miniaturized PAS sensors.

We are currently investigating the different sources of noise contributing to the PA signal to improve the performances of the micro-PA cell. Furthermore, we are developing the integration of QCL sources on silicon and their coupling to the active function, thus paving the way towards fully integrated PAS sensors.

Acknowledgements

This project has received funding from the European Union's Horizon 2020 research and innovation programme under grant agreement No 780240.

References

1. A. Miklós, P. Hess, Z. Bozóki, *Review of Scientific Instruments* 72 (4), 1937 (2001)
2. A. Glière, J.-G. Coutard, J.-M. Fedeli, H. Lhermet, J. Rouxel, A. Teulle, T. Verdot, S. Nicoletti, submitted to 20th International Conference on Photoacoustic and Photothermal Phenomena (ICPPP20) (Moscow, Russia, Jul. 7-12, n.d.).
3. H. Lhermet, T. Verdot, A. Teulle, A. Berthelot, A. Glière, B. Desloges, F. Souchon, M. Fournier, J.-M. Fedeli, J.-G. Coutard, to be presented at *Transducers 2019* (Berlin, Germany, Jun. 23-27, 2019)

Improved Analytical Platform for Spectroscopic Analysis of Air Gas Components in the Mid-IR

Alexandre KOLOMENSKII⁽¹⁾ *, James BOUNDS⁽¹⁾, Feng ZHU^(1,2), Junchao ZHOU⁽³⁾,
Paotai LIN⁽³⁾, Hans SCHUESSLER^(1,4)

1. Department of Physics and Astronomy, Texas A&M University, College Station, Texas 77843-4242, USA

2. School of Physics and Astronomy, Sun Yat-sen University, Zhuhai, Guangdong 519082, China

3. Department of Electrical and Computer Engineering, Texas A&M University

4. Science Program, Texas A&M University at Qatar, Doha 23874, Qatar

alexandr@physics.tamu.edu

The methane absorption spectrum was measured in the mid-IR in the wavelength interval around 3.3 mm using a frequency comb laser source produced by a difference frequency generation. The frequency comb vernier spectroscopy (FCVS) unlike dual frequency comb spectroscopy requires only one frequency comb [1], allowing for a broad spectral coverage. A scanning high-finesse cavity acts as a narrowband filter consequently transmitting sets of comb lines separated by a multiple $m \times f_r$ of the repetition rate frequency of the comb, f_r , where m is an integer. The transmitted radiation of these lines is forming an image consisting of dots on the pixel array detector, from which the spectrum is retrieved [2]. Unlike traditional FCVS approach, we used continuous recording of the images, while the length of the cavity was changing, so that the comb lines in the whole spectral range were continuously recorded with a mid-IR camera. Using these images from multiple exposures we can remove the constraint imposed on the bandwidth and also avoid the need for the scanning galvo mirror. The processing of 10000 images recorded during the scan allowed to retrieve the methane spectrum with the frequency comb spectral resolution of $\sim 0.01 \text{ cm}^{-1}$. This technique can be realized with a camera and due to high Q-value of the resonant cavity yields an effective path length in the 100 km range, providing in this way sensitive and broadband detection of the absorption spectra of gases in the mid-IR.

Acknowledgements

This work was supported by the Robert A. Welch Foundation, grant No. A1546 and the Qatar Foundation, grant NPRP 8-735-1-154.

References

1. C. Gohle, B. Stein, A. Schliesser, Th. Udem, and T. W. Hänsch, Phys. Rev. Lett. 99 (26-31), 263902 (2007) doi: 10.1103/PhysRevLett.99.263902
2. F. Zhu, J. Bounds, A. Bicer, J. Strohaber, A. Kolomenskii, C. Gohle, M. Amani and H. A. Schuessler, Optics Express 22 (19), 23026-23033 (2014) doi: 10.1364/OE.22.023026

Balanced-Detection Interferometric Cavity-Assisted Photothermal Spectroscopy

Johannes P. WACLAWEK, Christian KRISTAMENT, Harald MOSER, Bernhard LENDL

Research Unit of Environmental Analytics, Process Analytics and Sensors,
TU Wien, Getreidemarkt 9/164, 1060 Vienna, Austria

johannes.waclawek@tuwien.ac.at

Any photo-induced heating of sample gas caused by absorption of excitation radiation leads to a change in the refractive index of the gas [1]. The refractive index change in turn causes a phase shift of electromagnetic waves passing through the heated region. An optical cavity can be utilized as an excellent transducer for highly sensitive gas detection by monitoring intensity changes of a transmitted probe laser beam. The presented work reports on the novel implementation of balanced detection to *Interferometric Cavity-Assisted Photothermal Spectroscopy (ICAPS)*. Within this scheme, the probe beam is split into two beams, which are both transmitted through identical cavities with some lateral displacement and afterwards are detected separately, see Fig. 1. Differential amplification of the photodiode signals allows to extract the induced photothermal signal with very high sensitivity by efficient rejection of common mode noise. That way, excess noise which limited the sensitivity of previous cavity-based photothermal sensors [2, 3] can be effectively rejected down to the fundamental limit of shot noise. This setup links the general advantages of the optical cavity as transducer of photothermal spectroscopy with the advantages arising from balanced detection, by enhancing the sensitivity as well as ruggedness of the developed sensor.

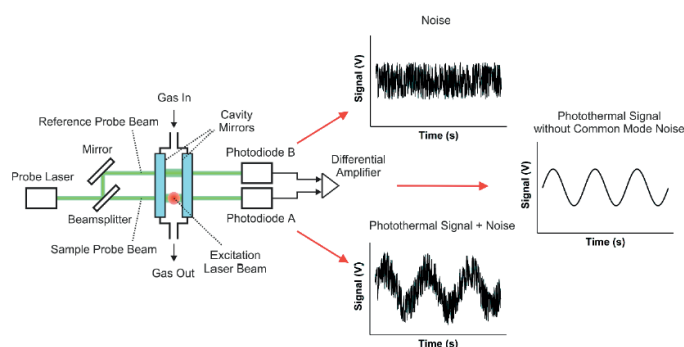


Fig. 1. Balanced-detection ICAPS scheme; the probe beam is split into a sample probe beam and a reference probe beam. The sample beam probes the photothermal signal, which is superimposed by noise, whereas the reference beam probes only noise. By subtraction of the two photodiode signals, the photothermal signal is received along with high rejection of common mode noise.

An excitation beam induced refractive index changes in the sample. The probe and excitation laser beams were arranged in transverse configuration, which enables the construction of simple, robust and compact trace gas sensors, which feature very small absorption volumes of a few 100 mm³ (see Fig. 2). Selectivity was achieved by signal generation via wavelength modulation at reduced sample pressure and detection at second harmonic ($2f$) [4]

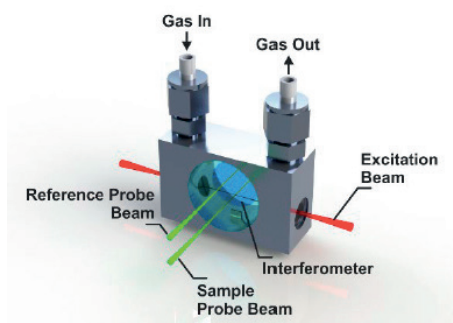


Figure 2. Illustration of the compact balanced-detection ICAPS gas cell including the interferometers with a mirror spacing of 1 mm.

The metrological qualities of the sensor were investigated by detection of sulfur dioxide (SO₂) using a quantum cascade laser (QCL) as powerful mid-infrared excitation source, whereas the induced refractive index changes were monitored by a near-infrared probe laser emitting around 1550 nm. For the targeted absorption band centered at 1380.93 cm⁻¹, a 5 ppbv minimum detection limit was

Session C3: Applied / Gas Analysis

achieved with a 1 second integration time, corresponding to a normalized noise equivalent absorption of $7.5 \times 10^{-9} \text{ cm}^{-1} \text{ W Hz}^{-1/2}$. Moreover, the sensor exhibits white-noise-determined characteristics, thereby resulting in an excellent long-term stability, which enables integration times of a few thousand seconds. Advantages and limitations of this method will be discussed.

References

1. S. E. Bialkowski, *Photothermal Spectroscopy Methods for Chemical Analysis* (John Wiley & Sons, 1996).
2. A. J. Campillo, S. J. Petuchowski, C. C. Davis, and H.-B. Lin, Fabry-Perot photothermal trace detection, *Appl. Phys. Lett.* 41(4), 327–329 (1982).
3. J. P. Waclawek, V. C. Bauer, H. Moser, and B. Lendl, 2f-wavelength modulation Fabry-Perot photothermal interferometry, *Opt. Express* 24, 28958-28967 (2016).
4. P. Werle, “A review of recent advantages in semiconductor laser based gas monitors,” *Spectrochim. Acta A* 54, 197-236 (1998).

KEYNOTE

Fluorescence quantum efficiency and upconversion measurements by thermal Lens with 1.53- μm excitation

Tomaz Catunda ^{(1)*}, Marcio S.Figueiredo ^(1,2), Vitor S.Zanuto ⁽¹⁾, Jessica F.M. Santos ⁽¹⁾

1. Instituto de Física de São Carlos – USP, São Carlos, Brazil

2. Universidade Federal da Grande Dourados, Dourados, Brazil

tomaz@ifsc.usp.br

Currently, Er^{3+} -doped crystals and glasses are attractive for the use in integrated optoelectronics because of the Er^{3+} intra-4f emissions at the standard telecommunications wavelength (at 1.54 μm) and host for laser emission (at about 2.7 μm), which is close to the most pronounced absorption band of water (at 3 μm). In the research reported here, we studied the effect of energy-transfer upconversion (ETU) on the fluorescence quantum efficiency of Er^{3+} -doped tellurite glasses by thermal lens spectrometry (TLS) [1]. The TLS were performed using the dual-beam (excitation and probe) mode-mismatched configuration with an Er^{3+} fiber laser as excitation beam and a HeNe laser as probe beam. The samples were obtained by conventional melt-quenching method, in which the powders were mixed in a crucible, melted in air at 850 $^{\circ}\text{C}$ for one hour, and afterwards they were annealed for 5h at a temperature close to the glass transition temperature [2]. The TLS signal amplitude is proportional to the phase shift parameter, θ , which is proportional to the heat power delivered into the sample, so it is proportional to the product $P_{abs} \cdot \phi$, where P_{abs} is the absorbed excitation power and ϕ the fraction of P_{abs} converted into heat. The basic idea of all photothermal methods for radiative quantum efficiency (η) measurements is to assume that $\phi = 1 - \eta \cdot (v_{em}) / v_e$, in the case of one photon excitation with energy $h\nu_e$ and average emission energy ($h\nu_{em}$), so [1]:

$$\theta = C \cdot P_{abs} (1 - \eta \langle v_{em} \rangle / v_e) \quad (1)$$

where C is a parameter that depends on the thermo-optical properties of the host matrice.

In a typical transient TL signal, the proper fit of the data give the parameters θ and t_c , where θ is proportional to the signal amplitude and t_c is the TL response time. Figure 1b shows the plot of $\theta \times P$ for different Er^{3+} concentrations. The linear behavior is more evident for low Er^{3+} concentrations, but for all samples a linear fit can be made in the low power regime. This linear regime is expected for a single excitation and emission process with (λ_{em}) = 1541nm and $\lambda_e = 1535$ nm (Fig.1.a). From these data, we obtained the parameter C and η , which decreases monotonically with Er^{3+} concentration from 0.81 to 0.16 for 0.05% of Er^{3+} and 4.0% of Er^{3+} respectively, as shown in Fig.2.a. Both C and η values are in excellent agreement with previous TLS measurements performed with 980 nm excitation [2]. Several processes can contribute to nonlinear behavior of $\theta \times P$ but ETU is expected to be the most important one in Er^{3+} -doped systems, with 1535 nm excitation, in resonant with the first excited state ($^4I_{13/2}$). ETU is a process between a pair of excited Er^{3+} ions where one ion decays and the other is promoted to a higher energy level. In this system, ETU generates emission emission at 980, 808, 650 and 545 nm due to population of several Er^{3+} levels. Consequently, Eq.1 is no longer valid in the nonlinear regime of $\theta \times P$ (Fig.1.b). In fact, the detailed description of the luminescence and population dynamics is very difficult since it involves several processes (with one, two and three pump photons) and consequently $\langle \lambda_{em} \rangle$ depends on excitation power. However, the relationship $\theta = C \cdot P_{abs} \cdot \phi$ remains valid and can be used to determine ϕ , as shown in Fig.2.b. Mainly for the samples with higher concentrations, it is observed a strong decrease of heat generation indicating a corresponding increase of the energy that is upconverted into light. The overall fraction of energy converted into light, by energy conservation, is given by $(1 - \phi)$. Finally, transient absorption measurements and results in Er^{3+} -doped fluoride glasses will be presented.

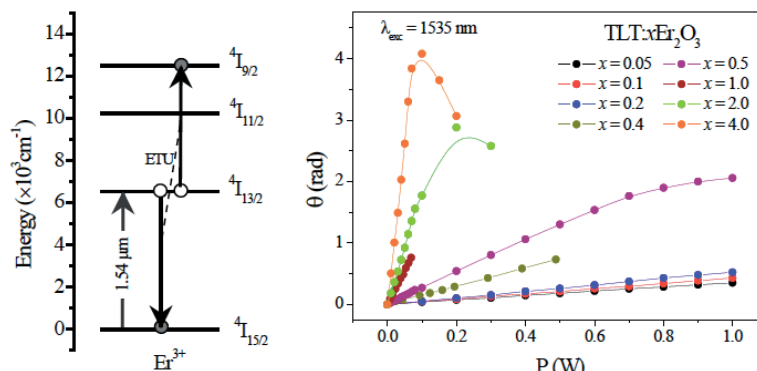


Fig. 1: (a) Partial energy level diagram of Er^{3+} ions in which ETU represents the Energy Transfer Upconversion; (b) the thermal lens phase shift (θ) as a function of excitation power (P) for different Er_2O_3 concentrations.

Session C4: Spectroscopy III

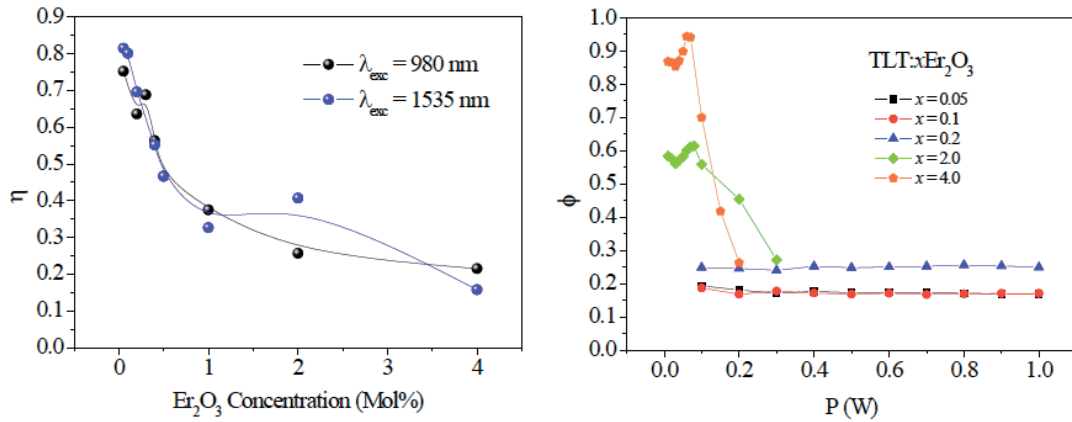


Fig. 2: (a) Er_2O_3 concentration behavior of the fluorescence quantum efficiency for 980 nm and 1535 nm pump and (b) ϕ is the fraction of heat generated as a function of excitation power (P) for some concentration.

Acknowledgements

We are grateful to the financial support of the Brazilian agencies CAPES and FAPESP.

References

1. W.Q. Santos, A. Benayas, D. Jaque, J. García-Solé, T. Catunda, C. Jacinto, Laser Physics Letters 13, 25004 (2016) doi:10.1088/1612-2011/13/2/025004
2. M.S. Figueiredo, F.A. Santos, K. Yukimitu, J.C.S. moraes, J.R. Silva, M.L. Baesso, L.A.O. Nunes, L.H.C. Andrade and S.M. Lima, Optical Materials 35, 2400 (2013) doi:10.1016/j.optmat.2013.06.041

Resonance Photoacoustics for Measurement of Low Absorption of Optical Materials

Aleksei KONYASHKIN ^{(1),(2)*}, Aleksei MOLKOV ⁽¹⁾, Oleg RYABUSHKIN ^{(1),(2)}

1. Moscow Institute of Physics and Technology, Dolgoprudnyy, Russia
 2. Kotelnikov Institute of Radio-engineering and Electronics of RAS, Fryazino, Russia

a.konyashkin@gmail.com

Output radiation powers of modern high-power laser systems far exceed kilowatt levels. This implies strong demands to the optical absorption properties of employed components, as even low absorption can induce its damage at such power levels. There are various methods used for measurements of low absorption coefficients of dielectric materials [1]. Standardized laser calorimetry technique relies on the temperature kinetics measurements of the irradiated sample using external detectors (e.g. thermocouples, RTDs etc.). However, absorption of scattered radiation by the detector can induce its additional heating and resulting measurement errors especially when the high-power radiation is involved. Conventional photoacoustic techniques rely on the detection of the acoustic response conditioned by the local density change of the material, induced by absorption of pulsed laser radiation. As a rule, these methods require calibration, i.e. presence of strong absorption bands that can be analyzed using some other methods or reference samples with the absorption known beforehand. An alternative approach that was recently proposed for precise measurements of low absorption coefficients of nonlinear-optical crystals is the piezoelectric resonance laser calorimetry (PRLC) [2]. The main idea of this method is that the thermodynamic temperature of the crystal interacting with laser radiation is characterized by its equivalent temperature, which is directly determined by measuring an induced frequency shift of any of the temperature calibrated piezoelectric resonances of the sample. However, this method is only applicable for the examination of piezoelectric materials, when the resonances can be excited noncontactly via application of the probe radiofrequency electric field.

For precise measurements of low optical absorption coefficients of dielectric samples, we propose to use temperature dependence of its acoustic resonance frequencies. Resonance frequencies of the investigated sample can be excited both by tuning the repetition rate of the incident pulse radiation or via external piezoelectric transducer. In order to validate this approach, we investigated the nonlinear-optical KH_2PO_4 (KDP) crystal ($20 \times 20 \times 45 \text{ mm}^3$). Here we were able to measure its optical absorption using both PRLC technique and an introduced one. A block-scheme of the experimental setup is shown in Fig. 1 (a). In the case of PRLC a voltage from the radiofrequency (RF) generator is applied to the metallic electrodes forming the capacitor, which is connected in series with the load resistor R. A voltage drop across R is measured using the lock-in amplifier. Piezoelectric resonances (PRs) can be observed when the generator frequency corresponds to KDP eigenmode frequencies Rf . Temperature calibration of Rf frequencies in uniform heating conditions reveals that in the first approximation Rf linearly depend on temperature: $Rf(T) - Rf(T_0) = K^{prt}(T - T_0)$, where K^{prt} – piezoelectric resonance thermal coefficient. When the sample is heated by laser radiation of power P , its nonuniform temperature distribution can be characterized by the equivalent temperature derived directly from measured $Rf(P, t)$ value: $\Theta_{eq}(P, t) = T_0 + [Rf(P, t) - Rf(0)] / K^{prt}$ [3], temperature T_0 corresponds to $P = 0$. In other series of experiments the RF signal from the generator drives the laser pulse repetition rate f . Single-mode Yb-doped pulsed fiber laser operating at 1064 nm wavelength (spectral linewidth 1.5 nm, pulse duration 200 ns, average power up to 20 W) was used. Acoustic resonances are excited whenever f corresponds to frequencies Rf . The acoustic response (AR) of KDP (see Fig. 1 (b)) was analyzed using the microphone via lock-in detection.

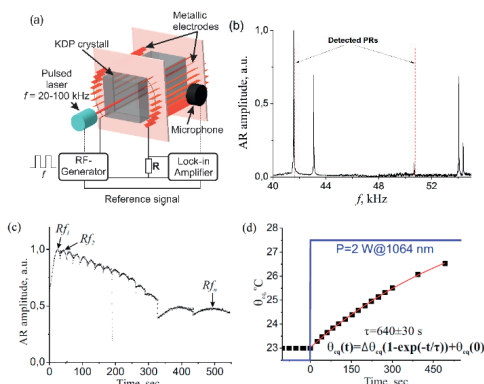


Fig. 1. Block scheme of the experimental setup (a). Acoustic response (AR) of the KDP measured via sweeping the laser pulse repetition rate frequency, red dashed lines denote the detected piezoelectric resonances of the KDP sample (b). Kinetics of the resonance frequency (c) and equivalent temperature (d) of the KDP irradiated by 2 W laser power.

The frequency kinetics of one of the KDP resonances measured during its heating by pulsed laser radiation ($P=2 \text{ W}$) is shown in Fig. 1 (c). The pulse repetition rate frequency f was subsequently changed in order to follow the resonance signal, the local maximums correspond to the time moments when the resonance frequency Rf equals to the preset f value. The equivalent temperature kinetics of KDP derived from Rf kinetics is presented in Fig. 1 (d). The optical absorption coefficient of KDP $\alpha = (4.2 \pm 0.2) \times 10^{-2} \text{ cm}^{-1}$ was determined from the solution of the nonstationary heat conduction problem relying on the temperature kinetics data. Its value is in good agreement with that measured using PRLC technique. Eventually we can testify that proposed method is applicable for the precise absorption testing of various optical components.

References

1. M. Leidinger, S. Fieberg, N. Waasem, F. Kuhnemann, K. Buse, and I. Breunig, *Optics Express* 23 (17), 21690 (2015) doi:10.1364/OE.23.021690
2. O. A. Ryabushkin, A. V. Konyashkin, D. V. Myasnikov, V. A. Tyrtshnyy, O. I. Vershinin, *Proc. SPIE* 8847, 88470Q (2013) doi: 10.1117/12.2023285
3. O. A. Ryabushkin, D. V. Myasnikov, A. V. Konyashkin, V. A. Tyrtshnyy, *Journal of the European Optical Society - Rapid Publications* 6, 11032 (2011) doi: 10.2971/jeos.2011.11032

Laser optoacoustic method for measurement of light extinction coefficient in colloid media

Yulia Sokolovskaya^{1*}, Natalia Podymova¹, Alexander Karabutov^{2,3,4}

1. Faculty of Physics, M.V. Lomonosov Moscow State University, Moscow, Russia

2. International Laser Center, M.V. Lomonosov Moscow State University, Leninskie Gory, Moscow, Russia

3. The National University of Science and Technology "MISIS", Leninskii prospect 4, Moscow, Russia

4. ILIT RAS Branch of the FSRC «Crystallography and Photonics» RAS, Shatura, Russia

yu.sokolovskaya@mail.ru

Optical methods of diagnostic are presently widely used in biology, chemistry and medicine [1]. One of the actual problems is analysis of structure, optical and thermophysical properties of colloid media, for example, blood, lymph, protein solutions

If the laser pulse with a duration, which is much less than an acoustical wave transition time over the heat release area, absorbed in the considered medium, the optoacoustic (OA) pulse profile repeats the heat sources spatial distribution in this medium [2,3]. In the approximation of a plane light wave, for a homogeneous absorbing and scattering media, the distribution of heat sources corresponds spatial distribution of light intensity in it, which is determined by the light absorption and scattering coefficients. So, the OA-method may be used for measurement of the optical characteristics of absorbing and scattering media, including biological ones. The advantage of this method is that the information about optical properties of investigated media is delivered by the acoustic waves, which have a relatively weak attenuation in biological media in comparison with the waves in optical range [3].

Many biological media represent colloid solutions. In such media, the distribution of light-absorption and scattering particles and, correspondingly, light extinction coefficient may be inhomogeneous depending on a number of external and internal factors. Thus, the actual problem is reconstruction of spatial distribution of optoacoustic sources in investigated medium and in-depth dependence for the extinction coefficient. The aim of the current work is demonstration of capabilities of the OA-method for optical properties diagnostics of colloid media by the example of magnetic fluids. We considered two types of fluids with different base liquids (water and kerosene) and with different concentration of magnetite particles.

Temporal profile of pressure $p(\tau)$ on the leading edge of OA pulse in general case is expressed by formula

$$p(\tau) \sim \alpha(-c_0\tau) \exp\left(-\int_0^{-c_0\tau} \alpha(\xi) d\xi\right),$$

where α is a light extinction coefficient, c_0 is sound velocity in media. So, spatial distribution of the light extinction coefficient can be determined from this formula.

Forward mode scheme of OA signal detection is used to measure the extinction coefficient [4]. Opto-acoustic pulses were excited by radiation of Nd:YAG laser with wavelength $\lambda=1064$ nm and pulse duration $\tau_L=10$ ns. In conditions of current experiment, the boundary between transparent and absorption medium was acoustical rigid, for which a cell with an investigated medium was covered with a quartz plate. The measurement results showed that the light extinction coefficient, averaged by whole depth of studied medium, depends linearly on magnetite concentration in solution. It was found that the in-depth spatial distribution in magnetic fluids is inhomogeneous in the case of the rigid acoustic boundary. Moreover, a relative in-depth change of extinction coefficient $\Delta\alpha/\alpha_{\max} = (\alpha_{\max} - \alpha_{\min})/\alpha_{\max}$ significantly depends on a concentration of studied solution. The existence of such inhomogeneity of magnetite particle distribution, which leads to extinction coefficient spatial change, may be explained that the rigid acoustic boundary (quartz plate) creates induced anisotropy in investigated liquid. It can appear because of an interaction between two media at liquid-solid phase boundary due to processes, caused by surface tension forces. It was shown that for water-base fluid $\Delta\alpha/\alpha_{\max}$ changes from 7% for high concentration of magnetite ($n_{\text{mag}}=0.9$) to 60% for low concentration ($n_{\text{mag}}=0.1$), but for kerosene-based fluid – from 2% for $n_{\text{mag}}=0.9$ to 40% for $n_{\text{mag}}=0.1$.

References

1. Zimnyakov D.A., Tuchin V.V. Quantum Electronics, 2002, Vol. 32, 10, p. 849-867
2. Gusev V.E., Karabutov A.A., Laser optoacoustics. American Institute of Physics, New York, 1993
3. Grashin P.S., Karabutov A.A., Oraevsky A.A., Pelivanov I.M., Podymova N.B., Savateeva E.V., Solomatina V.S. Quantum Electronics, 2002, Vol. 32, p.868-874
4. Karabutov A.A., Savateeva E.V., Podymova N.B., Oraevsky A. A. Journal of Applied Physics, 2000, Vol. 87, 4, p. 2003-2014

Photothermal spectrophotometer for measurements of low absorption in liquid samples

Jehan AKBAR^{(1,2)*}, Humberto CABRERA⁽²⁾, Dorota KORTE⁽³⁾

1. Department of Physics, Hazara University, Mansehra, Pakistan

2. International Centre for Theoretical Physics (ICTP), Strada Costiera 11, Trieste, ITALY

3. Laboratory of Environmental and Life Sciences, University of Nova Gorica, SLOVENIA

Jehan@ictp.it

We report on development of a highly-sensitive thermal lens spectrophotometer which allows measurements of absorption spectrum and lower detection limit for Fe(II) concentrations in liquid as well as solid samples. Our proposed experimental setup consists of a halogen lamp (for pumping) instead of excitation laser and a filter to provide nearly monochromatic and widely tunable pump source. The lower detection limit of our experimental setup was calculated to be $3.74 \mu\text{g L}^{-1}$

Introduction

The photothermal lensing (TL) method has been commonly employed for the detection of small amounts of analytes present in the low absorbing samples [1-3]. The TL method is based on probing local changes in temperature which are induced by an intensity modulated laser beam in a sample.

The TL technique have widespread applications [4-6], however several different wavelengths of pumping lasers are needed to measure full absorption spectra of different samples. This wider spectrum of wavelengths for the excitation could be easily obtained from a dye laser, F-centre laser or any other tunable lasers. For this purpose, Long et al. acquired wavelength tunability using a dye laser [7] and an optical-parametric-oscillator (OPO) have been used for this purpose by researchers as described in [8, 9]. The lasers are not very suitable choices for this purpose due to the high cost of tunable lasers and the wavelength range they offer.

In this paper we describe the development of a white light spectrophotometer using a low cost halogen light source to excite the sample. To select a particular wavelength, an interference filter is used. An optical cavity is formed between the walls of the cell containing the sample and the filter which magnifies the TL effect due to multiple passes.

Experimental Setup

Our experimental setup mainly consists of a lamp (halogen lamp) which is used as a pump source and a Helium Neon laser which is used as a probe for TL effect in the sample. The light from the pump is periodically modulated in intensity at a very lower frequency (around 1 Hz) using a mechanical chopper. The interference filter for wavelength selection is placed around 0.1 cm before the sample which also serves as a reflector and hence form a cavity which allow amplification of TL effect. The interference filter allows to select a narrower spectrum (8-10 nm wide) from the very broad spectrum obtained from the halogen lamp.

The photodiode produces analog signal, which is digitized using an Arduino board, the signal is then feed to PC via a USB port for further processing and analysis.

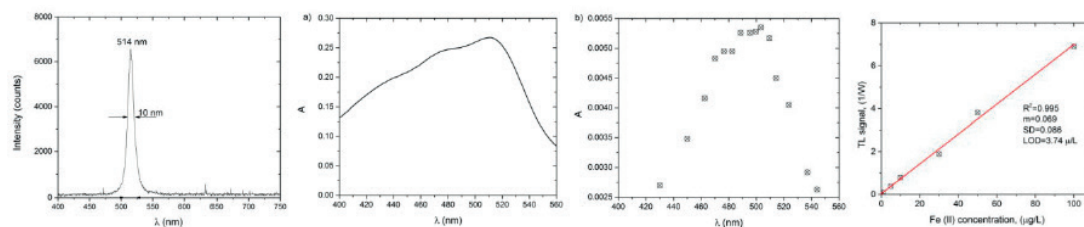


Figure 1. (a) Emission of the halogen lamp, which is quasi monochromatic, (b) Absorption spectrum of 1 mg L^{-1} (c) TL spectrum of $50 \mu\text{g L}^{-1}$ of Fe(II) dissolved in water. (d) measured calibration curve of Fe(II) solutions

Results and discussion

Figure 1 (b) and (c) shows the absorption spectra obtained using a commercial spectrometer (Ocean Optics) and TL spectrum for 1 mg L^{-1} and $50 \mu\text{g L}^{-1}$ solution of Fe(II) in water/ethanol solution respectively. From this figure, it is clear that both the spectra are in good agreement with each other. Similarly Figure 1 (d) shows the calibration curve obtained for samples prepared with different concentrations of Fe(II). Furthermore, the thermal lens signal shows a linear increase with increase in the Fe(II) concentration and the correlation parameter is around 0.99. The lower limit of detection was calculated to be $3.74 \mu\text{g L}^{-1}$

Session C4: Spectroscopy III

Conclusions

We developed a photothermal spectroscopy technique which employs a halogen lamp as a pumping light source and an interference filter to select a particular wavelength range. We utilized the partially reflecting surfaces of cell and interference filter which make an optical cavity and thus enhance the TL signal via multiple passes. The TL signal is detected using a Si photodetector and an Arduino board is used to convert signal from analog to digital and feed into a PC for further processing.

References

- [1] Leite R C C Moore R S Whinnery 1964 Appl. Phys. Lett. 5 141
- [2] Franko M and Tran C D 1996 Rev. Sci. Instrum. 67 1
- [3] Shen J Lowe R D and Snook R D 1992 Chem. Phys. 165 385
- [4] Divjak B, Franko M and Novic M 1998 J. Chromatogr. A 829 167
- [5] Miyaishi K, Imasaka T and Ishibashi N 1982 Anal. Chem. 54 2039
- [6] Miyaishi K, Imasaka T and Ishibashi N 1981 Anal. Chim. Acta 124 381
- [7] M. E. Long, R. L. Swofford and A. C. Albrecht, Science 191, 183 (1976)
- [8] S. Kawasaki, R. L. Lane and C. L. Tang, Appl. Opt. 33, 992 (1994)
- [9] T. Higashi, T Imasaka and N. Ishibashi, Anal. Chem. 55, 1907 (1983)

Quantitative pharmaceutical analysis based on the PCA of Raman spectra

Juan Carlos MARTINEZ-ESPINOSA⁽¹⁾, Rafael GUZMAN-CABRERA^{(2)*},
 José MARCOS FALCON-GONZALEZ⁽¹⁾, Teodoro CORDOVA-FRAGA⁽³⁾,
 Mauricio SANCHEZ-BARAJAS⁽⁴⁾, José Rafael GUZMAN-SEPULVEDA⁽⁵⁾

1. Instituto Politecnico Nacional-UPIIG, Guanajuato Puerto Interior, Silao de la Victoria, Guanajuato, MEX, 36275

2. Universidad de Guanajuato, km 3.5 + 1.8 road Salamanca-Valle de Santiago, Salamanca, Guanajuato, MEX, 36730

3. Universidad de Guanajuato-DCI, Loma del bosque 103 Fracc. Lomas del Campestre, Leon, Guanajuato, MEX, 37150

4. Hospital General de Zona con Medicina Familiar No 21 León Sur, Universidad de Guanajuato campus León, Guanajuato, MEX, 37380

5. CREOL, The College of Optics and Photonics, University of Central Florida, 4304 Scorpius St., Orlando, Florida 32826, USA

jcmartineze@ipn.mx

In the present work we examine the distribution of Ciprofloxacin drug as an active ingredient in tablets samples from eight different laboratories. Additionally, control samples with different concentration were prepared for calibration. Raman spectra were recorded from all samples, including controls, and a principal component analysis (PCA) was implemented on them. The results of the PCA were contrasted against mass spectrometry measurements, and they show that i) a clear discrimination among the different samples can be achieved, ii) such a distinction is corroborated by the mass spectrometry measurements, and finally, iii) the principal component of the Raman spectra has a well-defined, linear relation with the concentration of Ciprofloxacin (for all the samples measured). Such a strong, statistically significant correlation between the results of the PCA analysis and the mass spectroscopy measurements, supports the use of Raman spectroscopy for quantitative analysis of pharmaceutical compounds.

Raman spectroscopy can be used to measure the ‘fingerprint’ of chemical compositions, based on the frequency shift of the scattered light, which relates to transitions between different molecular vibration levels of the compounds in the sample [1-2]. These capabilities have proved useful to improve routine methods for cancer detection [3-4] and diagnosis [5], as well as for pharmaceutical analysis [6-8]. In this regard, a common methodology on the Raman spectra recorded relies on the analysis of principal components and linear discriminant analysis, which has proved robust and highly sensitive for the discrimination between different biochemical compounds [9-11]. In the present work we examine the distribution of Ciprofloxacin drug as an active ingredient, by means of the PCA applied on Raman spectra measured on both commercial samples from different laboratories and calibration samples prepared with known concentrations of the drug. We compared our results against mass spectroscopy measurements, and verified that a strong, linear dependence exists between the two. These results support the use of Raman spectroscopy for quantitative analysis of pharmaceutical compounds.

Results

Fig. 1 shows a representative processed Raman spectrum. Ciprofloxacin hydrochloride monohydrate presents different characteristic molecular vibrations at 638, 665, 718, 752, 787, 805, 1024, 1253, 1273, 1493, 1548, 1625 and 1708 cm^{-1} . The PCA was done in the spectral window from 1595 cm^{-1} to 1650 cm^{-1} . Within this range, the amplitude of the main peak, which is located at 1625 cm^{-1} (attributed to $\nu(\text{COOH})$, $\nu(\text{C50})$), is observed to increase with the concentration of ciprofloxacin.

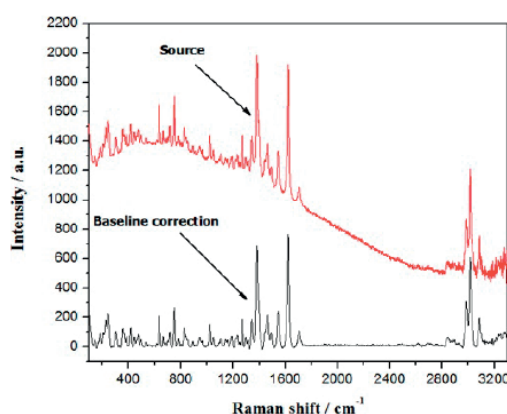


Fig. 1. Spectral preprocessing. baseline correction and smoothing: red line-raw spectrum, black line-spectrum processed.

Session C4: Spectroscopy III

In Fig. 2(a), we show the weight distribution for the first three principal components (PC1, PC2 and PC3). From the control group, the calibration curve was obtained based on the displacement of PC 1 as a function of the concentration of the active principle and the excipient (Fig. 2b). From our calibration, we were able to verify that the different laboratories have >80% of active principle in the tablets analyzed, as shown in Fig. 2(b).

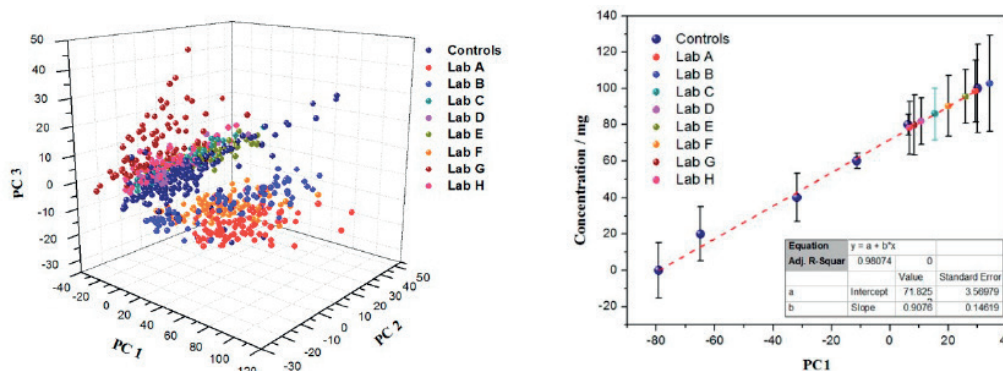


Fig. 2. Results of the PCA applied to the spectral database. LEFT. Plotting of the first three main components (PC1 vs PC2 vs PC3), control samples and different laboratories. RIGTH. Calibration curve generated from PC1, and the other PC1 weights corresponding to the different laboratories are superimposed on the graph in order to verify the associated concentration.

Conclusions

In this paper, we demonstrated the potential use of Raman spectroscopy as a quantitative tool for pharmaceutical analysis. Specifically, we worked on both control and commercial samples (from different laboratories) ciprofloxacin. Our methodology consists on the application of PCA to the Raman spectral maps recorded, which allows measuring the mutual correlations between the different spectral groups. The results of this analysis were found to be strongly correlated with independent mass spectroscopy measurements, thus validating our approach. Importantly, the methodology presented is general and it can be extended to other pharmaceutical compounds. The quantitative assessment provided by our approach can be useful either to improve the accuracy in the dosage in cases of delicate diagnoses, or to identify adulterations in the drug formulation.

Materials and Methods

Control samples. Reference compound: ciprofloxacin (Sigma Aldrich: CAS 85721-33-1, purity >98%). A solution of hydrochloric acid (HCl; CAS 7647-01-0) was added at $\pm 37.25\%$ purity, obtaining ciprofloxacin hydrochloride monohydrate (six control samples with concentrations from 0% (Excipient: Starch) to 100%, in steps of 20%). Each concentration was mixed with the excipient starch to gauge at 100%. **Commercial samples.** Eight samples of commercial ciprofloxacin tablets from different laboratories were purchased in different establishments. Each sample was completely pulverized to carry out the measurements by Raman spectroscopy. **Spectral mapping Raman.** An integrated Thermo Scientific DXR Raman Microscope system was used (laser excitation at 780 nm, 24 mW, 40X objective). One gram of sample was used in all cases. All spectral blocks were recorded in the range from 100 cm^{-1} to 3300 cm^{-1} (25 spectra per sample; 6 control samples plus 8 commercial samples; 350 spectra in total). All Raman mappings were taken in a square region of $5 \times 5 \mu\text{m}$. **Data processing.** The complete spectral block (350 spectra) was processed using Matlab 2014b. All the spectra were subjected to a baseline correction and smoothing in order to eliminate background noise (see Fig. 1). Finally, a PCA was implemented, and the corresponding dimensionless values were selected for the construction the calibration curve and 8-bit images representative of the concentration of the active substance.

References

1. G. Van Dalen, E.J. van Velzen, P.C. Heussen, Sovago M., K.F. van Malssen, J.P.M van Duynhoven. Journal of Raman Spectroscopy 48, 1075 (2017) doi.org/10.1002/jrs.5171
2. J.M. Ruvalcaba-López, T. Cordova-Fraga, G. de la Rosa-Alvarez, B.O. Murillo-Ortiz, J.C. Martínez-Espinosa, R. Guzman-Cabrera, J. Bernardo-Alvarado. Lasers in Medical Science, 1 (2018) doi: 10.1007/s10103-018-2576-8
3. P.R. Jess, V. Garcés-Chávez, D. Smith, M. Mazilu, L. Paterson, A. Riches, C.S. Herrington, W. Sibbett, K. Dholakia. Optics express 14(12), 5779 (2006) doi.org/10.1364/OE.14.005779
4. L. Chen, Y. Wang, N. Liu, D. Lin, C. Weng, J. Zhang, L. Zhu, W. Chen, R. Chen, S. Feng. Laser Physics 23(6), 065601 (2013) doi.org/10.1088/1054-660X/23/6/065601
5. W. Wang, J. Zhao, M. Short, H. Zeng. J. Biophotonics 8, 527 (2014) doi: 10.1002/jbpo.201400026
6. T. Vankeirsbilk, A. Vercauteren, G. Van der Weken, F. Verpoort, G. Vergote, J.P. Remon. TrAC Trends in Analytical Chemistry 21(12), 869 (2002) doi.org/10.1016/S0165-9936(02)01208-6
7. T. Lipiäinen, S.J. Fraser-Miller, K.C. Gordon, C.J. Strachan. Journal of Pharmaceutical and Biomedical Analysis 149, 343 (2018) doi.org/10.1016/j.jpba.2017.11.013
8. J.C. Martinez, J.R. Guzmán, G. Bolanos Evia, T. Cordova, R. Guzman-Cabrera. International Journal of Thermophysics 39,79 (2018) doi.org/10.1007/s10765-018-2391-2
9. G.S. Bumbrah, R.M. Sharma, Egyptian Journal of Forensic Sciences 6(3), 209 (2016) doi.org/10.1016/j.ejfs.2015.06.001
10. M. Edinger, D. Bar-Shalom, J. Rantanen, N. Genina. Pharmaceutical research 34(5), 1023 (2017) doi: 10.1007/s11095-017-2126-2
11. A.M. Martinez, A.C. Kak. IEEE transactions on pattern analysis and machine intelligence 23(2), 228 (2001) doi: 10.1109/34.908974

Study of charge transfer mechanism of PEDOT polymer for detection of solid explosives using pulsed Photoacoustic technique

Archana Kumari, D. Ganesh, B. K. Sikder and A.K. Chaudhary*

Advanced Centre of Research in High Energy Materials, University of Hyderabad, Hyderabad-500 046, India * Authors' anilphys@yahoo.com, akcphys@gmail.com

We report the charge transfer mechanism under visible 532 nm wavelength for detection of premium explosives like HMX, RDX and TNT, etc. in solid form using pulsed photoacoustic technique. The PEDOT plays the role of an effective sensing medium for the detection explosives when mixed in equal proportion and subjected to 532 nm wavelength without any chemical treatment. The study reveals that one milligram of PEDOT is sufficient to initiate the charge transfer mechanism between positive charge on the oxidised PEDOT and the lone pairs of electrons on the oxygen atoms of the nitro group of the explosives. The experimental results clearly show the shift of the NO₂ vibration mode and reduction in the intensity of Raman bands.

The strength of enhanced PA signal for HMX, RDX and TNT were of the order of 4000, 636 and 4 times, respectively. We have also verified the Lewis acid based interaction in solid state form as predicted by Toggeler's group [1]. Further, we used static optical pump and THz probe technique to identify the formation of new state of compound which is reflected in terms of change of refractive index for the first time.

1. Introduction

RDX, TNT and HMX do not absorb visible radiation, therefore, they can be detected either in UV region or in near infrared region using conjugated polymer matrix as a sensor. Most of the reports on optical detection of these explosives are based on photoluminescence (PL) or fluorescence techniques which arise due to radiative decay. Our group has used solid graphite powder as a sensing medium to detect TNT in visible region [2]. In addition, many more reports are available for detection of explosives in vapor state [3-4]. However, in the present report efforts have focused on sensing three commonly used explosives: 2,4,6-trinitro-toluene (TNT), 1,3,5-trinitro-1,3,5-triazinane (RDX) and HMX with PEDOT, a conjugated polymer matrix, using pulsed photoacoustic spectroscopy technique.

2. Experimental arrangements

Fig. 1 shows the schematic arrangement for recording of PA signal of solid sample in PA cell made of Al. The sample were irradiating with a 532 nm wavelength (visible wavelength). Data were recorded at various incident laser energies such as 0.5 mJ, 1 mJ, 1.5 mJ, 2 mJ and 2.5 mJ, respectively and the data acquisition time were 0.5 ms, 1.0 ms, 1.5 ms and 2.5 ms respectively. Solid samples were physically crushed into fine powder using motor pestle prior performing PA spectroscopy. Pristine conjugated polymer (PEDOT), pristine explosives (RDX, TNT, HMX) and PEDOT-explosive mixtures (PEDOT-TNT, PEDOT-RDX and PEDOT-HMX) are the samples of interest. The time domain PA signals for five different incident energies and four data acquisition time were recorded and converted into frequency domain using Fast Fourier Transform. The inset of fig. shows the charge transfer mechanism between PEDOT and explosive molecules

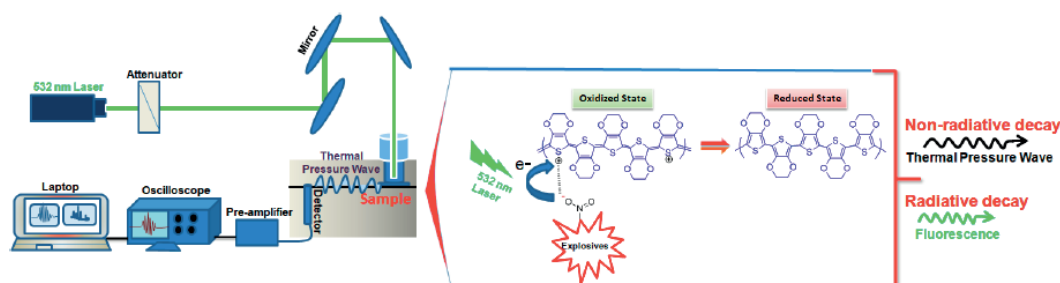


Fig. 1

3. Results and Discussion

The obtained results are shown in Fig. 2 (a,b and c). It is very much clear in case of RDX the PA signal without PEDOT was below 10mV which become more than 695 mV in case of RDX with PEDOT. Similarly for TNT and HMX the PA signal becomes from 25 mV to 160 mV and 0.031 mV to 187mV, respectively.

Session C4: Spectroscopy III

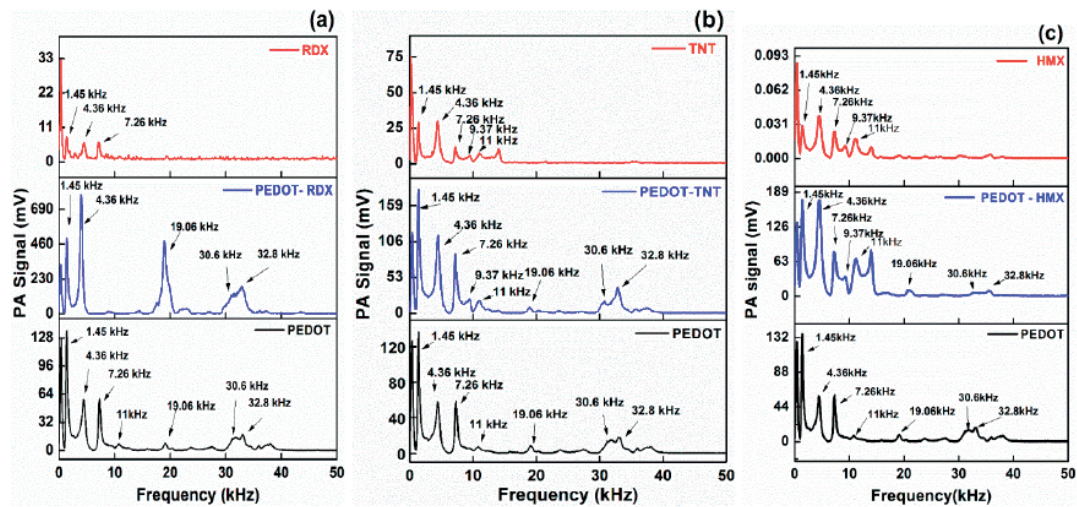


Figure 2: Plots of the various PA modes of frequency domain signal (a) PEDOT, PEDOT-RDX and RDX; (b) PEDOT, PEDOT-TNT and TNT; (c) PEDOT, PEDOT-HMX and HMX.

Acknowledgement

The Authors gratefully acknowledge the financial support provided by the DRDO, Ministry of Defence, Govt. of India under ACRHEM Phase-III No.ERIP/ER/1501138/M/01/319/D(R&D).

References

1. H. P. Martinez, C. D. Grant, J. G. Reynolds, and W. C. Silica Trogler, *J. Mater. Chem.* (22), 2908 (2012)
2. K. S. Rao, A. K. Chaudhary, F. Yehya, *Sensors Actuators B Chem.* (231), 830 (2016)
3. F. Yehya, A. K. Chaudhary, D. Srinivas, and K. Muralidharan, *Appl. Phys. B* 121, 193 (2015).
4. A. K. Chaudhary, K. S. Rao, and Sudheer Kumar *Appl. Optics*, 55(6), 1 (2016) [dx.doi.org/10.1364/AO.99.099999](https://doi.org/10.1364/AO.99.099999)

Photoinduced coherent acoustic phonons in phase change materials GeTe

R. Gu^{*(1)}, T. Perrault⁽¹⁾, V. Juvé⁽¹⁾, G. Vaudel⁽¹⁾, M. Weis⁽¹⁾, A. Bulou⁽¹⁾, N. Chigarev⁽²⁾, S. Raetz⁽²⁾, V. E. Gusev⁽²⁾, Z. Cheng⁽³⁾, H. Bhaskaran⁽³⁾, P. Ruello⁽¹⁾

1. Institut des Molécules et Matériaux du Mans, UMR CNRS 6238, Le Mans Université, 72085 Le Mans, France

2. Laboratoire d'Acoustique de Le Mans Université, UMR CNRS 6613, Le Mans Université, 72085 Le Mans, France

3. Department of Materials Science, University of Oxford, United Kingdom

pascal.ruello@univ-lemans.fr

GeTe is a typical phase change material which shows both semiconducting and ferroelectric behaviors in its crystalline phase (\square -phase). The Sb doped GeTe (GST alloy) is also famous since it is widely used in modern rewritable data storage devices (rewritable DVD), which is called phase change memory devices. The writing/erasing process is based on the phase transformation of metastable amorphous into rhombohedral phase and vice-versa. In order to extend the capability of this class of materials to be used in modern photonics with ultrafast writing/erasing processes, a profound understanding of the electron and phonon dynamics must be obtained. In this study, we therefore investigate these dynamics at short time scale, i.e. in the frequency range of tens to hundreds of GHz. The sample under investigation is a GeTe thin layer (300-400nm) which is deposited on SiO_2/Si substrate and covered by thin ITO layer. We used ultrafast optical spectroscopy method (two-color pump-probe) with an in-situ temperature monitoring [1,2], to investigate the electrons and phonons dynamics in GeTe lattice before and after the phase transformation at picosecond time scale. The spectrum of photogenerated/photodetected GHz acoustic phonons exhibits a drastic modification revealing large changes of optical, elastic and photoelastic properties of GeTe when the phase transition occurs. Only room temperature experiments in GST alloys were conducted up to now [3,4] and our results bring new insights in the description of the phase transformation. Besides the clear temperature dependence of the coherent acoustic phonon spectrum, the analysis of the acoustic pulse duration is discussed to establish the nature of the electron-acoustic phonon coupling mechanism involved in the light-induced generation process [5,6]. As shown in Fig. 1, a reasonable agreement is found between the detected signal and the calculated one while a clear discrepancy is observed for the crystalline phase whose origin will be discussed.

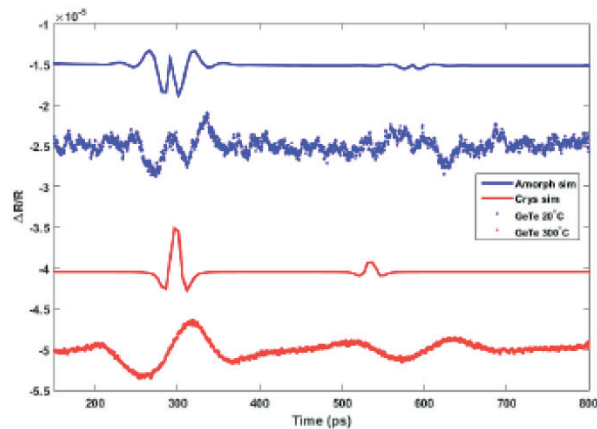


Fig. 1. Evolution of the picosecond acoustic pulses (two echoes) generated and detected in a thin film of GeTe when the material is transformed from an amorphous (blue) to a crystalline (red) phase. The solid (blue and red lines) correspond to a theoretical calculation showing a clear departure for the response in the crystalline material.

Acknowledgements

The authors acknowledge the projects Ferrotransducers (Lmac, Région Pays de la Loire France) and ANR UP-DOWN project (18-CE09-0026-04)

References

1. P Ruello, S Zhang, P Laffez, B Perrin, V Gusev, Phys. Rev. B 79 (9), 094303 (2009). doi.org/10.1103/PhysRevB.79.094303
2. M Lejman, C Paillard, V Juvé, G Vaudel, N Guiblin, L Bellaiche, M Viret, V. E Gusev, B. Dkhil, P. Ruello Phys. Rev. B 99 (10), 104103 (2019). doi.org/10.1103/PhysRevB.99.104103
3. M. Hase, P. Fons, A. V. Kolobov and J. Tominaga, J. Phys.: Condens. Matter 27, 485402 (2015). doi: 10.1088/0953-8984/27/48/485402.
4. M. J. Shu, I. Chatzakis, Y. Kuo, P. Zalden, and A. M. Lindenberg, Appl. Phys. Lett. 102, 201903 (2013). doi.org/10.1063/1.4807731
5. G. Ruizhe et al, to be submitted.
6. P Ruello, VE Gusev, Ultrasonics 56, 21-35 (2015) doi.org/10.1016/j.ultras.2014.06.004

Thermal transport in layered ferrielectric materials $M^{1+}M^{3+}P_2(S, Se)_6$ ($M^{1+} = Cu, Ag$; $M^{3+} = In, Bi$)

Alberto OLEAGA*, Agustin SALAZAR

Departamento de Física Aplicada I, Escuela de Ingeniería de Bilbao,
 UPV/EHU, Plaza Ing. Torres Quevedo 1, 48013 Bilbao, Spain

alberto.oleaga@ehu.es

Single crystals of layered ferroelectrics $CuInP_2(S,Se)_6$, $AgInP_2(S,Se)_6$, $AgBiP_2(S,Se)_6$ and $CuBiP_2Se_6$ have been grown and samples cut as plane parallel plates in two orientations, with surfaces perpendicular and parallel to the layered plane *ab*. An ac photopyroelectric calorimetric technique has been used to measure the thermal diffusivity *D* along the layered planes as well as perpendicular to them in the range 30-350K, highlighting a strong thermal anisotropy in all cases; at room temperature, the thermal diffusivity along the layers is roughly thrice the one in a direction perpendicular to them, presenting typical values for thermal insulators, where heat is mainly transported by phonons. The ferrielectric transitions in $CuInP_2S_6$ and $CuInP_2Se_6$ are signalled as dips superimposed to the monotonous background of the thermal diffusivity. For $CuBiP_2Se_6$ a faint first order phase transition has been found around 136K, in agreement with an antiferroelectric transition found in literature [1] while there is no sign of phase transitions in any of the other samples in this thermal property. Fig. 1(a) shows *D* for the samples containing S.

The background heat capacity *C* for all compositions has been either extracted from literature [2] or calculated through the evaluation of the phonon spectra using density-functional perturbation theory [3] (see Fig. 2 for $AgInP_2Se_6$, as an example) so that thermal conductivity *k* has been calculated by means of the equation $k = C D$.

It can be seen from Fig. 1(b) that ultra low values of thermal conductivity can thus be achieved playing with the concentration and the orientation of the sample. All samples, save for $CuBiP_2(S,Se)_6$, share a common behavior, with *k* following the law $k \sim T^{-1}$ at medium temperatures, confirming the dominant role of phonon scattering above the Debye temperature, while softening the decrease at about double that value. The differences in the thermal and ferroelectric properties among the compounds are explained in terms of the following mechanisms: the size and site occupancy of the Cu (Ag) ions together with their effective hopping motions and the possibility to freeze them, the covalency degree in the bonds with S or Se, and, finally, the differences in stereochemical activity between In and Bi.

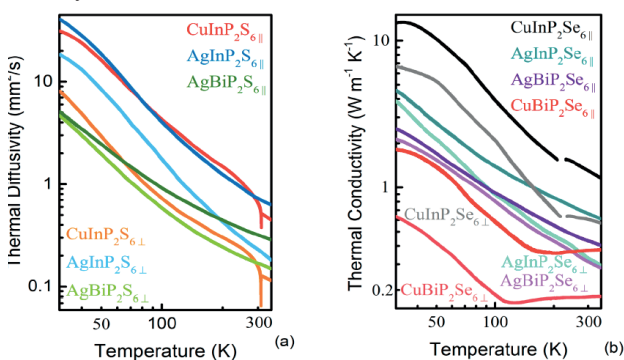


Fig. 1. (a) Thermal diffusivity for the samples with S; (b) Thermal conductivity for the samples with Se. Symbols || and \perp mean they are calculated along the layered planes or perpendicular to them.

Acknowledgements

This work has been supported by Universidad del País Vasco UPV/EHU (GIU16/93).

References

1. M. A. Gave, D. Bilc, S. D. Mahanti, J. D. Breshears, M. G. Kanatzidis, "On the Lamellar Compounds $CuBiP_2Se_6$, $AgBiP_2Se_6$ and $AgBiP_2S_6$. Antiferroelectric Phase Transitions Due to Cooperative Cu^{+} and Bi^{3+} Ion Motion", *Inorg. Chem.* 44, 5293 (2005).
2. L.M. Beley. "Thermodynamic properties of ferroelectric crystals $CuInP_2(S_{1-x}S_1-x)_6$ " PhD Thesis, Uzhhorod National University, Uzhhorod, (2007).
3. S. Baroni, S. de Gironcoli, A. del Corso, P. Gianozzi, "Phonons and related crystal properties from density-functional perturbation theory", *Rev. Mod. Phys.* 73, 515 (2001).

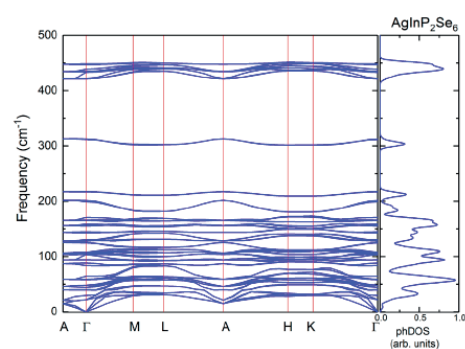


Fig. 2. Calculated phonon spectrum and phonon density of states for $AgInP_2Se_6$

Acoustic attenuation in silica via ultrafast optical techniques

A. HUYNH ^{(1)*}, X. LAFOSSE ⁽²⁾, A. LEMAITRE ⁽²⁾, E. PERONN ⁽¹⁾, B. PERRINE ⁽¹⁾, B. RUFFLÉ ⁽³⁾,
R. VACHER ⁽³⁾, M. FORET ⁽³⁾

1. Institut des Nanosciences de Paris, Sorbonne Université, CNRS-UMR 7588, F-75005 Paris, France

2. Centre de Nanosciences et de Nanotechnologies, Université Paris-Sud - Université Paris-Saclay CNRS-UMR 9001, 10 Boulevard
Thomas Gobert, F-91120 Palaiseau, France

3. Laboratoire Charles Coulomb, Université de Montpellier, CNRS-UMR 5221, F-34094 Montpellier

*Agnes.huynh@insp.jussieu.fr

We reinvestigate sound dispersion and attenuation in a SiO₂ layer as a function of temperature over the range 20–300 K by picosecond acoustics [1]. Indeed, thin films of amorphous SiO₂ are key materials for a variety of applications. It is therefore of fundamental interest to investigate the dissipative mechanisms at the origin of acoustic losses in amorphous dielectric layers and in particular to compare them to those of the bulk material, including the prototypical vitreous silica v-SiO₂. A pulse echo scheme is used, where a broadband strain-pulse (centered at 120 GHz) is detected in an Al transducer after propagating back and forth through the SiO₂ layer. The acoustic attenuation coefficient α within the SiO₂ layer is evaluated by fitting the echoes to a mismatch model including an effective local law for the frequency dependence of attenuation over the band of the pulse. In this way, the T dependence of α in SiO₂ layers could be extracted in this work for the first time.

In particular, these silica layers are found to have a similar anharmonic contribution to acoustic absorption than vitreous silica, while defects contribution decreases with frequency. We therefore explore acoustic modes in these silica layers at higher frequencies where we can reach vitreous silica properties. Thanks to the use of GaAs/AlAs superlattices as sensitive phonon detector, we can reach the difficult but crucial frequency region between around 0.1 and 1 THz. Indeed, a rather universal property of glasses is that a large excess of modes exists, with a maximum density of states near 1 THz, forming the so-called boson peak. The acoustic modes are expected to be strongly affected as their frequency nears the boson peak. The onset of this effect, which is expected to be dominant in the 0.5 to 1 THz range, is observed here for the first time at low temperature.

References

1. A. Huynh, E. Péronne, C. Gingreau, X. Lafosse, A. Lemaître, B. Perrin, R. Vacher, B. Rufflé, and M. Foret, Phys. Rev. B 96, 174206 (2017).

Squeezing of Phonoritons in Heterostructures

Que Huong NGUYEN

Marshall University, One John Marshall Drive, Huntington WV 25701, USA

nguyenh@marshall.edu

In this work we discuss the squeezing of phonoritons inside semiconductors from a theoretical point of view. When a semiconductor sample is illuminated by high-intensity electro-magnetic radiation near the resonance, the occupation number of polaritons in the same mode is large and the interaction between polaritons and phonons become very important. This interaction leads to the formation of a new kind of elementary excitation called phonoriton, a coherent superposition of excitons, photons, and longitudinal acoustic phonons under Brillouin scattering of an intense polariton. The phonoritons have been studied theoretically and experimentally and have been found in Cu_2O . To illustrate the formation of phonoritons, after diagonalization, the Hamiltonian of a system of excitons, photons and phonons is written as the following

$$H = \sum_p \{ \omega^{pol}(p) B_p^+ B_p + \Omega^c(p) C_p^+ C_p + \sum_q S'(p-q) B_{ip}^+ \langle B_{jq} \rangle (C_{(p-q)} + C_{-(p-q)}^+) + c.c. \}$$

We found that the phonoritons are intrinsically squeezed and found the squeezed states, or so called 'low-noise' states- the states of reduced quantum noise with reducing effect of vacuum fluctuation, for phonoritons. We introduce the new polariton-phonon mixed mode:

$$A_{\pm} = \alpha_p B_{\pm p} + e^{2i\chi} B_p C_{\pm(p-q)}$$

This mode leads to a two-mode squeeze operator, which will reveal the squeezed structure of the phonoritons.

From our results we also have the possibility to tune the squeeze amplitude, what is important both theoretically and experimentally. The results have been applied for phonoritons of inorganic-inorganic heterostructures.

KEYNOTE

Concept of Equivalent Temperature for the Investigation of Photothermal Phenomena in Dielectric Materials

Oleg A. Ryabushkin*

Kotelnikov Institute of Radio-engineering and Electronics of RAS, Moscow, Russia

e-mail: roa228@mail.ru

During propagation of laser radiation in any medium some part of its power is transformed into heat. Nonuniform heating is conditioned by both spatial distribution of laser beam intensity and anisotropy of the heat conductivity, as well as by cooling mechanisms of the irradiated substance. In such case application of the thermodynamic temperature concept for mathematical description of the material heating has considerable limitations. In our opinion for correct characterization of physical phenomena related to interaction of laser radiation with materials it is necessary to introduce novel “equivalent temperature” concept.

KEYNOTE

Ultrafast optoacoustic nanowire-to-nanowire surface acoustic wave excitation and detection

Oliver B. WRIGHT ^{(1)*}, Yuta IMADA ⁽¹⁾, Motonobu TOMODA ⁽¹⁾,
Osamu MATSUDA ⁽¹⁾, Vitalyi E. GUSEV ⁽²⁾

1. Division of Applied Physics, Faculty of Engineering, Hokkaido University, Sapporo 060-8628 Japan

2. Laboratoire d'Acoustique de l'Université du Mans (LAUM), UMR CNRS 6613, Le Mans Université,
Avenue Olivier Messiaen, 72085 LeMans, France

olly@eng.hokudai.ac.jp; yuta.imade@gmail.com; mtomoda@eng.hokudai.ac.jp;
omatsuda@eng.hokudai.ac.jp; vitali.goussev@univ-lemans.fr

Surface acoustic waves (SAWs) have been of great interest for the last 50 years, ever since the invention of interdigital transducers (IDTs) [1] and application of lasers for SAW generation [2]. SAWs in the ultrasonic range have been widely used in communication and signal-processing technologies, material characterization, photonic modulation, and optomechanics, for example.

One major drawback with IDTs is the need for a piezoelectric substrate for their operation. GHz SAWs can be excited by laser-induced mechanical stress localized within the SAW penetration depth, i.e. their wavelength, provided that the laser intensity temporal spectrum contains these frequencies and the spatial spectrum on the sample surface contains the required SAW acoustic wavenumbers [3]. The intensity envelope of ultrafast laser pulses (of sub-ps and fs duration) do contain these required frequencies. Reaching the required wave numbers involves laser-induced grating patterns on the sample surface [4,5], or deposited metal gratings [6,7], down to sub-100-nm spatial periods [7-9]. However, gratings require several spatial periods, thus imposing a limit on miniaturization.

Here we present experimental results for a miniaturized geometry for both optoacoustic excitation and detection of GHz SAWs, by means of a single nanowire SAW emitter and a single nanowire SAW receiver, localizing the transduction regions to ~70 nm in width.

Our emitter consists of a gold nanowire of thickness 50 nm, width 70 nm and length 5 mm on a glass substrate, whereas our receiver consists of a line of nanorods each of thickness 50 nm, width 70 nm and length 210 nm, separated by 100 nm gaps (Fig. 1 (a)), forming a nanowire-like line of length 5 mm. This line is arranged to be at a distance of 5 mm from the nanowire.

We apply 200 fs duration laser pulses at 410 nm wavelength for the generation of the coherent surface acoustic waves on the left-hand nanowire over a line source $\sim 70 \times 3 \text{ mm}^2$ set parallel to the nanowire, and at 820 nm wavelength for the detection on the right-hand nanowire over a spot of diameter $\sim 3 \text{ mm}$. The dimensions of the nanorods are chosen to increase the sensitivity of the detection process through their deformation by ensuring their longitudinal plasmon resonance is in the vicinity of the probe light wavelength [10-13], and the probe light is chosen to be polarized along the nanorods for optimum sensitivity. Figure 1(b) (top) shows the detected optical reflectivity change at the detector nanowire, corresponding to a time equal to the SAW propagation time from the left-hand nanorod. Figure 1(b) (bottom) shows the modulus of the temporal Fourier transform vs frequency. This indicates that SAW pulses centred at ~8 GHz are detected. Numerical modelling of the vibrations of the gold nanorods used for detection on the glass substrate reveals that the maxima in the detected frequency spectrum (Fig. 1(b), bottom) are in the vicinity of the two lowest longitudinal vibrational resonances of nanorod. Consequently, in the experiments the acousto-optic nano-detector effectively operates in vibrational resonance mode.

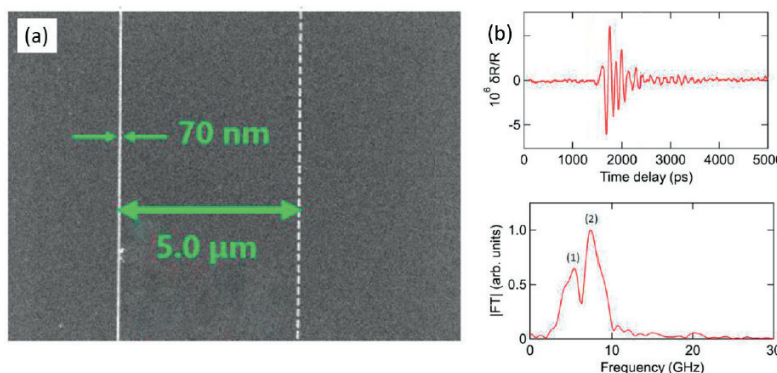


Fig. 1. (a): SEM image of the gold nanowires deposited on a glass substrate for optical generation (left) and optical detection (right) of coherent surface acoustic waves propagating to the right along the surface. (b) Transient reflectivity normalized variation $\delta R/R$ detected by at $5 \mu\text{m}$ distance between the generator and the detector (top) and its temporal Fourier spectrum ($|FT|$) (bottom), showing two main resonances.

Our emitter consists of a gold nanowire of thickness 50 nm, width 70 nm and length 5 μm on a glass substrate, whereas our receiver consists of a line of nanorods each of thickness 50 nm, width 70 nm and length 210 nm, separated by 100 nm (Fig. 1 (a)), forming a nanowire-like line of length 5 μm . This line is arranged to be at a distance of 5 μm from the nanowire.

We apply 200 fs duration laser pulses at 410 nm wavelength for the generation of the coherent surface acoustic waves on the left-hand nanowire over a line source $\sim 70 \times 3 \mu\text{m}^2$ set parallel to the nanowire, and at 820 nm wavelength for the detection on the right-hand nanowire over a spot of diameter $\sim 3 \mu\text{m}$. The dimensions of the nanorods are chosen to increase the sensitivity of the detection process through their deformation by ensuring their longitudinal plasmon resonance is in the vicinity of the probe light wavelength [10-13], and the probe light is chosen to be polarized along the nanorods for optimum sensitivity. Figure 1(b) (top) shows the detected optical reflectivity change at the detector nanowire, corresponding to a time equal to the SAW propagation time from the left-hand nanorod. Figure 1(b) (bottom) shows the modulus of the temporal Fourier transform vs frequency. This indicates that SAW pulses centred at ~ 8 GHz are detected. Numerical modelling of the vibrations of the gold nanorods used for detection on the glass substrate reveals that the maxima in the detected frequency spectrum (Fig. 1(b), bottom) are in the vicinity of the two lowest longitudinal vibrational resonances of nanorod. Consequently, in the experiments the acousto-optic nano-detector effectively operates in vibrational resonance mode.

Our results demonstrate that through the optimization of nano-detector wires along with the wavelength and polarization of the probe light, experiments with nano-localized nanowire-to-nanowire transduction with pulsed SAWs in the GHz range are feasible. This research therefore provides promising avenues for future development of wide-frequency-band localized opto-acoustic transducers for SAWs up to 1 THz.

References

1. R. M. White, F. M. Voltmer, *Appl. Phys. Lett.* 7, 314 (1965) doi.org/10.1063/1.1754276
2. R. E. Lee, R. M. White, *Appl. Phys. Lett.* 12, 12 (1968) doi.org/10.1063/1.1651832
3. V. Gusev and A. Karabutov, *Laser Optoacoustics* (Nauka, Moscow, 1991; AIP, New York, 1993).
4. J. J. Kasinski, L. Gomez-Jahn, K. J. Leong, S. M. Gracewski, and R. J. Dwayne Miller, *Opt. Lett.* 13, 710 (1988) doi.org/10.1364/OL.13.000710
5. A. Harata, H. Nishimura, T. Sawada, *Appl. Phys. Lett.* 57, 132 (1990) doi.org/10.1063/1.103964
6. B. Bonello, A. Ajinou, V. Richard, Ph. Djemia, S. M. Chérif, *J. Acoust. Soc. Am.* 110, 1943 (2001) doi.org/10.1121/1.1399034
7. M. Schubert, M. Grossmann, O. Ristow, M. Hettich, A. Bruchhausen, E. C. S. Barretto, E. Scheer, V. Gusev, T. Dekorsy, *Appl. Phys. Lett.* 101, 013108 (2012) doi.org/10.1063/1.4729891
8. M. Grossmann, O. Ristow, M. Hettich, C. He, R. Waitz, E. Scheer, V. Gusev, T. Dekorsy, M. Schubert, *Appl. Phys. Lett.* 106, 171904 (2015) doi.org/10.1063/1.4919132
9. Q. Li, K. Hoogeboom-Pot, D. Nardi, M. M. Murnane, H. C. Kapteyn, M. E. Siemens, E. H. Anderson, O. Hellwig, E. Dobisz, B. Gurney, R. Yang, K. A. Nelson, *Phys. Rev. B* 85, 195431 (2012) doi.org/10.1103/PhysRevB.85.195431
10. S. A. Maier, *Plasmonics: Fundamentals and Applications* (Springer, New York, 2007).
11. A. Crut, P. Maioli, N. Del Fatti, F. Vallée, *Phys. Rep.* 549, 1, (2015) doi.org/10.1016/j.physrep.2014.09.004
12. J. Cao, E. K. Galbraith, T. Sun, K. T. V. Grattan, *Sensors and Actuators B* 169, 360 (2012); doi.org/10.1016/j.snb.2012.05.019
13. J. Cao, T. Sun, K. T. V. Grattan, *Sensors and Actuators B* 195, 332 (2014); doi.org/10.1016/j.snb.2014.01.056

Application of photoacoustic method to thermophysical properties of ceramic coatings with different scattering properties of radiation

Atsumasa YOSHIDA*, Takuya AKIYAMA, Shinichi KINOSHITA

Department of Mechanical Engineering, Osaka Prefecture University, Sakai, Japan

Authors' e-mail ayoshida@me.osakafu-u.ac.jp

Introduction

Thermal barrier coating (TBC) is one of the applications of ceramics. Thermal spraying is a typical method and is applied to the formation of TBC for high-temperature equipment such as gas turbines. In order to evaluate the thermal performance of the formed coating, a technique is required to measure the thermophysical properties of the coating nondestructively.

Measurement Theory

The thermophysical properties of thermal sprayed coatings were measured nondestructively using photoacoustic method. A sample placed in an enclosed space was irradiated with periodically intensity-modulated light, and the phase lag for the incident light was measured by an acoustic signal as its thermal response. The thermal diffusivity and thermal effusivity of the sample were determined by performing inverse analysis of the signal. The conventional RG theory was applied to optically thin samples where absorption is dominant. For samples with optical scattering, we developed a method that does not irradiate the sample directly with a laser.

Sample

As a measurement sample, a cylinder (60 mm in diameter) made of carbon steel S45C was used as a base. For the thermal spray coating, $\text{Al}_2\text{O}_3 \cdot \text{TiO}_2$ (0.14 mm in thickness) whose optical absorption was dominant and YSZ (0.14 and 0.45 mm in thickness), which are typical materials for TBC, whose optical scattering was dominant were adopted. The sample surface was polished and $R_a = 1.0 \mu\text{m}$. For each material, three kinds of sample with different porosity were prepared, one sprayed under normal condition, one with doubled spraying distance, and one with diagonal spraying. Let $\text{Al}_2\text{O}_3 \cdot \text{TiO}_2$ be samples (a), (b) and (c) in order, and YSZ be samples (d), (e) and (f). For $\text{Al}_2\text{O}_3 \cdot \text{TiO}_2$, the optical flux was directly incident on the sample, and the thermal diffusivity and thermal effusivity were simultaneously measured based on the RG theory. On the other hand, for YSZ, we applied a new method that does not directly irradiate the sample with the optical flux. The thermal effusivity was first determined by adhering an optically opaque titanium thin plate (0.05 mm in thickness) to a thermally thick sample with 0.45 mm in thickness. The thermal diffusivity was calculated by performing the same measurement on a thermally thin sample with 0.14 mm in thickness, with this thermal diffusivity as known. The pressing pressure was set to 600 N where no effect was observed.

Results and Discussion

The measurement results of $\text{Al}_2\text{O}_3 \cdot \text{TiO}_2$ (0.14 mm in thickness) are shown in Fig. 1. The target samples are (a) and (b). The experiment was performed three times each, and the measurement precision was estimated to be less than about 10%. The solid and dotted lines in this figure represent the phase delay calculated from the thermophysical properties determined as the optimum values from the measured values. Figure 2 shows the measurement results of YSZ (0.14 and 0.45 mm in thicknesses). The target sample is (d). The solid line in Fig. 2 represents the phase lag calculated for the coating with 0.14 mm in thickness. The measurement results of the samples with different thickness were different in the low frequency range. It was judged that the coating of 0.45 mm in thickness

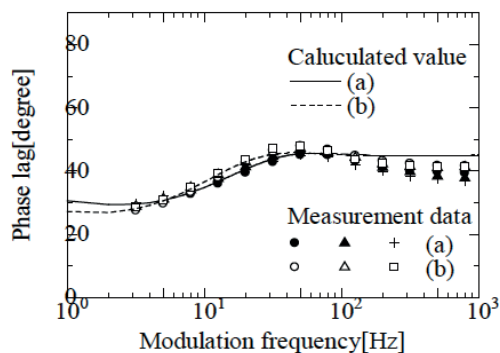


Fig. 1. Relation between phase delay and modulation frequency for $\text{Al}_2\text{O}_3 \cdot \text{TiO}_2$ (a) and (b).

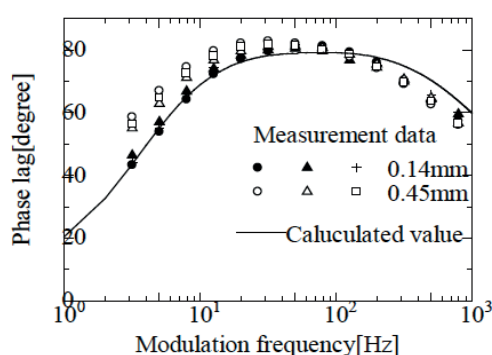


Fig. 2. Relation between phase delay and modulation frequency for YSZ (d).

was thermally thick and that the heat was sufficiently attenuated in the coating, and the thermal effusivity was first determined. Next, the thermal diffusivity was calculated using the measurement result of the coating with 0.14 mm in thickness that the heat could reach to the base, with the thermal effusivity as known. It was found that the thermal diffusion performance decreased as the porosity increased in both samples. The porosity was calculated by binarizing from a photomicrograph magnified 500 times of the sample cross section. The same tendency was seen for the thermal effusivity. The thermal diffusivity of $\text{Al}_2\text{O}_3 \cdot \text{TiO}_2$ (0.655 mm in thickness) and YSZ (0.698 mm in thickness) sprayed under normal condition was also measured by the laser flash method and compared with the measurement results obtained by photoacoustic method. As a result, the difference was about 10% and about 25%, respectively.

Conclusions

Thermophysical properties of thermal sprayed coatings could be measured nondestructively by the photoacoustic method regardless of the scattering characteristics of radiation. It was found that the higher the porosity, the lower the thermal diffusion performance. The measurement precision was confirmed by repeated measurement, and the results were compared with the measurement results by the laser flash method, and good results were obtained.

Acknowledgements

The provision of data to compare with the results of photoacoustic measurement was conducted by Dr. Megumi Akoshima and Dr. Haruka Abe, who belonged to National Metrology Institute of Japan, National Institute of Advanced Industrial Science and Technology. We express deeply our gratitude to them.

Time-domain Brillouin scattering by GHz shear acoustic waves generated in grating structures

Osamu MATSUDA ^{(1)*}, Kandai TSUTSUI ⁽¹⁾, Thomas PEZERIL ⁽²⁾, Gwenaëlle VAUDEL ⁽²⁾,
Vitalyi GUSEV ⁽³⁾

1. Division of Applied Physics, Faculty of Engineering, Hokkaido University, Sapporo 060-8628, Japan

2. Institut Molécules et Matériaux du Mans, UMR CNRS 6283, Le Mans Université, 72085 Le Mans, France

3. Laboratoire d'Acoustique de l'Université du Mans, UMR CNRS 6613, Le Mans Université,
72085 Le Mans, France

omatsuda@eng.hokudai.ac.jp

The absorption of short light pulses (pump light) in a medium may generate coherent acoustic waves therein, and their propagation can be detected by the delayed light pulses (probe light) through the transient optical reflectivity change. In transparent media, the reflectivity change shows long-lasting oscillation, so called Brillouin oscillation, which corresponds to the observation of Brillouin scattering in time-domain and provides opportunity to evaluate acoustical, optical, and photoelastic properties of the medium.

The usage of the grating structure formed on the surface of the transparent medium has been reported to monitor simultaneously the multiple Brillouin frequencies necessary for the precise material evaluation [1]. This is achieved via the diffraction of probe light by the grating before and/or after the light scattering by the acoustic waves. The study, however, has been limited only to the longitudinal acoustic waves, though it has been pointed out that the shear acoustic waves may also be generated by the grating-shaped source [2]. From the viewpoint of the material evaluation, it is desirable to get the information for both longitudinal and shear acoustic waves to get the full information of the elastic properties of the medium. The failure of the shear wave detection could be attributed to the choice of experimental configuration: the most of convenient configurations, such as normal incident probe light to the sample, for example, have too high symmetry and are not suitable for the shear wave detection [3].

Generally, the incident probe light induces the electric dipole moment in the medium. This induced dipole may be modulated by the acoustic waves through the photoelastic effect. The Brillouin oscillation is a result of interference between the light emitted from the modulated dipole and the non-modulated light. In an isotropic medium, the Brillouin scattering caused by the shear acoustic wave is efficient if the shear polarization has finite component perpendicular to the plane defined by the probe light before and after the scattering by the acoustic waves.

In this paper, we carry out the measurement with low symmetry probe configuration to detect the shear acoustic waves. The sample is a fused silica substrate (1 mm thickness) with Aluminum grating of 380 nm period. A standard optical pump-probe setup with a Ti-sapphire regenerative amplifier (wavelength 795 nm, pulse width < 200 fs, repetition frequency 260 kHz) is used. The probe light is incident on the surface without the grating. The expected shear acoustic wave polarization is in the plane perpendicular to the grating rods. To fulfill the condition for the shear acoustic wave detection, we use the following configuration for the probing: 1) First the sample is held perpendicular to the incident probe light. The incident probe light and the sample grating rods are in parallel to the optical table. 2) The sample is rotated with respect to the axis perpendicular to the table by 45° so that the reflected light is in parallel to the table and forms the right angle to the incident probe light. 3) Then the sample is further rotated (in our case by 48°) with respect to the axis in parallel to the grating rod so that the first order diffracted probe light is almost in parallel to the table. The transient intensity change in the first order diffracted probe light is monitored.

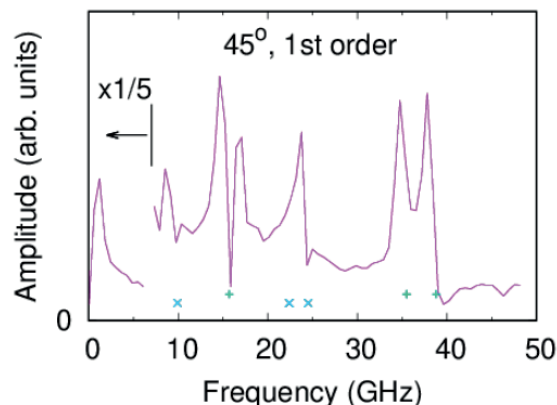


Fig. 1. Fourier spectrum of the Brillouin oscillations. The symbols are the calculated frequencies. +: longitudinal, x: shear.

Figure 1 shows the Fourier spectrum of the obtained Brillouin oscillation with the marked theoretically predicted frequencies for the longitudinal ($v_l=5968$ m/s) and shear ($v_t=3764$ m/s) sound velocities and the refractive index $n=1.47$. The peak around 24 GHz well agrees with the prediction for the shear waves. This opens a broad way of application of the time-resolved Brillouin measurement with grating structure for various material evaluations.

Acknowledgements

The reported research was conducted in the frame of the project PLUSDIL supported by ANR, under contract ANR-12- BS09-0031. O.M. is partially supported by the Acoustic HUB of Région des Pays de la Loire in France, by a Grant-in-Aid for Scientific Research from Japan Society for the Promotion of Science (17H02807), and by a research grant from Insight k.k.. We would like to thank OPEN FACILITY (Hokkaido University Sousei Hall) for the sample fabrication.

References

1. O. Matsuda, T. Pezeril, I. Chaban, K. Fujita, V. Gusev, *Physical Review B* 97, 064301 (2018) doi: 10.1103/PhysRevB.97.064301
2. V. Gusev, *Applied Physics Letters* 94, 164105 (2009) doi: 10.1063/1.3125243
3. M. Kouyaté, T. Pezeril, V. Gusev, O. Matsuda, *Journal of the Optical Society of America B* 33, 2634 (2016) doi: 10.1364/JOSAB.33.002634

Intracavity stimulated low-frequency Raman scattering

Maria Tareeva ⁽¹⁾*, Anna Kudryavtseva ⁽¹⁾, Maxim Karpov ⁽²⁾,
Mikhail Shevchenko ⁽¹⁾, Nikolay Tcherniega ⁽¹⁾

1. P.N. Lebedev Physical Institute of the RAS, Leninsky pr, 53, Moscow, 119991, Russia

2. FSUE VNIIA, ul.Sushchevskaya, 22, Moscow, 127055, Russia

tareeva@sci.lebedev.ru

The coherent interaction between optical and acoustic waves via stimulated scatterings (SS), mainly via stimulated Brillouin scattering (SBS) or stimulated low-frequency Raman scattering is an effective tool for manipulating light spectra in the gigahertz range. By using SBS, it is possible to obtain pulsed electromagnetic radiation in the optical range with modulation in the gigahertz frequency range. Modulation of the spectrum means the appearance in the spectrum of the scattered radiation the spectral components whose displacement relative to the line of exciting laser radiation lies in the gigahertz range. SBS generation gives the possibility to get several spectral Stokes and anti-Stokes components spaced by the spectral interval lying in the gigahertz range. The exact value of the spectral shift is defined by the acoustical properties of the active medium used. SLFRS is the stimulated analogue of spontaneous low-frequency Raman scattering [1], which represents inelastic scattering of electromagnetic radiation on acoustic vibrations of nano- and submicrometer particles. The frequency shift of the SLFRS is defined by the morphological properties of the particles used and can be easily varied in the range from several gigahertz up to terahertz by choosing for SLFRS excitation different nano or submicron particles systems. The very important characteristics of any type of stimulated scattering of light especially for practical applications are conversion efficiency and the threshold value. One of the most common ways to improve these characteristics is the use of intracavity stimulated scattering of light. Different schemes of intracavity scattering excitation make it possible to reduce the threshold value of the intensity of exciting laser radiation and to increase its conversion efficiency, which is actually equivalent to using optical feedback. Intracavity SBS allows not only lowering the threshold and increase the conversion efficiency but can be used for gigahertz comb generation. Also, intracavity SBS can be efficiently used to get the passive Q-switching mode at wavelengths for which conventional saturated absorbers are absent [2]. In this case, such effects as wave phase conjugation during SBS play an important role to achieve a high quality of the spatial distribution of laser radiation [3].

In the present work, we experimentally studied intracavity SLFRS for different submicron particles systems. We defined the threshold, conversion efficiency and SLFRS spectral structure (frequency shift and a number of the spectral components).

The frequency shift of SLFRS ranges from several GHz to 30 GHz for various systems. SLFRS modes together with frequency shift of SLFRS are controlled by nanoparticle's morphology.

Materials and Methods

The experimental setup for intracavity SLFRS generation was based on a ruby laser (wavelength 694.3 nm, pulse duration 20 ns, spectral width 0.015 cm⁻¹) (Fig. 1).

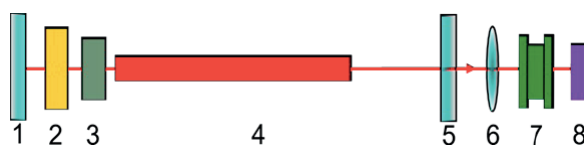


Fig. 1. Experimental scheme. (1) 99% mirror, (2) Q-switch (cryptocyanine solution in ethanol), (3) low-frequency Raman active medium (4) ruby rod with pumping lamps, (5) output mirror, (6) optical system, (7) Fabry Perot interferometer, and (8) interference pattern measuring system.

A few different nanosized media were studied upon excitation by radiation of the nanosecond ruby laser: aqueous suspensions of latex nanoparticles (average size of particles 200 and 600 nm) and silver nanoparticles (500 nm).

Raman active medium	Particle diameter, nm	SLFRS spectral shift, cm ⁻¹
latex particles	200	0.265
	600	0.100
silver particles	500	0.24
		0.48

Table 1. Parameters of nanosized media of different nature, which were used in the experiment as a low-frequency Raman active medium for optical comb generation.

The cell with an experimental sample was placed in the laser cavity of 0.5 m length. The laser pulse energy, duration, and the spectral composition of radiation were controlled during every experiment. The sample parameters and frequency shift of the intracavity SLFRS are presented in Table 1. For latex particles, only one Stokes component was registered for each size and for silver particles two Stokes components were registered. SLFRS spectral shifts for both cases agree well with the values of the acoustic frequencies of the particles used.

So, the intracavity SLFRS can be used as a spectral method for nano and submicron particles systems investigation and also as an effective source of radiation with a given spectral profile namely modulated in the gigahertz range.

Acknowledgements

This study was supported by the Russian Foundation for Basic Research (RFBR) project no. 19-02-00750-a

References

01. N. V. Tcherniega, K. I. Zemskov, V. V. Savranskii, et al., *Optics Letters* 38 (6), 824 (2013) doi:10.1364/ol.38.000824
02. A. Z. Grasyuk, V. V. Rogul'skii, and F. S. Faizulov, Formation of Powerful Nanosecond Pulses with the Aid of Mandel'shtam-Brillouin Scattering and Stimulated Raman Scattering, *Soviet Journal of Experimental and Theoretical Physics Letters* 9(1), 6 (1969)
03. N N Il'ichev, A V Kir'yanov, A A Malyutin, P P Pashinin, V S Sidorin, E I Shklovskii, Passive Q switching of a 1.3- μm laser resonator using a stimulated Brillouin scattering mirror, *Soviet Journal of quantum electronics*, 20 (11), 1383 (1990) doi:10.1070/QE1990v020n11ABEH007537

Rayleigh anomalies and disorder-induced mixing of polarizations at nanoscale in amorphous solids

Maria Grazia Izzo^{(1,2)*}, Stefano Cazzato^(3,4), Björn Wehinger⁽⁵⁾, Aleksandar Matic⁽⁴⁾,
Claudio Masciovecchio⁽⁶⁾, Alessandro Gessini⁽⁶⁾, Giancarlo Ruocco^(2,3)

1. Università degli studi di Roma "La Sapienza", Dipartimento di Ingegneria Informatica Automatica e Gestionale Antonio Ruberti, Via Ariosto 25, 00185 Roma, Italy

2. Istituto Italiano di Tecnologia - Center for Life Nanoscience, Viale Regina Elena, 291, 00161 Roma, Italy

3. Università degli studi di Roma "La Sapienza", Dipartimento di Fisica, Piazzale Aldo Moro 5, 00185 Roma, Italy

4. Chalmers University of Technology, Department of Applied Physics, Maskingränd 2, 412 58 Gothenburg, Sweden

5. University of Geneva, Department of Quantum Matter Physics, 24 Quai Ernest Ansermet, 1211 Genève 4, Switzerland

6. Sincrotrone Trieste S.C.p.A., S.S. 14 km 163,5 in AREA Science Park, I-34012 Basovizza, Italy

izzo@diag.uniroma1.it; mariagraziaizzo@gmail.com

Topologically disordered systems are characterized by macroscopic anomalies which characterize as a whole them with respect to long-range ordered solids. In particular, a hump over the level predicted by the Debye theory is observed in their specific heat, related to an excess over the Debye level of the Vibrational Density of States (VDOS). Even if the effort to link macroscopic anomalies to microscopic properties, extensively substantiated by the scientific literature, did not merge into a unified theory, it is noteworthy that all existing theories beg the question of the effect of elastic disorder on acoustic excitations at mesoscopic scale [1-4]. In this context, particular attention was drawn to the so-called Rayleigh anomalies [2,4]. They consist in a strong increase of the acoustic modes attenuation and softening of their phase velocity with respect to its macroscopic value. An acoustic excitation in a three-dimensional material is, however, characterized by its phase velocity, amplitude and polarization. The Rayleigh anomalies highlight how elastic disorder can affect the first two properties. Concerning polarization, acoustic excitations with mixed polarization (depolarization) have been observed by both Inelastic X-ray Scattering (IXS) and Inelastic Neutron Scattering (INS) experiments in several amorphous solids [5-7]. This latter phenomenon, however, has never been related to Rayleigh anomalies and quantitatively described as a phenomenon also originating from the disordered nature of the medium. This goal could in principle be grasped by solving the so-called Dyson equation, introduced in the framework of the Random Media Theory (RMT), which describes the ensemble averaged elastodynamic response of the system to an impulsive force [8]. The unavoidable recourse to approximate solutions, however, can hamper this task because of their limited range of validity in the acoustic excitations wavelength (l) domain. The Rayleigh anomalies and the mixing of polarizations arise at different l , respectively for l much lower or of the order of the average size of inhomogeneity domains (a), typically \sim nm in glasses. This makes difficult the building of an approximate solution encompassing both the wavelength ranges.

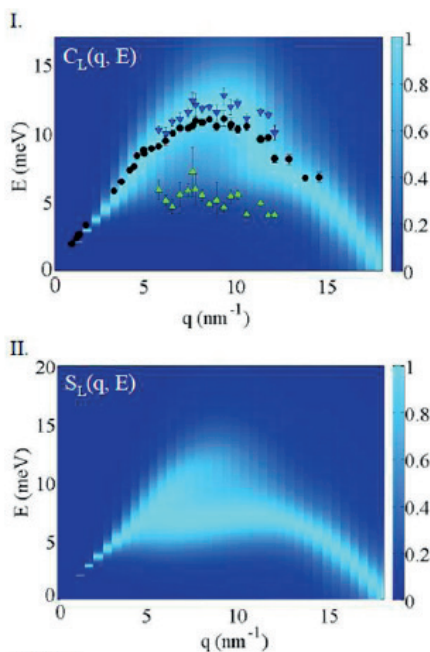


Fig. 1

Materials and Methods

In the framework of the RMT we developed an approximate solution of the Dyson equation, so-called Generalized Born Approximation (GBA) [9], holding up to $\lambda \sim a$. Theoretical results were corroborated by experimental characterization of longitudinal acoustic dynamics and VDOS, obtained respectively by IXS and INS, of 1-octyl-3-methylimidazolium chloride ([C8MIM] Cl) glass. The acoustic dynamics of a glass has been characterized in the present work with unprecedented precision in the wavevectors region where the mixing of polarizations occurs. Though the experimental methodology is standard, the choice of the testing material is not. The recent increase of discovery of novel materials with the consequent establishment of a wide range of heterogeneous structures at nanoscale, which can be experimentally characterized and, in some cases, tuned, offers indeed nowadays the opportunity of an unambiguous testing of the theory. The local structure of [C8MIM]Cl glass at nanoscale has been largely characterized both by experiments and MD simulations [7,10], thus permitting to fix non-trivial input parameters of the theory, such as α .

Results and Conclusion

The GBA permitted to achieve a quantitative, experimentally corroborated and unified description of acoustic dynamics properties in topologically disordered systems including both the Rayleigh anomalies and the mixing of longitudinal and transverse polarizations [4]. Their predictions are in qualitative agreement with experimental characterization of amorphous solids reported in literature. Comparison with experimental features of [C8MIM]Cl showed an excellent agreement. Fig. 1 shows, as an example of results, the projection in the wavevector (q) - Energy (E) plane of the longitudinal

current spectra, $C_L(q,E)$, (Panel I) and of the dynamic structure factors, $S_L(q,E)$, (Panel II) obtained by relying on GBA. The q trend of the longitudinal characteristic energy, corresponding to the maximum of $C_L(q,E)$, is highlighted. The mixing of polarizations, taking shape in the presence of a peak-like feature in $S_L(q,E)$ and $C_L(q,E)$ at energies near the ones characteristic of the transverse mode, is clearly observable at sufficiently high q . Symbols in Panel I mark experimental outcomes for the characteristic energies. The proposed model can be thought as a starting point for describing acoustic dynamics in glasses, composites, ceramics and geophysical systems. Since in solids acoustic excitations lead heat transfer, a reliable modeling of their properties can furthermore pave the way to identify the topological properties possibly forging the characteristics of these media as heat conductors.

References

1. H. Shintani, H. Tanaka, Nat. Mat. 7, 870 (2008) doi:10.1038/nmat2293.
2. A. I. Chumakov, G. Monaco, A. Monaco, W. A. Crichton, A. Bosak et al., Phys. Rev. Lett. 106, 225501 (2011) doi: 10.1103/PhysRevLett.106.225501.
3. W. Schirmacher, G. Ruocco, T. Scopigno, Phys. Rev. Lett. 98, 025501 (2007) doi: 10.1103/PhysRevLett.98.025501.
4. G. Monaco, V. Giordano, PNAS 106 3659 (2009) doi: 10.1073/pnas.0808965106.
5. B. Ruzicka, T. Scopigno, S. Caponi, A. Fontana, O. Pilla et al., Phys. Rev. B 69, 100201(R) (2004) doi: 10.1103/PhysRevB.69.100201.
6. F. Bencivenga, D. Antonangeli, Phys. Rev. B 90, 134310 (2014) doi: 10.1103/PhysRevB.90.134310. 7. M. G. Izzo, B. Wehinger, G. Ruocco, A. Matic, C. Masciovecchio, A. Gessini, S. Cazzato arXiv:1705.10338v2 and references therein.
8. S. M. Rytov, Y. A. Kravtsov, V. I. Tatarskii, Principles of Statistical Radiophysics 4 - Wave Propagation Through Random Media (Springer-Verlag, Berlin, 1989).
9. M. G. Izzo, G. Ruocco, S. Cazzato, Front. in Phys. 6, 108 (2018) doi: 10.3389/fphy.2018.00108.
10. E. Bodo, L. Gontrani, A. Triolo, R. Caminiti, J. Phys. Chem. Lett. 1, 1095 (2010) doi: 10.1021/jz100146r.

KEYNOTE

All-optical thermometry from DC till 100MHz

Lei MENG ⁽¹⁾, Pengfei ZHANG ⁽¹⁾, Olivier DESCHAUME ⁽¹⁾, Liwang LIU ⁽¹⁾, Kuo ZHONG ⁽²⁾,
Eduard FRON ⁽²⁾, Carmen BARTIC ⁽¹⁾, Mark VAN DER AUWERAER ⁽²⁾, Lionel LARBANOIX ⁽³⁾,
Sophie LAURENT ⁽³⁾, Christ GLORIEUX ^{(1)*}

1. *Laboratory for Soft Matter and Biophysics, Department of Physics and Astronomy, KU Leuven, Celestijnenlaan 200D, B3001 Heverlee – Belgium*
2. *Molecular imaging and photonics, Department of Chemistry, KU Leuven, Celestijnenlaan 200D, B3001 Heverlee – Belgium*
3. *Center for Microscopy and Molecular Imaging, Rue Adrienne Bolland 8, B-6041, Gosselies, Belgium*

Christ.glorieux@kuleuven.be

Besides many other measurable physical properties, the optical absorption and fluorescence spectrum of materials are changing with temperature, opening a pathway to measuring local temperature and temperature changes by optical probing. In this work, we report on the use of fluorescence thermometry¹⁻⁴ for monitoring the evolution of temperature after impulsive photothermal heating of glycerol¹ and extract from that the frequency dependence of the heat capacity in a wide range of frequencies. We also present our latest results on the exploitation of the proportionality between the photoacoustic signal strength and the optical absorption at the generating location, in combination with multispectral photoacoustic imaging⁵, to obtain a 2D/3D image of the temperature distribution in a region of interest.

Acknowledgements

The authors are grateful to KU Leuven Research Council for financial support (C14/16/063 OPTIPROBE). L.M. acknowledges the support from the China scholarship Council (CSC) for his scholarship (Grant No. 201503170257).

References

1. L. W. Liu, K. Zhong, L. Meng, D. Van Hemelrijck, L. Wang, and C. Glorieux, *Journal of Applied Physics* 119 (22), 224902 (2016) doi: 10.1063/1.4953591
2. L. W. Liu, K. Zhong, T. Munro, S. Alvarado, R. Cote, S. Creten, E. Fron, H. Ban, M. Van der Auweraer, N. B. Roozen, O. Matsuda, and C. Glorieux, *Journal of Applied Physics* 118 (18), 184906 (2015) doi: 10.1063/1.4935277
3. T. Munro, L. W. Liu, H. Ban, and C. Glorieux, *International Journal of Heat and Mass Transfer* 112, 1090-1097 (2017) doi: 10.1016/j.ijheatmasstransfer.2017.05.046
4. T. Munro, L. W. Liu, C. Glorieux, and H. Ban, *Journal of Applied Physics* 119 (21), 214903 (2016) doi: 10.1063/1.4953223
5. L. Meng, O. Deschaume, L. Larbanoix, E. Fron, C. Bartic, S. Laurent, M. Van der Auweraer, and C. Glorieux, *Photoacoustics* 13, 33-45 (2019) doi: 10.1016/j.pacs.2018.11.004

KEYNOTE

Moving photoacoustic sources, photoacoustic effect in a stratified atmosphere, and sensitive temperature determination

Wenyu Bai ^{*}, Gerald Diebold

Department of Chemistry, Brown University, Providence, RI 02906, USA

wenyubai@gmail.com

The versatility of controlling optical radiation offers a broad platform for exciting sound waves with widely differing characteristics through the photoacoustic effect. The moving photoacoustic source represents a typical example of taking advantage of the controllability of the laser beam. In particular, it has been shown that a Gaussian source moving at sound speed in a one-dimensional geometry will give rise to a plane wave whose amplitude increases with time without bound in the linear acoustic regime [1]. The first part of the talk will be focused on the properties of photoacoustic waves from moving sources in one, two, and three dimensions [2]. A frequency-domain technique based on the moving optical grating for trace gas detection will be introduced as well [3].

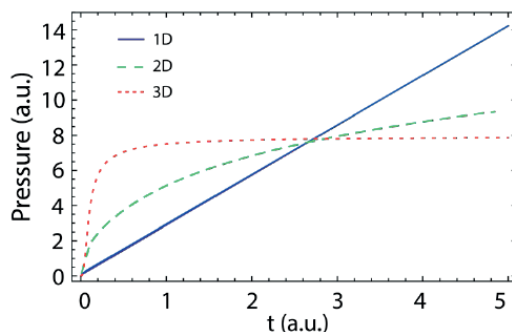


Fig. 1. Evolution of the maximum pressure with time when the source moves at the sound speed in different geometries. Due to geometric divergence, the pressure grows more slowly as the dimensionality increases and is eventually bounded in the three-dimensional case. This figure is adapted from Ref. 2 where the exact formula and parameters can be found.

Apart from laboratory applications, moving optical sources can also be found in natural events on the planetary scale such as the rotation of the earth terminator and the supersonic motion of moon shadow during the solar eclipse. Inspired by this connection, the second part of the talk will transit to the photoacoustic effect in a stratified atmosphere where the gravitational force will come into play and complicate the generation and propagation of the pressure waves. A generalized photoacoustic wave equation along with its associated Green's function will be introduced [4]. Properties of pressure waves generated from several typical optical excitation schemes will be covered as well.

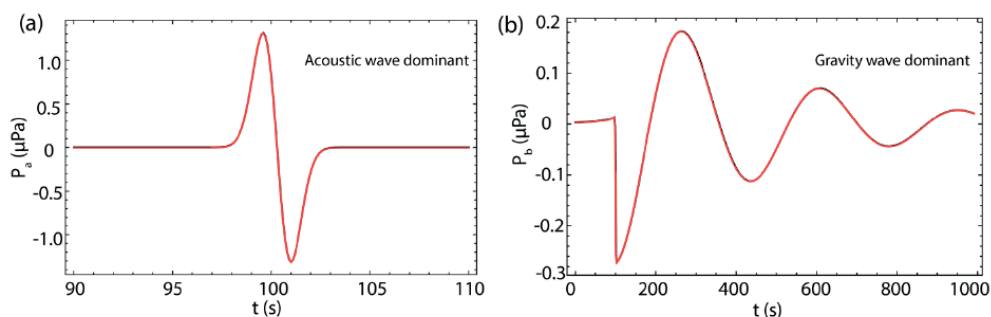


Fig. 2. Pressure waveforms resulting from a pulsed point source in the earth atmosphere. Apart from the bipolar acoustic waves as shown in (a), a low-frequency gravity wave as a result of the balance between the gravity force and the buoyant force is also found (b). This figure is adapted from Ref. 4 where the exact formula and parameters can be found.

At last, a differential pyrometer capable of detecting temperature variations on the microkelvin scale will be introduced. Infrared pyrometry refers to a noninvasive method of using infrared emission from an object to determine its temperature. However, the sensitivity of commercial infrared pyrometers is merely on the order of subkelvin scale which hinders their use in determining small temperature variations. In the last part of the talk, a sensitive differential pyrometer will be introduced which makes use of a resonant mirror and a liquid nitrogen cooled HgCdTe detector for radiation modulation and detection. Its capability of detecting microkelvin-scale temperature changes holds promise in monitoring the dynamics of chemical or biological systems.

Session D2: Thermometry / Scattering

References

- 1 V.E. Gusev, A.A. Karabutov, Laser Optoacoustics. (American Institute of Physics, New York, 1993). See section 1.3 for discussion on moving sources in the linear acoustic regime.
2. W. Bai, G.J. Diebold, Journal of Applied Physics 125 (6), 060902 (2019)
3. L. Xiong*, W. Bai*, F. Chen, X. Zhao, F. Yu, G.J. Diebold, Proceedings of the National Academy of Sciences of the United States of America 114 (28), 7246 (2017)
4. W. Bai, G.J. Diebold, Physical Review E 98 (3), 032125 (2018) doi:10.1103/PhysRevE.98.032125

Fluorescence based thermometry for photothermal signal detection

Pengfei Zhang*, Liwang Liu, Lei Meng, Christ Glorieux

*Laboratory for Soft Matter and Biophysics, Department of Physics and Astronomy,
KU Leuven, Celestijnenlaan 200D, Heverlee B-3001, Belgium*

christ.glorieux@kuleuven.be

Fluorescent probes, being molecular in size, allow temperature measurement to be performed locally and accurately with minimum interference with the medium being characterized. They provide a non-contact, all-optical, and emissivity independent approach for designing optical detection systems whereby changes in fluorescent intensity, spectral position, polarization, lifetime, and bandwidth of fluorescence can provide a local measurement of temperature [1]. Among these, intensity-based methods tend to be the most cost-effective approach to implement as it requires relatively simple instrumentation and data analysis. However, due to the effect of electrical, mechanical, and optical instabilities of the measurement arrangement, the accuracy of the intensity-based methods is hampered. In order to solve this problem, ratiometric fluorescence thermometry, which is based on the fluorescence intensity ratio at four selected emission bands, is proposed.

In this work, a ratiometric fluorescence thermometry approach is presented. The fluorescence intensity at different emission bands was recorded at temperatures ranging from 200K to 290 K with a step of 0.1 K. A neural network (NN) [2] was trained to extract the temperature from the spectrally resolved fluorescence data. The approach was implemented for monitoring the photothermally induced dynamic temperature evolution in Rhodamine B dyed glycerol, with the goal to extract information on the frequency dependence of the heat capacity.

References

1. D. Jaque, F. Vetrone, Luminescence nanothermometry. *Nanoscale*, 4 (15), 4301 (2012) DOI: 10.1039/c2nr30764b
2. V. M. Krasnopolsky, H. Schiller, *Neural Netw*, 16 (3), 321 (2003) DOI: 10.1016/S0893-6080(03)00027-3

Material characterization and detection of nanostructures through opaque layers by laser induced ultrasound

Hao Zhang ^{(1,3)*}, Alessandro Antoncetti ^(1,3), Stephen Edward ^(1,2), Paul Planken ^(1,2), Stefan Witte ^(1,3)

1. Advanced Research Center for Nanolithography, Science Park 110, 1098 XG Amsterdam, the Netherlands

2. Universiteit van Amsterdam, Science Park 904, 1098 XH Amsterdam, the Netherlands

3. Vrije Universiteit, De Boelelaan 1105, 1081 HV, Amsterdam, the Netherlands

*h.zhang@arcnl.nl

Ultrafast laser pulses incident on metals can lead to the generation of coherent phonon wave packets with frequencies in the gigahertz to terahertz range [1,2]. Material characterization using such ultrafast laser-induced ultrasound pulses provides access to a frequency range that is inaccessible by any other means. Our objective is to study the optical and acoustic properties of materials by generating and detecting ultrasound waves with ultrafast laser pulses. To generate high frequency acoustic waves in a way that also optimizes their detection, we use a pair of crossed 40 fs femtosecond pump pulses at 400 nm wavelength to project interference fringes on the surface of thin metal films. Because ultrasound is only generated in the interference maxima, this approach produces a spatially periodic array of acoustic pulses. The acoustic pulses propagate through the film and are reflected at the back surface. A delayed probe pulse (30 fs, 800 nm) then detects the returning acoustic echo by detecting a change in the optical response that occurs every time an acoustic echo returns to the surface. Because a periodic array of ultrasound waves was produced, we can detect the first order diffraction of the probe beam by this ‘acoustic grating’. By performing these measurements in thin free-standing metal membranes, the influence of substrate interfaces is eliminated, and acoustic attenuation is only caused by propagation in the metal, providing clean measurements of the metal parameters without external factors.

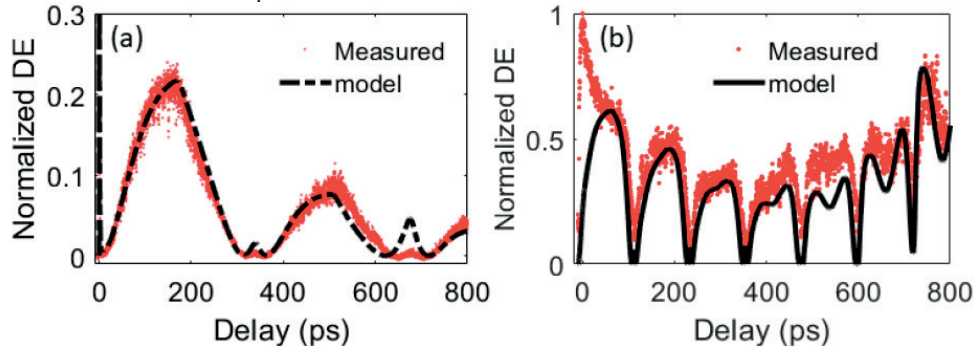


Fig. 1. Diffraction efficiency measurement (dots) on (a) a 500 nm Au free-standing membrane and (b) 400 nm Al free-standing membrane as a function of pump-probe delay. The solid lines are model calculations. Note that the model calculations shown here are not least-squares fits. The best-fit results that include multiple physical effects will be presented.

In parallel, we developed an advanced numerical model that captures the generation, propagation and detection of these acoustic waves. Evaluation of this model is sufficiently fast and accurate to perform least squares fitting of the experimental data, which enables quantitative extraction of multiple electronic and acoustic properties of thin metal films in this hitherto nearly inaccessible frequency range.

Figure 1 shows measured data on a 500 nm thick Au free-standing membrane and on a 400 nm Al free-standing membrane, along with model calculations. We find that we can accurately extract electron-phonon coupling, longitudinal speed of sound, acoustic attenuation and dispersion, as well as thermo-optic coefficients of the investigated materials by a least-squares fit of the model to the measured data. Note that the model calculations shown here are not least-squares fits. The best-fit results that include multiple physical effects will be presented.

We will present our methods and latest results on different materials, as well as our progress towards the detection of buried nanostructures through optically opaque layers.

References

1. C. Thomen, H. T. Grahn, H. J. Maris, and J. Tauc, Phys. Rev. B. 34 (6), 4129 (1986) doi: 10.1103/PhysRevB.34.4129
2. Osamu Matsuda, Maria Cristina Larciprete, Roberto Li Voti, and Oliver B. Wright, Ultrasonics. 56, 3-20 (2015). doi: 10.1016/j.ultras.2014.06.005

Detection of gratings underneath optically opaque layers using photoacoustics

Stephen EDWARD*, Hao ZHANG, Vanessa VERRINA, Alessandro ANTONCECCHI, Stefan WITTE, Paul PLANKEN

Advanced Research Center for Nanolithography (ARCNL), Science Park 106, 1098XG Amsterdam, Netherlands

*sedward@arcnl.nl

In semiconductor device manufacturing, it is often necessary to optically detect the presence of micro/nano structures buried underneath many dielectric and metallic layers. An example of a buried structure is a so-called alignment grating, which is a grating etched in Si. When light is diffracted off such a grating, a small change in position of the wafer changes the phase difference between the -1st and +1st order diffracted light beams, which can be used to determine the position of the wafer with great accuracy. However, when optically opaque dielectric and metallic layers are deposited on top of these gratings, it becomes very difficult to detect them. Here we demonstrate that we can detect the presence of grating buried under optically opaque metal and dielectric layer using photoacoustics in a fs-pump-probe scheme.

Detection of Au grating underneath 500 nm Au

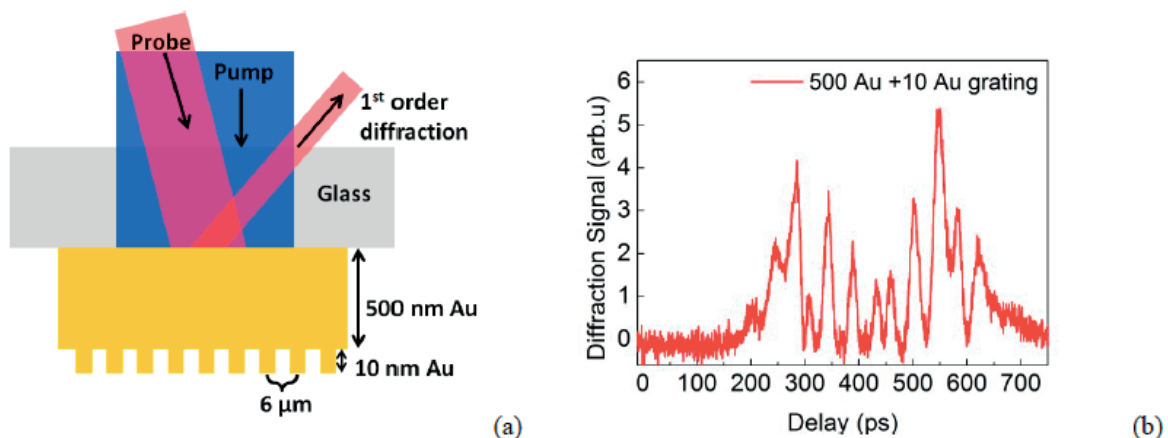


Fig.1 (a). Schematic of a buried 10 nm amplitude Au grating on 500 nm of Au on glass. Pump and probe pulses illuminate the sample from the glass side. (b) The experimentally measured diffracted probe signal plotted as a function of pump-probe delay.

We fabricated Au gratings on top of flat layers of Au on a glass substrate and performed pump-probe experiments from the substrate side. Hence, both the 400 nm pump pulse and the 800 nm probe pulse see a nominally flat surface and the grating is effectively optically hidden (Fig. 1(a)). The femtosecond pump pulse generates an acoustic wave in the metal layer that propagates through the metal and reflects off the buried grating. The acoustic wavefront returning to the Au-glass interface now has a shape resembling that of the buried grating. This gives rise to a ‘grating-like’ strain wave at the Au-glass interface. A delayed probe pulse diffracts off this grating and the diffracted signal is plotted as a function of time delay between the pump and the probe pulse. Fig. 1(b) shows the time-dependent diffracted probe signal for a 10 nm Au gratings buried underneath 500 nm Au. The time-dependent diffraction signal we observe in our measurements is proof that we detect the presence of the “buried” grating by measuring optical diffraction off an acoustic copy of the grating near the glass/metal interface. The 400 nm pump pulse which has a penetration depth of 15 nm in Au, excites the top layer of Au at the Au-glass interface. Due to the low electron-phonon coupling strength of Au, the hot electrons diffuse deep into the thick Au layer and heat up the region much larger than the optical penetration depth, up to 250 nm. The rapid heating of the lattice leads to a rapid expansion of the lattice which launches a longitudinal acoustic wave packet with an expected spatial extent corresponding to this electron energy diffusion depth. The slow, early, rise of the diffraction signal versus time is due to the arrival of part of the acoustic wave that has been generated deep inside the gold layer and thus is the earliest to reflect off the buried grating and to arrive at the glass/Au interface. The signal slowly increases for time delays up to 300 ps when the acoustic wave generated at the Au-glass interface returns to the Au-glass interface after reflecting off the buried grating. A part of the acoustic wave that reflected off the buried grating also enters the glass substrate after one round trip. The grating-shaped acoustic wave modifies the optical constants in glass due to the photoelastic effect (Brillouin scattering). This signal coherently adds up to the diffraction signal we measure and explains the peaks in between the two major maxima. The complex time-dependent diffraction signal we observe is well reproduced by numerical simulations.

Session D3: ND&E III / Thermography III

Detection of grating underneath a complex sample

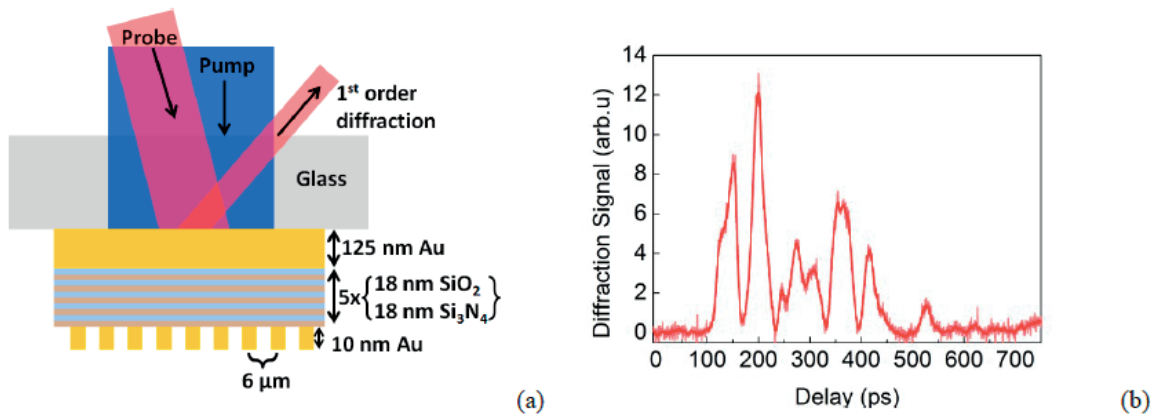


Fig.2 (a). Schematic of the experiment: The 400 nm pump and the 800 nm probe pulses illuminate a 125 nm flat Au layer with alternating layers of 18 nm silicon oxide and silicon nitride with a 10 nm gold grating on buried underneath. (b) The experimentally measured diffracted probe signal plotted as a function of pump-probe delay.

This technique also works for more complicated samples that are similar to those used in the semiconductor manufacturing industry. We fabricated a sample that partially mimics the materials/structure used in the fabrication of 3D NAND memory. The sample has alternating layers of silicon oxide and silicon nitride between the flat gold layer and the grating, as shown in Fig 2(a). In Fig 2 (b), we plot the time-dependent diffracted probe signal from the grating buried underneath the metal and dielectric stack. We emphasize that the observation of diffraction in itself implies an acoustic grating at the Au-glass interface, caused by the buried grating. We will present results obtained on more complicated samples consisting of 20 layers, as well as the dependence of the electron-phonon coupling strength of the flat metal layer on the time-dependent diffraction signal.

Pulsed thermography on semitransparent materials — what has to be considered?

Raphael BERNEGGER*, Simon J. ALTENBURG, Christiane MAIERHOFER

Bundesanstalt für Materialforschung und -prüfung (BAM), 12200 Berlin, Germany

raphael.bernegger@bam.de

Pulsed thermography is a well-known non-destructive testing technique and has proven to be a valuable tool for examination of material defects, to determine thermal material parameters, and the thickness of test specimens through calibration or mathematical models [1-4]. However, the application to semitransparent materials is quite new and demanding, especially for semitransparent materials like epoxy, polyamide 12, or glass fiber reinforced polymers with epoxy or polyamide matrix.

In order to describe the temporal temperature evolution in such materials, which are recorded with an infrared camera during pulse thermography experiments, much more influences have to be considered, compared to opaque materials:

- The wavelength of the excitation source and the spectral range of the infrared camera
- The angles between the specimen, the excitation source and the infrared camera
- The area behind the specimen
- The roughness of the material surface
- The scattering mechanism within the material

Here, we will consider all these influences and describe how they can be treated mathematically in analytical (based on [5, 6]) or numerical models (using COMSOL Multiphysics software). These models describe the temperature development during the pulse thermography experiment in reflection and transmission configuration. By fitting the results of the mathematical models to experimental data it is possible to determine the thickness or the optical and thermal properties of the specimen.

As an example for different roughness of the material surface, Figure 1 shows the experimentally obtained temperature differences of the surface of an uncoated pure epoxy specimen in reflection configuration of a pulse thermography experiment. One part of the front surface is roughened through 320-grit sandpaper (dots) and the other part is untreated (crosses). The sample was heated for 0.47 s with a widened laser beam with a wavelength of 840 nm and an energy density of 19.7 kW/m². The temperature was recorded with an infrared camera being sensitive from 3 μm to 5 μm.

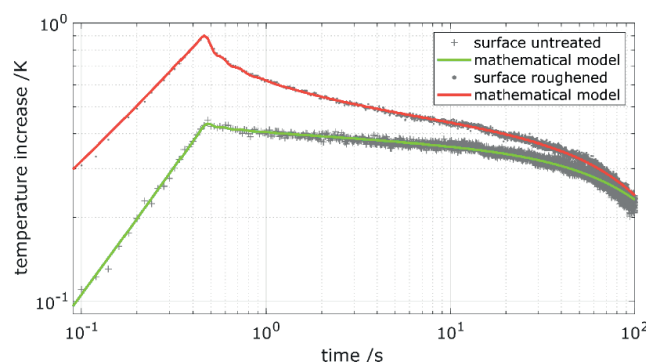


Figure 1: Results of laser pulsed thermography experiments performed in reflection configuration for a pure epoxy test specimen of 4 mm thickness. The experimentally obtained temperature difference by an infrared camera (grey dots and crosses) as well as the results of a fit using the proposed mathematical model (solid lines) are shown.

Taking into account the roughness of the material through surface absorption, the temperature development for both parts of the sample can be determined with a mathematical model (solid line) with the same set of parameters, only the front surface absorption and the front surface reflectivity changed due to the surface roughness.

References

1. C. Maierhofer, M. Röllig, M. Gower, M. Lodeiro, G. Baker, C. Monte, A. Adibekyan, B. Gutschwager, L. Knazowicka, A. Blahut, *Int. J. Thermophys* 39 (5), 61 (2018) doi:10.1007/s10765-018-2378-z
2. S. Agustín, M. Arantza, A. Estibaliz, P. Christophe, N. Frédéric, B. Jean-Christophe, *Measurement Science and Technology* 25 (3), 035604 (2014) doi:10.1088/0957-0233/25/3/035604
3. S.J. Altenburg, H. Weber, R. Krankenhagen, *QIRT* 0 (0,0), 1 (2017) doi:10.1080/17686733.2017.1331655
4. R. Bernegger, S.J. Altenburg, M. Röllig, C. Maierhofer, *Int. J. Thermophys* 39 (3), 39 (2018) doi:10.1007/s10765-018-2362-7
5. D. Maillat, S. André, J.-C. Batsale, A. Degiovanni, C. Moyne, *Thermal quadrupoles*. (2000),
6. A. Salazar, R. Fuente, A. Mendioroz, E. Apiñaniz, R. Celorrio, *Int. J. Thermophys* 33 (10), 1887 (2012) doi:10.1007/s10765-012-1251-8

Evaluation of defect depth in CFRP by long pulse thermography

Zijun Wang ^{(1)*}, Litao Wan ⁽¹⁾, Junzhen Zhu ⁽²⁾, Francesco Ciampa ^{(3)*}

1. School of Aeronautics and Astronautics, University of Electronic Science and Technology of China, Chengdu 611731, China.

2. School of Engineering, Newcastle University, Newcastle upon Tyne NE1 7UR, UK.

3. Centre for Engineering Materials, Department of Mechanical Engineering Sciences, University of Surrey, Guildford GU2 7XH, UK.

wangzijun@uestc.edu.cn; f.ciampa@surrey.ac.uk

Long pulse thermography (LPT) is an emerging non-destructive techniques that has been used for damage assessment in both metallic and composite components. This paper provides two analytical model for defect depth quantification in carbon fibre reinforced plastic specimen (CFRP) specimen by long pulse thermography. The methods are focused on the depth determine of flat-bottomed hole defects. The peak temperature-contrast method and peak temperature-contrast slope method are chosen for processing the thermal images data. The theoretical analysis and the experimental results reveal that the peak temperature-contrast time depends on the depth and the diameter, whilst the contrast time slope is proportional to the square of the defect depth but does not depend on the defect diameter.

1. Introduction

Long pulse thermography (LPT), which contained the simplest means of applying a thermal stimulation to a surface to a high intensity heat source for a few seconds, can be effective for some favourable applications. In long pulse thermography, the infrared camera recorded the thermal images during the test sample cools down, after the samples is heated for a selected period of time. The technical advantages of long pulse were that it produced higher heating energy easily than pulsed thermography which depended on high heating impulse to provide high energy.

2.Theoretical Analysis of LPT method

2.1 Peak temperature-contrast method

The LPT thermal contrast of a plate at the defect surface, $T_c(t)$, can be represented by the integration of the impulse response function [5]:

$$T_c(t) = \int_{\tau=0}^{t_p} \frac{2q}{\sqrt{\pi\rho ck(t+\tau)}} \left[\sum_{n=1}^{\infty} e^{-\frac{(nd)^2}{\alpha(t+\tau)}} - \sum_{n=1}^{\infty} e^{-\frac{(nL)^2}{\alpha(t+\tau)}} \right] \cdot \left(1 - e^{-\frac{(D/2)^2}{4\alpha(t+\tau)}} \right) d\tau$$

where, q is the heat power density created by the absorption of optical energy from lamps applied for a duration of t_p . D and d is defect's diameter and depth, respectively. L is the specified thickness of the plate.

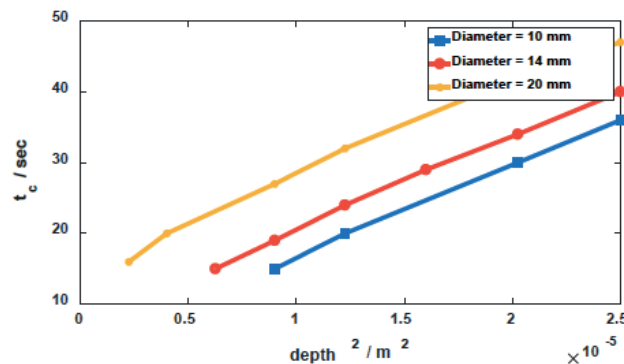


Fig. 1. contrast time t_c as a function of the square of depth by analytical data (equation model). The parameter t_c was influenced by defect diameter.

Long pulse thermography has one more parameter compared with pulse thermography, which is heating time t_p . In order to consider the relationship of t_p parameter with peak contrast time t_c , the same defect depth (3.5 mm) and diameter (14 mm) were chosen with different heating time. Figure 2 showed the temperature contrast as a function of recording time with different heating time. The peak contrast time was almost a constant. For the following analysis, the heating time was set to 2 sec.

2.2 Peak temperature-contrast slope method

The slope or first derivative of the temperature contrast has been examined for the prediction of the depth. The dimensionless temperature-contrast slope can be expressed as

$$\frac{dT_c(t)}{dt} = \int_{\tau=0}^{t_p} \frac{d}{dt} \left(\frac{2q}{\sqrt{\pi\rho ck(t+\tau)}} \left[\sum_{n=1}^{\infty} e^{-\frac{(nd)^2}{\alpha(t+\tau)}} - \sum_{n=1}^{\infty} e^{-\frac{(nL)^2}{\alpha(t+\tau)}} \right] \cdot \left(1 - e^{-\frac{(D/2)^2}{4\alpha(t+\tau)}} \right) \right) d\tau$$

It was found that the slope reaches a maximum at an early time instant. The value of t_s was approximately proportional to the square of the defect depth (d^2), and the proportionality coefficient did not depend on the defect size.

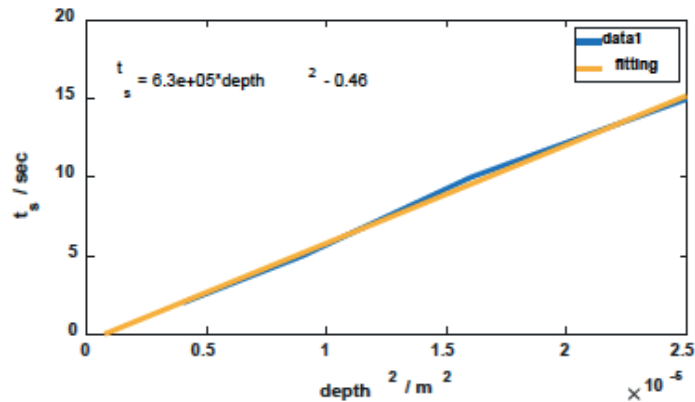


Fig.2. contrast time slope t_s as a function of the square of depth by analytical data (equation model) (for defect depth 5 mm to 20 mm)

KEYNOTE

Unexpected mismatch between amplitude and phase in lock-in thermography on moving samples

Agustín SALAZAR*, Laura ZAMANILLO, Mateu COLOM, Arantza MENDIOROZ

Departamento de Física Aplicada I, Escuela de Ingeniería de Bilbao, Universidad del País Vasco UPV/EHU, Plaza Ingeniero Torres Quevedo 1, 48013 Bilbao, Spain

agustin.salazar@ehu.es

In this work, we address the challenge of measuring the thermal diffusivity of moving samples. In particular, we focus on samples moving at constant velocity since it is the case of in-line production or in-line inspection in factories, where heterogeneities, i.e. local changes in the properties, must be detected in real time, without stopping the production chain. The method we propose is based on illuminating the moving sample with a modulated laser spot, which remains at rest, and recording the surface temperature with an IR video camera. First, we have obtained an analytical expression for the surface temperature, which predicts that while the isotherms of the amplitude of the temperature are elongated due to the sample movement, the isophases remain concentric circumferences. Figure 1 shows the experimental amplitude and phase thermograms obtained on an AISI-304 stainless steel sample that is moving along the horizontal direction at $v = 10$ mm/s. The surface is heated by a focused laser spot, which remains at rest, and is modulated at $f = 1$ Hz. This result confirms the surprising decoupling between the amplitude and phase of the surface temperature in moving samples.

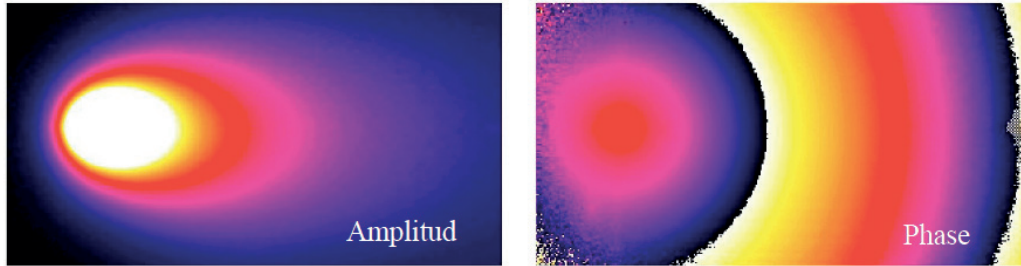


Fig. 1. Experimental amplitude and phase thermograms for an AISI-304 sample moving to the right at $v = 10$ mm/s and heated by a laser beam modulated at $f = 1$ Hz.

Regarding the amplitude and phase profiles along the transverse direction with respect to the sample movement, it is shown that they behave linearly as a function to the distance to the laser spot. The slopes (m) verify

$$m_{\text{Ln}(|r|_y)} \times m_{\text{phase}} = \frac{\pi f}{D}, \quad (1)$$

which allows measuring the thermal diffusivity of the sample D in the direction perpendicular to the motion.

Moreover, the amplitude and phase profiles along the direction of the sample movement also behave linearly as a function to the distance to the laser spot. In this case, the phase slope satisfies

$$m_{\text{phase}} = \sqrt{\frac{\pi f}{D}} \sqrt{\frac{e^{-b \left[\text{Log} \left(\frac{v^2}{Df} \right) - c \right]}}{1 + e^{-b \left[\text{Log} \left(\frac{v^2}{Df} \right) - c \right]}}}, \quad (2)$$

where $b = 2.72$ and $c = 1.273$. From this expression, the thermal diffusivity of the sample in the direction of motion can be obtained. Figure 2a shows the experimental amplitude and phase profiles of the surface temperature along the transverse direction with respect to the sample movement for the AISI-304 sample with $f = 1$ Hz and $v = 5$ mm/s. As predicted by the model, both amplitude and phase behave linearly but the slope of the phase is lower than the slope of the amplitude. By using Eq. (1), the thermal diffusivity is obtained: $D = 3.6$ mm²/s, which agrees with tabulated data.

In Fig. 5b we show the phase profile along the direction of the sample movement for the same values of frequency and velocity. As can be observed, the profile is a straight line from whose slope the thermal diffusivity is obtained using Eq. (2): $D = 3.5$ mm²/s, which is consistent with the value obtained from the transverse profiles and in agreement with the literature data.

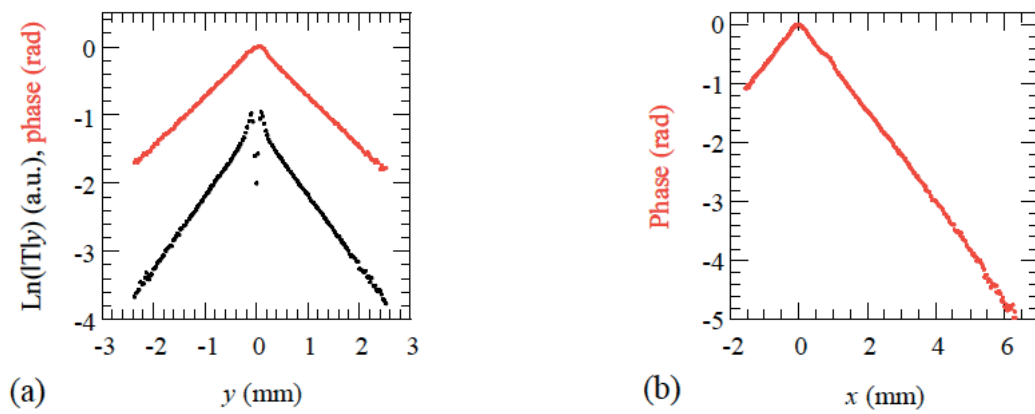


Fig. 2. (a) Experimental amplitude and phase profiles along the transverse direction and (b) longitudinal phase profiles for AISI-304 at $f = 1$ Hz and $v = 5$ mm/s.

Acknowledgements

This work has been supported by Ministerio de Economía y Competitividad (DPI2016-77719-R, AEI/FEDER, UE), by Gobierno Vasco (PIBA2018/15) and by Universidad del País Vasco UPV/EHU (GIU16/33). M. Colom acknowledges UPV/EHU for Research Grant PIFG18-18.

KEYNOTE

Thermographic Super Resolution Imaging Using Structured 1D Laser Illumination

Samim AHMADI ^{(1)*}, Mathias ZIEGLER ⁽¹⁾, Erik THIEL ⁽¹⁾, Philipp HIRSCH ⁽¹⁾, Christina KARAGIANNI ⁽¹⁾, Peter BURGHOLZER ⁽²⁾, Günther MAYR ⁽³⁾, Peter JUNG ⁽⁴⁾, Giuseppe CAIRE ⁽⁴⁾

1. Bundesanstalt für Materialforschung und -prüfung (BAM), 12200 Berlin, Germany

2. RECENDT, Research Center for Non-Destructive Testing, Linz, Austria

3. Josef Ressel Center for Thermal NDE of Composites, University of Applied Sciences Upper Austria, Wels, Austria

4. Technical University of Berlin, Department of Telecommunication System, Berlin, Germany

samim.ahmadi@bam.de

Thermographic nondestructive evaluation (NDE) is based on the interaction of thermal waves with inhomogeneities. These inhomogeneities are related to sample geometry or material composition. Although thermography is suitable for a wide range of inhomogeneities and materials, the fundamental limitation is the diffusive nature of thermal waves and the need to measure their effect radiometrically at the sample surface only. The propagation of the thermal waves from the heat source to the inhomogeneity and to the detection surface results in a degradation in the spatial resolution of the technique. A new concerted ansatz based on a spatially structured heating and a joint sparsity of the signal ensemble allows an improved reconstruction of inhomogeneities [1, 2]. As a first step to establish an improved thermographic NDE method, an experimental setup was built based on structured 1D illumination using a flash lamp behind a mechanical aperture [1]. As a follow-up to this approach, we now use direct structured illumination using a 1D laser array [3, 4]. The individual emitter cells are driven by a pseudo-random binary pattern and are additionally shifted by fractions of the cell period. The repeated measurement of these different configurations enables to illuminate each spot of the sample surface in lateral direction. This allows for a reconstruction that makes use of joint sparsity. The measurement procedure is illustrated in Fig. 1.

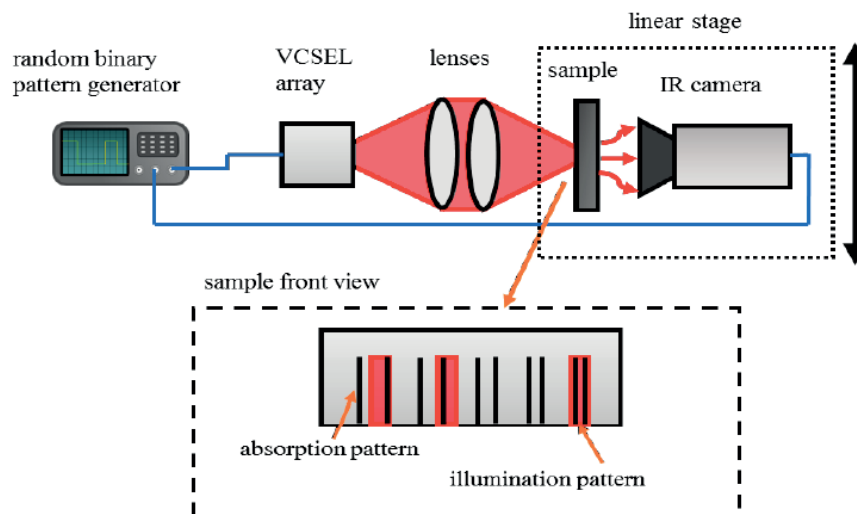


Fig. 1: Experimental setup for generating thermographic data that is suitable for super resolution image reconstruction in transmission configuration. The binary pattern generator controls the VCSEL array cells randomly so that blind structured laser illumination is realized. Using a linear stage enables to shine on different spots on the sample surface. The sample is a 3 mm thick blackened steel sheet where aluminum foil is glued on the sample front surface. The sample front view shows an example of an illumination pattern since the VCSEL array has 12 laser lines (cells) that are controlled randomly. In this case 3 of the 12 VCSEL array cells are turned on (illumination pattern). An absorption pattern was applied to the sample surface by cutting slits into the aluminum foil. This leads to increased heating in the slit region. The absorption pattern contains 5 slit pairs with varying distances (3.0, 2.0, 1.3, 0.9, 0.6 mm). The goal is to resolve even the slit pair with the smallest distance using the IR camera in transmission configuration. For this reason multiple measurements at different positions are done.

The measured data set is processed using super resolution image reconstruction algorithms such as the iterative joint sparsity (IJOSP) algorithm. Using this reconstruction technique and 150 different illumination patterns results in a spatial resolution enhancement of approximately a factor of four compared to the resolution of 5.9 mm for homogeneously illuminated thermographic reconstruction [5]. The reconstruction result is shown in Fig. 2.

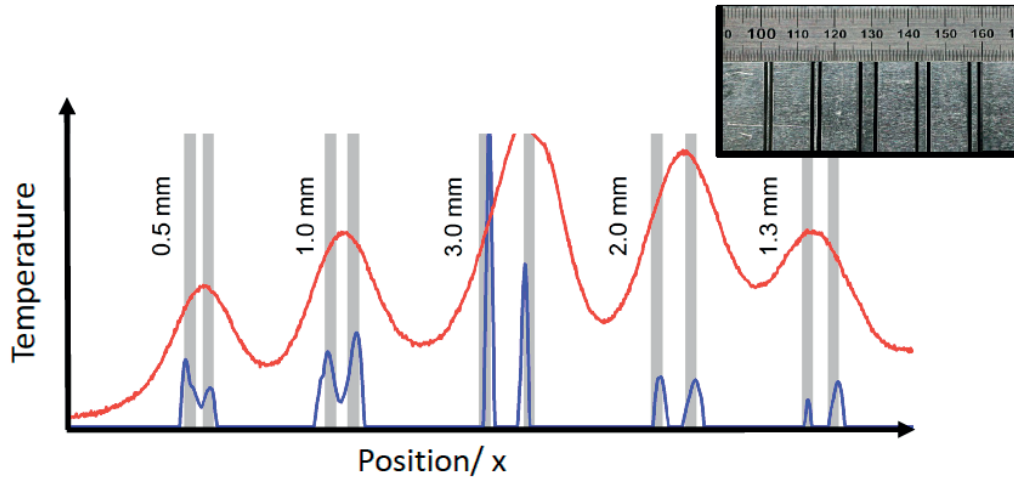


Fig. 2: Reconstruction results after applying super resolution reconstruction algorithm IJOSP (blue curve) vs mean over pixels in height and all measurements of thermographic raw data (red curve)

Further, new data processing techniques have been studied before applying the IJOSP algorithm that are more performant or less prone to errors regarding image reconstruction. The choice of regularization parameters in data processing as well as experimental parameters such as the illumination pattern as a variable heat flux density (i.e., the Neumann boundary condition for convolution with the constant Green's function) have a big influence on the reconstruction goodness. With analytical-numerical modelling and numerical FEM simulations, we studied the influence of the experimental parameters on the result of the non-linear IJOSP reconstruction. This has also been investigated experimentally e.g. using different laser line widths or more measurements per position. These studies are used to derive optimal conditions for a certain measurement image reconstruction technique.

References

1. P. Burgholzer, T. Berer, J. Gruber and G. Mayr, *Applied Physics Letters*, 111 (3), 031908 (2017)
2. T. W. Murray, M. Haltmeier, T. Berer, E. Leiss-Holzinger and P. Burgholzer, *Optica*, 4 (1), 17-22 (2017)
3. E. Thiel, M. Ziegler and T. Studemund, *Int J Thermophys*, 40 (2), 13-17 (2018)
4. M. Ziegler, E. Thiel and T. Studemund, *Materials Testing*, 60 (7-8), 749-757 (2018)
5. P. Burgholzer, T. Berer, J. Gruber, M. Ziegler, E. Thiel, S. Ahmadi, G. Mayr, G. Hendorfer, *QIRT Journal*, submitted (2019)

Massive parallel real-time data acquisition

Vassili IVANOV, Hans Peter BRECHT, Sergey ERMILOV

PhotoSound Technologies, Inc., 9511 Town Park Dr., Houston, Texas 77036, USA

Email: vi@pst-inc.com

PhotoSound specializes in the development of electronics solutions for massive parallel data acquisition for application in the field of photoacoustics (PA), X-ray acoustics (XA), and other multi-channel sensor monitoring. Current PhotoSound solutions are based on data acquisition (DAQ) systems with USB3 interface, which limits sustained data rate to about 3 Gbps or 380 MBps per board.

PhotoSound's data acquisition solutions are typically limited by PC interface data bandwidth (BW) and internal memory to triggered data acquisition with low duty cycle, low number of data points per trigger, and nearly periodic trigger. The duty cycle is a fraction of time DAQ is saving data. The number of data points per trigger is limited by the internal fast memory of DAQ capable to buffer all incoming data at peak data rate.

PhotoSound's ADC256, released in 2018, is a 256-channel 12-bit ADC with a sampling rate up to 40 MHz. The peak data rate of this DAQ is 123 Gbps. The maximal number of data points per trigger in all channels of ADC256 is 4096 points, which require storage of 12.6 Mb data per trigger in fast memory buffer. ADC256 can run over USB3 interface at ≥ 200 Hz frame rate or about 2% duty cycle. Reduction of the number of data points per trigger allows proportional increase of the trigger rate. For example, data acquisition of 2024 point per channels in all channels is possible at ≥ 400 Hz.

PhotoSound ADC32, released in 2019, is 32-channel ADC 12-bit 80 MHz and 14-bit 65 MHz sampling modes selectable on software level, which is twice faster data rate compared to ADC256. The peak data rate of this ADC is 30.7 Gbps. Taking into account USB3 data BW of 3Gbps the duty cycle can be close to 10%. Sustained trigger rate of ADC32 is limited by only data BW and the number of points per trigger. The maximal number of data points per trigger in all channels of this DAQ is not practically limited and can be as high as 100'000 or more, because ADC32 is equipped with 1 GB DDR memory buffer with data BW exceeding 30.7 Gbps. Until DDR memory buffer is full DAQ can collect the data up to 100% duty cycle, but the memory buffer will be full in about 0.3 second. The implementation cost of fast DDR memory is equal or higher to connection of matching ADC channels. Instead of DDR the same architecture might be equipped with extra 32 data acquisition channels up to 64-channels total. 64-channels of ADC32 would be equivalent to 128-channels of ADC256, which have twice slower data rate. ADC256 might be equipped with twice faster ADC chips (like ADC32 has), if the number of the channels is reduced from 256 to 128. Note, that increase of the data-rate or the number of channels require modification on hardware level.

PhotoSound ADC1, planned for 2020, is ADC with multiple programmable configurations with 1 or 2 or 4 channels. The programmable data acquisition modes are 1-channel 8-bit 1 GHz sampling or 12-bit 640 MHz, 2-channels 8-bit 500 MHz or 12-bit 320 MHz, 4-channels 8-bit 250 MHz or 12-bit 160 MHz or 14-bit 105 MHz. ADC1 will have up to 100% data acquisition duty cycle in all modes.

PhotoSound DAQ systems allows full parallel operation of multiple boards with synchronized ADC clocks and distributed trigger. With daisy chain architecture operation up to 4 ADC256 boards can operate fully in parallel with up to 1024 channels connected over USB3 ports to a single computer. The master board serves as a clock and trigger source for the slave board. Each board use its own USB3 interface, with combined data BW for 4 boards up to 12 Gbps or 1.5 GBps. On software level slave DAQs are visible as extra channels on the master board. More than 4 ADC256 boards can operate in parallel using simple clock and trigger hub serving as universal master board for all ADC256 boards. Different ADC256 boards might be connected to the same or different computers. Parallel operation of ADC32 using the same protocol is planned for the next hardware revision of ADC32.

PhotoSound DAQ systems have amplifiers integrated to ADC boards and optional preamplifiers optimized for PA and XA applications. ADC256 has an integrated amplifier with programmable gain up to 51 dB, and ADC32 has programmable gain up to 54 dB. The standard analog input for all ADCs is 50 Ohm, AC coupled. ADC1 will have analog configurations equivalent to digital storing oscilloscope with DC coupling, programmable gain, and DC offset.

The typical applications for PhotoSound DAQ systems are XA for systems with multiple ADC256 and PA. Other applications include PA microscopy, optical coherence tomography (OCT), and optical fiber sensor DAQ, and other general oscilloscope applications for ADC1.

References

1. Ivanov V, Brecht HP, Ermilov SA. Real-time photoacoustic data acquisition with a thousand parallel channels at hundreds frames per second. Proceedings SPIE. 2019; 10878:108784Z.
2. H.P. Brecht, V. Ivanov, D.S. Dumani, S.Y. Emelianov, M.A. Anastasio, S.A. Ermilov, "A 3D imaging system integrating photoacoustic and fluorescence orthogonal projections for anatomical, functional and molecular assessment of rodent models", Proceedings SPIE, Vol. 10494, 1049411 (2018)
3. Ermilov, S., Brecht, H. P., Ivanov, V., "Instrument for acquiring co-registered orthogonal fluorescence and photoacoustic volumetric projections of tissue and methods of its use", 2018-01-25, US20180020920A1, US patent application.

Real-time laser ultrasound tomography with toroidal sensor array

Anton BYCHKOV ⁽¹⁾, Varvara SIMONOVA ^{(2,3)*}, Vasily ZARUBIN ⁽¹⁾, Igor KUDINOV ⁽³⁾,
Elena CHEREPETSKEYA ⁽¹⁾, Alexander KARABUTOV ^(1,2,3)

1. NUST MISiS - The National University of Science and Technology MISiS, Moscow, Russia
2. ILIT RAS Branch of the FSRC «Crystallography and Photonics» RAS, Shatura, Moscow region, Russia
3. ILC MSU - International Laser Center, Lomonosov Moscow State University, Moscow, Russia

vas@optoacoustic.ru

The appearance of confocal PZT arrays and active development of computer equipment have significantly expanded the capabilities of photoacoustic (PA) and laser-ultrasound (LU) tomography of the internal structure of rocks and composite materials, as well as the tomography of biological and other heterogeneous media [1–2]. In most problems concerning biological object diagnostics and nondestructive testing, real-time 2D visualization of inhomogeneities is very important.

To form a sufficiently “thin” image plane, the array is focused in the direction perpendicular to it [3]. Focusing of the array in the image plane itself can increase the angular aperture and improve the spatial resolution [4] due to the decrease in the size of the sensitivity area. Confocal arrays are focused both in the image plane and perpendicular to it. Therefore, real-time 2D-systems equipped with such arrays are promising for studying the internal structure of a wide class of objects with high spatial resolution in a bounded spatial region: biological objects [2–5], filaments [6], etc.



Fig. 1. Real-time OA and LU 16-channel system setup (left) and 3D-model (right).

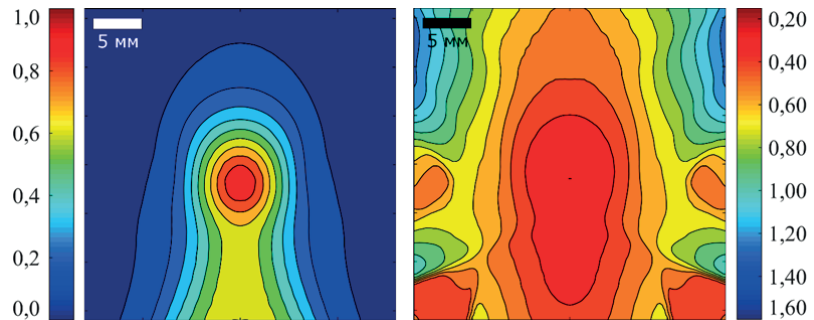


Fig. 2. Numerical sensitivity map for OA and LU toroidal 16-channel array with 0.2 mm resolution (left) and the map of transverse resolution of this array (right).

We discuss the combined LU and PA real-time imaging integrated into one system. Such combined transducer array will allow simultaneously receiving LU and PA images in real time with high spatial resolution. Advantages of the system (penetration depth through investigated object, optical contrast of the reconstructed image and high resolution of the images) are also discussed. 3D-model and prototype of focused transducer array with advantages described above is proposed.

We present typical numerical maps of sensitivity $I(x, z)$ (left) and transverse resolution $L(x, z)$ (right) for toroidal array and discuss experimental maps of the considerable prototype array. We compare and discuss the images from cylindrical and toroidal LU and PA arrays.

References

1. Y. Zhou, J. Yao, and L. V. Wang, *J. Biomed. Opt.* 21 (6), 061007 (2016).
2. T.D. Khokhlova, I.M. Pelivanov, A.A. Karabutov, *Acoust. Phys.* 55 (4–5), 674–684 (2009).
3. V. A. Simonova, I. M. Pelivanov, V. Ya. Panchenko, A. A. Karabutov, *Acoust. Phys.* 56 (5), 748–752 (2010).
4. I. M. Pelivanov, V. A. Simonova, T. D. Khokhlova, A. A. Karabutov, *Proc. SPIE* 7564, 756428 (2010).
5. A. S. Bychkov, E. B. Cherepetskaya, A. A. Karabutov, V. A. Makarov, *Laser Phys. Lett.* 13 (8), 085401 (2016).
6. A. S. Bychkov, E. B. Cherepetskaya, A. A. Karabutov, V. A. Makarov, *Acoust. Phys.* 64 (1), 77–82 (2016).

Characterization of piezoelectric cantilevers by optic techniques

A. Vargas-Vargas*, J. A. I. Díaz Góngora, A. Cifuentes

Centro de Investigación en Ciencia Aplicada y Tecnología Avanzada del Instituto Politécnico Nacional, Legaria 694. Colonia Irrigación, 11500 México D. F.

The growing number of remote electronic devices (such as wireless sensor networks) has resulted in the constant research and development of technologies in energy transformation and storage for the support of such devices, given that in many of the cases, due to the distance and accessibility to which they are subject, it is convenient the autonomy of these. Where the main challenges for the autonomy of these devices are: the development of sustainable energy sources, longer duration of load, smaller dimensions for equal or greater loads, friendly with the environment and low cost. There are certain types of sources that try to comply with these objects, the residual energy sources, which are the ones we will discuss in this work. The residual energy sources are the energy that certain processes, from nature and the hand of man, cannot be used entirely and are emitted to the environment in the form of heat, vibration, electromagnetic radiation, etc. This is achieved by using specific transducers for each of the energy sources, such as solar cells for the electromagnetic radiation sources, kinetic energy harvesters for the sources of vibration, etc.

The main objective of this work was to characterize devices that will be used as harvesters of residual energies (with commercial piezoelectric materials), more precisely, devices that take advantage of the kinetic energy coming from vibration. It was possible to characterize the resonance frequency, the oscillation modes, the oscillation amplitude, powers, voltages and output currents, which are essential parameters to be able to perform the appropriate synchronization to the frequencies required by the applications, since these devices reach Its maximum efficiency when the frequency of the application and the frequency of the system are equal or very close. In this way it was possible to approximate the power that the harvester will be able to deliver along different frequencies close to those of the possible applications.



References

- Erturk, A., & Inman, D. J. (2011). Piezoelectric energy harvesting. John Wiley & Sons.
- Priya, S., & Inman, D. J. (Eds.). (2009). Energy harvesting technologies (Vol. 21). New York: Springer.

Laser ultrasonic imaging of solids with complex surface geometry

Vasily Zarubin^{(1,2)*}, Anton Bychkov^(1,2), Alexander Karabutov^(1,2), Elena Cherepetskaya⁽²⁾

1. Lomonosov Moscow State University, Leninskie Gory, 1, 119234, Moscow, Russia

2. National University of Science and Technology MISiS, Leninskiy ave., 4, 119991, Moscow, Russia
zarubin.vasily@gmail.com

One of the most reliable ways of measuring the dimensions of solid parts is x-ray computed tomography. However, it requires the access to the inspected part from all sides and thus it is often inapplicable on the production line. Other methods include various types of profilometry, coordinate-measuring machines, which require access to the inspected side of part. Ultrasonic methods can have a higher speed of operation and allow inspecting of sample interior and both sample sides requiring the access from one side. However, in this case a transverse resolution is rather low. Nowadays several types of ultrasonic inspection systems are developed. They use phased arrays for control of planar samples [1] and flexible phased arrays for control of samples with smooth surface [2].

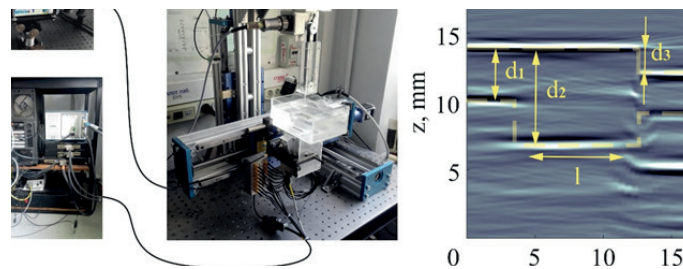


Fig. 1. A photo of the automatized 4-axis experimental setup, (b) a laser ultrasonic tomogram of PMMA cylinder with piecewise linear surface profile.

Materials and Methods

In this study we develop a real-time experimental system (Fig. 1, a) [3] and algorithm for 2D laser ultrasonic imaging of solid parts with complex surface geometry immersed in liquids [4]. The principle of the proposed technique is the following. The optoacoustic effect is used for excitation of wideband ultrasonic probe pulse with duration of ~ 100 ns. This pulse is focused by an acoustic lens on the inspected object. A wideband piezoelectric sensor array records acoustic waves reflected from object surface, internal cracks and other acoustic inhomogeneities. The recorded waveforms are processed to reconstruct a 2D cross-sectional image of a part of the object – a laser ultrasonic tomogram.

The proposed technique allows real-time inspecting of solid parts with high spatial resolution due to combined advantages of laser generation of ultrasound, array signal detection and tomographic image reconstruction. In this study, we assume that the 2D surface profile of the object can be represented as a piecewise linear curve which is relevant for a wide class of industrial tasks (e.g. composite pipes with varying diameter).

The algorithm is based on the heuristic ray-tracing technique and has four stages [4]: 1) reconstruction of a 2D laser ultrasonic tomogram using standard filtered back-projection algorithm for homogeneous media; 2) segmentation of the 2D surface profile of the object from the tomogram; 3) refraction-corrected re-reconstruction of the part of the tomogram corresponding to the interior of the object; 4) segmentation of solid part boundaries based on a provided virtual model of the part. The model is a set of equations that define the boundaries of the object.

The comparison of plexiglas and duralumin samples dimensions measured by laser ultrasonic imaging (Fig. 1, b) and by standard gauge shows good agreement within 0.1 mm. The algorithm can be efficiently implemented using parallel computing techniques on a single PC. Thus, the proposed technique allows verification of complex-shaped workpiece tolerance with high speed and sufficient resolution for a set of industrial tasks.

Acknowledgements

The work is supported by the Ministry of Science and Higher Education of the Russian Federation grant № K2-2019-004.

References

- Advances in Phased Array Ultrasonic Technology Applications. Olympus NDT, 2007.
- K. Nakahata, S. Tokumasu, A. Sakai, Y. Iwata, K. Ohira, Y. Ogura, NDT & E International 82 (2016), doi: 10.1016/j.ndteint.2016.04.002
- V. Zarubin, A. Bychkov, A. Karabutov, V. Simonova, E. Cherepetskaya, Applied Optics 57 (10), 2018, doi: 10.1364/AO.57.000C70.
- V. Zarubin, A. Bychkov, V. Simonova, V. Zhigarkov, A. Karabutov, E. Cherepetskaya, Applied Physics Letters 112 (21), 2018, doi: 10.1063/1.5030586.

KEYNOTE

Acoustic Image Reconstruction for Photothermal Measurements

Peter BURGHOLZER ^{(1)*}, Günther MAYR ⁽²⁾, Gregor THUMMERER ⁽²⁾, Holger PLASSER ⁽²⁾

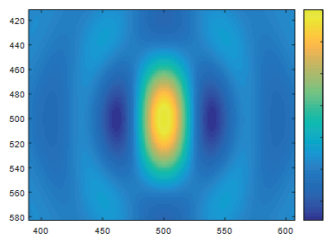
1. RECENDT - Research Centre for Nondestructive Testing, Linz, Austria

2. Josef Ressel Centre for Thermal NDE of Composites, University of Applied Sciences Upper Austria, Wels, Austria

peter.burgholzer@recendt.at

Thermographic imaging using an infrared camera for signal detection has a big advantage compared to ultrasonic imaging using acoustic transducers: it does not need any coupling media and parallel detection of many camera pixels is possible. The main disadvantage of pulsed thermography is the degrading spatial resolution with increasing depth. This is the reason why often only one-dimensional thermographic reconstruction is performed, which can be applied for layered structures, where the lateral extension is big compared to their depth. For other structures, using a one-dimensional reconstruction gives additional artifacts, as the heat propagates not only perpendicular to the surface but also in the lateral direction. Solving directly the inverse three-dimensional heat diffusion equation is rather ambitious, even for simple geometries of embedded structure, e.g. rectangular vertical cracks [1].

In this work, it is shown that image reconstruction methods from ultrasonic imaging can be employed for thermographic signals.



Before using these imaging methods, a virtual signal is calculated by applying a local transformation to the temperature evolution measured on a sample surface. The introduced transformation describes all the irreversibility of the heat diffusion process and can be used for every sample shape in two and three dimensions.

Figure 1. Thermographic point-spread function: Thermographic reconstruction of a point signal: the lateral resolution (vertical) is approximately twice the axial resolution (horizontal). The axial resolution for pulsed thermography is proportional to the depth of the point source divided by the natural logarithm of the signal-to-noise ratio.

In acoustical or optical imaging this blurring of structures is usually modeled by convolution with a point - spread - function. We can introduce such a point – spread – function for thermographic imaging (Fig. 1), which shows that the lateral resolution (vertical direction in Fig. 1) is approximately twice the axial resolution (horizontal direction in Fig. 1). The axial resolution for pulsed thermography is proportional to the depth of the point source divided by the natural logarithm of the signal-to-noise ratio [2]. The virtual temperature signal T_{virt} is calculated by applying a local transformation at the point r to the measured surface temperature data T . This transformation is a linear inverse problem and can be formulated as a Fredholm integral of the first kind

$$\int_{-\infty}^{\infty} K(t, t') T_{virt}(\mathbf{r}, t') dt' = T(\mathbf{r}, t), \quad (1)$$

where the right-hand side T and the kernel K are in principal known functions, while T_{virt} is the unknown solution. The aim is to find the virtual wave field T_{virt} from the measured temperature field T and the corresponding model K . The kernel K allows a transformation between the heat conduction equation and the wave equation

$$K(t, t') \equiv \frac{c}{\sqrt{\pi \alpha t}} \exp\left(-\frac{c^2 t'^2}{4 \alpha t}\right) \text{ for } t > 0, \quad (2)$$

where α is the thermal diffusivity and c the virtual speed of sound. It can be discretized to produce a matrix equation

$$\mathbf{T} = \mathbf{K} \mathbf{T}_{virt}, \quad (3)$$

where T and T_{virt} are the vectors of the measured temperature signal and the virtual wave signal. For regularization several different methods are used: the truncated singular value decomposition, and various iterative methods, using positivity and sparsity [3].

References

4. A. Mendioroz, R. Celorrio, A. Salazar, Rev. Sci. Instrum. 86, 064903 (2015).
5. P. Burgholzer, M. Thor, J. Gruber, G. Mayr, Journal of Applied Physics (2017) doi:10.1063/1.4978010
6. R.C. Aster, B. Borchers, C.H. Thurber, Parameter estimation and inverse problems (Elsevier, Amsterdam, Netherlands, 2019)

KEYNOTE

Solvable splines for direct and inverse modeling of media with graded properties

Jean-Claude KRAPEZ

ONERA, The French Aerospace Lab, 13661 Salon de Provence, France

krapez@onera.fr

Graded media, i.e. media with continuous variation in their properties, are ubiquitous. Examples can be found at different scales in nature (soils, wood, living tissues: e.g. skin, teeth, boundary layers in the atmosphere and the ocean) and in manmade materials (functionally graded materials -FGM- as for examples composites, thermal barriers, optical thin films, Bragg gratings, tapered transmission lines and many others). In 1D graded media, thermal diffusion is driven by the effusivity profile. On the other side, electromagnetic (EM) wave propagation is driven by the EM admittance profile (or simply the refractive index, in non-magnetic materials). A method has recently been described for the construction of sequences of effusivity profiles that are “solvable”, which means profiles leading to exact analytical solutions for the time- (or frequency-) dependent temperature [1]. The proposed profiles are expressed in closed-form, involving elementary functions only (the same holds for the corresponding temperature solution when expressed in the Fourier or Laplace space). Similar sequences have been proposed in the context of Maxwell’s equations for lossless media, more generally for a class of wave equations to which acoustic waves and electric waves in LC transmission lines also belong, just to name a few [2]. In all these cases, the solvable profiles together with their joint field-solutions are generated by applying repeatedly the Darboux transformation in the Liouville space (PROFIDT method: PROperty and FieId Darboux Transformation method). At each iteration, the number of leading parameters increases, which improves the fitting capability of the profiles. In the Liouville space, depending on the considered problem, i.e. thermal diffusion or (optical/acoustical) wave scattering, the new independent-variable corresponds to the (square-root of) diffusion-time (SRDT), resp. the optical-depth (or acoustical-depth). In the Liouville space, the solvable profiles share the same form, for both considered problems (diffusion or wave scattering). One class of solvable profiles is particularly interesting, we dubbed it “profiles of $\text{sech}(\hat{\xi})$ -type” because they are defined through a linear combination of two independent functions, the first one being the hyperbolic secant function ($\text{sech}=1/\cosh$) of the linearly deformed $\hat{\xi}$ -variable, namely $\hat{\xi} = \xi/\xi_c + \tau$. In the thermal context, the $\text{sech}(\hat{\xi})$ -type profiles of effusivity are defined by:

$$b^{+1/2}(\xi) = A_B B(\xi) + A_D D(\xi) \quad ; \quad \begin{cases} B(\xi) = \text{sech}(\hat{\xi}) \\ D(\xi) = \sinh(\hat{\xi}) + \hat{\xi} \text{sech}(\hat{\xi}) \end{cases}$$

The “+1/2” exponent refers to profiles called of $\langle T \rangle$ -form and the “-1/2” exponent refers to profiles called of $\langle \phi \rangle$ -form (as a matter of fact, they originate from the heat equation expressed in temperature, resp. in heat flux).

In addition to the outstanding properties already mentioned, these four-parameter profiles are extremely flexible. This means that we can adjust the four parameters ξ_c , τ , A_B and A_D so that the considered property (either thermal effusivity, EM admittance or refractive index) and its slope at both boundaries of a given layer reach any given set of four values. Hence, composite profiles of arbitrary shape can be built by assembling such elementary bricks [3, 4]. The corresponding (exact) field-solution (temperature or electric field) is then obtained based on transfer-matrix multiplications like in the classical quadrupole method. As opposed to the classical quadrupole method where each layer is assumed to be homogeneous, the individual layers now present continuously variable properties. The whole functional may be continuous at the nodes up to the second derivative. Hence, it can be manipulated like an interpolating spline function. It is the first known class of “solvable splines” aimed at modeling both diffusion and wave-like problems in graded media.

The next figure intends to illustrate the case of a graded coating in which, starting from the surface, the effusivity first decreases to a minimum and then increases to the bulk value. In this figure, the effusivity is normalized by the bulk value and the depth is represented through the SRDT which has been normalized by the value ξ_{end} corresponding to the depth where effusivity reaches the bulk value. Three curves have been plotted. The blue curve is the classical cubic spline as obtained after specifying the position and height of three nodes together with the slope at both ends of the coating (this corresponds to a “clamped spline”; in this example, the normalized slope is set to -2 at left-end and 0 at right-end). On each of two intervals, two $\text{sech}(\hat{\xi})$ -type profiles have been evaluated, one of $\langle T \rangle$ -form (in black) and one of $\langle \phi \rangle$ -form (in red). The value and derivative of the cubic spline at both ends of each interval provide the four constraints used to evaluate the four parameters of each $\text{sech}(\hat{\xi})$ -type profile. For the effusivity values and derivatives considered in this example, the $\langle T \rangle$ -form and $\langle \phi \rangle$ -form profiles are very close one to the other. Furthermore, they are not very

Session E1: Thermography I / Data Handling

different from each element of the cubic spline. Then, a composite profile is obtained by stitching two successive $\text{sech}(\frac{\xi}{\xi})$ -type profiles. Notice that profiles of $\langle T \rangle$ -form and $\langle \varphi \rangle$ -form can be freely mixed, which, in the example described here, gives four (slightly) different composite profiles. Remember that each composite profile is a *solvable profile* in the sense that temperature and heat flux at each position can be analytically calculated by combining in due order the quadrupoles related to each elementary profiles. This is not the case with the cubic-spline profile for which there is no closed-form analytic solution.

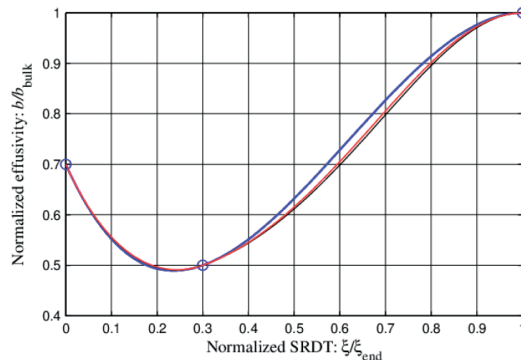


Fig. 1. Comparison between the classical cubic spline (in blue) and the solvable splines of $\langle T \rangle$ -type of either $\langle \varphi \rangle$ -form (in black) or $\langle T \rangle$ -form (in red).

The inversion problem consists in finding the *composite solvable profile* whose temperature solution best matches with the experimental temperature data measured on the surface of the functionally graded material. One possible strategy is to select a small number of nodes and perform the fitting by adjusting the ξ -position of the internal nodes, together with the effusivity and slope at each node. Different avenues can be explored regarding the constraint on the left vs. right values of effusivity or its derivative at each node (i.e. continuous vs. discontinuous profile or broken vs. smooth profile).

The differential equations to which the proposed PROFIDT method can be applied are quite general, which means that the proposed tools can be implemented to find exact analytical solutions in graded media for a whole bunch of problems in addition to those already quoted: matter diffusion (Fick's law), Stokes problems, advection-diffusion, microfluidic, tapered RC or LC transmission lines, longitudinal acoustic waves, shear waves, ocean gravity waves, etc.

Several examples of applications will be presented related to thermal problems (photothermal characterization), to advection-diffusion problems (pollutant dispersion in the atmosphere, footprint modeling for soil-atmosphere flux studies) and to photonic problems (rugate filters, chirped mirrors, antireflection layers).

References

1. J.-C. Krapez, Int. J. Heat Mass Transfer, 99, 485-503 (2016) <https://doi.org/10.1016/j.ijheatmasstransfer.2016.03.122>
2. J.-C. Krapez, J. Modern Optics, 64(19), 1988-2016 (2017) <https://doi.org/10.1080/09500340.2017.1330975>
3. J.-C. Krapez, Int. J. Thermophysics, 39(7), 86 (2018), <https://doi.org/10.1007/s10765-018-2406-z>
4. J.-C. Krapez, J. Opt. Soc. Am. A, 35(6), 1039-1052 (2018), <https://doi.org/10.1364/JOSAA.35.001039>

Characterization of mid-wave quantum infrared cameras using the photon transfer technique

Stefan BREITWIESER*, Gerald ZAUNER, Günther MAYR

Josef Ressel Centre for Thermal NDE of Composites, University of Applied Sciences Upper Austria, Wels, Austria

stefan.breitwieser@fh-wels.at

The photon transfer technique is a well-established method for characterizing the performance parameters of optical camera systems, e.g. CCD (charge coupled device) and CMOS (complementary metal oxide semiconductor) [1,2]. In this study, the photon transfer technique is adapted for the noise characterization of mid-wave infrared (IR) cameras. The mean value and the standard deviation are calculated from IR camera signals, which are recorded at different irradiation intensities. The standard deviation (noise) is plotted versus the mean value (signal) in a double logarithmic representation (Fig. 1). This photon transfer curve allows a determination of various camera parameters, such as the camera gain, read noise, dark current, quantum yield, full well, linearity, pixel nonuniformity, sensitivity, signal-to-noise ratio, offset and the dynamic range [3].

Three different IR cameras with indium antimonide (InSb) and cadmium mercury telluride (CMT) detectors were examined with the photon transfer technique. The experimental study shows that the camera noise corresponds to Poisson noise with increasing intensity. The local detector noise, i.e. the noise of the individual pixels in relation to each other, corresponds to a normally distributed noise with a standard deviation of 24.2 mK for the InSb detector and 58.5 mK for the CMT detector. The photon transfer technique couldn't be applied to the third IR camera due to the high pixel crosstalk. This systematic error was evaluated by the computation of the correlation coefficients for the detector array.

The sensitivity of the cameras was determined in the form of the camera gain constants. The camera gain constant is a parameter describing how many photons have to reach the detector to cause a signal change at the output of the camera system.

The camera gain constants of the InSb detector and CMT detector were determined with 433 photons per signal level in digital numbers (DN) respectively 281 photons per DN.

The results of the experimental study were verified by a theoretical examination of the photon irradiation on the detector. The radiation of a blackbody was calculated using Planck's law and converted into detector irradiation using various camera parameters and manufacturer specifications. This made it feasible to calculate the theoretical camera gain constants.

The theoretical camera gain constant of the InSb detector were determined to be 431 photons per DN.

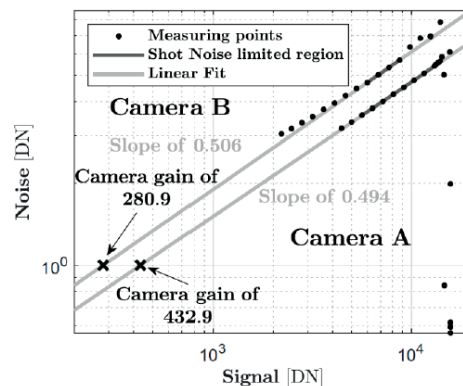


Fig. 1. Photon transfer curve of camera A (InSb detector) and B (CMT detector). The black points represent the results of the measurement. The region which was used for the evaluation is marked with dark grey.

Acknowledgements

The financial support by the Austrian Federal Ministry of Science, Research and Economy and the National Foundation for Research, Technology and Development is gratefully acknowledged.

References

- L. Li, M. Li, Z. Zhang, Z.-L. Huang, Assessing low-light cameras with photon transfer curve method, *Journal of Innovative Optical Health Sciences* 09 (03) (2016) 1630008. doi:10.1142/S1793545816300081.
- H. T. Hytti, Characterization of digital image noise properties based on raw data, in: L. C. Cui, Y. Miyake (Eds.), *Image Quality and System Performance III*, SPIE Proceedings, SPIE, 2006, pp. 60590A–60590A–12. doi:10.1117/12.640500.
- J. R. Janesick, *Scientific charge-coupled devices*, Vol. PM83 of SPIE Press monograph, SPIE, Bellingham, WA, 2001.

Edge Recognition of Debonding Defects in Carbon Fiber Composites Based on Infrared Image Segmentation with Iterative Threshold Algorithm

Tang Qingju*, Gao Shuaishuai, Liu Yongjie

School of Mechanical Engineering, Heilongjiang University of Science and Technology, Harbin, 150022, China

tangqingju@126.com

In infrared thermal wave nondestructive testing of debonding defective components of carbon fiber reinforced composites, large noises exist in the collected infrared thermograms affected by the detection system itself, the surrounding environment and the test conditions, which result to low contrast and signal-to-noise ratio of the infrared images. An edge recognition method of debonding defects in carbon fiber composites based on infrared image segmentation with iterative threshold algorithm was presented in this paper. The implementation steps are as follows: Firstly, a threshold is determined. Generally, the average value of the maximum and minimum gray value of an image is taken as the initial iteration threshold. Then the image is divided into two parts using this threshold, the part greater than the threshold and the other part less than or equal to the threshold. Finally, calculating the average value of the two parts' thresholds, and taking it as the new threshold. It illustrates the iteration has converged, when the new threshold does not change or the range of change is less than the specified value compared with the previous iteration result. And the final threshold will be used for image segmentation. The results show that, compared with iterative threshold segmentation effect enhanced by linear gray level transformation and gamma transform algorithm, that enhanced by high-pass filtering is better, which not only effectively suppresses a large amount of redundant information, but also makes the edge of debonding defects display more clearly.

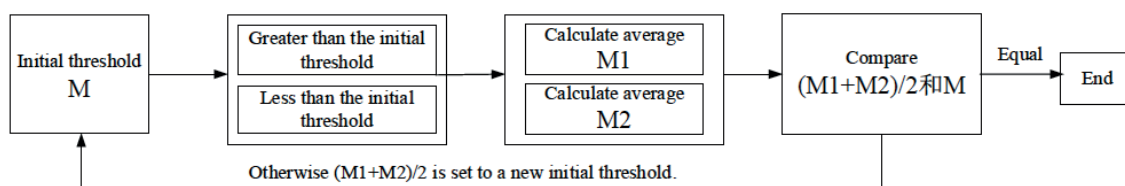


Fig. 1. The procedure of iterative threshold method

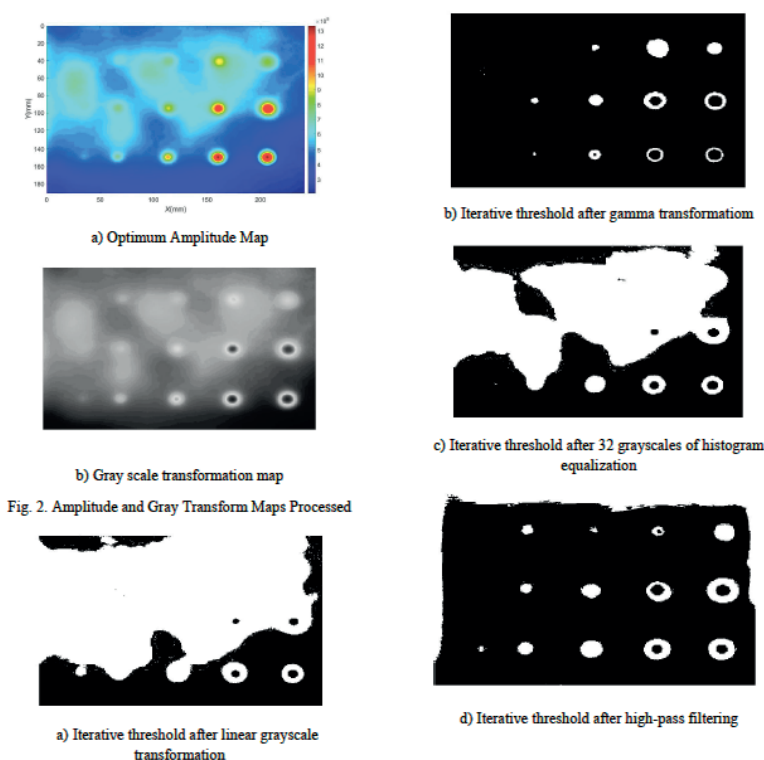


Fig. 2. Amplitude and Gray Transform Maps Processed

Fig. 3 Results of iterative threshold segmentation

On the effect of the electron subsystem on the thermoelasticity of real metals

Kyrill MURATIKOV ^{(1)*}, Alexey GLAZOV ⁽¹⁾, Nikita MOROZOV ⁽²⁾

1. Ioffe Institute, St. Petersburg, Russia

2. Institute of Problems of Mechanical Engineering, Russia

klm.holo@mail.ioffe.ru

The classical theory of thermoelasticity is based on the development of a general approach to materials of different nature. The classical theory of thermoelasticity makes no distinction between dielectrics and metals [1] while metals in contrast with dielectrics along with lattice atoms have an electronic subsystem. In ideal metals it is assumed that electrons form electron gas in their conduction bands. In slow thermodynamic processes, their presence does not play a fundamental role, but with fast thermal effects can significantly affect the course of thermoelastic processes. Such situation is usually realized for metals under exposure to short laser pulses. Short laser pulses may strongly affect on the electron subsystem and influence on thermoelastic processes in metals, in particular, due to the so-called “electron blast” effect [2]. In ideal metals besides of the temperature relaxation time thermoelastic processes are ruled by rather short times such as electron-to-phonon and phonon-to-phonon relaxation times. At the same time, in a number of experiments it was found that in real metals under short-pulse laser impact a rather long thermoelastic response can be observed [3]. The main goal of this paper is to propose the model of thermoelastic effect in real metals and discuss its results using experimental data from the work [3] and our data obtained in experiments with stressed metals.

The structure of real metals, along with a regular lattice, assumes the presence of various kinds of defects such as vacancies, the boundaries of clusters and grains, microcracks, heterogeneity of the composition, etc. Such structure of the real metal is resulted in inhomogeneous behavior of potential energy of electrons, which can vary within the metal randomly. Under these conditions near the conduction band appears a range of energies for which an electron can move only by the activated hopping from one localized state to another (Mott conductivity [4]). Therefore in real metals there is both a significant amount of free electrons and a certain number of trapped ones. Under equilibrium conditions, their quantities remain constant. However, under external excitations, electron transitions from one state to another can occur and the quantities of free and bound electrons can vary. The electrons excited from localized states go over into the conduction band and are converted into free ones. This process leads to a change in the concentration of free electrons in the metal which resulted in the change of their pressure. The purpose of this paper is to analyze the influence of such processes on dynamic thermoelastic phenomena in metals under laser action. The description of such dynamic processes may require the use of additional parameters that are not presented in the conventional theory of thermoelasticity.

The proposed model assumes the transition of a part of electrons between different localized states. This behavior of the electron – lattice system is clearly demonstrated in experiments studying behavior of the electron conductivity of disordered metallic films [5]. In the simple form the thermoelastic problem for metal under short-pulse laser irradiation can be presented by equations

$$\rho \frac{\partial^2 u_i}{\partial t^2} = \frac{\partial \sigma_{ik}}{\partial x_k} - m_e \frac{\partial (nv_i)}{\partial t}, \quad m_e \frac{\partial (nv_i)}{\partial t} = - \frac{\partial p_e}{\partial x_i},$$

where u_i is the displacement of the lattice, ρ is its density,

$$\sigma_{ij} = \lambda \frac{\partial u_k}{\partial x_k} \delta_{ij} + \mu \left(\frac{\partial u_i}{\partial x_j} + \frac{\partial u_j}{\partial x_i} \right) - (3\lambda + 2\mu) \alpha_T (T - T_0) \delta_{ij},$$

λ and μ are the Lamé constants, α_T is the thermal expansion coefficient, T is the temperature, m_e is electron mass, n is electron concentration, v_i is electron velocity,

$$p_e = \frac{2}{5} n E_F + \frac{\pi^2}{6} n E_F \left(\frac{k_b T}{E_F} \right)^2$$

is the pressure of degenerate electron gas, E_F is the Fermi energy. The dynamics of electron concentration can be described by the expression $\frac{\partial n}{\partial t} + \frac{n}{\tau} = J$, where J is the source term, τ is the relaxation time.

The source term for electrons can be chosen in the form of Arrhenius form [5]. Analysis of the formulated problem shows that when a short laser pulse $P \delta(t) \delta(x)$ (P is the power of laser pulse) is applied to the surface of a metal sample, the piezoelectric photoacoustic signal $V_e(t)$ from the sample can be represented as

Session E1: Thermography I / Data Handling

$$V_e(t) = KP \int_0^{t-d/c-t'} e^{\frac{t-d/c-t'}{\tau}} \frac{1}{\sqrt{t'}} dt',$$

where d is the sample thickness, c is the velocity of sound, K is the coefficient of proportionality.

The result obtained is in good agreement with the experimental results of the paper [3], and also allowed us to explain a number of features of photoacoustic signals obtained on metallic samples with stresses.

Acknowledgements

This study was supported by Russian Science Foundation (Project No.15-19-99182).

References

1. W. Nowacki, "Thermoelasticity", 2nd Edition, Pergamon Press, Oxford, (1986)
2. D. Y. Tzou, J. K. Chen, and J. E. Beraun, J. Thermal Stresses. 28 (6-7), 563 (2005) doi.org/10.1080/01495730590929359
3. Yu. V. Sudenkov, B. A. Zimin, Int. J. Heat Mass Transfer. 85, 781 (2015) doi.org/10.1016/j.ijheatmasstransfer.2015.01.119
4. M. Cutler, N. F. Mott, Phys. Rev., 181 (3), 1336 (1969)
5. A. Eisenbach, T. Havdala, J. Delahaye, T. Grenet, A. Amir, and A. Frydman, Phys. Rev. Lett., 117, 116601 (2016). doi.org/10.1103/PhysRevLett.117.116601

Remote detection of hidden defects on metal surfaces using the method of pulsed laser thermography

Leonid A. SKVORTSOV*, Pavel I. ABRAMOV, Eugene V. KUZNETSOV,
Peter Y. LOBANOV, Oleg E. SIDORYUK

JSC Polyus Research Institute of M. F. Stelmakh, Moscow, Russia

lskvortsov@gmail.com

Recently, more and more attention has been paid to the development of an active thermographic method of non-destructive testing (NDT), which allows us to investigate the surface of tested objects in a non-contact manner.

In the classic active thermographic method NDT (*flash thermography*) the object's surface is heated by radiation from one or more flash lamps, after which its cooling is recorded using an IR camera. Heating the surface with flash lamps is almost uniform, thereby causing a one-dimensional heat flux directed from the surface into the bulk of the material. This method has long been used for non-destructive and non-contact study of the interfaces between the surface layer (coating) and the base material (substrate), for example, to detect defects of adhesive origin (peeling of the coating), local corrosion sites, surface cracks that change the one-dimensional heat flux from the surface.

A significant divergence of radiation from flash lamps and its low spectral brightness significantly limit the scope of flash thermography, in particular, in the implementation of NDT objects that are far away from the heating source. At the same time, this task is now becoming increasingly important and attention of researchers, as it relates to remote monitoring of metal structures in the form of bridges, tanks for transportation and storage of petroleum products, liquefied gas, etc.

The aim of this work is to demonstrate the possibility of remote thermographic method of NDT of the surface of metal structures at considerable distances from the heating source, which uses pulsed laser radiation.

The source of laser radiation in the work was the assembly of semiconductor laser diodes with a wavelength of 915 nm, having a common fiber output. The duration of the laser exposure was set by the timer associated with the mechanical chopper of the laser radiation channel and was 5 s. The radiation power density at the target was $\sim 0.05 \text{ W/cm}^2$.

As a target, samples were used in the form of bars, made of structural St3 steel, which were covered with a layer of protective paint coating of dark color. The iron corrosion centers on the surface of the tested areas did not appear in any way during remote observation of the samples by means of CCD or thermal imaging camera, which used the infrared camera FLIR Tau2 (NETD = 50 mK, resolution 336×256 , pixel size $17 \mu\text{m}$, lens diameter 35 mm).

At the same time, when a sample is irradiated with laser radiation, hidden defects in the form of rust-affected areas are clearly seen when observed with an infrared camera located at a distance of 10 m from it, coupled with a laser-sensing system (Fig. 1). The same figure shows the result of visualization in similar conditions of the hidden defect in the form of cross-shaped surface cracks with a depth of 2 mm, obtained by spark erosion, covered with polyester putty, followed by polishing and painting the surface with alkyd enamel. Despite the perfect masking in the visible range of the spectrum and the indistinguishability of the defective area, even at high magnification, it can be visualized by pulsed laser thermography (Fig. 1b).

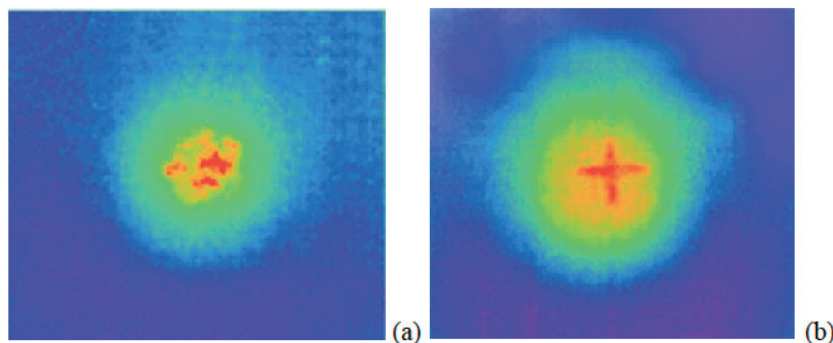


Fig. 1. Thermographic images observed after laser irradiation of a metal plate with local defects under a layer of paint: (a) iron corrosion centers, (b) cross-shaped surface cracks filled with polyester putty.

In the above figures, the thermal footprint is clearly visible, due to the violation of the heat sink in the defective area of the test sample, hidden by the protective coating. The paint coating absorbed at least 80% of the radiation energy, and its emissivity in the region of $7.5 - 13 \mu\text{m}$ was 0.9.

Session E1: Thermography I / Data Handling

To assess the sensitivity of the method, the time dependences of the temperature increment of the sample surface depending on the thickness of the layer subjected to corrosion (Fig. 2 (a)) and the thickness of the protective layer hiding cross-shaped surface cracks (Fig. 2 (b)) were studied.

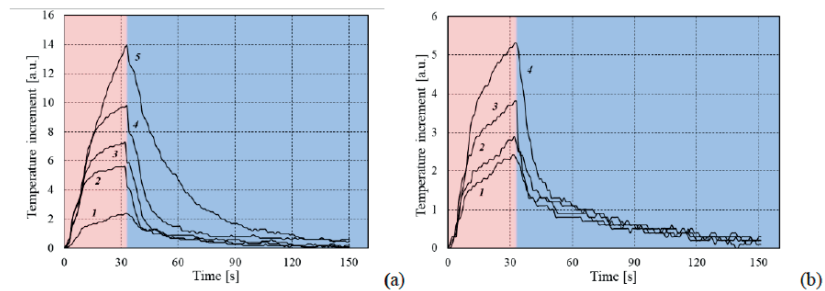


Fig. 2. Time dependences of changes in the surface temperature of plates made of St3 steel when exposed to laser radiation with a power density of 0.4 W/cm^2 for 33 seconds and subsequent cooling for different thicknesses h of the surface layers of

(a) corrosion products of hydrated iron oxide: 1- $h = 0,25 \text{ mm}$, 2- $h = 0,5 \text{ mm}$, 3- $h = 0,8 \text{ mm}$, 4- $h = 1,1 \text{ mm}$, 5- $h = 2,3 \text{ mm}$;

(b) polyester putty: 1- $h = 0,25 \text{ mm}$, 2- $h = 0,5 \text{ mm}$, 3- $h = 1,6 \text{ mm}$, 4- $h = 2,5 \text{ mm}$.

As follows from the graphs presented, the method of pulsed laser thermography is of sufficient sensitivity to detect hidden defects with a thickness $h \sim 100 \mu\text{m}$ and less at distances exceeding 10 m.

Designing Ultra-Sensitive Sensors for Photoacoustic Imaging

James A GUGGENHEIM*, Edward Z ZHANG, Paul C BEARD

*Department of Medical Physics and Biomedical Engineering,
University College London, UK*

Biomedical photoacoustic (PA) imaging provides detailed images of soft tissue but achieving multi-cm scale penetration depth is challenging as the signals encountered are extremely weak, necessitating high-performance detectors. Unfortunately, due to a range of factors including the challenging nature of detector characterisation and incompleteness of reporting in the literature, it is extremely difficult to effectively compare detectors and select the best one for achieving maximal penetration depth. This talk will address this by providing a rigorous review of the capabilities of PA detectors and demonstrating the different ways in which the choice of detector critically impacts upon image depth and quality.

Photo-acoustic Characterization in Nanophotonics

Emilija PETRONIJEVICH ^{(1)*}, Grigore LEAHU ⁽¹⁾, Alessandro BELARDINI ⁽¹⁾, Roberto LI VOTI ⁽¹⁾,
Teemu HAKKARAINEN ⁽²⁾, Mircea GUINA ⁽²⁾, Tiziana CESCO ⁽³⁾, Giovanni MATTEI ⁽³⁾,
Concita SIBILIA ⁽¹⁾

1. Sapienza University of Rome, SBAI Department, Rome, Italy

2. Tampere University of Technology, Optoelectronics Research Centre, Tampere, Finland

3. University of Padova, Physics and Astronomy Department, Padua, Italy

emilija.petronijevic@uniroma1.it

Absorption properties of nanostructured materials are of essential importance for applications spanning from light harvesting to lasing. Moreover, chiral properties of nanostructures with broken symmetry lead to different absorption for circularly polarized light of opposite handedness, which is a property of circular dichroism, CD; direct characterization of CD at the nanoscale could pave the way to enantioselectivity and chiral detection [1]. However, conventional characterization techniques of absorption properties are usually based on indirect measurements by means of transmission/reflection, photocurrents or photoluminescence, which includes complicated post-processing and interpretation of results; moreover, many effects are hidden due to the influence of scattered light. We have therefore proposed photo-acoustic spectroscopy (PAS) as a reliable characterization tool of absorption effects at the nanoscale.

PAS is a type of photothermal techniques, where absorption of light leads to a non-radiative de-excitation process which generates heat, which in return changes the thermal state of the sample. If the intensity of the light is modulated in time, a sample in an air-tight chamber heats up and cools down in cycles and, as it does not have time to expand and contract, changes in pressure arise. These pressure changes produce an acoustic signal which is then directly converted into an electrical signal by a close and sensitive microphone [2]. The microphone receives the signal from the sample through the small diameter tunnel, therefore the scattered light cannot directly reach the microphone; this way scattering effects are largely reduced. The amplitude of the measured signal finally corresponds to the near field absorption. Our PAS set-up includes either the white light lamp followed by a monochromator, or a laser operating in VIS or near-IR range; the light is then modulated by a mechanical chopper, and finally reaches the PAS cell with the sample.

We use PAS to measure absorption properties of different types of nanostructures: GaAs-based nanowires (NWs) [2,3] (self-assembled or periodically arranged), polystyrene-metal nanoparticles [4], localized surface plasmons, silver NW films etc. In Fig. 1(a) PAS spectra show resonant absorption peaks of GaAs-based NW samples with different dimensions. Specifically, the main peak position corresponds to the excitation of HE_{11} and red-shifts with the diameter increase. In Fig. 1(b) the same samples were asymmetrically covered by Au, and PAS spectra show mode broadening due to Au losses. These samples are then characterized in terms of CD at 532 nm and 980 nm; the breaking of symmetry at oblique angles leads to CD increase, typical for extrinsic chiral behavior. In all cases, experimental PAS results were in good agreement with theoretical predictions and numerical simulations [5,6]; moreover, the demonstration of CD in absorption led us to idea that CD is also present in emission of Au-covered NW samples [7].

Recently, we used PAS to characterize polystyrene metasurfaces, asymmetrically covered by Au, Ag, or Cr. In Fig. 1(c) we show CD dependence on incidence angle θ defined as:

$$CD[\%] = 200 \frac{A_{LCP} - A_{RCP}}{A_{LCP} + A_{RCP}},$$

where A_{LCP} and A_{RCP} are absorption of left and right circular polarization, respectively. We demonstrate extrinsic chirality for Au- and Cr-covered samples, while for the Ag-covered one we note slight intrinsic chirality (CD at $\theta=0^\circ$).

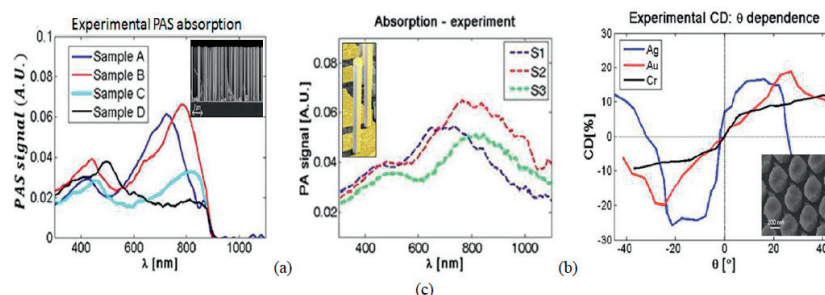


Fig. 1. (a) PAS spectra of GaAs-based NW samples of different dimensions; the resonant peaks demonstrate the excitation of leaky guided modes, and red-shift with the diameter increase [2]. (b) PAS spectra of GaAs-based NWs partially covered by Au [3]. (c) CD measurements of polystyrene metasurfaces partially covered by different metals [3], at 633 nm. Insets show Scanning Electron Microscope images of the samples.

In conclusion, PAS offers advantages of being scattering-free, stable, low-cost characterization technique for direct measurements of absorption in nanomaterials. Both qualitatively and quantitatively, PAS can be used to control and improve design of nanophotonic components.

References

1. E. Petronijevic, M. Centini, A. Belardini, G. Leahu, T. Hakkarainen, C. Sibilìa, *Opt. Express* 25 (13), 14148 (2017).
2. G. Leahu, E. Petronijevic, A. Belardini, M. Centini, R. Li Voti, T. Hakkarainen, E. Koivusalo, M. Guina, C. Sibilìa, *Sci. Rep.* 7 (1), 2833 (2017).
3. G. Leahu, E. Petronijević, A. Belardini, M. Centini, C. Sibilìa, T. Hakkarainen, E. Koivusalo, M. Rizzo Piton, S. Suomalainen, M. Guina, *Adv. Opt. Mater.* 5 (16), 1601063 (2017).
4. E. Petronijevic, G. Leahu, R. Li Voti, A. Belardini, C. Scian, N. Michieli, T. Cesca, G. Mattei, C. Sibilìa, *Appl. Phys. Lett.* 114, 053101 (2019).
5. E. Petronijevic, G. Leahu, A. Belardini, M. Centini, R. Li Voti, T. Hakkarainen, E. Koivusalo, M. Rizzo Piton, S. Suomalainen, M. Guina, C. Sibilìa, *Int. J. Thermophys.* 39 (4), 46 (2018).
6. E. Petronijevic, G. Leahu, A. Belardini, M. Centini, R. Li Voti, T. Hakkarainen, E. Koivusalo, M. Rizzo Piton, S. Suomalainen, M. Guina, C. Sibilìa, *Int. J. Thermophys.* 39 (3), 45 (2018).
7. T. Hakkarainen, E. Petronijević, M. Rizzo Piton, and C. Sibilìa, *Sci. Rep.* 9, 5040 (2019).

Improved imaging of polycrystalline materials via time-domain Brillouin scattering by shear acoustic waves

Théo THRÉARD (1), Samuel RAETZ (1), Elton DE LIMA SAVI (1), Nikolay CHIGAREV (1), Sergey AVANESYAN (2), Vincent TOURNAT (1), Zilong HUA (3), Andreas ZERR (4), David H. HURLEY (3), and Vitalyi E. GUSEV (1)*

1. Laboratoire d'Acoustique de l'Université du Mans, UMR 6613 CNRS, Le Mans Université, Le Mans, France

2. Department of Life and Physical Sciences, Fisk University, Nashville, TN 37208, USA

3. Idaho National Laboratory, P.O. Box 1625, Idaho Falls, ID 83415, USA

4. Laboratoire des Sciences des Procédés et des Matériaux, UPR 3407 CNRS, Université Paris 13, Villetaneuse, France

theo.threadard@univ-lemans.fr, samuel.raetz@univ-lemans.fr, elton_savi@hotmail.com, nikolay.chigarev@univ-lemans.fr, savanesyan@fisk.edu, vincent.tournat@univ-lemans.fr, zilong.hua@inl.gov, zerr@univ-paris13.fr, david.hurley@inl.gov, vitali.goussev@univ-lemans.fr

In material science, the time-domain Brillouin scattering (TDBS) technique, initially known as the picosecond acoustic interferometry technique [1], allows imaging either of a continuous change of (or of inhomogeneities occurring due to a mismatch in) acoustical, optical, and/or photo-elastic parameters in transparent materials [2]. In this technique, acoustic waves are generated by an ultrashort optical (pump) pulse absorbed by the tested material or by an optoacoustic transducer in contact with it. In the most general case, up to three waves could be generated and propagate in the sample: one longitudinal (or quasi-longitudinal) and two shear (or quasi-shear) waves. Propagation of these waves is monitored by a second time-delayed ultrashort optical (probe) pulse with the wavelength in the transparency region of the tested material. In that case, a part of the probe beam is reflected at stationary surfaces/interfaces and another part is reflected at the propagating acoustic pulses. These reflected parts interfere on the photodetector and give rise to an oscillatory signal having the same frequencies as the Brillouin oscillations. In the most general case, several frequencies could be present in the signal, the values of which being defined by the combinations of the acoustic sound velocity, the optical refractive index, and the probe light wavelength. In a polycrystalline material, tracking of the changes of those frequencies with lateral position and with delay time should allow a precise 3D imaging of the crystallites (or of crystallites groups having the same preferential orientation) and of the boundaries between them. Yet, contrast in the TDBS imaging, such as in the evaluation of texture [3], of position of grain boundaries [4], and of elastic moduli [5] in polycrystalline materials, comes usually from the value of the Brillouin frequency associated to the longitudinal acoustic pulses only. However, a parallel monitoring of both longitudinal and transverse acoustic pulses has recently demonstrated an enhanced ability in determining grains orientation near the surface of a polycrystalline ceria (CeO₂) sample [6].

We propose here to extend the technique to three dimensions by making use of the three acoustic pulses, if available, and/or by taking benefit from the fact that Brillouin frequencies depend on the local refractive index and the local sound velocities. Indeed, accurate and simultaneous estimates of the variations of the three Brillouin frequencies with respect to time in collected TDBS signals gives access to the variations of the material parameters as a function of the sample depth. Combining the latter with a 2D lateral scanning over the sample leads to a three-dimensional imaging. Some applications of the TDBS technique for 3D imaging of polycrystalline materials, both at atmospheric and at high pressures, will be presented, together with the signal processing procedure/software developed for this purpose. The experimental results have been collected with an ASOPS-based picosecond acoustic microscope (JAX-M1, NETA, France), which allows a fast image acquisition. The Figure 1 presents examples of the images for a polycrystalline sample of ceria (CeO₂) at atmospheric pressure obtained with the Brillouin frequencies associated with (a) longitudinal, (b) fast and (c) slow quasi-shear acoustic pulses, demonstrating their complementarity in determining the grain boundary positions in the vicinity of the sample surface. The nanoscale imaging ability of TDBS is improved by the use of shear acoustic waves, which is expected to be even more evident by the gain in contrast obtained on the imaging of buried grain boundaries.

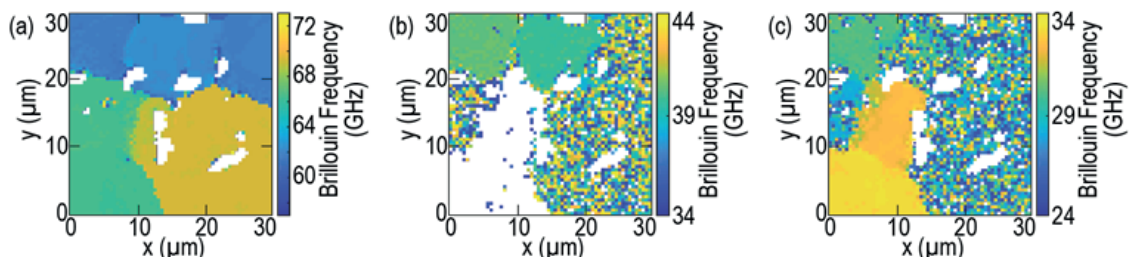


Fig. 1. Examples of the images obtained with the Brillouin frequencies associated with (a) quasi-longitudinal, (b) fast and (c) slow quasi-shear acoustic pulses for a polycrystalline sample of ceria (CeO₂) at atmospheric pressure.

Acknowledgements

This research is supported by the project <ANR-18-CE42-I2T2M>, the Acoustic Hub® program and the LMAc project NANOSHEAR.

References

1. C. Thomsen, H.T. Graham, H.J. Maris, J. Tauc, *Optics Communications* 60, 55 (1986); doi:10.1016/0030-4018(86)90116-1
2. V. E. Gusev, and P. Ruello, *Applied Physics Reviews* 5, 031101 (2018); doi:10.1063/1.5017241
3. S. M. Nikitin, N. Chigarev, V. Tournat, A. Bulou, D. Gasteau, B. Castagnede, A. Zerr, V. E. Gusev, *Scientific Reports* 5, 9352 (2015); doi:10.1038/srep09352
4. M. Khafizov, J. Pakarinen, L. He, H. Henderson, M. Manuel, A. Nelson, B. Jaques, D. Butt, D. Hurley, *Acta Materialia* 112, 209–215 (2016); doi: 10.1016/j.actamat.2016.04.003
5. M. Kuriakose, S. Raetz, Q. M. Hu, S. M. Nikitin, N. Chigarev, V. Tournat, A. Bulou, A. Lomonosov, P. Djemia, V. E. Gusev, A. Zerr, *Physical Review B* 96, 134122 (2017); doi:10.1103/PhysRevB.96.134122
6. Y. Wang, D. H. Hurley, Z. Hua, G. Sha, S. Raetz, V. E. Gusev, M. Khafizov, *Scripta Materialia* 166, 34– 38 (2019); doi: 10.1016/j.scriptamat.2019.02.037

Three-dimensional imaging of H₂O ice at high pressure by time-domain Brillouin scattering

Elton DE LIMA SAVI⁽¹⁾, Nikolay CHIGAREV⁽¹⁾, Samuel RAETZ⁽¹⁾, Vincent TOURNAT⁽¹⁾,
Alain BULOU⁽²⁾, Andreas ZERR⁽³⁾, Vitalyi E. GUSEV^{(1)*}

1. Laboratoire d'Acoustique de l'Université du Mans, UMR 6613 CNRS, Le Mans Université, Le Mans, France

2. Institut des Molécules et Matériaux du Mans, UMR 6283 CNRS, Le Mans Université, Le Mans, France

3. Laboratoire des Sciences des Procédés et des Matériaux, UPR 3407 CNRS, Université Paris Nord, Villetaneuse, France

elton_savi@hotmail.com, nikolay.chigarev@univ-lemans.fr, samuel.raetz@univ-lemans.fr, vincent.tournat@univ-lemans.fr, alain.bulou@univ-lemans.fr, zerr@univ-paris13.fr, vitali.goussev@univ-lemans.fr

Time-domain Brillouin scattering (TDBS) is applied for the first time to perform the 3D imaging of polycrystalline water ice phases, VII and VI, coexisting at a pressure of 2.1 GPa in a diamond anvil cell (DAC) at room temperature.

Materials and Methods

The TDBS is a non-destructive opto-acousto-optic pump-probe technique [1] which allows the study of a variety of transparent materials [2]. In this method, an optical pump pulse from a femtosecond laser is absorbed by an optoacoustic transducer contacting the sample. As a result, a picosecond acoustic pulse is emitted into the sample. It scatters a time-delayed optical probe pulse from the same or another femtosecond laser. Thus, via detection of the changes of the transient optical reflectivity in time, the evolution of the acoustic pulse with its propagation distance can be probed when it traverses the sample. The TDBS signal contains information on the characteristics of the acoustic pulse and the parameters of the material in the current spatially localized position of the acoustic pulse. The length of this pulse is commonly at nanometers spatial scale. Therefore, the technique is suitable for imaging of materials along the pulse propagation path with a spatial resolution better than optical. Two-dimensional (lateral and depth) TDBS imaging has been earlier applied for revealing the texture of solid H₂O [3] and Ar [4], the phase transitions [5] and the reliable pressure dependences of elastic moduli [6] in water ice. We report here the extension of the TDBS technique to the 3D imaging of samples compressed in a DAC.

To accelerate the data acquisition and to make 3D imaging possible in reasonable time, we applied, for the first time, to a sample at high pressure in a DAC, an ultrafast laser technique called asynchronous optical sampling (ASOPS). In ASOPS technique, the time delay between the pump and the probe is controlled electronically by an offset of the repetition rate frequency of two lasers without the use of a slow mechanical delay line.

The experiments were conducted on water ice in a DAC at 2.1 GPa. The opto-acoustic generator (iron plate of approximately 40 μm thickness [5]) inside the sample chamber has the diameter of $\sim 110 \mu\text{m}$. The full width at half maximum of the laser beams at the surface of the generator is 1.4 μm . When irradiated by the pump optical pulses at 515 nm wavelength from our ASOPS-based picosecond acoustic microscope (JAX-M1, NETA, France), it emits picosecond acoustic pulses in 14.5 μm layer of water ice on the top of laser irradiated Fe surface [5]. The maximum analyzable time delay (1.9 ns) of the probe laser pulses at 532 nm wavelength provided opportunity for imaging the ice layers up to $\sim 10 \mu\text{m}$ distances from the generator. The image in the volume of $40 \times 40 \times 10 \mu\text{m}^3$ is obtained with the lateral step of 2 μm in 2 hours.

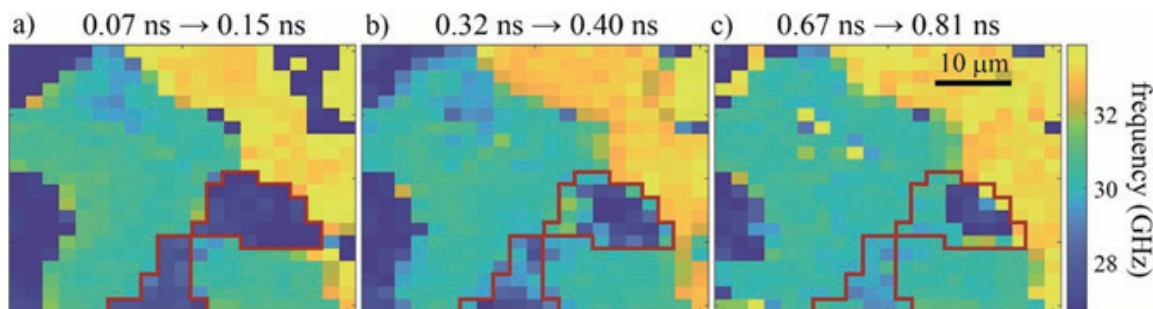


Fig.1. 2D maps of the Brillouin frequencies distribution in the $40 \times 40 \mu\text{m}^2$ cross sections of the tested ice volume at 2.1 GPa for shifting time slices. The red line highlights one of the lateral regions with important variations of the Brillouin frequency as a function of the distance from the generator.

Results

Maps of the Brillouin frequencies in the moving time windows of the acoustic pulse propagation in the ice are presented in Fig.1. They were obtained using a time-frequency analysis based on the synchronous detection principle [6]. The delay times between the probe and the pump laser pulses inside the time windows are marked above each of the cross-sectional maps (a)-(c) and, thus, correspond to different depth layers in the sample. The red line attracts the eyes to the variations of the Brillouin frequency with time in a selected lateral region. Note that, because acoustic waves propagate at different velocities in different lateral points, the same time window corresponds to different depth windows in different lateral points. The estimates demonstrate that the highest and the lowest detected Brillouin frequencies are the fingerprints of presence of the ice VII, while the intermediate frequencies in the lower half of the frequency spectrum could be due to the presence of ice VI.

Conclusions

We demonstrated the ASOPS-based 3D TDBS imaging of water ice in a DAC. This 3D imaging allows us to visualize shapes of the crystallites formed in the sample volume and their transformation with increasing load. In perspective, the 3D imaging of the transient processes at high pressures with nanometers depth resolution could be possible.

Acknowledgement

This research is supported by the grant <ANR-18-CE42-017>.

References

1. C. Thomsen, H.T. Graham, H.J. Maris, J. Tauc, *Optics Communications* 60, 55 (1986); doi:10.1016/0030-4018(86)90116-1
2. V. E. Gusev, and P. Ruello, *Applied Physics Reviews* 5, 031101 (2018) doi:10.1063/1.5017241
3. S. M. Nikitin, N. Chigarev, V. Tournat, A. Bulou, D. Gasteau, B. Castagnede, A. Zerr, V. E. Gusev, *Scientific Reports* 5, 9352 (2015); doi:10.1038/srep09352
4. M. Kuriakose, S. Raetz, N. Chigarev, S. M. Nikitin, A. Bulou, D. Gasteau, V. Tournat, B. Castagnede, A. Zerr, V. E. Gusev, *Ultrasonics*, 69, 201 (2016); doi:10.1016/j.ultras.2016.03.007
5. M. Kuriakose, N. Chigarev, S. Raetz, A. Bulou, V. Tournat, A. Zerr, V. E. Gusev, *New Journal of Physics* 19, 053026 (2017); doi:10.1088/1367-2630/aa6b3d
6. M. Kuriakose, S. Raetz, Q. M. Hu, S. M. Nikitin, N. Chigarev, V. Tournat, A. Bulou, A. Lomonosov, P. Djemia, V. E. Gusev, A. Zerr, *Physical Review B* 96, 134122 (2017); doi:10.1103/PhysRevB.96.134122

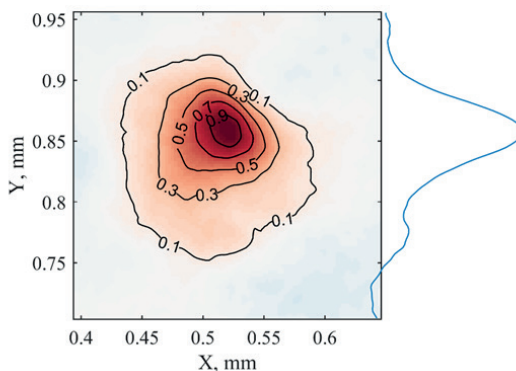
Photoacoustic imaging for visualization of laser energy deposition under femtosecond filamentation

Anton BYCHKOV ^{(1,3)*}, Fedor POTEKIN ^(1,2), Evgenii MAREEV ^(1,2), Boris RUMIANTSEV ^(1,2),
Alexander KARABUTOV ^(2,3), Elena CHEREPETSKEYA ^(1,3), Vladimir MAKAROV ^(1,2,3)

1. Faculty of Physics, Lomonosov Moscow State University, Leninskie Gory bld. 1/2, Moscow, Russia
2. International Laser Center, Lomonosov Moscow State University, Leninskie Gory bld. 1/62, Moscow, Russia
3. The National University of Science and Technology MISIS, Leninski Prospekt 6, Moscow, Russia

E-mail: abychkov@optoacoustic.ru

Photoacoustic (PA) tomography is a unique method for visualization of the energy deposition during femtosecond laser filamentation directly and non-invasively. When the power of a laser pulse exceeds the critical power of Kerr self-focusing the beam collapses and the light intensity increases. When the intensity is high enough, the medium is ionized, and the resulting plasma defocuses the beam, stopping the collapse. Filamentation is a laser pulse propagation regime when the Kerr self-focusing and plasma defocusing are dynamically balanced [1]. In the case of monofilamentation, a single elongated plasma column is formed. The plasma eventually



recombines, and the energy is released, heating the medium and generating acoustic waves thermoelastically. In water, the recombination and thermalization take tens of picoseconds, while the mechanical relaxation time is in the nanosecond range and the thermal relaxation time is in microsecond range for the characteristic filament core diameter of $\sim 20 \mu\text{m}$ [2]. Therefore, the stress and thermal confinement conditions are satisfied, and the methods of classical PA imaging can be used. Figure 1 shows an example of the monofilament PA tomogram.

Fig. 1. The 2D PA image of the monofilament and its 1D cross-section through the point with maximum amplitude. The full width at half maximum (FWHM) of the image is $66 \pm 6 \mu\text{m}$, which corresponds to the Gaussian PA source with the FWHM of $55 \pm 7 \mu\text{m}$. The FWHM of the filament, estimated from the single-shot darkening of photographic plates was $58 \pm 6 \mu\text{m}$.

PA tomography can be used to estimate the position and width of the plasma column of the monofilament with an accuracy of $\sim 10 \mu\text{m}$ in water [2]. The spatial resolution of this method is limited by acoustic attenuation in the medium and the size of the sensors [3]. In addition, due to linear and non-linear light absorption in the medium, PA tomography may be used to visualize the electromagnetic energy reservoir of the filament, which contains $\sim 90\%$ of the laser pulse energy [4].

Current research has focused on the use of PA tomography for characterization of multi-filamentation, where the distance between individual filaments is $\sim 10 \mu\text{m}$, and super-filamentation, where the energy deposition is so high that the approximation of linear acoustics may not be valid. It will be shown that PA response and PA images of the filament can be used to determine the peak energy deposition in different regimes (mono-, multi- and super-) of filamentation.

Acknowledgements

The reported study was funded by RFBR according to the research project No. 18-32-00696, The image reconstruction algorithm was developed under the funding of NUST MISIS Competitiveness Program by the Ministry of Education and Science of the Russian Federation (K2-2019-004).

References

1. A. Couairon, A. Mysyrowicz, Physics Reports 441 (2–4), 47 (2007) doi:10.1016/j.physrep.2006.12.005
2. F.V. Potemkin, E.I. Mareev, B.V. Rumiantsev, A.S. Bychkov, A.A. Karabutov, E.B. Cherepetskaya, V.A. Makarov, Laser Physics Letters 15 (7), 075403 (2018) doi:10.1088/1612-202X/aabc99
3. A.S. Bychkov, E.B. Cherepetskaya, A.A. Karabutov, V.A. Makarov, Laser Physics Letters 13 (8), 085401 (2016) doi: 10.1088/1612-2011/13/8/085401
4. F.V. Potemkin, E.I. Mareev, B.V. Rumiantsev, A.S. Bychkov, A.A. Karabutov, E.B. Cherepetskaya, V.A. Makarov, Journal of Physics: Conference Series 1141, 012060 (2018) doi: 10.1088/1742-6596/1141/1/012060

Time Domain Photoacoustics: Transient Signals Measured with Solid-Gas-Microphone Detection

Dragan M. TODOROVIC ^{(1)*}, Dragan D. MARKUSHEV ⁽²⁾,
Katarina RADULOVIC ⁽³⁾, Vesna JOVIC ⁽³⁾

1. IMSI, University of Beograd, K. Viseslava 1, 11030 Beograd, Serbia

2. Institute of Physics, University of Belgrade, Pregrevica 118, 11080 Belgrade-Zemun, Serbia

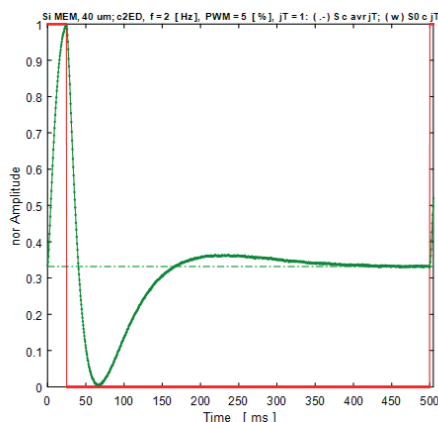
3. IHTM, University of Beograd, Njegoseva 12, 11000 Beograd, Serbia

dmtodor@afrodita.rcub.bg.ac.rs

Photoacoustic (PA) effect is suitable for the development of experimental non-contact and non-destructive methods and allows examining the optical, thermal, carrier transport and elastic characteristics of microstructures [1].

PA signals versus the time (optical pulse excitation) were measured and analyzed for thin Si square membranes (thickness 30 – 80 μm). The PA amplitude of the membranes was measured by using the PA cell with the solid-gas-microphone (SGM) detection configuration. The SGM detection has enabled the development of a range of measurement techniques and specific fields of application (PA spectroscopy, PA microscopy, PA non-destructive material evaluation, PA solid material, thin film, multilayer and microstructure characterizations, etc). The experimental PA signals of the Si membranes were measured by using the SGM detection technique with transmission configuration. The sample is optically excited at one side, and the acoustic response (PA signal) in the gas which is in contact with the sample is detected with a microphone on the opposite side of the sample.

The experimental setup consists of an Optical & Acoustical part (optical source, PA cell) and Signal processing & Control unit (modulator, digital acquisition system and computer). The samples were excited by an electronically modulated high power LED (the wavelength ~ 630 nm).



PA measuring conditions: optical pulse excitation - pulse period, $T = 500$ ms; pulse width, $T_w = 24.512$ ms; Time resolution, $T_{res} = 0.5$ [ms]; digital acquisition: number of samples, $N_s = 10000$ samples; scan duration, $T_s = 5000$ ms; scan rate, $F_s = 2000$ sample/s; samples / periode, $N_{sT} = 1000$ samples. Each experimental signal is the averaged result of at least three measurements.

Fig. 1 shows typical normalized experimental signals (optical excitation pulse and PA amplitude) for Si membrane. Normalized signal is defined as $(S_{max} - S_{min}) / S_{max}$, where S_{max} and S_{min} are signal maximum and minimum, respectively.

Fig. 1. Normalized experimental PA amplitude versus time for Si membrane (Si chip, $<100>$, frame 5×5 mm, square membrane $\approx 3.0 \times 3.0$ mm, 40 μm thick), excited with 24.5 ms optical square pulse: (· red) optical signal; (* green) PA signal; (-.-) mean value of the PA signal. Normalized signal is defined as $(S_{max} - S_{min}) / S_{max}$, where S_{max} and S_{min} are signal maximum and minimum, respectively.

An analysis of the experimental results shows that in the observed case the PA response is established (reaches its maximum) after about $T_{max1} = T_w = 24.5$ ms. During this time, while the optical excitation is switch on, the PA signal increases with rise time, $T_{rise1} = 14.85$ [ms]. Subsequently, when optical excitation is switched off, the PA signal is relaxed with a complex time function. The PA signal rapidly decreases (with fall time $T_{fall} = 11.23$ ms) from its maximum to minimum value after approximate $T_{min} = 65.0$ ms. Then, the PA signal increases again and after $T_{max2} = 235$ ms, it reaches a new lower maximum (with rise time, $T_{rise2} = 84.25$ ms). Finally, the signal decreases slightly so that after time $T_{mean} = 470$ ms, it will reach its mean value. The mean PA signal value is statistically determined and corresponds to a third of the maximum signal value.

Theoretical model for optically (square-pulse) excited thin semiconductor elastic plate, which includes thermodiffusion, plasmaelastic, and thermoelastic mechanisms, is given in order to study the experimental time-dependent PA signals.

References

1. D. M. Todorovic, M. D. Rabasovic, D. D. Markushev, V. Jovic, K. T. Radulovic, Int. J. Thermophys, 33, 2222 (2012).

Hypersound scattering by silica nanoparticles in water probed by picosecond opto-acoustics

Bertrand AUDOIN^{(2)*}, Marie-Fraise PONGE⁽¹⁾, Liwang LIU⁽²⁾, Serge RAVAINÉ⁽³⁾

1. Bordeaux INP, Physical Acoustics Department, I2M, CNRS UMR 5295, Talence, France,

2. University of Bordeaux, Physical Acoustics Department, I2M, CNRS UMR 5295, Talence, France

3. University of Bordeaux, CRPP, CNRS UMR 5031, Pessac, France

bertrand.audoin@u-bordeaux.fr

Picosecond ultrasonics (PU) enables the mechanical characterization of transparent media by means of the time-resolved Brillouin oscillations.^{1,2} However, when the sample of interest has to be kept in a liquid medium during experiments, the acoustic wave front propagates through the sample-liquid interface, and measurements can be hampered by the strong Brillouin scattering in the surrounding liquid. This is notably critical when probing the elastic properties of live cells since the Brillouin frequencies in the sample is very close to that of the culture medium.³ In this work, we propose the use of silica nanoparticles to discriminate the Brillouin oscillations in a soft transparent medium immersed in water.

The PU technique is based on the interaction of a probe light beam with a propagating acoustic wave. Two femtosecond lasers with slightly different repetition rates generate and probe the acoustic waves in the GHz range. By heating the bottom of a metallic transducer, the pump beam generates ultrashort acoustic waves. The probe beam is focused at the top of the transducer and faces exactly the pump beam.⁴ We consider silica beads sedimented in water. The size of the beads is chosen so that the frequency of their acoustic resonance matches the Brillouin frequency for water at the probe wavelength. As a result, there is no coherent acoustic propagation in water at this frequency and consequently no Brillouin oscillations. The phenomenon is enhanced by the high contrast of acoustic impedance between silica and water. Moreover, the refractive index for silica is close to that for water at the probe wavelength and there is no diffusion of the probe light due to the beads.

We have first demonstrated that when a sapphire/titanium transducer is immersed in water, nanoparticles cause a large decrease of the spectrum amplitude at the Brillouin frequency for water. In a second configuration, a layer of a transparent medium covers the optoacoustic transducer. The addition of nanoparticles attenuates the Brillouin oscillations in water, whereas the Brillouin signature for the transparent medium remains unaffected.

Acknowledgements

Authors acknowledge financial support from the Agence Nationale de la Recherche (grant ANR-17-CE11-0020-01), from the Region Nouvelle-Aquitaine (grant 2016-1R-60301) and from Université de Bordeaux.

References

1. C. Thomsen, H. T. Grahn, H.J. Maris, and J. Tauc, *Optics comm.* 60, 55 (1986).
2. V. Gusev and P. Ruello, *Appl. Phys. Rev.* 5, 031101 (2018).
3. C. Rossignol, C. Nikolay, M.-C. Durrieu, B. Audoin, F. Guillaume, and M.-C. Durrieu, *Appl. Phys. Lett.* 93, 123901 (2008).
4. T. Dehoux and B. Audoin, *J. Appl. Phys.* 112, 124702 (2012).

KEYNOTE

Radiative Memristor Based on The Thermal Hysteresis of VO₂

Jose ORDONEZ-MIRANDA ^{(1)*}, Younès EZZAHRI ⁽¹⁾, Jose A. TIBURCIO-MORENO ⁽²⁾,
Karl JOULAIN ⁽¹⁾, Jérémie DREVILLON ⁽¹⁾

1. Institut Pprime, CNRS, Université de Poitiers, ISAE-ENSMA, F-86962 Futuroscope Chasseneuil, France

2. Universidad Nacional Jorge Basadre Grohmann, Facultad de Ciencias,
Av. Miraflores s/n, Ciudad Universitaria, Tacna, Perú

jose.ordonez@cnsr.pprime.fr

Based on the thermal hysteresis of a phase change material exchanging radiative heat with a phase invariant one, we propose a radiative thermal memristor (Fig. 1(a)) characterized by a Lissajous curve between their exchanged heat flux and temperature difference periodically modulated in time (Fig. 1(b)). For a memristor with terminals of VO₂ and a blackbody, it is shown that: (i) the temperature variations of its memristance follow a closed loop determined by the thermal hysteresis width of VO₂, (ii) The thermal memristance on/off ratio is determined by the contrast of VO₂ emissivities for its insulating and metallic phases and is equal to 3.59. The analogy of the proposed memristor to its electrical counterpart makes it promising to lay the foundations of the thermal computing with photons.

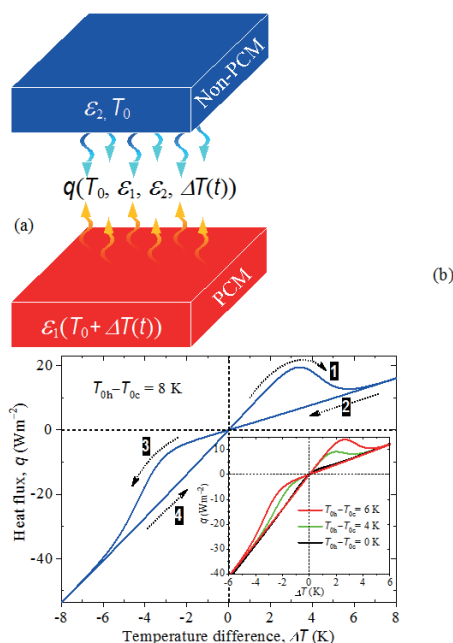


Figure 1: (a) Scheme of a radiative thermal memristor: a PCM exchanging radiative heat with a non-PCM through a vacuum gap, due to their temperature difference $\Delta T(t) = 8 \sin(2\pi \nu t)$ periodically modulated in time t . (b) Lissajous q vs ΔT curve characterizing the thermal memristor. Calculations were done for four hysteresis widths $T_{0h} - T_{0c}$.

Improved QTF preamplifier for QEPAS applications

TOMASZ STARECKI*, Piotr Z. WIECZOREK

Warsaw University of Technology, Institute of Electronic Systems, Nowowiejska 15/19, 00-665 Warsaw, POLAND

t.starecki@ise.pw.edu.pl

The quartz enhanced photoacoustic spectroscopy (QEPAS) is a very sensitive spectroscopic technique, in which detection of the gas absorption induced with a laser is performed with a quartz tuning fork (QTF) [1-4]. Preamplifiers for piezoelectric sensors are implemented as voltage amplifiers or charge / transimpedance amplifiers [5]. Until recently, all the QTF amplifiers dedicated for the QEPAS were based on a transimpedance configuration. However, it can be easily proved that properties of the preamplifier can be substantially improved if it is implemented in the voltage configuration. Preliminary measurements of the QTF preamplifier implemented in both mentioned configurations (voltage and transimpedance) showed, that the signal produced in the voltage amplifier configuration is over one order of magnitude higher than a signal from the transimpedance circuit [6]. In addition, evaluation of the signal-to-noise ratio (SNR) performed in the neighborhood of the QTF resonant frequency showed that the voltage configuration has the highest SNR, which is important, taking into consideration that the QEPAS technique is typically used in low concentration measurements.

Signal to Noise Ratio (SNR) is a major factor that limits the sensitivity of QEPAS sensors. The higher is the electrical signal level compared to the noise amplitude, the lower concentration of gases can be detected. For this reason, the preamplifier circuits used in QEPAS should be optimized for the low-frequency narrow-band applications. Moreover, special care should be taken when choosing a particular operational amplifier in either transimpedance or voltage (differential) configuration. It turns out, that depending on the preamplifier topology different operational amplifier noise parameters should be carefully considered when the highest possible SNR of the whole QEPAS system is required. In the presentation, we will discuss operation of the sensor in both (i.e. transimpedance and voltage) configurations and in particular we will analyze the influence of the operational amplifier characteristics on noise properties of the preamplifiers dedicated for QEPAS applications.

References

- [1] P. Patimisco, G. Scamarcio, F.K. Tittel, V. Spagnolo "Quartz-enhanced photoacoustic spectroscopy: A review." *Sensors* 14, 6165–6206 (2014).
- [2] A.A. Kosterev, Y.A. Bakhrkin, R.F. Curl, F.K. Tittel, "Quartz-enhanced photoacoustic spectroscopy." *Opt. Lett.* 27, 1902–1904 (2002).
- [3] A.A. Kosterev, F.K. Tittel, D.V. Serebryakov, A.L. Malinovsky, I.V. Morozov, "Applications of quartz tuning forks in spectroscopic gas sensing." *Rev. Sci. Instrum.* 76, 043105-1–9 (2005).
- [4] A.A. Kosterev, L. Dong, D. Thomazy, F.K. Tittel, S. Overby "QEPAS for chemical analysis of multi-component gas mixtures." *Appl. Phys. B* 101, 649–659 (2010).
- [5] T. Starecki, "Analog front-end circuitry in piezoelectric and microphone detection of photoacoustic signals" *Int. J. Thermophys.* 35, 2124-2139 (2014).
- [6] T. Starecki, P. Z. Wieczorek "A high sensitivity preamplifier for quartz tuning forks in QEPAS (Quartz Enhanced PhotoAcoustic Spectroscopy) applications" *Sensors* 17, 2528 (2017).

QEPAS sensor with radial and longitudinal acoustic resonators

Maxime Duquesnoy ^{(1,2)*}, Guillaume Aoust ⁽¹⁾, Jean Michel Melkonian ⁽²⁾, Raphaël Levy ⁽²⁾,
Myriam Raybaut ⁽²⁾, Antoine Godard ⁽²⁾

1. Mirsense, Nanno-INNOV, building 863, 8 Avenue de la Vauve, 91120 Palaiseau, France

2. DPHY, ONERA, Université Paris Saclay, F-91123 Palaiseau, France

maxime.duquesnoy@mirsense.com

We present a quartz enhanced photoacoustic sensor based on a custom quartz tuning fork associated with different acoustic devices to enhance the sensitivity. We study the influence of the addition of different types of acoustic resonators, on the signal-to-noise ratio, quality factor and frequency, through finite element simulations together with analytical modeling. The studied resonators are longitudinal dual tube resonators used with or without an acoustic recovery cavity. We also propose the study of a new acoustic resonator configuration for QEPAS consisting in an acoustic radial mode.

Motivation

Over the last decades, photoacoustic detectors were designed using microphones placed in acoustic resonators [1, 2]. In 2002, a new technology emerged – called quartz enhanced photoacoustic spectroscopy (QEPAS) – using quartz tuning forks (QTF) instead of microphones for acoustic detection [3].

In classical PAS many works have already been conducted to determine the optimal geometry of the acoustic resonators to reach the best sensitivity [2] (Figure 1a). In QEPAS, an acoustic resonator can be used to enhance the sensitivity, usually taking the form of tubes placed on each side of the QTF, inside which the laser passes. It is called on-beam configuration (Figure 1b). Surprisingly, there has been very little deviation from the longitudinal resonator geometry for QEPAS.

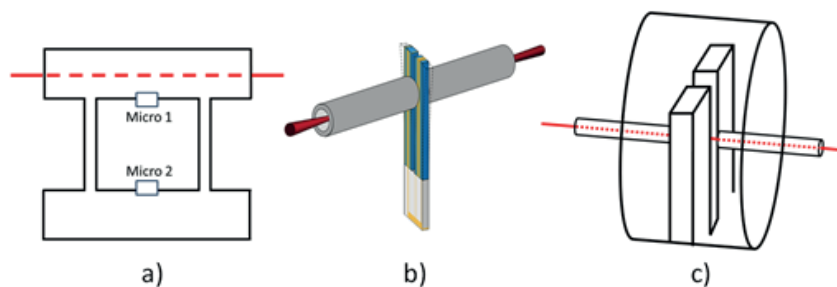


Fig. 1. (a) Schematic of a differential Helmholtz resonator with microphones [4]. (b) Schematic of a QEPAS sensor in on-beam configuration, the tuning fork is surrounded by two longitudinal acoustic resonators in which the laser passes. (c) Schematic of our custom tuning fork with adapted longitudinal resonators as well as a cylindrical cavity for acoustic recovery.

Our work

We recently presented a custom QTF with adapted acoustic resonators [5, 6] (schematic in Figure 1c). This QTF, optimized to present the best quality factor in air at atmospheric standard conditions, is associated with an acoustic recovery cavity in order to avoid the important acoustic losses that would occur due to the emission of acoustic waves by the QTF's prongs. In order to enhance its sensitivity in a QEPAS experiment, the recovery cavity is coupled with adapted on-beam longitudinal resonators, enhancing the quality factor from 8000 to 75 000.

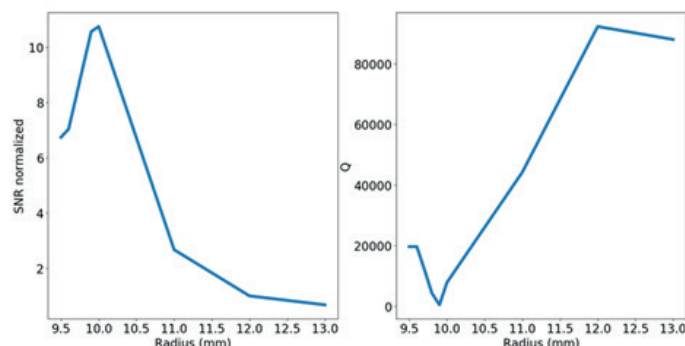


Fig. 2. Study of the influence of the resonator's radius on the system's signal to noise ratio and quality factor. The SNR is normalized with the SNR obtained at the best quality factor (radius equal to 12.5 mm).

Session E3: Instrumentation

We now propose a new configuration for our custom QTF (similar to Figure 1c), where the acoustic cavity is made resonant through adaptation of its design. This resonator was modelled through finite element simulations to study the influence of its geometry on the sensor's response (Figure 2). An optimal coupling with the QTF is obtained by modifying the resonator's radius, enhancing the signal-to-noise ratio by a factor ten compared to our previous non-resonant cavity.

We will provide a comparison of the key parameters – Q, SNR, frequency – of our sensor with both acoustic resonators. We will show how to design the system to obtain a better coupling between acoustical and mechanical resonances.

Acknowledgements

M.D.'s PhD grant was funded by MirSense and Association Nationale de la Recherche Technologique. The project was partially funded by the FCS Campus Paris-Saclay under grant 2014-0455I (MICSI).

References

1. Jr. D.F. Dewey, R.D. Kamm, et C.E. Hackett. (1973) <https://doi.org/10.1063/1.1654774>
2. B. Kost, B. Baumann, M. Germer, M. Wolff, et M. Rosenkranz. (2011) <https://doi.org/10.1007/s00340-010-4170-z>
3. A. A. Kosterev, Y. A. Bakirkin, R. F. Curl, et al. (2002) <https://doi:10.1364/OL.27.001902>
4. V. Zeninari, R. Vallon, C. Risseret B. Parvite (2016). <https://doi.org/10.1007/s10765-015-2018-9>
5. G. Aoust, R. Levy, B. Verlhac, et O. Le Traon. (2018) <https://doi.org/10.1016/j.sna.2017.12.026>
6. M. Duquesnoy, G. Aoust, J.M. Melkonian, R. Lévy, M. Raybaut, et A. Godard (2019) <https://doi.org/10.3390/s19061362>

Laser and Acoustic Radiation Input and Output Devices for Optoacoustics

Vladimir PETROV

Saratov State University, Saratov, Russia

petrovvv@info.sgu.ru

The main part of optoacoustic analytical system is the set of elements that provide the laser energy input to investigating media and excited acoustical energy reception for further analysis. The configuration of these elements depends on the destination and the task that are required and expected from optoacoustic system. For example, when investigating the cancer tumor in woman breast the laser pulse is directed by angle scanning to the breast body in the framework of “therapeutic window” spectral area. At the same time the set of acoustical sensors are situated surrounded and at the surface on the breast body, receiving the side lobes of ultrasonic radiation. But in many practical cases it is required to analyze the backside ultrasonic waves radiated immediately after laser pulse acting and closed to the area of sound excitation. Such situation might take place when for example investigating the cancer blood particles in the vessels closed to the skin surface. The wedge shape optical beam having fast repetition time over covers the cross section of blood vessel. So, when the optical beam is crossed by high absorption black cancer particle the ultrasonic reply is excited and is registered by ultrasonic lens sensor.

In present report the variants of coaxial configuration of optical and acoustical system for photo acoustical investigation are discussed. The main idea of such optoacoustic geometry based on the fact that the angular spectrum of wave radiation or reception by round shape antenna is much differ in two cases: if the antenna has the disc shape and if the antenna has ring shape. In the last case the amplitude zero order lobe of directivity diagram occurs about 10% higher in comparison to zero order lobe of disc shape antenna, but second order side lobes of ring shape antenna on about 10% less than second order side lobes of disc shape antenna. That fact allows providing the crystal sound conductor having the ring shape piezo transducer on the one butt end and the acoustical lens on another butt end by cylindrical tube channel on the axis of ultrasonic sound conductor. This channel might serve for several aims: 1) to deliver immersion liquid to opto acoustical interaction area; 2) to channelize the optical radiation from laser right to investigating area; 3) to place the optical lens directly into the channel that could be combined with acoustical lens so that to provide optoacoustic process in minimal geometrical area with coincided optical and acoustical focuses.

Based on above mentioned approach the series of optoacoustic devices where developed and patented.

Some of experimental realizations of different construction of suggested optoacoustic devices geometry in present report are discussed.

Terahertz Acoustic Parametric Oscillator

Thomas Edward WILSON

Department of Physics, Marshall University, One John Marshall Drive, Huntington, WV 25701 USA

wilsons@marshall.edu

A narrowband coherent source of acoustic phonons of either polarization could find widespread applications in science and technology [1]. We report experimental evidence for a 1.0 THz self-starting mirrorless acoustic phonon parametric oscillator (MAPPO) in a doping superlattice (DSL) structure pumped by nanosecond-pulsed 1.0 THz laser radiation [2]. It is based upon acousto-optic (AO) phase-conjugate degenerate four-wave mixing (D4WM) of counter-propagating fields [3]. Coherent nanosecond-pulsed THz compressional and shear waves with different pumping thresholds were observed. We have designed the DSL period to provide spatially-distributed feedback. The DSL [4] was grown by molecular beam epitaxy on a (100)-oriented boron doped silicon substrate. Superconducting granular aluminum bolometric detection, coupled with Si:B piezophonon spectroscopy, revealed excitation of THz coherent longitudinal acoustic (LA) and transverse acoustic (TA) phonons, along the $\langle 111 \rangle$ direction only. The Bragg condition for distributed feedback, and the energy conservation requirement for the D4WM process, were both verified. The delta-doped DSL [5] consisted of 30 n-i-p-i sequences of period $d = 8.1$ nm with B and Sb doping levels $N^{2D} = 3.3 \times 10^{13} \text{ cm}^{-2}$. The smallest subband energy level spacing in the V-shaped potential wells for both electrons and holes is of order 50-meV in our DSL, much larger than the 4.3-meV pump radiation. Accordingly, the AO D4WM process should lie in the reactive regime [6] where the frequency of the far-infrared (FIR) laser pump radiation is below the onset of absorption by electronic transitions in the DSL. Electrostriction-coupling is posited to result from the direct action of the electric field acting upon the ion sheets of the DSL. The experimental arrangement is shown in Fig. 1(left). We use a superconducting NbTiN sub-wavelength grating-coupler (period 10- μm) to convert the incident pump radiation into counter-propagating evanescent surface waves within the DSL, and a superconducting Al bolometer for both photon and phonon detection. The Si substrate was boron doped at a density of $N_B = 10^{15} \text{ cm}^{-3}$ to allow Si:B piezophonon spectroscopy [7]. Fig.1 (right) illustrates schematically our posited 1.04-THz D4WM process. Fig. 2(left) shows a stacked sequence of digitized bolometer traces (signal versus time) in response to single laser pulses of progressively increasing power. The first pulse observed (at 0-ns) in all traces is the bolometer response to the arrival of undiffracted grating-coupled FIR laser radiation. As the laser radiation pump power reaches a threshold power of 6.4-mW, ballistic $\langle 111 \rangle$ LA phonons appear at a delay time of 110 ± 2 ns. As the incident FIR power increases further, the LA signal at the 110-ns delay grows progressively stronger, and at a 8.8-mW pump power, a second $\langle 111 \rangle$ TA signal appears at 210 ± 2 ns. The observed phonon signal delays agree with calculated transit times, 110-ns and 203-ns for $\langle 111 \rangle$ LA and TA phonons, respectively, across the 0.6 mm thick Si substrate. Fig. 2(right) shows phonon spectra acquired by the Si:B-spectrometer. The LA and TA phonons are observed at 4.3-meV (1.0-THz), yielding evidence for energy conservation for the D4WM process. Estimates for the LA peak power, phonon occupation number, and strain were $10 \mu\text{W}$, 10^8 , and 10^{-4} , respectively for a FIR pump power 10 mW in a 5 ns duration.

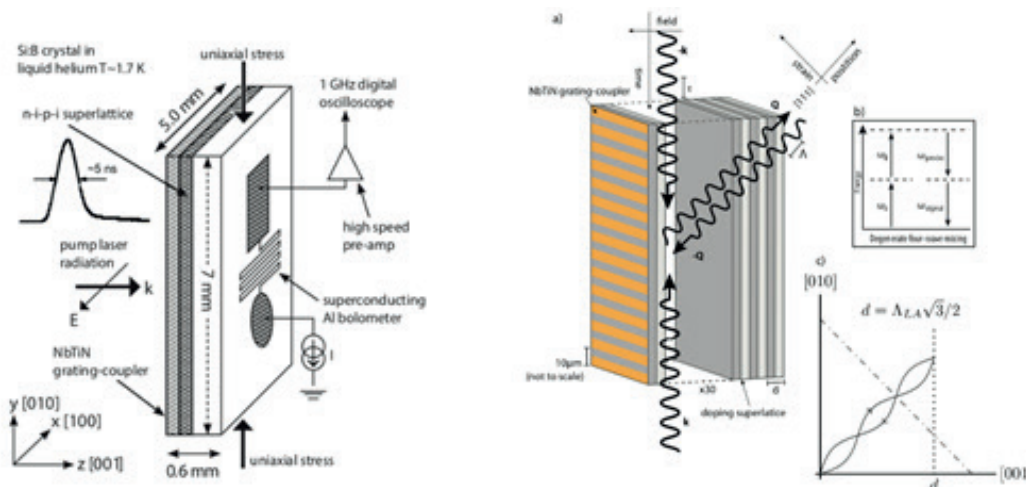


Fig. 1. (Left) Schematic diagram of experimental arrangement. Thicknesses of grating-coupler and DSL (crosshatched) not to scale. THz pump laser radiation incident from left with wavevector k , E-field, and typical digitized pulse envelope shown. (Right) (a) Schematic diagram of MAPPO showing k - k evanescent electromagnetic fields, and $\langle 111 \rangle$ -directed Q-Q (PC) acoustic fields. (b) Energy conservation diagram for D4WM (c) Distributed feedback phase-matching, projected onto (100) plane, results in a standing LA wave (solid lines) for Q-Q. DSL (dotted line) of period d . Gain grating (dash-dotted line) shown. LA wavelength: Λ_{LA}

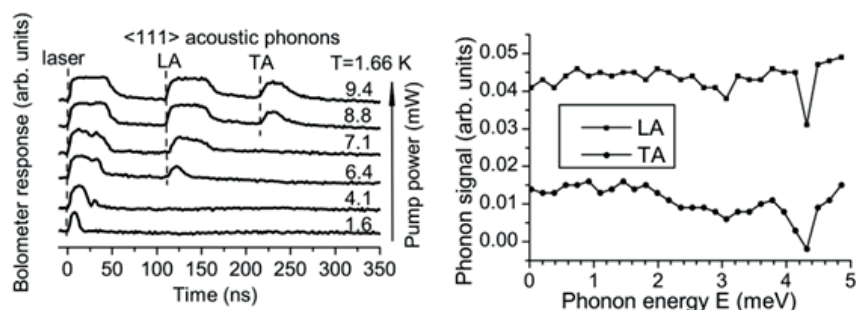


Fig. 2. (Left) Stacked sequence of digitized bolometer signals (arb. units) for increasing (estimated) pump power (mW) listed above traces. (Right) Resonant scattering from Si:B spectrometer indicating 4.3-meV energy for both LA (top) and TA (bottom) phonons.

A self-starting MAPPO operating at 1.04 THz and providing TA and LA phonons may prove useful both as a source (and detector [8]) for probing material properties at the nanoscale, and to provide a testbed for studies of non-classical acoustic phonon fields.

References

1. D. G. Cahill, P. V. Braun, G. Chen, D. R. Clarke, S. Fan, K. E. Goodson, P. Keblinski, W. P. King, G. D. Mahan, A. Majumdar, H. J. Maris, S. R. Phillpot, E. Pop, and L. Shi, *Appl. Phys. Rev.* 1, 011305-1-46 (2014) doi:10.1063/1.4832615
2. T. E. Wilson, *Int. J. Infrared Millimeter Waves* 14, 303-310 (1993) doi:10.1007/BF02282072
3. A. Yariv and D. M. Pepper, *Opt. Lett.* 1, 16-18 (1977) doi:10.1364/OL.1.000016
4. G. H. Dohler, *Crit. Rev. Solid State Mater. Sci.* 13, 97-141 (1986) doi:10.1080/01611598608241264
5. H.-J. Gossmann and E. F. Shubert, *Crit. Rev. Solid State Mater. Sci.* 18, 1-67 (1993) doi:10.1080/10408439308243415
6. C. Flytzanis, in *Nonlinear Acoustics – Fundamentals and Applications: 18th International Symposium on Nonlinear Acoustics – ISNA 18*, edited by B. Enflo, C. M. Hedberg, and L. Kari, AIP Conf. Proc. Vol. 1022 (AIP, Melville, NY, 2008), p. 471
7. M. Schwarte and P. Berberich, *J. Phys. C: Solid State Phys.* 18, 3225-3229 (1985) doi: 10.1088/0022-3719/18/16/017
8. D. Rogovin, *Phys. Rev. A* 41, 6805-6812 (1990) doi:10.1103/PhysRevA.41.6805

Multi-laser-based photoacoustic system using double-phase synchronous detection

Ricardo DÍAZ FUENTES*, Suren STOLIK ISAKINA, Alma Rosa VALOR REED,
José Manuel DE LA ROSA VÁZQUEZ

Instituto Politécnico Nacional, Higher School of Mechanical and Electrical Engineering (ESIME), Zacatenco Unit, Biophotonics Laboratory, Mexico City, Mexico.

rdiazfuentes90@gmail.com

The optical absorption coefficient is a measure of how much the electromagnetic radiation of a certain wavelength can penetrate a material before being absorbed. This magnitude depends on the material properties and on the wavelength of the incident light. It is a very important tissue property, which has to be known for the accurate planning of phototherapy treatments; since the effectiveness of this type of therapies depends on the absorption of light by the tissue to be treated. Therefore, this magnitude must be accurately studied to achieve the desired results with a proper dosimetry.

This work presents the design and construction of a photoacoustic system that allows the measurement of optical absorption coefficients of a certain substance when it is exposed to modulated light of several wavelengths.

The device is based on the photoacoustic effect, according to which, when modulated light is absorbed by a material enclosed in a cavity containing a gas, a pressure wave of the same frequency as that of the light modulation is generated. This wave is the result of periodic absorption processes and subsequent heating of the sample and the surrounding gas within the cell. The measurement of the absorption coefficient is possible due to the fact that the pressure produced inside the photoacoustic cell is directly proportional to the optical absorption coefficient of the absorbing medium. The pressure wave can be detected using a microphone.

The proposed system consists of a cabinet, a photoacoustic cell, a laser array with its driver module, a module for temperature control of the lasers, a synchronous detection system, a control software, and a power source.

The system uses the method of synchronous double-phase detection to measure weak signals in environments with high levels of electromagnetic, luminous, and acoustic noise. This technique was implemented in a home-made excitation-detection module that avoids the use of expensive laboratory equipment such as a Lock-in Amplifier. This module is responsible for the generation of in-phase and quadrature signals and their subsequent demodulation after the pressure wave is detected. The sensing module is composed by an electret microphone and a preamp circuit that allow the detection of the photoacoustic signals. The microphone is mounted in an appropriate slot in the developed photoacoustic cell where the studied sample, solid or liquid, is also enclosed. The eight semiconductor lasers are mounted on a disk, pointing to a prism located in its center; the control system allows the irradiation of the sample with a modulated signal selected among eight different wavelengths. The system has a control module for eight different lasers, which allows the irradiation of the sample with a modulated signal at eight different wavelengths, as well as the selection of the laser to be used. The laser selection is carried out by means of a simple optical array that includes a rotating prism. The prism rotation movement is performed using a stepper motor which is controlled by means of a home-made control circuit. Also, Peltier cells were implemented to maintain a correct control of the lasers temperature, which is monitored throughout the measurements by a circuit that includes temperature sensors. The system has a power supply provides the different voltages used for each part of the system. The system uses a computer for data storage, while the control and communication interface has been developed using an Arduino Mega 2560 and the LabVIEW platform.

Every part of the system was properly characterized with respect to its stability and response at the different working frequencies. Several measurements were performed on phantoms to evaluate the system performance at modulation frequencies of 30 Hz, 100 Hz, 500 Hz, 1000 Hz and 2000 Hz. The preliminary results are presented and discussed.

Investigation of EM-free audible sound producing based on photoacoustic effect

Bengi Derya MUSDAL*, Mustafa KURT

Department of Phsyic, Çanakkale Onsekiz Mart University, 17100 Çanakkale, Turkey

bengiderya.musdal@gmail.com, mkurt@comu.edu.tr

The ability to transfer audible sound lacking any electronic apparatus which effect to human brain will open up many innovative possibilities: e.g., EEG (Electroencephalography) sound module. The modulated optical signal can be converted into an audible signal occurs via the absorption of light by the specific molecules. When the specific molecule is irradiated with IR light, the atomic bound of the molecule is vibrated and occurred a damping signal. If the damping signal is sufficiently high, the photoacoustic sound can be achieved. We design a cell which is filled with the highly IR resonant molecules and illuminate with modulated optical signal. The optical signal is transfered to cell from the source via optical fiber. Conceptually we achieved 50 – 80 dB (SPL) in our design.

Infrared Thermal Defect Detection of Fiber Metal Laminates Based on PCA-Morphological Algorithms

Chiwu BU ^{(1)*}, Guozeng LIU ⁽¹⁾, Xibin ZHANG ⁽¹⁾, Qingju TANG ⁽²⁾

1. College of Light Industry, Harbin University of Commerce, Harbin, 150028, China

2. School of Mechanical Engineering, Heilongjiang University of Science and Technology, Harbin, 150022, China

buchiwu@126.com

Fiber-reinforced metal laminates have been widely used in aerospace, supersonic vehicle, nuclear power, rail transit and other fields due to their excellent fatigue damage tolerance, impact resistance, corrosion resistance, high flame retardancy and easy processing. The fabrication conditions of fibre metal laminates are complex and the service environment is harsh. It is easy to produce defects such as overall cracking, uneven curing or even breaking of fibers, debonding of fibers and substrate, which will directly endanger the service life, operation safety and controllability of the equipment. Infrared thermal wave nondestructive testing technology has many advantages, such as safety, high efficiency, wide application fields, visual testing results, etc. It provides a new method for the detection of debonding defects of fibre metal laminates. A linear frequency modulation (LFM) excitation method for detecting debonding defects of fibre metal laminates was developed. Using halogen lamp as infrared thermal excitation source, infrared thermal imager collects infrared images of fiber metal laminates. Using pulse phase method (PPT), polynomial fitting and reconstruction are carried out first. After Fourier transform, the amplitude and phase maps are obtained, and the best amplitude maps are selected for comparative analysis. Then the amplitude map is processed by discrete cosine transform (DCT) to reduce the noise interference. Finally, the infrared image is processed by expansion and corrosion using the PCA (principal component analysis) - morphology algorithm to obtain the edge recognition of the defect of the fiber metal laminate. The results are compared with those obtained by Canny, LOG, Robert and other classical edge recognition operators. It is verified that the PCA-Morphology algorithm has more edge recognition ability and can improve the infrared detection ability of the defects in fibermetal laminates.

Theoretical Study on Infrared Thermal Wave Imaging Detection of Semiconductor Silicon Chip Microcrack Defects

Qingju TANG ^{(1)*}, Shuaishuai GAO ⁽¹⁾, Yongjie LIU ⁽¹⁾, Chiwu BU ⁽²⁾

1. School of Mechanical Engineering, Heilongjiang University of Science and Technology, Harbin, 150022, China

2. College of Light Industry, Harbin University of Commerce, Harbin, 150028, China

tangqingju@126.com

As the main substrate material of integrated circuits, semiconductor wafers have become the semiconductor materials with the largest production scale, the largest single crystal diameter and the most complete production technology. Surface damage of silicon wafers can be divided into surface damage and subsurface damage. The surface damage mainly includes scratches, micro cracks, broken, orange peel and pits. The subsurface damage mainly includes amorphous layer, poly-crystalline layer and micro Cracks, dislocations, stacking faults, elastic distortions, and residual stresses. Surface/subsurface damage during semiconductor wafer processing will have a direct impact on the processing time and processing efficiency of the subsequent polishing process, due to the shallow surface damage of the silicon wafer and its crystallographic properties of the single crystal. Many conventional inspection techniques are not suitable for the study of wafer surface/subsurface damage. The micro crack defects detection of semiconductor wafers by infrared heat wave testing technology was studied under linear frequency-modulated laser excitation. The heat transfer process and temperature field distribution of semiconductor wafers with chirp modulation were studied. The numerical simulation analysis confirmed the time-frequency domain response characteristics of the thermal wave radar signal are analyzed. The influence of scanning period and laser power and defect geometry on the characteristics of thermal wave radar signals was analyzed. The results show that for the 10 μm wide micro crack, this test method can be theoretically detected. With the deepening of the crack defect depth, the larger the temperature difference between the two sides of the crack, the easier it is to be detected; as the crack width increases, the larger the temperature difference between the two sides of the crack, the easier it is to be detected. Under the condition that the semiconductor wafer not damaged twice and the performance of the detection system is allowed, the laser power can be used to identify the micro crack defects, and the scanning period has little effect on the crack detection on both sides of the semiconductor silicon micro crack. The results of this test play a major role in the surface/subsurface damage detection of semiconductor wafers, provide important technical support for the production of semiconductor wafers, and have broad application prospects. In addition, the research results can provide some reference and reference for other semiconductor materials, optical material damage and defect detection.

High Resolution Three-Dimensional Photoacoustic Microscopy based on Linear Frequency-Modulated Optical Excitation

Zahra Kavehvasht*, Seyed Masood Mostafavi, Mohammadreza Amjadian

Sharif University of Technology, Tehran, Iran

mosatafavi_sm@ee.sharif.edu, mohammadreza.amjadiang@ee.sharif.edu, kavehvasht@sharif.edu

Photoacoustic microscopy (PAM) is an emerging imaging modality where the variation in optical absorption coefficient of tissues is detected via ultrasonic transducers. Photoacoustic microscopy, even though having high lateral resolution, suffers from low depth of field (DOF). In an attempt to improve the DOF of PAM structure single pixel photoacoustic Fourier imaging has been proposed to achieve a 3D image with no mechanical scanning [2]. In this structure, each two-dimensional (2D) image at a specified depth is considered as a weighted sum of 2D sinusoidal light fringes with different frequencies [1]. Propagation-invariant sinusoidal fringes (PISFs) are generated in space by interference of two symmetrical tilted plane waves. In this method, a digital micro-mirror device (DMD) is utilized in order to steer the input optical beams in different inclination angles. Therefore, the effective wavenumber, $k_{eff} = k \cos \theta$, is being changed by θ . Because of the limited tilting angle of DMDs, the achievable range for k_{eff} would be limited resulting in loss of some spatial frequency components. This in turn would limit the spatial resolution and contrast of this structure.

In this work, the above limitation is overcome through employing a frequency-swept (chirped) optical excitation for producing the input sinusoidal fringe patterns instead of changing the beam angle via DMD. In this approach, the optical wavelength is continuously altered with time, like the structure presented in [3]. Change in optical wavelengths would result in variation of the frequency of sinusoidal fringes. Therefore, the effective wavenumber would cover a wider frequency bandwidth resulting in improved spatial frequency bandwidth and thus resolution of the captured image. The proposed single-pixel Fourier photoacoustic imaging structure with chirped optical excitation is shown in Fig. 1.

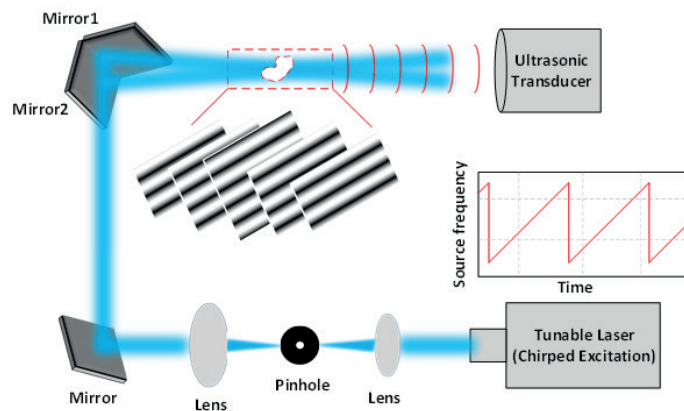


Fig 1. Schematic of the 3D Photoacoustic Microscopy based on Linear Frequency-Modulated Optical Excitation.

As an example, the DLP4500NIR DMD [4] tilts the beam angle in the range of ± 12 degree that yields a relative effective wavenumber bandwidth equal to 2.2 percent. In contrast, by using CF125 [5] as a tunable laser source in the proposed structure, k_{eff} relative bandwidth would be around 65 percent. This improved relative bandwidth results in better resolution of final reconstructed 3D image.

References

1. J. Yang, L. Gong, X. Xu, P. Hai, Y. Shen, Y. Suzuki, L.V. Wang, Nature communications 8, no. 1 (2017): 780, doi: 10.1038/s41467-017-00856-2.
2. Z. Zhang, M. Xiao, Z. Jingang, Nature communications 6 (2015): 6225, doi: 10.1038/ncomms722.
3. S. Telenkov, M. Andreas, L. Bahman, F. Michael, Journal of Applied Physics 105, no. 10 (2009): 102029, doi: 10.1063/1.3116136.
4. www.ti.com/product/DLP4500NIR
5. www.solinstruments.com/en/lasers/tunable-lasers/cf125/description



**POSTER
CONTRIBUTIONS**

FTIR Photoacoustic Spectroscopy for physicochemical analysis of a self-etch adhesive containing 10-MDP with dentin in noncarious cervical lesions

Mauro Luciano Baesso ^{(1)*}, Bruna Medeiros Bertol de Oliveira ⁽²⁾, Adriana Lemos Mori Ubaldini ⁽²⁾, Luis Humberto da Cunha Andrade ⁽³⁾, Sandro Márcio Lima ⁽³⁾, Marcelo Giannini ⁽⁴⁾, Luzmarina Hernandez ⁽⁵⁾, Renata Correa Pascotto ⁽²⁾

1. Physics Department, State University of Maringá, Maringá, PR, Brazil

2. Department of Dentistry, State University of Maringá, Maringá, PR, Brazil

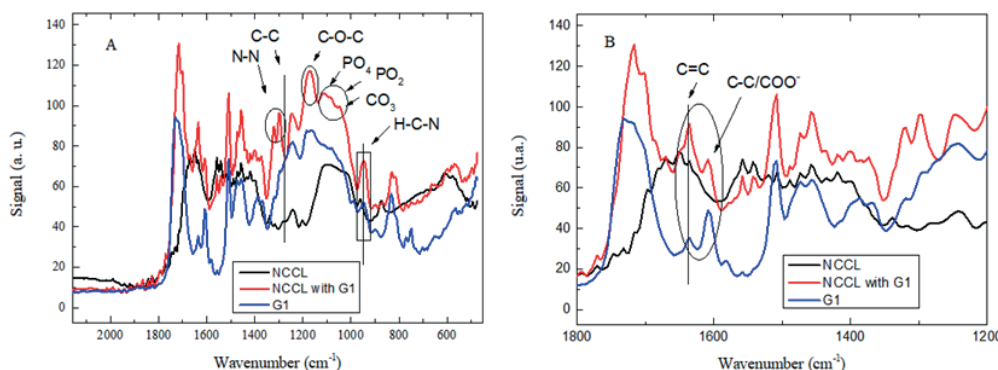
3. Physics Department, State University of Mato Grosso do Sul, Dourados, MS, Brazil

4. Department of Restorative Dentistry, UNICAMP, Campinas, SP, BR

5. Morphological Sciences Department, State University of Maringá, Maringá, PR, Brazil

*Email: mlbaesso@uem.br

The chemical interaction and morphology at the interface of self-etch adhesives and the dentin in noncarious cervical lesions depend on the functional monomer present in the adhesive. This fact is essential to evaluate the requirement for additional substrate preparation before adhesive procedures(1,2). It is well known that photothermal methods permit the identification of biochemical changes without the need for reagents or complicated sample preparation(3,4). This study aimed to evaluate the interaction of restorative adhesive system with dentin, especially the study of resin-dentin interfaces. The dynamics of materials setting, formation of chemical bonds and depth profile analysis will be discussed. FTIR Photoacoustic methods was used in the rapid scan mode to quantitatively analyse the formation of chemical bonds and depth profiling in adhesive-dentin restoration. Human teeth were used in order to investigate the chemical interaction between the restorative adhesive material and the dentin tissue with or without natural non-carious cervical lesions (NCLL) (Research ethics protocol:47305015.7.0000.0104). Specimens had their spectra measured with Fourier transform infrared photoacoustic spectroscopy (FTIR-PAS) before and after being submitted to the adhesive treatment. The experiments were performed with a Nicolet Spectrometer (MTEC Photoacoustics, Ames, USA) equipped with a MTEC 200 photoacoustic cell model. All spectra were collected at a resolution of 8 cm^{-1} , with scanning speed of 0.5 cm/s . The spectral region of the measurements was between 4000 and 400 cm^{-1} . Figure 1 illustrate the results for noncarious cervical lesions (NCCL) before and after application of the self-etch adhesive system containing the 10-MDP monomer (Clearfill SE Bond 2, Kuraray Noritake Dental Inc., Tokyo, Japan). Circles and bars indicate changes in spectra, suggesting chemical interactions between the dentin and the adhesive system. The detection of chemical bonds between adhesives and dentin has been shown to be a controversial topic in the literature. As a consequence, several techniques have been used in order to provide a better understanding of the involved chemical processes(5). This technique has been used before to investigate the occurrence of adhesive chemical bonds in dentin; exploring the finger print characteristics of the optical absorption bands in the infrared spectral region. It has already been demonstrated that the 10-MDP functional monomer present in the adhesive system used in this work is capable of forming chemical bonds with the hydroxyapatite (calcium salts-MDP), improving adhesion and the longevity of restorations (5). The FTIR-PAS analysis confirmed that the peak intensities related to the chemical interactions in health dentin tissue were similar to those in teeth with NCCLs. Considering that the lack of durability of dentin-resin bonding is still a challenge in clinical restorative dentistry, resulting in frequent restoration replacements due to its short lifetime, these analyses supplied important information since they detected chemical interaction between the dentin tissue and the adhesive system. The findings of this study may benefit dentistry clinical practice since the improvement



of chemical bonds on resin-dentin interface enhances the restoration stability.

Fig.1 Photoacoustic absorption spectra obtained from the adhesive and the NCCL before and after application of the adhesive system. (A) Spectral region $2100\text{-}550\text{ cm}^{-1}$, and (B) Spectral region $1800\text{-}1200\text{ cm}^{-1}$.

Acknowledgements

We are thankful to CNPq, CAPES, FINEP and Fundação Araucária for the financial support of this work.

References

1. B.M.B Oliveira A.L.M. Ubaldini, F. Sato, M.L. Baesso, A.C. Bento, L.H.C. Andrade, S.M. Lima , R.C. Pascotto. *Operative Dentistry*, 42(4), 357 (2017). doi:10.2341/16-062-L
2. B.M.B Oliveira A.L.M. Ubaldini, F. Sato, M.L. Baesso, A.C. Bento, L.H.C. Andrade, S.M. Lima , R.C. Pascotto. *Operative Dentistry*, 43(5), E253 (2018). doi:10.2341/17-366-L
3. W. Wang, A. Mandelis, J. *Biomedical Optics*, 21(6), 06618 (2016). doi:10.1117/1.JBO.21.6.066018
4. A.L.M. Ubaldini, M.L. Baesso, A.N. Medina, F. Sato, A.C. Bento, R.C. Pascotto. *J. Dent Res*, 92 (7), 661 (2103). doi:10.1177/0022034513488893
5. Y. Wang, X. Yao, R. Parthasarathy. *J Biomed Mater Res* 91 (A), 014020 (2009). doi:10.1117/1.2857402.

AP 002

Mechanobiological studies of ultrasound-mediated cell junction interruption using fluorescence super-resolution microscopy

Andriy CHMYROV *, Yu-Shan HUANG, Vasilis NTZIACHRISTOS

Institute for Biological and Medical Imaging, Helmholtz Zentrum München, 85764 Neuherberg, Germany

andriy.chmyrov@helmholtz-muenchen.de

The ability to spatiotemporally disassemble and re-assemble the intercellular adhesion allows the researchers and tissue engineers to break and build multicellular biosystems in a specific manner. Examples of clinical applications include a precise spatiotemporal modulation of tissue integrity through complete opening and recovery of cell junctions at the blood-brain barrier (BBB) for efficient drug delivery.

Although various kinds of strategies have been developed to facilitate the efficiency of drug delivery across the BBB to date, a safer and more efficient way is still desperately in need due to the complexity of the brain. Therefore, either too firm or too loose state of the cell junctions leads to the imbalances of the health conditions. To appropriately open and to stabilize the cell junctions are equally momentous from the therapeutic point of view.

One of the suitable tools for achieving this goal is the microbubble-engaged ultrasound irradiation. However, a clear understanding of the mechanism has been limited due to the complexity and the meticulous scale in the signal regulations and architectural changes therein.

Among the reasons that there are still many unanswered questions in the field is an insufficient spatial resolution of the images obtained. For instance, how the tight junction proteins redistribute due to the ultrasound irradiation is still unclear. The fluorescence super-resolution microscopy, which normally yields the lateral resolution in the 20~50 nm range, is an excellent tool to tackle this problem

Based on our expertise and experience in fluorescence super-resolution imaging, we plan to establish a multi-functional super-resolution imaging platform integrated with Stimulated Emission Depletion (STED) microscopy, soundwave, and microfluidic cell culture systems to investigate the spatiotemporal correlations between the molecular and architectural events in ultrasound-mediated TJ modulation.

LRSP- based structures for interferometric biosensing

Carlos G. MARTÍNEZ-ARIAS ⁽¹⁾, Jose R. GUZMAN-SEPULVEDA ⁽²⁾,
 Juan C. MARTINEZ-ESPINOSA ⁽³⁾, Daniel A. MAY-ARRIOJA ⁽⁴⁾, Miguel TORRES-CISNEROS ⁽¹⁾,
 Rafael GUZMAN-CABRERA ^{(1)*}

1. Applied Physics Group, College of Engineering, Universidad de Guanajuato, km 3.5 + 1.8 road Salamanca-Valle de Santiago, Salamanca, Guanajuato, MEX, 36730

2. CREOL, The College of Optics and Photonics, University of Central Florida, 4304 Scorpius St., Orlando, FL, USA

3. Instituto Politecnico Nacional-UPIIG, Guanajuato Puerto Interior, Silao de la Victoria, Guanajuato, MEX, 36275

4. Centro de Investigaciones en Óptica, Prol. Constitución 607, Aguascalientes, Ags. 20200, México

In this work, we present a numerical parametric study of an integrated Mach-Zehnder Interferometer (MZI), where one of the arms has been replaced by a Long Range Surface Plasmon Polariton (LRSP) waveguide, as is shown schematically in Figure 1(a). The rest of the structure of the MZI is all-dielectric, and it consists of waveguides made of the commonly used SU8 photoresist, which are embedded into a CYTOP host polymer matrix. Our structure is designed specifically for biologically relevant situations, where high-sensitivity sensing of refractive index in aqueous environments is critical for tracking small changes in the concentration of the suspended species.

Figure 1(b) shows in detail the region of the sensing arm having the LRSP waveguide. The waveguide itself consists of a thin stripe of gold [thickness ~35nm; see Figure 1(c)]. The thickness of the LRSP waveguide has been strategically chosen in order to balance the sensitivity and the losses [1]. The top cladding of the LRSP waveguide is removed in order to expose the waveguide to interact with the analyte, i.e., basically, the analyte plays the role of the top cladding of the LRSP. Due to the significant sensitivity of the mode supported by the LRSP waveguide to the optical symmetry of the claddings, small variations in the effective refractive index of the analyte can be detected. Figure 1(d) shows the intensity distribution of the mode supported by the LRSP waveguide, for the case of symmetric claddings.

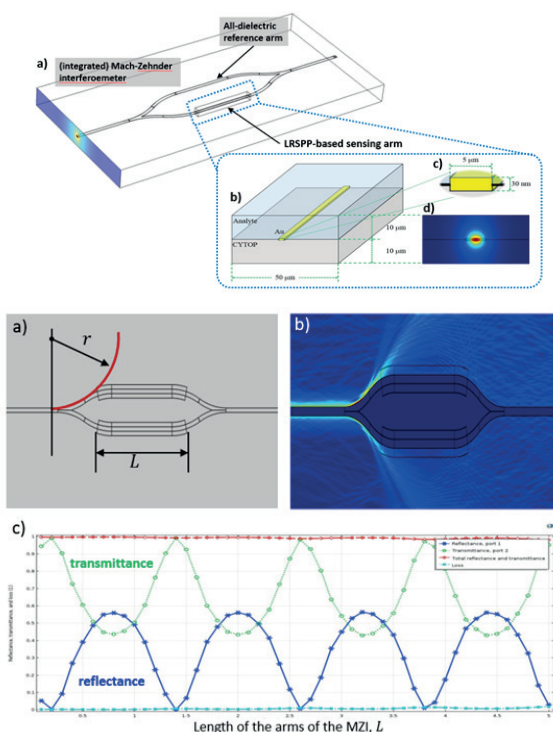
In the first stage of our parametric study, we focus our attention to the geometrical optimization. More specifically, we study the dependence on the length of the arms of the MZI, as well as the S-bend radius [see Figure 2(a)]. As a preliminary result, we show the reflectance/transmittance characterization as a function of the length of the arms of the MZI, i.e., as a function of the length of the LRSP waveguide, as indicated in Fig. 2. The simulations were performed using COMSOL Multiphysics®. The wavelength of operation in

the simulations is the telecom standard $\lambda_0 = 1550$ nm. For the simulations, the thickness of the top and bottom claddings was $15\mu\text{m}$ in all parts of the structure. The simulations were performed for an S-bend radius $r = 6.5$ mm; the curvature is set to be the same in both the input and the output of the device. The length of the arms of the MZI was varied in a range from 0.1 mm to 5mm [Figure 2(c)].

Fig. 1. (a) Schematic of the simulated device, consisting of a LRSP waveguide incorporated into the sensing arm of an integrated MZI. (b) Zoom-in into the sensing region. The top cladding of the LRSP waveguide is removed in order to expose the waveguide to interact with the analyte. (c) Dimensions of the LRSP waveguide. (d) the intensity distribution of the optical mode supported by the LRSP waveguide.

Fig. 2. Reflectance/transmittance of the device as a function of the length of the arms of the MZI. (a) The geometry of the simulation; r and L are the radius of curvature of the S-bend and the length of the arms, respectively. (b) A typical result of the intensity distribution. (c) transmittance (at the output port) and reflectance (at the input port) as a function of the length of the arms of the MZI.

In the complete study, which includes the dependence on the bending radius, we were able to find optimal geometries, with minimal losses and a suitable length, for which the contrast of the transmittance/reflectance response is maximum [see Fig. 2(c)]. This result is the best condition possible for interference, which is critical for sensing small changes in refractive index with high sensitivity.



A Biomedical Sciences and Biophotonics

Acknowledgements

The authors are indebted with Consejo Nacional de Ciencia y Tecnología (CB2016-286368), (CB2016-286629); Universidad de Guanajuato (CIIC 160/2019)

References

1. Martínez-Arias, C. G., Escobar, M. A., Guzman-Sepulveda, J. R., Torres-Cisneros, M., & Guzman-Cabrera, R. (2018, September). Biosensing using long-range surface plasmon structures. In *Biosensing and Nanomedicine XI* (Vol. 10728, p. 107280F). International Society for Optics and Photonics.

AP 004

Using photoacoustics to study protein aggregation abnormalities in organs of the gastrointestinal tract

Sharmila Anandasabapathy⁽¹⁾, Ivan Pelivanov⁽²⁾, Matthew O'Donnell⁽²⁾, Elena V. Petrova^{(1)*}

1. Department of Medicine and Gastroenterology, Baylor College of Medicine, Houston, TX, USA

2. Department of Bioengineering, University of Washington, Seattle, WA, USA

elena.petrova@bcm.edu

Aggregation of misfolded proteins can lead to formation of fibrils and further loss of protein functions (i) in cells, like aggregation of tumor suppression proteins associated with cancer pathogenesis [1], or (ii) in extracellular matrix, like amyloid formation in type-2 diabetes, neurodegenerative diseases, and hereditary systemic or organ-specific amyloidosis [2,3]. Thus, protein amyloid formation is a target for drug therapy to address an aggressive array of diseases, and methods to quantify and assess therapeutic response are needed to optimize specific treatment protocols. Screening new agents against protein aggregation is very challenging, however, due to the stochastic character of aggregate nucleation.

We hypothesize that protein fibril formation can be controlled by small molecular catalysts and inhibitors rather than by altering the concentration of protein macromolecules, and resultant phase transition phenomenon can be detected photoacoustically. To test this hypothesis, we use natural antimicrobial enzyme lysozyme, a model protein known for genetic lysozyme amyloidosis with manifestation in the gastrointestinal tract [4].

Here we study time-dependent changes in the photoacoustic (PA) response from optically contrasted solutions contained the protein Ly and salt-precipitant NaCl [5]. Crystallization from solution is accompanied by heat release and, consequently, by reduced specific heat capacity C_p and concomitant increased PA signal amplitude p at the first stage of the phase transition. Note that changes in the volumetric thermal expansion coefficient β and speed of sound V_l are negligible for this type of phase transition.

The PA signal amplitude was measured as a function of laser excitation energy E . A principle schematic of the non-contact PA measurement system used here can be found in [6]. A key advantage of a non-contact approach is that the protein solution can be probed in its natural environment using standard laboratory cuvettes and other containers conventionally used in other analytic instruments to characterize the solution.

The solutions were contrasted with carbon microparticles and placed in a chamber. A narrow beam of a diode-pumped nanosecond laser at 750 nm wavelength was directed to a measurement cuvette. The signal was detected by the double differential fiber-optic Sagnac interferometer.

If there is no phase transition, then $C_p = \text{const}$ and $\frac{p}{E}(E)$ is a linear function at a fixed laser beam diameter. If there is a phase transition, however, then $\frac{p}{E}(E)$ will diverge from linearity corresponding with $1/C_p$. We obtained data for a variety of aqueous mixtures of Ly+NaCl and the results clearly demonstrate the potential of the proposed method to detect aggregation in real time.

These results can be used to develop a PA instrument for high-throughput *in vitro* screening of agents designed for protein aggregation control and *ex vivo* examination of protein aggregation precursor to facilitate early stage diagnostics and therapy of amyloid-related diseases.

References

1. G.D.D.S. Ferretti, D.C.F. da Costa, J. Silva, R.L. Pereira, *Methods in Molecular Biology* 1873, 265 (2019) doi: 10.1007/978-1-4939-8820-4_17
2. R.R.Vanga, S. Dhingra, K. Patel, *Clinical Gastroenterology and Hepatology* 15, A35 (2017) doi: 10.1016/j.cgh.2017.06.034
3. F. Chiti, C.M. Dobson, *Annual Review of Biochemistry* 75, 333 (2006) doi: 10.1146/annurev.biochem.75.101304.123901
4. S. Freudenthaler, U. Hegenbart, S. Schönland, H.-M. Behrens, S. Krüger, C. Röcken, *Virchows Arch* 468, 569 (2016) doi: 10.1007/s00428-016-1916-y
5. E.V. Petrova, S.J. Yoon, I. Pelivanov, M. O'Donnell, *Proc. SPIE Photon Plus Ultrasound: Imaging and Sensing* 10494, 1049464 (2018) doi: 10.1117/12.2290482
6. I. Pelivanov, E.V. Petrova, S.J. Yoon, Z. Qian, K. Guye, M. O'Donnell, *Scientific Reports* 8, 14425 (2018) doi:10.1038/s41598-018-32580-2

Enhancing the Sensitivity and Detection Limit of Lateral Flow Immunoassays using Lock-In Thermography

Nima Tabatabaei*, Damber Thapa, Ashkan Ojaghi, Pouya Rezai

Department of Mechanical Engineering, York University, Toronto, ON, Canada

nima.tabatabaei@lassonde.yorku.ca

Lateral flow immunoassays (LFIAs) are simple paper-based devices used for non-laboratory diagnostics in many fields, such as agriculture, medicine, environmental testing, biosafety control, and water and food quality control. The LFIA provides rapid analysis of analytes without the need for sophisticated equipment and specially trained personnel, however, they suffer from low detection limits. They have low detection limits because most of the commercially available LFIA technologies incorporate optical scattering properties of antibodies and gold nanoparticles (GNPs) for colorimetric interpretation of test results. However, our recent research findings [1], indicate that the detection cutoff limit of LFIA can be significantly improved by recording the localized surface plasmon resonance responses of GNPs. In this study, we demonstrate improvement in analytical sensitivity and detection limit of commercially available LFIA test strips for detection of THC (Δ^9 -tetrahydrocannabinol; the psychoactive substance of cannabis) and hCG (aka pregnancy hormone) by interrogating their photothermal responses in a lock-in thermography (LIT) platform.

Materials and Methods

Experimental setup includes a conventional LIT illumination sub-system in which intensity-modulated near-infrared light (808nm; Jenoptik, Jena, Germany) is collimated, homogenized, and illuminated the sample. Detection is synchronously carried out via a long-wave infrared camera (Xenics Gobi 640, Belgium) at a maximum frame rate of 50 fps. Lock-in demodulation of signals is performed in LabVIEW for obtaining amplitude and phase images.

THC test strips: The LIT interpretation of THC was performed using NarcoCheck™ saliva test strips procured from Kappa city Biotech SAS (Montluçon, France) with a nominal detection limit of 25ng/ml. Saliva sample containing Δ^9 -THC was prepared by adding a known volume of non-stabilized artificial saliva (Chromatographic Specialties Inc.; Brockville, Canada) to Δ^9 -THC stock solution (MilliporeSigma; Oakville, Canada) to achieve the desired THC concentrations of 25, 10, 5, and 1 ng/ml. The sample solutions were then pipetted into three polypropylene sample vials and one saliva test strip was dipped into each vial. Upon immersion, the solution flowed upward by capillary action towards the test and control bands on the nitrocellulose membrane and interact with antibodies in order to create a colorimetric contrast difference. After 10 minutes, the test strips were removed from the vial and dried at room temperature for LIT interpretation. The process was repeated for solutions of different concentrations. Amplitude and phase images of the spiked test strips were obtained using LIT. The images were analyzed for quantitative evaluation of LFIA at different THC concentrations.

hCG pregnancy test strips: The hCG LFIA test was performed using the Rapid Response™ 20 mIU/ml test strips and the 20 mIU hCG urine control positive solution procured from BTNX Inc. (Markham, ON, Canada). To prepare solutions with different hCG concentrations, the urine control positive solution was pipetted into seven polypropylene sample vials and subsequently diluted with DI water to achieve spiked control positive solutions with concentrations of 16, 12, 8, 4, 2, 1 and 0.2 mIU. One test strip was dipped into each vial of different concentrations. After completion of the test, the LFIA strips were removed from the vial, dried and obtained LIT amplitude and phase images. In order to extract quantified information from the images of strips with different hCG concentrations, a normalization process was applied to compensate for sources of systemic error.

Results

Quantitative analysis of experiments was performed by calculating the mean and standard deviation (STD) from the test band of the amplitude images of spiked LFIAs. Fig 1(a) illustrates the average normalized amplitude values within the test band for strips with different THC concentrations ranging from 0 to 25 ng/mL, obtained at a laser modulation frequency of 2 Hz. One can see that the LIT amplitude value decreases with an increase in the THC concentrations in oral fluid. Since the STDs of any two concentrations do not overlap, results suggest that interrogation of thermal signature of GNPs through LIT significantly improves the detection threshold (1ng/ml vs the nominal 25 ng/ml limit of the LFIA used) of these low-cost and accessible point-of-care devices. Moreover, our results show that LIT provides a way to quantify the concentration of oral fluid THC.

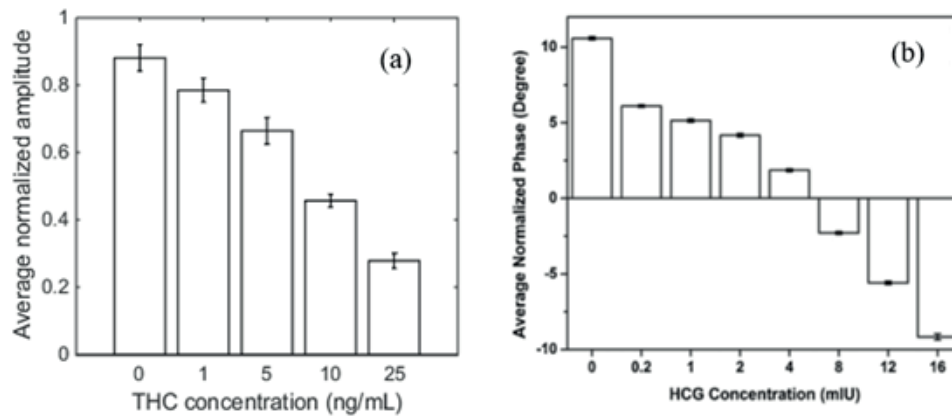


Fig. 1. (a) Average normalized amplitude values within the test band for THC test strips with different THC concentrations and (b) average normalized phase values for hCG test strips [1].

Fig 1(b) depicts the average normalized phase values within the test band for stripes with different hCG concentrations ranging from 0 to 16 mIU, obtained at the modulation frequency of 2 Hz. The LIT phase value decreases monotonically with an increase in the hCG concentration. The error bars do not overlap for any two concentrations which indicate that the detection limit of commercially-available hCG test strips is significantly improved by examining thermal signatures of GNPs (0.2 mIU vs. nominal LFIA cut-off of 20 mIU).

References

1. A. Ojaghi, M. Pallapa, N. Tabatabaei, and P. Rezai, *Sensors and Actuators A: Physics* 273, 189 (2018) doi:<https://doi.org/10.1016/j.sna.2018.02.036>

In pursuit of an optimum optical imaging technology for early detection of dental caries

Nima Tabatabaei, Elnaz B. Shokouhi

Department of Mechanical Engineering, Lassonde School of Engineering, York University, Toronto, Canada

Nima.Tabatabaei@Lassonde.Yorku.ca

Dental caries continues to be a major public health challenge in both children and adults [1]. Over the past decades, the state of the art in preventive dentistry has provided promising therapeutic techniques for preventing the progression of early dental caries to cavities and complete tooth decay [2]. However, the effectiveness of these preventive provisions rely on detection of caries at very early stages of formation; a task not achievable by clinical detection methods such as x-ray radiography and visual-tactile inspection [2]. As such, in recent years, several optics-based imaging methods have been proposed for early detection of caries. From biomedical physics perspective, these technologies rely on either enhanced scattering of light or enhanced absorption of light at early caries sites. While optical coherence tomography (OCT) is known as the mainstream scattering-based technology in the field, thermo-phonic imaging (TPI) is, arguably, the mainstream choice of detection of early caries based on absorption of light. This paper aims to review the development of a spectrum of dental OCT and thermo-phonic imaging methods over the past decade by leading research groups in the field as well as to present our recent results on a comparative study on the detection of early dental caries using thermo-phonic imaging and optical coherence tomography. Based on the outcomes of the comparative study, recommendations supported by preliminary results are made for a light-absorption based imaging modality with the ability to produce tomographic and depth-resolved images, combining the key advantages of OCT and TPI [3].

Experimental setup of TPI system, Fig. 1(a), includes an illumination sub-system in which intensity-modulated near infrared light (808nm; Jenoptik, Jena, Germany) is collimated and intensity-homogenized before illuminating the dental sample. Detection is synchronously carried out via a long-wave infrared camera (Xenics Gobi 640, Belgium) at a maximum frame rate of 50 fps. Based on the modulation scheme used lock-in demodulation or cross-correlation of signals is performed in LabVIEW for obtaining amplitude and phase images. On the other hand, the OCT system, Fig. 1(b), uses broadband light of a superluminescent diode centered at 1310 nm (+/- 75 nm at 10 dB) and a 2048-pixel line scan camera spectrometer with a maximum acquisition rate of 147 kHz to form tomographic images of light scattered back from dental samples via interferometry with axial and lateral resolutions of 11 μm and 10 μm, respectively. Verification tests were carried out by micro Computed Tomography (Skyscan 1272 high-resolution μCT system, Bruker MicroCT, Kontich, Belgium). Samples used in the studies were healthy extracted human teeth which were subsequently artificially demineralized using a standard acidic gel for different treatment periods.

Fig. 2 represent data from one of the studies carried out aimed at comparing performances of OCT and TPI in detecting well-developed early caries on proximal and occlusal surfaces. While these results demonstrate sufficient detection sensitivity of both technology, more specific nature (i.e., less false positive readings) of TPI is clearly demonstrated. Figure 3 depicts results of the statistical analysis carried out on a time-lapse artificial demineralization study. Panels (a) and (b) highlight pixels statistically identified as demineralized (i.e., yellow pixels) by OCT and TPLI, respectively, at different stages of demineralization. The tabulated sensitivity and specificity data in panel (c) as well as the ROC plot in panel (d) clearly show the more specific nature of TPI over OCT, especially at early stages of caries formation.

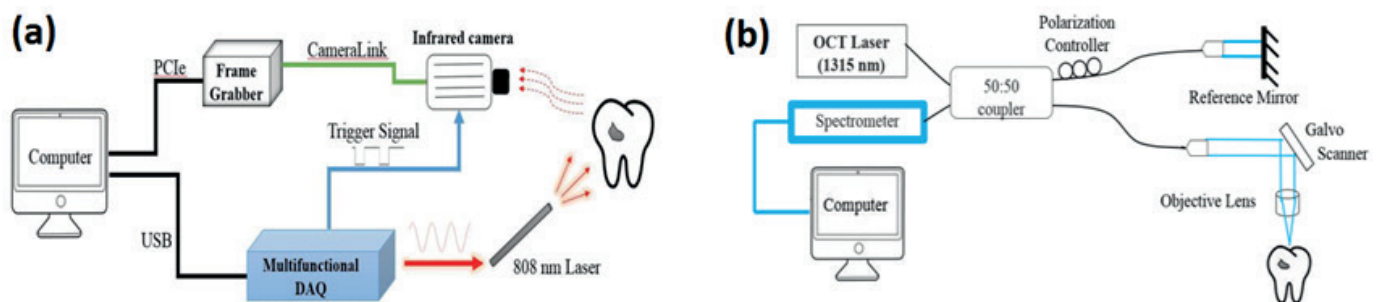


Fig. 1 Schematic representation of the developed (a) TPI and (b) OCT systems [3].

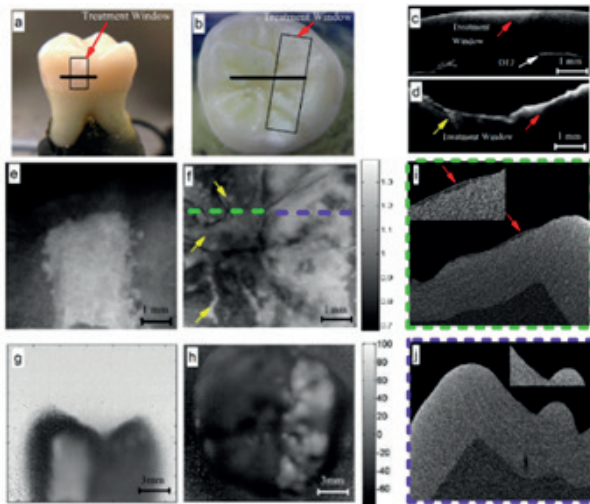


Fig. 2 Schematic Photographs of simulated caries on (a) smooth and (b) occlusal surfaces; rectangles depict the location of treatment windows. Representative OCT B-mode images of (c) smooth surface and (d) occlusal caries samples along the solid lines indicated in panels (a) and (b), respectively. Integrated en-face OCT images at 10 days of treatment of (e) smooth and (f) occlusal caries samples. TPLI phase images obtained at 2-Hz modulation frequency at 10 days of treatment for (g) smooth surface (h) occlusal caries samples. (i) and (j) represent the μ CT slices along the green and blue dashed lines in panel (f), respectively. Red and yellow arrows point to treatment window and false positives, respectively. [3]

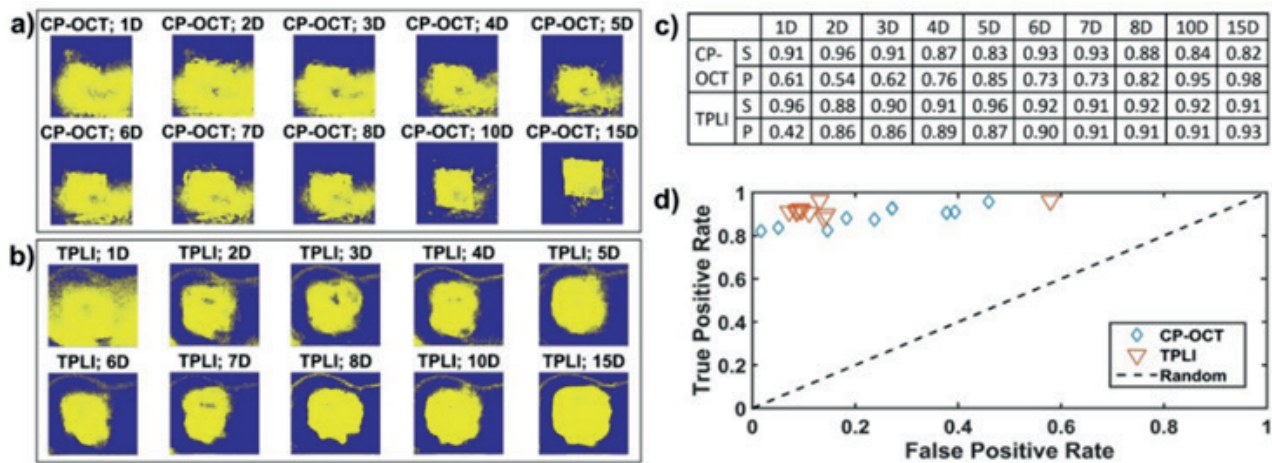


Fig. 3 Statistically (CI: 95%) identified healthy (blue pixels) and demineralized (yellow pixels) at various stages of demineralization by (a) OCT and (b) TPLI. (c) Corresponding sensitivity (S) and specificity (P) values and (d) receiver operating characteristic curve. [3]

References

1. Bagramian, R.A., F. Garcia-Godoy, and A.R. Volpe, The global increase in dental caries. A pending public health crisis. *Am J Dent*, 2009. 22(1): p. 3-8.
2. Mohanraj, M., V. Prabhu, and R. Senthil, Diagnostic methods for early detection of dental caries - A review. *International Journal of Pedodontic Rehabilitation*, 2016. 1(1): p. 29-36.
3. Shokouhi, E.B., et al., Comparative study on the detection of early dental caries using thermo-photonic lock-in imaging and optical coherence tomography. *Biomedical Optics Express*, 2018. 9(9): p. 3983-3997.

Modeling of an open photoacoustic resonator for blood glucose measurement

Marcus WOLFF ^{(1)*}, Said EL-BUSAIDY ^(1,2), Bernd BAUMANN ⁽¹⁾, Lars DUGGEN ⁽²⁾

1. Hamburg University of Applied Sciences, Hamburg, Germany

2. University of Southern Denmark, Mads Clausen Institute, Sønderborg, Denmark

marcus.wolff@haw-hamburg.de

Photoacoustic spectroscopy has been demonstrated as an effective technique for non-invasive measurement of blood glucose concentration [1-3]. The measurement is done by probing the glucose molecules in the interstitial fluid with an infrared laser source. The interstitial fluid lies a few micrometers under the skin surface and the glucose concentration in the interstitial fluid and in the blood is correlated [4-5]. If the acoustic resonator of the sensor was closed, skin transpiration during measurements would result in the build-up of humidity inside the resonator causing strong absorption of the infrared radiation. Leaving one end of the resonator open has been shown as possible solution that enables continuous non-invasive monitoring of the blood glucose concentration.

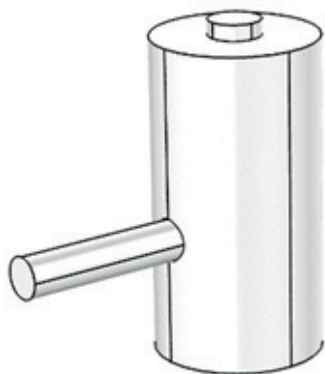


Fig. 1. T-shaped resonator made from Aluminum. The small opening at the top of the resonator is closed by skin of the patient, while the opening at the bottom of the large cylinder is left open. A microphone is mounted at the end on the narrow side cylinder.

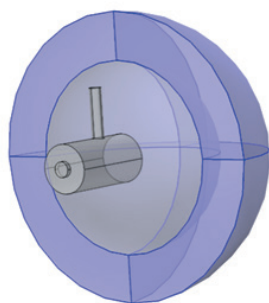


Fig. 2. The resonator with the additional hemisphere (grey) and the perfectly matched layers (blue).

We demonstrate an accurate method for simulating the photoacoustic signal in an open resonator using finite element modelling. The resonator consists of three interconnected cylinders forming a T-like structure as shown in Fig.1.

This simulation method is based on the linearized Navier-Stokes equations in which viscous and thermal loss are the main sources of signal attenuation. The open end of the resonator is modelled by adding a hemisphere as an additional domain. The hemisphere represents the infinite free space. To avoid reflections of the radiated sound waves, it is terminated by perfectly matched layers (Fig. 2).

The simulation results show good agreement with the experimental results as all the major acoustic resonances have been experimentally confirmed. The small frequency shifts of the resonances are mainly attributed to experimental inaccuracies.

The simulation method provides an accurate tool for modelling the performance of an open resonator. This is particularly useful when designing and optimizing the photoacoustic sensor for blood glucose measurements.

References

1. M.A. Pleitez, T. Lieblein, A. Bauer, O. Hertzberg, H.V. Lilienfeld-Toal, W. Mäntele1, Review of Scientific Instruments 84 (8), 084901 (2013) doi:10.1063/1.4816723
2. W.V. Gonzales, A.T. Mobashsher, A. Abbosh, Sensors 19 (4), 800 (2019) doi:10.3390/s19040800
3. J. Kottmann, J.M. Rey, M.W. Sigrist, Sensors 16 (10), 1663 (2016) doi:10.3390/s16101663
4. C. Laugel, N. Yagoubi, A. Baillet, Chemistry and Physics of Lipids 135 (1), 55 (2005) doi: https://doi.org/10.1016/j.chemphyslip.2005.02.001
5. P. Garidel, Physical Chemistry Chemical Physics 4 (22), 5671 (2002)

AP 008

The study of photosynthetic light-harvesting antenna supercomplexes in the xanthophyll cycle by infrared nanospectroscopy

Jiangtao Zhou ^{(1)*}, Sergey Sekatskii ⁽¹⁾, Renata Welc ⁽²⁾, Giovanni Dietler ⁽¹⁾, Wieslaw I. Gruszecki ⁽²⁾

1. Laboratory of Physics of Living Matter, Ecole Polytechnique Fédérale de Lausanne (EPFL), CH-1015 Lausanne, Switzerland

2. Department of Biophysics, Institute of Physics, Maria Curie-Skłodowska University, 20-031 Lublin, Poland

Jiangtao.zhou@epfl.ch

Light-harvesting complex II (LHCII), as the primary antenna complex in the green plants, is playing a fundamental role in the initial steps of the photosynthesis by harvesting solar light and transferring excitation energy to the plant photosystem II core complex¹. The LHCII complexes contain multiple chlorophyll and carotenoids with substoichiometric amounts of xanthophylls, including violaxanthin or zeaxanthin^{2,3}. The xanthophyll cycle is one of the possible mechanisms of regulating dissipation and energy transfer in the photosynthetic apparatus of plants, by converting the level of violaxanthin to zeaxanthin. However, studying on this regulation and antenna organization between LHCII supercomplexes is challenging because of the difficulties in nanoscale characterization of antenna supercomplexes in the presence of chloroplast lipid membranes.

In this work, we applied single molecular techniques based on atomic force microscopy-infrared spectroscopy (AFM-IR), a novel hybrid technique of AFM and infrared spectroscopy, providing new insights into the chemical analysis in nanoscale, as illustrated in Fig. 1. This technique allows us to characterize the morphological properties of the lipoprotein multilayer and access the conformational conversion of LHCII protein on the chloroplast lipid due to the effect of violaxanthin or zeaxanthin. The IR absorption map on the chloroplast lipid membrane are shown in Fig. 2.

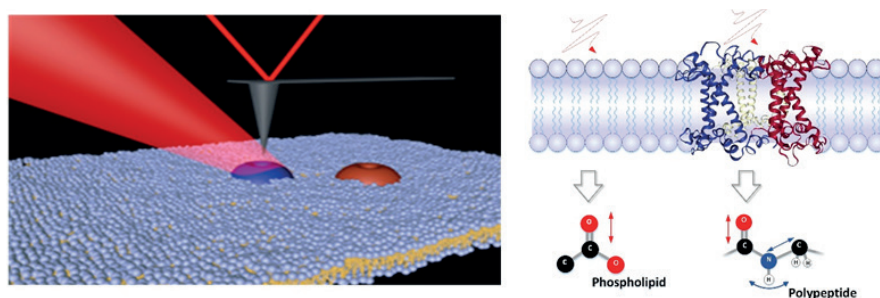


Fig. 1. Scheme of infrared nanospectroscopy of the LHCII complex on the lipid membrane.

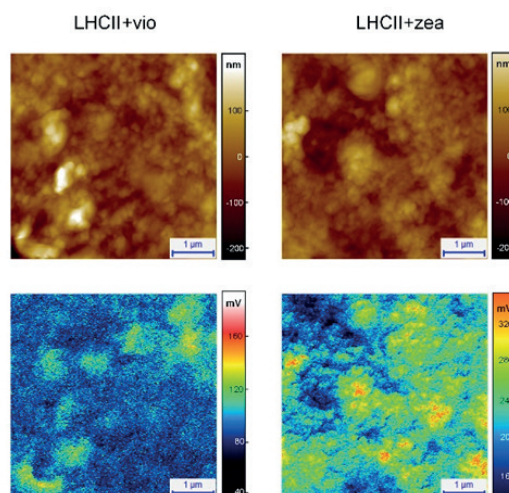


Fig. 2. The surface morphology image and IR absorption (1645 cm^{-1}) map of lipoprotein multilayer, consisting of chloroplast lipids and the antenna complex LHCII, in the presence of violaxanthin (middle) or zeaxanthin (right).

Our results reveal that, from the IR absorption map at 1645 cm^{-1} in Fig. 2, the existence of xanthophylls can lead to specific stabilization between LHCII supercomplexes, by promoting the interaction between intramembrane complexes embedded in the photosynthetic membranes or intermembrane complexes from vertical stacked membranes. Moreover, zeaxanthin shows more pronounced effect in linking and stabilizing these supercomplexes than that of violaxanthin, and induces intermolecular aggregates between supercomplexes. While, violaxanthin indicates the ability of linking the LHCII antenna and preseaving their conformational structure without formed aggregation. These dynamics of xanthophyll cycle form the basis for controlling LHCII antenna rearrangement and promotes our understanding on biological regulation of photosynthesis.

References

1. van Amerongen, H. & van Grondelle, R. Understanding the Energy Transfer Function of LHCII, the Major Light-Harvesting Complex of Green Plants. *Journal of Physical Chemistry B* 105 (3), 604 (2001) doi: 10.1021/jp0028406
2. Liu, Z. et al. Crystal structure of spinach major light-harvesting complex at 2.72 \AA resolution. *Nature* 428, 287 (2004) doi: 10.1038/nature02373
3. Schlau-Cohen, G. S. et al. Single-Molecule Identification of Quenched and Unquenched States of LHCII. *Journal of Physical Chemistry Letters* 6 (5), 860 (2015) doi: 10.1021/acs.jpcllett.5b00034

Energy Transfer Processes in Solar Cell Materials by Photoacoustic Spectroscopy

Mauro Luciano Baesso^{(1)*}, Antonio Carlos Bento⁽¹⁾, Leonardo de Oliveira Mendes⁽¹⁾,
Jurandir Hillmann Rohling⁽¹⁾, Francine Baesso Guimarães⁽¹⁾, Otávio Augusto Capeloto⁽¹⁾,
Luis José Borrero-González⁽²⁾, Luiz Antonio de Oliveira Nunes⁽²⁾, Helion Vargas⁽³⁾

1. Departamento de Física, Universidade Estadual de Maringá, Maringá, PR, Brazil

2. Instituto de Física, Universidade de São Paulo, São Carlos, SP, Brazil

3. Laboratório de Física, Universidade Norte Fluminense, RJ, Brazil

*mlbaesso@uem.br

Solar cell efficiency is known to be highly dependent on the spectral matching between the solar spectrum and the active material bandgap. Despite its low efficiency to produce electrical energy, ~15%, silicon panels are nowadays worldwide used as an important energy generator. This so low performance has encouraged researchers towards the development of new solar energy converters aiming to produce more efficient devices (1-3). Glasses and ceramics doped with lanthanide ions have been shown to be an alternative route for this purpose due to their abilities to promote efficient downconversion processes. Then, they can be used to convert high-energy photons from the visible range into low-energy ones close to the silicon band gap in the near infrared, being candidates as sensitizers to improve silicon solar cell performance. Under this aspect, the knowledge of energy transfer mechanisms is crucial to develop this class of solar energy converters. Here we used Photoacoustic Spectroscopy (PAS) to investigate the energy transfer processes of lanthanide ions in glasses aiming to evaluate their feature as sensitizers for efficient emission at the silicon band gap spectral region.

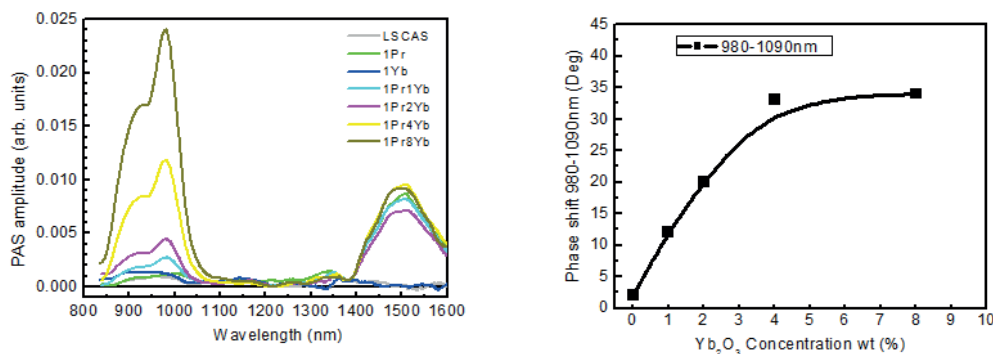
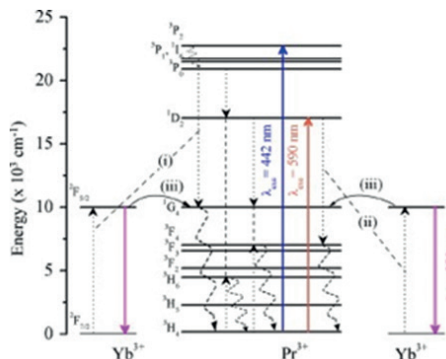


Figure 1. a. PAS spectra of Pr-Yb co-doped aluminosilicate glasses; b. Relative phase shift with respect to 1 wt% of Pr₂O₃ sample.

The experiments were performed in aluminosilicate glasses (LSCAS) with 1 wt% of Pr₂O₃ and X wt% of Yb₂O₃. The PAS spectra are shown in Fig. 1a and the relative phase shift with respect to the sample with 1wt% of Pr₂O₃ is shown in Fig. 1b. The bands between 800 and 1000 nm are attributed to the photothermal effect of Yb³⁺ absorption, while that around 1480 nm is associated to Pr³⁺ ions. The linear increase of Yb³⁺ bands as well as its relative phase shift in relation to that of Pr³⁺ are confirmations of prevalent occurrence of heat transfer processes instead of luminescence of this Pr-Yb system. Previously (1), we used luminescence techniques to

evaluate the energy transfer mechanisms of these glasses, as illustrated in Fig. 2. The observed dominance of back transfer energy processes from Yb³⁺ to Pr³⁺, under 442 nm excitation, with consequent multiphoton relaxation was shown. In other words, the PAS data shown the Yb³⁺ band around 980 nm is a direct detection of predominant multiphoton relaxation through ¹G₄, ³F₄ → ³H₄ transitions, as illustrated in Fig. 2, as a consequence of back-energy transfer from Yb³⁺:²F_{5/2} to the Pr³⁺:¹G₄ level.

Figure 2. (i) Cross relaxation (Pr³⁺:³P₀ → ¹G₄; Yb³⁺:²F_{7/2} → ²F_{5/2}), resulting in the emission of one photon by Yb³⁺ (²F_{5/2} → ²F_{7/2}) and multiphoton relaxation from Pr³⁺:¹G₄ to lower levels. (ii) Cross relaxation (Pr³⁺:¹D₂ → ³F₄; Yb³⁺:²F_{7/2} → ²F_{5/2}) followed by the emission of one photon by Yb³⁺ (²F_{5/2} → ²F_{7/2}) and multiphoton relaxation from Pr³⁺:³F₄ to lower levels. The back-energy transfer from Yb³⁺:²F_{5/2} to the Pr³⁺:¹G₄ level is also depicted.



B Materials Science and Characterization

Therefore, the photoacoustic data highlighted this technique usefulness in terms of quantitative evaluation of solar cell converters. Comparison of Pr-Yb data with other systems like Nd-Yb and Tb-Yb will also be presented.

Acknowledgements

We are thankful to Companhia Paranaense de Energia Elétrica (COPEL) for the financial support of this work. Project P&D number PD-2866-0466/2017.

References

1. L.J. Borrero-González, L.A.O. Nunes, J.L. Carmo, F.B.G. Astrath, M.L. Baesso, J. Lumin. 145 615–619, (2014). [dx.doi.org/10.1016/j.jlumin.2013.08.036](https://doi.org/10.1016/j.jlumin.2013.08.036).
2. L.J. Borrero-Gonzalez, L.A.O. Nunes, G. S. Bianchi, F.B.G. Astrath, M.L. Baesso. J. Appl. Phys. 114, 013103 (2013). doi.org/10.1063/1.481237
3. A. Cruz-Orea, I. Delgadillo, H. Vargas, A. Gudino-Martinez, E. Marin, C. Vazquez-Lopez, A. Calderon, and J.J. Alvarado-Gil, J. App. Phys. 79 (12), 8951 (1996). doi.org/10.1063/1.362626

Study of overtones and combination bands in solvents using near near-infrared thermal lens spectroscopy

Maryleide VENTURA⁽¹⁾, Junior REIS SILVA⁽¹⁾, Luis Humberto DA CUNHA ANDRADE⁽¹⁾,
Tomaz CATUNDA^{(2)*}, Sandro Marcio LIMA⁽¹⁾

1. Grupo de Espectroscopia Óptica e Fototérmica, Programa de Pós-Graduação em Recursos Naturais, Universidade Estadual de Mato Grosso do Sul, CP 351, Dourados, MS, Brazil.

2. Instituto de Física de São Carlos, Universidade de São Paulo, São Carlos, SP, Brazil.

maryleide.ventura@gmail.com; juniorrsilva@uems.br; luishca@uems.br; tomaz@ifsc.usp.br; smlima@uems.br

Introduction

It is well known that the anharmonicity of chemical bonds can influence the absorption of molecules, especially in the near-infrared (NIR) and near near-infrared (N-NIR) spectral regions. Specifically, it affects its dipole moment, which in an anharmonic model does not present a linear dependence on the interatomic distance. Hence, determination of the anharmonicity of a chemical bond is important in order to know its absolute absorption. The background absorption can be due to overtone vibrations, so careful choice of a solvent is required in order to minimize the effect of the blank absorption [1].

Materials and Methods

The dual-beam mode-mismatched Thermal Lens (TL) technique in the near-near infrared (N-NIR), was applied in the study of solvents using a tunable cw excitation laser (Ti³⁺:Sapphire) in the range 9600 to 11500 cm⁻¹. Absorption spectra due to overtones and combination bands of the C-H and O-H stretching bonds were obtained and the anharmonicity constants (χ), dissociation energies and thermo-optical properties were calculated.

Results and discussion

Figure 1 shows the TL absorption spectra in the N-NIR for the chloroform (a) and methanol (b), attributed to overtones and combination bands. In the chloroform spectrum is noted an absorption due to the third overtone of the C-H stretching mode (4v C-H) at 11325 cm⁻¹ and combination band at 9823 cm⁻¹. Figure 1.b shows the methanol spectrum with 4v C-H and 3v O-H lines, much broader than compared to the lines observed in Fig.1.a. Similar spectra were obtained for dichloromethane and ethanol.

The anharmonicity constants obtained are: $\chi = (1.9 \pm 0.1) \times 10^{-2}$; $(1.9 \pm 0.1) \times 10^{-2}$; $(2.2 \pm 0.1) \times 10^{-2}$ and $(2.2 \pm 0.1) \times 10^{-2}$ for chloroform, dichloromethane, methanol and ethanol, respectively. The thermal diffusivity values were also determined in all solvents: chloroform $(0.85 \pm 0.02) \times 10^{-3}$ cm²/s⁻¹, dichloromethane $(0.93 \pm 0.03) \times 10^{-3}$ cm²/s⁻¹, methanol $(1.06 \pm 0.02) \times 10^{-3}$ cm²/s⁻¹ and ethanol $(0.89 \pm 0.03) \times 10^{-3}$ cm²/s⁻¹. All these values are in good agreement with the literature [2, 3].

Conclusions

Most of TL results reported in the literature have no selectivity since they were obtained with single wavelength excitation. In this paper the lineshapes of combination overtones could be fully characterized using a tunable N-NIR laser (cw Ti-sapphire laser). The spectra presented high selectivity since the signal due to the absorption lines are two order of magnitude higher than the background (blank) absorption $\sim 2 \times 10^{-4}$ cm⁻¹. In conclusion, we demonstrate that the TL technique with N-NIR tunable excitation is a technique that provides high selective and sensitivity suitable for many analytical applications such as environmental monitoring [4].

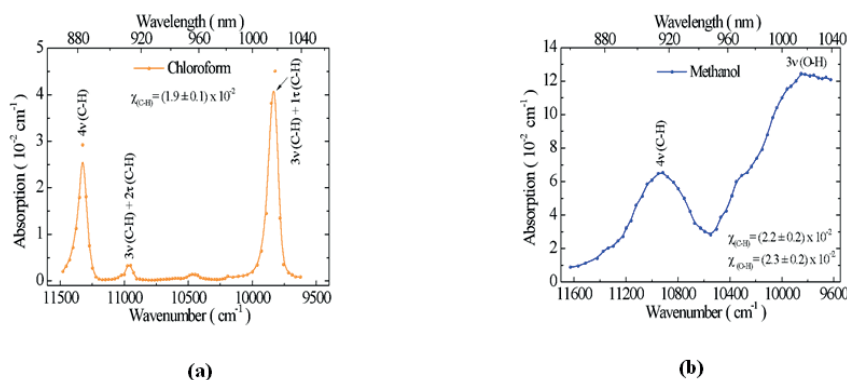


Fig. 1. Thermal Lens absorption spectra in the N-NIR: chloroform (a) and methanol (b).

B Materials Science and Characterization

Acknowledgements

The authors thank the Brazilian agencies: Coordenação de Aperfeiçoamento de Pessoal de Nível Superior (CAPES), Fundação de Apoio ao Desenvolvimento do Ensino, Ciência e Tecnologia do Estado de Mato Grosso do Sul (FUNDECT) and Conselho Nacional de Desenvolvimento Científico e Tecnológico (CNPq).

References

1. R. Iwamoto, *Applied Spectroscopy* 63 (3),354 (2009) doi: 10.1366/000370209787598942.
2. W. Groh, *Makromol. Chem.* 189 (12), 2861 (1988) doi: /10.1002/macp.1988.021891213.
3. F. Kollipost, K. Papendorf, Yu-F. Lee, Yuan-P. Lee, M.A. Suhm, *Phys. Chem.* 16 (30), 15948 (2014) doi:10.1039/c4cp01418a.
4. M. Ventura, J. R. Silva, L. H. C. Andrade, R. P. Scorza-Júnior, S.M. Lima, *Spect. Acta Part A: Mol. and Biomol. Spectrosc.* 188 (1), 32 (2018) doi: 10.1016/j.saa.2017.06.043.

Near-near infrared thermal lens spectroscopy to monitor transesterification reaction during biodiesel production

Maryleide VENTURA⁽¹⁾, Warley BATISTA DEUS⁽¹⁾, Junior REIS SILVA⁽¹⁾,
Luis Humberto DA CUNHA ANDRADE⁽¹⁾, Tomaz CATUNDA^{(2)*}, and Sandro Marcio LIMA⁽¹⁾

1. Grupo de Espectroscopia Óptica e Fototérmica, Programa de Pós-Graduação em Recursos Naturais, Universidade Estadual de Mato Grosso do Sul, CP 351, Dourados, MS, Brazil.

2. Instituto de Física de São Carlos, Universidade de São Paulo, São Carlos, SP, Brazil.

maryleide.ventura@gmail.com; warleydeus@hotmail.com; juniorrsilva@uems.br;
luishca@uems.br; tomaz@ifsc.usp.br; smlima@uems.br

The main analytical procedures that are used to monitor and quantify the concentrations of the compounds involved in the transesterification reaction include chromatography and/or spectroscopic methods [1,2]. The chromatography is not suitable for monitoring the reaction produced in industry, so they require sample preparation, complex calibration and long time of analysis. On the other hand, spectroscopic techniques appear relevant to monitor the transesterification reaction because they involve the observation of different physical, dielectric, optical and chemical parameters. They have been studied and tested directly in the reaction, so that they may be employed in the industry without changing substantially the routine of production. In this study the Thermal Lens Spectroscopy in the near-near infrared region [3] was used to monitor the biodiesel production, by inspecting the thermo-optical properties of aliquots extracted during the reaction.

Materials and Methods

Fifteen aliquots were extracted from the reaction during 20 minutes and their thermo-optical properties were measured as a function of the reaction time. The spectroscopic investigation was performed between 855 and ~1000 nm to identify overtone absorptions bands (markers), which can be used as marker to control the ester production.

Results and discussion

The results show that the OH absorption overtone (~ 970 nm) from alcohol, which is used in the reaction, is the most appropriated marker to monitor the biodiesel production. The time dependence of the thermo-optical parameter $A(dn/dQ)$, which is the product between the absorption coefficient (A) and the refractive index dependence with the sample deposited heat (dn/dQ), exhibits a very good correlation with the ester production measured by chromatography (Fig. 1). Besides, the measured thermal diffusivity values as function of reaction time indicates a strong dependence with the viscosity of the aliquots (Fig. 2). By the results it is possible to affirm that the reaction reached the end in ester production around 5 minutes, indicating that a longer reaction time is not needed for ester production.

Conclusions

It is possible to conclude that the used TLS in the N-NIR region contributes to the optimization of biodiesel production process by indicating the best time to stop the reaction.

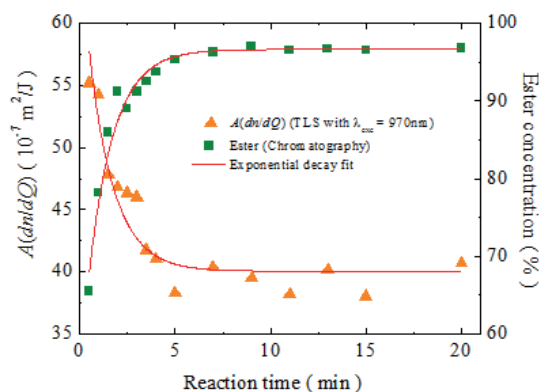


Fig. 1. $A(dn/dQ)$ for $\lambda_{exc} = 970\text{nm}$ and ester concentration determined by chromatography as a function of the reaction time. A single exponential decay function was used to fit the experimental data using the same time constant $\tau = 0.91\text{ s}$.

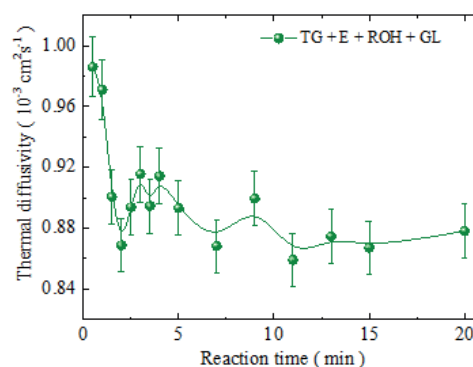


Fig. 2. Thermal diffusivity (D) determined for the aliquots as a function of the reaction time.

B Materials Science and Characterization

Acknowledgements

The author thank the following Brazilian agencies: Coordenação de Aperfeiçoamento de Pessoal de Nível Superior (CAPES) for an undergraduate fellowship awarded to the first author, Fundação de Apoio ao Desenvolvimento do Ensino, Ciência e Tecnologia do Estado de Mato Grosso do Sul (FUNDECT) and Conselho Nacional de Desenvolvimento Científico e Tecnológico (CNPq).

References

1. E.F. Aransiola, T.V. Ojumu, O.O. Oyekola, T.F. Madzimbamuto, D.I.O. Ikhu-Omoregbe, *Biomass and Bioenergy* 61 (1), 276 (2014) doi: 10.1016/j.biombioe.2013.11.014.
2. L.A.B. Boni, I.N.L. Silva, *Fuel Process Technology* 92 (5), 1001 (2011)doi: 10.1016/j.fuproc.2010.12.022.
3. M. Ventura, W.B.Deus, J.R.Silva, L.H.C.Andrade, T. Catunda, S.M.Lima, *Fuel*212(15), 309 (2018) doi: 10.1016/j.fuel.2017.10.069.

Statistical methods for the analysis of thermal images obtained from corn seeds

**José Ernesto ROJAS-LIMA*, Claudia HERNÁNDEZ-AGUILAR,
Flavio Arturo DOMÍNGUEZ-PACHECO**

SEPI-ESIME Zacatenco, Instituto Politécnico Nacional, Ciudad de México, 07738, México

errojas@ipn.mx

During the last decades, digital image processing algorithms, have been developed to objectively measure external characteristics of agricultural products due to the great diversity and potential that these methods offer [1]. So in this research, analysis of thermal images obtained using thermographic instrumentation, which consists of a thermographic camera and a laser light source at 650 nm [2], was used to irradiate samples of two genotypes of maize seed: crystalline and floury in their natural state for exposure times of 15 s and 35 s. The methods applied in the analysis were [3]: a) histogram to obtain the distribution of gray levels of images, b) mean that represents a measure of brightness, c) variance which provides a measure of contrast, d) entropy of images applying both Shannon [4] and Tsallis [5] definitions, which indicates the average self-information contained in images, e) Probability density estimation of the temperature variations on seeds samples in order to quantitatively characterize them from thermal images. According to the results in the case of thermal images obtained from crystalline seeds, higher mean and variance values were obtained indicating higher brightness and contrast. Furthermore, the thermal images for floury seeds exhibited higher Shannon entropy indicating that they have greater disorder respect to the thermal images of crystalline seeds, due to the molecular structure of the floury seed is less organized.

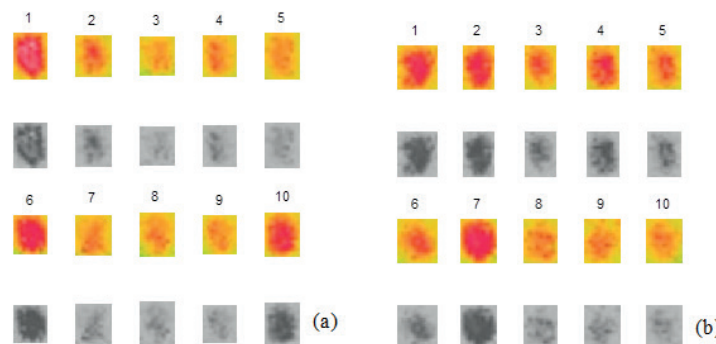


Fig. 1. Collection of thermal images and their grayscale equivalent of corn seed samples. (a) Crystalline seeds, exposure time of 15 s. (b) Crystalline seeds, exposure time of 35 s.

In the case of Tsallis entropy, since the value of the entropic index q characterizes each collection of images [6], this index could also be used for characterization of seeds. Thermal images obtained from seeds with floury structure, provides higher redundancy value for a shorter exposure time to laser light. In this way it can be observed the viability of the statistical methods of digital image processing applied to thermal imaging for the characterization of seeds.

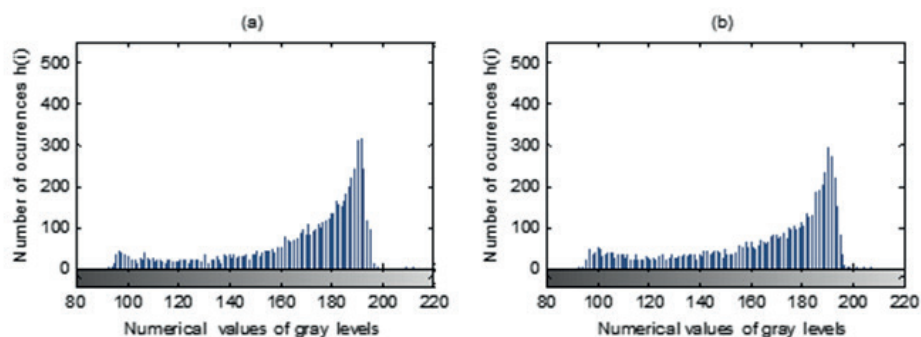


Fig. 2. Histograms of thermal images in gray scale. (a) Crystalline seeds, exposure time of 15 s. (b) Crystalline seeds, exposure time of 35 s.

B Materials Science and Characterization

Table 1. Mean, variance, Shannon entropy, Tsallis entropy and q index for collections of 10 thermal images of crystalline and floury seeds for exposure times of 15 and 35 s.

Genotype of corn seeds	Mean 15 s	Variance 15 s	Mean 35 s	Variance 35 s	Shannon Entropy 15 s	Shannon Entropy 35 s	Tsallis Entropy 15 s	q index 15 s	Tsallis Entropy 35s	q index 35 s
Crystalline	169.055	797.298	164.312	837.030	4.275	4.345	216.699	-0.14	498.206	-0.340
Floury	164.702	684.751	157.281	761.837	4.354	4.5061	368.123	-0.28	330.377	-0.252

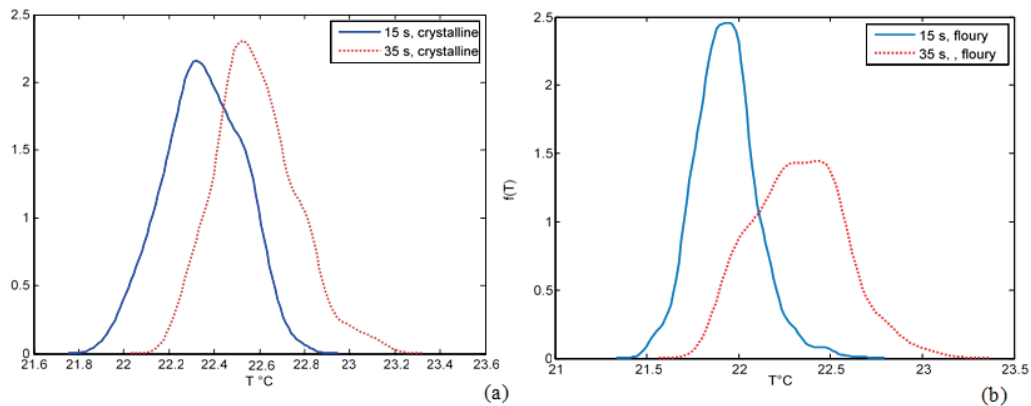


Fig. 3. Probability density functions of temperature variations (a) crystalline seeds (b) floury seeds

References

1. M. Latha, A. Poojith, B.A. Reddy, G.V. Kumar, *Int. J. Innov. Res. Electr. Electron. Instrum. Control Eng.* 2, 1562, (2014).
2. C. Hernández Aguilar, F.A. Dominguez Pacheco, A. Cruz Orea, A. C., R. Tsonchev, R. I. (2015). Thermal effects of laser irradiation on maize seeds. *International Agrophysics*, 29(2), 147-156.
3. W.K. Pratt, *Introduction to digital image processing*, 1st edn. (CRC Press, 2013), p. 756.
3. C.E. Shannon, *Bell Syst. Tech. J.*, 27, 379, (1948).
4. S. Sarkar, S. Das, *IEEE Trans. Image Process.* 22, 4788, (2013).
5. A. Ramírez-Reyes, A.R. Hernández-Montoya, G. Herrera-Corral, I. Domínguez-Jiménez, *Entropy*, 18, 299, (2016).

Optical properties in textile materials added with UV protective biomaterials

Arturo DOMINGUEZ-PACHECO ^{(1)*}, Claudia HERNANDEZ-AGUILAR ⁽¹⁾,
Benjamin GOMEZ-UZETA ⁽¹⁾, Alfredo CRUZ-OREA ⁽²⁾

1. Posgrado en Ingeniería de Sistemas, Instituto Politécnico Nacional, SEPI-ESIME-Zac., Av. Instituto Politécnico Nacional, s/n, Col. Lindavista C. P. 07730, Ciudad de México, México.

2. Departamento de Física, CINVESTAV-IPN, A. P. 14-740, C. P. 07360, Ciudad de México, México.

fatur@hotmail.com

Currently applied technology is developed to improve material properties [1-2], by adding other materials or bio-materials by means of different methods in order to increase their capacities to make them functional with improved absorbent, resistant or flexible properties. Textiles are the most used materials to protect us from different harmful agents and they have acquired a great importance, for protection of diverse climatic and environmental factors. A great variety of functional textiles have been developed for UV, anti-microbial, humidity, irradiation and temperature protections. [3-4]. the characterization of these type of materials by non-destructive techniques, such as Photothermal (PT) techniques, is desirable [5-7]. By means of PT techniques the optical and thermal properties of different materials can be obtained, then the optical absorption coefficient (β), thermal diffusivity, thermal effusivity and thermal images, have been obtained by using PT techniques. Among the PT techniques the photoacoustic spectroscopy (PAS) has been used to optical characterization of different materials. In the present study natural pigments extracted from maize seeds, and added to textiles in order to improve their UV protection capacity, were optically characterized by photoacoustic spectroscopy, as it can be seen in Figure 1.

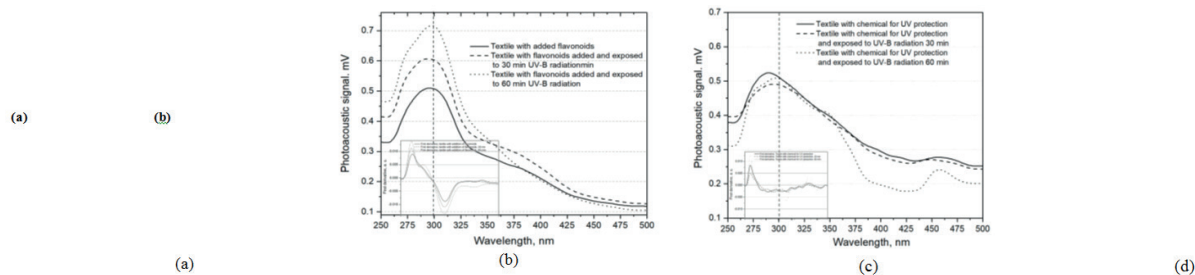


Fig. 1. Photoacoustic spectra, a) Flavonoid extracts by different methods, b) Textile added with flavonoids, c) Textile with UV protective chemistry, d) Differences between textiles with flavonoids vs UV protective chemical.

References

- Davidovits, J. (1991). Geopolymers: inorganic polymeric new materials. *Journal of Thermal Analysis and calorimetry*, 37(8), 1633-1656.
- Berglund, L. A., & Burgert, I. (2018). Bioinspired wood nanotechnology for functional materials. *Advanced Materials*, 30(19), 1704285.
- Mahltig, B., Haufe, H., & Böttcher, H. (2005). Functionalisation of textiles by inorganic sol-gel coatings. *Journal of Materials Chemistry*, 15(41), 4385-4398.
- Xin, J. H., Daoud, W. A., & Kong, Y. Y. (2004). A new approach to UV-blocking treatment for cotton fabrics. *Textile Research Journal*, 74(2), 97-100.
- Kovács, M., Dóka, O., Bicanic, D., & Ajtony, Z. (2017). Application of laser-based photoacoustic spectroscopy and colorimetry for quantification of anthocyanin in hard boiled candy. *Microchemical Journal*, 135, 100-104.
- Tavakolian, P., & Mandelis, A. (2018). Perspective: Principles and specifications of photothermal imaging methodologies and their applications to non-invasive biomedical and non-destructive materials imaging. *Journal of Applied Physics*, 124(16), 160903.
- Delgado-Vasallo, O., Valdes, A. C., Marin, E., Lima, J. A. P., Da Silva, M. G., Sthel, M., ... & Cardoso, S. L. (2000). Optical and thermal properties of liquids measured by means of an open photoacoustic cell. *Measurement Science and Technology*, 11(4), 412.

Characterization of vegetables lubricants with Nanoparticles by PAS

Joel Eduardo VALENCIA-HERNANDEZ ⁽¹⁾, Arturo DOMINGUEZ-PACHECO ^{(1)*},
 Ezequiel Alberto GALLARDO HERNANDEZ ⁽¹⁾, Claudia HERNANDEZ-AGUILAR ⁽¹⁾,
 Alfredo CRUZ-OREA ⁽²⁾, Eduardo SAN MARTIN-MARTINEZ ⁽³⁾

1. Posgrado en Ingeniería de Sistemas, Instituto Politécnico Nacional, SEPI-ESIME-Zac., Av. Instituto Politécnico Nacional, s/n, Col. Lindavista C. P. 07730, Ciudad de México, México.

2. Departamento de Física, CINVESTAV-IPN, A. P. 14-740, C. P. 07360, Ciudad de México, México.

3. Calzada Legaría No. 694 Col. Irrigación, C.P. 11500, Ciudad de México, México

fatur@hotmail.com

Environmental pollution is a global problem that increases day to day, and is caused by various fuels, lubricants, industrial waste, chemical products, etc. In order to reduce the use of mineral lubricants various alternatives have been proposed, highlighting lubricants of vegetable origin [1]. From this, many investigations have focused on studying and improving the tribological and thermal properties of lubricants [2], incorporating a wide variety of additives. Also in the last decades there is a great interest in the incorporation of nanoparticles of various materials in the additives [3-4]. The objective of this research is to characterize vegetable oils such as: coconut, castor, paraffin and Jatropa, added with calcium carbonate nanoparticles (CaCO₃) to be used as possible additives in lubricants. By means of photoacoustic spectroscopy (PAS), photoacoustic (PA) spectra of vegetable oils were obtained and their optical absorption coefficient obtained (β) was calculated. Figure 1a shows the different types of oil samples and Figure 1b shows the PA spectra of the pure oils that were obtained. Figure 2 (a, b, c, d) shows the differences between the PA spectra of the pure oils and the oils added with CaCO₃ nanoparticles. The changes presented by the PA spectra are similar to the changes presented by the tribological properties.

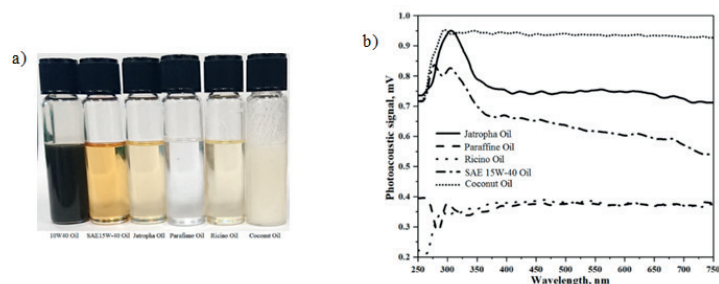


Fig 1. a) Samples oils, b) Photoacoustic signals of lubricants without nanoparticles.

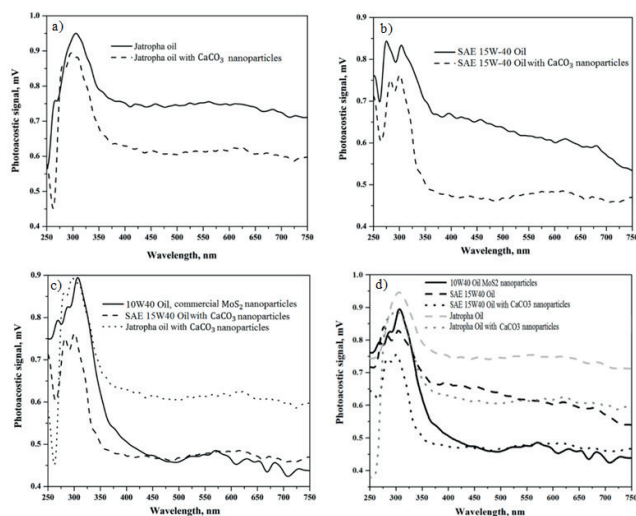


Fig. 2. a) Jatropa alone and with nanoparticle concentration of CaCO₃ 1 wt%, b) Mineral SAE 15w-40 alone and with 1 wt% of CaCO₃, c) Comparison of lubricants: mineral and jatropa with 1 wt% of CaCO₃, with 10W40 semisynthetic lubricant. d) Comparison of oils with and without nanoparticles, with 10W40 semisynthetic oil.

Acknowledgements

The authors thank the IPN through the support SIP, EDI, COFFA, etc. Joel Eduardo Valencia-Hernandez thank for the support, for Doctorate studies, through the grant awarded by Conacyt.

References

1. H. Mobarak, E. Mohamad, H. Masjuki, M. Kalam, K. Al Mahmud, M. Habibullah y A. Ashraful, *Renewable and Sustainable Energy Reviews*, n° 33, p. 34–43, 2014. doi.org/10.1016/j.rser.2014.01.062
2. Gallardo-Hernández, E. A., Lara-Hernández, G., Nieto-Camacho, F., Domínguez-Pacheco, A., Cruz-Orea, A., Hernández-Aguilar, C., ... & Flores-Cuautle, J. J. A. (2017). Thermal and Tribological Properties of Jatropa Oil as Additive in Commercial Oil. *International Journal of Thermophysics*, 38(4), 54. DOI 10.1007/s10765-017-2185-y
3. H. Spikes, *Tribol Lett*, pp. 1-26, 2015. DOI: 10.1007/s11249-015-0589-z
4. M. Gulzar, H. H. Masjuki, M. A. Kalam, M. Varman, N. W. M. Zulkifli, R. A. Mufti y R. Zahid, *Journal of Nanoparticle Research*, vol. 18, n° 223, pp. 1-25, 2016. DOI: 10.1007/s11051-016-3537-4
5. J. C. J. Bart, E. Gucciardi y S. Cavallaro, *Biolubricants Science and technology*, Oxford Cambridge Philadelphia New Delhi, Woodhead Publishing, 2013, pp. 24-68.
6. S. Qiu , J. Dong y G. Chen, *Lubrication Science*, vol. 12, n° 2, pp. 205-212, 2000/. doi.org/10.1002/ls.3010120207.
7. E. Prakash, R. Rajaraman y D. Sivakumar, *IOSR Journal of Mechanical and Civil Engineering*, vol. 6, pp. 68-74, 2014. e-ISSN: 2278-1684, p-ISSN: 2320-334X

Optical characterization of essential oils of Mexican aromatic plants

Mariana PALMA-TENANGO ⁽¹⁾, Arturo DOMINGUEZ- PACHECO ^{(1)*},
 Claudia HERNANDEZ-AGUILAR ⁽¹⁾, Rosa SÁNCHEZ-FERNÁNDEZ ⁽²⁾,

Marcos SOTO-HERNÁNDEZ ⁽²⁾, Alfredo CRUZ-OREA ⁽³⁾, Baldomero ESQUIVEL-RODRÍGUEZ ⁽⁴⁾

1. Posgrado en Ingeniería de Sistemas, Instituto Politécnico Nacional, SEPI-ESIME-Zac., Av. Instituto Politécnico Nacional, s/n, Col. Lindavista C. P. 07730, Ciudad de México, México.

2. Posgrado en Botánica, Colegio de Postgraduados, Campus Montecillo, Texcoco, Estado de México, 56230 México.

3. Departamento de Física, CINVESTAV-IPN, A. P. 14-740, C. P. 07360, Ciudad de México, México.

4. Instituto de Química, UNAM, Circuito Ext. s/n, Ciudad Universitaria, Alcaldía Coyoacán, C.P. 04510, Ciudad de México, México.

fatur@hotmail.com

Table 1. Composition of the essential oil of A. Mexicana

Compound	red toronjil	white toronjil
1-Octen-3-ol	✓	✓
β-Myrcene	✓	✓
Limonene *	✓	✓
Linalool *	✓	✓
Menthone	✓	✓
Isomenthone	✓	
Isomenthol	✓	
trans-Isopulegone	✓	
Estragole	✓	✓
Pulegone	✓	✓
Piperitone	✓	
β-Caryophyllene	✓	
Humulene	✓	
Germacrene D	✓	
Bicyclogermacrene	✓	
Caryophyllene oxide	✓	
Elixene		✓
Humulene		✓
Methyleugenol		✓
Caryophyllene		✓

* Compounds identified by comparison of mass and KI spectra of authentic standards.

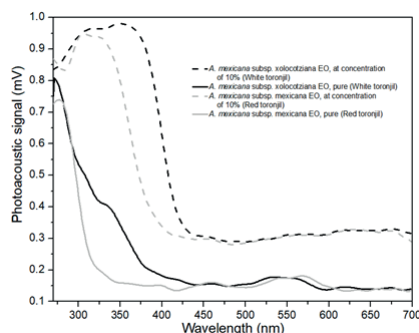


Figure 1. Photoacoustic signals of EO of Mexican aromatic plants.

The aromatic plants have a great potential for their high content of essential oils (EO). This type of substances is used in various industries, such as perfumes, cosmetics, pharmaceutical, agricultural and food products. It has been found that the biological activity of the EO is a function of the plant species and their chemical composition [1]. The common technique for its analysis is gas chromatography coupled to the mass (GC-MS). These types of materials could be characterized by techniques that do not require prior preparation, not destroy the samples. The photothermal techniques (PT) have been used to study the thermal and optical properties of a wide range of biological samples, such as agricultural seeds, seedlings and food [2]. In the present investigation, the objective was to obtain the optical characteristics of EO, which allow us to characterize two different species of Mexican aromatic plants. The optical absorption spectra obtained from the pure and diluted EO (10%) were obtained by photoacoustic spectroscopy. using the experimental configuration according to Hernández et al. (2011) [3]. In the essential oil of "red toronjil", were identified, as main compounds estragole (89.88%) and limonene (10.02%). In the "white toronjil" were identified, as major compounds pulegone (31.69%) and menthone (20.46%). The differences in the photoacoustic signals are highly correlated with the chemical differences of the EO.

Acknowledgements

CONACYT is thanked for the support to the postdoctoral research of Mariana Palma Tenango

References

1. Bakkali, F., Averbeck, S., Averbeck, D., & Idaomar, M. Food and Chemical Toxicology (2008). <http://doi.org/10.1016/j.fct.2007.09.106>
2. A. D. Pacheco, C. Hernández-Aguilar, A. C.O. International Journal of Thermophysics. (2017) <http://doi.org/10.1007/s10765-017-2244-4>
3. Hernández-Aguilar, C., Cruz-Orea, A., Ivanov, R., Dominguez, A., Carballo, A., Moreno, I., & Rico, R. (2011). Food Biophysics, 6(4), 481. doi:10.1007/s11483-011-9229-9

Thermal analysis and artificial vision of laser irradiation on maize

Hermenegildo CISNEROS CARRILLO*, **Claudia HERNANDEZ-AGUILAR**,
Arturo Dominguez-Pacheco, **Rosalba ZEPEDA BAUTISTA**

*Posgrado en Ingeniería de Sistemas, Instituto Politécnico Nacional, SEPI-ESIME-Zac.,
Av. Instituto Politécnico Nacional, s/n, Col. Lindavista C. P. 07730, Ciudad de México, México.*

hermes.cisneros82@gmail.com, clauhaj@yahoo.com, rzb0509@hotmail.com

Different researches have shown the thermal effects of laser irradiation on biologics objects where chemical reactions and temperature variations are caused by the components inner, properties and physical features [1-2]. So, it is important to know the temperature variations that the maize seed (*Zea mays L.*) could experience because it could be a strategy to identify and classify them. The objective of this research work was to analyze the thermal effects of laser irradiation on crystalline-type corn grain and get characteristic patterns of color and geometrical measurements using an Artificial Vision System (AVS). Three color categories were implemented: intense, middle and transparent of the same variety. The temperature variation of corn grains caused by laser light exposition during 60 s was captured through a thermal camera according to Hernández (2015b). The results point out, to a time of 60 s, it is possible to identify significant variations in the increase temperature when the three maize grains category implemented were compared. The highest variation of temperature was obtained by corn kernels of intense color with 1.075 oC with respect to the initial temperature, attained at 60 s of exposure of laser light, where the temperature reached to 23.975 oC, having an increment of 4.69% with respect to its initial temperature and an average increase of 0.1075 oC (Table 1). Likewise, the results of AVS (Table 2) indicated that the grains, with the original color, had greater difference in color intensities than the thermal images color intensities in RGB space. In this way, the thermal images analysis with the results obtained by AVS, could be a useful strategy to identify and classify maize.

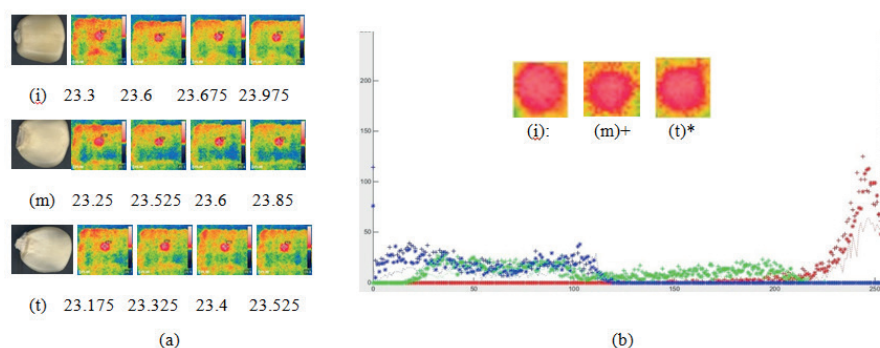


Fig. 1. Thermal images analysis. a) Temperature evolution, b) Color intensity graph RGB to thermal images, i - intense, m - middle, t-transparent.

Table 1. Comparison of mean temperature at various times during and after the incidence of laser light.

Parameter	Variety	t_0	t_2	t_4	t_6	t_8	t_{10}
Changes of temperature (°C) with turned on laser							
	Intense	22.9a	23.3a	23.6a	23.675a	23.85a	23.975a
	Middle	22.9a	23.25a	23.525a	23.6a	23.825a	23.85 ab
	Transparent	22.9a	23.175a	23.325a	23.4a	23.5a	23.525b
LSD (0.05%)		0	0.2099	0.3146	0.3351	0.4402	0.3613
R ²		0	0.671827	0.715311	0.757848	0.714985	0.845776
Temperature decay (°C) turned off laser							
	Intense	23.975a	23.675a	23.65a	23.45a	23.425a	23.4a
	Middle	23.85ab	23.6a	23.425a	23.4a	23.375a	23.3a
	Transparent	23.525b	23.35a	23.25a	23.225a	23.175a	23.175a
LSD (0.05%)		0.3613	0.5294	0.4458	0.4047	0.4505	0.5403
R ²		0.845776	0.69626	0.801742	0.81012	0.774387	0.784066

Means with the same letter in a column are statistically equal (LSD, $p \leq 0.05$), t - time (t_0, t_2, \dots, t_{10}) represent the time 0, 6, ..., 54 y 60 s.

B Materials Science and Characterization

Table 2. Comparison of mean values of characteristics obtained with con AVS.

Category	Color characteristics			Physical characteristics	
	R	G	B	Major axis	Minor axis
Values of images in original color					
Intense	159.217625	148.6801	116.5466	43.60425	37.05105
Middle	165.095275	156.407275	133.765275	49.88495	40.752675
Transparent	149.593275	142.900475	125.737275	40.96515	33.994275
Values of thermal images					
Intense	242.8905	96.6515	62.6636	37.6287	36.241
Middle	239.9074	107.6872	48.2508	47.9881	44.091
Transparent	242.2245	103.2385	54.361	47.4829	41.9369

Acknowledgements

The authors thank the IPN through the support SIP, EDI, COFFA, etc. Hermenegildo Cisneros Carrillo thank for the support, for Doctorate studies, through the grant awarded by Conacyt.

References

1. Hernandez-Aguilar, C., Dominguez-Pacheco, A., & Cruz-Orea, A. (2015). *International Journal of Thermophysics*, 36(9), 2401-240C, DOI 10.1007/s10765-015-1882-7
2. A.Yu. Popov, N.A. Popova, A.V. Tyurin, *Optics and Spectroscopy*, 2007, Vol. 103, No. 4, dio:10.1134/S0030400X07100232
3. Aguilar, C. H., Pacheco, F. A. D., Orea, A. C., & Tsonchev, R. I. (2015). *International Agrophysics*, 29(2), 147-156, doi: 10.1515/intag-2015-0028

Photoacoustic spectroscopy on the evaluation of seedlings from seed treated by polluting gases

Joel Eduardo VALENCIA-HERNANDEZ, Arturo DOMINGUEZ-PACHECO*,
Claudia HERNANDEZ-AGUILAR, Alfredo CRUZ-OREA

1. Posgrado en Ingeniería de Sistemas, Instituto Politécnico Nacional, SEPI-ESIME-Zac., Av. Instituto Politécnico Nacional, s/n, Col. Lindavista C. P. 07730, Ciudad de México, México.

2. Departamento de Física, CINVESTAV-IPN, A. P. 14-740, C. P. 07360, Ciudad de México, México.

fartur@hotmail.com

Spectroscopy is the study of the interaction of electromagnetic radiation with atoms and molecules to provide qualitative and quantitative chemical and physical (structural) information, that is contained within the wavelength or frequency spectrum of energy that is either absorbed or emitted [1,2]. PAS is a sort of spectroscopy, nondestructive based on photothermal phenomena, which allows spectroscopic studies [3]. Thanks to the technological advances, is a convenient option to be incorporated in the agriculture for the study of seedlings, due to that allows to obtain optical qualities of various objects of study in different states e.g. liquids and solids. In this way, it could be possible to qualitatively evaluate the quality of seedlings from seed treated with car exhaust emissions. The pollutants emitted by the vehicles are mainly nitrogen oxide, carbon monoxide (CO), and carbon dioxide (CO₂). So, it was proposed in this investigation to evaluate by PAS, the seedlings from maize, lentil and bean seeds treated with CO and CO₂ to compare the photoacoustic signals within the spectral ranges belonging to the chlorophyll. Figure 1 shown the experimental setup used, where it is observed, the exhaust without catalyst of a car and a container system, adapted with CO, CO₂, humidity and temperature sensors, used for the treatment of the seeds to different times. Short-term and long-term exposure to toxic substances suspended in the air has a different toxicological impact on humans and the environment. Carbon monoxide has a great negative effect on human life when the gas emitted by the exhaust system of the vehicles is inhaled [4]. In this investigation it was found that the spectra of the seedlings are modified according to the time of exposure to the pollutants from a car exhaust (Fig. 2).

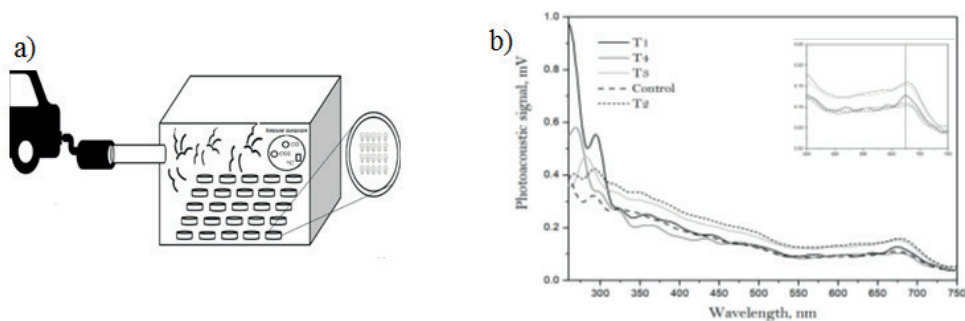


Fig. 1 a) Experimental setup for treatment of seeds, b) Photoacoustic spectra obtained from seedlings

Acknowledgements

The authors thank the IPN through the support SIP, EDI, COFFA, etc. Joel Eduardo Valencia-Hernandez thank for the support, for Doctorate studies, through the grant awarded by Conacyt.

References

1. Hernández-Aguilar, C., Domínguez-Pacheco, A., Cruz-Orea, A., & Ivanov, R. (2019). Journal of Spectroscopy, 2019. <https://doi.org/10.1155/2019/5920948>
2. R. Martel, C. N. N'Soukpoe-Kossi, P. Paquin, and R. M. Leblanc, Journal of Dairy Science, vol. 70, no. 9, pp. 1822–1827, 1987. DOI: 10.1021/jf00081a023
3. D. D. Bicanic, Journal of Molecular Structure, vol. 993, no. 1–3, pp. 9–14, 2011. <https://doi.org/10.1016/j.molstruc.2010.12.061>
4. Chamberlain, O. (2016). Carbon-Monoxide (CO): A Poisonous Gas Emitted from Automobiles, Its Effect on Human Health. Adv Automob Eng, 5(151), 2, DOI: 10.4172/2167-7670.1000151

Thermal Effusivity Investigations of Solid Thermoelectrics Using the Front Photopyroelectric Detection

Carmen TRIPON^{(1)*}, Dorin DADARLAT⁽¹⁾, Katalin KOVACS⁽¹⁾, Mladen FRANKO⁽²⁾

1. National R&D Institute for Isotopic and Molecular Technologies, Donat Str. 67-103, Cluj-Napoca, Romania.

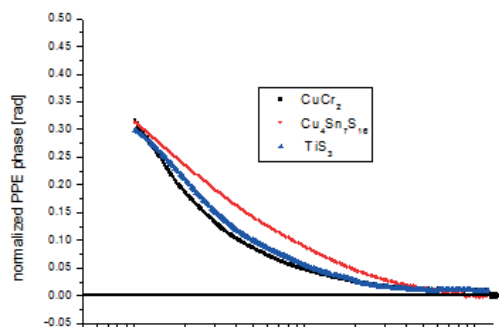
2. Laboratory for Environmental and Life Sciences, University of Nova Gorica, Nova Gorica, Slovenia.

Carmen.Tripon@itim-cj.ro

The thermoelectric (TE) materials are intensively studied in connection with their energy applications. The efficiency of a TE device depends on material characteristics such as the Seebeck coefficient (S_0), thermal (κ), and electrical (σ) conductivities, and the figure of merit $zT = TS_0^2\sigma/\kappa$ is used to compare TE materials performances. Together with these “classical” applications, last years, the TE materials were proposed to be used as radiation sensors. For both applications the knowledge of the TEs’ thermal parameters is important.

Many solid thermoelectrics are sintered porous materials, whose thermal parameters are difficult to be measured by contact PT techniques especially due to their porosity. Several PPE/PTE investigations, in various configurations, have been made with the purpose of retrieving the static and dynamic thermal parameters of different types of solid thermoelectric materials but, unfortunately, the influence of the coupling fluid could not be eliminated. Recently, Salazar and colab. proposed a new FPPE model in which the coupling fluid between a porous solid sample and the pyroelectric sensor is replaced by air [1]. In such a way there is no penetration of the coupling fluid inside the porous sample, but the model has to take into account the heat losses by convection and radiation in the surrounding gas. In this paper we use Salazar’s method to measure accurately the thermal effusivity of some largely used solid thermoelectric materials.

The theory of the FPPE configuration (including the heat losses by convection and radiation) was largely described in Ref. [1]. We will use in the paper the same equations with the particularity that the coupling fluid between sensor and sample is air.



As test samples we selected CuCrO_2 , $\text{Cu}_4\text{Sn}_7\text{S}_{16}$ and TiS_3 and the detection configuration is the FPPE one, in the thermally thin and optically opaque regime for the sensor and thermally thick for the sample. Practically, we will perform a frequency scan of the phase of the normalized FPPE signal (normalization with the signal obtained with empty sensor), with three fitting parameters: sample’s thermal effusivity “ e_s ”, heat losses by convection and radiation “ h ” and air gap thickness “ L_{air} ”.

The results obtained for the thermal effusivity (together with the remaining two thermal parameters) of the investigated TE materials are presented in Fig.1 and Table 1.

Fig. 1. Frequency scan of the normalized FPPE phase for the investigated TE solids.

Table 1. The values of the thermal effusivity for the investigated TEs together with the two fitting parameters (L_{air} and h).

Thermoelectric material	e_s , $\text{Ws}^{1/2}\text{m}^{-2}\text{K}^{-1}$	h , $\text{Wm}^{-2}\text{K}^{-1}$	L_{air} , μm
CuCrO_2	822 +/- 45	36	26
$\text{Cu}_4\text{Sn}_7\text{S}_{16}$	565 +/- 31	40	10
TiS_3	698 +/- 35	40	19

In conclusion the method described in the paper seems very suitable for thermal effusivity measurements of solid porous TE materials, due to the fact that it eliminates any influence of the coupling fluid on the results.

Acknowledgements

This work was financially supported by Romanian Ministry of Research and Innovation, through the Core Program, Project No. PN 19 35 02 01. The authors acknowledge Prof E. Guilmeau for preparing and delivering the TE samples.

References

1. A. Salazar, A. Oleaga, A. Mendioroz and E. Apiñaniz, Measurement, 121, 96 (2018).

Photothermoacoustic evaluation of local thermal properties of soldered joints in photovoltaic solar cells

Alexey GLAZOV*, Vitaliy KALINOVSKII, Alexey NASHCHEKIN, Kyrill MURATIKOV

Ioffe Institute, St. Petersburg, Russia

Glazov.holo@mail.ioffe.ru

One of the problems of modern concentrated photovoltaics is an effective heat removal from a photovoltaic structure. Concentrated radiation results in overheating of solar cells what has a negative impact on quantum efficiency [1] and can cause accelerated degradation. The efficiency of concentrator modules based on nanoheterostructure cascade solar cells has already reached 40 - 44% [2, 3] and that of photodiodes has raised up to 50% [4]. Active life of these devices requires perfect thermal contacts between the semiconductor substrate and the heat sink. A soldered joint which mainly used in these constructions is one of the bottlenecks in the heat sink system.

The choice of soldering composition is determined by many reasons, primarily mechanical reliability. Thermal properties of a solder alloy are usually taken from handbooks. These data are determined on the basis of stationary tests of bulk samples. However, as it was shown earlier [5, 6], the thermal conductivity of the joint may differ significantly from reference data due to different soldering conditions. The thermal conductivity of the alloy is determined not only by the thermal conductivity of the components, but also by its structure. Interphase boundaries play a significant role in the processes of heat transfer. On the other hand, it is known that during reflow, penetration of contact materials into the depth of the solder layer occurs, which leads to the formation of various intermetallic complexes. Such complexes, for example, in the form of whiskers, can significantly degrade the mechanical properties of the joints. Their influence on heat-conducting properties is studied much less.

This paper presents a study of the local heat-conducting properties of a soldered joint based on a eutectic lead-tin alloy in the structure of nanoheterostructure photovoltaic solar cell on AlN ceramic heat sink and their correlation with local metal composition of the solder alloy.

Before studying the thermal characteristics of the joint, its structure was examined by a scanning electron microscopy (SEM) and X-ray spectroscopy (EDS). SEM revealed two regions in the solder layer with different structures along the interfaces. The EDS microanalysis confirmed that the elemental composition of each of the regions is very different. The contact layers were made of different metals. For example, before soldering, AlN ceramics has a thick cover layer of gold. The SEM and EDS showed the complete dissolution of the gold layer the presence of a significant amount of gold right up to the middle of the joint, which is consistent with the data on the solubility of gold in lead-tin alloys [7]. In fact, dissolved gold displaced lead into region closer to Ge wafer. Obviously, such a redistribution of the elemental composition should result in a change in the thermophysical properties of the alloy.

Probe beam deflection (PBD) and piezoelectric photoacoustic (PA) methods were applied to study local thermophysical properties in the soldered joint. Fig. 1 shows the schema of a sample and the behavior of the PBD and PA signals when scanning a sample across a soldered joint. The resulting graphs demonstrate the inhomogeneity of the solder layer, where one can also select two main parts with different signal amplitude, corresponding to the previously selected areas on the SEM micrograph.

For a quantitative analysis of the PBD signal, we apply the approach proposed for the study of similar objects [6, 8]. The calculation was made for a multilayer sample with vertical interfaces. The solder layer was considered as the 3-layer structure. The fitted curve describes well the experimental PBD data.

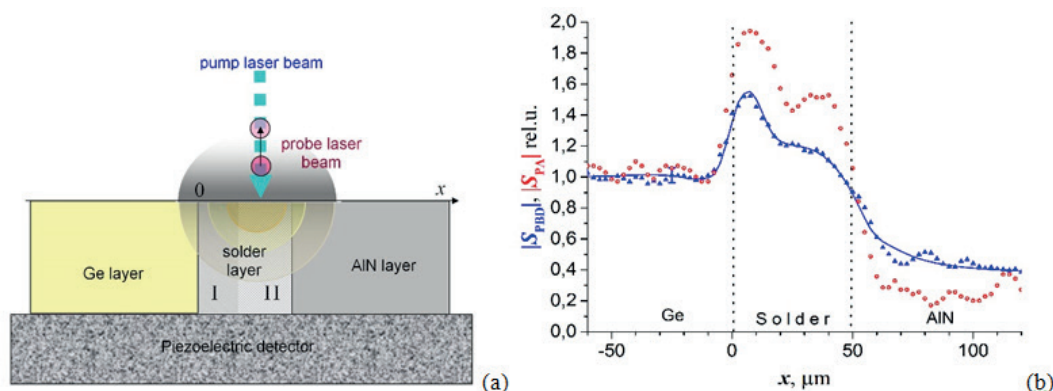


Fig. 1. (A) Layout of the sample relative to the PBD and PA detectors. (B) The PA (red circles) and PBD (blue triangles) signals vs pump beam position. Solid curve is a fitting of PBD experimental data.

B Materials Science and Characterization

Thus, multilayer metal contacts on the surface of semiconductors and ceramics to be jointed by soldering may lead to forming solder layers with a complex distribution of metal components during reflow. In accordance with the data obtained the composition inhomogeneity results in the variation of local thermal properties of the solder layer. This inhomogeneity can lead to local overheating and thermal stresses, which result in disruption of the mechanical strength of a joint and degradation of a semiconductor device.

References

1. J. R. Wilcox, "Solar Cell Temperature Dependent Efficiency and Very High Temperature Efficiency Limits," Open Access Dissertations. Paper 19. (2013)
2. W. Guter, J. Schone, S.P. Philipps, M. Steiner, G. Siefer, A. Wekkeli, E. Welsler, E. Oliva, A.W. Bett, and F. Dimroth, *Appl. Phys. Lett.* 94 (22), 223504 (2009) doi.org/10.1063/1.3148341
3. <http://www.greentechmedia.com/articles/read/Sharp-Hits-Record-44.4-Efficiency-For-Triple-Junction-Solar-Cell>.
4. V. S. Kalinovskii, E. V. Kontrosh, G. V. Klimko, T. S. Tabarov, S. V. Ivanov, and V. M. Andreev, *Tech. Phys. Lett.*, 44, 1013 (2018)
5. A. L. Glazov, V. S. Kalinovskii, E. V. Kontrosh, K. L. Muratkov, *Tech. Phys. Lett.*, 42 (6), 570 (2016)
6. A. L. Glazov, V.S. Kalinovskii, K.L. Muratkov, *Int. J. Heat Mass Transfer.* 120, 870 (2018) doi.org/10.1016/j.ijheatmasstransfer.2017.12.049
7. B. Kobe, N.S. McIntyre, *Acta Materialia* 50 (18), 4667 (2002) doi.org/10.1016/S1359-6454(02)00319-1
8. A. Ocariz, A. Sanchez-Lavega, A. Salazar, D. Fournier, and A. Boccard, *J. Appl. Phys.* 80 (5) 2968 (1996) doi.org/10.1063/1.363154

Thin film photothermal characterization: Photoacoustic thermal wave interferometry on low thermal diffusivity materials

Kai HERRMANN, Nelson Wilbur PECH-MAY, Markus RETSCH

Department of Physical Chemistry, University of Bayreuth

kai.herrmann@uni-bayreuth.de

Despite the solid theoretical fundament, the photoacoustic technique did not receive a lot of recognition in thermal characterization.^[1,2] For characterizing thermally thin samples, not only the amplitude but also the phase shift signal can be evaluated. Bennett and Patty proposed the so-called thermal wave interferometry as a potential application of the photoacoustic effect for thermally thin samples.^[3] Due to partial reflection of thermal waves at the sample backing interface, thermal wave interference effects at the sample surface are apparent for thermally thin samples.^[4] Depending on the materials inherent thermal diffusivity the thermally thin regime can be accessed by either adjusting the sample thickness or by adapting the thermal penetration depth via the measurement frequencies. In this work, we establish a generalized description of measurement parameters depending on the sample parameters, demonstrated by a well-known reference sample of thermally grown SiO₂. Furthermore, the applicability is demonstrated by using PMMA thin films on silicon dioxide, silicon and silicon carbide.

Thermal wave interferometry

Thermal wave interference is implicitly contained in the Rosenzweig-Gersho theory, still, it is worth pointing out the role of interference effects. Due to the periodic nature of the thermal excitation, rapidly damped so-called thermal waves are generated. The magnitude of the thermal reflection coefficient R for normal incidence is determined by the ratio of thermal effusivities, which may be regarded as a measure of the thermal mismatch between two media.

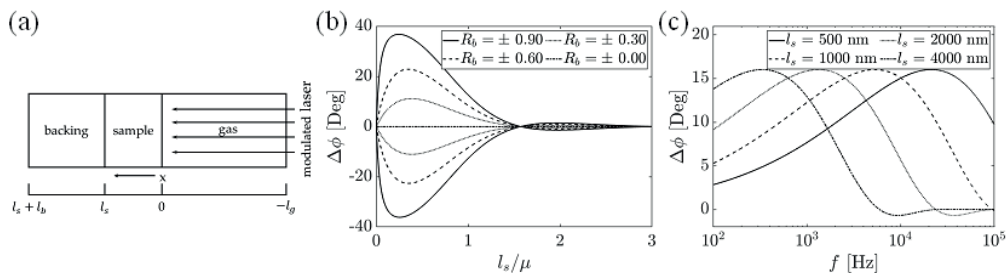


Fig. 1. (a) General structure of a two-layered sample. (b) Theoretical phase shift of a two-layered sample for different reflection coefficients R_b at the sample backing interface, as a function of thermal thickness with μ being the thermal penetration depth.^[3] (c) Influence of sample thickness for a polymeric sample for a fixed reflection coefficient ($R_b = -0.43$) and thermal diffusivity ($\alpha = 1.2 \cdot 10^{-7} \frac{m^2}{s}$).

Performing photoacoustic measurements on thermally thin samples offers the possibility to evaluate the phase shift of the generated acoustic signal related to the thermal excitation. This phase shift is linked to the thermal effusivity ratio between sample and backing and, furthermore, to a phase shift caused by heat propagation through the sample and reflection at the sample backing interface. The phase shift due to propagation depends on the sample thickness l_s and its thermal diffusivity α . With the method being sensitive to both, thermal diffusivity and thermal effusivity, it is possible to extract the samples thermal conductivity.

Results

The concept of thermal wave interferometry is adapted for samples with low thermal diffusivities. Depending on the thermal properties, a suitable sample thickness has to be adjusted to obtain an extremum of the phase shift within the accessible frequency regime. Only then, a meaningful fit to the measurement data can be conducted. Due to the limited accessible frequency regime for photoacoustic measurements, thin films can only be significantly analyzed for low thermal diffusivity samples. Thermally grown silicon dioxide on a silicon wafer was utilized as an established reference sample. Data analysis using Levenberg-Marquardt least-square fitting using the multilayer theory from Wang et al. provides excellent agreement between literature and determined thermal properties.^[5] Furthermore, the influence of the reflection coefficient between sample and backing, and the influence of the samples thermal thickness could be confirmed by measurements.

B Materials Science and Characterization

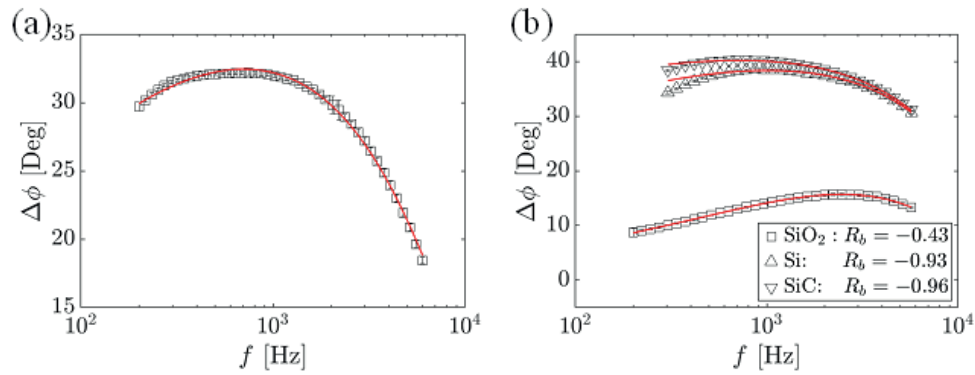


Fig. 2. Phase shift data of (a) 5 μm thermally grown SiO_2 on a Si substrate and (b) a 2 μm PMMA film on SiO_2 , Si and SiC with the performed data analysis. Continuous lines represent the fit to the model.[5]

Deviations in the low-frequency regime for samples on Si and SiC can be attributed to the absence of thermally thick substrates at those frequencies.

Acknowledgments

This work was funded by the German Research Foundation (DFG) by the SFB840.

References

1. A. Rosencwaig, A. Gersho, J Appl Phys 47 (1), 64 (1976) doi:10.1063/1.322296
2. H. Du, H. Hu, IOP Conference Series: Earth and Environmental Science 69, (2017) doi:10.1088/1755-1315/69/1/012176
3. C.A. Bennett, Jr., R.R. Patty, Appl Opt 21 (1), 49 (1982) doi:10.1364/AO.21.000049
4. D.P. Almond, P.M. Patel, Photothermal Science and Techniques. (Chapman & Hall, 1996)

Investigation of morphology, thermal and electron properties of thin oxide films

Anna Kaźmierczak-Bałata^{(1)*}, Jerzy Bodzenta⁽¹⁾, Maciej Krzywiecki⁽¹⁾, Lucyna Grządziel⁽¹⁾,
Marek Guziewicz⁽²⁾, Vishnukanthan Venkatachalapathy⁽³⁾, Andrej Kuznetsov⁽³⁾

1. Institute of Physics CSE, Silesian University of Technology, Konarskiego 22B, 44-100 Gliwice, Poland

2. Institute of Electron Technology, Al. Lotników 32/46, 02-668 Warszawa, Poland

3. Department of Physics, University of Oslo, Sem Saelands vei 24, 0316 Oslo, Norway

*Author's e-mail: akazmierczak@polsl.pl

In this work the morphology, thermal and electron properties of thin oxide films were investigated. The zinc oxide thin films were deposited by Atomic Layer Deposition (ALD) method and their thickness varied from 15 nm to 118 nm. ZnO is typically n-type semiconductor with a direct band gap of 3.3 eV at 300 K, that emits light in the near-UV region. ZnO found numerous applications in electronics and optoelectronics as a transparent conductor in solar cells, polycrystalline channels in film transistors, etc [1-4]. While doped with Aluminium ZnO is promising material for thermoelectric applications. The thermal conductivity of thin ZnO films is typically two orders of magnitude lower than for bulk crystal and depends on inner structure of the layer and film fabrication method. Typical value of few $\text{Wm}^{-1}\text{K}^{-1}$ for ALD thin film is very low comparing to $80 \text{ Wm}^{-1}\text{K}^{-1}$ for bulk crystal [1].

The ZnO thin films were deposited on Si(100) wafers at 200°C substrate temperature. The surface morphology was determined by the atomic force microscopy. The thin films were fine grained, while the thicker films were formed with larger, elongated grains. The X-ray diffraction measurements revealed polycrystalline structure of the thin films with preferred orientation 100. Determination of the thermal conductivity of oxide thin films was realized by the use of scanning thermal microscopy. The thermal conductivity was dependent on layer thickness and grain diameter and varied from 0.28 W/mK to 4.29 W/mK. The variations in thermal conductivity followed the changes in morphology of layers. X-ray photoelectron spectroscopy (XPS) was used to reveal surface chemical and electronic properties and to correlate the properties with results of the thermal investigations. The surface topography was determined by the RMS, which varied in range from 1.1 nm to 2.6 nm. An exemplary AFM, XRD and XPS results are presented in the Fig. 1 a), b) and c) respectively.

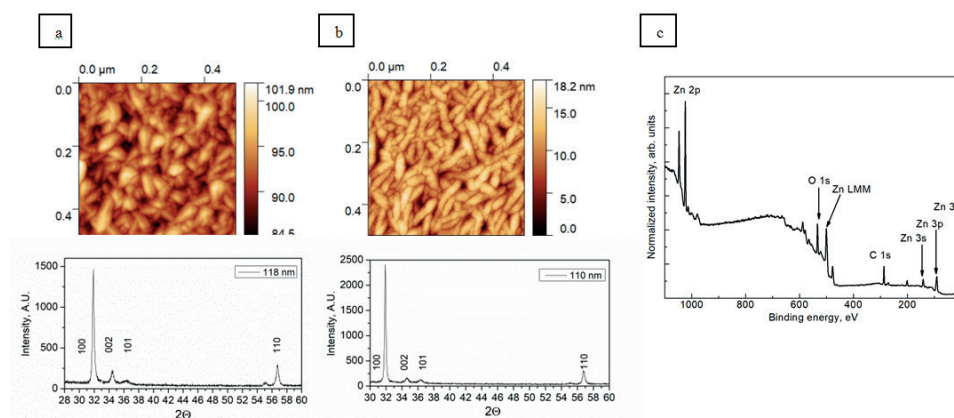


Fig. 1. Surface topography and X-ray diffraction patterns of oxide thin films deposited on Si substrate at 200°C for: (118 nm) ZnO layer a), (110 nm) Al doped ZnO layer b), exemplary XPS spectra of (110 nm) Al doped ZnO sample surface c).

Acknowledgements:

This work was supported through pro-quality grant by the Silesian University of Technology (project number 14/990/RGJ18/0101). The authors acknowledge ESPEFUM laboratory at Institute of Physics – CSE, Silesian University of Technology for access to SThM, XPS experimental setup.

References

- [1] U. Ozgur, Ya. I. Alivov, C. Liu, A. Teke, M. A. Reshchikov, S. Doğan, V. Avrutin, S.-J. Cho, H. Morkoc., J. Appl. Phys. 98, 041301 (2005)
- [2] S.J. Pearton, D.P. Norton, M.P. Ivill, A.F. Hebard, J.M. Zavada, W.M. Chen, I.A. Buyanova, IEEE Trans. Electron Devices 54, 1040–1048 (2007)
- [3] U. Ozgur, D. Hofstetter, and H. Morkoc, Proceedings of the IEEE 98 (7), 1255 (2010).
- [4] E. Fortunato, A. Gonçalves, A. Pimentel, P. Barquinha, G. Gonçalves, L. Pereira, I. Ferreira, R. Martins, Appl. Phys. A Mater. Sci. Process. 96, 197 (2009)

In-plane thermal diffusivity measurements of PES woven textiles

Maria Cristina LARCIPRETE*, Stefano PAOLONI, Roberto LI VOTI, Concita SIBILIA

1. Dipartimento di Scienze di Base ed Applicate per l'Ingegneria, Sapienza Università di Roma, Roma, Italy

2. Dipartimento di Ingegneria Industriale, Università degli Studi di Roma Tor Vergata, Roma, Italy

mariacristina.larciprete@uniroma1.it

In this work we carried a remote and non-destructive analysis for the characterization of different PES textiles. We applied the lock-in thermography technique for the evaluation of thermal diffusivity of the investigated samples. Thermal diffusivity is expected to depend on several factors, including the local density of the sample induced by the woven structure of the fabric. Experimental results obtained on three different samples are presented and discussed.

Thermal properties of textiles such as thermal conductivity, thermal absorptivity and thermal diffusivity are influenced by fabric characteristics such as material of fibers, structure, density, air permeability and many other factors. As a consequence, a local inter-dependence between thermal diffusivity and textile density is to be expected. Following these considerations, we characterized the thermal diffusivity of three different PES (polyethersulfone) textiles in the infrared regime, i.e. 3.3-5.1 microns. All the investigated textile structures are composed by the same PES fibers, while differing by woven structure characteristics such as fiber density, and weaving patterns.

In particular, we employed the lock-in thermography technique for the evaluation of thermal diffusivity of the investigated samples. Lock-in thermography technique is based on the application of an input modulated heating to the surface of an object. The resulting temperatures oscillation on sample surface is thus analyzed as a function of distance from the center of the heating laser-spot. The experimental set up is composed by a modulated Argon laser system whose frequency is locked to an infrared lock-in camera, operating in the IR range, pointing the sample surface. Here, the synchronized IR camera provides images of both the amplitude and phase of the oscillating temperature variation. In particular the diffusivity value can be retrieved from the slope of the asymptotic linear dependence of the phase as a function of the lateral offset from the center of the heated spot [1]. The spatial dependence of thermal diffusivity, i.e. isotropy or anisotropy, with respect to the direction of the applied laser field, can be found, thus resulting a reliable indicator of the density of fibers into a textile structure.

References

1. E. Wu, Q. Gao, M. Li, Y. Shi and A. Mandelis, "Study on in-plane thermal conduction of woven carbon fiber reinforced polymer by infrared thermography", *NDT and E International*, 94, 56-61 (2018).

Electronic transport characterization of B⁺ ion-implanted silicon wafers using nonlinear two-layer frequency-domain photocarrier radiometry model

Xiaoke LEI, Bincheng LI*, Qiming SUN, Jing WANG, Chunming GAO

School of Optoelectronic Science and Engineering, University of Electronic Science and Technology of China, Chengdu 610054, China

bcli@uestc.edu.cn

Mounting experimental evidences have confirmed that the nonlinearity between photocarrier radiometry (PCR) amplitude and excitation power is ubiquitous for silicon (Si) materials and devices [1-4]. A nonlinearity coefficient β has been proposed as an ad hoc modification of the linear PCR model to address the PCR nonlinearity [2]. Wang *et al.* [3] have performed a further study on nonlinearity with a single-layer model and found that β usually ranges between 1 to 2, and has a positive correlation with wafer resistivity. Subsequently, a nonlinear two-layer theoretical model has been proposed for the investigation of ion-implanted Si samples [5], and both experimental results and theoretical simulations have corroborated that the existence of nonlinearity and the negative correlation between the nonlinearity coefficient and the implantation dose in the samples. Electronic transport parameters are further quantitatively characterized using the nonlinear two-layer frequency-domain PCR model.

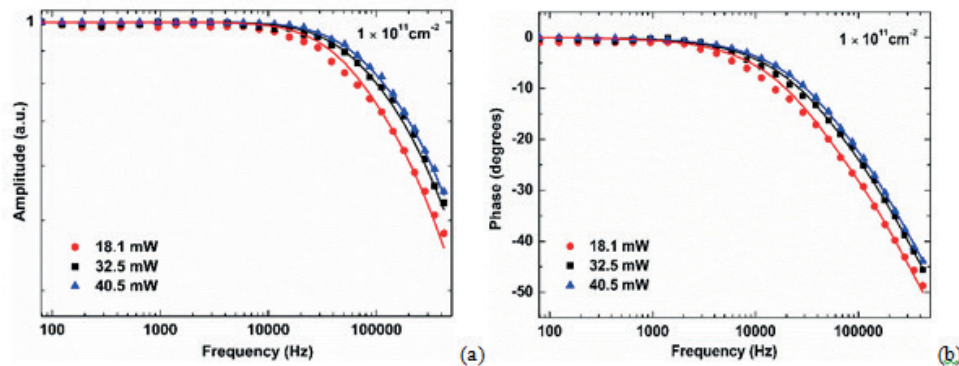


Fig. 1. Dependences of PCR amplitude (a) and phase (b) on frequency at three different excitation powers for B⁺ ion-implanted silicon wafer. The implantation dose was $1 \times 10^{11} \text{ cm}^{-2}$. Symbols represent the experimental data and solid lines represent the corresponding linear fits

In this presentation, several Si samples with implantation doses from 10^{11} to 10^{16} cm^{-2} are tested using PCR frequency scans at three different excitation laser powers, and good agreements between theory and experiment are presented, as shown in Fig. 1. Both the nonlinearity of excitation power versus PCR amplitude and phase and the dependence between nonlinearity and implanted dose are analyzed separately in frequency domain. The electronic transport parameters (e.g. minority carrier lifetimes, carrier diffusivities, and surface recombination velocities etc.) of samples are measured by simultaneously fitting the three-group experimental results to the nonlinear two-layer PCR model with different doses. The comparison of fitting results for electronic transport parameters between linear and nonlinear two-layer model via multi-parameter estimation procedure is fully discussed. The theoretical simulations are devoted to analyzing the error of fitting experimental data with traditional linear approximation model.

Acknowledgements

The authors thank the financial support by the Natural Science Foundation of China (Grant Nos. 61601092, and 61771103).

References

- [1] D. Guidotti, J. S. Batchelder, A. Finkel, and J. A. Van Vechten, *Phy. Rev. B* 38, 1569 (1988); doi:10.1103/PhysRevB.38.1569
- [2] J. Tolev, A. Mandelis, and M. Pawlak, *J. Electrochem. Soc.* 154, H983 (2007); doi:10.1149/1.2780862
- [3] Q. Wang and B. C. Li, *J. Appl. Phys.* 118, 215707 (2015); doi:10.1063/1.4936958
- [4] Q. M. Sun, A. Melnikov, J. Wang, and A. Mandelis, *J. Phys. D: Appl. Phys.* 51, 15LT01 (2018); doi:10.1088/1361-6463/aab395
- [5] X. Lei, B. Li, Q. Sun, J. Wang, and C. Gao, *AIP Advances* 9, 035125 (2019); doi: 10.1063/1.5092621

CCD-based thermal lensing for fast localization of microscale absorptive defects on large-sized laser components

Liangjia LI, Bincheng LI *, Qiming SUN

School of Optoelectronic Science and Engineering, University of Electronic Science and Technology of China, Chengdu, 610054, China

bcli@uestc.edu.cn

Large-sized laser components with diameters over 100 mm have been widely used in high power/energy laser systems. Most studies have shown that one of the key factors leading to laser-induced damages of laser components and limiting the operation fluence of the laser systems is strongly absorptive defects (usually with microscale sizes) on the surface/ subsurface of the optics [1].

Thermal lensing (TL) has proven to be a powerful technique to measure optical absorption of various materials with sub-ppm sensitivity and nm-scale resolution, and it is one of the non-destructive methods to characterize the absorptive defects of optical components. In previous studies modulated TL techniques with focused pump beams and point-by-point scanning were used to locate the strong absorptive defects. This raster-scan method is very time consuming and not practical for defect imaging of large-sized optical components.

In this presentation we propose a CCD-based pulse TL approach in which a probe pulse is employed to detect the TL signal of a large region induced by the irradiation of a high-energy, large-sized pump pulse. A theoretical model is developed to analyze and quantitatively evaluate the feasibility of this proposal. From Fresnel diffraction theory the complex electric-field distribution of the probe beam in the detection plane is [2,3]:

$$U_2(r_2, z_1 + z_2, t) = \frac{j2\pi}{\lambda z_1} \exp\left[-jk\left(z_2 + \frac{r_2^2}{2z_2}\right)\right] \times \int_0^\infty U_1'(r_1, z_1, t) J_0\left(k \frac{r_1 r_2}{z_2}\right) \exp\left(-jk \frac{r_1^2}{2z_2}\right) r_1 dr_1$$

Where, $U_1'(r_1, z_1, t)$ is complex amplitude of the probe beam on the exit surface of the sample, in which a pump pulse induced optical phase shift is added into the Gaussian probe beam. z_1 is the distance from the probe beam waist to the sample plane, z_2 is the distance from the sample plane to the detection plane, r_2 is the radial coordinate at the detection plane.

In order to show the TL signal caused by the pump pulse induced phase shift, the change of the intensity $\Delta I/I$ on the detection plane with and without the pump pulse excitation is used to describe the TL amplitude [4]:

$$S(z_2, t) = \frac{I(z_2, t) - I(z_2, t = \infty)}{I(z_2, t = \infty)} = \frac{I(z_2, t)}{I(z_2, t = \infty)} - 1$$

Where, $I(z_2, t)$ is intensity distribution of the probe beam on the detection plane (with a distance z_2) at time t where a CCD is used to detect the intensity profile.

The time delay (t) between the pump and probe pulses and the distance (z_2) between the sample surface and the detection plane are the two critical parameters for the optimization of the experimental configuration for sensitive detection of absorptive defects. Some simulation results aiming at the case of a $1\text{-}\mu\text{m}^3$ absorptive defect on the surface of a fused silica are shown in Fig. 1. The simulation results with two defects are presented in Fig. 2.

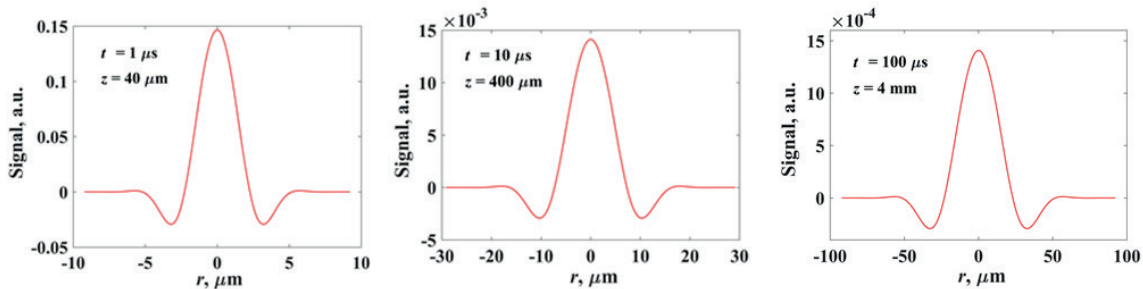


Fig. 1. TL signal of a $1\text{-}\mu\text{m}^3$ absorptive defect on the surface of a fused silica, under a 4 J/cm^2 short-pulse excitation. The results of three selected moments after the excitation are shown, i.e. $1\text{ }\mu\text{s}$, $10\text{ }\mu\text{s}$, and $100\text{ }\mu\text{s}$.

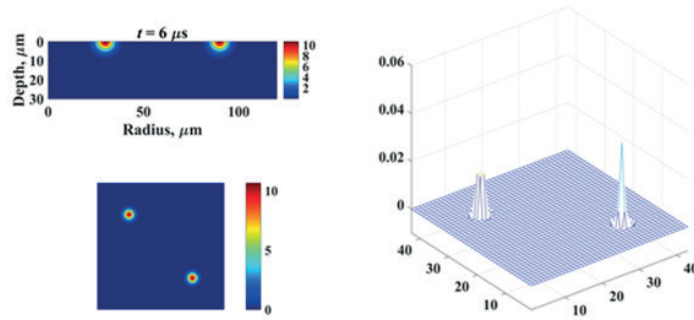


Fig.2. TL signals of two adjacent $1\text{-}\mu\text{m}^3$ absorptive defects at 6-s delay. with the only difference being one at the best while the other at the worst conditions.

Acknowledgements

The authors are grateful to National Natural Science Foundation of China (Grant No. U1830132).

References

1. H. J. Liu, J. Huang, F. R. Wang, X. D. Zhou, X. Ye, X. Y. Zhou, L. X. Sun, X. D. Jiang, Z. Sui, and W. G. Zheng, *Opt. Express* 21(10):12204-12217 (2013) doi:10.1364/OE.21.012204
2. J. F. Power, *Applied Optics* 29 (1): 52-63 (1990) doi:10.1364/AO.29.000052
3. J. Shen, R. D. Lowe, and R. D. Snook, *Chemical Physics* 165, 385-396(1992) doi:10.1016/0301-0104(92)87053-c
4. B. C. Li and E. Welsh, *Applied Optics* 38(24): 5241-5249 (1999) doi:10.1364/Ao.38.005241

Photoacoustic Spectroscopy of noble metal functionalized nanoparticles based networks

I. FRATODDI ⁽¹⁾, R. MATASSA ⁽²⁾, G. FAMILIARI ⁽²⁾, G. LEAHU ⁽³⁾, A. BELARDINI ⁽³⁾,
R. LI VOTI ^{(3)*}, and C. SIBILIA ⁽³⁾

1. Department of Chemistry, Sapienza University of Rome, P.le A. Moro 5, 00185, Rome Italy

2. Department of Anatomical, Histological, Forensic and Orthopaedic Sciences, Section of Human Anatomy, Sapienza University of Rome, Via A. Borelli 50, 00161 Rome, Italy.

3. Department of Basic and Applied Sciences for Engineering, Sapienza University of Rome, Via Antonio Scarpa 16, 00161 Rome, Italy.

roberto.livoti@uniroma1.it

Functionalized metal nanoparticles are transforming many research fields, from biomedicine to catalysis and energy conversion with the intellectual excitement associated to the chance of finding new materials with synergic properties. The large surface area of MNPs leads to high local concentrations of ligands on the surface, providing enhanced opportunities for drug delivery [1]. Additionally, MNPs can be functionalized with optically active organic or organometallic molecules and the optical/electronic properties of the metallic core can be tuned together with the optical behavior of the ligands [2]. Moreover, the easy manipulation of colloidal MNPs allows their self-assembly into complex structures, 2D or 3D networks that show collective properties. A fundamental role in properties and potential applications is played by the functionalizing ligand; for example, organic thiols, [3] organometallic systems [4] or polymers [5] can make NPs based colloids easily handy in organic or aqueous media.

In this paper silver nanoparticles (AgNPs-FL) functionalized with the π -conjugated dithiol, 9,9-didodecyl-2,7-bis-thiofluorene (FL) have been studied by means of spectroscopic and morphological techniques. For the characterization of the AgNPs-FL we have applied the photoacoustic spectroscopy (PAS) which is a suitable technique for the optical and thermal analysis of scattering materials giving a complementary information to optical transmittance [6,7]. In particular we applied the PAS technique in the UV/VIS range from 300 to 600 nm to investigate the changes of the light diffusion and absorption across the plasmonic resonances for the solution of AgNPs in chloroform. PAS confirms to be the most appropriate technique to determine separately the absorption and scattering coefficients. From their ratio one eventually obtains information on the size of the cluster of nanospheres bridged by the ligands, that in our case has been calculated of about 100 nm as also validated by TEM image.

References

1. Fratoddi, I. et al, NanoResearch, 2015, 8, 1771
2. Quintiliani, M. et al. J. Mater. Chem. C, 2014, 2, 2517
3. Fratoddi, I. et al Nanoscale, 2014, 6, 9177
4. Matassa, R. et al Phys. Chem. C 2012, 116, 15795–15800
5. Fratoddi, I. et al Nanoscale Research Letters. 2011, 6, 98(8)
6. A. Belardini et al., Scientific RepoRts 6:31796 (2016)
7. R. Li Voti et al., Int J Thermophys Vol.36: pp.342–1348 (2015)

BP 018

Unique determination of photocarrier transport parameters using combined quantitative heterodyne lock-in carrierography imaging and homodyne photocarrier radiometry

Peng SONG ^{(1,2)*}, Junyan LIU ^{(1,2)*}, Alexander MELNIKOV ⁽³⁾, Qiming SUN ^(3,4),
 Andreas MANDELIS ^{(3)*}

1. School of Mechatronics Engineering, Harbin Institute of Technology, Harbin, 150001, China

2. State Key Laboratory of Robotics and System, Harbin Institute of Technology, Harbin, 150001, China

3. Center for Advanced Diffusion-Wave and Photoacoustic Technologies (CADIPT),
 University of Toronto, Toronto, M5S 3G8, Canada

4. School of Optoelectronic Science and Engineering, University of Electronic Science and Technology of China, Chengdu, 610054, China

*Corresponding Authors' e-mail: ljywlfj@hit.edu.cn and mandelis@mie.utoronto.ca

The accurate determination of minority carrier transport parameters (i.e., carrier lifetime, diffusion coefficient, and surface recombination velocities) in silicon is important for process control and device modeling in the semiconductor, and more specifically, the photovoltaics industry. Simulations were carried out to study the uniqueness range of Heterodyne Lock-in Carrierography (HeLIC) [1, 2] imaging measurements of carrier transport parameters (bulk lifetime, diffusion coefficient, and front and back surface recombination velocities) of silicon wafers. Theoretically, HeLIC can resolve all four transport parameters, however, in practice the presence of experimental noise does not allow all those parameters to be measured reliably and uniquely from the HeLIC amplitude images alone. An extended range of simultaneously determined unique transport parameters was attained through a combination of HeLIC camera pixel and Homodyne Photocarrier Radiometry (HoPCR) experimental frequency response data via a multi-parameter fitting procedure [3]. Two n- and p-type wafers with different surface recombination velocities were used to illustrate the simulation results. Quantitative HeLIC images of diffusion coefficients and surface recombination velocities were obtained, with bulk lifetime values determined from HoPCR frequency scan measurements. The combined approach was shown to be able to resolve all four transport parameters uniquely and thus reliably.

Table 1 shows the ability of HeLIC to resolve the transport parameters for various combinations of lifetime and surface recombination velocity values. The diffusion coefficient can always be resolved in all cases. Bulk lifetimes or SRVs can be resolved with added noise on the order of 10%.

Table 1. Value ranges of HeLIC-determined bulk lifetimes and/or surface recombination velocities from calculated data with added random noise simulating experimental signal levels.

		τ_b (ms)			
		0.1	1	10	100
τ_b (ms)	34.03				
	3.426				
	0.366				
	0.06				
	0.029				

where

τ_b and s unresolved	τ_b resolved	s resolved
-----------------------------	-------------------	--------------

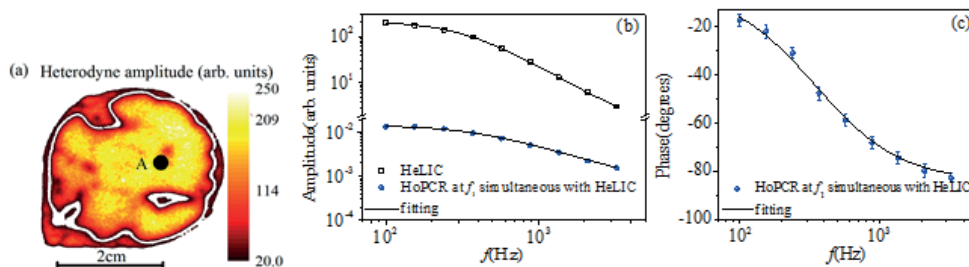


Fig. 1. A heterodyne image of the n-type wafer at 100 Hz (a) as well as HoPCR amplitude (b) and phase (c) at point A of the n-type wafer in Fig. 1a measured at f_1 simultaneously with HeLIC frequency responses

B Materials Science and Characterization

Figure 1a shows a HeLIC image of the *n*-type wafer. Point A was selected to derive the transport parameters and to compare the fitted parameters using HeLIC and HoPCR measurements which are shown in Figs. 1b and 1c. Theoretical best fits to the data are also shown in Table 2. Good agreements were found between HoPCR and HeLIC. In summary combined simultaneous HeLIC and HoPCR measurements were effective and sufficient for uniquely resolving all four transport parameters.

Table 2. Best-fit results using HoPCR and HeLIC at Point A

Methods	τ_b (ms)	D (cm ² /s)	s (m/s)
HoPCR	1.30±0.18	2.44±0.03	0.19±0.02
HeLIC	1.30(fixed)	3.31	0.20

References

1. A. Melnikov, A. Mandelis, J. Tolev, P. Chen, S. Huq, J. Appl. Phys. 107 114513 (2010)
2. Q. Sun, A. Melnikov, A. Mandelis, Phys. Status Solidi A 213(2) 405 (2016)
3. P. Song, A. Melnikov, Q.M. Sun, A. Mandelis, J.Y. Liu, J. Appl. Phys. 125 065701 (2019)

Contactless non-destructive imaging of doping density and electrical resistivity of semiconductor Si wafers using lock-in carrierography

Peng SONG ^(1,2), Junyan LIU ^{(1,2)*}, Alexander MELNIKOV ⁽³⁾, Qiming SUN ^(3,4),
 Andreas MANDELIS ^{(3)*}

1. School of Mechatronics Engineering, Harbin Institute of Technology, Harbin, 150001, China

2. State Key Laboratory of Robotics and System, Harbin Institute of Technology, Harbin, 150001, China

3. Center for Advanced Diffusion-Wave and Photoacoustic Technologies (CADIPT),
 University of Toronto, Toronto, M5S 3G8, Canada

4. School of Optoelectronic Science and Engineering, University of Electronic Science and Technology of China, Chengdu, 610054, China

ljywlj@hit.edu.cn and mandelis@mie.utoronto.ca

A contactless non-destructive imaging method for spatially resolved dopant concentration, N_d , and electrical resistivity, N_d of n - and p -type silicon wafers using lock-in carrierography (LIC) [1] images at various laser irradiation intensities is presented. Amplitude and phase information from wafer sites with known resistivity was employed to derive a calibration factor for accurate determination of the absolute carrier generation rate. A frequency-domain model based on the nonlinear nature of photocarrier radiometric signals was used to extract dopant density images [2, 3]. Lateral variations in the resistivity of an n -type and a p -type wafer obtained by means of this methodology were found to be in excellent agreement with those obtained with conventional 4-point probe measurements.

Figure 1 shows the resistivity images of the n -type and the p -type wafer obtained by LIC as well as the comparison results between LIC and conventional 4-point probe measurements. In summary LIC was shown to offer surface-wide non-contacting *quantitative* images of wafer resistivity profiles, a major step forward over conventional localized contacting 4-point probe measurements.

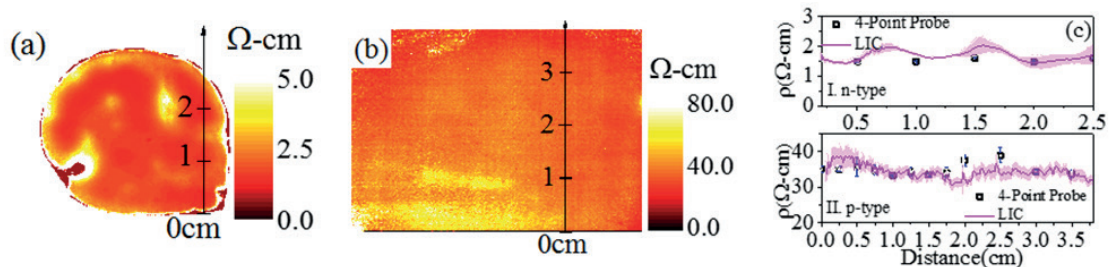


Fig. 1. Resistivity images of the n -type wafer (a) as well as p -type wafer (b) and the comparison of resistivity profiles between LIC and 4-point probe (c).

References

1. A. Melnikov, A. Mandelis, J. Tolev, P. Chen, S. Huq, J. Appl. Phys. 107 114513 (2010)
2. Q. M. Sun, A. Melnikov, J. Wang, A. Mandelis, J. Phys. D: Appl. Phys. 51 15LT01(2018)
3. P. Song, A. Melnikov, Q.M. Sun, A. Mandelis, J.Y. Liu, Semicond. Sci. Technol. 33 12LT01(2018)

Characterization of the Interface Between a Silicon Substrate and CVD Silicon Epitaxial Layer by Frequency-Domain Photocurrent Radiometry

Alexander MELNIKOV ^{(1)*}, Andreas MANDELIS ⁽¹⁾, Robert H. PAGLIARO ⁽²⁾

1. Center for Advanced Diffusion-Wave and Photoacoustic Technologies (CADIPT), Department of Mechanical and Industrial Engineering, University of Toronto, Toronto, ON, M5S 3G8, Canada

2. Advanced Processing Equipment Technology (APET) Co., Ltd. 20-15, Sukwoo-Dong, Hwaseong-City, Gyeonggi-do 463-802, South Korea

mandelis@mie.utoronto.ca

The growing application of epitaxial layers for electronic devices requires non-contact and non-destructive methods for characterization of such multilayer systems. A theoretical one-dimensional two-layer frequency-domain photocurrent radiometry (PCR) model involving front, interface, and back surface recombination velocities, diffusion coefficients, and recombination lifetimes in the upper and lower layers, and the fraction of unoccupied trap states [1-2] was used for characterization of interface between silicon wafer, epitaxial layer, and substrate. The PCR signal is obtained by solving the carrier transport equation and integrating the carrier density diffusion wave over the thickness of the processed wafer:

$$\begin{aligned} \frac{d^2}{dx^2} N_1(x, \omega) - \sigma_1^2 N_1(x, \omega) &= -\frac{I_0(1-R)\beta_1}{2D_1} e^{-\beta_1 x}, & 0 \leq x < L_1 \\ \frac{d^2}{dx^2} N_2(x, \omega) - \sigma_2^2 N_2(x, \omega) &= -\frac{I_0(1-R)\beta_2}{2D_2} e^{-\beta_2(L_1 - \beta_2(x-L_1))}, & L_1 < x \leq L_2 \\ D_1 \frac{d}{dx} N_1(x, \omega) \Big|_{x=0} &= S_1 N_1(0, \omega), & N_1(L_1, \omega) - N_T(L_1) &= N_2(L_1, \omega), \\ -D_1 \frac{d}{dx} N_1(x, \omega) \Big|_{x=L_1} &+ D_2 \frac{d}{dx} N_2(x, \omega) \Big|_{x=L_1} &= S_i n_{TF}, & -D_2 \frac{d}{dx} N_2(x, \omega) \Big|_{x=L_2} &= S_2 N_2(L_2, \omega), \end{aligned}$$

$$\text{Where } \sigma_j = \sqrt{\frac{1 + i\omega\tau_j}{D_j\tau_j}}, \quad j=1,2; \quad N_T(L_1) = n_{TF}.$$

The PCR signal can be expressed as follows:

$$S_{PCR}(\omega) = C_{L_1} \int_0^{L_1} N_1(x, \omega) dx + C_{L_2} \int_{L_1}^{L_2} N_2(x, \omega) dx$$

Here, N_j , D_j , τ_j , and β_j are, respectively, excess CDW concentration, ambipolar diffusion coefficient, excess carrier lifetime, and absorption coefficient in the epitaxial layer. N_2 , D_2 , τ_2 , and β_2 are the respective quantities in the substrate. S_f , S_i and S_2 are front-surface, interface, and back-surface recombination velocities. ω is the angular frequency of laser power modulation. I_0 is surface photon flux, R is surface reflectivity, and n_{TF} is the number density of free (unoccupied) traps at the interface $x=L_1$.

A homogeneously spread 808-nm modulated laser beam was used for excitation of diffusion carrier waves in the range 0.1-100 kHz. Several 200-mm CZ grown p-type (100) silicon wafers with a ~250-nm low temperature (650-680C) CVD deposited silicon epitaxial layer, following various kinds of surface preparation, were investigated by full optical PCR in homodyne and heterodyne modes [3]. It was shown that fundamental transport parameters of the composite structure can be evaluated from the PCR frequency dependence. The best fitting results showed the interface recombination velocity S_i to be very sensitive to interface contamination. Samples with high S_i demonstrated significant reduction of bulk lifetime in the epitaxial layer. The figure shows experimental data of wafers with and without an *in-situ* high temperature prebake (HTB) in the epi reaction chamber at 1100 °C, and 20 Torr in H₂ for 120 s, which is used to desorb non-chemically bound contamination (particularly adsorbed organic matter and moisture from the ambient) and removes the native oxide from the surface before the low temperature deposition, using silane (SiH₄) as the source gas. Theoretical best fits to the data are also shown.

B Materials Science and Characterization

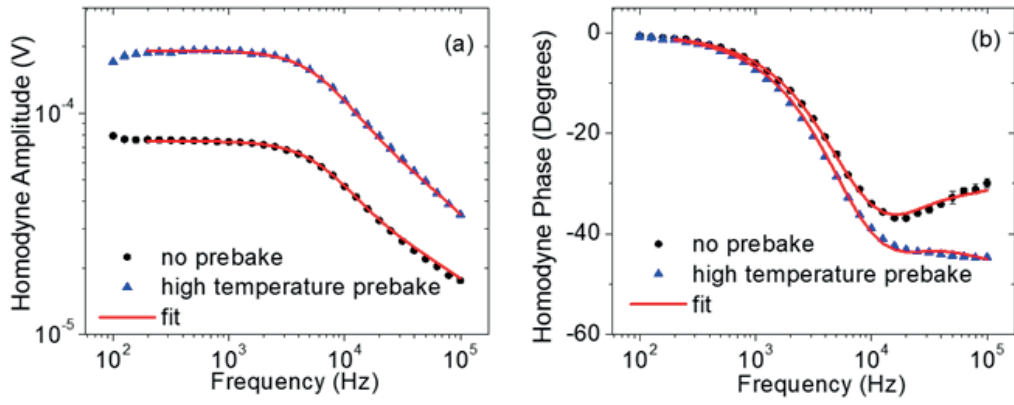


Fig. 1. Homodyne frequency scans of silicon wafers with and without high temperature prebake before epitaxial deposition. Amplitude (a), phase (b)

Table 1. The best fitted τ_p , S_p , τ_2 , and n_{Tr}

Description	No clean, no HTB	No clean, HTB	APET clean
τ_2 , s	1.49×10^{-4}	1.52×10^{-4}	1.59×10^{-4}
S_i , m/s	83 ± 16	0.66 ± 0.49	0.17 ± 0.23
τ_1 , s	$<1 \times 10^{-10}$	$5 \times 10^{-4} \pm 2.4 \times 10^{-4}$	$8.4 \times 10^{-4} \pm 1.6 \times 10^{-4}$
n_{Tr} , m^{-3}	$6.1 \times 10^{-20} \pm 1 \times 10^{-20}$	$8.3 \times 10^{-20} \pm 4.1 \times 10^{-18}$	$8.4 \times 10^{-20} \pm 2.1 \times 10^{-18}$

References

- 1 A. Mandelis, Diffusion-Wave Fields: Mathematical Methods and Green Functions, (Springer, New York, 2001), pp. 643-653
- 2 A. Melnikov, A. Mandelis,, B. Halliop, and N. P. Kherani, J. Appl. Phys. 114, 244506 (2013)
- 3 Q. Sun, A. Melnikov, and A. Mandelis, Phys. Stat. Sol. A 213, 405-411 (2016)

Laser thermal wave mid-IR technique for studying pyroelectric properties of bulk materials and thin films

Gennadiy Gavrilov, Alexandr Kapralov, Kyrill MURATIKOV, Galina Sotnikova

Ioffe Institute, St. Petersburg, Russia

g.sotnikova@mail.ioffe.ru

Currently, much attention is paid to the study of the pyroelectric properties of bulk materials and thin films [1]. The pyroelectric properties of materials are important when creating detectors of IR radiation and creating devices for energy harvesting [2]. Laser radiation are considered very useful for non-stationary non-contact heating of samples when conducting experiments for determination of pyroelectric parameters of materials. Both the methods of periodic laser heating [3] and pulsed laser heating are widely used [4].

Most experiments to determine the pyroelectric coefficients of materials are carried out in cells filled with air. Under these conditions, convective heat transfer takes place between the sample and the gaseous medium. It is known that convective heat transfer depends on the parameters of the gas medium and the sample, as well as on the structure of the chamber. The control of this parameter during pyroelectric experiments is a serious problem. It is usually considered that convective heat losses are small. As a result, the interpretation of most experimental data is performed under the assumption that the convective heat transfer weakly influences the dynamic thermal processes in the samples. This assumption leads to certain poorly controlled inaccuracies in the determination of pyroelectric parameters of materials. Therefore, one of the main tasks of this work was to develop a technique for measurement of pyroelectric parameters of bulk materials and thin films that allows one to reliably control and determine the value of the parameter of convective heat exchange for a sample directly during the experiment.

The pyroelectric coefficient of a sample is determined in quasi-equilibrium thermodynamic conditions in which there is no temperature gradient inside it. The establishment of such a regime after the start of laser irradiation is achieved at a time $t \geq \tau_{th} = L/\kappa$, where L is the thickness of the sample, κ is the thermal diffusivity of the material. Under this condition the pyroelectric current of the sample is determined by the equation

$$i_p = Ap \frac{dT(t)}{dt},$$

where A is the surface area of the sample electrodes and p is the integral over the sample thickness pyroelectric coefficient of the material.

In accordance with the results of the work [5] a change in the temperature of the sample over time at $t \geq t_{th}$ occurs in accordance with the expression

$$T(t) = \frac{(1-R)I_0}{\rho CL} \int_{t_1}^t dt' e^{-\frac{2H}{C\rho}(t-t')} f(t') + T_0,$$

where R is the light reflectance of the sample surface, I_0 is the laser-radiation intensity, t_1 is the time of starting the laser irradiation, ρ is the density of the sample material, C is its specific heat capacity, H is the heat transfer coefficient between the sample and surrounding gas, T_0 is the temperature of the medium, and $f(t)$ is the function describing the temporal characteristic of the laser radiation.

Independent measurements of $i_p(t)$ and $T(t)$ allowed to control the measurement mode and determine independently the pyroelectric coefficient of the sample p and the coefficient of convective heat transfer H . The temperature of the sample was measured by sensitive mid-IR photodiodes. The electronic system of the photodiodes provided the signal detection in kilohertz band for temperatures above 20°C with accuracy not worse than 0.1°C. The pyroelectric current $i_p(t)$ was also simultaneously measured. All the registered signals were digitized (12 bit) and transmitted to a PC, which provided the online calculation, displaying the results on the monitor, and recording of the information on the dynamics of the registered signals to a file with a temporal resolution of 1.5 ms.

Test experiments were carried out on a bulk sample of a single crystal of well-studied ferroelectric lithium tantalate LiTaO₃ [6]. Processing the experimental data made in accordance with equations for $i_p(t)$ and $T(t)$ led to a pyroelectric coefficient value that is in good agreement with known results. For the first time the pyroelectric coefficient was determined for aluminum nitride (AlN) single crystal [7]. The results are presented for the pyroelectric parameters of AlN thin films with thicknesses in the range 10 μm – 140 μm grown by hydride – chloride vapor phase epitaxy (HVPE) processes on SiC 400 μm substrates. The transformation of the pyroelectric properties of AlN films with thickness is investigated. The data obtained allow performing a comparative analysis of the pyroelectric properties of the obtained films with similar parameters of AlN bulk crystals.

References

1. S. Jachalke, E. Mehner, H. Stocker, J. Hanzig, M. Sonntag, T. Weigel, T. Leisegang, and D. C. Meyer, *Appl. Phys. Rev.* 4 (2), 021303 (2017) doi.org/10.1063/1.4983118
2. G. Sebald, E. Lefeuvre, and D. Guyomar, *IEEE Trans. Ultrason. Ferroelectr. Freq. Control* 55, 538 (2008) doi: 10.1109/TUFFC.2008.680.
3. S. B. Lang and D. K. Das Gupta, *J. Appl. Phys.* 59, 2151 (1986) doi.org/10.1063/1.336352
4. P. Bloss, A. S. DeReggi, and H. Schafer, *Phys. Rev. B* 62, 8517 (2000).
5. S. E. Aleksandrov, G. A. Gavrilov, A. A. Kapralov, K. L. Muratikov, and G. Yu. Sotnikova, *Tech. Phys. Lett.* 43 (7), 684 (2017) doi.org/10.1134/S106378501707015X
6. S. E. Aleksandrov, G. A. Gavrilov, A. A. Kapralov, K. L. Muratikov, and G. Yu. Sotnikova, *Tech. Phys. Lett.* 43 (12), 1084 (2017) doi.org/10.1134/S1063785017120021
7. G. A. Gavrilov, A. F. Kapralov, K. L. Muratikov, E. A. Panyutin, A. V. Sotnikov, G. Yu. Sotnikova, and Sh. Sh. Sharofidinov, *Tech. Phys. Lett.* 44 (8), 709 (2018) doi.org/10.1134/S1063785018080199

Photoacoustic spectra and thermal diffusivity measurements of GaN thin films

Marcos Macias Mier^{(1)*}, Marlene Camacho Reynoso⁽²⁾, Mario Alberto Zambrano Serrano⁽²⁾, Briseida Guadalupe Pérez Hernández⁽²⁾, Yenny Lucero Casallas Moreno⁽³⁾, Alfredo Cruz Orea⁽¹⁾, Máximo López López⁽¹⁾

1. Dep. Física, Cinvestav-IPN, Mexico
 2. Dep. Nanociencias, Cinvestav-IPN, México
 3. UPIITA, IPN, México.

mmacias@fis.cinvestav.mx

Gallium Nitride holds a vital position for technological development due to its many unique properties, such as its wide bandgap, high electron mobility, and high thermal conductivity. Besides its more frequent use in LEDs, this promising semiconductor is very suitable for high power and high frequency devices, spintronics, solar cells, and optoelectronic devices.

In this work, we use photoacoustic (PA) spectroscopy to study the optical and thermal properties of thin films of GaN deposited by plasma-assisted molecular beam epitaxy (MBE) on GaAs (001) substrates. The optical absorption spectra and the thermal diffusivity of the samples were obtained. As PA spectroscopy is a relatively inexpensive and reliable technique, these analyses can be helpful to study growth conditions of cubic GaN, transport properties and defects on the samples.

Three samples, labeled in this abstract as S620, S621, and S622, of thin films of GaN were grown by the MBE technique in a Riber C21 system, equipped with a radio frequency gas source for supplying atoms of nitrogen. The structure of the three samples is shown in Figure 1, and they were grown under the conditions displayed in table 1. A 200 nm buffer layer of GaAs was grown at 490 °C on the GaAs (001) substrate. In order to evaluate the effects of growth temperature of GaN nucleation layers on the structure, three different values for this parameter were chosen. The temperature of the final GaN layer is the same for all samples (620 °C). The corresponding beam equivalent pressure (BEP) of the Ga Knudsen cell for both the nucleation and final GaN layer was 2.06×10^{-7} Torr.

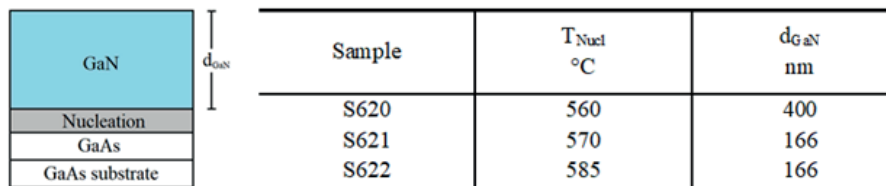


Fig. 1. Schematic representation of the samples and growth conditions. The growth temperature of the final GaN is 620 °C for all the samples.

The photoacoustic signal is obtained by using the experimental set-up shown in Figure 2. According to the Rosencwaig and Gersho model of the photoacoustic effect in solids [1], the amplitude of the complex signal is directly proportional to the absorption coefficient of the samples. As the band gap energy (E_g) of GaN in wurtzite crystal structure is expected to be around 3.32 eV [2], we use light with wavelengths from 300 to 540 nm in order to use a Tauc plot to estimate it. The thermal diffusivity of samples was obtained with another PA experimental set-up, with a 500 mW laser emitting at 405nm, used in the open PA cell configuration [3]. As the PA signal depends explicitly on the chopper frequency, the photoacoustic signal was acquired for values from 10 to 210 Hz.

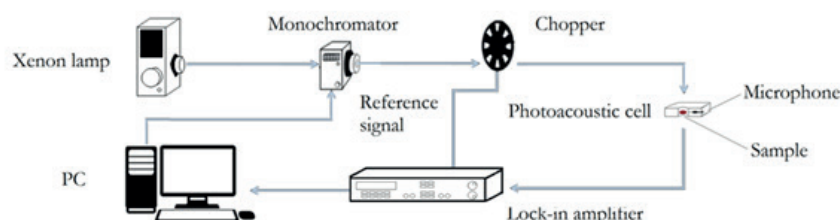


Fig. 2. Experimental set-up of the PA spectroscopy experiment.

The Tauc plot of the three samples and their thermal diffusivities are shown in Figure 3. Preliminary identifications of the absorption bands indicate the presence of the zinc blende structure of GaN. Complementary characterizations such as x-ray diffraction and Raman scattering experiments, not shown in this abstract due to space limitations, also show the presence of this phase.

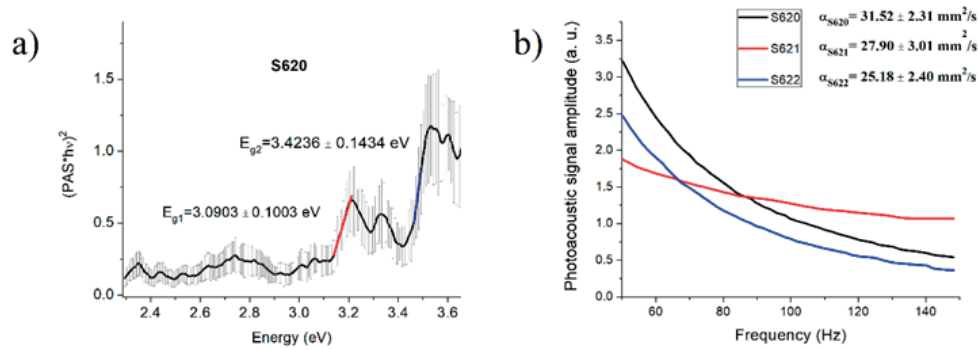


Fig. 3. Experimental results. a) Tauc plot of the sample S620. b) PA spectroscopy as function of the chopper frequency and the obtained thermal diffusivity values.

On the other hand, thermal diffusivity is an essential parameter to study further transport parameters, like the surface recombination velocity of carriers and the diffusion coefficient of carriers. The results of this work indicate the potential of PAS as a support in the thermal and optical characterization of GaN samples and their surface properties, especially in the study of growth conditions of the zinc blende structured phase.

References

1. Rosencwaig, A., & Gersho, A. (1976). Theory of the photoacoustic effect with solids. *Journal of Applied Physics*, 47(1), 64-69. Rinke, P., Scheffler, M., Qteish, A., Winkelkemper, M., Bimberg, D., & Neugebauer, J. (2006).
2. Rinke, P., Scheffler, M., Qteish, A., Winkelkemper, M., Bimberg, D., & Neugebauer, J. (2006). Band gap and band parameters of InN and GaN from quasiparticle energy calculations based on exact-exchange density-functional theory. *Applied physics letters*, 89(16), 161919.
3. Marquezini, M. V., Cella, N., Mansanares, A. M., Vargas, H., & Miranda, L. C. M. (1991). Open photoacoustic cell spectroscopy. *Measurement Science and Technology*, 2(4), 396.

Photoacoustic spectroscopy of thin film semiconductor heterostructure deposited on transparent substrate

I. Riech^{(1)*}, M.A. Zambrano-Arjona⁽¹⁾, F. Maldonado⁽¹⁾, R. A. Medina-Esquivel⁽¹⁾, J.L. Peña⁽²⁾

1. *Facultad de Ingeniería, Universidad Autónoma de Yucatán, A.P. 150, Cordemex, Mérida, Yucatán, México*

2. *Departamento de Física Aplicada, Centro de Investigación y de Estudios Avanzados del IPN-Unidad Mérida, Carretera Antigua a Progreso km. 6, A.P. 73 Cordemex, Mérida, Yucatán, México*

Photoacoustic Spectroscopy (PAS) is an excellent technique for studying the optical bandgap of semiconductor materials. Several works have been devoted to determination of absorption edge from thin film semiconductor deposited on backing material which can be thermally thick semiconductor substrate [1] or optically transparent substrate as glass [2]. In the first case, the PAS technique is able to separate the absorption contribution of thin film material from that of the semiconductor substrate. However the structure composed by two thin semiconductor layers deposited on transparent substrate is especially important in thin films electronic devices as solar cells, where the analysis of phenomena that occur in the interface between two thin films is fundamental for the devices performance. The reported experimental works, about PAS study of thin heterostructure are scarce. In this work the CdS/CdTe bilayers of different thicknesses grown onto glass were studied by PAS. The energy of the optical band edge from CdTe layer is clearly identified in the amplitude of PA spectra and its position, 1.44 eV, is not related to its thickness. The second transition was observed around the CdS bandgap energy, despite this layer is semitransparent and thermally thin. This band is shifted to lower energies from 2.33 to 1.92 eV as the thickness of the structure increases. We discuss two possible contributions, one associated to the lattice mismatch between wider and narrower band gap layers and the other related to the optical absorption of each layer. The theoretical model was compared with the experimental results.

Acknowledgements

This work has been supported by CONACYT-SENER 254667

References

1. M. Malinski, L. Bychto, J.L. Nzodoum Fotsing, K. Jungue and A. Patryn, *J. Phys. IV France* 117, 29 (2004)
2. L. Bychto, M. Malinski, *Opto-Electronics Review* 26, 217(2018)

Thermal properties of superhydrophobic films when applied in ceramics

J. Sanabria-Mafaile ⁽¹⁾, E. San Martín-Martínez ^{(1)*}, A. Cruz-Orea ⁽²⁾

1. Centro de Investigación en Ciencia Aplicada y Tecnología Avanzada del Instituto Politécnico Nacional, Legaria 694. Colonia Irrigación, 11500, CDMX, México

2. Departamento de Física, Centro de Investigación y de Estudios Avanzados del IPN, Av. IPN No. 2508, Col. San Pedro Zacatenco, C.P. 07360, CDMX, México

esanmartin@ipn.mx

In the present work, the study of thermal properties in thin films with superhydrophobic properties is reported. Superhydrophobic coatings have a wide potential for applications in self-cleaning, anti-fouling, anti-ice, anti-corrosion, enhancement of heat transfer and so on. By using Aluminum Tri-sec-butoxide the synthesis of films, with super repellent properties to water, was carried out and applied on substrates of clay ceramics tiles. It was used the technique of spray with airbrush to deposit the films, previously elaborated by de Sol-Gel method. When polytetrafluoroethylene is coated on the alumina films, the surface energy is reduce and improves its hydrophobic properties, resulting in an increase of the water contact angle (<160°). In this study, superhydrophobic films were characterized by the analysis of surface roughness, surface wettability and thermal properties. The thermal effusivity (e), and thermal diffusivity (α), and thermal conductivity (k) of the superhydrophobic films were determined using photothermal techniques.

Materials and Methods. Preparation of dual-layer superhydrophobic coatings

The alumina films (Al_2O_3) were prepared by the Sol-Gel method according to the following procedure: Aluminum tri-sec-butoxide ($Al(O\text{-}sec\text{-}Bu)_3$) and isopropyl alcohol (i-PrOH) they were mixed and stirred at room temperature during 1 hour. Ethyl acetoacetate (EAcAc) was added as a chelating agent and the solution was stirred during 3 hours. To the partial solution is carefully added distilled water to hydrolyse it and the solution is used for the coating. Different solution concentrations were prepared, from 0.03M to 0.37M, with the purpose of understanding the effect of these concentrations in the microstructure formations. The coating was carried out on ceramic clay tile (Baldosín) by means of airbrush spray technique. The obtained films were thermally treated at different temperatures and time intervals, 349-601 °C and 3-38 minutes, respectively. Finally, polytetrafluoroethylene (PTFE) was used as a water repellent agent; the surface of the substrate was coated with PTFE polymer followed by a heat treatment at 380-480 °C for 1 hour.

Results

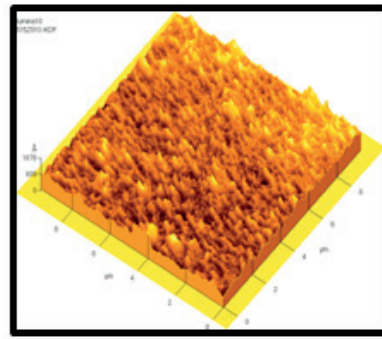
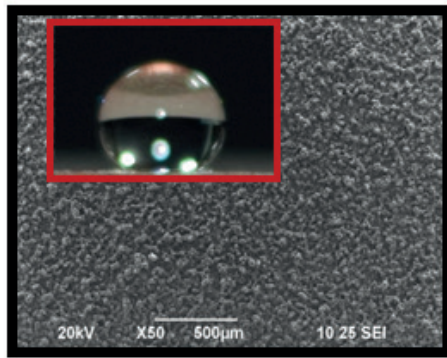
Thermal diffusivity (α) and effusivity (e) experimental values for the samples are show in Table 2. From the relationship of e and α it is possible to calculate the thermal conductivity (k) of samples ($k=e \sqrt{\alpha}$).

Table 1 Values of thermal diffusivity, thermal effusivity and thermal conductivity for the samples

Sample	Thickness [μm]	Diffusivity α [$10^{-7} \text{m}^2\text{s}^{-1}$]	Effusivity e [$\text{Ws}^{1/2}\text{m}^{-2}\text{K}^{-1}$]	Conductivity k [$\text{Wm}^{-1}\text{K}^{-1}$]
SST0	555.8 ± 4.1	4.17 ± 1.68	628.57 ± 5.27	0.41 ± 0.018
SST349	592.6 ± 3.2	24.01 ± 1.19	475.33 ± 5.68	0.73 ± 0.020
SST400	596.8 ± 4.3	31.31 ± 1.74	455.58 ± 6.35	0.79 ± 0.025
SST475	598.2 ± 3.5	28.45 ± 1.08	487.85 ± 6.15	0.82 ± 0.019
SST550	658.5 ± 3.3	19.40 ± 0.45	428.05 ± 9.25	0.60 ± 0.015
SST601	610.1 ± 4.2	17.98 ± 1.00	391.55 ± 8.81	0.53 ± 0.019

The k value of the uncoated sample (SST0), obtained from experimental configurations, is close to the value of reported k for clay ceramic roof tiles ($0.46 \text{Wm}^{-1}\text{K}^{-1}$). However, the values of the thermal conductivity for the samples coated with alumina and PTFE micro-particles show significant changes. Comparing the sample SST0 with others, it can be seen that when the layer of alumina and PTFE is coated, the thermal conductivity is increased in the samples. In the case of sample SST475, it was performed with a solution concentration at 0.20M and calcination time at 20 min; it was observed the highest thermal conductivity compared to other samples (see Table 2). With these processing conditions, we achieve the best static contact angle (SCA) up to $159.80^\circ \pm 0.47$ (Figure 1), in all the experimentation.

B Materials Science and Characterization



Conclusions

We have prepared super-water-repellent coating film of alumina on Baldosín ceramic by a combination of geometric and chemical approaches. Alumina thin films with roughness from 1.10 μm to 1.35 μm were formed by spray coating prepared by the Sol-Gel method. When polytetrafluoroethylene was coated on the alumina films, the static contact angle for water was increased. In this research was obtained films with roughness of 1.31 μm and static contact angle up to $159.80^\circ \pm 0.47$.

References

1. Quéré, D., *Annu. Rev. Mater. Res.*, 2008. 38: p. 71-99.
2. Zhang, P. and F. Lv., *Energy*, 2015. 82: p. 1068-1087.

BP 025

Influence of skin depth and of photo-injected carriers in photothermally modulated magnetic resonance studies with magnetic foils, tapes and thin films

Thallis Custódia CORDEIRO ⁽¹⁾, Max Erik SOFFNER ⁽¹⁾, Antonio Manoel MANSANARES ⁽²⁾,
Edson Corrêa da SILVA ⁽¹⁾ *

1. Universidade Estadual do Norte Fluminense Darcy Ribeiro - UENF, Rio de Janeiro, Brazil

2. Universidade Estadual de Campinas, São Paulo, Brazil

ecorrea329@gmail.com

In this article, we followed the frequency dependence of the photothermally modulated magnetic resonance (PMMR) signal in a wide range of frequencies (100 Hz to 100 kHz) in several samples in the form of foils (Fe and Ni), layers (γ -Fe₂O₃ cassette tape), thin films (Co and Permalloy deposited on glass and Si substrates), and the Si substrate itself.

It is shown that the skin depth of the microwaves deeply influences the signal behavior by selecting the portion of the sample that is probed. Clear differences in the frequency dependence are observed between the metallic Ni and Fe foils and the dielectric γ -Fe₂O₃ cassette tape. Furthermore, the thermal mismatch between the magnetic films and substrates also plays a crucial role, once the modulation of the temperature is strongly dependent on the substrate thermal parameters at low modulation frequencies. The non-resonant signal from the diamagnetic Si is also analyzed. It is produced by the absorption of microwaves by the photo-injected free carriers and presents characteristic behavior in the investigated frequency range.

Materials and Methods

Nickel and iron foils are cold laminated and 50 μ m thick. The cassette tape was a Nipponic type I tape, not recorded, which is made up of 15 μ m polyester backing and a 5 μ m magnetic layer of γ -Fe₂O₃ needle shaped particle immersed into a polyester matrix. Cobalt and Permalloy films, with 150 nm thickness, were deposited by sputtering on 150 μ m corning glass and 535 μ m Si (111) wafer substrates, which were kept at room temperature.

The experimental setup was based on a Bruker Elexys 500 Electron Spin Resonance spectrometer operating in microwaves X-band. For the PMMR experiments, an optical access ER4104OR cavity with a Q-factor of 7000 was used. A Newport LQA660-110C laser, 110 mW nominal power, 660 nm wavelength, and pump beam radius of 1.0 mm, was used as a periodic intensity light source by modulating its electronic power source. The surface of the sample was fully illuminated and its dimensions are much larger than thickness, what allows consider one-dimension treatment. Equation (1) represents the PMMR signal, which is originated in the sample temperature oscillation produced by laser light absorption and is proportional to the temperature derivative of the imaginary part of magnetic susceptibility [1-2]. $T(\vec{r})H_{mw}(\vec{r})$ corresponds to the temperature oscillation times the microwave magnetic field.

$$\text{PMMR}_{\text{signal}} \propto \int \left(\frac{\partial \chi''(\vec{r})}{\partial T} \right) T(\vec{r}) H_{mw}(\vec{r}) d\mathbf{v} \quad (1)$$

In order to include the influence of the skin depth δ the equation (2) presents the exponential term times the temperature oscillation in the depth x , integrated over the thickness l of the medium. T_H is the temperature variation integrated over the sample thickness and weighted by the microwaves magnetic field amplitude in the sample. It is actually a temperature multiplied by a characteristic length.

$$\text{PMMR}_{\text{signal}} \propto T_H = \int_0^l e^{-\frac{x}{\delta}} T(x) dx \quad (2)$$

With this equation, simplified expressions for the studied specific cases were obtained [3].

Results

Figure 1 illustrates the distinct behaviors of a metallic (50 μ m Fe foil) and a dielectric sample (μ -Fe₂O₃ cassette tape), showing the predicted slopes of the frequency dependence of the PMMR signal amplitude obtained using Eq. 2.

B Materials Science and Characterization

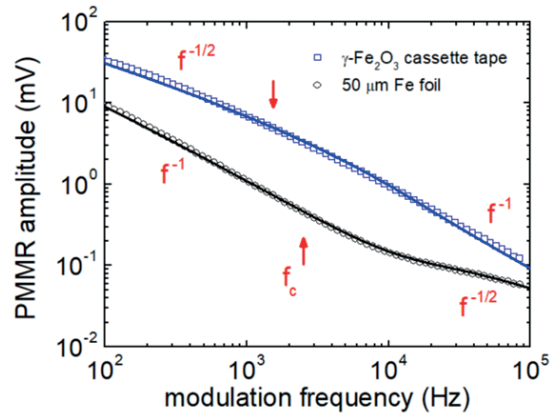


Figure 1: PMMR signal amplitude versus laser modulation frequency for a metallic and a dielectric sample.

Acknowledgements

The authors acknowledge the Brazilian agencies FAPERJ, FAPESP, CNPq, and CAPES for financial support.

Isabel Merino and Elisa Saitovitch, from the Brazilian Center for Research in Physics (CBPF), are acknowledged for the preparation of the Co and Permalloy films on glass and Si substrates.

References

1. T. Orth, U. Netzelmann, J. Pelzl, Applied Physics Letters, 53 (20), 1979 (1988) doi: 10.1063/1.100338
2. A.M. Neto, F.G. Gandra, J.A. Romano, A.C.R.M. Cortez, E.C. da Silva, S. Gama, F. Galembeck, H. Vargas, S.A. Niktov, Journal of Magnetism and Magnetic Materials, 128 (1), 101 (1993) doi: 10.1016/0304-8853(93)90862-V
3. T.C. Cordeiro, M.E. Soffner, A.M. Mansanares, E.C. da Silva, Journal of Applied Physics 124 (16), 163901 (2018) doi: 10.1063/1.5049683

Underwater optoacoustic detection and characterization of oil films: laboratory study

Pavel Subochev*, Roman Belyaev, Maxim Prudnikov, Vladimir Vorobyev, Ilya Turchin, Alexander Bugrov, Alexandra Pyanova, Alexey Ermoshkin, Ivan Kapustin, and Alexander Molkov

Institute of Applied Physics RAS, Nizhny Novgorod, Russia

Pavel.Subochev@gmail.com

The study of the physical properties of organic films on the water surface is an important problem related to the development of methods for the ecological monitoring of the ocean and inland water. Even in the laboratory, the detection and characterization of oil films is a challenging task, while the use of existing laboratory methods in the full-scale experiments is not yet possible. This laboratory study was devoted to transmission-mode optoacoustic (OA) [1] characterization of oil films based on OA microscope of Institute of Applied Physics RAS [2] equipped with disk-shaped ultrasonic detector.

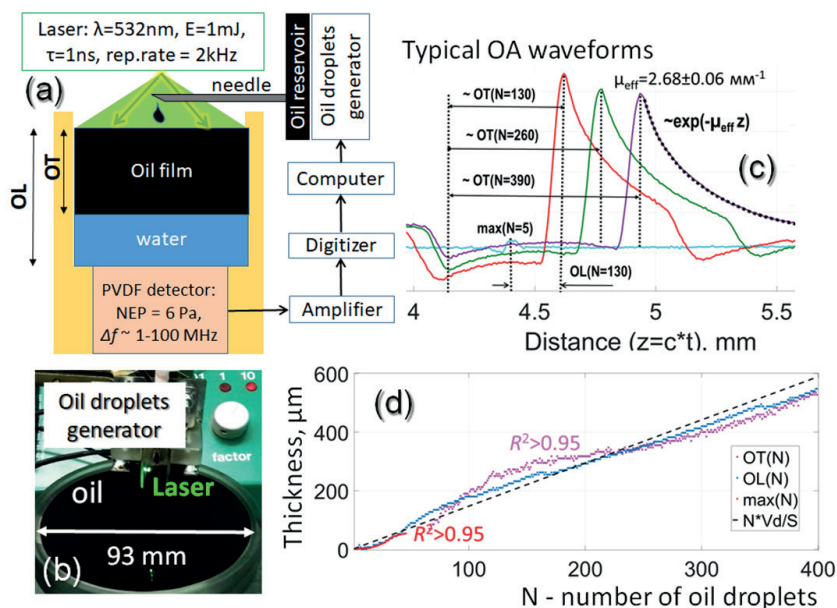


Fig. 1. Underwater optoacoustic (OA) detection of oil films: (a) – scheme of the experimental setup; (b) – photograph of oil droplets generator; (c) – examples of OA A-scans acquired after different number N of oil droplets were generated; (d) – experimental estimations of oil thickness based on the independent measurements of pulse delay (dotted blue), maximum pulse amplitude (dotted red), effective pulse duration (dotted magenta) being compared to theoretical model of oil thickness (dashed black).

The experiments were performed using cylindrical cuvette with 93 mm diameter (fig. 1 a-b) filled with distilled water and containing PVDF ultrasonic detector with 5 mm diameter, with noise equivalent pressure (NEP) of 6 Pa and the bandwidth Δf of 0-100 MHz. Signals from PVDF detector were transmitted through custom-made 1-100 MHz matching amplifier and digitized by 16-bit analog to digital converter Razor16 (GaGe, USA) at 200 MHz sampling rate.

Crude Urals oil (Lukoil, Russia) was dropped to the cuvette (fig. 1 a-b) using custom-made oil droplet generator providing 9 mg oil droplets at the rate of 4 droplets per minute. Assuming homogeneous superficial distribution of oil at the water surface, the effective increment of oil thickness was estimated as 1.5 μm per droplet (dotted black curve at figure 1d). After each oil droplet, oil film was illuminated by the series of $n=50$ optical pulses at 532 nm wavelength using laser Wedge HB (Bright Solutions, Italy). Each laser pulse had ~ 0.1 mJ energy and 1 ns pulse duration. Each series of A-scan was averaged for noise reduction purposes.

Assuming 1.5 mm/ μs sound speed, the axial OA profiles of each oil film were obtained (figure 1c). Due to the difference in acoustic impedance at liquid-air interface, the straight-propagating OA pulses were followed by the reflected ones. Due to the finite optical attenuation (μ_{eff}) of oil, OA waveforms corresponding to the thicker (>100 μm) oil films expressed the exponential decays corresponding to $\mu_{\text{eff}} = 2.68 \pm 0.06$ mm^{-1} . OA waveforms (fig. 1c) were used to estimate the oil level (OL) based on the delay in ultrasound propagation as well as oil thickness (OT) based on the thickness-dependent changes in OA amplitudes or OA pulse durations. The results of OA characterization of oil film level and thickness are presented in figure 1d. Table 1 represents the thickness ranges potentially accessible by the proposed OA methods with the noise equivalent thickness (NET) of 10 μm .

B Materials Science and Characterization

Table 1. Applicability of underwater OA measurements for independent estimations of OL, OT, and μ_{eff} .

Film thickness tested range	$R^2 > 0.95$ estimations of oil level (OL) based on OA pulse delays	$R^2 > 0.95$ estimations of oil thickness (OT) based on OA amplitudes	$R^2 > 0.95$ estimations of oil thickness (OT) based on OA pulse duration	$R^2 > 0.95$ estimations of effective optical attenuation μ_{eff}
<10 μm	NA	NA	NA	NA
10-70 μm	+	+	—	—
70-100 μm	+	—	—	—
100-600 μm	+	—	+	+

Acknowledgements

This study was supported by RFBR grant #18-35-20054

References

1. V.E. Gusev, A.A. Karabutov. "Laser optoacoustics." NASA STI/Recon Technical Report" (1991).
2. P.V. Subochev "Cost-effective imaging of optoacoustic pressure, ultrasonic scattering, and optical diffuse reflectance with improved resolution and speed" Optics letters, 41(5), 1006-1009, (2016).

Cross-plane variation of thermal conductivity in swift heavy ion irradiated sapphire: modulated picosecond thermoreflectance

Abdullaev^{1*}, B. Muminov², J. O'Connell³, V. A. Skuratov⁴, V. S. Chauhan⁵, M. Khafizov⁵,
Z. N. Utegulov^{1*}

1. Department of Physics, School of Science and Technology, Nazarbayev University, Astana, Kazakhstan

2. Department of Mechanical Engineering, University of California, Riverside, CA, USA

3. Centre for HRTEM, Nelson Mandela Metropolitan University, Port Elizabeth, South Africa

4. Flerov Laboratory of Nuclear Reactions, Joint Institute for Nuclear Research, Dubna Russia

5. Department of Mechanical and Aerospace Engineering, Ohio State University, Columbus, OH, USA

azat.abdullaev@nu.edu.kz, zhutegulov@nu.edu.kz

We studied degradation of thermal conductivity in single crystalline sapphire ($\alpha\text{-Al}_2\text{O}_3$) irradiated by 167 MeV Xe *swift heavy ions* (SHI) at $10^{12} - 10^{14}$ ions/cm² fluences. Near-surface cross-plane nanoscale thermal transport measurements were performed by a non-contact ultrafast optical pump-probe technique called picosecond time domain thermo-reflectance (TDTR). Modulation frequency-dependent thermal characterization with variable heat penetration depths combined with multi-layer and multi-modulation rate data analysis allowed us to isolate for the first time the thermal conductivity of sub-surface thin amorphous layer from ion track regions both resulting from damage caused by ionization effects of SHI. These results demonstrate the applicability of modulated thermoreflectance method to resolve thermal transport behavior in SHI-irradiated oxides having non-homogeneous damage depth profile. It can also facilitate future studies aiming at resolving the impact of damage resulting from electronic and nuclear stopping regions.

Influence of Carbon Nanofibers Reinforcements on the Effective Thermal Conductivity of Magnetorheological Fluids

Caridad VALES PINZON ^{(1)*}, Rubén Arturo MEDINA ESQUIVEL ⁽¹⁾, Miguel Ángel ZAMBRANO ARJONA ⁽¹⁾, Alejandro VEGA FLICK ⁽²⁾

1. Facultad de Ingeniería-UADY, Av. Industrias no Contaminantes por Periférico Norte, Apdo. Postal 150 Cordemex, 97310 Mérida, Yucatán, Mexico

2. Instituto Tecnológico y de Estudios Superiores de Monterrey, Campus Chihuahua, Avenida Heroico Colegio Militar 4700, Nombre de Dios, 31300 Chihuahua, Chihuahua, Mexico, 31300

caridad.vales@correo.uady.mx, ruben.medina@correo.uady.mx, miguel.zambrano@correo.uady.mx, avegaflick@tec.mx

The development of composite materials has shown excellent improvement in recent years with the inclusion of nanostructured filler materials. Additionally, the geometric manipulation of these nanostructured fillers has allowed the modulation of the material properties. This represents one of the most important features in the development of new materials for applied science and engineering. Magnetorheological (MR) fluids are a type of smart materials that have been shown to be exceptionally valuable in the development of heat transfer and mechanical applications such as fast-acting clutches, brakes, shock absorbers, among others [1,2]. MR fluids consists of dispersions of highly magnetizable microparticles in a non-magnetic carrier fluid. Under an external magnetic field, they can change their mechanical properties from a fluid-like state to a solid-like state. This effect is due to the preferential aggregation of the microparticles that leads to the formation of chain-like structures in the direction of the applied field [3-5]. The thermal properties of these materials can be modified with the addition of nanostructures with high thermal conductivity. In a similar manner, the structural dynamics of the MR fluid can also be improved by the inclusion of carbonaceous nanostructured materials [6,7].

In the present work, we studied the thermal properties of MR fluids based on carbonyl iron powder (CIP) with the addition of carbon nanofibers (CNF). We analyzed the thermal diffusivity of the MR fluid samples as a function of the volume concentration of CIP and CNF. The thermal diffusivity was measured using a photopyroelectric technique under the influence of low intensity, homogeneous magnetic fields. Additionally, we determined the effective thermal conductivity of the samples as a function of the CIP and CNF volume concentration as well as the applied magnetic field. In the absence of an external field, the thermal conductivity of the MR fluid shows an increase proportional to the CNF load, even at low concentrations. This is due to the extraordinary thermal conductivity of the carbonaceous nanostructure material. Furthermore, with the application of an external magnetic field, the increase in the thermal conductivity becomes hindered compared to the case without a magnetic field. For example, samples with 5% of CIP and 5% of CNF show an increase in the thermal conductivity of 17% when comparing measurements with and without an applied magnetic field. In addition, the experimental measurements were found to be in agreement with an effective medium model (modified Lewis-Nielsen model). In this model, the form factor, i. e., the relation between the dimensions and the shape of the structures in the MR fluid, was used as a fitting parameter. These results provide evidence that the presence of the fibers interfere with the formation of the chain-like structures of CIP microparticles.

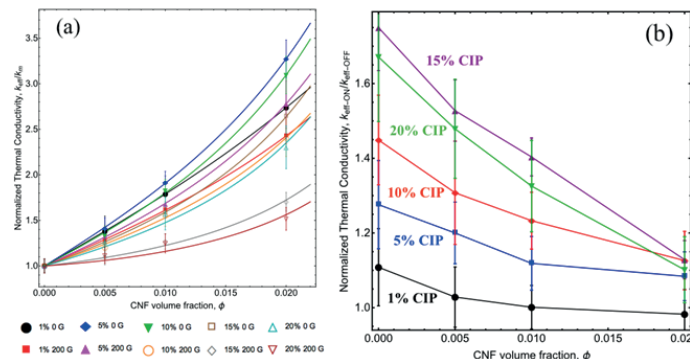


Fig. 1. Enhancement of the thermal conductivity of MR Fluids with loads of CNF (a) respect to the matrix and (b) due to the applied magnetic field of 200 G.

Acknowledgements

This work was supported by SEP- CONACYT-CB-2015-256497

References

1. O. Machacek, M. Kubik, Z. Strecker, J. Roupec, I. Mazurek, *Advances in Mechanical Engineering* 11 (3), 1-8 (2019) doi: 10.1177/1687814019827440
2. I.Y. Forero-Sandoval, A. Vega-Flick, J.J. Alvarado-Gil, R.A. Medina-Esquivel, RA, *Smart Materials and Structures* 26 (2), 025010 (2017) doi: 10.1088/1361-665X/26/2/025010
3. B. Reinecke, J. Shan, K. Suabedissen, A. Cherkasova, *Journal of Applied Physics* 104, (2008) doi: 10.1063/1.2949266
4. M.R. Jolly, J.D. Carlson, B.C. Muñoz, *Smart Materials and Structures* 5 (5), 607-614 (1996) doi: 10.1088/0964-1726/5/5/009
5. K.J. Jin, W.J. Wen, *Physics Letters* 286 (5), 347-352 (2001), doi: 10.1016/S0375-9601(01)00397-8
6. W. Kaddouri, A. El Moumen, T. Kanit, S. Madani, A. Imad, *Mechanics of Materials* 92, 28-41 (2016) doi: 10.1016/j.mechmat.2015.08.010
7. M. Cvek, M. Mrlik, R. Moucka, M. Sedlacik, *Colloids and Surfaces A* 543, 83-92 (2018) doi: 10.1016/j.colsurfa.2018.01.046

Photoacoustic Study of Rare-Earth-Containing Liquid Crystals

Yuetao YANG*, Xiaojun LIU, Shuyi ZHANG

Key Laboratory of Modern Acoustics, Ministry of Education, Institute of Acoustics,
Nanjing University, Nanjing 210093, China

yyang@nju.edu.cn

In order to combine the properties of liquid crystals and metal compounds, a substantial amount of efforts have been devoted to the design of liquid-crystalline metal compounds. Rare earth ions have sharp emissions in the visible and near-infrared region. Rare-earth-containing liquid crystals have been considered as a promising kind of light-emitting liquid crystals [1]. Though some studies have been performed on rare-earth-containing liquid crystals, only few of these compounds have luminescent properties and most of them have transition temperatures above room temperature.

Photoacoustic technique, which is sensitive to both the thermal and optical properties of the sample, has been widely used to study the physical and chemical properties of many kinds of materials. Photoacoustic spectroscopy can be a direct monitor of energy levels and non-radiative relaxation channels of rare earth compounds [2]. Additionally, photoacoustic technique has been successfully introduced to study the phase transition of liquid crystals. In this work, $\text{Ln}(\text{TTA})_3\text{L}_2$ (Ln^{3+} : La^{3+} , Eu^{3+} , Gd^{3+} and Er^{3+} , TTA: 2-thenoyltrifluoroacetato, L: 2-hydroxy-N-octadecyloxy-4-tetradecyl-oxybenzylaldimine) liquid-crystalline compounds were prepared. The spectral properties and phase transitions of these compounds have been studied by photoacoustic and fluorescence spectroscopy.

Materials and Methods

$\text{Ln}(\text{TTA})_3\text{L}_2$ compounds were prepared by the adduct formation reaction between L (0.2 mmol) and $\text{Ln}(\text{TTA})_3(\text{H}_2\text{O})_2$ (0.1 mmol) in dry toluene at 60 °C for 5 h. After the solution was allowed to cool to room temperature, the solvent was removed, and the product was dried in vacuum.

Photoacoustic spectra were recorded on a single-beam spectrometer constructed in our laboratory. The excitation source was a 500 W xenon lamp. The optical system included a monochromator and a mechanical chopper at a frequency of 33 Hz. The photoacoustic spectra were recorded in the region of 300~800 nm. The fluorescence spectra and fluorescence lifetime of the compounds were measured on an Edinburgh Instruments FS-900 spectrofluorimeter. The lowest triplet state was detected from the phosphorescence of $\text{Gd}(\text{TTA})_3\text{L}_2$ compound. In situ energy-dispersive X-ray diffraction experiments were performed in the Beijing Synchrotron Radiation Facility. The optical textures of the mesophase were taken with an Olympus BX60 polarizing microscope.

Results

As shown in Fig. 1, the mesophase of the title compounds was identified as smectic A phase on the basis of the typical fan-like texture which can be found by polarizing microscopy when the liquid sample was cooled into the mesophase. In situ energy-dispersive X-ray diffraction experiments were performed, and the periodicity d for the layer structure of the title compounds was determined to be around 26 Å.

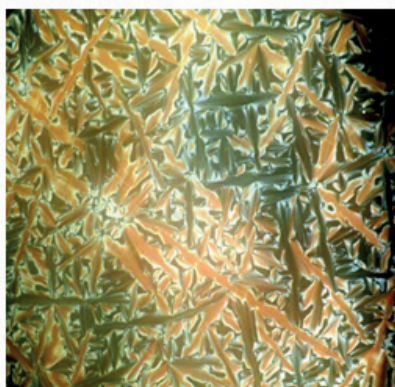


Fig. 1. Texture of $\text{Eu}(\text{TTA})_3\text{L}_2$ in smectic A phase.

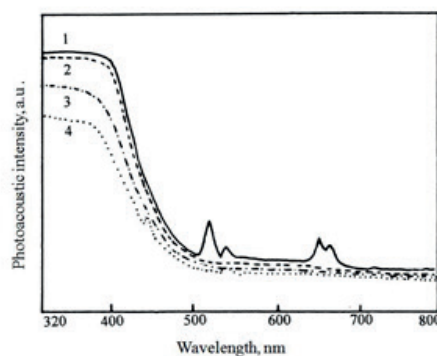


Fig. 2. Photoacoustic spectra of $\text{Er}(\text{TTA})_3\text{L}_2$, 1; $\text{Gd}(\text{TTA})_3\text{L}_2$, 2; $\text{La}(\text{TTA})_3\text{L}_2$, 3; $\text{Eu}(\text{TTA})_3\text{L}_2$, 4.

B Materials Science and Characterization

Photoacoustic spectra of the title compounds are shown in Fig. 2. The broad absorption around 390 nm is attributed to π - π^* transition of the ligand. Photoacoustic intensity of the ligand increases in the order of $\text{Eu}(\text{TTA})_3\text{L}_2 < \text{La}(\text{TTA})_3\text{L}_2 < \text{Gd}(\text{TTA})_3\text{L}_2 < \text{Er}(\text{TTA})_3\text{L}_2$. As the thermal property of $\text{Ln}(\text{TTA})_3\text{L}_2$ is basically the same at room temperature, photoacoustic spectra indicate that the probability of non-radiative relaxation is the lowest for $\text{Eu}(\text{TTA})_3\text{L}_2$, and the largest for $\text{Er}(\text{TTA})_3\text{L}_2$. The fluorescence quantum yields (Q) of the title compounds have been measured. The value of Q increases for $\text{Er}(\text{TTA})_3\text{L}_2$, $\text{Gd}(\text{TTA})_3\text{L}_2$, $\text{La}(\text{TTA})_3\text{L}_2$ and $\text{Eu}(\text{TTA})_3\text{L}_2$, respectively. The result of fluorescence measurements is coincident with photoacoustic spectra. Additionally, photoacoustic technique has been used to monitor the phase transitions of the title compounds, and the variations of photoacoustic signals have been interpreted based on the theoretical prediction for reversible first-order phase transitions.

Conclusions

Rare-earth-containing liquid crystals have been synthesized and studied by photoacoustic and fluorescence spectroscopy. The results show that photoacoustic technique may serve as a new tool for investigating the relaxation processes and phase transitions of these metallomesogens.

Acknowledgements

This work was supported by the National Natural Science Foundation of China (No. 11834008)

References

1. S. Guerra, T. Dutronc, E. Terazzi, K.L. Buchwalder, L. Guenee, R. Deschenaux, S.V. Eliseeva, S. Petouda, C. Piguet, *Coordination Chemistry Reviews* 340, 79 (2017)
2. H.X. Zhang, B. Gao, Y.T. Yang, X.J. Liu, S.Y. Zhang, *International Journal of Thermophysics* 36, 1336 (2015)

Photothermal Spectroscopy of CdZnSe Mixed Crystals

Jacek ZAKRZEWSKI⁽¹⁾, Karol STRZAŁKOWSKI⁽¹⁾, Mirosław MALIŃSKI⁽²⁾

1. Institute of Physics, Nicolaus Copernicus University, ul. Grudziądzka 5/7, 87–100 Torun, POLAND

2. Department of Electronics, Technical University of Koszalin, ul. Sniadeckich 2, 75–328 Koszalin, POLAND

jzakrzew@fizyka.umk.pl

Photothermal spectroscopy has found the wide range of applications as a method of monitoring the thermal, optical and recombination parameters of semiconductors. It involves irradiating of light onto a sample and then, detecting of the periodic temperature fluctuations in the sample. In piezoelectric method, the stresses and strains of a sample due to absorption of optical radiation are detected by a piezoelectric transducer.

The paper presents results of both experimental and theoretical studies of CdZnSe crystals for different methods of the surface preparation and different content of zinc. Mechanical, chemical and thermal treatment of the surface can create the damaged subsurface layer which introduces additional defects states in the material. The increase of the zinc content can also be associated with the creation of volume defects in the material.

The investigated crystals were grown by the high pressure Bridgman method under argon overpressure. The crystals were cut into 1–1.2 mm thick plates and mechanically grounded, polished and chemically etched. The influence of zinc content and preparation method on the amplitude and phase spectra is observed.

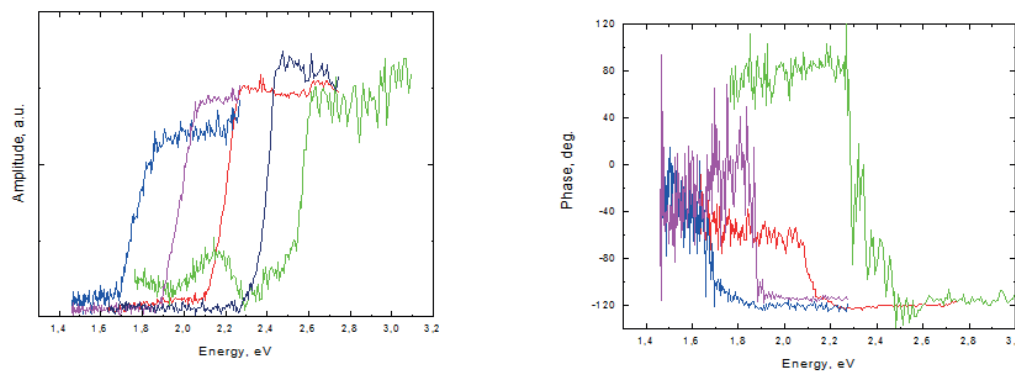


Fig. 1 Amplitude and phase spectra of as-grown CdZnSe mixed crystals with different Zn content

The temperature distribution in the sample is the basis for the finding of the theoretical amplitude and phase of photothermal spectra. In contrast to the microphone detection, which needs only the temperature at one of the sample surfaces, in the piezoelectric one, it is necessary to know the spatial temperature distribution along the thickness of the sample.

The paper presents both amplitude and phase piezoelectric spectra, for different content of zinc in CdZnSe crystals. Several features of the crystals were revealed from the spectra, with the increase of zinc content: shift of the energy gap, broadening of the absorption band, increase of the surface absorption.

For semiconductors there are three main sources of photothermal signal: thermal, plasma waves (associated with diffusion and recombination of carriers). In photoacoustic investigation of transport in semiconductors one can also take into account immediate thermalization of carriers and nonradiative surface recombination. Their influence on the character of amplitude and phase piezoelectric spectra is showed and discussed.

Measurement of the thermal and infrared properties of thin AlGaAs films using spectrally resolved photothermal infrared radiometry

Michał PAWLAK (1)*, Jacek ZAKRZEWSKI (1), Nicolas HORNY (2), Arne LUDWIG (3), Carsten EBLER(3), Sven SCHOLZ(3), Josef PELZL (3), and Andreas WIECK (3)

1. Institute of Physics, Nicolaus Copernicus University, Grudziadzka 5, 87-100 Torun, Poland

2. Multiscale Thermophysics Lab. GRESPI, Université de Reims Champagne Ardenne URCA, Moulin de la Housse BP 1039, 51687 Reims, France

3. Chair of Applied Solid-State Physics, Experimental Physics VI, Ruhr-University Bochum, Universitaetsstrasse 150, 44780 Bochum, Germany.

mpawlak@fizyka.umk.pl

In this work, we demonstrate that it is possible to measure simultaneously thermal and infrared properties of semiconductor thin films by spectrally-resolved photothermal infrared radiometry. Measurements are conducted on undoped and doped AlGaAs thin films epitaxially grown on the heavily Zn doped GaAs substrate. Typical results are shown in figure 1 that presents the best fits of the theoretical model to amplitude ratios and phase differences for undoped $\text{Al}_{0.33}\text{Ga}_{0.67}\text{As}$ alloy and C-doped $\text{Al}_{0.33}\text{Ga}_{0.67}\text{As}$ alloy (open squares) thin films. In the case of undoped $\text{Al}_{0.33}\text{Ga}_{0.67}\text{As}$ alloy, the infrared absorption coefficient of the thin layer and thermal boundary resistance were set constant, and the fitting was performed with thermal conductivity and diffusivity of the thin film as unknown parameters [1]. In turns for C-doped $\text{Al}_{0.33}\text{Ga}_{0.67}\text{As}$ alloy thermal conductivity and diffusivity were set constant and the fitting was performed with thermal boundary resistance and infrared absorption coefficient of the thin film as unknown parameters [2].

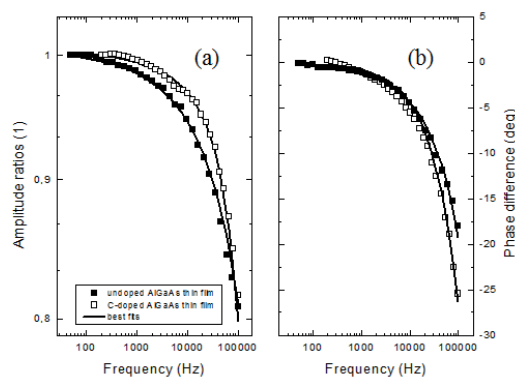


Fig. 1. Amplitude ratios (a) and phase differences (b) as a function of the modulation frequency for undoped and C doped $\text{Al}_{0.33}\text{Ga}_{0.67}\text{As}$ alloys using filter F9 [2].

It is worth emphasizing that the phase difference at low frequencies (up to about 500 Hz) is very small (less than 1 degree), which indicates that at low frequencies the PTR signal is emitted from the substrate. At high frequencies, the PTR signal yields information about the thin film. Besides, it can also be observed that at the frequency of 100 kHz the PTR amplitude of the $\text{Al}_{0.33}\text{Ga}_{0.67}\text{As}/\text{GaAs}$ sample decreases only by 20%, while the phase difference varies by about 20 degrees for undoped AlGaAs, and 25 degrees for C-doped AlGaAs. From the normalized experimental data one can estimate either the thermal conductivity and thermal diffusivity of the thin film or the infrared absorption coefficient and thermal boundary resistance. The supplementary FTIR experiments in reflection configuration of undoped AlGaAs thin film provide reliable information about the layer thickness. It was also found that with increasing infrared absorption coefficient of the thin film the sensitivity of the method for the estimation of the infrared absorption coefficient of the thin film increases, while the experimental errors decrease.

Acknowledgements

This work was funded by the National Science Centre Poland, grant based on Decision no. 2015/19/D/ST3/02388. A.L., and A.D.W. acknowledge the support of the DFH/UFA CDF A-05-06. We thank Nadine Viteritti for sample preparations.

References

1. M. Pawlak, S.Pal, S.Scholz, A.Ludwig, A.D.Wieck, *Thermochim Acta* 662 (2018), 69-74
2. M. Pawlak, N. Horny, S.Scholz, C. Ebler, A. Ludwig, A.D. Wieck, *Thermochim. Acta* 667 (2018) 73-78

Analysis on luminescent highly absorbing materials by thermal lens technique

Vitor Santaella ZANUTO ^{(1)*}, Jéssica Fabiana Mariano dos SANTOS ⁽¹⁾, Diego da Silva MANOEL ^(1,2),
 Maryleide VENTURA ⁽¹⁾, Fábio Simões de VICENTE ⁽²⁾, Vinicius Granatto CAMARGO ⁽²⁾,
 Luis Carlos MALACARNE ⁽³⁾, Tomaz CATUNDA ⁽¹⁾

1. Instituto de Física de São Carlos - USP, São Carlos, Brazil

2. Departamento de Física – UNESP, Rio Claro – Brazil

3. Departamento de Física – UEM, Maringá - Brazil

vszanuto@gmail.com

Assessment of luminescent quantum efficiency is essential for evaluating quality and applicability of luminescent material in numerous modern photonic devices, such as lasers, LEDs and solar concentrators. Thermal lens (TL) spectroscopy has been successfully applied in the study of these materials with low and very low optical absorption coefficients [1,2]. The technique is a nondestructive, remote and high-sensitive photothermal method. In the mode-mismatched TL configuration, an excitation beam is focused in the material. The material absorbs part of the incident energy, which may induce a local temperature change. The temperature change profile generates a refractive index gradient that acts as a lens, phase-shifting the second laser beam, as-called probe beam. Monitoring the intensity at center of the probe beam, the technique can quantify the temperature change. This capacity is essential for the characterization of luminescent samples, assessing the fluorescence quantum efficiency (η).

Usually the method is applied to very low absorbing samples, which present a homogeneous temperature change profile along the sample thickness, being described theoretically by a 2D temperature profile [3],

$$T_{2D}(r, t) = \frac{(1-R)P_e A_e}{4\pi K} \phi \left[Ei\left(-\frac{2r^2}{\omega_e^2}\right) - Ei\left(-\frac{2r^2}{\omega_e^2(2t+t_c)}\right) \right], \quad (1)$$

where P_e and ω_e are the incident power and the radius of excitation beam, respectively. A_e , R and K are the optical absorption coefficient, reflectivity and thermal conductivity of the sample, respectively. $\phi = 1 - \eta \lambda_e / \langle \lambda_{em} \rangle$ is the fraction of absorbed energy converted into heat, where λ_e is the excitation wavelength and $\langle \lambda_{em} \rangle$ is the mean emission wavelength. The parameter t_c relates the excitation beam radius with the thermal diffusivity of the sample ($t_c = \omega_e^2 / (4D)$), which is named as characteristic TL response time

The 2D theory is a simple and effective model for samples presenting $A_e L \ll 1$, where L is the sample thickness. For highly absorbing materials, which the product $A_e L$ are greater than unity, the temperature profile can be immensely changed, which should be taken into account the theoretical 3D description. However, solving the thermal lens 3D model considering a finite sample, with no heat flux from sample to the coupling fluid, obtains a temperature equivalent to the simple 2D model with the introduction of Beer's law [3],

$$T_{3D}(r, z, t) \approx e^{-A_e z} T_{2D}(r, t). \quad (2)$$

Using these considerations, the normalized TL signal is described by the expression,

$$\frac{I(t)}{I(0)} = 1 - \frac{\theta}{2} \left(\frac{1 - e^{-A_e L}}{A_e L} \right) \arctan \left(\frac{2mV}{[(1+2m)^2 + V^2] \frac{t_c}{2t} + 1 + 2m + V^2} \right), \quad (3)$$

where $\theta = (1-R) P_e A_e L (ds/dT) \phi / (K \lambda_p)$, (ds/dT) being the temperature coefficient of the optical path of the sample, and λ_p the probe laser wavelength. V and m are geometrical setup parameters.

To investigate the validity of this expression, high concentrated RhB - doped 3-glycidoxypopyltrimethoxysilane (GPTS)/tetraethyl orthosilicate (TEOS) – derived organic/silica monolithic xerogels were prepared by sol-gel process and studied by TL method. The RhB concentration varied from 0.036 to 19.49 mM. Figure 1.a presents the normalized absorption and emission spectra of the sample with the lowest concentration (0.036 mM of RhB). Since the samples present high optical absorption coefficients, conventional TL low absorption theoretical model was evaluated and compared to high absorption model. The thermal diffusivities and luminescent quantum efficiency values were determined considering both models. The dye-doped organic/silica xerogels present high luminescent quantum efficiency values (up to 90 %) for the lower concentrations, which decreases as the concentration increases, reaching 8 % for the higher concentration, as shown in Fig. 1.b.

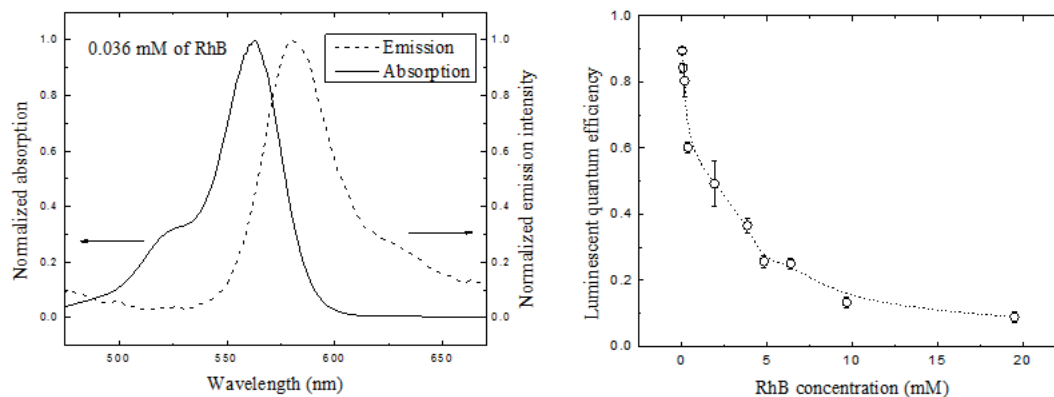


Fig. 1. (a) Normalized absorption (solid line) and emission (dashed line) spectra of the lowest concentration of RhB-doped GPTS/TEOS xerogels (0.036 mM of RhB). (b) Luminescent quantum efficiency of RhB-doped GPTS/TEOS xerogels with the concentration.

Acknowledgements

The authors thank the financial support of the Brazilian agencies CAPES, CNPq and FAPESP (V.S. Zanuto, processo 2017/19392-6).

References

1. J. Shen, R.D. Lowe, R.D. Snook, *Chem. Phys.* 165, 385 (1992). doi: 10.1016/0301-0104(92)87053-C
2. M.L. Baesso, J. Shen, R.D. Snook, *Chem. Phys. Lett.* 197, 255 (1992). doi: 10.1016/0009-2614(92)85764-2
3. M.P. Belancon, L.C. Malacarne, P.R.B. Pedreira, A.N. Medina, M.L. Baesso, A.M. Farias, M.J. Barbosa, N.G.C. Astrath, J. Shen, *Journal of Physocs: Conference Series*, 214 (1), (2010) doi:10.1088/1742-6596/214/1/012016

BP 033

Study of Thermal Emissivity in Porous Silicon by Means of Infrared Photothermal Radiometry

Lizbeth LUVIANO ELIZALDE^{(1)*}, Joel HERNÁNDEZ WONG⁽²⁾, Uriel NOGAL LUIS⁽²⁾,
José Bruno ROJAS TRIGOS⁽¹⁾, Ernesto MARÍN MOARES⁽¹⁾, José Antonio CALDERÓN ARENAS⁽¹⁾

1. Instituto Politécnico Nacional, Centro de Investigación en Ciencia Aplicada y Tecnología Avanzada, Av. Legaria # 694, Col. Irrigación, C.P. 11500, Ciudad de México, México.

2. CONACyT-Instituto Politécnico Nacional, Centro de Investigación en Ciencia Aplicada y Tecnología Avanzada, Unidad Legaria. Legaria No. 694, C.P. 11500, Ciudad de México, México.

calder62@hotmail.com, lle-01liz@hotmail.com

The determination of the thermal emissivity of porous silicon samples by means of infrared photothermal radiometry technique is reported. The porous silicon samples were elaborated by electrochemical etching from crystalline silicon wafers of 500 μm of thickness, phosphorus doped, orientation 100 and resistivity of 1.75 Ωcm . During the electrochemical etching process, it was used a current density of 40mA/cm², hydrofluoric acid at a concentration of 40% volume and etching times of 5, 10, 20, 30, 40, 50 y 60 minutes.

The thermal conductivity and diffusivity were determined by means the photoacoustic technique in a heat transmission configuration and the porosity through gravimetric method.

Results show a significant dependence of the thermal emissivity with the etching time, and therefore with the porosity.

References

1. Canham, L.T., Applied Physics Letters 57 (10), 1046 – 1048 (1990).
2. Calderon A, Alvarado-Gil JJ, Gurevich YG, Cruz-orea A, Delgadillo I, Vargas M, Miranda LCM, Phys Rev Lett 79:5022–5025(1997).
3. Suarez V, Hernández Wong J, Nogal U, Calderón A, Rojas-Trigos JB, Juárez AG, Marín E, Appl. Rad. Isot. 83: 260-263(2014).
4. A. Rojas-Marroquin, L. Luviano, J. Hernández Wong, U. Nogal, J. Calderón, I. G. Fernández, J. B. Rojas Trigos, E. Marín and A. Calderón, Lat. Am. J. Phys. Educ. Vol. 11 No. 4, 4311 (2017).
5. J. Hernández-Wong, J.B. Rojas-Trigos, U. Nogal, V. Suárez, E. Marín, and A. Calderón, Rev. Mex. Fis. 65, 54–64 (2019).

CP 001

Thermal properties of herbal extracts of calendula, basil and thyme by using photopyroelectric techniques

N.P. ARIAS ^{(1)*}, G. LARA HERNANDEZ ⁽²⁾, Wilfred ESPINOSA MANRIQUE ⁽¹⁾,
A WILCHES TORRES ⁽¹⁾, A. CRUZ OREA ⁽³⁾, C. HERNANDEZ AGUILAR ⁽²⁾, J.J.A. FLORES CUAUTLE ⁽⁴⁾

1. Universidad de Boyacá, Facultad de Ciencias e Ingeniería, Carrera 2ª Este No. 64 – 169, Tunja, Boyacá

2. Escuela Superior de Ingeniería Mecánica y Eléctrica, SEPI-ESIME-Zacatenco-Instituto Politécnico Nacional, C. P. 07738, Ciudad de México, México

3. Departamento de Física, CINVESTAV-IPN, C. P. 07360, Ciudad de México, México.

4. CONACYT-Tecnológico Nacional de México/I.T. Orizaba, Orizaba, Ver. México

* Corresponding Author: nparias@uniboyaca.edu.co

Author's e mail: larag_139otmail.com, weespinosa@uniboyaca.edu.co, andreawilches@uniboyaca.edu.co, oreais.cinvestav.mx, clauhajahoo.com, jflores_cuautleotmail.com

The Saboyá Municipality is considered one of the most prolific agricultural producers at Colombia; also, the medicinal and aromatic plants are part of its biodiversity. Among the plants cultivated at the mentioned area Calendula (*Calendula officinalis*), Albahaca (*Ocimum basilicum*) and Tomillo (*Thymus vulgaris*) stands out because of the importance for the local economy. Herbal extracts from aromatic plants are essential in the pharmaceutical and cosmetic industry, and adequate quality control is needed for both raw and final products [1]. Physicochemical properties of aromatic plants depend on several factors; the soil conditions, weather, and local conditions make a difference in the final raw plant [2]. Afterward, the next critical step is the extraction method used for getting the bioactive compound. In this work, maceration was used. After the extraction procedure, the polyphenol content in the herbal extracts was tested by Folin-Ciocalteu method, and the thermal properties of this herbal extracts were studied by using the so-called inverse photopyroelectric method (IPPE) [3]

Acknowledgments

The authors thanks Fondo de Ciencia, Tecnología e Innovación del Sistema General de Regalías, Fondo Nacional de Financiamiento para la Ciencia, la Tecnología y la Innovación "Francisco José de Caldas," COLCIENCIAS, Programa Colombia BIO, Gobernación de Boyaca, through FP44842-298-2018 contract and Vicerrectoría de Investigación, Ciencia y Tecnología-Universidad de Boyacá for the financial support

References

- [1] J.G, Zeng. M.L, Tan, X. Peng, and Q. Luo. Ch.9. Standardization and Quality Control of Herbal Extracts and Products. In Traditional Herbal Medicine Research Methods, Edited by Willow J.H. Liu. 2011 John Wiley & Sons, Inc. doi:10.1002/9780470921340.ch9
- [2] A. Signore, M. Renna and P. Santamaria (2019). Annual Plant Reviews 2, 1–24 (2019) doi: 10.1002/9781119312994.apr0687
- [3] G. Lara-Hernández, E. Suaste-Gómez, A. Cruz-Orea, J. G. Mendoza-Alvarez, F. Sánchez-Sinécio, J. P. Valcárcel and A. García-Quiroz. International Journal of Thermophysics 34(5): 962-971 (2013) doi:10.1007/s10765-013-1419-x

CP 002

Wheat germ, mamey seed, walnut, coconut, and linseed oils thermal characterization using photothermal techniques

Gemima LARA HERNANDEZ ⁽¹⁾, Claudia HERNANDEZ AGUILAR ⁽¹⁾, Alfredo CRUZ OREA ⁽²⁾,
Nayda Patricia ARIAS DUQUE ⁽³⁾, Andrea WILCHES TORRES ⁽³⁾,
Jose Jesus Agustin FLORES CUAUTLE ^{(4)*}

1. *Escuela Superior de Ingeniería Mecánica y Eléctrica, SEPI-ESIME-Zacatenco-Instituto Politécnico Nacional, C. P. 07738, Ciudad de México, México*
2. *Departamento de Física, CINVESTAV-IPN, C. P. 07360, Ciudad de México, México.*
3. *Universidad de Boyacá, Facultad de Ciencias e Ingeniería, Carrera 2ª Este No. 64 – 169, Tunja, Boyacá*
4. *CONACYT-Tecnológico Nacional de México/I.T. Orizaba, Orizaba, Ver. México*

jflores_cuautle@hotmail.com

The cosmetic industry has turned its attention to using vegetable products; the number of different vegetable oils used in the cosmetic industry has risen in the last years. In this work, the so-called photopyroelectric techniques are used for studying the thermal effusivity and diffusivity of wheat germ, mamey seed, walnut, coconut, and linseed oils.

The thermal conductivity was calculated using a mathematical relationship. Therefore, full thermal characterization is achieved. The obtained values for the studied oils are closed to other vegetable oils already reported. This similarity is partially a consequence of the similar chemical structure presented in this type of materials.

The results point out values are close to those of vegetable oils, as previous studies, the vegetable oils thermal properties present similar values, even though those values strongly depend on the origin region, type of sample and management processes

Acknowledgements

The authors thanks Fondo de Ciencia, Tecnología e Innovación del Sistema General de Regalías, Fondo Nacional de Financiamiento para la Ciencia, la Tecnología y la Innovación "Francisco José de Caldas," COLCIENCIAS, Programa Colombia BIO, Gobernación de Boyaca, through FP44842-298-2018 contract and Vicerrectoría de Investigación, Ciencia y Tecnología-Universidad de Boyacá for the financial support

References

1. Lara-Hernández, G., et al., Thermal Characterization of Edible Oils by Using Photopyroelectric Technique. *International Journal of Thermophysics*, 2013. 34(5): p. 962-971.
2. Oliphant, T. and R. Harper, Skin barrier protection with jojoba esters. *Journal of the American Academy of Dermatology*, 2013. 68(4): p. AB37.

CP 003

Photoacoustic FTIR spectroscopy for investigation of nanodiamond surface

Petr KRIVOSHEIN, Dmitry VOLKOV*

*Department of Chemistry, Lomonosov Moscow State University,
Leninskie gori 1, building 3, Moscow, 119991, Russia*

dmsvolkov@gmail.com

Since their discovery, detonation nanodiamonds have been considered almost as an abrasive material only due to their hardness. However, in addition to this property, they also possess other equally interesting properties as optical transparency, a low thermal expansion coefficient, an extremely high resistance to various aggressive chemicals, and a high surface area [1, 2]. As nanodiamonds (ND) are considered promising ion exchangers [3], it is necessary to have the information about their surface as completely as possible.

In previously published papers, KBr-pellet techniques of absorbance FTIR spectroscopy were mainly used to study the ND surface. Other techniques as attenuated total reflectance FTIR (ATR-FTIR) or diffuse reflectance (DR-FTIR) spectroscopy were used less often. However, ATR-FTIR requires a tight contact between the crystal and the sample surface; and thus, diamond is the only material of the ATR crystal that is applicable in ND measurements. DR-FTIR requires sample dilution with KBr and milling to obtain fine powders. Also, KBr can react with surface groups and is very hygroscopic. Photoacoustic FTIR is free from these disadvantages. But as far as we know, IR photoacoustic techniques have not used for ND measurements yet. Thus, we compare PA-FTIR and ATR-FTIR of several ND samples, for the first time, to demonstrate the possibilities of PA-FTIR spectrometry for ND surface investigation.

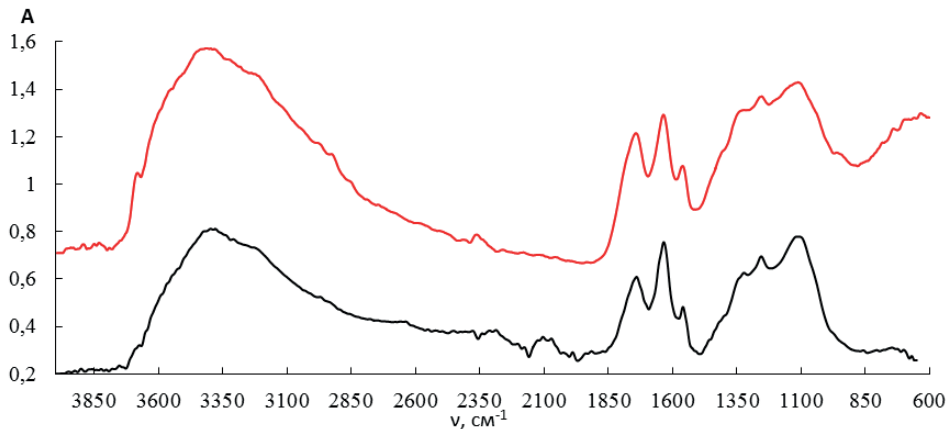


Fig.1. Comparison of PA-FTIR (red) and ATR-FTIR (black) spectra of a nanodiamond sample.

FTIR spectra of ND powders were collected using a Vertex 70 FTIR spectrometer (Bruker Optik GmbH, Germany) with a PAC300 photoacoustic accessory (MTEC Photoacoustic, Inc., USA) for PA-FTIR spectra with different modulation frequencies of IR radiation and a diamond-crystal GladiATR accessory (Pike Technologies, USA) for ATR-FTIR spectra.

We collected spectra of 8 commercially available ND samples. Figure 1 shows an example of PA-FTIR and ATR-FTIR spectra of nanodiamonds. In general, both techniques provide similar spectra. In the region of 3800–3000 cm^{-1} , there is a wide OH band of surface OH-groups and adsorbed water. In the region of 1800–1500 cm^{-1} , there is a characteristic band of stretching vibrations of carbonyl C=O group (1750–1720 cm^{-1}) and a peak of bending OH vibrations (1620–1635 cm^{-1}). For some ND samples, a weak peak at 1550 cm^{-1} is observed. In the range of 1500–800 cm^{-1} , several overlapping peaks of various surface groups are observed.

In comparison with ATR-FTIR, PA-FTIR spectrometry results in more informative spectra. In an ATR mode, the spectral information in the region of 2300–1900 cm^{-1} is lost due to the diamond crystal absorption. PA-FTIR modality reveals weak peaks due to larger radiation penetration depth. For instance, overlapping peaks of CH_x vibrations at 2950–2750 cm^{-1} are observed in PA-FTIR spectra while almost unobservable in ATR-FTIR spectra. In addition, PA-FTIR allows varying the radiation penetration depth with the interferometer frequency. Thus, PA-FTIR spectroscopy provides the additional information about the ND surface and demonstrates advantages over more widespread FTIR techniques such as ATR-FTIR and others.

Acknowledgements

This work was supported by the Russian Foundation for Basic Research, project 19-33-70068 mol_a_mos.

References

1. Buchatskaya, Y., et al., Sorption of actinides onto nanodiamonds. *Radiochimica Acta*, 2015. 103(3). doi:10.1515/ract-2014-2336
2. Peristy, A., et al., Ion-exchange properties of High Pressure High Temperature synthetic diamond. *Diamond and Related Materials*, 2017. 75: p. 131-139. doi:10.1016/j.diamond.2017.02.022
3. Peristy, A., B. Paull, and P.N. Nesterenko, Ion-exchange properties of microdispersed sintered detonation nanodiamond. *Adsorption*, 2016. 22(3): p. 371-383. doi:10.1007/s10450-016-9786-9

Spectral responses of nucleation events and source related correction of Aethalometer data using multi-wavelength photoacoustic spectroscopy

Fruzsina Anna KUN-SZABÓ^{(1)*}, Máté PINTÉR⁽¹⁾, Tibor AJTAI^{(1),(2)}, Zoltán BOZÓKI^{(1),(2)}, Gábor SZABÓ^{(1),(2)}

1. Department of Optics and Quantum Electronics, University of Szeged, Hungary

2. University of Szeged, Interdisciplinary Excellence Centre, Department of Optics and Quantum Electronics

kszfrusina@titan.physx.u-szeged.hu

Atmospheric aerosol has severe impact on climate on human health and air quality. The light absorbing carbonaceous aerosol is responsible for the major fraction of uncertainty in climate forcing calculation and one of the most harmful atmospheric constituents too. Therefore, precise and accurate measurement of that is deemed essential. The researcher is in common platform in that the photoacoustic spectroscopy is one of the most powerful methodology for precise and accurate determination of light absorption of aerosol. In this study, we perform results of the field measurement campaign focussing on the correlation between the aerosol size distribution and photoacoustic responses of ambient.

The measurement was made under wintry urban meteorological conditions from late winter until early spring of 2015, in Budapest, the capital of Hungary. Optical absorption coefficient (OAC) by aerosol is generally measured by two different methodologies. One was the most commonly applied Aethalometer [1]. The other was the recently developed multi wavelength photoacoustic instrument (4- λ -PAS) [2]. The number concentration and size distribution of ambient aerosol was measured by a single mobility particle sizer (SMPS equipped with a Vienna-type DMA+CPC, Grimm Aerosol Technik GmbH & CO. Austria, with a size range of 10,1-1093 nm). The wavelength dependency of the measured OAC data quantified by the Aerosol Angstrom Exponent (AAE) was also deduced and analysed from the measured responses of the ambient at the operational wavelength of 4- λ -PAS.

Based on the data evaluation of size distribution, the measurement period can be classified into two categories such as normal and nucleation days. On 5 measurement days clear nucleation events were observed. At normal days three characteristic size modes were defined with count median diameters of circa 15, 25 and 110nm that association with nucleation, traffic and heating activities. We also identified diurnal variations of the strengths of those characteristic modes and AAE values. Investigating the correlations between the photoacoustic and size distribution data we revealed and quantified relationship between the mode structure and the AAE. During the campaign we also identified characteristic spectral responses of nucleation events first. Moreover, in daily regulation, we experimentally demonstrated so called uncompleted nucleation events with characteristic AAE values in normal days.

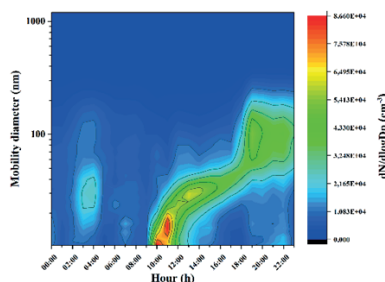
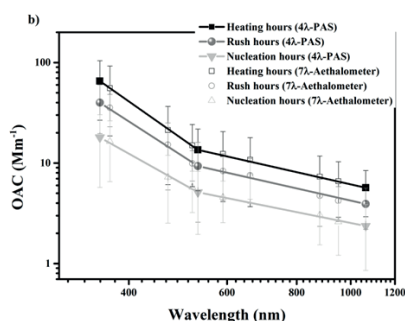


Fig.1. The banana curve demonstrating a nucleation event



From the simultaneous measurement of OAC by the 7 λ -Aethalometer and a 4 λ -Photoacoustic Spectrometer as reference instrument, wavelength dependent correction factors (f and C) was defined in weingartner posterior correction schemes [3]. We found that the correction factor of C has source specific diurnal variations, while correction factor of f no clear trend could be observed during the measurement period.

Acknowledgements

This work was supported by the project GINOP-2.3.2-15-2016-00036 and EFOP-3.6.1-16-2016-00014. This paper was supported by the János Bolyai Research Scholarship of the Hungarian Academy of Sciences. Ministry of Human Capacities, Hungary grant 20391-3/2018/FEKUSTRAT is acknowledged.

References

1. J. Hansen, A. Lacis, D. Rind, G. Russell, P. Stone, I. Fung, Climate processes and climate sensitivity, 130-163 (1984) doi: 10.1029/GM029p0130
2. T. Ajtai, Á. Filep, G. Kecskeméti, B. Hopp, Z. Bozóki, G. Szabó, Appl. Phys. A 103, 1165– 1172. (2010) doi: 10.1007/s00339-010-6068-3
3. E. Weingartner, H. Saathoff, M. Schnaiter, N. Streit, B. Bitnar, U. Baltensperger, Journal of Aerosol Science, 34(10), 1445-1463. (2003) doi: 10.1016/S0021-8502(03)00359-8

Fig.2. Absorption responses of ambient measured at different periods of the nucleation days using 4 λ -PAS the 7 λ -Aethalometer using Cref values

Protein Characterization by Steady-State and Transient Thermal Lens Spectrometry

Polina A. GALKINA, Dmitry VOLKOV, Mikhail A. PROSKURNIN

Chemistry Department, Lomonosov Moscow State University, 119991, Moscow, Russia

proskurnin@gmail.com

Thermal-lens spectrometry (TLS) is used for sensitive and reliable quantification of the absorption bands of proteins [1, 2]. These applications usually require microscopic techniques and precise instrumentation combined with data visualization and rather sophisticated data treatment [2, 3]. However, TLS can be implemented as simpler setups still providing high sensitivity of measurements in rather small-volume samples [4]. This approach is considered straightforward and useful for the determination of optical absorption and photothermal properties of solvents only. However, the dynamic nature of photothermal effects provide very informative transient data, which can be used with non-microscopic schematics for the characterization of photothermal and size-based parameters of protein solutions.

Carotenoid proteins are photoactive molecules responsible for the photoprotection of cyanobacteria from the oxidative damage. They have photosensitive chromophores and long hydrocarbon chains with many double bonds and, thus, very efficient quenchers of excitation energy absorbed by the light-harvesting complex of cyanobacteria under high light intensities [5, 6]. Carotenoid proteins have a physiological function to deliver carotenoids with antioxidant properties to the cells that need protection from active singlet oxygen [5]. Various species of these proteins show different energy-transfer properties that hence can be attributed to thermal and, thus, photothermal parameters. Orange carotenoid protein (OCP) is the main energy-transfer protein. Violet carotenoid protein is a C-domain only 'version' of OCP, which is known to quench singlet oxygen more efficiently than OCP. Purple carotenoid protein is a mutant, always stable photoactive form of OCP, similar to which it turns when illuminated with a green-blue light [5]. Thus, the comparison of photothermal properties of these various species may be attributed to the chromophore and structure differences.

Bovine serum albumin, haemoglobin, and also myoglobin (as an oxygen-binding protein in the heart and skeletal muscles [7]) were selected as heme proteins with known properties and different molecular weights.

A special protocol for handling transient curves based on changes in thermal diffusivity during the experiment was proposed. Heme proteins, albumin, carotenoid proteins, and their supramolecular complexes at submicromolar levels as well as ferroin and cobalt nitrate (used as reference systems of true solutions) were characterized by steady-state and transient thermal-lens experiments. The detection limits of heme proteins by TLS are at nanomolar level, which is 50-fold lower than those by optical absorption methods.

TLS not only shows high sensitivity of the assessment of protein chromophores, but also provides a change in the calibration slopes compared to the theoretical values due to changes in the heat transfer in disperse media. The dependences of the thermal lens signal vs. the excitation laser power was determined for carotenoid proteins (orange, purple, and violet) and myoglobin.

From transient curves, thermal diffusivities of protein solutions were assessed, and the differences in heat transfer in carotenoid protein species were estimated. Thermophysical properties of these species will be discussed. The data obtained by TLS were compared with the results obtained from other relevant methods of spectrochemical analysis.

References

1. D.A. Nedosekin, E.I. Galanzha, S. Ayyadevara, R.J. Shmookler Reis, V.P. Zharov, *Biophys. J.* 102 (3), 672 (2012) doi:10.1016/j.bpj.2011.12.035
2. M.A. Proskurnin, T.V. Zhidkova, D.S. Volkov, M. Sarimollaoglu, E.I. Galanzha, D. Mock, D.A. Nedosekin, V.P. Zharov, *Cytometry A* 79A (10), 834 (2011) doi:10.1002/cyto.a.21127
3. J.W. Kim, E.I. Galanzha, E.V. Shashkov, H.M. Moon, V.P. Zharov, *Nat Nanotechnol* 4 (10), 688 (2009) doi:10.1038/nnano.2009.231
4. K. Tishchenko, M. Muratova, D. Volkov, V. Filichkina, D. Nedosekin, V. Zharov, M. Proskurnin, *Arab. J. Chem.* 10 (6), 781 (2017) doi:10.1016/j.arabj.2016.01.009
5. E.G. Maksimov, N.N. Sluchanko, Y.B. Slonimskiy, E.A. Slutskaya, A.V. Stepanov, A.M. Argentova-Stevens, E.A. Shirshin, G.V. Tsoraev, K.E. Klementiev, O.V. Slatinskaya, E.P. Lukashev, T. Friedrich, V.Z. Paschenko, A.B. Rubin, *Sci. Rep.* 7 (1), 15548 (2017) doi:10.1038/s41598-017-15520-4
6. D. Kirilovsky, C.A. Kerfeld, *Photochem. Photobiol. Sci.* 12 (7), 1135 (2013) doi:10.1039/C3PP25406B
7. D.J. Garry, S.B. Kanatous, P.P.A. Mammen, *Trends Cardiovasc. Med.* 13 (3), 111 (2003) doi:https://doi.org/10.1016/S1050-1738(02)00256-6

CP 006

Numerical Simulations in COMSOL in Photothermal Beam-Deflection Spectroscopy

Aleksandr POTEKIN, Dmitry VOLKOV, Mikhail PROSKURNIN

Chemistry Department, Lomonosov Moscow State University, 119991, Moscow, Russia

proskurnin@gmail.com

Finite element numerical calculations (COMSOL Multiphysics software) was used to simulate the whole cycle of photothermal beam-deflection (PBD) measurements — the thermal perturbation (field), the distribution of the refractive index in the surrounding medium as a result of photothermal heating of the sample, and the propagation of a probe beam through a photothermal element. The thermal model assumes the absence of radiative transitions in the sample upon the absorption of radiation, constant thermophysical parameters during the experiment, the linear temperature dependence of refractive index, and the absence of diffusion. Numerical implementation of mathematical models (sample geometry, materials and irradiation times) for PBD experiments facilitates replacement of empirical optimization. The aim of this study was to test COMSOL Multiphysics with the new *Ray Tracing* module for modeling PBD experiments without any other software/simulations.

The numerical part of the simulation consisted in (i) setting the geometry of PBD experiments; (ii) setting the expressions for constraints and boundary conditions; (iii) setting the physical parameters of the sample and parameters of the optical schematic of the setup; (iv) setting up the division to finite elements; and (v) solving the heat transfer equation, which was followed by the data handling. The model gives either a 2D time-dependent temperature distribution in radial coordinates $\Delta T(r, t)$, a simplified model, or a 3D distribution $\Delta T(r, z, t)$, the basic model for PBD measurements [1]. The simulation is implemented for times from 0.1 ms to 1000 s. The simulation showed that to solve the problem of numerical simulation of the thermal response in PBD, it is enough to further process only the thermal field corresponding to the medium contacting the sample.

At the stage of ray tracing optimization and a geometry optics calculations, a 'Release from Grid' node was used for setting up the number of rays and their origin, a 'Wall' node was set up for the detection position, and a 'Ray Termination' node was used for stopping ray tracing at the detector plane. The amplitude signal of photothermal beam deflection can be measured only; the phase signal is not implemented. The approach has sufficient simplicity and provides significant accuracy of the solution of the problem. The examples of the application of the proposed model will be discussed.

References

1. J. Bodzenta, A. Kaźmierczak-Bałata, R. Bukowski, M. Nowak, B. Solecka, *Int. J. Thermophys.* 38 (6), 93 (2017) doi:10.1007/s10765-017-2219-5

CP 007

Model for Heat Transfer in Disperse Systems in Thermal-Lens and Related Experiments

Evgeny VYRKO, Dmitry S. VOLKOV, Mikhail A. PROSKURNIN

Chemistry Department, M.V. Lomonosov Moscow State University, Moscow 119991, Russia.

proskurnin@gmail.com

Disperse systems play more important roles in photothermal experiments and they involve various types of systems — from protein and micellar solutions to nanodiamonds, quantum dots, and metal nanoparticles. Photothermal modalities used to study these systems also vary and include large scale relatively slow techniques like photothermal-lens spectrometry, fast techniques like photothermal grating and various microscopic techniques. The correct interpretation of sophisticated and time-resolved photothermal signals are required for the relevant results. In this study, a model involving heat transfer in pulsed and cw thermal lens experiments in solution with nano-sized chromophores of various origin in light-absorbing and non-absorbing dispersive media was developed. Simulation software, COMSOL Multiphysics (finite element numerical simulation) and MATLAB software were used. The results for various photothermal modalities and disperse systems will be discussed.

Photoacoustic Evaluation of the Formation of Rare Earth Chelate in Silica Matrices

Yuetao YANG *, Haixiao ZHANG, Xiaojun LIU, Shuyi ZHANG

Key Laboratory of Modern Acoustics, Ministry of Education, Institute of Acoustics,
Nanjing University, Nanjing 210093, China

yyang@nju.edu.cn

Rare earth chelates have received great attention due to their important roles in the study of fluorescent reagents, optical materials and NMR shift reagents. However, rare earth chelates are usually soft, easily melted, and have few desired mechanical properties. Thus these compounds have been impeded from direct applications as fluorescent phosphors or other optical materials. One way to solve this problem is to dope these chelates into inorganic matrices by the sol-gel method, which has been proved to be an excellent method to prepare inorganic-organic composite materials under mild conditions [1].

Photoacoustic technique has been widely used to study the physical and chemical properties of many kinds of samples. It has the advantage to detect optical and thermal properties of light-scattering or opaque samples. Photoacoustic spectroscopy has been found to be suitable for investigating rare earth compounds according to the recent work. In this paper, neodymium chelate with dipyrindine (dipy) was incorporated into silica matrices by the sol-gel method. The formation of the neodymium chelate in silica gels has been studied by photoacoustic spectroscopy.

Materials and Methods

For the sol-gel preparation, ethanol and tetraethoxysilane were mixed. The pH value was adjusted to 2 with addition of HCl. The mole ratio of ethanol, tetraethoxysilane and water was 4: 1: 4. Then Nd(dipy)₂Cl₃•2H₂O chelate was introduced to the precursor solution. Thermal densification of the gels was performed at 150 oC for 3 h. The term ‘wet gel’ in this paper was to refer to the sample that had undergone drying and aging at room temperature only.

Photoacoustic spectra were recorded on a single-beam spectrometer. The excitation source was a 500 W xenon lamp. The optical system was a CT-30F monochromator with a variable-speed mechanical chopper. The acoustic signal was monitored using an indigenous photoacoustic cell fitted with an electret microphone. The microphone output was processed using a SR-830 lock-in amplifier. The final signal was normalized by use of the carbon black reference. Infrared spectra were measured using conventional KBr pellet technique.

Results

Photoacoustic spectra of Nd³⁺ chelate-doped silica samples are shown in Fig. 1. The broad absorption band around 30000 cm⁻¹ is assigned to π - π^* transition of dipy. Photoacoustic bands of different energy levels of Nd³⁺ are clearly shown in Fig. 1. Rare earth ions are frequently used as spectral probes for inorganic matrices and biological systems. It is interesting to study photoacoustic bands of Nd³⁺ in different silica gels to evaluate the formation of rare earth chelates. The “degree of covalency” can be estimated from bonding parameter $b^{1/2}$, nephelauxetic ratio β and Sinha parameter δ [2]. Values of covalency parameters have been calculated based on photoacoustic assignments.

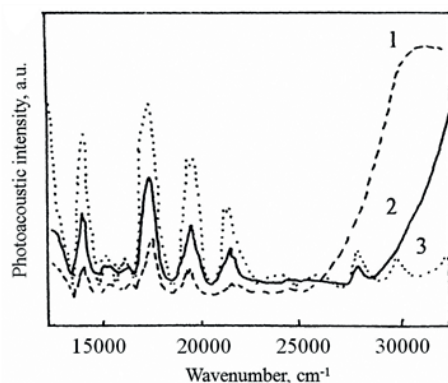


Fig. 1. Photoacoustic spectra of Nd³⁺ chelate-doped silica gel after heat treatment, 1; Nd³⁺ chelate-doped wet gel, 2; Nd³⁺ ion doped-wet gel, 3.

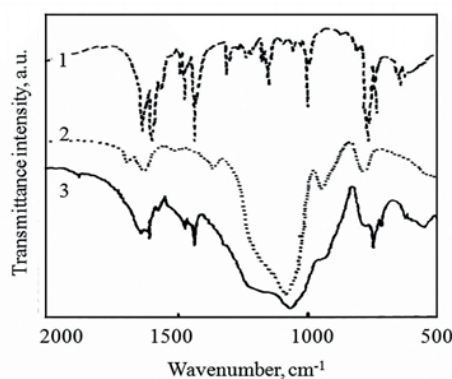


Fig. 2. Infrared spectra of pure Nd³⁺ chelate, 1; Nd³⁺ chelate-doped wet gel, 2; Nd³⁺ chelate-doped-silica gel after heat treatment, 3.

The values of β , $b^{1/2}$ and δ of Nd^{3+} chelate-doped wet gel are 99.50%, 0.050 and 0.50, respectively, which are consistent with those of only Nd^{3+} ion in wet gel. The result indicates that the Nd^{3+} ion does not coordinate with dipy due to the acidic environment of the wet gel. The nephelauxetic ratio decrease to 98.62% for the sample after heat treatment. Upon heat treatment, ethanol, water and HCl vaporize further. The flexibility of siloxane network still allows easy diffusion of rare earth ions and dipy molecules, which can result in the formation of rare earth chelates. IR spectra are shown in Fig. 2. For the sample upon heat treatment, absorption peaks of the neodymium chelate, C=C, C=N stretching (1455 and 1598 cm^{-1}) and C-H vibration (766 cm^{-1}), can be found. Those infrared peaks are superimposed on the original patterns of the silica matrix, which further supports the above discussion.

Conclusions

The formation of the neodymium chelate in silica matrices has been evaluated by photoacoustic technique. Based on the assignments of photoacoustic bands, nephelauxetic parameters of neodymium chelate-doped samples have been determined. Spectral results indicate that dipy does not coordinate with the neodymium ion in silica gels without a suitable heat treatment.

Acknowledgements

This work was supported by the National Natural Science Foundation of China (No. 11834008)

References

1. V. Levchenko, R. Reisfeld, *Optical Materials* 74, 187 (2017)
2. H.Y. Wang, Y.T. Yang, W.S. Chen, Y. Wang, X.J. Liu, S.Y. Zhang, *Journal of Physics and Chemistry of Solids* 71, 971 (2010)

CP 009

Application of Photoacoustic Spectroscopy and Phase Resolved Technique in The Study of Photoprotective Pigments in Golden Delicious Apple (*Malus Domestica*)

Alejandro ROJAS MARROQUIN ^{(1)*}, Joel HERNÁNDEZ WONG ⁽²⁾, Uriel NOGAL LUIS ⁽²⁾, José Bruno ROJAS TRIGOS ⁽¹⁾, Ernesto MARÍN MOARES ⁽¹⁾, José Antonio CALDERÓN ARENAS ⁽¹⁾

1. Instituto Politécnico Nacional, Centro de Investigación en Ciencia Aplicada y Tecnología Avanzada, Av. Legaria No. 694, Col. Irrigación, C.P. 11500, Ciudad de México, México.

2. CONACyT-Instituto Politécnico Nacional, Centro de Investigación en Ciencia Aplicada y Tecnología Avanzada, Unidad Legaria. Legaria No. 694, C.P. 11500, Ciudad de México, México.

calder62@hotmail.com; marroquin-m@hotmail.com

We report the application of the Photoacoustic Spectroscopy (PAS) and the phase resolved technique (PRT) to study the change in the optical absorption spectra of the photoprotective pigments in Golden Delicious Apple (*Malus domestica*) as a function of the maturation time.

Unlike optical absorption spectra reported with conventional methods, the application of PRT on the data of amplitude and phase measured with PAS provides the spectral separation of optical absorption centers corresponding to the pigments in the cuticle and epidermal tissue.

Results show a clear definition of the absorption bands associated to each one of the separate absorption centers of the surface layers of the apple samples. On the other hand, remarkable changes are observed in the characteristics of the absorption bands as a function of the maturation time in Golden Delicious Apple (*Malus domestica*) samples.

References

1. C.L. Cesar, H. Vargas, J. Pelzl, L.C.M. Miranda, J. Appl. Phys. 55, 3460 (1984)
2. R.A. Muñoz Hernández, A. Calderón, A. Cruz-Orea, S.A. Tomas, F. Sánchez Sinencio, G. Peña Rodríguez, High Temperatures-High Pressures, 32, 379 (2000)
3. A. Solovchenko, M. Merzlyak, Photochem. Photobiol. Sci., 2, 861 (2003)
4. A. Rojas-Marroquin, J. Calderón, J. Jaime, J. Hernández Wong, U. Nogal, J. B. Rojas Trigos, A. G. Juárez Gracia, E. Marín, A. Calderón, Lat. Am. J. Phys. Educ., 2 (12), 2308 (2018).

Photoacoustics of Soils: Measurement Methodology and Comparison of Various IR Modalities for Soil Fractions of Various Agrogenesis

Dmitry VOLKOV^{(1,2)*}, Olga Rogova⁽²⁾, Mikhail PROSKURNIN⁽¹⁾

1. Chemistry Department, Lomonosov Moscow State University, 119991, Moscow, Russia

2. V.V. Dokuchaev Soil Science Institute, Pyzhevsky per., 7/2, Moscow 119017, Russia

dmsvolkov@gmail.com

Currently, the studies of the influence of anthropogenesis on the changes in physical and physicochemical properties of soils experience a notable shift. Apart from traditional approaches to determining the properties of the bulk soil, the new information level is to determine soil fractions and aggregate structures including the evaluation of changes at the meso- and microaggregate levels. IR photoacoustic spectroscopy is a promising instrument for more delicate measurement and modeling of the dependence of soil properties on its physical and elemental composition, moisture, porosity, and density. Also, photoacoustic spectroscopy can be on demand for studies of changes of properties of entities of different hierarchical levels under the action of agrogenesis and anthropogenesis.

In this study, the dependence of mid-IR photoacoustic spectra of chernozem soils of various agrogenesis conditions was studied. Photoacoustic modality provides measurements of soil aggregates up to 2–5 mm without sample destruction, which a unique property of this modality. The quality of the spectra does not change for various size fractions (Fig. 1). Photoacoustic spectra very clearly show the organic matter region from 2000 to 1300 cm^{-1} with some differences in the composition. Below 1300 cm^{-1} , the bands are weak in comparison, which differs this case from photoacoustic measurements of other types of samples like nanomaterials. In our opinion, it requires theoretical modeling and experimentally studying model systems.

For soil, photoacoustic and ATR modalities are complementary (Fig. 2), ATR provides the mineral part of soil perfectly visible, while the organic part is rather poorly revealed, and vice versa for photoacoustic measurements. ATR spectra of soil fractions in the mineral part are different, and IR photoacoustic and ATR measurements taken together may be used for studying soil degradation and recultivation processes.

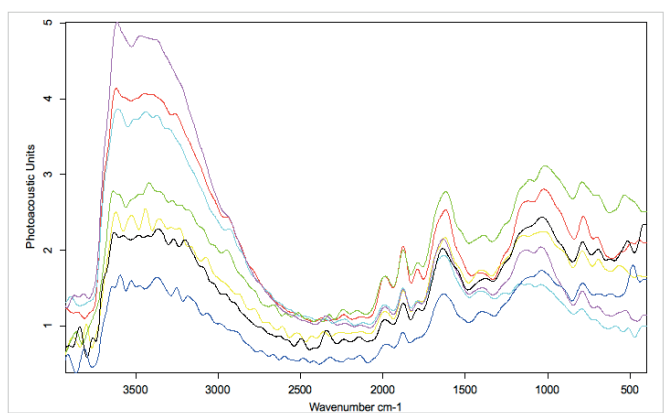


Fig. 1. Photoacoustic spectra (Bruker Vertex 70, 1.6 kHz) of Kursk chernozem bare fallow fractions of less than 50 μm (red); 50–100 μm (green); 100–250 μm (cyan); 250–500 μm (yellow); 0.5–1 mm (blue); 1–2 mm (black); and 2–5 mm (magenta).

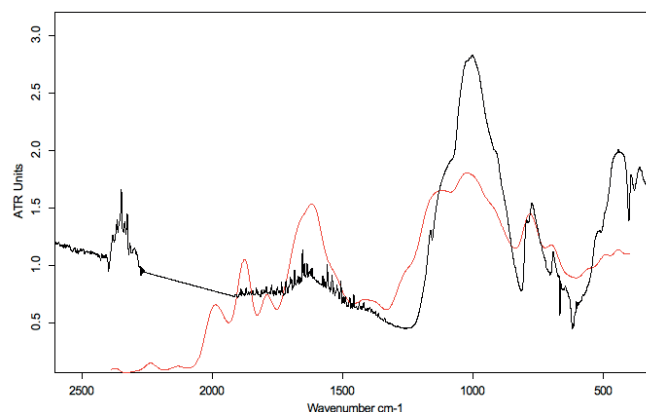


Fig. 2. Photoacoustic (red) and ATR (black) spectra (1.6 kHz) of Kursk chernozem bulk bare fallow.

Acknowledgements

The Russian Science Foundation, grant no. 19-13-00117.

CP 011

Optical Characterization of Mixed Halide Perovskite by using Photoacoustic Spectroscopy in The Visible Spectrum

Jorge Andrés RAMIREZ RINCÓN*, Alejandra María CASTRO CHONG,
Juan José BECERRIL GONZÁLES, Gerko OSKAM, Juan José ALVARADO GIL

Física Aplicada, Cinvestav-Unidad Mérida, Carretera Antigua a Progreso km. 6, 97310, Mérida, Yucatán, México.

jorge.ramirezr@cinvestav.mx

Optical characterization of semiconductor materials with band gap near to the visible spectrum has been an important and widely topic, since the 20th century due to its potential applications in solar cells technology. In the last years the materials of perovskite crystalline structure have been received special attention, due to its low fabrication cost and easy scale up, as a substitute of silicon in conventional solar cells for the absorption of solar spectrum and its conversion in electricity [1]. The efficiency of the photovoltaic conversion process depends mainly on: i) the optical absorption of the material in the solar spectrum, which is conventionally determined by using UV-VIS spectroscopy and ellipsometry [2], ii) the radiative quantum efficiency, i.e. the photons reemitted which are quantify by photoluminescent techniques [3] and iii) the light-into-heat conversion efficiency (non-radiative), related with the amount of light dissipated as heat through the crystalline lattice, which have not been deeply explore in these new materials. Photoacoustic spectroscopy (PAS) is a versatile, well established and widely used technique for the thermal and optical characterization of different kind of materials [4-5]. Additionally, its direct dependence with the non-radiative quantum efficiency makes this technique very suitable to perform this optical characterization.

In this work a mixed halide perovskite deposited on glass have been characterized optically combining conventional optical spectroscopy, photoluminescent and PAS techniques in the spectral range of 400-800 nm, where the perovskite shows its maximum optical absorption to solar spectrum, in order to quantify the efficiency of photovoltaic conversion process.

References

1. K. Akihiro, K. Teshima, Y. Shirai, T. Miyasaka, *Journal of the American Chemical Society* 131, (17) 6050-6051. (2009)
2. J. Yajie, M. A. Green, R. Sheng, A. Ho-Baillie, *Solar Energy Materials and Solar Cells* 137 253-257 (2015)
3. Z. Wenhui, Y. Ding, Y. J. M. Zheng, S. Wu, X. Lu, M. Zeng *RSC Advances* 7, 63 39523-39529 (2017).
4. A. Rosencwaig, G. Allen. *Science* 190 556-557 (1975).
5. J.A. Ramírez-Rincón, O. Ares-Muzio, J. D. Macias, M. A. Estrella-Gutiérrez, F. I. Lizama-Tzec, G. Oskam, J. J. Alvarado-Gil. *Applied Physics A* 124, (3) 252 (2018).

DP 001

Determination of bioavailable Fe redox fractions of sediment pore waters by DGT passive sampling and BDS detection

Hanna BUDASHEVA ⁽¹⁾, Dorota KORTE ^{(1)*}, Arne BRATKIČ ^(2,3), Mladen FRANKO ⁽¹⁾

1. University of Nova Gorica, Laboratory for Environmental and Life Sciences,
Vipavska 13, SI-5000 Nova Gorica, Slovenia

2. Vrije Universiteit Brussel, Analytical, Environmental and Geo-Chemistry, Boulevard de la Plaine 2,
1050 Brussels, Belgium

3. Université de Liège, Chemical Oceanography Unit, Allée du 6 Août 17, 4000 Liège, Belgium

dorota.korte@ung.si

The bioavailability and toxicity of contaminants in sediments to benthic organisms depend on the speciation of the contaminant [1]. The level of iron supply to sediments creates contrasting chemical pathways, each producing distinctive mineral assemblages. Reliable measurement of Fe redox species (Fe^{2+} and Fe^{3+}) in sediments is essential for studies of pollutants or trace-element cycling. This is, however, a difficult task, because the distribution of chemical species often changes during sampling and storage.

In this work the Diffusive Gradients in Thin-films technique (DGT) is investigated as a passive sampling approach used in combination with photothermal beam deflection spectroscopy (BDS) as a detection method for determination of labile Fe-redox species in sediments and natural waters. DGT offers the advantage of pre-concentration of labile (i.e. bioavailable) Fe species from the total dissolved Fe pool in sediment pore waters [2]. The advantage of using BDS [3-4] is also in avoiding contamination by using additional steps as extraction or pre-concentration. Furthermore, combined DGT-BDS provides 2D information about distribution of Fe^{2+} and the total Fe content in the resin hydrogels [5].

The goal of this research is to show the repeatability of this technique for determining trace amounts of Fe redox species in environmental samples.

Materials and Methods

The concentration of iron redox species in solution or their amount on the gel was determined using 1,10-phenanthroline (PHN) as colorimetric reagent. The Fe^{2+} -PHN complex shows broadband absorption in the visible range, with a maximum at 508 nm. This overlaps well with the wavelength of the excitation beam in applied BDS spectrometer (532 nm).

Two methods of sample preparation were examined. In the first approach, each piece (5 mm x 5 mm x 0.04 mm) of the gel was loaded with different mass of Fe^{2+} in the range 0-168 ng. Iron was deposited on the surface of the gel by applying different volumes (0 - 300 μL) of Fe^{2+} solution prepared in double-deionized H_2O ($C = 10 \mu\text{molL}^{-1}$) and leaving overnight until the diffusion of the solution into gel was completed. After deposition of iron, gels were immersed in 25 mL flasks containing 30 μmolL^{-1} PHN solution and put in a horizontal shaker at 250 rpm for 1 day. The BDS signals for each point of calibration curve were obtained by measurements at 3 different parts of gel for 1 minute and calculating the average BDS signal. The procedure was repeated 5 times for each amount of loaded iron. The equation of the regression line was $y = 0.0041x - 0.0077$ ($r^2 = 0.97$). The within day precision of calibration curves' slopes, expressed as RSD, was 6.4 %, and the achieved LOD was a total of 36 ng Fe^{2+} in the loaded gel.

In the second case, the gels were loaded with iron by immersing the same size pieces of gel in 25 mL flasks containing Fe^{2+} solutions prepared in double-deionized H_2O in the concentration range 0-1000 nmolL^{-1} (0-1400 ng) for 24 hours and treating the gels with PHN as described above before performing BDS measurements. The equation of the regression line was $y = 0.0046x - 0.0136$ ($r^2 = 0.98$). The achieved LODs were 31 nmolL^{-1} Fe^{2+} in the solution, which corresponds to 43 ng of iron diffused into the gel.

The RSD values for both calibrations of DGT-BDS technique were 5 - 17 % over the investigated range of concentrations.

The analytical yields of the method were determined by exposing the DGT gels to water samples prepared by spiking deionized water with known amounts of iron at 400 nmolL^{-1} , 600 nmolL^{-1} and 800 nmolL^{-1} concentration levels, and derivatizing them with PHN before BDS measurements. The achieved analytical yields were 92 %, 115 % and 95 %, respectively, which indicates good specificity of the DGT-BDS technique.

The achieved LODs are comparable with other commonly used techniques, such as ICP-MS or ICP-AES [6].

D Fundamentals of Photothermics, PA/OA, and Related Phenomena

The DGT sampling technique combined with BDS detection provides highly sensitive chemical analysis with good repeatability and low detection limits. Thus, it is a promising tool for monitoring concentrations of biologically relevant Fe species in aquatic environment.

Acknowledgements

This work was supported by ARRS - Slovenian Research Agency within the research program P2-0393; Advanced materials for low-carbon and sustainable society. H.B. acknowledges the Young Researchers' grant by the ARRS.

References

1. A. Altier, M. Jiménez-Piedrahita, R. Uribe, C. Rey-Castro, J. Galceran, and J. Puy, *Analytica Chimica Acta* 1060, 114 (2019).
2. D. J. Koppel, M. S. Adams, C. K. King, and D. F. Jolley, *Environmental Toxicology and Chemistry* (2019).
3. D. Korte, H. Cabrera, J. Toro, P. Grima, C. Leal, A. Villabona, and M. Franko, *Laser Physics Letters* 13, 125701 (2016).
4. M. A. Proskurnin, D. Korte, O. B. Rogova, D. S. Volkov, and M. Franko, *International Journal of Thermophysics* 39, 13 (2018).
5. H. Budasheva, A. Kravos, D. Korte, A. Bratkič, Y. Gao, and M. Franko, *Acta Chimica Slovenica* 66, 239-246 (2019).
6. R. Parker, T. Bolam, J. Barry, C. Mason, S. Kröger, L. Warford, B. Silburn, D. Sivyver, S. Birchenough, A. Mayes, and G. R. Fones, *Science of The Total Environment* 575, 1074 (2017).

DP 002

Study of ancient paper and detection of microbiological contamination using photoacoustics

Dalia CASTILLO HERNANDEZ⁽¹⁾, José Francisco SANCHEZ RAMIREZ⁽²⁾,
José Luis JIMENEZ PEREZ^{(1)*}, Alfredo CRUZ OREA⁽³⁾, Mario PÉREZ GONZÁLEZ⁽¹⁾

1. Unidad Profesional Interdisciplinaria en Ingeniería y Tecnologías Avanzadas-Instituto Politécnico Nacional, Av. Instituto Politécnico Nacional No. 2580, Col. Barrio la Laguna Ticomán, Del. Gustavo A. Madero, C.P. 07340 Mexico, D.F
2. Instituto Politécnico Nacional-CIBA. Ex-Hacienda San Juan Molino Carretera Estatal Tecuexcomac-Tepetitla Km 1.5, Tlaxcala, C.P. 90700, Mexico.
3. Departamento de Física, CINVESTAV- IPN, México.

*Authors' e-mail jimenezp@fis.cinvestav.mx

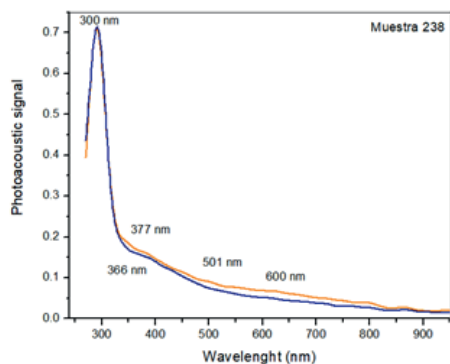
In this work the characterization of fragments of ancient paper (obtained from the Franciscan Library of San Pedro Cholula) that comes from various bibliographic materials was performed. From photoacoustic spectra results, absorption bands from 280 nm to 400 nm associated with cellulose were detected. In addition, the presence of pigments generated by microorganisms for the absorption bands in the region from 450 to 550 nanometers were detected. Photoacoustic spectroscopy has proven to be a versatile technique for the detection highly sensitive systems.

Materials and Methods

The sol-gel technique was employed for the synthesis of TiO₂ nanoparticles. After the synthesis of TiO₂ nanoparticles, three washes with distilled water were carried out to obtain the amorphous phase. On the other hand, to obtain the anatase crystalline phase, the sample was subjected to a heat treatment in a muffle at 450 °C for 2 hours. Then, the dry weight was determined and the nanoparticles from both phases were characterized by UV-vis spectrophotometry, TEM and photoacoustic spectroscopy [1, 2]. Paper discs of 0.5 cm were cut, to be analyzed by using photoacoustic characterization. Four types of measurements were carried out using photoacoustic spectrophotometry. First, different samples of old paper without contaminating were characterized. Second, five species of filamentous fungi which are the most frequent in the ancient papers such as *Aspergillus sp*, *Penicillium sp*, *Mucor sp*, *Alternaria sp* and *Rizopuz sp*, which cause irreversible effects on paper were analyzed. Third, the photoacoustic spectrum to the TiO₂ dioxide was taken. Finally, contamination of the paper with the fungi was induced, inducing the fragments of paper in a solution of spores. Once the contamination of the paper was verified monthly, the discs were immersed in a solution of nanoparticles of TiO₂ and were placed in small boxes to be irradiated with a lamp of UV at 365 nm for 1 h in the anatase phase.

Results and discussion

The synthesized NPsTiO₂, were characterized in ultraviolet light with a main peak located at a wavelength of 352 nm. The obtained result indicates that the TiO₂ with heat treatment of 450, 30 °C, for an hour and a half, has a prohibited bandwidth of 3.78 eV. In the TEM micrographs, nanoparticles of mean particle size of 70 nm were observed. The UV photoacoustic spectrum for the ancient paper fragments revealed intense absorption bands with a broad absorption band in the range from 300-400 nm. Hernández-Aguilar et al., 2019 detected cellulose at 350-400 nm while Gould (1982), found cellulose and hemicellulose in different species of pines at 300-400 nm. Figure 1 shows the photoacoustic absorption spectra of the 238 book catalogue, where cellulose was detected at 300 nm [3, 4].



Conclusions

It was demonstrated that photoacoustic spectroscopy is an alternative technique of high sensitivity for the detection of organic pigments and biological compounds in ancient documents.

Figure 1. Photoacoustic absorption spectra of the sample from a book 238 a) without microorganism, and b) contaminated with a microorganism.

D Fundamentals of Photothermics, PA/OA, and Related Phenomena

References

1. S. Manente, A. Micheluz, R. Ganzerla, G. Ravagnan, and A. Gambaro (2012). Chemical and biological characterization of paper: A case study using a proposed methodological approach. *International Biodeterioration & Biodegradation* 74, 99-108.
2. S. Sequeira, E.J. Cabrita and M.F. Macedo (2012). Antifungals on paper conservation: An overview. *International Biodeterioration & Biodegradation* 74, 67-86.
3. J. Gould Michael Characterization Of Lignin In Situ By Photoacoustic Spectroscopy. *Plant Physiol.* (1982) 70, 1521-1525.
4. C. Hernández-Aguilar, A. Domínguez-Pacheco A. Cruz-Orea and R. Ivanov (2019). Photoacoustic Spectroscopy in the Optical Characterization of Foodstuff: A Review *Journal of Spectroscopy*, pag. 34.

Thermal property measurement of gold nanoshells

Angel NETZAHUATL⁽¹⁾, José Francisco SANCHEZ RAMIREZ⁽²⁾, José Luis JIMENEZ PEREZ^{(1)*}, Genaro GAMBOA LOPEZ⁽³⁾, Zormy Nacary CORREA PACHECO⁽⁴⁾

1. Unidad Profesional Interdisciplinaria en Ingeniería y Tecnologías Avanzadas-Instituto Politécnico Nacional, Av. Instituto Politécnico Nacional No. 2580, Col. Barrio la Laguna Ticomán, Del. Gustavo A. Madero, C.P. 07340 Mexico, D.F

2. Instituto Politécnico Nacional-CIBA.

Ex-Hacienda San Juan Molino Carretera Estatal Tecuexcomac-Tepetitla Km 1.5, Tlaxcala, C.P. 90700, Mexico.

3. Universidad Politécnica del Valle de Toluca, Km 5.6 Carretera Toluca-Almoloya de Juárez, Santiaguillo Tlalcalcali, C.P. 50904, Almoloya de Juárez, México.

4. CONACYT-Instituto Politécnico Nacional. Centro de Desarrollo de Productos Bióticos. Carretera Yautepec-Jojutla, km. 6, Calle CEPROBI, No. 8, San Isidro, Yautepec, C.P. 62731, Morelos. México

jimenezp@fis.cinvestav.mx

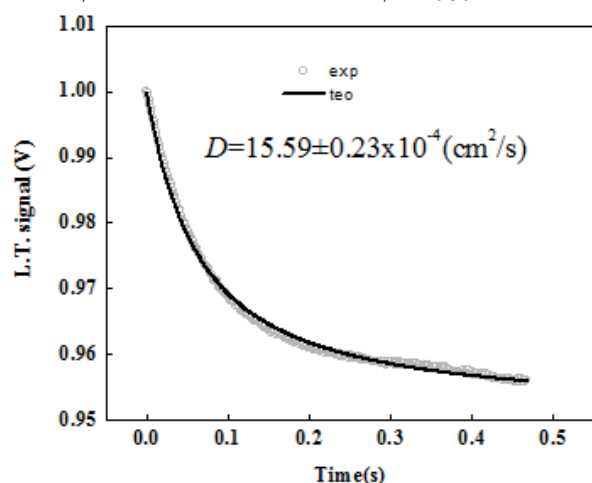
In this work, SiO₂-Au nuclei-shell structures were prepared, the SiO₂ synthesized by the Stöber method were used to growth an Au thin nanoshell. From transmission electron microscopy (TEM) micrographs, homogeneous SiO₂ spherical nanoparticles with an average size of 90 nm and Au shells 13 nm were observed. The Au nanoshells were attached to a dielectric base by the deposition-precipitation process. An absorption band located in infrared region from the UV-vis spectra showed new structures synthesized. Thermal diffusivity for different concentrations lower than 1 mg / ml core-shells SiO₂-Au nanofluids dispersed in water was measured by thermal lens spectroscopy. From the results, it was observed an increase in the thermal diffusivity as the concentration of nanoshells increased. Finally, a possible interpretation to our results is given.

Materials and Methods

For the preparation of the SiO₂-Au nanoshells, tetraethyl orthosilicate (TEOS), ammonium hydroxide, (3-aminopropyl) triethoxysilane (APTES), tetrachloroauric acid, sodium borohydride and sodium citrate dehydrate were employed. In addition, methanol, ethanol, sodium hydroxide and deionized water were used. SiO₂ spherical structures were synthesized using the Stöber method [1], which involves the hydrolysis and condensation of TEOS. For the preparation of the Au shell, an a solution of SiO₂-AuOH₃ seed was added to an Au hydroxide solution. Different concentrations lower than 1 mg / ml of nanofluids containing core-shell dispersed in water and the thermal diffusivity was measured by using thermal lens technique. Moreover, the samples were characterized by TEM, X-ray, UV-vis spectroscopy and Fourier Transform Infrared Spectroscopy (FTIR).

Results and discussion

It was observed from TEM micrographs that the SiO₂ mean particle size was 90 nm and for Au shells it was 13 nm. From UV-vis spectroscopy a band at around 750 nm, associated to surface plasmon resonance (SRP), confirmed the Au nanoshells formation. From FTIR, the characteristic peaks absorption bands were: at 550 cm⁻¹ related to longitudinal vibration of Si-O-Si, at 800 cm⁻¹ due to the symmetric tension of Si-O-Si, at 1080 cm⁻¹ and at 1200 cm⁻¹ due to the asymmetric tension of Si-O-Si. At 955 cm⁻¹ related to



bond tension in Si-OH and at 1640 cm⁻¹ and 3362 cm⁻¹ related to bending and stretching of water on the surface of SiO₂ spheres. The thermal diffusivity value obtained by thermal lens spectroscopy was $15.7 \pm 0.23 \times 10^{-4} \text{ cm}^2/\text{s}$ for a concentration of 0.1 mg / ml. In Figure 1, the typical spectra of thermal lens evolution vs time is shown. The obtained value was greater than that of the water-base fluid, which is $14.2 \times 10^{-4} \text{ cm}^2/\text{s}$. It can be seen, that as core-shell of SiO₂-Au concentration increases, the thermal diffusivity increases. This behavior can be explained as follows: there is an increase in the optical and heat absorption, according to $D = k/\rho c_p$. In SiO₂ the specific c_p is decreased in nanofluids causing and improvement of the thermal diffusivity. At higher concentration, there is a thermal enhancement due to scattering phonon in the liquid-solid interphase [2, 3].

Fig. 1. Thermal lens signal for the core-shell SiO₂-Au nanofluid.

D Fundamentals of Photothermics, PA/OA, and Related Phenomena

Conclusions

Gold nanoshells over a SiO₂ dielectric platform were synthesized. This was achieved by mixing the seed solution and more Au-hydroxide solution. Thermal diffusivity was measured by thermal lens spectroscopy, the results revealed an increase of thermal diffusivity according to concentration of core-shells SiO₂-Au. This investigation also have applications in the treatment of cancer cells treated by photothermal effects.

References

1. W. Stöber, A. Fink, Journal of colloid and interface science 26, 62 (1968)
2. J.L. Jiménez-Pérez, J.F. Sánchez-Ramírez, D. Cornejo.-Monroy, R. Guitierrez.-Fuentes, J.A. Pescador.-Rojas, A. Cruz-Orea, C. Jacinto, International Journal of Thermophysics 33, 69 (2012) doi:10.1007/s10765-011-1139-z
3. Shahriari, E., Moradi, M., Raeisi, M. Journal of Theoretical and Applied Physics, 10(4), 259-263. doi:10.1007/s40094-016-0224-x

Study of Moringa Oleifera extract by photothermic techniques

Rigoberto CARBAJAL VALDEZ ⁽¹⁾, José Luis LUNA SANCHEZ ⁽¹⁾, José Luis JIMENEZ PEREZ ^{(1)*},
Claudia HERNANDEZ AGUILAR ⁽²⁾, Arturo DOMINGUEZ PACHECO ⁽²⁾,
Zormy Nacary CORREA PACHECO ⁽³⁾

1. Unidad Profesional Interdisciplinaria en Ingeniería y Tecnologías Avanzadas-Instituto Politécnico Nacional, Av. Instituto Politécnico Nacional No. 2580,

Col. Barrio la Laguna Ticomán, Del. Gustavo A. Madero, C.P. 07340 Mexico, D.F

2. Instituto Politécnico Nacional, Sepi-Esime, Zacatenco, Unidad Profesional "Adolfo López Mateos". Col. Lindavista. México D.F., CP 07738, México ²Colegio de Postgraduados.

IREGEP. Programa de Semillas. Montecillo. Edo. de México, CP 56180, México.

3. CONACYT-Instituto Politécnico Nacional. Centro de Desarrollo de Productos Bióticos. Carretera Yautepec-Jojutla, km. 6, Calle CEPROBI, No. 8, San Isidro, Yautepec, C.P. 62731, Morelos. México.

jimenezp@fis.cinvestav.mx

In this work, the method used for the elaboration and characterization of Moringa oleifera extract are presented. An aqueous extract of Moringa oleifera was prepared. The Moringa oleifera leaf powders were characterized by the XPS (X-ray photoelectron spectroscopy) technique and the aqueous extract was characterized by UV-VIS absorption spectroscopy, Fourier transform infrared spectroscopy (FTIR) and thermal lens spectroscopy (TLS). The variation of the thermal diffusivity at different concentrations was measured by TLS.

Materials and Methods

To obtain the aqueous extract of Moringa oleifera, distilled water was placed in a flask, brought to boiling temperature. Then, dried leaves of Moringa oleifera were added. After that, the aqueous solution was allowed to cool [1-3]. For the characterization by the XPS technique, the powder obtained from dried and ground of Moringa oleifera leaves was used. As a result from this characterization, the following elements were found: Potassium (K), Calcium (Ca), Iron (Fe), Silicon (Si), Phosphorus (P), Sulfur (S), Carbon (C), Oxygen (O) and Nitrogen (N) (Fig. 1), from the FTIR technique, the functional groups observed were OH and NH₃⁺ [2]. Finally, with the TLS technique the variation of the thermal diffusivity was obtained with the concentration, from 0.00175 cm²/s to 0.00196 cm²/s (Fig. 2).

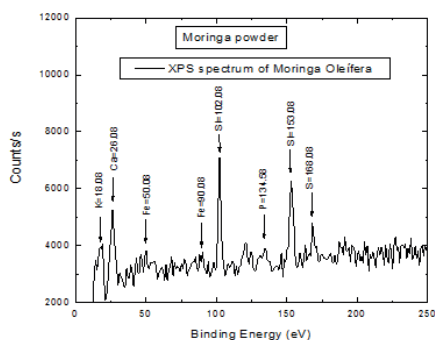


Fig. 1. XPS spectrum of powdered dried ground leaves of Moringa oleifera

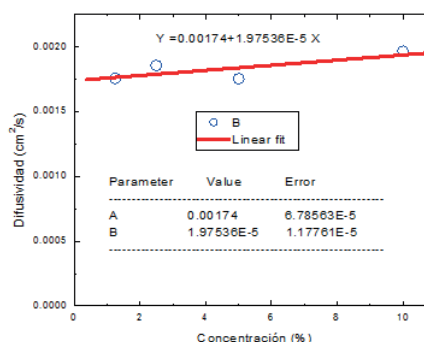


Fig. 2. Graph of the concentration vs diffusivity obtained with the TLS technique from the extract of Moringa oleifera.

References

1. Vivek Patidar, Preeti Jain . (2017). Green Synthesis of TiO₂ Nanoparticle Using Moringa Oleifera Leaf Extract. International Research Journal of Engineering and Technology (IRJET), 04, 470-473.
2. Matinise, N., Fuku, X. G., Kaviyarasu, K., Mayedwa, N., & Maaza, M. (2017). ZnO nanoparticles via Moringa oleifera green synthesis: Physical properties & mechanism of formation. Applied Surface Science, 406, 339-347.
3. Shivashankar, M., & Sisodia, G. (2012). Biosynthesis of silver nanoparticles obtained from plant extracts of Moringa oleifera. Int. J. Life Sci. Biotechnol. Pharm. Res, 1, 180-185.

DP 005

Photothermal study and Photoacoustic Spectroscopy to crosslink a Silver-Acrylic nanocomposite resin

José Luis LUNA SÁNCHEZ ⁽¹⁾, José Luis JIMÉNEZ PÉREZ ^{(1)*}, Alfredo CRUZ OREA ⁽²⁾, Marcos MACIAS MIER ⁽²⁾, Zormy Nacary CORREA PACHECO ⁽³⁾, Mario PÉREZ GONZÁLEZ ⁽²⁾, Adrián Antonio CASTAÑEDA GALVAN ⁽¹⁾

1. Unidad Profesional Interdisciplinaria en Ingeniería y Tecnologías Avanzadas-Instituto Politécnico Nacional, Av. Instituto Politécnico Nacional No. 2580, Col. Barrio la Laguna Ticomán, Del. Gustavo A. Madero, C.P. 07340 Mexico, D.F

2. Physics Department, CINVESTAV-IPN, AP 14-740, 07360 Mexico City, Mexico

3. CONACYT-Instituto Politécnico Nacional. Centro de Desarrollo de Productos Bióticos. Carretera Yautepec-Jojutla, km. 6, Calle CEPROBI, No. 8, San Isidro, Yautepec, C.P. 62731, Morelos. México

jimenezp@fis.cinvestav.mx

Abstract

In the present research, Photoacoustic Spectroscopy (PAS) was employed to polymerize and to measure the thermal constants of an acrylic resin composite with silver nanoparticles (AgNPs). The AgNPs were synthesized by a green method and their properties were determined by TEM (transmission electron microscopy), XRD (X-ray diffraction), EDS (energy dispersive X-ray spectroscopy), FE-SEM (field emission scanning electron microscopy) and FTIR (Fourier transform infrared spectroscopy). The nanocomposite resin was polymerized in a PAS (photoacoustic spectroscopy) open cell experimental set up. The polymerization characteristic time, τ , presented a lineal increase behavior for AgNPs concentration.

Materials and Methods

To synthesize the AgNPs the methodology of Li [1] was used. A juice extractor with a power of 250 W and a centrifuge at 4000 rpm were used. Capsicum Annum var Annum, distilled water, AgNO₃, acrylic resin were the reagents used. The AgNPs were dispersed into the acrylic resin using an ultrasonic bath. UV-vis analysis of absorption coefficients were performed in the range (190-1100) nm, with a step of 5 nm. The chemical functional groups were determined using a FTIR spectrometer in the range from 400 to 4000 cm⁻¹, with a step of 2 cm⁻¹. TEM analysis of nanoparticle size were taken with an electron microscope at 60 kV. The surface morphology of the samples was assessed with FE-SEM at 10.0 kV and 3 mm working distance. The chemical composition of the nanoparticles was investigated by EDS. The acrylic resin was also investigated by FTIR and UV-visible to identify its chemical characteristics and absorption range (200 – 405 nm). The nanocomposite was formed by adding 5 – 20 x10⁻⁴ g of

AgNPs into the resin and dispersed by ultra-sonication for 1h. The nanocomposite samples were deposited in a circular sample holder 5 x 2 mm on the acoustic cell. PAS experimental set up variables were: laser wavelength 405 nm, power 2.2 mW and frequency 17 Hz.

Results and discussion

In agreement to Li *et al.*, [1], it was found that the synthesized AgNPs were formed with the following characteristics: size 17.5 nm, rounded shape, hexagonal structure, polycrystalline nature and chemical composition (Ag: 85.76± 3.61; O 14.24 ± 1.57). They were stabilized by the green extract, with an organic film on the particle surface. Such film acted as a surfactant during the incorporation to the acrylic resin allowing a good dispersion into the polymer that was stable at normal temperature and pressure conditions. The incorporation of AgNPs into the resin was confirmed by the formation of a band in the 1500 – 1580 cm⁻¹ region in the FTIR spectra, assigned to the presence of AgNPs as a highly charged group in the proximity of the acrylic double bond [2]. Fig 1 shows the linear enlargement of polymerization characteristic time, τ , versus AgNPs concentration into the composite.

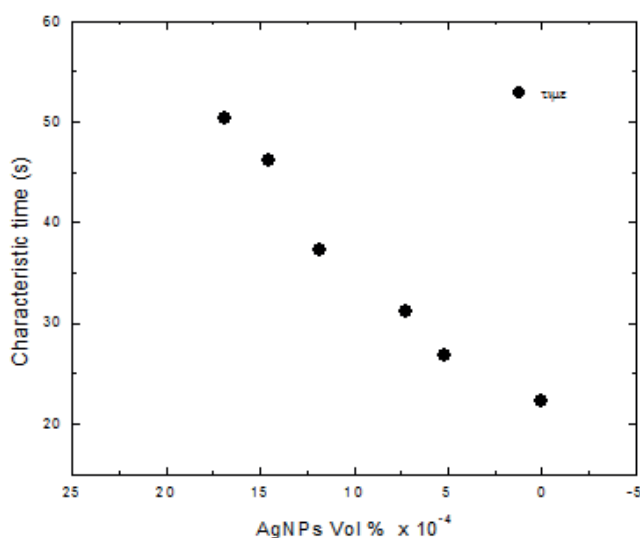


Fig. 1. Characteristic polymerization time

D Fundamentals of Photothermics, PA/OA, and Related Phenomena

Conclusions

Green synthesis is a reliable technique to get AgNPs. The obtained nanoparticles facilitated the incorporation into the acrylic resin, increasing τ for the nanocomposite, compared to pure resin. Further characterization analyses will help us to describe the microstructure and mechanical properties of cured samples. Then, the polymerized samples will be microstructural and mechanically characterized.

References

1. Shikuo Li, Yuhua Shen, Anjian Xie, Xuerong Yu, Lingguang Qiu, Li Zhanga and Quingfeng Zhanga. Green synthesis of silver nanoparticles using *Capsicum annuum* L. extract. *Green Chem.*, 2007, 9, 852–858.
2. C. Suresh, M. Vasubabu and R. J. Kumar. FTIR Investigations on the Structure of Acrylic Resin Based Dental Biomaterials. *Res. J. Pharm. Biol. Chem. Sci.*, 2016, (4), 1157-1159.

DP 006

The use of Artificial Neural Networks for modeling thermal conductivity of nanobiodiesels

José Luis JIMÉNEZ PÉREZ^{(1)*}, Genaro LOPEZ GAMBOA^(1,3), Zormy Nacary CORREA PACHECO⁽²⁾, M.L. ALVARADO NOGUEZ⁽⁵⁾, Marcenilda AMORIM LIMA⁽⁶⁾, Alfredo CRUZ OREA⁽⁷⁾

1. Unidad Profesional Interdisciplinaria en Ingeniería y Tecnologías Avanzadas-Instituto Politécnico Nacional, Av. IPN, No. 2580, Col. Barrio la Laguna Ticomán, Gustavo A. Madero, CP 07340 Ciudad de México, México
2. CONACYT- Instituto Politécnico Nacional – Centro de Desarrollo de Productos Bióticos, Carretera Yautepec–Jojutla, km 6. San Isidro, C.P. 62731, Yautepec, Morelos, México
3. Universidad Politécnica del Valle de Toluca, Km 5.6 Carretera Toluca-Almoloya de Juárez, Santiaguillo Tlalcalcali, C.P. 50904, Almoloya de Juárez, México.
4. Centro de Investigación en Biotecnología Aplicada, Instituto Politécnico Nacional, Ex-Hacienda San Juan Molino Carretera Estatal Tecuexcomac-Tepetitla Km 1.5, Tlaxcala C.P. 90700, México
5. SEPI-ESIME-Instituto Politécnico Nacional, Unidad Profesional “Adolfo López Mateos”, Edificio 5, C.P. 07738, Mexico City, Mexico
6. Laboratory of Physics Sciences, North Fluminense State University, 28.013-602, Campos dos Goytacazes, Rio de Janeiro, Brazil.
7. Departamento de Física, CINVESTAV-IPN, Av. Instituto Politécnico Nacional No. 2508, Col. San Pedro Zacatenco, C.P. 07360 Ciudad de México, México

jimenezp@fis.cinvestav.mx

Thermal conductivity of two types of nanobiodiesels (NBs) were investigated theoretically and experimentally. The first type of NBs was composed of C4 biodiesel (Purchased from Biofuels of Mexico) filled with Au nanoparticles (Au-NPs) and the second type was composed of soybean biodiesel filled with Ag nanoparticles (Ag-NPs). It has been demonstrated in the literature that the addition of Au-NPs or Ag-NPs to biodiesel can lead to a significant increase in thermal properties. The photo thermal techniques were used to determine the thermal diffusivity (D), thermal effusivity (e) and thermal conductivity (k) of biodiesel filled with Au-NPs or Ag-NPs in different concentrations. For about two decades researchers have made the effort to predict the enhancement of the thermal conductivity of nanofluids based on experiments and several theoretical models have been proposed. One of these analytical models that have allowed researchers, calculate the thermal conductivity of the nanofluids is the Hamilton-Crosser Model, this model is based on the classical theory of compounds and mixtures containing particles of the order of millimeters or micrometers and fails dramatically in predicting the thermal conductivity of nanofluids. In that sense, the so-called Hamilton-Crosser model (H-C) cannot represent adequately the enhancement in k as a function of NP's concentration. So to predict the thermal conductivity of the two NBs, the so-called artificial neural networks (ANNs) were used [1-6].

Results and discussion

The figure 1 shows the k vs. volume percentage for both NBs, experimentally, with the H-C model and using the ANN model, from the thermal properties of the NB of C4 filled with Au-NPs and NB of Soybean biodiesel filled with Ag-NPs.

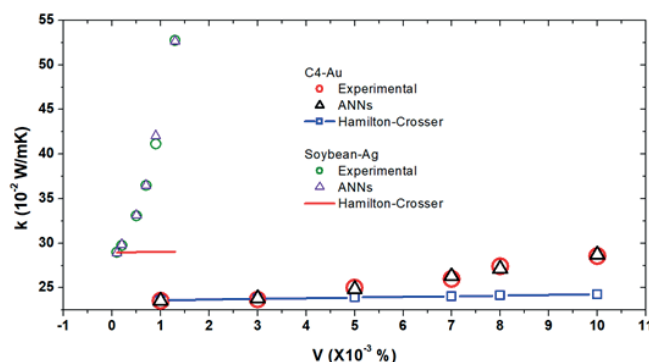


Figure 1. Thermal conductivity (k) vs. volume percentage for AgNPs/Soy biodiesel and C4/Au biodiesels for Hamilton-Crosser and ANN models.

D Fundamentals of Photothermics, PA/OA, and Related Phenomena

As can be seen in figure 1, it should be noted that the k of the NBs is not described adequately by the classical theories as Hamilton – Crosser for nanofluids. The comparisons indicate that the ANN model can successfully predict the k of nanofluids with applications on heat transfer performance of nanofluids.

Conclusions

It was found that biodiesel containing a small amount of AgNPs have higher thermal conductivity than of C4 biodiesel containing a higher amount of AuNPs. The thermal conductivity of nanobiodiesels increases remarkably with increasing concentration of nanoparticles. The chemical composition of the biodiesel does not influence the k enhancement of nanofluids. It was found that the experimental results are higher than those predicted by ANN models for nanofluids, while the H-C model was not satisfactory for low and high NPs concentrations. In summary, the addition of NPs to biodiesel increases the thermal properties. The values obtained in the literature, are in the range of typical biodiesel oils. This study is important for nanofluids having potential applications in many important fields such as heat transfer or cooling technologies, microfluids, transportation, medical and several thermal systems.

References

1. J.L. Jiménez-Pérez, G. López-Gamboa, Z.N. Correa-Pacheco, J.F. Sánchez-Ramírez, M. Sánchez-Rivera, M. Salazar-Villanueva, Int. J. Eng. Tech. Research 3, 162 (2015)
2. D. Kumar, H. Patel, V. Rajeev, T. Sundararajan, T. Pradeep, S. Das, Phys. Rev. Lett. 93, 144301 (2004)
3. J. L. Jiménez-Pérez, P. Vieyra Pincel, A. Cruz-Orea, Z. N. Correa-Pacheco, Appl. Phys. A 122, 556 (2016)
4. J. L. Jiménez-Pérez • R. Gutiérrez Fuentes, Z. N. Correa-Pacheco • J. Tánori-Cordova • A. Cruz-Orea • G. López Gamboa, Int. J. Thermophys, 36, 1086-1092 (2015)
5. J. L. Jiménez-Pérez, G. López-Gamboa, A. Cruz-Orea, Z.N. Correa-Pacheco, Rev. Mex. Ing. Quim. 14, 481 (2015)
6. R. L. Hamilton, O.E. Crosser, Ind. Eng. Chem. Res. I(3), 187-191 (1962)

DP 007

Optical-Thermal Characterization of Lime in the Talavera House from the Historical Center of Mexico City

Joel JIMENEZ PEREZ ⁽¹⁾, Alicia Bracamontes ⁽¹⁾, José Luis JIMENEZ PEREZ ^{(2)*},
Zormy Nacary CORREA PACHECO ⁽³⁾, Mario PEREZ⁽¹⁾, Alfredo CRUZ OREA⁽⁴⁾

1. Escuela Nacional de Antropología e Historia, Periférico Sur y Zapote, Col. Isidro Fabela, CP 14030 México DF. México

2. Unidad Profesional Interdisciplinaria en Ingeniería y Tecnologías Avanzadas-Instituto Politécnico Nacional, Av. Instituto Politécnico Nacional No. 2580, Col. Barrio la Laguna Ticomán, Del. Gustavo A. Madero, C.P. 07340 Mexico, D.F

3. CONACYT-Instituto Politécnico Nacional. Centro de Desarrollo de Productos Bióticos. Carretera Yautepec-Jojutla, km. 6, Calle CEPROBI, No. 8, San Isidro, Yautepec, C.P. 62731, Morelos. México

4. Departamento de Física, Centro de Investigación y de Estudios Avanzados, Instituto Politécnico Nacional, Av. Instituto Politécnico Nacional 2508 Col. San Pedro Zacatenco, CP 07360 DF, México

Authors' e-mail jimenezp@fis.cinvestav.mx

X-ray Photoelectron Spectroscopy (XPS), Dispersive Energy Spectroscopy (EDS) and Photoacoustic (PA) techniques are useful to identify the structure of chemical compounds used for various applications, archaeology, among others. In the following work, these techniques were used for the analysis of seven samples that were obtained in Talavera House during the works corresponding to the years 2012-13 in which conservation and restoration works were carried out. Talavera House is located between the streets of the República del Salvador, Talavera and Roldán in the historic center of Mexico City [1, 2]. The objective of this work were to study the chemical compounds that were added to the lime when burned in the furnace and its use in the tanneries during the 18th century, both elements located in the second yard, as well as in the construction of the corridor in the 20th century located in the first courtyard. The samples were collected at these points and analyzed with the XPS and EDS techniques and by Photoacoustic (PA), comparing these results with other excavated sites

Results and discussion

XPS, EDS and Photoacoustic (PA) were used to determine the composition of lime manufacture in Talavera House. From the seven samples studied, the first five and the last sample belong to materials used in the year of its construction (eighteenth century) when the building was a tannery factory, and the sixth sample corresponds to a modification in the building made in 1912 when at that time, it was a primary school. In Fig. 1, photographs of the flattened interior of the tub corresponding to sample 2 (a) and the lime kiln corresponding to sample 5, can be seen. In Fig. 2, the Ca 2p peaks corresponding to sample 2 and sample 5 from Fig 1, opposite sides of sample 2 (sample 1) and sample 5 (sample 4) and flattened exterior wall of the building located opposite one side of the calera in the second yard (sample 3) are observed. From the physicochemical techniques used for the characterization, we were able to know the composition of the lime and the nature of the material. These samples were compared for the function they had in each space, their morphological composition and the manufacture of lime.



Fig. 1. Talavera house: a) flattened interior of the tub and (sample 2) b) lime kiln (sample 5)

D Fundamentals of Photothermics, PA/OA, and Related Phenomena

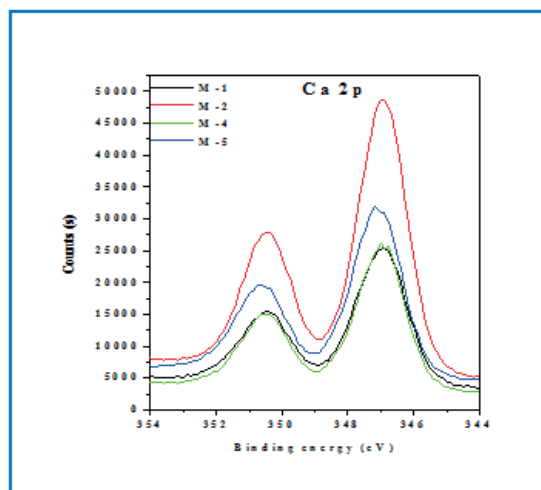


Fig. 2. Ca 2p peaks corresponding to sample 2 and sample 5 from Fig 1, opposite sides of sample 2 (sample 1) and sample 5 (sample 4)

Conclusions

In summary, the functions of the use of lime were determined in the Talavera House, recognizing areas of activity within the architectural spaces of the building. In the results of the chemical analysis of Talavera House, nine elements were found: O, C, Ca, Si, Mg, P, Na, Fe and K, varying their percentages according to the sampled site. It was concluded that in the tubs (sample 2) and in the heat furnaces (samples 4 and 5), a relatively higher percentages of Ca and P were found, reason why it is justified that these locations were used to cut the skins and to perform calcination of the lime. On the other hand, it was found for samples 3 and 7, chemical elements such as Na, Si and K, the different in proportion compared to the samples of the eighteenth century, so there are differences in to the proportion of chemical elements for these two different periods of construction of the Talavera house.

References

1. M. Toussaint, *Arte Colonial en México*, Instituto de Investigaciones Estéticas, Universidad Nacional Autónoma de México (UNAM), 1983
2. J. Jiménez, A. Bracamontes, J. Jiménez, Z. Correa, A. Cruz, *La Casa Talavera*, Restauro Compás y Canto S.A. de

DP 008

Photothermal Deflection Study of V/V_2O_5 alternating layers Structure: Effect of Annealing Temperature and Time on Thermal and Optical Properties

Anouar Khalfaoui^{(1)*}, Soufiene Ilahi^(1,2), Mohamed Abdel-Rahman^(3,4), Muhammad Alduraibi⁽⁵⁾, Bouraoui Ilahi⁽⁵⁾, Nouredine Yacoubi⁽¹⁾

1. Laboratoire de recherche de caractérisation photo-thermique, IPEIN, Université de Carthage, 8000 Nabeul, Tunisie
2. Université de Monastir, Faculté des sciences de Monastir, Département de physique, Université de Tunis
3. Department of Electrical Engineering, College of Engineering, King Saud University, Riyadh, Saudi Arabia
4. Prince Sultan Advanced Technologies Research Institute (PSATRI), King Saud University, Riyadh, Saudi Arabia
5. King Saud University, Department of Physics and Astronomy, College of Science, Riyadh, Saudi Arabia

anouar_khalfaoui@yahoo.fr

Vanadium oxides (V_xO_y) have been widely studied as smart materials because of their capability of going through a reversible metal-insulator-transition. They are of considerable technological interest for a wide range of applications. This work, present deposition method proposed to achieve vanadium oxide V_2O_5/V thin films with high (TCR), intended to be used as functional material in microbolometer applications. We have applied a suitable thermal annealing by sputtering method to three samples composed of nine alternating layers of vanadium pentoxide (V_2O_5), 15 nm, and vanadium V (V), 5 nm, which were annealed for different times at 300°C in O_2 atmosphere. We have applied raman spectroscopy for microstructure characterization and Photothermal Deflection Techniques “PDT“ for thermal characterization and PDS for optical characterization. The results show that annealing atmosphere has an effect on microstructure, optical and thermal properties of the mixed phase.

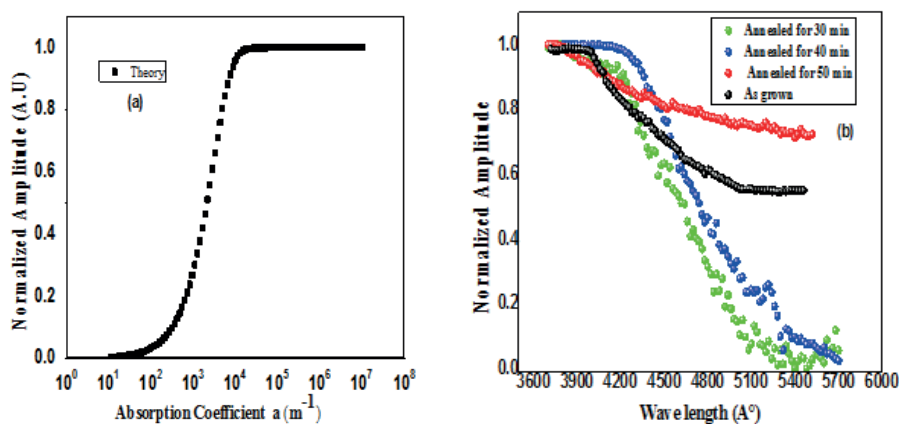


Fig 1 Experimental and theoretical amplitude of PDS signal versus wavelength and absorption coefficient respectively of the as-grown sample and annealed in O_2 atmosphere at 300°C for different annealing times

DP 009

Excitation of surface and bulk coherent phonons in diamond using embedded microstructure based on the graphitized layer

Andrey Yur'evich KLOKOV*, Andrey Ivanovich SHARKOV, Vitalii Anatolevich TSVETKOV, Roman Abramovich KHMELNITSKY, Valerii Abramovich DRAVIN

P.N.Lebedev Physical Institute of the Russian Academy of Sciences, Leninskii pr. 53, Moscow, 119991, Russia

klokov@lebedev.ru

For optical excitation of surface (SAW) and bulk (BAW) coherent phonons in transparent media, thin-film coatings or planar nanostructures formed on the surface are widely used. When an optical pulse is absorbed, coherent phonons are generated through various electron-phonon or photon-phonon mechanisms.

Another method of forming micro/nanostructures in the sample under study is ion implantation, which allows one to create a region with modified properties that absorbs the exciting optical pulse.

In this work, for the optical excitation of SAW and BAW in diamond, a microstructure in the form of a strip of $1000 \times 40 \mu\text{m}$ based on a graphitized layer [1], obtained by implantation of He^+ ions, was used. The depth of the layer is $\sim 700 \text{ nm}$ and the thickness $\sim 120 \text{ nm}$.

The interferometric technique [2] was used, which allows one to simultaneously register changes in the amplitude and phase of the reflection coefficient from the sample caused by propagating coherent phonons.

In Figure 1 the spectra of the amplitude and phase of the response are shown when the center of the strip is excited by a femtosecond laser pulse.

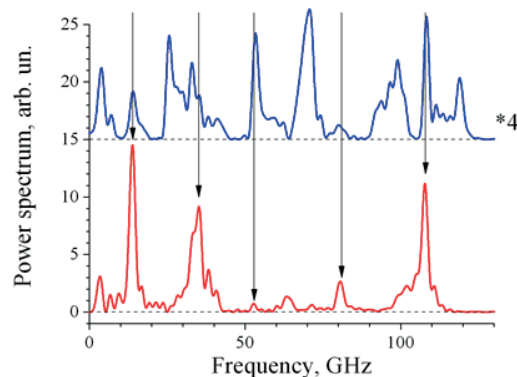


Fig. 1. The spectra of the amplitude and phase of the response to propagating BAW generated when the center of the strip is excited by a femtosecond laser pulse. Blue curve – the spectrum of $\text{Im}(\Delta R/R)$, red curve – the spectrum of $\text{Re}(\Delta R/R)$. The line at $\sim 108 \text{ GHz}$ corresponds to Brillouin scattering.

One can see that the spectra consist of a set of lines in the range from 5 to 120 GHz, and there is no complete line matching. This can be explained by the different "optical activity" of the various vibrational modes of the structure under study.

A similar difference in the spectra of the amplitude and phase of the response was observed previously for diamond samples implanted with carbon ions [3].

Figure 2 shows a picture of propagating SAW. It is seen that the fronts of the surface wave are almost not distorted when crossing the boundaries of the strip. This is due to the small thickness of the strip ($\sim 120 \text{ nm}$) as compared to the SAW wavelength ($\sim 2 \mu\text{m}$). As a result, the perturbation ("softening") of the effective elastic properties of the near-surface layer is small. The propagation velocity of SAW along the strip at frequencies lower than 1 GHz is $\sim 3\%$ lower than the velocity of the Rayleigh wave on the diamond surface. At frequencies above 1GHz, SAW normal dispersion is visible (Fig.2).

D Fundamentals of Photothermics, PA/OA, and Related Phenomena

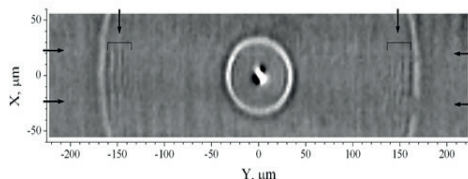


Fig.2. SAW pattern obtained on the sample surface. Repetitive circles are pulses of SAW corresponding to two excitation pulses, following with a period of ~ 13 ns. In the figure the boundaries of the embedded layer are marked by horizontal arrows. At the back front of the SAW pulse, which passed $170 \mu\text{m}$ along the embedded layer, one can see the structure caused by the dispersion (marked by vertical arrows).

Comparison of the experimental data with the results of mathematical modeling of the response allowed us to determine the elastic and photoelastic properties of the graphitized layer.

Acknowledgements

This work was supported by Russian Foundation for Basic Research, grant no 19-02-00952-a.

References

1. A.V. Khomich, R.A. Khmel'nitsky, V.A. Dravin, A.A. Gippius, E.V. Zavedeev and I.I. Vlasov, *Physics of the Solid State* 49 (9), 1661-1665 (2006) DOI: 10.1134/S1063783407090107
2. T. Tachizaki, T. Muroya O. Matsuda, Y. Sugawara, D. Hurley and O. Wright, *Review of Scientific Instruments* 77, 043713 (2006) DOI: 10.1063/1.2194518
3. A. Klovov, A. Sharkov, V. Vershkov, R. Khmel'nitsky, D. Aminev and V. Tsvetkov, *Book of Abstracts 19th International Conference on Photoacoustic and Photothermal Phenomena* (July 16-20, 2017 Bilbao) 181 (2017)

DP 010

Photothermoacoustic transformation of Kummer-Gaussian light beam in semiconductor sensor structures

George S. MITYURICH⁽¹⁾, Victor P. VELESHCHUK⁽²⁾, Sergei S. GIRGEL⁽¹⁾,
Ekaterina V. LEBEDEVA⁽³⁾, Aleksandr I. VLASENKO⁽²⁾, Sergei N. LEVITSKIY⁽²⁾

1. Francisk Skorina Gomel State University, Gomel, Belarus
2. V.E. Lashkarov Institute of Semiconductor Physics NAS of Ukraine, Kiev, Ukraine
3. Belarusian Trade and Economics University of Consumer Cooperatives, Gomel, Belarus

george_mityurich@mail.ru

Laser photothermoacoustic (FTA) formation of CdTe-based sensor structures with high energy resolution of gamma radiation is one of the actual tasks of radiation monitoring systems [1]. In this regard, there is an interest in finding new solutions for optical fields, through which one can realize controlled laser irradiation of semiconductor sensor structures.

Theoretical model

Along with Bessel light beams, narrowly directed Kummer – Gaussian circular laser beams [2] seem to be quite effective, the amplitude of which with an accuracy of a constant can be represented as [3]

$$E = G \left(\frac{P}{Q_B} \right)^{\nu} \left(\frac{R}{Q_B} \right)^m {}_1F_1(-\nu, m + 1, R_2^2) \cdot e^{im\varphi}, \quad (1)$$

where the Gaussian $G(R, Z)$ is

$$G(R, Z) = \frac{1}{Q_B} \exp\left(i \frac{R^2}{Q_B}\right) {}_1F_1(-\nu, m + 1, R_2^2)$$

is confluent hypergeometric function, often referred to as the Kummer function,

$$Q_B = Z - Q_0$$

is dimensionless complex parameter of the light beam; $Q_0 = iQ_0''$ is complex value; $P = Z - P_0$; $X = x / x_0$; $Y = y / y_0$; $Z = z / z_0$; $R = \sqrt{X^2 + Y^2}$ is dimensionless radius;

$$R_2^2 = iR^2 \left(\frac{1}{P} - \frac{1}{Q} \right)$$

$z_0 = (k'x_0^2) / 2$, x_0 is characteristic linear transverse beam size. The factor $\exp(kz - \omega t)$ in expression (1) is omitted. The characteristics of these beams when describing them in a cylindrical coordinate system are functions of the variables R, z, φ and four free parameters: m, ν, P_0, Q_0 . Based on relation (1) for Kummer-Gaussian circular beams, it is easy to find the energy dissipation rate

$$Q = \text{div}(S) = \frac{\omega}{8\pi} |E|^2$$

of Gaussian-like 3D light beams in the selected coordinate system.

The power density of heat sources will be taken into account on the right side of the heat equation [4]

$$\nabla^2 T - \frac{1}{\beta_S} \frac{\partial T}{\partial t} = -\frac{1}{k_S} Q \cdot f(\Omega),$$

where $f(\Omega)$ is the pulse modulation function. As a result of solving this equation, one can determine the temperature field distribution in the semiconductor structure under study.

D Fundamentals of Photothermics, PA/OA, and Related Phenomena

The dependence of the spatial intensity distribution of Kummer-Gaussian light beams on the X coordinate at $m = 0$ is graphically illustrated in the figures, an analysis of which clearly shows that by varying the parameters P , Q , v , m you can achieve a uniform illumination of the semiconductor sensory structure under irradiation with a light pulse. In this case, the barodiffusion mechanism for introducing indium impurity In into the CdTe can be implemented as efficiently as possible. The formation of the required profile of Kummer-Gaussian beams is achieved using binary diffractive optical elements, as in [5].

In an experimental study of the impact on the semiconductor In / CdTe structure of Gaussian-like pulses of nanosecond duration, p-CdTe (111) crystals with an end surface area of $5 \times 5 \text{ mm}^2$ and a thickness of 0.5 mm, characterized by a specific resistance $(2 \div 4) \cdot 10^9 \text{ Ohm}\cdot\text{cm}$. Inn film with a thickness of 400 nm was deposited by thermal spraying in vacuum at a pressure 10^{-5} atm . The sample was irradiated with second-harmonic laser pulses from the YAG:Nd laser ($\lambda = 532 \text{ nm}$, $\tau_{\text{imp}} = 7 \text{ ns}$) in air and in a cell with distilled water. The diameter of the irradiated zone was equal to 1 mm, and the distribution of energy over the area was fairly uniform.

Conclusions

Thus, it has been established that, when irradiated in water of a semiconductor In / CdTe structure with Gaussian-like laser pulses ($\tau = 7 \text{ ns}$), the pressure in the energy release region is significantly higher than when irradiated with air. Before reaching the melting threshold of indium, when the photothermoacoustic effect takes place, the pressure values at the location of the sample in the indicated media differ by 17 times. It has also been shown that using hypergeometric light beams (Kummer-Gaussian beams), one can effectively control photothermoacoustic conversion of laser pulses in semiconductor structures used to create highly sensitive ionizing radiation detectors.

References

1. V.A. Gnatyuk, S.N. Levytskyi, O.I. Vlasenko, T. Aoki, The Journal of Nanoscience and Nanotechnology 2 (1), 7 (2016)
2. S. S. Girgel, Problems of physics, mathematics and technics 30 (1), 13 (2017)
3. S.S Girgel, Problems of physics, mathematics and technics 38 (1), 16 (2019)
4. G.S Mityurich, E.V. Chernenok, V.V. Sviridova, A.N. Serdyukov, Crystallography Reports 60 (2), 273 (2015) doi: 10.1134/S1063774515020194
5. V.V. Kotlyar, A.A. Kovalev, R.V. Skidalkov, S.N. Khonina, Computer optics 32 (2), 180 (2008)

Photoacoustic transformation of Bessel light beams in dense layer of carbon nanotubes

George S. MITYURICH^{(1)*}, Przemyslaw RANACHOWSKI⁽²⁾, Ekaterina V. LEBEDEVA⁽³⁾,
Mikolaj ALEKSIEJUK⁽²⁾, Anatoly N. SERDYUKOV⁽¹⁾

1. Francisk Skorina Gomel State University, Gomel, Belarus

2. Institute of Fundamental Technological Research PAS, Warsaw, Poland

3. Belarusian Trade and Economics University of Consumer Cooperatives, Gomel, Belarus

george_mityurich@mail.ru

Bessel light beams (BLB) are used and widely used in laser photoacoustic methods to diagnose the structure of various samples as a source of sound excitation [1–4]. In particular, the use of Bessel light beams in optical-acoustic microscopy makes it possible to effectively increase the focal depth of the resulting photoacoustic image in comparison with a conventional Gaussian light beam. The use of different types of BLB polarization modes is explained by the fact that BLBs have a number of unique properties, for example, non-diffraction of propagation in space. This paper is devoted to the construction of a model of photoacoustic conversion of BLB modes in a layer of chiral and achiral carbon nanotubes for the case of piezoelectric recording of the resultant signal.

Dissipation of energy of Bessel light beams in chiral and achiral carbon nanotubes

The effect of a Bessel light beam on the absorbing layer of chiral nanotubes leads to a periodic change in the temperature field, which can be described by the equation of thermal conductivity

$$\nabla T^2 - \frac{1}{\beta_s} \frac{dT}{dt} = -\frac{1}{k_s} Q(1 + e^{i\Omega t})$$

where $\beta_s = k_s / \rho_0 \cdot C$ is effective coefficient of thermal diffusivity, k_s is coefficient of thermal conductivity, ρ_0 is density of a layer of carbon nanotubes, C is specific heat of a layer of CNTs, Ω is modulation frequency.

Thus, in cylindrical coordinates, the energy dissipation TE-mode of Bessel light beams (BLB) in the layer of absorbing carbon chiral nanotubes can be represented as follows

$$Q^{TE} = \frac{2|\sigma_{cn}|I_0}{c\sqrt{\varepsilon'\varepsilon_0}} \frac{c}{4\pi} k_0 \varepsilon_\alpha (n_1^2 + n_2^2) \left[\frac{m^2}{q\rho} J_m^2(q\rho) + J_m'^2(q\rho) \right] \exp(-\alpha_{eff}z),$$

where $\alpha = 2k_{zz}$, $|\sigma_{cn}| = 2\pi \cdot |\sigma_{zz}|/\lambda$ is conductivity of the CNT layer.

The Resulting Photoacoustic Signal

The simultaneous solution of the heat equation and the equations for thermoelastic deformations in the sample and piezoelectric transducer II allows us to find an expression for the photoacoustic signal. Under conditions where the boundaries of the "sample-piezoelectric detector" system are fixed ($U(0) = 0$, $U(l + l_p) = 0$) or alternately loaded ($\sigma(0) = 0$, $U(l + l_p) = 0$; $\sigma(l + l_p) = 0$, $U(0) = 0$), other expressions for the potential difference are obtained. However, even in these particular situations, the main regularities of the photoacoustic transformation of the TE-mode of the BLB in magnetically low-dimensional structures correspond to those revealed on the basis of the model of free boundaries.

Using expression for the idling voltage, it is possible to determine the amplitudes of photoacoustic signals for the system "sample-piezoelectric transducer" with alternately loaded boundaries.

As a result of the graphical analysis of expressions of photoacoustic signal, a resonant increase in the amplitude was detected. It should be noted that the amplitude and position of the resonant peaks depend on the type of the boundary conditions imposed on the "sample-piezoelectric converter" system. At the same time, the tendency is generally to decrease the amplitudes of the resonance coordinates, as well as to identify and eliminate inconsistencies.

It can also be seen from the figures that an increase in the cone angle of a BLB affects the frequency of the appearance of resonant peaks as a function of the radial coordinate ρ .

D Fundamentals of Photothermics, PA/OA, and Related Phenomena

The amplitude of the photoacoustic signal is determined in a rather complicated manner and depends on many parameters of the "sample-piezoelectric converter" system. In addition, the magnitude of the resulting signal is significantly affected by the modulating action of Bessel light beams (Fig. 1)

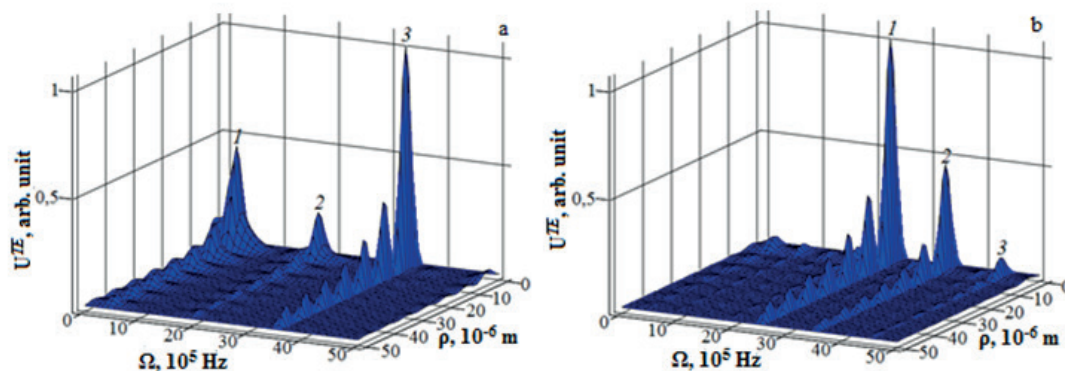


Fig. 1. Dependence of the amplitude of the photoacoustic signal UTE on the radial coordinate when receiving the modulation frequency Ω : a – the dependence under the boundary conditions ($\sigma(l) = \sigma_p(l), U(l) = U_p(l), \sigma(0) = 0, U_p(l_r) = 0$); b – dependence under the boundary conditions ($\sigma(l) = \sigma_p(l), U(l) = U_p(l), \sigma_p(l_r) = 0, U(0) = 0$)

Thus, the model of photoacoustic transformation in the layer of chiral and achiral carbon nanotubes irradiated by the TE-mode of a Bessel light beam is constructed.

References

1. G.S. Mityurich, M. Aleksiejuk, P. V. Astakhov, P. A. Khilo, A. N. Serdyukov, International Journal of Thermophysics 32 (4), 844 (2011) doi: 10.1007/s10765-010-0749-1
2. J. Shi, L.Wang, C.Noordam, L.V. Wang, Journal of Biomedical Optics 20(11), 11600 (2015) doi: 10.1117/1.JBO.20.11.116002
3. T.A. Planchon, L. Gao, D.E. Milkie, M.W. Davidson, J.A. Galbraith, C.G. Galbraith, E. Betzig, Nature Methods 8 (5), 417 (2011) doi: 10.1038/nmeth.1586
4. T. Zhao, S.C. Lao, Y. Wang, Y. Su, H. Wang, A. Cheng, K. Herrup, N.Y. Ip, S. Du, M.M.T. Loy, Scientific Reports 6, 26159(2016) doi: 10.1038/srep26159

DP 012

Laboratory study of sound generation on water surface covered by surfactant films due to its illuminating by intensive IR radiation

Alexander MOLKOV*, Ivan KAPUSTIN, Stanislav ERMAKOV

Institute of Applied Physics of the Russian Academy of Sciences, Nizhny Novgorod, Russia

a.molkov@inbox.ru

The study of the physical properties of organic films on the water surface is an urgent problem related to the development of methods for the ecological monitoring of the oceans and inland waters. Even in the laboratory, the determination of films characteristics is a complicated task, while the use of existing laboratory methods in the full-scale experiments is not yet possible. In this regard, the most important task is to develop new methods for the operational study of the characteristics of films on the water surface. One of these methods can be a new opto-acoustic method, not previously described in the literature, which consists in generating of sound at frequencies of several kHz when the near-surface water layer with surfactant film is illuminated by intensive IR radiation. The physical mechanism of sound generation is due to self-oscillations of a small near-surface water volume associated with periodic film ruptures when it is illuminating by continuous radiation.

This paper presents the results of the first laboratory experiments aimed to the studying the sound characteristics due to film substance, its thickness and radiation intensity. The surface film was created onto the surface of distilled water pre-poured into a small round cuvette by calibrated pipette. The film thickness was changed by dosed addition of specified substance volumes. Several types of oil, diesel, motor oil, oleic acid and vegetable oils were used as the test samples. Illuminating was performed using 10.5 μm 40 W CO₂ CloudRay laser. It was located at a distance of 100 mm above the water surface. Sound recording was carried out in digital form using microphones. Visual recording of the processes of film deformation and heating during interacting with intensity IR radiation was carried out using a webcam and a high-speed thermal camera.

In result, it was found that when there was a film on the water surface, sound signals were recorded at frequencies of several kHz with varying intensity and periodicity. Moreover, in the case of an oil film, the generation of sound at a frequency of about 5 kHz was the most intense. The effect was weaker for thinner films of oleic acid, but nevertheless it was also recorded with confidence. In the absence of a film, sound excitation was absent. The obtained results will serve as a basis for the practical implementation of a new optic-acoustic method for the remote sensing of films of different nature in real marine conditions, promoting the development of new systems for operational environmental monitoring of the ocean and inland water.

Acknowledgements

This work was supported by the Russian Foundation for Basic Research # 18-35-20054

DP 013

Steady-state temperature component within an n-type silicon plate illuminated with a laser beam of modulated intensity

**Dragana K. MARKUSHEV⁽¹⁾, Marica N. POPOVIĆ⁽²⁾, Slobodanka P. GALOVIĆ⁽²⁾,
Katarina Lj. DJORDJEVIĆ⁽³⁾, Dragan D. MARKUSHEV⁽⁴⁾, Jose ORDONEZ-MIRANDA⁽⁵⁾**

1. Faculty of Electronic Engineering, University of Niš, Aleksandra Medvedeva 14, 18000 Niš, Serbia
2. Vinča Institute of Nuclear Sciences, P.O. Box 522, 11001 Belgrade, Serbia
3. Faculty of Physics, University of Belgrade, Studentski Trg 12, 11000 Belgrade, Serbia
4. Institute of Physics, University of Belgrade, Pregrevica 118, 11080 Belgrade-Zemun, Serbia
5. Institut Pprime, CNRS, Université de Poitiers, ISAE-ENSMA, F-86962 Futuroscope Chasseneuil, France.

maricap@vin.bg.ac.rs

As is well known, the dynamic component of temperature is required to describe the photoacoustic signal of semiconductors [1,2]. However, the steady-state temperature component is also relevant for the proper interpretation of the photoacoustic response in presence of the photogenerated excess carrier density [2,3]. In this work, a short summary of the preliminary results for this latter temperature component is presented and analyzed aiming at assessing the impact of the photogenerated excess carriers.

Let us consider a semitransparent n-type silicon plate of thickness $l = 1000 \mu\text{m}$ and absorption coefficient β , whose front surface $x=0$ is uniformly illuminated by a modulated laser beam of the intensity $I_0 = 10 \text{ W/m}^2$. When the energy ($\varepsilon = h\nu \geq \varepsilon_g$) of a laser beam is equal to or greater than the band gap (ε_g) of the n-type semiconductor, the absorbed photons generate excess carriers. Based on the previous works [1,2], the steady-state excess carrier density δn_p^{st} is given by:

$$\frac{d^2 \delta n_p^{st}(x)}{dx^2} - \frac{\delta n_p^{st}(x)}{L_p^2} = -\frac{\beta I_0}{\varepsilon D_p} e^{-\beta x}, \quad (1)$$

where $L_p = \sqrt{D_p \tau}$ is the excess carrier (holes) diffusion length characterized by their diffusion coefficient D_p and lifetime τ . The solution of Eq. (1) is determined by the following boundary conditions

$$D_p \left. \frac{d\delta n_p^{st}(x)}{dx} \right|_{x=0} = s_1 \cdot \delta n_p^{st}(0) \quad \text{and} \quad D_p \left. \frac{d\delta n_p^{st}(x)}{dx} \right|_{x=l} = -s_2 \cdot \delta n_p^{st}(l). \quad (2)$$

Here s_1 and s_2 are the surface recombination speeds at sample front ($x=0$) and back ($x=l$) surfaces, respectively. On the other hand, the steady-state temperature component $T_{st}(x)$ (ambient temperature is omitted) has the form [3]:

$$\frac{d^2 T_{st}(x)}{dx^2} = -\frac{1}{k} [H_{\text{them}}(x) + H_{\text{tr}}(x)], \quad (3)$$

where k is the sample thermal conductivity and heat sources are given by

$$H_{\text{them}}(x) = \frac{\varepsilon - \varepsilon_g}{\varepsilon} \beta I_0 \exp(-\beta x), \quad (4)$$

$$H_{\text{tr}}(x) = \frac{\varepsilon_g}{\tau} \delta n_p^{st}(x). \quad (5)$$

The boundary conditions on the front ($x=0$) and back ($x=l$) sample surfaces for solving Eq. (3) are given by:

$$-k \left. \frac{dT_{st}(x)}{dx} \right|_{x=0} = s_1 \delta n_p^{st}(0) \cdot \varepsilon_g \quad \text{and} \quad -k \left. \frac{dT_{st}(x)}{dx} \right|_{x=l} = -s_2 \delta n_p^{st}(l) \cdot \varepsilon_g. \quad (6)$$

The preliminary results for δn_p^{st} and $T_{st}(x)$ are shown in Figure 1, as functions of the position x inside a Si plate of thickness $l = 1000 \mu\text{m}$.

D Fundamentals of Photothermics, PA/OA, and Related Phenomena

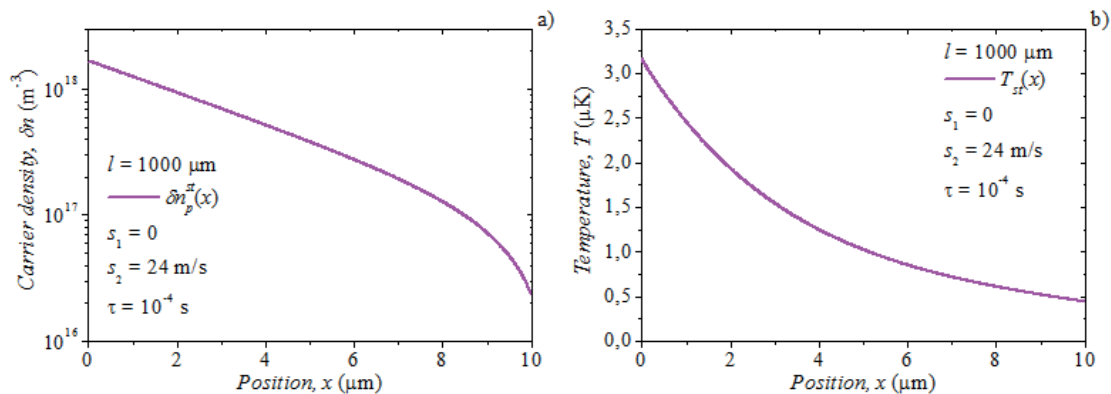


Figure 1. Steady-state component of the a) photogenerated excess carrier density and b) temperature as functions of the position inside a Si plate of thickness $l = 1000 \mu\text{m}$.

Acknowledgements

This work has been supported by the Ministry of Education, Science and Technological Development of the Republic of Serbia under the grants ON171016 and ON172026.

References

1. D. M. Todorovic, P. M. Nikolic, M. D. Dramicanin, D. G. Vasiljevic, Z. D. Ristovski, Journal of Applied Physics, 78 (9), 5750 (1995) <https://doi.org/10.1063/1.359637>
2. Dragana K. Markushev, Dragan D. Markushev, Slobodanka Galović, Sanja Aleksić, Dragan S. Pantić, Dragan M. Todorović, FactaUniversitatis, Series: Electronics and Energetics, 31, (2), 2018, pp. 313 – 328, <https://doi.org/10.2298/FUEE1802313>
3. Zlatan Šoškić, Slobodanka Galović, Nebojša Bogojević, Slobodan Todosijević, FactaUniversitatis, Series: Electronics and Energetics, 25, (3), 2012, pp. 213 – 224, DOI: 10.2298/FUEE1203213S

DP 014

Detection of elastic waves generated by radiation pressure

Tomaž POŽAR ^{(1)*}, **Jernej LALOŠ** ⁽¹⁾, **Aleš BABNIK** ⁽¹⁾, **Max BETHUNE-WADDELL** ⁽²⁾,
Kenneth J. CHAU ⁽²⁾, **Gustavo Vinicius Bassi LUKASIEVICZ** ⁽³⁾,
Nelson Guilherme Castelli ASTRATH ⁽⁴⁾, **Rok PETKOVŠEK** ⁽¹⁾

1. Faculty of Mechanical Engineering, University of Ljubljana, Ljubljana 1000, Slovenia

2. School of Engineering, The University of British Columbia, Kelowna, BC V1V-1V7, Canada

3. Department of Physics, Universidade Tecnológica Federal do Paraná, Medianeira, Paraná 85884-000, Brazil

4. Department of Physics, Universidade Estadual de Maringá, Maringá, Paraná 87020-900, Brazil

tomaz.pozar@fs.uni-lj.si

Electromagnetic momentum carried by light can be measured by employing the mechanical effects radiation pressure exerts on illuminated objects. Momentum transfer from electromagnetic field to matter launches elastic waves within solid objects [1,2]. This transfer is caused by a string of electrodynamic and elastodynamic phenomena, collectively bound by momentum and energy continuity. The details of this conversion, as predicted by different theories, have yet to be validated by experiments, as it is difficult to distinguish transients driven by different light-induced mechanisms [1–5].

We used an experimental configuration in which a dielectric mirror was illuminated by short laser pulses from air. Laser pulse reflections generated transient elastic waves which were detected by a piezoelectric sensor as transient ripples on both surfaces of the mirror (Figure 1). These picometer-sized, out-of-plane displacements were measured with sufficient spatial (1 mm lateral and 40 fm vertical) and temporal (0.2 μ s) resolutions to visualize the elastic wave propagation. We used ab initio modelling of the momentum and energy deposition from the electromagnetic field to the dielectric mirror [1,4] and of the subsequent creation and propagation of multicomponent elastic waves [1,3,5] to determine the generation mechanisms of the measured waveforms. Complete consistency between our predictions and the absolute measurements of surface displacements offers compelling evidence that the elastic transients were driven predominantly by the momentum of light transferred by radiation pressure, since the thermoelastic component was minimized to within the measurement uncertainty of the experiment. This work provides a method to quantitatively measure the momentum coupling between electromagnetic field and matter. It can be applied to characterize materials, to further advance optical manipulation technology of deformable matter, and to provide the means to empirically validate differing electrodynamic formalisms, commonly known as the Abraham–Minkowski controversy [1,4].

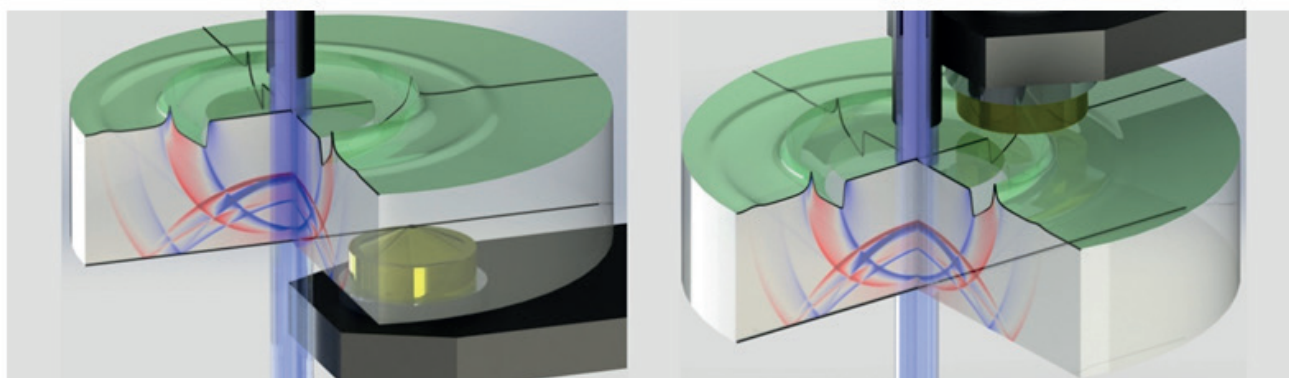


Fig. 1. Perspective view of the experimental setup used for the detection of elastic waves driven by the momentum of light with the sensor deployed on the highly reflective impact surface (right) and on the uncoated opposite surface (left). The laser pulse (indigo) from the Nd:YAG laser impinges on the highly reflective surface (green top layer) of the cylindrical sample (grey) to which the sensor head (gold) is coupled. The radiation pressure launches elastic waves which propagate from the source and carry the momentum and energy transferred from the laser pulse. For visualization purposes, the calculated out-of-plane displacements at 1.96 μ s after the initial pulse reflection are presented as exaggerated ripples on the surface, while the instantaneous z-velocity field of the bulk waves is colour-coded in the cutout of the sample [1].

Acknowledgements

T.P., J.L., A.B., and R.P. acknowledge the financial support from the Slovenian Research Agency (research core funding No. P2-0270 and P2-0392). G.V.B.L. and N.G.C.A. acknowledge the financial support from the Brazilian agencies CAPES, CNPq, and Fundação Araucária. T.P. and N.G.C.A. acknowledge the support from PVE-CAPES (grant No. 23038.010102/2013-34). K.J.C. acknowledges support from NSERC Discovery Grants program.

D Fundamentals of Photothermics, PA/OA, and Related Phenomena

References

1. T. Požar, J. Laloš, A. Babnik, R. Petkovšek, M. Bethune-Waddell, K.J. Chau, G.V.B. Lukasiewicz, N.G.C. Astrath, *Nature Communications* 9, 3340 (2018) doi:10.1038/s41467-018-05706-3
2. T. Požar, J. Možina, *Physical Review Letters* 111 (18), 185501 (2013) doi:10.1103/PhysRevLett.111.185501
3. N.G.C. Astrath, L.C. Malacarne, M.L. Baesso, G.V.B. Lukasiewicz, S.E. Bialkowski, *Nature Communications* 5, 4363 (2014) doi:10.1038/ncomms5363
4. M. Bethune-Waddell, K.J. Chau, *Reports on Progress in Physics* 78 (12), 122401 (2015) doi:10.1088/0034-4885/78/12/122401
5. J. Laloš, M. Jezeršek, R. Petkovšek, T. Požar, *Ultrasonics* 81, 158 (2017) doi:10.1016/j.ultras.2017.06.018

DP 015

The effect of temperature-dependent optical absorption on the second harmonic of nonlinear photoacoustic signal

Tagaymurod Salikhov ⁽¹⁾, Jumakhon Sharifov ⁽²⁾, Umarkhon Madvaliev ⁽³⁾, Zhandos N. Utegulov ⁽²⁾

1. Research Institute of Science, Tajik National University, Tajikistan.

2. Department of Physics, School of Science and Technology, Nazarbayev University,
Nur-Sultan, Kazakhstan

3. S.U.Umarov Physical Technical Institute of Tajik Academy of Science, Dushanbe, Tajikistan.

During modulated incident high laser optical powers the nonlinear photoacoustic phenomena take place in laser irradiated solids. The theory of nonlinear photoacoustic (PA) response of solids developed earlier [1] assumed that that irradiated sample is optically homogeneous, i.e. its optical absorption coefficient $\beta = \text{constant}$. Usually nonlinear PA response consists of the set of harmonics, where the main ones are the fundamental and second harmonics. It is known that in photoacoustic (PA) cell experiments the substantial heating of the sample and the PA cell causes an inhomogeneous temperature field distribution. On the other hand, elevated laser-induced temperature modulations cause optical and thermophysical parameters of the sample to become temperature-dependent [2], i.e. the sample becomes optically inhomogeneous. The goal of the present report is to formulate theory of nonlinear PA response in optically inhomogeneous isotropic solids. The nonlinear PA signal is due to temperature dependence of thermodynamic and optical parameters of the sample, as well as thermal parameters of the buffer gas and the substrate. We assume that sample's optical absorption coefficient has spatio-temporal dependence $\beta(t, x) = \beta(T(t, x))$. Therefore, the constitutive equations describing nonlinear heat conduction for all three layers of the PA cell, i.e. gas buffer layer, sample and substrate are as follows:

$$C_{pg}(T_g) \frac{\partial T'_g}{\partial t} = \frac{\partial}{\partial x} (\kappa_g(T_g) \frac{\partial T'_g}{\partial x}), \quad 0 \leq x \leq l_g, \quad (1)$$

$$C_{ps} \frac{\partial T'_s}{\partial t} = \frac{\partial}{\partial x} [k_s(T) \frac{\partial T'_s}{\partial x}] + 0.5I_0 A(T_s) (1 + e^{i\alpha t}) \frac{\partial}{\partial x} e^{\int_0^x \beta(t,y) dy}, \quad -l_s \leq x \leq 0, \quad (2)$$

$$C_{pb}(T_b) \frac{\partial T'_b}{\partial t} = \frac{\partial}{\partial x} (\kappa_b(T_b) \frac{\partial T'_b}{\partial x}), \quad -(l_b + l_s) \leq x \leq -l_s, \quad (3)$$

where $C_{pi}(T_i)$ is heat capacity per unit volume and $K_{pi}(T_i)$ -thermal conductivity of the respective layers, $A(T)$ - emissivity of sample. Temperature-dependent $C_{pi}(T)$, $k_i(T)$, $A(T)$ and $\beta(T)$ values are presented in the form:

$$C_{pi}(T) = C_{pi}^{(0)} (1 + \delta_1 T_i), \quad \kappa_i(T) = \kappa_i^{(0)} (1 + \delta_2 T_i), \quad A(T) = A^{(0)} (1 + \delta_3 T_i)$$

and $\beta(T) = \beta^{(0)} (1 + \delta_4 T_i)$, where $C_{pi}^{(0)} = C_{pi}(T_0)$, $\kappa_i^{(0)} = \kappa_i(T_0)$, $A^{(0)} = A(T_0)$ -initial value,

$$\delta_1 = (1/C_{pi}^{(0)}) (\partial C_{pi} / \partial T), \quad \delta_2 = (1/\kappa_i^{(0)}) (\partial \kappa_i / \partial T), \quad \delta_3 = (1/A^{(0)}) (\partial A / \partial T), \quad \delta_4 = (1/\beta^{(0)}) (\partial \beta / \partial T)$$

are thermal coefficients of the these parameters. In our case, the last terms in the equation (2) play a crucial role, namely the function $\exp[\int_0^x \beta(t,y) dy]$, which after expression substitution $\beta(T) = \beta^{(0)} [1 + \delta_4 T'_i(t,x)]$ takes the form $\exp\{\beta^{(0)} [x + \delta_4 \int_0^x T'_i(t,y) dy]\}$. Since the second term in the exponent is much less than unity, we expand this function in a series by this small parameter and we will have $\exp\{\beta^{(0)} [x + \delta_4 \int_0^x T'_i(t,y) dy]\} = e^{\beta^{(0)} x} [1 + \beta^{(0)} \delta_4 \int_0^x T'_i(t,y) dy]$.

Given this circumstance, equation (2) takes the following form:

$$C_{ps} \frac{\partial T'_s}{\partial t} = \frac{\partial}{\partial x} [k_s(T) \frac{\partial T'_s}{\partial x}] + 0.5I_0 A_s(T) (1 + e^{i\alpha t}) \frac{\partial}{\partial x} e^{\beta^{(0)} x} [1 + \beta^{(0)} \delta_4 \int_0^x T'_s(t,y) dy] \quad (4)$$

In equations (1), (2) and (4) the temperature modulation $T'_i(t,x)$ is the sum of the equilibrium $T_{0i}(x)$ and oscillatory temperature $\Phi_i(t,x)$ parts. $\Phi_i(t,x)$ values are presented as the superposition of the linear $\Phi_{Li}(t,x)$ and nonlinear $\Phi_{Ni}(t,x)$ components, where $\Phi_{1N}(t,x)$ and $\Phi_{2N}(t,x)$ the same fluctuations on the fundamental and second harmonics. This allowed us to get a following system of coupled equations for $\Phi_{2N}(t,x)$ and boundary conditions:

D Fundamentals of Photothermics, PA/OA, and Related Phenomena

$$\frac{\partial^2 \Phi_{2Ng}(x,t)}{\partial x^2} - \frac{1}{\chi_g^{(0)}} \frac{\partial \Phi_{2Ng}(x,t)}{\partial t} = -\frac{1}{2} \left(\delta_{2g} \frac{\partial^2}{\partial x^2} - \frac{\delta_g}{\chi_g^{(0)}} \frac{\partial}{\partial t} \right) [\Phi_{Lg}^2(t,x)], \quad (5)$$

$$\frac{\partial^2 \Phi_{2Ns}(x,t)}{\partial x^2} = \frac{1}{\chi_{1s(1)}^{(0)}} \frac{\partial \Phi_{2Ns}(x,t)}{\partial t} - 0,5 \left(\delta_{2s} \frac{\partial^2}{\partial x^2} - \frac{\delta_{1s}}{\chi_{1s(1)}^{(0)}} \frac{\partial}{\partial t} \right) \Phi_{Ls}^2(x,t) - \frac{I_0 A_s^{(0)} \beta^{(0)} e^{\beta^{(0)} x}}{2k_{s(1)}^{(0)}} \times \{ \delta_3 \Phi_{Ls}(0,t) + \delta_4 [\Phi_{Ls}(x,t) + \beta^{(0)} \int_0^x \Phi_{Ls}(y,t) dy] \} \cdot \exp[i\omega t] \quad (6)$$

$$\frac{\partial^2 \Phi_{2Nb}(x,t)}{\partial x^2} - \frac{1}{\chi_b^{(0)}} \frac{\partial \Phi_{2Nb}(x,t)}{\partial t} = -\frac{1}{2} \left(\delta_{2b} \frac{\partial^2}{\partial x^2} - \frac{\delta_b}{\chi_b^{(0)}} \frac{\partial}{\partial t} \right) [\Phi_{Lb}^2(t,x)]. \quad (7)$$

$$\Phi_{2Nb}(t, -l_s - l_b) = \Phi_{2Ng}(t, l_g) = 0, \Phi_{2Ns(1)}(t, 0) = \Phi_{2Ng}(t, 0), \Phi_{2Nb}(t, -l_b - l_s) = \Phi_{2Ns(2)}(t, -l_b - l_s), \quad (8)$$

$$\left\{ \frac{\partial \Psi_{2g}(t,x)}{\partial x} \right\} \Big|_{x=0} = \frac{\kappa_s^{(0)}}{\kappa_g^{(0)}} \frac{\partial \Psi_{2s}(t,x)}{\partial x} \Big|_{x=0}, \quad \frac{\partial \Psi_{2b}(t,x)}{\partial x} \Big|_{x=-l_s} = \frac{\kappa_s^{(0)}}{\kappa_b^{(0)}} \frac{\partial \Psi_{2s}(t,x)}{\partial x} \Big|_{x=-l_s} \quad (9)$$

where $\Psi_{2i}(t,x) = \Phi_{2Ni}(t,x) + 0,5\delta_{2i}\Phi_{Li}^2(t,x)$. The system of equations (5)-(7) together with boundary conditions (8), (9) allowed us to obtain the required expression for $\Phi_{2ng}(t,x)$, and then the oscillatory pressure in buffer gas layer on the second harmonics $\delta p_2(2\omega)$. The analysis of $\delta p_2(2\omega)$ and $T_{st}(x)$ expressions for limiting cases has been performed.

References:

- (1) U. Madvaliev, T. Kh. Salikhov, D. M. Sharifov, Tech. Phys. 51, 765 (2006).
- (2) A. Sala, "Radiant properties of materials" //Poland, Warsaw, Elsevier. 1986. P. 478.
- (3) A. Rosencwaig, A. Gersho, J. Appl. Phys. 47, 64 (1976).

DP 016

Study of laser generated longitudinal wave interacting with internal defects by using time delay method

Kaihua Sun*, Jianwen Li, Zengyong Wang, Chaoming Sun, Wei Gao, Jiqiang Ge

Institute of Mechanical Manufacturing Process, China Academy of Engineering Physics, Mianyang China

sundoom@126.com

Laser ultrasound (LU) has attracted increasing attention on testing the internal defects because of its ability to generate broadband high-frequency ultrasonic waves and its non-contact, nondestructive feature. LU technique can use ‘pulse-echo’^[1], ‘transmitted wave’^[2] and ‘time of flight diffraction (TOFD)’^[3] methods for the inspection of internal defects in thick materials. According to the changes of the bulk wave’s amplitude, the internal defects can be determined. However, in the LU scanning test process, if the material has high scattered property or rough surface, the signal-noise-ratio (SNR) of the detected ultrasonic signals will decrease and lead to the fluctuation of the signal amplitude. Then the testing accuracy for the internal defects will decrease, especially to the sub-millimeter defects. In this work, in order to improve the accuracy and stability of the LU in the scanning process, we present a time delay method, which is based on the transmitted delay time of the longitudinal wave signal to test the internal small defects in aluminum alloy.

Theory and Methods

The interacting process of the longitudinal wave propagating through the internal defect hole was studied by the theory and finite element method (FEM). In order to improve the excitation efficiency of the laser generated longitudinal wave, a thin transparent glass film was added on the sample surface. As shown in Fig.1(a), when the laser generated longitudinal wave encounters the internal defect, it cannot only be reflected but also be partly converted into creeping waves (green dash line) on the cavity surface. The creeping wave^[4-6] will propagate around the surface of the defect, and it becomes attenuated by leaking energy into the surrounding material. The leaking energy will convert into bulk wave and reradiate along the tangent direction of the defect surface. After interacting with the cavity, the transmitted longitudinal wave will couple with the reflected longitudinal wave and the reradiated longitudinal wave, then forms a new transmitted wavefront. Compared with the wavefront without interacting with the cavity, a small time delay (Δt) can be found in the center region of the transmitted wavefront, as shown in Fig.1(a). According to Fig.1(b), the delay time Δt of the transmitted wave after interacting with the cavity can be expressed as

$$\Delta t = \frac{\sqrt{h_1^2 + a^2 - r_0^2} + \sqrt{h_2^2 - r_0^2} - h_1 - h_2}{c_l} + \frac{r_0[\pi - \arctan(a/h_1) - \arctan(\sqrt{h_1^2 + a^2 - r_0^2}/r_0) - \arccos(r_0/h_2)]}{c_{lp}}$$

Where c_l and c_{lp} are the velocity of the longitudinal wave and the creeping wave, respectively. The delay time has a quantitative relationship with the cavity size, which is our study point.

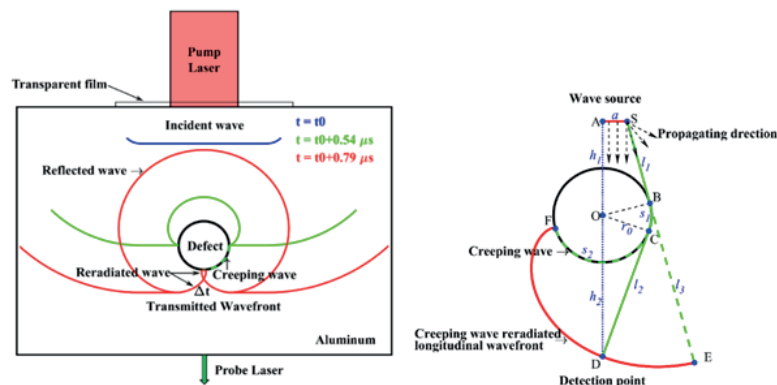


Fig.1. (a)The schematic of laser generated longitudinal wave scattering from a cavity and (b) the wave's propagation path

D Fundamentals of Photothermics, PA/OA, and Related Phenomena

Results

As shown in Fig.2, the quantified relationship between the time delay and the defect radius was determined by theory and FEM. These results are in good agreement, which demonstrates that the size of the defect can be evaluated by using the time delay.

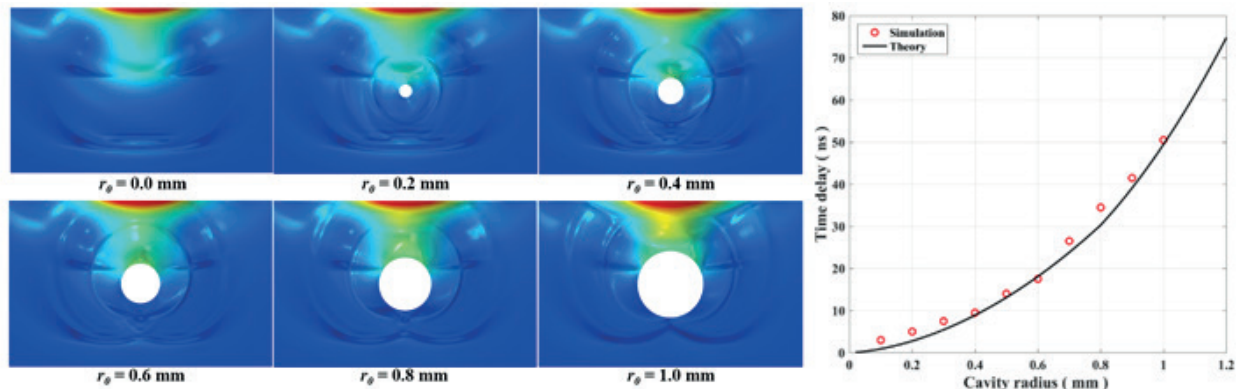


Fig.2. (a) the FEM results with different defect radius and (b) the quantified relationship between the time delay and defect.

Conclusions

In this paper, according to the velocity of the creeping wave and the wavefront distribution of the transmitted and reradiated longitudinal waves, the quantified relationship between the time delay and the defect diameter is determined by theory and FEM, respectively. The results demonstrate that the LU time delay method is a promising approach for evaluating the internal defect accurately and stably in the scanning process.

Acknowledgments

This work was supported by the National Natural Science Foundation of China (No.61801451).

References

1. A. Blouin, D. Lévesque, C. Néron, et al. *Opt. Exp.* 2, 531 (1998)
2. R. Quinteroa, F. Simonettia, P. Howardb, et al. *NDT&E Int.* 88, 8 (2017)
3. C. Pei, T. Fukuchi, H. Zhu, etc., *IEEE Trans. Ultrason. Ferroelectr. Freq. Control* 59, 2702 (2012)
4. P. Hurst, J. A. G. Temple, *Int. J. Pres. Ves. & Piping* 10, 451 (1982)
5. P. B. Nagy, M. Blodgett, M. Golis, *NDT & E Int.* 27, 131 (1994)
6. J. C. A. P. Blodgett, E. A. Lindgren, G. J. Steffes, et al., *J. Acoust. Soc. Am.* 129,3661 (2011)

DP 017

Frequency-scanned photoacoustic piezoelectric mapping of subsurface defects in metals

Binxing ZHAO, Jize JIANG, Ying ZHOU*, Qiming SUN, Chunming GAO*

School of Optoelectronic Science and Engineering,
University of Electronic Science and Technology of China, Chengdu, 610054, China

Corresponding Authors' e-mails: yzhou@uestc.edu.cn, gaocm@uestc.edu.cn

The photoacoustic piezoelectric (PAPE) technique has proved to be an effective method for nondestructive evaluation of thermal properties of a wide range of materials [1-3]. PAPE uses an intensity-modulated cw laser to excite samples and generate thermal waves; the consequent periodic thermoelastic strains are detected by a piezoelectric transducer attached to the sample; a lock-in amplifier demodulates the signals and outputs PAPE amplitudes and phases. By virtue of the fact that the thermal-wave penetration depth is controlled by both the sample thermal diffusivity and the laser modulation frequency, the frequency-scan mode is usually employed to quantitatively determine thermal properties of samples under investigation, as well as to investigate the depth profiles of inhomogeneous material properties, such as nondestructive testing and imaging of samples with surface/subsurface defects [4,5]. In this work we present a further study of the behaviors of PAPE signals of metals with artificial subsurface defects.

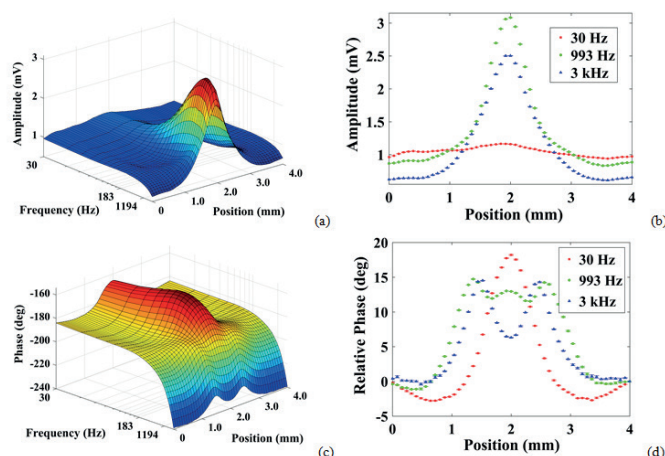


Fig. 1. PAPE line- and frequency-scan data of an aluminum sample with a 0.5-mm deep artificial hole, located at the 2-mm position indicated in the figures. (a & c) PAPE amplitudes and phases as functions of position and laser modulation frequency; (b & d) PAPE amplitude and phase dependences on the line-scan position at three selected frequencies featuring different behaviors.

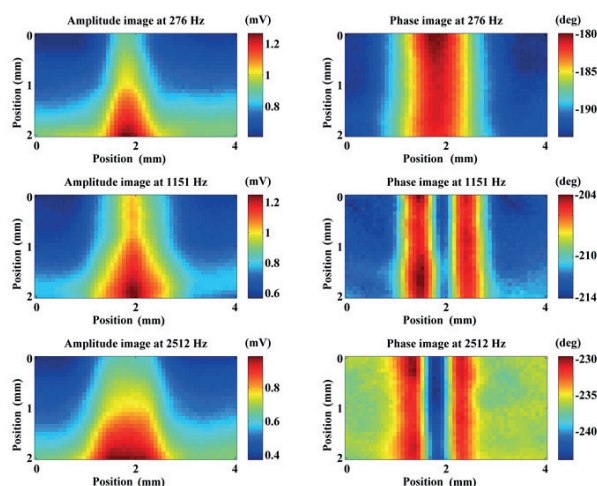


Fig. 2. PAPE amplitude and phase images of the aluminum sample at three modulation frequencies.

D Fundamentals of Photothermics, PA/OA, and Related Phenomena

Samples under investigation were aluminum, steel, and tin, with artificial subsurface defects sized from 50 to 500 μm . Results show that these defects can be clearly distinguished from the line-scan data shown in Fig. 1, and from the images shown in Fig. 2, as long as the modulation frequency is optimized. From Fig. 1 one can see that the line dependences of amplitude and phase exhibit quite different behaviors at different frequencies: in the region outside the subsurface defect, both amplitude and phase have a monotonically decreasing dependences on frequency; in the area near / right above the defect, amplitude shows a peak at 1194 Hz, which cannot be predicted by classical PAPE models [1,6,7], while the behavior of phase is even more complicated. A theoretical model taking into account the spatial non-uniformity of sample properties will be presented in order to semi-quantitatively interpret the behavior of PAPE phase-frequency dependences with the existence of subsurface defects.

Acknowledgements

The authors are grateful to National Key R&D Program of China (Grant No. 2017YFB1103002) and National Natural Science Foundation of China (Grant No. 51706036).

References

5. I. V. Blonskij, V. A. Tkhoryk, M. L. Shendeleva, *J. Appl. Phys.* 79, 3512 (1996)
6. L. Sun, S. Y. Zhang, Y. Z. Zhao, Z. Q. Li, L. P. Cheng, *Rev. Sci. Instrum.* 74, 834 (2003)
7. C. M. Gao, S. Y. Zhang, Y. Chen, X. J. Shui, Y. T. Yang, *Chin. Sci. Bull.* 49, 2273 (2004)
8. L. J. Yan, C. M. Gao, B. X. Zhao, X. C. Ma, N. Zhuang, and H. Y. Duan, *Int. J. Thermophys.* 33, 2001 (2012)
9. B. X. Zhao, C. M. Gao, L. J. Yan, Y. F. Wang, *Int. J. Thermophys.* 37, 121 (2016)

DP 017

Frequency-scanned photoacoustic piezoelectric mapping of subsurface defects in metals

Binxing ZHAO, Jize JIANG, Ying ZHOU*, Qiming SUN, Chunming GAO*

School of Optoelectronic Science and Engineering, University of Electronic Science and Technology of China, Chengdu, 610054, China

Corresponding Authors' e-mails: yzhou@uestc.edu.cn, gaocm@uestc.edu.cn

The photoacoustic piezoelectric (PAPE) technique has proved to be an effective method for nondestructive evaluation of thermal properties of a wide range of materials [1-3]. PAPE uses an intensity-modulated cw laser to excite samples and generate thermal waves; the consequent periodic thermoelastic strains are detected by a piezoelectric transducer attached to the sample; a lock-in amplifier demodulates the signals and outputs PAPE amplitudes and phases. By virtue of the fact that the thermal-wave penetration depth is controlled by both the sample thermal diffusivity and the laser modulation frequency, the frequency-scan mode is usually employed to quantitatively determine thermal properties of samples under investigation, as well as to investigate the depth profiles of inhomogeneous material properties, such as nondestructive testing and imaging of samples with surface/subsurface defects [4,5]. In this work we present a further study of the behaviors of PAPE signals of metals with artificial subsurface defects.

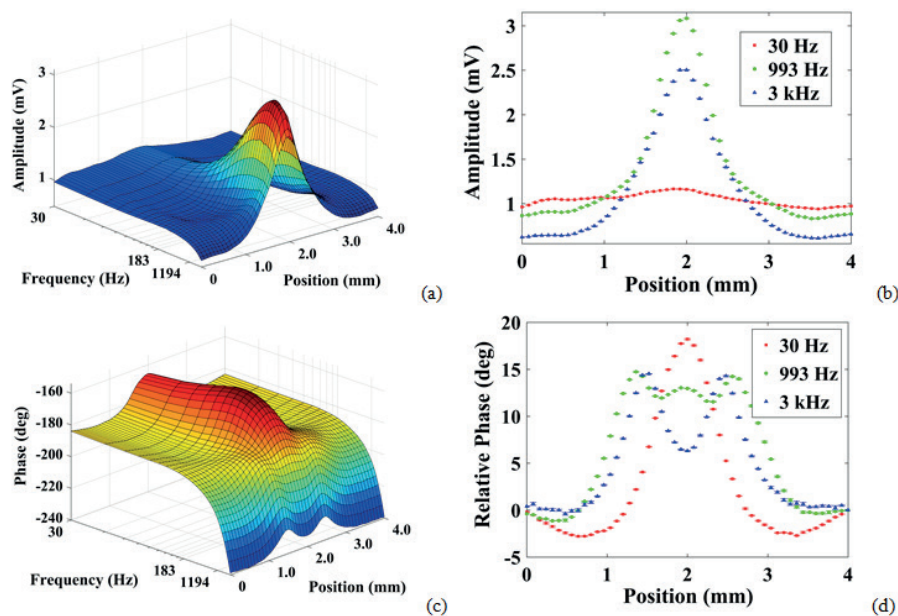


Fig. 1. PAPE line- and frequency-scan data of an aluminum sample with a 0.5-mm deep artificial hole, located at the 2-mm position indicated in the figures. (a & c) PAPE amplitudes and phases as functions of position and laser modulation frequency; (b & d) PAPE amplitude and phase dependences on the line-scan position at three selected frequencies featuring different behaviors.

Samples under investigation were aluminum, steel, and tin, with artificial subsurface defects sized from 50 to 500 μm . Results show that these defects can be clearly distinguished from the line-scan data shown in Fig. 1, and from the images shown in Fig. 2, as long as the modulation frequency is optimized. From Fig. 1 one can see that the line dependences of amplitude and phase exhibit quite different behaviors at different frequencies: in the region outside the subsurface defect, both amplitude and phase have a monotonically decreasing dependences on frequency; in the area near / right above the defect, amplitude shows a peak at 1194 Hz, which cannot be predicted by classical PAPE models [1,6,7], while the behavior of phase is even more complicated. A theoretical model taking into account the spatial non-uniformity of sample properties will be presented in order to semi-quantitatively interpret the behavior of PAPE phase-frequency dependences with the existence of subsurface defects.

D Fundamentals of Photothermics, PA/OA, and Related Phenomena

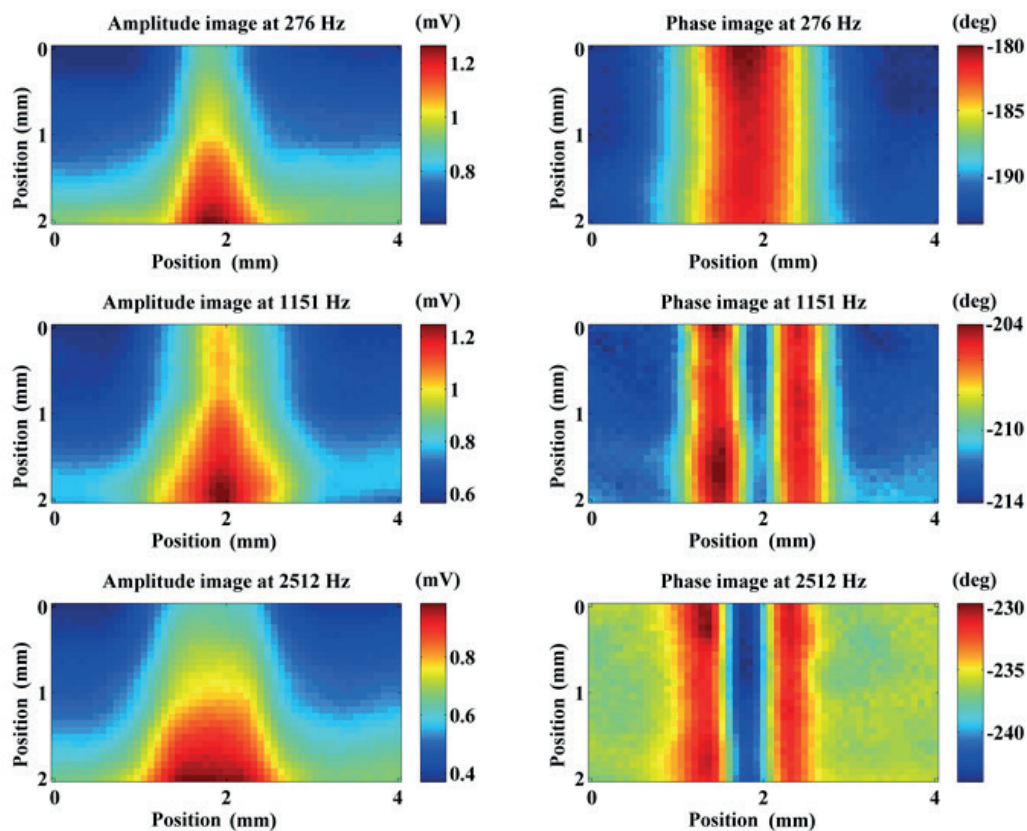


Fig. 2. PAPE amplitude and phase images of the aluminum sample at three modulation frequencies.

Acknowledgements

The authors are grateful to National Key R&D Program of China (Grant No. 2017YFB1103002) and National Natural Science Foundation of China (Grant No. 51706036).

References

5. I. V. Blonskij, V. A. Tkhoryk, M. L. Shendeleva, *J. Appl. Phys.* 79, 3512 (1996)
6. L. Sun, S. Y. Zhang, Y. Z. Zhao, Z. Q. Li, L. P. Cheng, *Rev. Sci. Instrum.* 74, 834 (2003)
7. C. M. Gao, S. Y. Zhang, Y. Chen, X. J. Shui, Y. T. Yang, *Chin. Sci. Bull.* 49, 2273 (2004)
8. L. J. Yan, C. M. Gao, B. X. Zhao, X. C. Ma, N. Zhuang, and H. Y. Duan, *Int. J. Thermophys.* 33, 2001 (2012)
9. B. X. Zhao, C. M. Gao, L. J. Yan, Y. F. Wang, *Int. J. Thermophys.* 37, 121 (2016)
10. Q. M. Sun, C. M. Gao, B. X. Zhao, and H. B. Rao, *Chin. Phys. B* 19, 118103 (2010)
11. Q. M. Sun, C. M. Gao, B. X. Zhao, and Y. F. Bi, *Int. J. Thermophys.* 31, 1157 (2010)

DP 018

The process of heat transfer in the formation of the thermoelastic and thermoelectric response of metals on impact of the laser pulse

Boris Alexandrovich ZIMIN ^{(1),(3)}, **Yuriy Vasilevich SUDENKOV** ⁽²⁾,
Elizaveta Sergeevna YALYCH ⁽¹⁾

1. *Baltic State Technical University "VOENMEH" named after D.F. Ustinov, St. Petersburg, Russia*

2. *St. Petersburg State University, St. Petersburg, Russia*

3. *Admiral Makarov State University of Maritime and Inland Shipping, St. Petersburg, Russia*

bazimin@mail.ru, y.sudenkov@yandex.ru, urban863@mail.ru

A solution to the dynamic problem of the thermoelasticity for the stresses caused by heat impact was obtained by V. I. Danilovskaya [1]. The time forms of stress pulses described by these solutions are a bipolar compression-tension pulse commensurate with values of amplitude for the durations whose order of magnitude is the same as that of radiation pulse. The subsequent investigations of the dynamic thermoelasticity problem has not made fundamental changes in the solution determining the parameters of thermoelastic stresses [2].

In dielectrics, the induced heat source is practically localized in the radiation absorption region, and the thermoelastic effect is well described in the framework of the above-mentioned models of the dynamic thermoelasticity problem (Fig.1a). However, in some experimental works devoted to studying the pulsed laser impact on solids [3, 4], that where is a significant difference between the parameters of thermoelastic stressed in dielectrics and metals. In metals, as it turned out, the stage of heat transfer after the end of the irradiation pulse is of fundamental importance to the formation of thermoelastic stresses happen (Fig.1b).

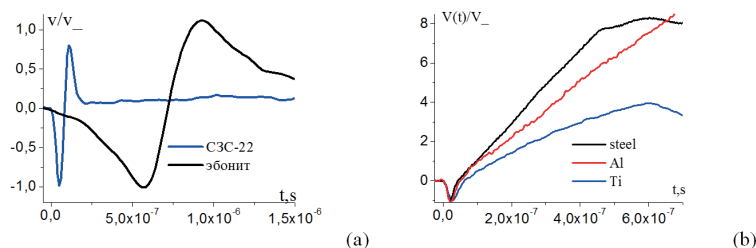


Fig.1 Elastic pulses excited in dielectrics-a, metals-b under the action of Nd:YAG laser pulse

The two-stage analysis of the thermoelasticity and thermoelectric effect in metals are suggested. The first stage is the action of the irradiation pulse. The second is the action of the "thermal piston," which is the process of heat transfer. This approach allowed us to show the determining effect of the electronic mechanism of heat transfer on the fundamental difference of thermal stress pulses in metals. The consequence of this is demonstrated in [4] the possibility of moving metal objects in the direction of the heating source under the action of the electron recoil pulse [4].

It is shown that at the stage of heat transfer (at $t > \tau_L$) solutions for both the mass velocity of particles and the electric current are similar and proportional to the integral of the temperature gradient.

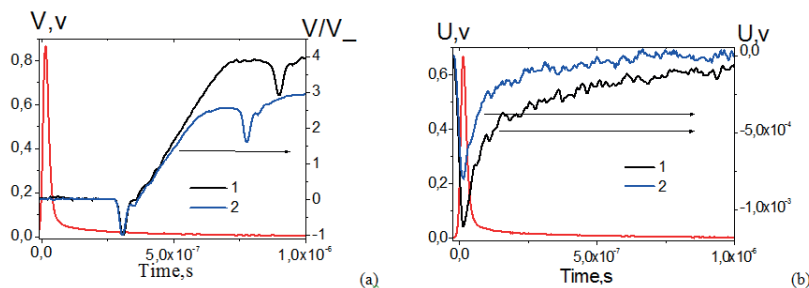


Fig.2 Pulse Nd:YAG laser (red curve) and the elastic impulses in specimens of copper M1; pulse Nd:YAG laser (red curve) and the electrical response of the samples медиM1 - b

D Fundamentals of Photothermics, PA/OA, and Related Phenomena

For Fig.2a, b the results of measurements of thermoelastic and thermoelectric effect in copper samples in the delivery state (1) and samples after severe plastic deformation (2) with a grain size of 0.7-0.8 microns are presented.

A two-stage approach for the analysis of thermoelastic and thermoelectric processes in metals under pulsed laser action allowed to obtain an adequate description of the thermoelastic and thermoelectric effect in metals. It is shown that the nature of the heat transfer process in metals significantly determines the parameters of both thermoelastic and thermoelectric responses of metals to pulsed laser action. At the same time, it is noted that the parameters of the thermoelastic and thermoelectric response of metals are very significantly dependent on the microstructure, which shows the possibility of developing a highly effective method of non-destructive testing of metals.

Acknowledgements

Work performed on the № 15-19-00182 RSF Project.

References

1. Danilovskaya V. I. Temperature field and temperature stresses arising in the elastic half-space due to the flow of radiant energy falling on the boundary of the half-space. *Izv. USSR ACADEMY OF SCIENCES. Mechanics and mechanical engineering.* - 1959. - № 3. - pp. 129-132.
2. Hamdy M. Yusef, Ahmed S. Al-Felali. Generalized Thermoelasticity Problem of Material Subjected to Thermal Loading Due to Laser Pulse // *Applied Mathematics*, 2012, 3, pp.142-146
3. Vovnenko, N. V., Zimin B. A., Sudenkov Y. V. Experimental study of thermoelastic stresses in thermal and non-conductive solids at submicrosecond the duration of laser heating // *ZhTF*, 2011, vol. 81, issue.6, pp. 57-62
4. Zimin B. A., Sudenkov Y. V. The Movement of a metal disk under the action of thermoelastic stresses towards the pulsed laser radiation // *Technical physics letters*, 2012, T3, no. 24, pp. 26-32

DP 019

Photoacoustic pressure behavior in metals irradiated with intensity modulated nanosecond laser pulses

Alexander A. Samokhin, Evgeny V. Shashkov, Nikolai S. Vorob'ev, Aleksei E. Zubko

Prokhorov General Physics Institute of the Russian Academy of Sciences, Moscow, Russia

asam40@mail.ru

Acoustical pressure response in target absorbing nanosecond laser pulses with modulated intensity contains also information about irradiated zone displacement as it is demonstrated in [1] for the case of absorbing dielectric liquids and harmonically modulated laser pulses due to mode beating. This information can be inferred from the time delay between laser and acoustic modulated parts which arises due to acoustic Doppler effect.

However for metals such harmonic intensity modulation procedure is less appropriate than pulsed modulation with the help of mode locking process. In the case of pulsed modulation generated pressure signal is mainly due to photoacoustic mechanism while harmonic modulation gives rise to interference between photoacoustic and vaporization mechanisms which affects the procedure of displacement determination using the form of generated pressure pulses [2, 3].

Maxima of acoustic modulation pulses localization t_{at} in time depend on the distance between irradiated surface and acoustic transducer and differs from the intensity modulation pulses t_{li} . The difference $t_{at} - t_{li} = \tau_i$ is positive (or negative) in the case of irradiated surface displacement $d(t_{at}) = d_i$ from (or towards) the transducer.

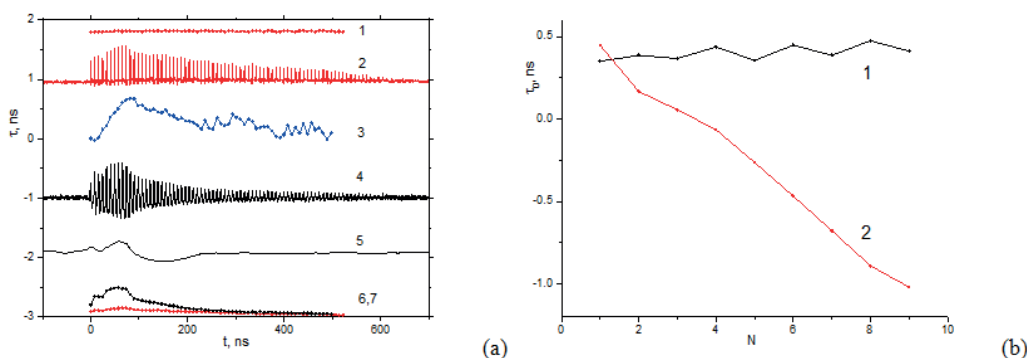


Fig. 1. (a) Behavior of modulated laser and acoustic signals, along with the changes in the delay τ_i and smooth acoustic-signal components: (curve 1) time delays τ_i of the peaks of laser pulses relative to the linear time scale; (2) trains of laser pulses normalized to unity in maximum; (3) time delays τ_i of the peaks of acoustic pulses with respect to optical ones; (4, 5) trains of acoustic pulses without a slow component and their slow component, respectively; (6, 7) envelopes of acoustic-pulse train matched in amplitudes at $t > 300$ ns. Incident laser train fluence is 2 J/cm^2 with pulse duration ≈ 60 ps. (b) Dependences of the train averaged acoustic delay τ_0 on the train number $N = 1-9$ (curve 1) without and (curve 2) with an additional heating pulse between two neighboring trains. Incident additional laser fluence is 7 J/cm^2 with pulse duration ≈ 70 ns.

First experiments [4, 5] show rather large displacement $d_i > 0$ which can not be explained as simple heat expansion of the irradiated metal [5]. This fact is probably due to sound velocity c diminishment in the heat affected region adjacent to the irradiated metal surface while the resulting total surface displacement $d_0 = c\tau_0$ after the irradiation pulse is negligible because ablation effect at the considered laser fluences is small.

The fact of negligible ablation can be seen from fig. 1b (curve 1) where the train averaged acoustic delay τ_0 without additional heating pulse does not depends on the subsequent train number. In the presence of additional laser pulse between the neighbor trains τ_0 diminishes almost linearly with respect to train numbers (curve 2) at the rate $\Delta\tau_0 = 180 \text{ ps}$ ($\Delta d_0 = 0.4 \text{ }\mu\text{m}$) for each additional heating pulse which is consistent with the absorbing heating pulse fluence 2.5 J/cm^2 .

It should be mentioned that sound velocity temperature dependence does not affect the procedure of displacement $d(t)$ determination in the case of steady-state ablation regime where the temperature distribution ahead of vaporization front does not changes in time in moving reference frame [6]. Short acoustic pulses propagation in the target as well as plasma formation effects on the considered acoustical monitoring of laser ablation needs further investigations.

D Fundamentals of Photothermics, PA/OA, and Related Phenomena

References

1. A.A. Samokhin, N.N. Il'ichev, *Quantum Electronics* 40 (8), 659–660 (2010), doi: 10.1070/QE2010v040n08ABEH014382
2. A.A. Samokhin, S.I. Kudryashov, A.E. Zubko, A.V. Sidorin, *Mathematica Montisnigri* 37, 76–90 (2016)
3. A.E. Zubko, A.A. Samokhin, *Engineering Physics* (3), 47–52 (2017), (in russian)
4. A.A. Samokhin, E.V. Shashkov, N.S. Vorob'ev, A.E. Zubko, *JETP Letters* 108 (6), 364–367 (2018), doi: 10.1134/S0021364018180108
5. A.A. Samokhin, E.V. Shashkov, N.S. Vorob'ev, A.E. Zubko, *Physics of Wave Phenomena* 27 (1), 42–50 (2019), doi: 10.3103/S1541308X19010084
6. A.A. Samokhin, *First-order phase transitions induced by laser radiation in absorbing condensed matter, Effect of laser radiation on absorbing condensed matter*, Nova Science Publishers, ed. by V.B. Fedorov, (1990).

DP 020

Photothermal and Thermographic Monitoring of The Curing of Constructive Materials

Jorge Iván GONZALEZ^(1,2), Juan Daniel MACIAS⁽¹⁾, Arantza MENDIOROZ⁽²⁾,
Agustín SALAZAR^{(2)*}, Juan José ALVARADO GIL⁽¹⁾

1. Física Aplicada, Cinvestav-Unidad Mérida, Carretera Antigua a Progreso km. 6, 97310, Mérida, Yucatán, México.

2. Departamento de Física Aplicada I, Escuela de Ingeniería de Bilbao, Universidad del País Vasco UPV/EHU, Plaza Ingeniero Torres Quevedo 1, 48013 Bilbao, España.

juan.alvarado@cinvestav.mx

Non-invasive methods for monitoring of hardening and setting process in constructive materials have been a subject of broad interest for its impact in the development, conservation and reconstruction of physical infrastructure [1]. Photothermal radiometry has shown to have the sensitivity to analyze, and at real time, in a non-destructive and non-invasive mode the dehydration and polymerization as well as water evaporation process in various systems [2-3]. In this paper photothermal radiometry and thermography are used to monitor the curing, of a variety of constructive materials. The technique consists in directing a modulated light beam onto the sample and monitoring the resulting temperature profiles on the surface of the sample. It is shown that the time evolution of the setting of the constructive materials can be followed by the changes in the photothermal and thermographic signals, occurring in a wide range of time scales [4]. Our measurements are complemented by mechanical tests of the obtained pieces.

References

- [1] Yunsheng Zhang, Wenhua Zhang, Wei She, Ligu Ma, Weiwei Zhu. Ultrasound monitoring of setting and hardening process of ultra-high performance cementitious materials. *NDT & E International*. Volume 47, April 2012, Pages 177-184
- [2] P. Martínez-Torres, A. Mandelis, J. J. Alvarado-Gil. Photothermal determination of thermal diffusivity and polymerization depth profiles of polymerized dental resins. *Journal of Applied Physics*. Volume 106, December 2009.
- [3] P. Martínez-Torres, A. Mandelis, and J. J. Alvarado-Gil. Optical and thermal depth profile reconstructions of inhomogeneous photopolymerization in dental resins using photothermal waves. *Journal of Applied Physics*. Volume 108. September 2010.
- [4] M. A. Zambrano-Arjona¹, R Medina-Esquivel² and J. J. Alvarado-Gil¹. Photothermal radiometry monitoring of light curing in resins. *Journal of Physics D: Applied Physics*. Volume 40, August 2007, Pages 6098–6104.

EP 001

Measuring the width of vertical interfaces separating two different media using lock-in thermography

A. Bedoya^(1,2), J. González^(2,3), A. Mendioroz⁽²⁾, A. Salazar⁽²⁾

1. Instituto Politécnico Nacional (IPN), Centro de Investigación en Ciencia Aplicada y Tecnología Avanzada (CICATA), Unidad Legaria, Legaria 694, Col. Irrigación, C.P. 11500, Ciudad de México, Mexico, adrian_filipo@hotmail.com

2. Departamento de Física Aplicada I, Escuela de Ingeniería de Bilbao, Universidad del País Vasco UPV/EHU, Plaza Ingeniero Torres Quevedo 1, 48013 Bilbao, Spain, agustin.salazar@ehu.es

3. Department of Applied Physics, CINVESTAV Unidad Mérida, carretera Antigua a Progreso km6, A.P. 73 Cordemex, Mérida Yucatán 97310, Mexico,

jorge.gonzalez860824@hotmail.com

A method to measure the width (L) of the vertical interface between two different materials using lock-in infrared thermography with laser spot heating is proposed. The thermal contact resistance (R_{th}) is obtained and from this value we calculate the width considering the direct relation between these parameters as $(R_{th})=L/K$, where K is the thermal conductivity of the material of the interface, air in this case. An analytical expression that represents the temperature on the surface of the two media when one of them (medium 1) is illuminated by a modulated and focused laser spot is presented. In order to check the validity of the technique, a setup was built to measure the calibrated thermal resistance between the illuminated medium 1 and a second medium 2 that is either a better or a worse conductor. The width of the vertical interface was measured by fitting of the experimental temperature profiles perpendicular to the interface, through the center of the laser spot to the analytical expression. The nominal and retrieved values of the width are in good agreement confirming the validity of the model and method.

EP 002

Infrared Nondestructive Detection of Fiber Metal Laminate Defects by Linear Frequency Modulation Excitation and Numerical Simulation

Chiwu BU^{(1)*}, Guozeng LIU⁽¹⁾, Xibin ZHANG⁽¹⁾, Qingju TANG⁽²⁾

1. College of Light Industry, Harbin University of Commerce, Harbin, 150028, China

2. School of Mechanical Engineering, Heilongjiang University of Science and Technology, Harbin, 150022, China

buchiwu@126.com

Fiber Metal Laminates (FMLs) have excellent fatigue damage tolerance, impact resistance and easy processing, and are widely used in the aviation industry. During the preparation and service of FMLs and its components, defects such as overall cracking, uneven curing or even breaking of fibers, and debonding of fibers and matrix are prone to occur. These defects and damages will have a direct impact on the quality, performance and service life of FMLs, and even pose a serious threat to the operational safety and reliability of aircraft and spacecraft using this material. A linear frequency modulation excitation method for detecting debonding defect of fibre metal laminates was established. Halogen lamp was used as thermal excitation source. Infrared camera was responsible for collecting infrared images of FMLs. Pulse phase method (PPT) was used to extract the relationship between temperature of each pixel in infrared thermal image and time. Fourier transform was used to obtain the amplitude spectrum and phase spectrum. Amplitude spectrum was selected in the amplitude spectrum. The simulation experiments were carried out to analyze the influence of light source power, initial frequency and termination frequency in linear frequency modulation on the detection results of different defect diameters and defect depths. The conclusions are as follows: with the increase of initial frequency, the contrast between defect and defect-free parts is also increasing; with the increase of termination frequency and heating power, the defect detection effect is better; with the increase of defect size, defects with smaller defect diameter and shallower defect depth can be detected; Chirp modulation is beneficial to defect detection of FMLs.

Pulse Infrared Thermal Wave Nondestructive Detection of Defects in Pure Titanium/Aluminum Alloy A6061 Metal Laminate

ChiWu BU^{(1)*}, Guozeng LIU⁽¹⁾, Xibin ZHANG⁽¹⁾, Qingju TANG⁽²⁾

1. College of Light Industry, Harbin University of Commerce, Harbin, 150028, China

2. School of Mechanical Engineering, Heilongjiang University of Science and Technology, Harbin, 150022, China

buchiwu@126.com

Titanium-aluminium alloy has been developed rapidly with its excellent properties such as high temperature resistance, corrosion resistance and light material. It has been widely used in aerospace, biomedical and other fields. Compared with common titanium-aluminium alloy materials, titanium-aluminium alloy laminates overcome the shortcomings of traditional aluminum alloys and titanium alloys, and have excellent comprehensive properties, such as better yield resistance, oxidation resistance and flame retardancy, which meet the material performance requirements of large aircraft. The interface between aluminium alloy laminates and pure titanium laminates is pasted by colloids. It is easy to cause colloidal solidification of the interface between the aluminum alloy laminates and pure titanium laminates under the harsh environment of high temperature and high pressure for a long time, thus causing debonding defects and affecting the performance of the laminates. Therefore, timely detection is needed. Infrared thermal wave nondestructive testing technology has been widely concerned by domestic scholars and experts in recent years because of its fast detection speed, large detection area and high detection accuracy. Infrared thermal wave nondestructive testing technology includes pulse thermal imaging method, Phase-locked thermography and ultrasonic thermal imaging method. Pulse thermography is the most mature method with low cost, simple junction and high detection efficiency. In this study, finite element method is used to discuss the influence of different defect diameter, defect depth and heat flow power on the measurement results, and the following conclusions are drawn: the larger the defect diameter is, the more obvious the detection results are; the deeper the defect depth is, the easier the defect location is detected; the greater the heat flow power is, the better the detection effect is. The research results can provide theoretical guidance for nondestructive testing of titanium-aluminium alloy and other metal laminates.

EP 004

Confocal Thermoreflectance Microscope and Applications to Thermal Characterization of Semiconductor Devices

Ki Soo CHANG *, Dong Uk KIM, Jung Dae Kim, Ilkyu HAN, Chan Bae JEONG

Division of Scientific Instrumentation, Korea Basic Science Institute, Daejeon, Korea

*ksc@kbsi.re.kr

As the integration density and speed of semiconductor devices has increased, heat generated under operation of devices has become an important factor in degrading device performance and shortening the device lifetime. Especially, in the structure of TSV(Through-Silicon-Via)-based three-dimensional semiconductor packaging for increasing the degree of integration of semiconductor circuits, heat generation is an inevitable problem. In order to solve the heating problem of a semiconductor devices, it is first necessary to measure where and how much heat is generated and how it is distributed in the device. Therefore, there is a growing need for a thermal imaging microscope that measures and images the temperature distribution of a devices on a microscale.

Several thermal imaging microscope techniques, such as scanning thermal microscopy, micro-Raman thermography, and infrared micro-thermography, have been developed to investigate thermal properties in micro- and nano-scale devices. In particular, thermo-reflectance microscopy (TRM) is an optical imaging technique that provides a two-dimensional thermal image of sample with high spatial and thermal resolution.

Thermo-reflectance microscopy is based on measurement of the relative change in the reflectivity of a sample (device) surface as a function of change in temperature. As the temperature of the sample changes, the refractive index, and therefore the reflectivity, varies. In this presentation, we report on a confocal thermo-reflectance microscope system that can provide sub-surface thermal image of semiconductor devices through the substrate [1]. Figure 1 (a) shows a schematic of the laser scanning confocal thermo-reflectance microscope. Figure 1 (b) represents the design of a micro-heater that was used as the test device, and also shows the illumination directions for the topside and backside measurements. Figure 2 shows the backside reflection and thermo-reflectance images obtained by the wide-field and confocal TRM systems using a 100× objective lens (NA 0.5). The image contrast in the wide-field backside image shown in Figure 2(a) was decreased by ~35 % from that of the backside measurement using the 50× objective lens. However, the confocal backside imaging with an optimized pinhole (50 μm diameter), i.e., the optical sectioning capability, was much more robust in the presence of strong reflections, as shown in Figures 2(b) and 2(d). As a result, the confocal backside thermo-reflectance measurement was found to exhibit a ~23 times improvement in the thermal sensitivity over that of the wide-field systems, from the ratio between the variations $\Delta R/R$ shown in Figures 2(c) and 2(d). Therefore, we believe that the developed confocal TRM system is particularly valuable for investigating the thermal characteristics of micro-electronic devices.

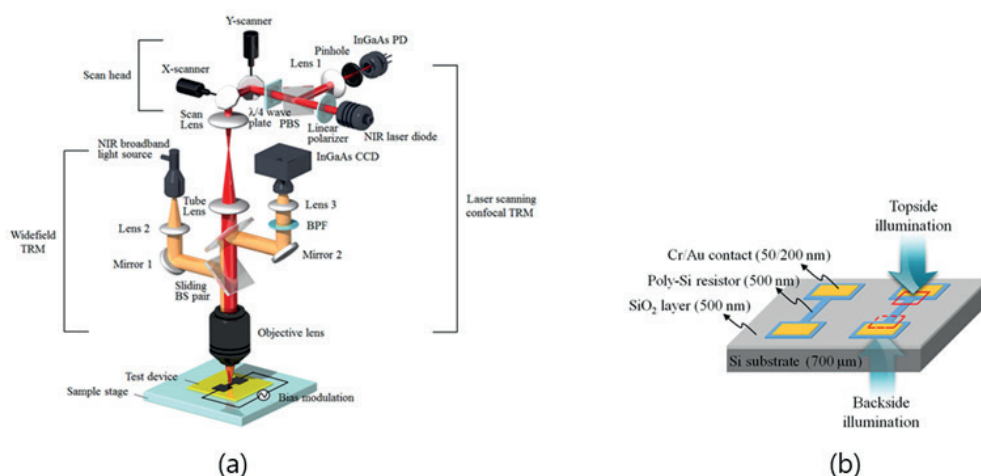


Fig. 1. (a) Schematics of laser scanning confocal thermo-reflectance microscope (b) Polycrystalline silicon micro-resistor on a SiO₂ layer/silicon substrate and the illumination direction for topside and backside measurements.

E Methodologies of Photothermics, PA/OA, and Related Techniques

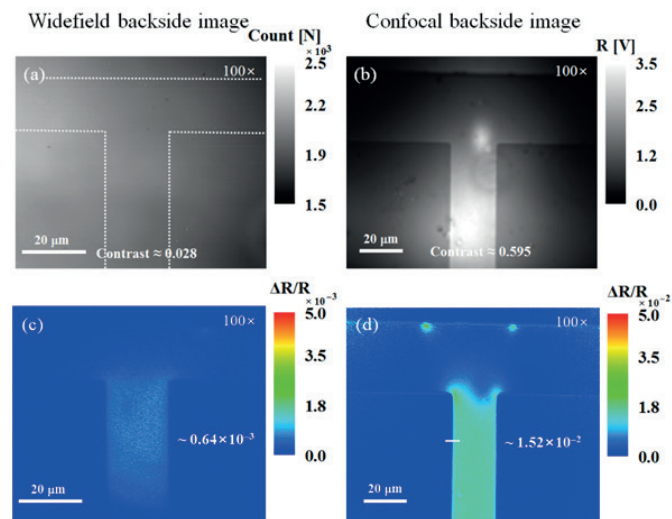


Fig. 2. Through the substrate reflection (top) and thermo-reflectance (bottom) images of the poly-Si micro-resistor obtained by (a, c) wide-field and (b, d) confocal TRM systems with a 100× objective lens (NA 0.5), respectively. The numbers inside (c, d) indicate the $\Delta R/R$ value of the micro-resistor.

Acknowledgements

This work was supported by the Korea Basic Science Institute Grant (grant number: D39615)

References

1. D. U. Kim, C. B. Jeong, J. D. Kim, K. Lee, H. Hur, K. Nam, G. H. Kim, and K. S. Chang, *Sensors* 17 (2), 2774 (2017) doi:10.3390/s17122774

EP 005

Anisotropic propagation of surface elastic waves in inclined columnar thin films

Asma CHARGUI *, Raya EL BEAINOU, Sébastie EUPHRASIE, Alexis MOSSET,
Nicolas MARTIN, Pascal VAIRAC

*Institut FEMTO-ST, CNRS UMR 6174, Université Bourgogne Franche-Comté,
15B, avenue des Montboucons, 25030 Besançon, France*

asma.chargui@femto-st.fr

In thin film deposition, some specific techniques allow producing anisotropic structures. The GLancing Angle Deposition (GLAD) approach is among the most attractive ways to produce original surface morphologies, especially for designing anisotropic architectures [1]. The technique consists of depositing thin films using oblique incidence of the sputtered particles flux and on a fixed or mobile substrate. This leads to the creation of thin films presenting a columnar architecture with different angles to the normal.

A femtosecond heterodyne pump probe setup [2] is used for the acoustic characterization of the GLAD films. This technique allows the visualization of surface acoustic waves and the calculation of their dispersions. The elastic waves are generated by the absorption of the first laser (pump). The second laser (probe) measures the reflectivity variations of the sample's surface, which are linked to the temperature and acoustic changes. Thanks to a lens mounted on a 2D translation stage, the pump-probe distance can also be scanned.

Two kinds of metallic films (W, Au) are deposited by GLAD sputtering using a constant inclination angle of 80° . The choice of these metals is motivated by their propensity to create morphological columnar features, which is connected to their film growth process. Scanning electron microscopy (SEM) are used to view the surface and the structural morphologies of the films. It is shown that W GLAD growth gives rise to asymmetric columns with elliptical sections linked by void regions that is especially favored by the atomic shadowing effect occurring during the growth of the inclined columns. Such architecture leads to important anisotropic behaviors for the group velocities of the pseudo-Rayleigh waves (fig.1). Au GLAD films produce a rather circular and more symmetric columnar growth with an isotropic propagation [3].

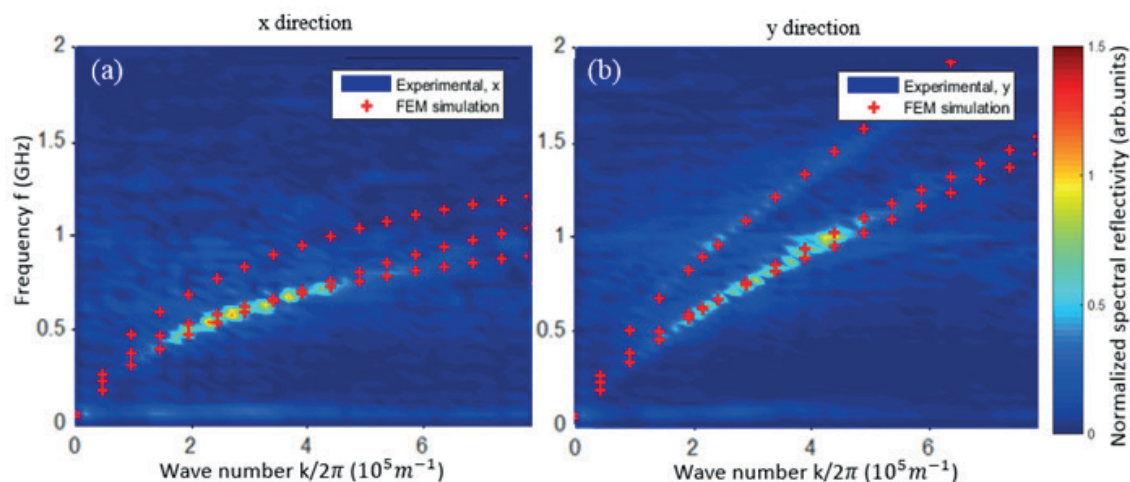


Fig. 1. Dispersion curves for x (a) and y (b) directions obtained from the variation of relative reflectivity versus spatial and time frequencies, compared with FEM simulation for W GLAD.

Numerical simulations of the surface acoustic wave propagation are performed with the finite element method. It is proved that acoustic anisotropy is related to the structural anisotropy of the film's architecture.

A systematic change of the W films thickness allows tuning the morphology of the columnar microstructure: from nearly circular shape to elongated as the thickness increases. The same phenomenon is noticed with a change of the argon sputtering pressure from 15×10^{-3} up to 2.5×10^{-3} mbar. This leads to tunable column angles and more interestingly significant changes of the columnar microstructure. Here again, some anisotropic behaviors are investigated and discussed.

E Methodologies of Photothermics, PA/OA, and Related Techniques

Acknowledgements

This work was supported by the Region of Franche-Comté (project PHOTAS), the French RENATECH network, the EIPHI Graduate School (contract ANR-17-EURE-0002). This research was also sponsored by the French National Agency for Research (ANR) funds through the PHEMTO project. The authors also thank the BQR ENSMM for financial support through the COSET project.

References

1. K. Robbie, J. C. Sit. M. J. Brett, *J. Vac. Sci. Technol.*, 16 (1988) 1115-22 doi.org/10.1116/1.590019
2. E. Coffy, G. Dodane, S. Euphrasie, A. Mosset, P. Vairac, N. Martin, H. Baida, J.M. Rampnoux, S. Dilhaire, *J. Phys. D: Appl. Phys.*, 50 (2017) 484005-8 doi.org/10.1088/1361-6463/aa92ad
3. R. El Beainou, A. Chargui, P. Pedrosa, A. Mosset, S. Euphrasie, P. Vairac, N. Martin, *Appl. Surf. Sci.* 475 (2019) 606-614 doi.org/10.1016/j.apsusc.2019.01.041

EP 006

Laser Scanning thermography for Coating Thickness Measurement

Fei CHEN ^{(1)*}, Zhonghua SHEN ⁽¹⁾, Kai ZHANG ⁽²⁾, Li CHEN ⁽²⁾

1. Nanjing University of Science and Technology, Nanjing, China
2. University of Electronic Science and Technology, Chengdu, China

218113010221@njjust.edu.cn

Coatings are widely applied for protecting underlying materials from corrosion and high temperature damages. The thickness is a very important parameter that needs to be well controlled to insure the optimal performance of the coatings. A number of efforts have been made for coating thickness measurement [1-3]. However, it remains a challenge to develop a safe, simple and effective method for coating thickness measurement in a non-destructive way.

This presentation describes a new technique based on laser scanning thermography for coating thickness measurement. Traditional thermographic thickness measurement involves taking the temperature decay curve after a pulsed heating. In order to obtain enough data points, it usually requires a high frame rate thermal camera. This is very expensive and for very thin coating layers, it may even be impossible. In this new technology, it utilizes a high power linear laser beam to scan the coating surface and captures the image with an IR camera. The laser beam scans across the sample surface at a speed of v . Along the scanning direction, there is a time delay dt in laser heating across a distance dl . Where,

$$(dt=dl)/v$$

In other words, in the IR image, along the scanning direction, different pixels represent data points on the decay curve with different timing. In this setup, a lower frame rate IR camera can be used for very thin coating thickness measurement.

A 2D model was established to describe the characteristics of the sample temperature distribution under linear laser scanning. The temperature field expression for limited thickness sample was derived by using the method of mirror images, as following:

$$T(x, y, t) = \int_0^t \frac{\sqrt{2\pi[R^2 + 8 \cdot \alpha(t - t')]} }{4} \times \left\{ \operatorname{erf} \left[\frac{\sqrt{2}(L + y)}{\sqrt{R^2 + 8 \cdot \alpha(t - t')}} \right] + \operatorname{erf} \left[\frac{\sqrt{2}(L - y)}{\sqrt{R^2 + 8 \cdot \alpha(t - t')}} \right] \right\} \times \frac{2\rho_0 P_0 \sqrt{\alpha}}{k\pi^{3/2} [8 \cdot \alpha(t - t')^{3/2} + R^2 \cdot (t - t')^{1/2}]} \times e^{-\frac{(x-vt')^2}{R^2 + 8 \cdot \alpha(t - t')}} \cdot [1 + 2 \cdot r \cdot e^{\frac{d^2}{\alpha(t - t')}}] dt$$

Where, α is the thermal diffusion coefficient, R is the laser beam width, ρ_0 is the density of the coatings, P_0 is the laser power and d is the coating thickness.

A set of specimens with different coating thickness were fabricated. Experiments were carried out by a laser scanning thermographic system. Figure 1(a) shows the IR image with different coating thickness. Figure 1(b) shows the thermal signals along the direction of the laser scanning.

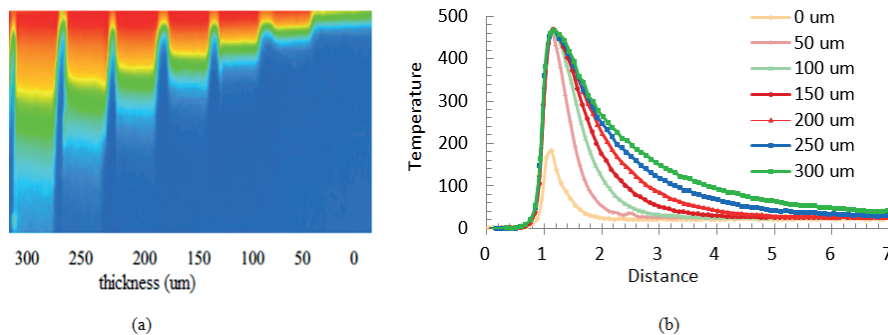


Fig. 1. Laser scanning thermal image of coating specimen with different coating thickness.

E Methodologies of Photothermics, PA/OA, and Related Techniques

The stability and reliability of the system are verified and the results indicate that in the range of 50-300 um coating thickness, the accuracy is within 5%.

References

1. Zixue Qiu, Tianchi Zheng, Liping Wan, Guan Lu, Jianxin Shao, Jiang Yuan, Review of Scientific Instruments 88 (1), (2017) doi:10.1063/1.4973668
2. S. Dixon, B. Lanyon, G. Rowlands, Applied Physics Letters 88 (14), (2006) doi:10.1063/1.2192144
3. M.H. Henderson, J.J. Peters, D.K. Walmer, G.M. Couchman, Review of Scientific Instruments 76 (3), (2005) doi:10.1063/1.1863832 .

EP 007

Equation of state and sound velocity of metallic liquids by picosecond acoustics at high pressure and temperature

Frédéric Decremps, Simon Ayrinhac, Michel Gauthier, Daniele Antonangeli,
Marc Morand, Yiuri Garino, and Paraskevas Parisiades

*Institut de Minéralogie, de Physique des Matériaux, et de Cosmochimie, Sorbonne Université - Université Pierre et Marie Curie, 4
Place Jussieu, 75005 Paris, France*

frederic.decremps@sorbonne-universite.fr

The determination of acoustic properties under pressure is a powerful method to treat fundamental problems in physics of solid and liquid states since (i) pressure is one of the most useful thermodynamical parameters to tune physical properties and (ii) sound velocity is very sensitive to subtle changes in local or long-range order as well as electronic properties of matter. However, up to recently, no laboratory technique was available to measure the sound velocity and the density in metallic liquids at pressure higher than 1 GPa and high temperature.

To overcome these limitations, picosecond acoustics in diamond anvil cell (called Apicoced) has been developed and enables measurements of both sound velocity and equation of state in any kind of materials under extreme conditions, including nanocrystals or metallic liquids [1]. Principle and feasibility described, we will also show that such technical improvement should certainly be useful in several fundamental and applied problems in physics as well as many other areas ranging from nonlinear acoustics or material research to earth and planetary science.

Finally, in order to illustrate Apicoced capabilities, the fascinating case of liquid cesium (l-Cs) at high densities will be given [2]. At 2 GPa, the l-Cs sound velocity goes first through a maximum versus pressure. A softening of the l-Cs visco-elastic properties is then observed from 2.0 up to 4.0 GPa, pressure at which the reflectometric signal is abruptly reversed. These anomalous behaviors could be related to structural and/or electronic transformations within the liquid state.

References

- [1] F. Decremps, M. Gauthier, S. Ayrinhac, L. Bove, L. Belliard, B. Perrin, M. Morand, G. Le Marchand, F. Bergame, J. Philippe, Ultrasonics (2014)
- [2] F. Decremps, S. Ayrinhac, M. Gauthier, D. Antonangeli, M. Morand, Y. Garino, and P. Parisiades, Phys. Rev. B. 98, 184103 (2018)

Cell constant determination via combined photoacoustic and direct optical absorption measurement

János Fekete⁽¹⁾, Ervin Jász⁽²⁾, Tibor Ajtai⁽¹⁾, Anna Szabó^(1,3), Gábor Szabó⁽¹⁾, Zoltán Bozóki^(1,3)

1. Department of Optics and Quantum Electronics, University of Szeged, Hungary

2. Bosch CC/ENG 1-Bp, Budapest, Hungary

3. Hobre Laser Technology Ltd., Algyő, Hungary

jfekete@titan.physx.u-szeged.hu, zbozoki@physx.u-szeged.hu

Photoacoustic (PA) spectroscopy is one of the most reliable methods for measuring gas or aerosol concentration. Whenever a PA instrument is operated under field conditions it needs regular calibration, which is typically performed by using a calibration gas cylinder or cylinders are required. Unfortunately, calibration not only limits the reliability of the instrument (via the uncertainty of the concentration of the calibration gas), but it also increases operational cost significantly, and takes off valuable measurement time, as a typical field calibration lasts about 30 minutes or even more.

Here we suggest an alternative calibration method aiming at eliminating these problems. The proposed method is applicable whenever there is a component which is present in the measured gas sample in a sufficiently high concentration making possible to perform both photoacoustic and optical absorption measurement on its strong absorption line by using the PA cell to be calibrated. Our goal was to reduce the calibration time down to a few minutes.

Based on the combination of the basic equation of photoacoustics [1,2] and the Beer-Lambert law, one can calculate the so called PA cell constant (C_{cell} in unit of $mV/(mW \cdot cm^{-1})$) from the measured PA signal (S in unit of mV), the decrease in the light power due to absorption within the PA cell (ΔP in unit of mW) and the length of the PA resonator (L in unit of cm):

$$C_{cell} = \frac{S \cdot L}{\Delta P}$$

In case of atmospheric aerosol measurement, water vapor is a evident choice as e.g. at 1371 nm it has a strong absorption line which is accessible by a fiber coupled single mode DFB diode laser. This example will be shown in the following.

The proposed calibration procedure starts by recording the power of the diode laser as a function of the driving current of the laser under no modulation with a power meter placed right behind the PA cell. The temperature of the diode laser is set in a way to ensure that the recorded power-current (P-I) curve includes a well measurable absorption line (see Figure 1). The software which is developed for this calibration procedure identifies the absorption line, fits a Lorentzian line profile on it, and calculates ΔP corresponding to the peak of the absorption. Next the laser current is set to be modulated while the laser temperature is unchanged and the PA signal corresponding to the peak of the absorption is determined. Finally the equation above is applied and the cell constant is determined

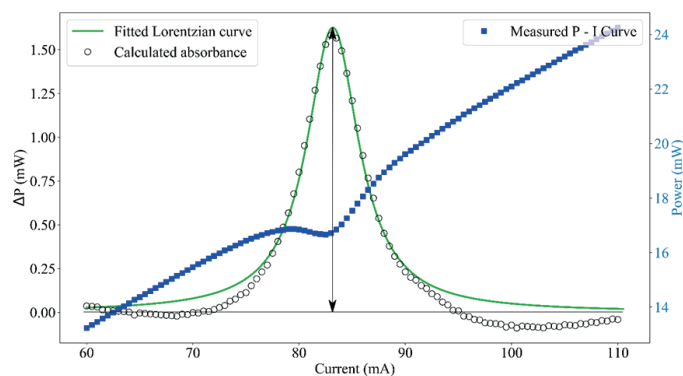


Figure 1. The blue curve shows the light-power as a function of the diode laser current measured by a power meter placed right after the PA cell. The green curve is the fitted Lorentzian curve on the light power decrease due to light absorption within the PA cell.

E Methodologies of Photothermics, PA/OA, and Related Techniques

The execution of the proposed method on a longitudinal differential cell yielded a calibration constant of $C_{cell} = 18 \text{ mV}/(\text{mW}\cdot\text{cm}^{-1})$. By taking into account that the applied microphone has the sensitivity of $10 \text{ mV}/\text{Pa}$, our result is in good agreement with the literature value [1, 2]. Furthermore the cell constant determination takes only about 2 minutes, which is a very significant time reduction.

Acknowledgements

Ministry of Human Capacities, Hungary grant 20391-3/2018/FEKUSTRAT and GINOP-2.2.1-15-2017-00101 project are acknowledged.

References

1. Zoltán Bozóki, Árpád Mohácsi, Gábor Szabó, Zsolt Bor, Miklós Erdélyi, Weindong Chen and Frank K. Tittel, Applied spectroscopy, Volume 56, Number 6 (2002), 715-719
2. András Miklós, Peter Hess, Zoltán Bozóki, Review of Scientific Instruments, Volume 72, Number 4 (2001), 1937-1955

EP 009

Thermoreflectance microscopy as a method for accurate determination of thermal properties of layered samples

Christian FRETIGNY ^{(1)*}, Danièle FOURNIER ⁽²⁾

1. Laboratoire SIMM, Sorbonne Université, PSL Research University, UMR 7615, CNRS, UPMC, ESPCI, 10 rue Vauquelin, Paris, 75005, France

2. Sorbonne Université, UPMC, Univ. Paris 06, CNRS, UMR 7588, Institut des NanoSciences de Paris, 75005, Paris, France

christian.fretigny@espci.fr ; danièle.fournier@insp.jussieu.fr

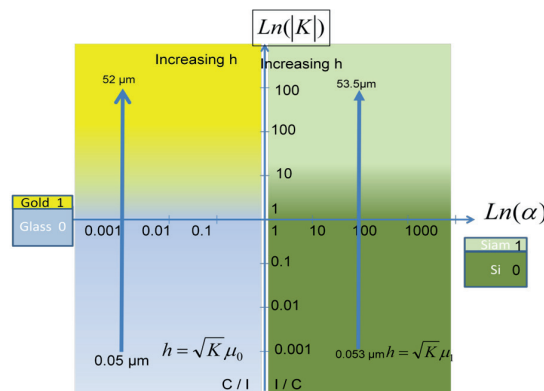
We report on thermal properties determination when the sample is a layer deposited on a substrate with known properties (layered sample) or is inserted between a known substrate and a known surface layer. The experimental setup is a thermoreflectance microscope in which the modulated pump beam, focused at a micrometer size, creates a thermal wave in the sample. The spatio-temporal heat diffusion is detected through the variation of the reflectivity of the probe beam which is scan on the sample surface. Experimental amplitude and phase are recorded versus the distance of the two beams. It is well known that a multiparameter best fit can find the thermal values required. Instead of a numerical approach, we show here that asymptotic behaviour of the heat diffusion in layered structures can be calculated and used to

$$T(r, 0, \omega) = \Phi \int_0^\infty \frac{1}{k_1 \sigma_1} \frac{k_1 \sigma_1 + k_0 \sigma_0 \tanh(\sigma_1 h)}{k_0 \sigma_0 + k_1 \sigma_1 \tanh(\sigma_1 h)} J_0(\lambda r) \lambda d\lambda$$

recover thermal properties [1,2]. The integral is evaluated using incomplete Bessel functions

$$T(r, 0, \omega) = \frac{\Phi}{k_1 h} \left[\frac{e^{-\rho \varepsilon \theta_0}}{\rho} + \sum_{n=0}^\infty R_n K_0(\rho y_n, w_n) \right]$$

where $\rho=r/h$, r is the distance from the heat source, h is the layer thickness and the other parameters are related to the relative thermal properties of the system. Domains of applicability of the different regimes are discussed and illustrated with examples in the plane of Figure 1.



Where $\alpha = \frac{k_0}{k_1}$ is the ratio of the thermal conductivities and $K = h^2 \left(\frac{1}{\mu_0^2} - \frac{1}{\mu_1^2} \right)$ (the μ 's are the thermal length) and subscripts 0 and 1 stand respectively for the substrate and the layer.

References

1. C.Fretigny C, J.-Y. Duquesne, D. Fournier , F. Xu, J. Appl. Phys 111 , 084313 (2012)
2. C. Fretigny, J.-P. Roger, V. Reita, D. Fournier, J. Appl. Phys 102 , 116104 (2007)

EP 010

Photocatalytic degradation of paracetamol and its monitoring with thermal lens microscopy (TLM)

Luz Amparo HERNÁNDEZ CARABALÍ^{(1)*}, Ramón Enrique CEDEÑO BERNAL⁽²⁾, Salvador ALVARADO RAMÍREZ⁽¹⁾, Ernesto MARÍN MOARES⁽¹⁾, José Bruno ROJAS TRIGOS⁽¹⁾, Antonio Manoel MANSANARES⁽²⁾

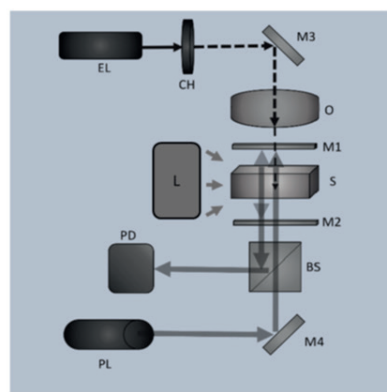
1. Instituto Politécnico Nacional, Centro de Investigación en Ciencia Aplicada y Tecnología Avanzada, Unidad Legaria. 2. Legaria No. 694, Ciudad de México 11500., México. (2) Gleb Wataghin Physics Institute, University of Campinas - UNICAMP, 13083-859, Campinas, SP, Brazil.

luam30_09@hotmail.com; emarinm@ipn.mx

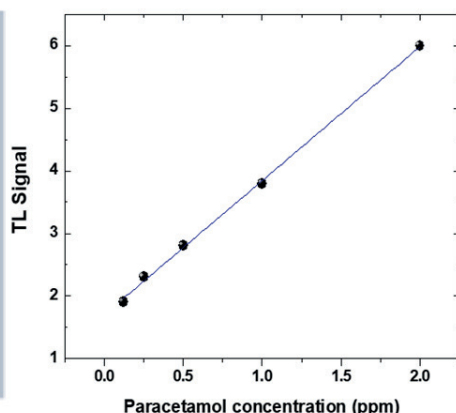
The presence of pharmaceuticals in wastewaters has been documented and reported as an emerging environmental issue [1]. The presence of trace pharmaceuticals in drinking water is also of public concern since little is known about chronic health effects associated with long-term ingestion [1]. Paracetamol is a common analgesic and anti-inflammatory widely used for humans and animals. It has been reported to be present with a concentration up to $6 \mu\text{gL}^{-1}$ in European Sewage Treatment Plant (STP) effluents, up to $10 \mu\text{gL}^{-1}$ in natural waters in USA and even more than $65 \mu\text{gL}^{-1}$ in the Tyne river [2-4]. Currently, interest is focusing on treating contaminated water for stopping further pollution, for example using photocatalysis. But to monitor minor concentrations of pollutants in very small samples' volumes, precise sensors must be developed.

Materials and Methods

In this work, a micro-spatial thermal lens spectroscopy setup (thermal lens microscope, TLM) with coaxial counter-propagating pump and probe laser beams and an integrated passive optical Fabry-Perot resonator is proposed (shown schematically in Fig. 1a) for monitoring trace amounts of paracetamol in water, at levels attainable when it is reduced by a photocatalytic reaction. The method is described with more detail elsewhere [5, 6]. A pump laser (EL) beam (OBIS 640 nm LX 100 mW), with a 640 nm wavelength and a beam power of 4 mW, at the sample position is focused onto a very small region of the sample (S) by using a microscope objective (O), which was previously modulated in intensity, using a frequency of 1 Hz, by a mechanical optical chopper (CH, Thorlabs MC 2000). The probe laser (PL, continuous LSR 532NL-300, 532 nm wavelength and 4 mW nominal power) beam is highly collimated. Both beams are coaxially counter propagating. The optically passive Fabry-Perot cavity formed between the mirrors M1 (dichroic) and M2 causes several times the forward and back propagation of the probe beam through the sample, increasing the sensitivity of the system around 10-times. Before of that, the resulting intensity is measured using a photodiode (PD, Thorlabs Det-36). Additionally, a pinhole (500 μm diameter Thorlabs- P500S, not shown in the figure) is located in front of the photodiode, in order to allow that only the contribution of the central region of the probe beam be sensed, which contains the information related to the thermal lens effect. Then, the signal from the photodiode is measured using a digital oscilloscope (Bk Precision 2542B). In the figure, M3 and M4 are mirrors and BS represents a beam splitter. A lamp (represented by L) was used to induce the photocatalytic reaction.



(a)



(b)

A colorimetric method was applied, and it is based on the formation of a colored complex (prussian blue), when the paracetamol react with Fe(III)/hexacyanoferrate(III), this complex have the same concentration as paracetamol with a broad absorption band centered at 710 nm. A calibration curve (Fig. 1b) was constructed by measuring the thermal lens signal at different paracetamol concentrations. From this curve a limit of detection of 60 ppb was obtained with a sensitivity of 2.14 V/ppm (linear curve slope). This calibration curve will allow the determination of the paracetamol concentration as a function of time during a photocatalytic degradation process.

Fig. 1. a) Experimental setup for the measurement of paracetamol concentrations using LTM technique. b) Calibration curve for paracetamol measuring using TLM

E Methodologies of Photothermics, PA/OA, and Related Techniques

Acknowledgements

This work was financial supported by SIP, IPN (Research Grants SIP: 20180376, 20195617) and CONACYT (2016-01-2482). COFAA-IPN by the SIBE and BEIFI programs is also acknowledged. L. A. Hernández-Carabalí thanks CONACyT and BEIFI for scholarships support. E. Cedeño gratefully acknowledges the support of the SECITI for granting a postdoctoral fellowship under the agreement SECITI/077/2017. A. M. M. acknowledges the support of the Brazilian Agencies CNPq and FAPESP.

References

1. J.L Tambosi, L.Y Yamanaka, H.J. José, R.D.F. Peralta, H. F. Schröder, *Quim. Nova*, 33 (2), 411 (2010) doi: 10.1590/S0100-40422010000200032
2. R. Andreozzia, V. Caprioa, R. Marotta, D. Vognab, *Water Research* 37, 993 (2003) doi: 10.1016/S0043-1354(02)00460-8.
3. *Pharmaceuticals in the Environment: Sources, Fate and Risks*, K. Kümmerer, Editor, Springer, Berlin _2001.
4. K. Dana, F. Edward, M. Michael, T. Michael, Z. Steven, B. Larry, B. Herbert *Environ. Sci. Technol.*, 36, 1202 (2002) doi: 10.1021/es020136s.
5. E. Cedeño, H. Cabrera, A.E. Delgadillo-López, O. Delgado-Vasallo, A.M. Mansanares, A. Calderón and E. Marín *Talanta* 170, 260 (2017). doi: 10.1016/j.talanta.2017.04.008.
6. L. A. Hernández-Carabalí, E. Cedeño, A. Mantilla, S. Alvarado, H. Cabrera, A. M. Mansanares, A. Calderón and E. Marín *J. Environ. Manag.* 232, 305 (2019). doi:10.1016/j.jenvman.2018.11.044

EP 011

The absorption spectrum of several Mexican agricultural products obtained through the photoacoustic spectroscopy

Blanca Estela ZENDEJAS-LEAL⁽¹⁾, Francisco HERNÁNDEZ-ROSAS⁽²⁾,
V́ctor Rodrigo BARRIENTOS-SOTELO⁽³⁾, Margarita Lizeth ALVARADO-NOGUEZ⁽⁴⁾,
Ahtziri Guadalupe ALVARADO-ESTRADA⁽³⁾, Rubén PERALTA-HERNÁNDEZ⁽²⁾,
Juan HERNÁNDEZ-ROSAS^{(3)*}, Alfredo CRUZ-OREA⁽¹⁾

1. Departamento de Física, Centro de Investigación y de Estudios Avanzados del IPN,
Apartado Postal 14-740, México D.F. 07360, México

2. Colegio de Postgraduados, Campus Córdoba, Km.348 Carretera Federal Córdoba-Veracruz,
Congregación Manuel León, Amatlán de los Reyes, Ver., 94946, México

3. Instituto Politécnico Nacional UPIITA, Av. IPN, No. 2580, Col. La Laguna Ticomán,
Del. Gustavo A. Madero, México D.F., 07340, México

4. Instituto Politécnico Nacional SEPI-ESIME, Unidad Profesional "Adolfo López Mateos", Col. San Pedro Zacatenco, Del. Gustavo
A. Madero, Ciudad de México, 07738, México.

juhernandezro@ipn.mx (Juan Hernández-Rosas)

The aim of this work is to remark the usefulness of the photoacoustic spectroscopy as a technique that can characterize *in situ* the optical properties of biological systems. In our case, we have studied several products representative of the Mexican agriculture. Thus, we have obtained the absorption spectra of chili peppers, Persian lime, sugar cane and also avocado. This technique can help us to monitoring the quality, the nutritional content but also the ripening process or the evolution of diseases on plants. In some cases, is necessary to get the second derivative of the spectra or to use the phase resolved method in order to gain a better understanding of the convolved signals of these non trivial systems. However, once the spectrum is taken on these samples, a richness of scientific information is generated that can be used in benefit of the farmers.

Thickness and defect detection by linear-frequency-modulated laser ultrasonic radar (LUR)

Huiting Huan ^{(1)(2)*}, Lixian Liu ⁽²⁾, Alexander Melnikov ⁽²⁾, Andreas Mandelis ⁽²⁾, Xiaolong Chen ⁽¹⁾

1. School of Mechano-Electronic Engineering, Xidian University, Xi'an 710071, China

2. Center for Advanced Diffusion-Wave and Photoacoustic Technologies (CADIPT), Department of Mechanical and Industrial Engineering, University of Toronto, Toronto, ON, M5S 3G8, Canada

huanht90@sina.com

Radar systems usually adopt frequency modulation to generate pulse compression and matched filtered signals [1]. In this presentation radar principles were applied in developing a frequency-modulated laser ultrasonic radar (LUR) system which was used for nondestructive thickness and defect detection. The laser ultrasonic radar relies on cost-effective, small-footprint CW laser diode sources and narrowband piezoelectric transducers [2]. We report on a LUR validation system for performing B-scan thickness measurements and defect diagnostics in the time and frequency domains.

The back-propagated LUR signal can be well described by a hybrid model that combines 1-D and 3-D thermoelastic generation schemes [2]. The 1-D model treats the LUR signal as a result of pure longitudinal stress. It can well describe the back-propagated signal but also lead to unrealistic echo amplitudes with respect to the direct response peak. On the other hand, the 3-D model treats the sample as a laterally infinite elastic solid of finite thickness and should be modeled in the spatial frequency domain with the help of the Hankel transformation [3]. Together the 1D-3D hybrid model combined in a hybrid manner can give a good prediction by cross-correlating the received ultrasonic chirp with the reference linear frequency modulation signal.

Materials and Methods

Two sets of experiments were conducted in terms of thickness and defect depth detection. In the first test, a step-shaped sample and a wedge were used as the testing objects, as shown in Fig. 1(a). The linear frequency modulated laser beam spot and the immersion ultrasonic transducer were confocally calibrated and scanned together on the flat front surface. By match filtering, the back-surface-echoes (BSE) were obtained in the time domain and compared with the theoretical prediction. In addition, a stainless steel sample with three horizontally drilled holes acting as subsurface defects was used as shown in Fig. 1(b). The test results were analyzed with the proper linear frequency modulated LUR theory.

Results

The thickness measurement results of the step-shaped sample are illustrated in Fig. 2(a). A gradual shift of BSEs indicates an increase in local thickness. The results from the wedge-shaped sample (not shown) also exhibited similar features. Thickness differences were also revealed from frequency spectra changes with respect to the echo signal, as shown in Fig. 2(b). Figure 2(c) shows the difference between the theoretical prediction and the experimental result. By combining 1D and 3D linear frequency-modulated thermoelastic theory, the prediction shows general agreement with the experimental LUR signal.

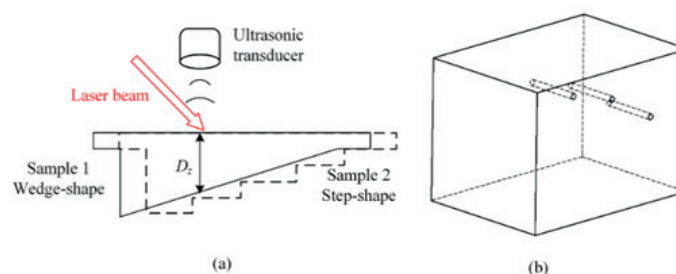


Fig. 1. (a) The thickness LUR test scheme and (b) defective sample under test

For the detection of subsurface defects, the described thickness testing modality was applied to the defect-bearing stainless steel sample. By following a standard linear LUR B-scan procedure, the time signature of the echoes was acquired and fitted to a simple geometric model. The calculated thickness is shown in Tab. 1. In summary, it was experimentally proven that the proposed linear frequency modulated LUR system is able to detect echoes from subsurface defects and determine their actual depths.

E Methodologies of Photothermics, PA/OA, and Related Techniques

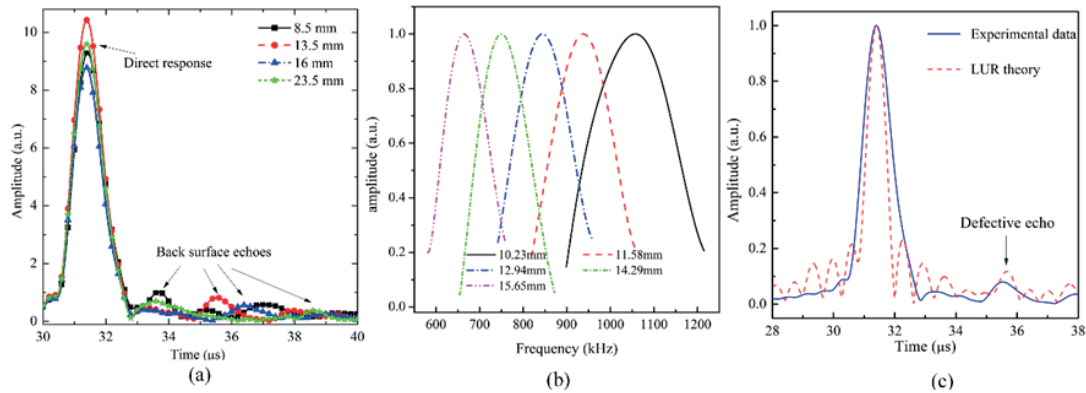


Fig. 2. (a) time domain back surface echo (BSE) signal from experiments, (b) spectra of BSEs and (c) LUR theory prediction

Table 1. Subsurface defect location detection by the LUR technique showing actual and estimated depths.

Defect real depth value	LUR detected value
5 mm	5.13 ± 0.47 mm
10 mm	9.59 ± 0.04 mm
20 mm	19.89 ± 0.07 mm

Acknowledgements

This work was supported by Natural Sciences and Engineering Research Council of Canada (NSERC) for a Discovery Grant to A.M. H.H. acknowledges the National Natural Science Foundation of China with Grant No. 61801358, 61805187 and 61727804.

References

1. E.C. Farnett and G.H. Stevens, "Pulse compression radar," in Radar Handbook (McGraw-Hill, New York, 1990), Chap. 10
2. H. Huan, A. Mandelis, Lixian Liu, et al., "Application of linear frequency modulated laser ultrasonic radar in reflective thickness and defect non-destructive testing" NDT&E Int. 102, 84-89 (2019)
3. H. Huan, A. Mandelis, B. Lashkari, L. Liu. "Frequency-domain laser ultrasound (FDLU) non-destructive evaluation of stress/strain behavior in an aluminum alloy," Int. J. Thermophys. 38, 62 (2017)

EP 013

Numerical simulation study on optimizing the metric and the modal function in sensorless adaptive optical microscopy

Hwan Hur, Dong Uk Kim, Kye-Sung Lee*, and Ki Soo Chang*

Division of Scientific Instrumentation, Korea Basic Science Institute, Daejeon 34133, South Korea

kslee24@kbsi.re.kr and ksc@kbsi.re.kr

Adaptive optics (AO) is becoming a valuable tool for correcting aberrations induced by refractive index mismatch of the sample and misalignment of the optical system in microscopy applications. Sensorless AO corrects aberration without wavefront sensor that needs to have a beacon or “guide star” as an artificially generated point source. Sensorless AO estimates the amplitude of aberrations based on the use of an image quality metric. A summation of orthogonal modes like Zernike polynomials and Lukosz polynomials expresses the aberrations. A combination of the modes applies to the adaptive element such as a deformable mirror and a spatial light modulator. The set of images is obtained corresponding to the combination of the modes. The image quality metric is calculated using the set of images. The sensorless AO performs the optimization process to find the optimal correction of wavefront aberrations using the results of the image quality metric. In this paper, we numerically investigate the image quality metric and the orthogonal modes governing the accuracy of the optimal correction in the sensorless AO. Entropy, second moment, intensity variance, and sharpness are chosen as an image quality metric. The aberration is expressed in terms of the Lukosz polynomials and the Zernike polynomials. We propose the combination method between the Zernike modes for small aberration and the Lukosz modes for large aberration (larger than RMS 1 radian). We believe that this work is potentially applicable to any form of microscopy.

EP 014

Thermal diffusivity of silicone rubber composite insulators determined by photothermal radiometry

Haitao Jiang, Bincheng Li *, Binxing Zhao, Qiming Sun, Chunming Gao

*School of Optoelectronic Science and Engineering,
University of Electronic Science and Technology of China, Chengdu, Sichuan 610054, China*

bcli@uestc.edu.cn

Silicone rubber composite insulators are widely used in high-voltage power systems due to their excellent hydrophobicity, light weight and hydrophobicity recovery after exposure to electrical discharges^[1-2]. In this presentation the thermal properties of fresh composite insulators with different mechanical and/or electrical behaviors and from different manufacturers are measured by photothermal radiometry (PTR) and compared. As organic polymer materials, the main component of most composite insulators is high temperature vulcanizing (HTV) silicone rubber, which is made via mixing and vulcanization from base polymer and a variety of fillers and additives, such as alumina trihydrate (ATH) and silica^[3-4]. Accordingly, the insulation performances as well as aging process of silicone rubber composite insulators manufactured by different formulations may differ widely.

In this presentation the thermal diffusivities of various fresh silicon rubber composite insulators are measured to find a base for possible link between the thermal properties and the insulation performance aging of composite insulator. Modulated PTR technique [5] is employed to determine the thermal diffusivity of the composite insulator. The silicone rubber composite insulators used in the experiment are got from two vendors named Shuyue Electric co. LTD in Sichuan (SY Insulator) and Tianrun Electric co. LTD in Hebei (TR Insulator), China. Experimentally, the measured modulation frequency dependences of PTR amplitude and phase are fitted to an explicit theoretical model to determine the thermal diffusivity^[5]. The corresponding fits are presented in Fig. 1 and the fitted results are presented in Table 1.

Table 1. Fitted thermal diffusivity values of three composite insulators with different voltage grade and the same mechanical load grade (70KN) from two vendors

Voltage Grade	SY insulator	TR insulator
35KV	$(2.58 \pm 0.01) \times 10^{-7}$	$(2.12 \pm 0.01) \times 10^{-7}$
110KV	$(2.56 \pm 0.02) \times 10^{-7}$	$(1.95 \pm 0.01) \times 10^{-7}$
220KV	$(2.44 \pm 0.02) \times 10^{-7}$	$(1.98 \pm 0.01) \times 10^{-7}$

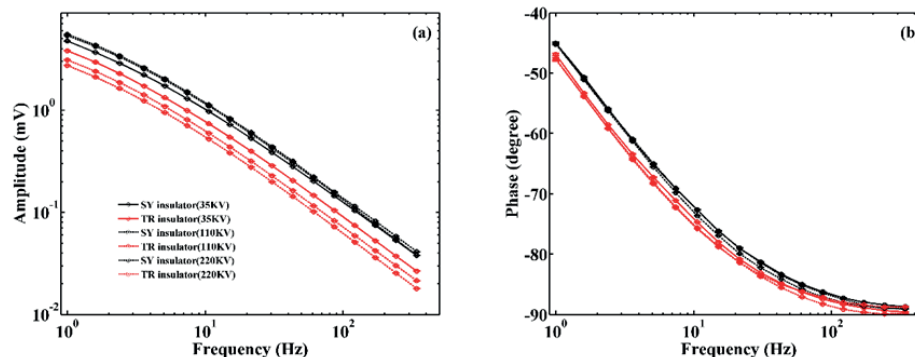


Fig. 1. PTR amplitude (a) and phase (b) versus modulation frequency for three silicon rubber composite insulators with different voltage grades and same mechanical load grade: 70KN, from two vendors.

The results presented in Table 1 show that significant difference exists between the thermal diffusivities of fresh silicon rubber composite insulators from different vendors. The thermal diffusivity also slightly relates to the voltage grade. These results will be helpful to the understanding of aging process of silicon rubber composite insulator via aging induced thermal property change of the composite insulator in operation.

E Methodologies of Photothermics, PA/OA, and Related Techniques

References

1. Tu, Y. , Zhang, H. , Xu, Z. , Chen, J. , & Chen, C., IEEE Transactions on Power Delivery 28(3), 1865-1871 (2013) doi: 10.1109/TPWRD.2013.2244103
2. Vlastos A E, Sherif E, IEEE Transactions on Power Delivery, 5(4):2030-2038,doi: 10.1109/61.103698
3. Meyer, L. , Grishko, V. , Jayaram, S. , Cherney, E. , Duley, W. W, Conference on Electrical Insulation & Dielectric Phenomena. IEEE. (2002),doi: 10.1109/CEIDP.2002.1048928
4. Su, F. , Zhidong, J. , Haifeng, G. , & Zhicheng, G. , Conference on Electrical Insulation & Dielectric Phenomena. IEEE.(2007),doi: 10.1109/CEIDP.2007.4451459
5. Haitao Jiang, Bincheng Li , Binxing Zhao, Qiming Sun, Chunming Gao, Lincong Chen, Journal of Physics D: Applied Physics, 51 425304(2018), doi: 10.1088/1361-6463

EP 015

Photo-acoustic spectrum of ambient atmospheric NO₂ and aerosol based on a low power blue diode laser

Jin Hua Wei ^{(1) (2) (3)*}, Hu Ren Zhi ^{(1) (2)}, Xie Pin Hua ^{(1) (2)}, and Huang Chong Chong ^{(1) (2)}

1. Key Laboratory of Environmental Optics & Technology, Anhui Institute of Optics and Fine Mechanics, Chinese Academy of Sciences, Hefei, China

2. University of Science and Technology of China, Hefei, China

3. School of Mechanical Engineering, Anhui University of Science and Technology, Huainan, China

hwjin@aiofm.ac.cn

Photo-acoustic technology based on a low power blue diode laser for the measurement of the ppb level NO₂ and ambient atmospheric aerosol is presented in this paper. A low cost NO₂ and aerosol measurement system based on traditional photo-acoustic technology is established. The 405 nm blue diode laser with an external modulation is used as the light source. The central wavelength of the laser is 403.56 nm, the half-peak full width is 0.84 nm, and the power is 65.3 mW. The effective absorption cross section of NO₂ is obtained, and the interferences of the water vapor and other trace gases are investigated. The resonant frequency is tested to be 1.35 kHz by frequency scanning fitting. An internally polished and coated PTFE aluminum cylindrical cavity is used as the photo-acoustic resonator (the inner diameter is 8 mm and the length is 120 mm). The influence factors caused by cavity parameters, optical windows and power supply are studied. System is optimized to reduce background noise and improve signal-to-noise ratio. Then the noise signal is dropped to 0.02 μv . An additional buffer chamber is integrated on the original buffer chamber to form a two-level buffer. The two-stage buffer structure significantly suppresses the effects of airflow noise, and improves the system stability.

At the same time, the influence of absorption coefficient of ambient atmospheric aerosol on polystyrene based on standard microspheres as aerosol generator is analyzed. The absorption coefficients of particles with different concentration and different diameters at the same concentration are measured. The absorption coefficient of ambient atmospheric aerosol is directly proportional to the number concentration. The slope after linear fitting is 10.598 ± 0.64196 , and the correlation coefficient is 0.993. The variance of the absorption coefficient curve is between 3Mm^{-1} - 4Mm^{-1} , and the absorption coefficient is affected by particles of different particle sizes. At the same time, the absorption coefficient increases with the increase of particle size.

The slope of the calibration curve of the system after linear fitting is $0.016 \mu\text{v/ppb}$, and R^2 is 0.998. The NO₂ detection limit of system is 2 ppb (3σ) with an average time of 60 s. To verify the results of the system, a diode laser cavity ring-down spectroscopy system (CRDS system, using a 409 nm the diode laser, with a system detection limit of 6.6×10^{-11}) is used to measure ambient NO₂ and atmospheric aerosol simultaneously on Lake Dong-Pu in western Hefei, Anhui province, China. During the experiment, the measured NO₂ concentration ranges from 8 to 30 ppb, with an average concentration of 20.8 ppb. The results of two systems have good consistency, with the linear fitting slope of 0.94 ± 0.009 , the intercept of 1.89 ± 0.18 and the correlation coefficient of 0.87. At the same time, the change trend of ambient atmospheric aerosol with $5 \mu\text{m}$ is obtained. The experimental results show that the system can realize the low-cost on-line detection of the ppb level NO₂, can be used for the real-time detection of NO₂ concentration field.

In November 2018, the system started to measure the concentration of NO₂ in the atmosphere of the Dong-Pu reservoir in Hefei, Anhui province, China (Google: latitude 31.89, longitude 117.20). The NO₂ in the ambient atmosphere is filtered through the filter membrane and buffer chamber by a small pump (KNF, N83KNE). The flow rate is controlled by a flow meter (CS200) at 0.2 L/min. After the preliminary background measurement, the system automatically records the photo-acoustic signal (time resolution 1 s) every 1 s, and the average measurement result after 60 s is shown in the blue line of figure 2a. The concentration of NO₂ is 8-30 ppb, and the average concentration is 20.8 ppb. In order to confirm the measurement results of the system, the diode laser cavity damping spectroscopy system developed by the research group itself (CRDS) was used to synchronously measure the concentration of NO₂ in the atmosphere at the same place. The measurement results are shown in the red line of figure 9a. The measurement results shows the good correlation between the PAS system and CRDS system, and the correlation coefficient is 0.87. The slope after linear fitting is 0.94 ± 0.009 , and the intercept is 1.89 ± 0.18 . The differences are mainly caused by system

E Methodologies of Photothermics, PA/OA, and Related Techniques

error, position difference, automobile exhaust, measurement environment and other influences. At the same time, the ambient atmospheric aerosol with $5\mu\text{m}$ is obtained.

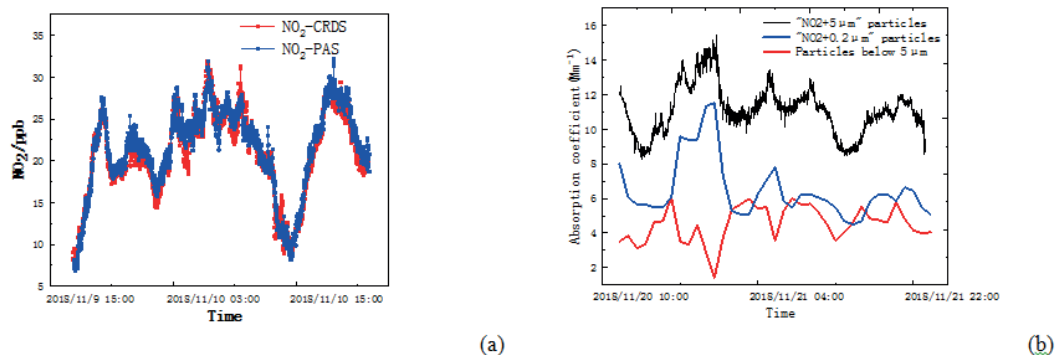


Fig.2 (a). Measurement of atmospheric NO₂ concentrations; (b). Measurement of ambient atmospheric aerosol with $5\mu\text{m}$

Acknowledgements

Acknowledgements the project support with the National Natural Science Foundation of China (Grant No.: 91644107, 61575206, 61805257), the National Key R&D Program of China (2017YFC0209401, 2017YFC0209403, 2017YFC0209902), and the Outstanding Young Talents Program of Anhui University of China (2019 Jin Huawei).

References

1. L. Dong, F.K. Tittel, C.G. Li, N.P. Sanchez, H.P. Wu, C.T. Zheng, Y.J. Yu, A. Sampaolo, R.J. Griffin, *Optics Express*, 24 (6), A528(2016) doi:10.1364/OE.24.00A528
2. H. Fuchs, W.P. Dube, B.M. Lerner, N.L. Wagner, E.J. Williams, S.S. Brown, *Environmental Science & Technology*, 43 (20), 7831(2009) doi: 10.1021/es902067h
3. X. Lu, M. Qin, P.H. Xie, J. Duan, W. Fang, L.Y. Ling, L.L. Shen, J.G. Liu, W.Q. Liu, *Chinese Physics B*, 25 (2), 024210(2016) doi: 10.1088/1674-1056/25/2/024210

EP 016

Experimental methods for determination the refractive indices of materials

Valentina Maratovna KASIMOVA ^{(1,2)*}, Nina Semenovna KOZLOVA ⁽¹⁾,
Anna Petrovna KOZLOVA ⁽¹⁾, Evgeniya Viktorovna ZABELINA ⁽¹⁾, Zhanna Anatolievna GOREEVA ⁽¹⁾

1. National University of Science and Technology "MISiS", Moscow, Russia
2. FRC "Crystallography and Photonics" of the Russian Academy of Sciences, Moscow, Russia

kasimovavalya@mail.ru

The refractive index is fundamental parameter of any materials (in particular the dielectric materials) that determines the character of the interaction between light and matter. The most widely used methods of refractive index determination are the goniometric methods, the ellipsometric methods, the Kramers-Kronig method, the spectrophotometric methods [1, 2, 3].

The method of measuring the refractive index should be chosen depending on the maximum measurement error, the technical feasibility of the requirements fulfillment for the manufacture of the investigated sample [4].

In the Accredited Testing Laboratory "Single Crystals and Stock on their Base" of NUST "MISiS" some methods of the refractive indices determination are realized:

- the goniometric method of the minimum deviation (prism method) using the "GS-2" goniometer;
- spectrophotometric methods using a spectrophotometer "Cary 5000" with the universal measuring accessory "UMA" ("Agilent Technologies"): the method of reflection at near-normal incidence and the Brewster method.

In this paper we consider the features of the implementation of these methods, their accuracy and the requirements for investigated samples.

For the prism method we need the sample in the form of a prism with isosceles triangle at the base. It is necessary to measure the refractive angle θ of the sample and the angle of minimum deviation φ_{λ}^{min} of a beam with wavelength λ passing in a prism parallel to its base [4]. The refractive index n_{λ} is calculated due to the formula (1):

$$n_{\lambda} = \frac{\sin\left[\frac{(\theta + \varphi_{\lambda}^{min})}{2}\right]}{\sin[\theta/2]} \quad (1)$$

This method allows to estimate the refractive index n with the accuracy $\sim 10^{-5}$. However, a number of stringent sample preparation requirements are imposed for such measurements carrying out. The trihedron prism as the investigated sample should be manufactured with the accordance [4].

Due to the fact that the implementation of these requirements is a non-trivial task, alternative methods for determination of the refractive indices can be used.

For two spectrophotometric methods of n determination the following parameters are measured: the spectrum of reflection from one surface at low angle of incidence close to normal and the Brewster angles obtained at p-polarized light. Nevertheless, the accuracy of these methods doesn't exceed the 0,001 [5]. At the same time, the requirements for the sample preparation are less stringent: it must have one polished face.

As for materials with the low absorption and the non absorption the refractive index can be calculated at a low angle of light incidence (2) [3]:

$$n = \frac{1 + \sqrt{R}}{1 - \sqrt{R}} \quad (2)$$

In this case, to obtain the dispersion of the refractive index of the material, the reflection coefficient R in this formula must be measured from one face.

According to the Brewster method [6], we get the values of the refractive indices of the material n_{λ} for a certain wavelength of incident light using the measured Brewster angle φ_{Br} (3):

E Methodologies of Photothermics, PA/OA, and Related Techniques

$$\operatorname{tg} \varphi_{Br} = \frac{n_2}{n_1} \quad (3)$$

where n_1 – the refractive index of air ($n_1=1$).

The determination of the refractive indices by the Brewster method doesn't depend on the intensity of the reflected light and requires the samples to have a significant size of the polished face. This method is valid for determination of the ordinary refractive index, and the values of n_2 are separately measured. To obtain the dispersion the special approximation equations are used [3]. This method is laborious and requires the accumulation of statistical data and their further metrological study.

The considered methods have been successfully applied for the refractive indices measurements of such crystals: LiNbO₃, crystals of the langasite type (La₃Ga₅SiO₁₄), Gd₃Al₂Ga₃O₁₂:Ce, CaMoO₄, a number of biaxial crystals and etc. [7, 8]. The results of the research are given in the report.

References

1. C.F. Bohren, D.R. Huffman, Absorption and Scattering of Light by Small Particles (Wiley Professional Paperback Edition Published, New York, 1998)
2. Application note // Spectrophotometric Methods of Refractive Indices Measurement. - URL :<https://www.agilent.com/cs/library/applications/application-refractive-index-cary-5000-uv-vis-5994-0052en-us-agilent.pdf>
3. E.D. Palik Handbook of optical constants of solids (Academic press, New York, 1998)
4. GOST 28869-90, Optical materials. Methods of measurement of the refractive index.
5. N.S. Kozlova, A.P. Kozlova, Zh.A. Goreeva, IEEE 2nd International Ural Conference on Measurements (UralCon), 281 (2017) doi: 10.1109/URALCON.2017.8120724
6. G.S. Landsberg, Optics.General Physics Course (Nauka, Moscow, 1976)
7. N.S. Kozlova, O.A. Buzanov, V.M. Kasimova, A.P. Kozlova, E.V. Zabelina, Modern Electronic Materials 4 (1), 7 (2018) doi: 10.3897/j.moem.4.1.33240
8. N.S. Kozlova, O.A. Buzanov, A.P. Kozlova, E.V. Zabelina, Zh.A. Goreeva, V.M. Kasimova, A.G. Chernykh, Crystallography Reports 63 (2), 216 (2018) doi: 10.1134/S1063774518020128

Sensitivity Enhancement of Laser Scanning Thermoreflectance Microscopy with Auto-Balanced Detection

Dong Uk KIM, Jung Dae Kim, Ilkyu HAN, Chan Bae JEONG, Ki Soo CHANG*

Division of Scientific Instrumentation,
Korea Basic Science Institute, 169-148 Gwahak-ro, Yuseong-gu, Daejeon, 34133, South Korea

ksc@kbsi.re.kr

Thermal management becomes major issue for integrated circuit (IC) design because local excess heating causes the performance, reliability and lifetime degradation in the microelectronic devices. Thermoreflectance microscopy (TRM) is a simple optical imaging technique which is well adapted to non-contact thermal measurement for IC devices [1-3]. Especially in this paper, we proposed a sensitive thermoreflectance imaging system for visualizing thermal faults through the backsides of IC devices. We employed the auto-balancing scheme for low-noise thermal measurement via laser scanning confocal thermoreflectance microscopy that previously demonstrated in Ref. [3]. By taking advantage of the inherent system noise suppression under the optimized auto-balancing conditions, ~5-fold improvement of the system signal to noise ratio (SNR) over that attainable via normal detection was achieved. Moreover, we proved that optical zooming provides further inherent noise reduction. As shown in Fig. 1, our system successfully enabled clear distinction of a localized thermal fault, which was dimly visible in the normal backside detection results, by auto-balanced backside detection. Therefore, the sensitivity-enhanced confocal TRM system is valuable for localizing individual thermal faults induced by sub-micron-sized defects through the backsides of IC devices.

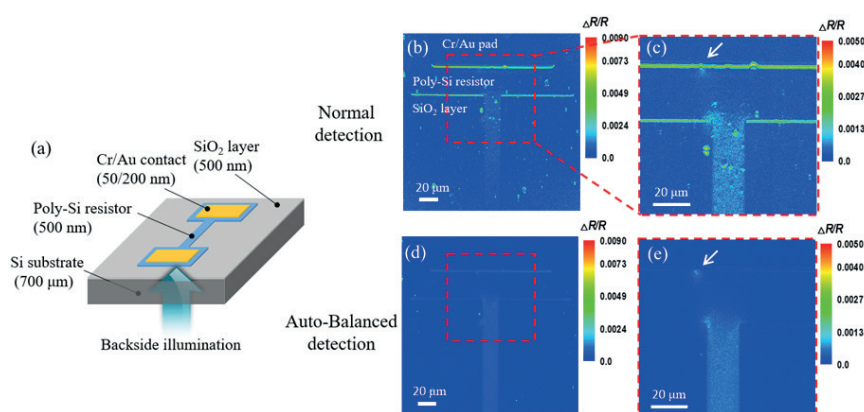


Fig. 1. Test sample schematic (a), Back-side thermoreflectance images obtained by normal detection (b, c) and auto-balanced detection (d, e) using the TRM system with a 50× objective lens (NA 0.42), respectively. The dotted line in (c, e) represents the region of the dotted line in (b, d), which was obtained by 2× optical zooming.

Acknowledgements

This work was supported by the Korea Basic Science Institute Grant (grant number: D39615)

References

1. S. Grauby, A. Salhi, J.-M. Rampnoux, H. Michel, W. Claeys, and S. Dilhaire, Rev. Sci. Instrum. 78, 074902 (2007) doi:10.1063/1.2757473
2. M. Farzaneh, K. Maize, D. Lüerßen, J. A. Summers, P. M. Mayer, P. E. Raad, K. P. Pipe, A. Shakouri, R. J. Ram, and J. A. Hudgings, J. Phys. D: Appl. Phys. 42 (14), 143001 (2009) doi:10.1088/0022-3727/42/14/143001
3. D. U. Kim, C. B. Jeong, J. D. Kim, K. -S. Lee, H. Hur, K.-H. Nam, G. H. Kim, and K. S. Chang, Sensors 17 (12), 2774 (2017) doi:10.3390/s17122774

Wide-field photothermal reflectance microscopy for fast detection of a single nanoparticle

Jung Dae KIM, Dong Uk KIM, Chan Bae JEONG, Ilkyu HAN, Ki Soo CHANG*

Division of Scientific Instrumentation, Korea Basic Science Institute, 169-148 Gwahak-ro, Yuseong-gu, Daejeon 34133, Korea

ksc@kbsi.re.kr

There is a limit to the observation of sub-micro sized objects due to the diffraction limit of light by general optical microscopy. Although fluorescence microscopy can overcome this problem, observation time is very short due to photobleaching [1]. In addition, because of the need for fluorescent dye, types of samples which could be observed are very limited. On the other hand, photothermal microscopy allows long-time observation of nano-samples with high resolution [2-7]. In this presentation, we demonstrate wide-field photothermal reflection microscopy for observing a single gold nanorod. It is well-known an indirect optical absorption technique which achieves high detection sensitivity while discriminating absorption from scattering. Photothermal reflectance image is expressed by signal of temperature-dependent optical reflectivity changes. In experiment, two types of lasers were used: an 808 nm laser beam (pump beam) for photothermal excitation of a single gold nanorod with sinusoidal modulation and a 635 nm laser (probe beam) for measurement of thermorefectance signal. Figures 1(a) and 1(b) illustrate dark field and SEM images, respectively. Gold nanorod was spin-coated on the coverglass with covering PDMS for enhancement of photothermal effect as shown in Fig. 1(c). Figure 1(d) presents a photothermal reflectance image of gold nanorods (SNR=5.38). The proposed system not only acquires photothermal images in short-period time (~0.02 mm² per minute), but also allows detection of a single nanoparticle in large area (200 x 150 μm²).

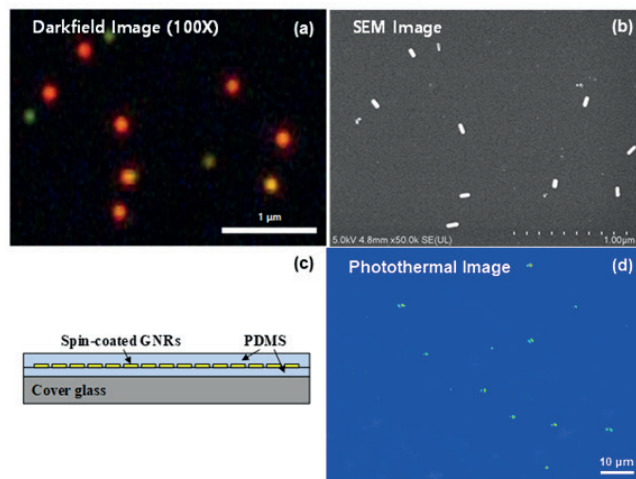


Fig. 1. Dark field (a) and SEM (b) image of gold nanorods. (c) Gold nanorod sample preparation for photothermal experiment. (d) Photothermal reflectance image of a single gold nanorod.

Acknowledgements

This work was supported by the Korea Basic Science Institute Grant (grant number: D39615)

References

1. A.S. Stender, K. Marchuk, C. Liu, S. Sander, M.W. Meyer, E.A. Smith, B. Neupane, G. Wang, J. Li, J.-X. Cheng, B. Huang, N. Fang, *Chemical Reviews* 113 (4), 2469 (2013) doi:10.1021/cr300336e
2. D. Boyer, P. Tamarat, A. Maali, B. Lounis, M. Orrit, *Science* 297 (5584), 1160 (2002) doi:10.1126/science.1073765
3. S. Berciaud, L. Cognet, G.A. Blab, B. Lounis, *Physical Review Letters* 93 (25), 257402 (2004) doi:10.1103/PhysRevLett.93.257402
4. M. Selmke, M. Braun, F. Cichos, *ACS Nano* 6 (3), 2741 (2012) doi:10.1021/nn300181h
5. S. Arunkarthick, M.M. Bijeesh, G.K. Varier, M. Kowshik, P. Nandakumar, *Journal of Microscopy* 256 (2), 111 (2014) doi:10.1111/jmi.12164
6. W.J. Choi, S.Y. Ryu, J.K. Kim, J.Y. Kim, D.U. Kim, K.S. Chang, *Optics Letters* 38 (22), 4907 (2013) doi: 10.1364/OL.38.004907
7. D.U. Kim, C.B. Jeong, J.D. Kim, K.-S. Lee, H.H., K.-H. Nam, G.H. Kim, K.S. Chang, *Sensors* 17 (12), 2774 (2017) doi:10.3390/s17122774

Response Time Optimization of Photoacoustic Gas Analyzers

Diána Kiss⁽¹⁾, Anna Szabó^(1,2), Attila Czirják⁽³⁾, Gábor Szabó⁽¹⁾, Zoltán Bozóki^(1,2)

1. University of Szeged, Department of Optics and Quantum Electronics, Szeged, Hungary

2. Hobre Laser Technology Ltd., Algyő, Hungary

3. University of Szeged, Department of Theoretical Physics, Szeged, Hungary

kissdiana@titan.physx.u-szeged.hu, zbozoki@physx.u-szeged.hu

Monitoring and controlling of short-term physico-chemical processes frequently require gas analyzers with high time resolution. In-situ and real time gas measurements are essential to detect rapid changes and allow continuous optimization of industrial processes. Photoacoustic (PA) spectroscopy-based gas measuring systems meet the requirements of process analysis due to their high sensitivity, wide dynamic range, robust construction, automatic operation and short response time. The typical response time of a PA system is around 2-3 seconds, it is expected that the scope of applications can be extended by improving response time of the analyzers [1]. The scope of the present study was to shorten the response time of the longitudinal-differential cell-based PA systems [2].

Finite element analysis and visual investigation of the gas flow indicated that in the longitudinal-differential PA cell the purge of the gas sample is limited. Therefore, a diffuser allowing quicker purging was attached to the first buffer of the cell. Response time measurements of a PA system with longitudinal-differential cell (with and without diffuser) were performed with nitrogen monoxide (NO), nitrogen dioxide (NO₂), carbon monoxide (CO) and carbon dioxide (CO₂). Results showed that the diffuser reduces the response time on average by 35%. Furthermore, several factors influencing the response time were investigated (e.g. material of the cell and pipes, temperature, flow rate etc.). For NO and NO₂ measurement, heated polytetrafluoroethylene (PTFE) pipe was found to have the lowest response time. In case of NO and NO₂ measurement it is also important to operate the PA cell at elevated temperature, the optimal temperature was found to be 80°C. Moreover, the most important parameter is the flow rate of the gas sampling, which is highly limited by the PA cell, because above a certain flow rate the flow becomes turbulent resulting in rapidly decreasing signal-to-noise-ratio. It was found that the present system can be operated with a flow rate up to 1 liter/min, which in combination with the low volume of the cell results in short rinse time [3]. The optimization of these parameters and the use of the diffuser resulted in a reduced response time, which was found to be around 1 second. The efficiency of the diffuser was investigated by a finite element modelling performed in COMSOL Multiphysics 5.3. The results of the model proved efficiency of the diffuser. Figure 1. shows the streamlines of a PA cell without diffuser (a) and with diffuser (b).

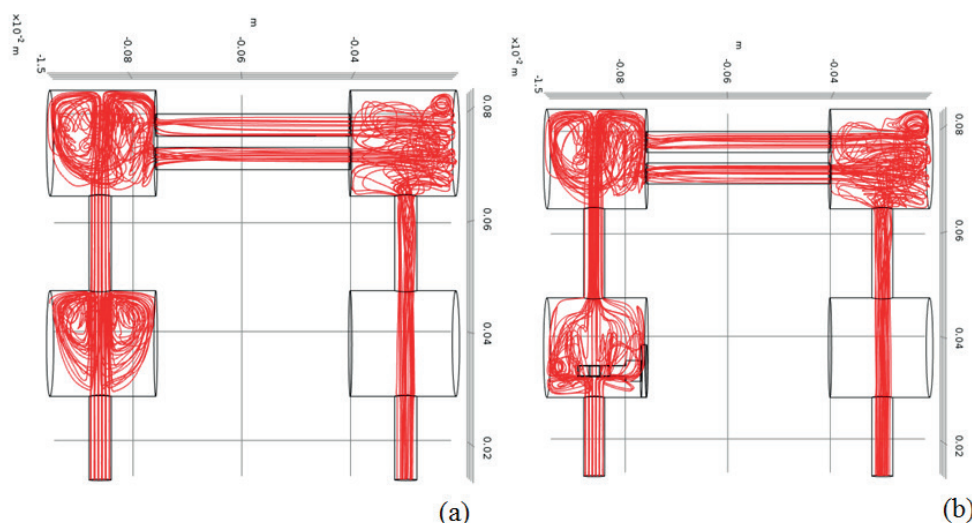


Fig. 1. Streamlines (a) PA cell without diffuser (b) PA cell with diffuser

In addition, the transfer function of the system can be calculated based on response time characteristics. If the transfer function of the system is known and the response of the system is measured, then convolution based analysis can be used to study real-time physico-chemical processes affecting the response time (e.g. adsorption-desorption).

E Methodologies of Photothermics, PA/OA, and Related Techniques

Acknowledgements

Our project was supported by GINOP-2.2.1-15-2017-00036 „LaserBox Rapid emission measurement technology”. Ministry of Human Capacities, Hungary grant 20391-3/2018/FEKUSTRAT is acknowledged.

References

1. D. Tátrai, Z. Bozóki, H. Smit, C. Rolf, N. Spelten, M. Kramer, A. Filegs, C. Gerbig, G. Gulyás, G. Szabó *Atmos. Meas. Tech. Discuss.*, 7, 6359-6384, (2014) doi:10.5194/amtd-7-6359-2014
2. A. Miklós, P. Hess, Z. Bozóki, *AIP Review of Scientific Instruments*, 72, 4, (2001) doi:10.1063/1.1353198
3. A. Schmohl, A. Miklos, P. Hess, *Applied Optics*, 40, 15, (2001) doi:10.1364/AO.40.002571

EP 020

Opto-Acoustic Frequency Combs

Alexandre KOLOMENSKII ^{(1)*}, Jian DONG ⁽¹⁾, Hans SCHUESSLER (1,2)

1. Department of Physics and Astronomy, Texas A&M University, College Station, Texas 77843-4242, USA

2. Science Program, Texas A&M University at Qatar, Doha 23874, Qatar

alexandr@physics.tamu.edu

Recently there was considerable interest in optical frequency combs broadly used for precision spectroscopy and metrology [1,2]. A frequency comb originates from a regular sequence of ultrashort pulses and in the spectral domain it presents a ruler with regularly spaced spectral lines. An acoustic frequency comb can be naturally produced by conversion of an optical pulse sequence into a sequence of acoustic pulses via opto-acoustic generation. The main features of frequency combs are their precision and stability. These are assured by locking the repetition rate and fixing the carrier-envelope phase. Typical frequencies in the optical domain determined by the repetition rate of pulses are in hundreds of MHz to GHz. The number of coherent spectral components (comb lines) in the frequency comb is determined by the ratio of the bandwidth of an individual pulse to the repetition rate. An acoustic frequency comb obtained with an 80MHz repetition rate of the optical frequency comb is shown in Fig. 1.

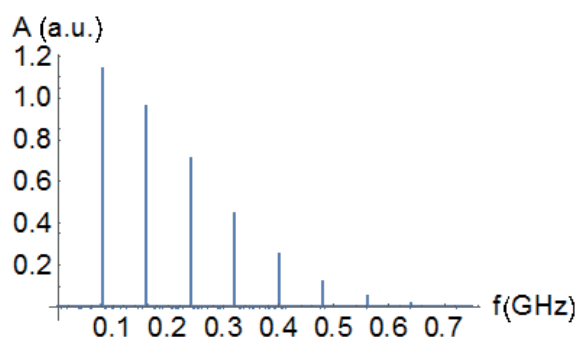


Fig. 1. Acoustic frequency comb obtained with an 80MHz repetition rate of the optical frequency comb.

If optical pulses are very short (of femtosecond duration), they can be assumed having temporal dependence of a δ -function in practical calculations of the generated acoustic pulses. Consequently, the upper limit for the obtained frequencies depends mainly on the parameters of the photo-acoustic conversion, such as the optical absorption coefficient, as well as on the bandwidth of the detection system. The possible applications of such acoustic frequency combs that carry massive amplitude as well as phase information include profilometry, ranging, calibration of microphones, determination of media absorption, studies of nonlinearities and precision frequency tuning and metrology.

Acknowledgements

This work was supported by the Robert A. Welch Foundation, grant No. A1546 and the Qatar Foundation, grant NPRP 8-735-1-154.

References

1. Th. Udem, R. Holzwarth, and T. W. Hänsch, *Nature* 416, 233-237 (2002) doi: 10.1038/416233a
2. F. Zhu, J. Xia, A. Bicer, J. Bounds, A. A. Kolomenskii, J. Strohaber, L. Johnson, M. Amani, and H. A. Schuessler, *Applied Optics* 56, 6311 (2017) doi: 10.1364/AO.56.006311

E Methodologies of Photothermics, PA/OA, and Related Techniques

EP 021

The Design of Windowless Photoacoustic Cell for Trace Gas Detection

Lixian Liu^{(1,2,3)*}, Huiting Huan^(1,2), Ming Zhang⁽¹⁾, Xiaopeng Shao⁽¹⁾, Andreas Mandelis⁽²⁾

1. School of Physics and Optoelectronic Engineering, Xidian University, Xi'an 710071, China

2. Center for Advanced Diffusion-Wave and Photoacoustic Technologies (CADIPT), Department of Mechanical and Industrial Engineering, University of Toronto, Toronto, Ontario M5S 3G8, Canada

3. CAS Key Laboratory of Spectral Imaging Technology, Xi'an 710119

Lixianliu@xidian.edu.cn

Photoacoustic Spectroscopy (PAS) technology is a widely recognized method for its excellent performance in trace gas detection and simplified experimental setups [1,2]. The detectivity of laser PAS reaches ppm~ppb levels, thanks to the high power and ultra-narrow spectral emission bandwidth of laser sources, and the high sensitivity of resonant cells. Although very weak, common mode interference signals generated from light absorption by resonator windows present a challenge for improving signal-to-noise ratio and gas detection sensitivity. Unless the noise is incoherent [3] i.e., unrelated to the incident light, the noise originated by window absorption is inevitable and almost impossible to remove by classical filtering methods, e.g. amplitude modulation. The application of closed photoacoustic resonators may be limited due to the requirement for externally linked circulation of the target gas. Unlike our recent windowed T-resonator design comprising resonance and absorption cylinders and its use in a PA cell [4], Fig. 1(a), a windowless photoacoustic cell is able to sufficiently suppress common mode interference by disposing of the glass windows and facilitating an open cell situation for light absorption by gases. In this presentation, a novel design of windowless photoacoustic T-resonator cell is presented. Use of a T-resonator is appropriate for the windowless cell design because its resonant frequency is mainly determined by the resonance cylinder perpendicular to the light absorption path.

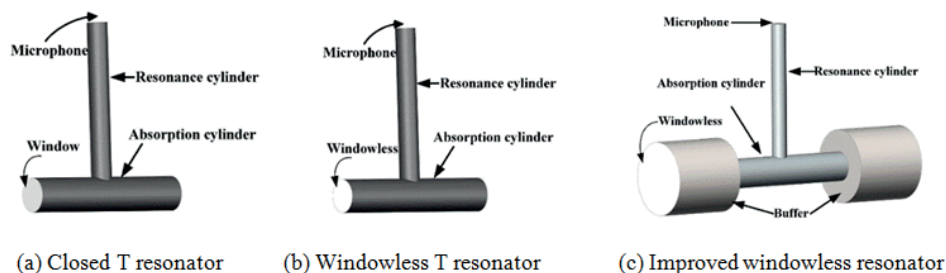


Fig. 1 T-type resonator models

Two possible designs of windowless cell are shown in Figs. 1(b) and 1(c). Both structures consist of T-type resonators with open ends on the absorption cylinders. In Fig. 1(c) two buffer cylinders are aligned on both ends through which the external acoustic noise is attenuated. The volumes of the buffers are designed so that the buffer acoustic impedance is relatively high at the resonance frequency. The performance of the windowless cells in Fig. 1 was tested by the finite element method (FEM).

The three different T-type resonators shown in Fig.1 were modeled with Comsol Multiphysics 5.2. The geometry of the absorption and resonance cylinders was identical for the three resonators and the lossy boundary conditions were adopted due to thermal and viscous losses at the resonator boundary. The FEM simulated amplitude response results are presented in Fig.2 which indicates optimal performance of the improved windowless resonator shown in Fig. 1(c). The latter was subsequently built and tested in the laboratory. In Table 1, although there is a large deviation of the resonance frequency of the three cells, the full width at half maximum (FWHM) of the improved windowless resonator is similar to the closed one and they are both much better than the characteristics of the windowless resonator. The improved windowless resonator with two buffers at both ends of the absorption cylinder has the capability for noise suppression and can be used as an open cell in trace gas detection applications.

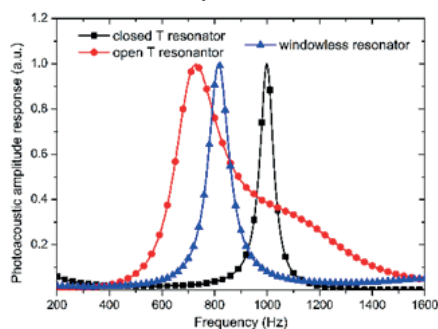


Fig. 2. The photoacoustic amplitude simulated response of three different resonators

E Methodologies of Photothermics, PA/OA, and Related Techniques

Due to non-window related coherent noise rejection and isolation from the ambient background noise, the improved T-type based windowless resonator is a competitive photoacoustic design for trace gas detection.

Table 1. The simulation results of the three T typed resonators

Cell Type	Resonance frequency (Hz)	FWHM (Hz)
Closed resonator	998	28
Open resonator	728	105
Windowless resonator	816	34

Acknowledgements

A.M. acknowledges the Natural Sciences and Engineering Research Council of Canada (NSERC) for a Discovery Grant. L. L. and H. H. are grateful to the National Science Foundation of China (Grant No. 61805187 and 61801358). This project was supported by the Open Research Fund of CAS Key Laboratory of Spectral Imaging Technology.

References

1. Z. Yu, J. Assif, G. Magoon, P. Keabian, W. Brown, W. Rundgren, J. Peck, R. Miake-Lye, D. Liscinsky, B. True, *Aerosol Science and Technology* 51 (12), 1438 (2017) doi: 10.1080/02786826.2017.1363866
2. L. Liu, A. Mandelis, H. Huan, K.H. Michaelian, *Optics Letters* 42 (7), 1424 (2017) doi: 10.1364/OL.42.001424
3. L. Liu, A. Mandelis, H. Huan, A. Melnikov, *Applied Physics B* 122, 268 (2016) doi: 10.1007/s00340-016-6545-2
4. L. Liu, A. Mandelis, H. Huan, K.H. Michaelian, A. Melnikov, *Vibrational Spectroscopy* 87, 94 (2016) doi: 10.1016/j.vibspec.2016.09.013

Determination of Soil Heavy Metal Contaminants based on Photoacoustic Spectroscopy

Lixian Liu ^{(1,2)*}, Huiting Huan ⁽¹⁾, Xiaopeng Shao ⁽¹⁾, Ming Zhang ⁽¹⁾

1. School of Physics and Optoelectronic Engineering, Xidian University, Xi'an 710071, China

2. CAS Key Laboratory of Spectral Imaging Technology, Xi'an 710119

lixianliu@xidian.edu.cn

Soil is one of the basic elements for ecosystem, as well as an indispensable natural resource to life on the Earth. However, soil pollution has become a worldwide focus, due to urban-industrial expansion and agricultural development[1]. Heavy metal contaminant issue is especially emphasized because of their toxicity and persistence, therefore there is an urgent need for cost-effective devices capable of recognizing and detecting various metals[3]. In this paper, we presented an alternatively approach based on photoacoustic spectroscopy (PAS) for high performance and non-destructive detection of heavy metal contamination in soil.

The broadband PAS configuration based on a Xenon lamp is depicted in Fig. 1. The incident light was directed into the photoacoustic chamber with 50% square-wave duty cycle chopper, using a monochromator for the optical wavelength scan. The photoacoustic signal generated by the sample in the cell was detected by a lock-in amplifier[4].

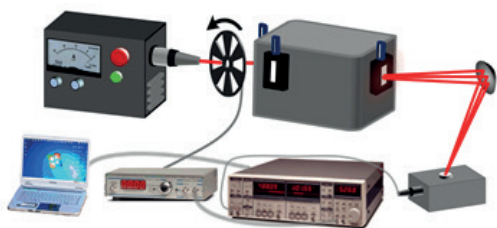


Fig. 1. The broadband PAS experimental schematic.

We chose cadmium nitrate tetrahydrate as the preferred test heavy contaminant. The reagent was of analytical pure and diluted with distilled water. The above 10 group soil samples with several Cd contaminant concentrations premixed with the artificial Cd reagent to stimulate industrial discharge pollution.

All the soil absorption spectra were normalized by the photoacoustic spectrum of carbon black. The typical photoacoustic absorption spectra of contaminated soil were depicted in Fig 2(a) with two predominant absorption peaks around 1400 nm and 1900 nm. These are correlated to clay humus and minerals which are abundant in the experimental soil samples (OH features of free water at

1400 nm and 1900 nm, Lattice OH features at 1400 nm). The characterized spectra illustrate a gradual increase of the photoacoustic amplitude signal with the rise in metallic ion contaminant concentration. This phenomenon indicates that the PAS configuration has potential for the featureless heavy mental contamination detection.

In order to establish a reliable and robust prediction model and improve the estimation accuracy, the obtained absorption spectra were pre-processed with five methods of mean centering (MC), first derivative (FD), standard normal variate (SNV), multiplicative scatter correction (MSC) and continuum removing (CR), and the results were shown in Fig. 2(b)-(f). All approaches strengthen the absorption features around 1900 nm where the peaks become more prominent. The preprocessed spectra indicate more obviously that the absorption peaks of soil decreases as the Cd concentration rises. These spectra processed by CR algorithm were more distinguishable than the others as the absorption peaks at 1400 nm are also revealed and steepened.

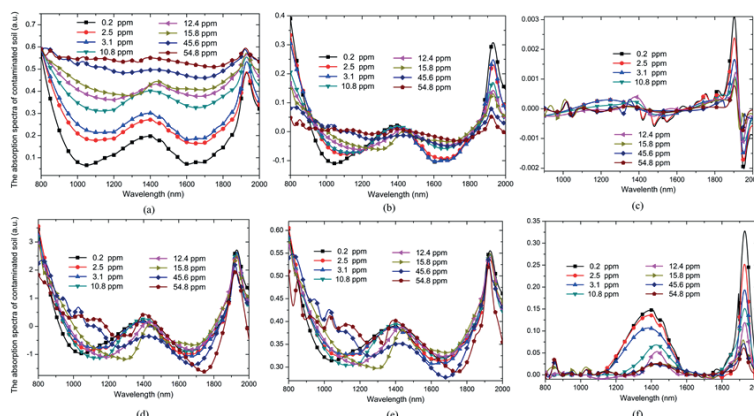


Fig. 2. The photoacoustic absorption spectra of contaminated soil preprocessed with different methods (a) The original spectra; (b) MC; (c) FD; (d) SNV; (e) MSC; (f) CR.

E Methodologies of Photothermics, PA/OA, and Related Techniques

A three-layer BP neural network was established for the quantification analysis of Cd residual. The whole absorption spectra acted as the net input as well as heavy metal Cd concentrations as the net output. Two-third of the sample data in each group were undertook for training the network, while the other one-third were set as test group. The best correlation coefficient was greater than 0.90 for the absorption data preprocessed with CR method. The experimental results exhibit the broadband PAS system with BP network has the capability for the quantification analysis of featureless toxic heavy mental contaminants in soil.

Acknowledgements

The authors are grateful to the National Science Foundation of China (Grant No. 61805187 and 61801358). This project was supported by the Open Research Fund of CAS Key Laboratory of Spectral Imaging Technology.

References

1. E. Ben-Dor, A. Banin, *Soil Science Society of America Journal*, 59, 364 (1995).
2. V.H. Dale, S. Brown, R.A. Haeuber, N.T. Hobbs, N. Huntly, R. J. Naiman, W. E. Riebsame, M.G. Tunner, T. J. Valone, *Journal of Applied Ecology*, 10, 63 (2000).
3. L. Liu, Y. Wang, C. Gao, H. Huan, *International Journal of Thermophysics*, 36(5), 868 (2015).

Neuro and neuro-fuzzy absorption efficiency determination by photoacoustic signal intensity sensing

M. Lukić¹, Ž. Čojbašić², D. D. Markushev³

1. Faculty of Occupational Safety, University of Niš, Čarnojevića 10a, Niš 18000, Serbia.

2. Mechanical Engineering Faculty, University of Niš, Aleksandra Medvedeva 14, Niš 18000, Serbia.

3. Institute of Physics, University of Belgrade, Pregrevica 118, Belgrade-Zemun 11080, Serbia.

Laser fluence Φ plays an important role in multiphoton absorption experiments. Variations of this parameter are the most common cause of error in photoacoustic (PA) measurements, as they can disguise the actual relationship between the absorption efficiency of different gases. In order to avoid adjusting the experimental set-up by repeating the experiment and the long procedure of calculating the signal parameters, the intelligent techniques [1] with the real-time results were applied. The Adaptive Neuro Fuzzy Inference System (ANFIS) [2] allows working with imprecise data, whereas the neural network, owing to its ability to adapt and learn from experience, automates the parameters change to the system phase and significantly accelerates it. The problem solved by ANFIS is the estimation of the energy density of laser radiation Φ based on the intensity I of the experimental photoacoustic (PA) signal. ANFIS training involved theoretical PA signals obtained by solving the wave equation using the Green functions for the Lorentzian profile with a hole, i.e. for conditions corresponding to the experimental set-up used. The intensities of the maximum (I_+) and the minimum (I_-) signals were the adaptive network input, while the value Φ was the network output. The experimental signals were generated in the $\text{SF}_6 + \text{Ar}$ mixture in the multiphoton regime, for the mixture pressure in the range of 10-100 mbar and the laser power Φ density in the range of 0,4–1,5 Jcm^{-2} . The pressure of the SF_6 absorber was constant and amounted to 0.47 mbar. ANFIS was tested with experimental PA signals.

Thanks to the significant contributions of ANFIS [3,4] in approximating functions, working with imprecise data, adapting to the environment as well as in error tolerance, there were better results in estimating Φ parameter compared to the results obtained by the neural network. The parameter Φ was estimated by ANFIS with a mean error of 9.32%, which is twice more precise than the value estimated by the neural network (18.18%). Working in real time and a simple description of the signals offer wide possibilities for the application of intelligent techniques in situ measurement of the trace gases concentration in the pulsed photoacoustics.

References

1. M.Lukić, Ž.Čojbašić, M.D.Rabasović, D.D. Markushev, D.M. Todorović Int.J.Thermophys.38:165 (2017)
2. J.S.R. Jang IEEE Trans. Syst., Man., Cybern. 23(3), 665-684 (1993)
3. K.L. Du, M.N.S. Swamy, Neural Networks and Statistical Learning. (Springer-Verlag London 2014)
4. A.P. Engelbrecht, Computational Intelligence. 2nd edition. (John Wiley and Sons 2007)

EP 024

Diffusion-Wave Inverse Problem Thermal Conductivity Depth-Profile Reconstructions Using an Integral Equation Approach

Andreas MANDELIS ^{(1)*}, Daren ZHENG ^(1,2), Alexander MELNIKOV ⁽¹⁾, Sahar KOOSHKI ^(1,3)

1. Center for Advanced Diffusion-Wave and Photoacoustic Technologies (CADIPT), University of Toronto, Toronto M5S 3G8, Canada
2. School of Energy and Power Engineering, Xi'an Jiaotong University, Xi'an, China
3. Mechanical Engineering, Yazd University, Yazd, Iran

mandelis@mie.utoronto.ca

The thermal-wave boundary-value problem in a semi-infinite thermophysically inhomogeneous solid can be described as follows:

$$\frac{\partial}{\partial x} \left[k(x) \frac{\partial T(x,t)}{\partial x} \right] = C(x) \frac{\partial T(x,t)}{\partial t}; \quad t \geq 0; \quad 0 \leq x < \infty \quad (1)$$

$$\text{with } -k(0) \frac{\partial T(x,t)}{\partial x} \Big|_{x=0} = \frac{1}{2} F_0 e^{i\omega_0 t} \quad \text{and } C(x) \equiv \rho(x)c(x) \quad , \quad (2)$$

where F_0 is the incident (photo)thermal flux, $p(x)$ is the density, $k(x)$ is the thermal conductivity and $c(x)$ the specific heat of the material; ω_0 is the modulation angular frequency. Introducing the Green function, $G(x|x_0)$, approach yields the formal solution to the inhomogeneous problem in the frequency domain in the form of a Fredholm-type integral equation:

$$T(x; \omega_0) = -i\omega_0 \int_0^\infty G(x|x_0) T(x_0; \omega_0) C(x_0) dx_0 - k(0) G(x|0) \left[\frac{dT(x_0; \omega_0)}{dx_0} \Big|_{x_0=0} \right] \quad (3)$$

Solving this equation using a trial function $T(x_0; p) = e^{-px_0}$ in the integrand and

$$\frac{dT(x; p)}{dx_0} \Big|_{x_0=0} = -p \quad (4)$$

where $p = (i\omega_0/\alpha_0)^{1/2}$ is a spatial Laplace variable with α_0 being the thermal diffusivity of the homogeneous solid substrate on which the inhomogeneous thermophysical properties have been imposed, results in an inverse relation between the thermal conductivity depth profile and the inverse Laplace transform of the thermal diffusion-wave frequency response:

$$\frac{1}{k(x)} = \frac{d}{dx} \left(L^{-1} \left[\frac{T(0; p)}{p} \right] \right) \quad (5)$$

Here, L^{-1} denotes inverse spatial Laplace transformation

Fig. 1 shows inversion pairs (conductivity and frequency response) in the case of constant, increasing, and decreasing thermal conductivity depth profiles, the constant case being in agreement with the well-known analytical solution [1]. Fig. 2 shows the inversion pair in the case of $k(x)$ depth profiles with maximum and minimum. The method is currently being applied to the non-destructive reconstruction of thermophysical depth profiles in manufactured solids such as metal powder compacts used for parts in the automotive industry.

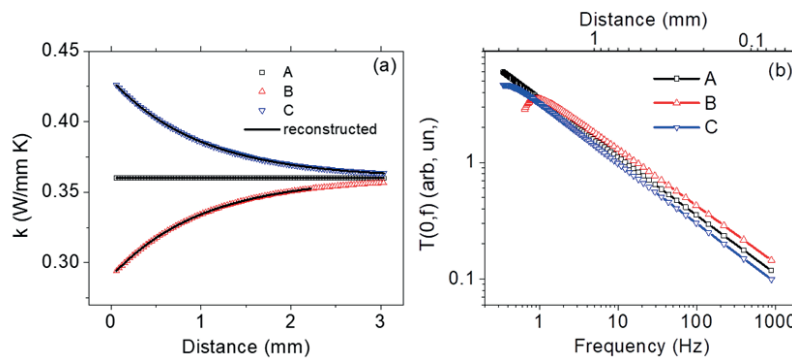


Fig. 1. Thermal conductivity depth profiles (a) and corresponding frequency responses (b) in case of constant (A), increasing (B), and decreasing (C) thermal conductivity. The reconstructed conductivity profiles are also shown in (a) superposed on the assumed profiles.

E Methodologies of Photothermics, PA/OA, and Related Techniques

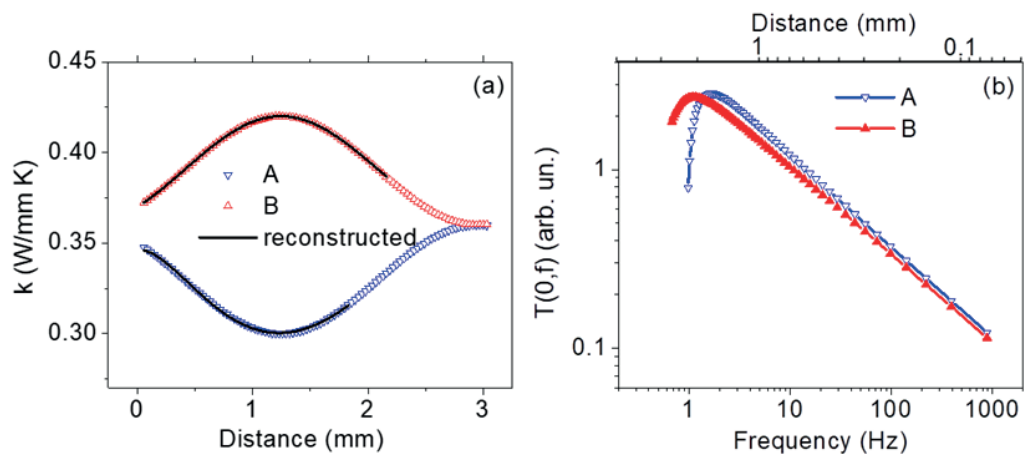


Fig. 2. Thermal conductivity depth profiles (a) and corresponding frequency responses (b) in case of non-monotonic distributions with minimum (A) and maximum (B) profiles. The reconstructed conductivity profiles are also shown in (a) superposed on the assumed profiles.

References

1. A. Mandelis, Diffusion-Wave Fields, Springer, New York 2001, Chap. 2.

EP 025

Measurement of Space-Dependent Thermal Diffusivities by Photo-Activated Thermography

Mario MARINI, Margaux BOUZIN, Amirbahador ZEYNALI, Laura SIRONI,
Laura D'ALFONSO, Giuseppe CHIRICO, Maddalena COLLINI*

1. Physics Department, Università degli Studi di Milano-Bicocca, Piazza della Scienza 3, 20126, Milano, Italy

**maddalena.collini@unimib.it*

The ability to monitor, control and predict thermal conduction is beneficial in a variety of research areas ranging from bio- and nano-technology to electronics and materials engineering. The assessment of thermo-physical properties enables the characterization of newly synthesized materials, allows targeting photo-thermal biomedical applications of nanostructured devices, and ensures the long-lasting good performance of electronic and mechanical components subject to intensive heat load. However, structural defects, disorder, porosity-related effects and/or anisotropies inherent in the fabrication process largely impact on the thermal properties of any material: accurate theoretical prediction of thermal conductivity and diffusivity values is hard to achieve, and methods aimed at their direct non-invasive experimental measurement are constantly being developed.

Visible to near infrared pulsed laser-light illumination of absorbing samples, coupled to the space-time monitoring of the front-face diffusion of the thermal wave by conventional far infrared thermography, allows the accurate and non-contact on-site quantification of thermal diffusivities. In this work, we build on the well-established flash method and investigate the possibility of deriving and spatially mapping in-plane thermal diffusivity values under low-power modulated Gaussian illumination of thin IR-opaque solid slabs.

We first write the fully analytical Fourier-space solution for the two-dimensional heat-transfer equation in the presence of a Gaussian, temporally extended, laser pulse impinging on an ideally infinite isotropic absorbing surface. The space and time dependence of the laser-induced temperature variation in the direct space is then deduced by numerical integration and simulated. With the aim of a direct measurement of the thermal diffusivity, we devise a protocol to extract this parameter from the temporal broadening of the temperature profiles width, irrespectively of the laser power, excitation laser beam waist and material grey-body emissivity. The impact of first-order heat losses by both radiation and convection to the surrounding atmosphere is accounted for and included in the model.

The correctness of the theoretical framework and the accuracy of the diffusivity measurement procedure are tested at first against finite-elements numerical simulations. By implementing laser-primed heat transfer on standard metallic and polymeric materials of known thermo-physical properties, we confirm that the analysis of simulated temperature peaks enables accurate retrieval of the adopted diffusivity values. Furthermore, we quantify the negligible impact of a \sim millimeter-sized sample thickness on the recovered parameters and evaluate heat-confinement effects due to the finite (\sim cm²) sample extension in the measurement plane. Results are further corroborated by experimental validation with room-temperature diffusivity measurements on thin uniform glass slides.

Finally, numerical simulations performed in the simplest case of homogeneous slabs are extended to composite and anisotropic materials aiming at the spatial mapping of diffusivity values on laser-scanned discontinuous materials with space-dependent thermal properties. The space resolution is quantified as a function of the (\sim 10-100 μ m) waist of the scanned excitation laser beam and of the observed thermal diffusivities. Current investigation is being directed towards the experimental proof-of-principle recovery of spatial maps of diffusivity values, to be combined with the usual temperature-based content of infrared images.

Resonant opto-acoustic cells. Data processing algorithm optimization

A. A. Markelov ^{*(1,2,4)}, A. I. Karapuzikov ^(1,4), M. Yu. Shtyrov ⁽¹⁾,
M. B. Miroshnichenko ^(1,2), A. V. Boykova ^(3,4)

1. *Special technologies Ltd., Novosibirsk, 630060, Russia.*
2. *Institute of Strength Physics and Materials Science SB RAS, Russia.*
3. *Novosibirsk State Technical University, Novosibirsk, Russia.*
4. *Institute of laser physics SB RAS, Novosibirsk, Russia.*

markellexa@mail.ru, ir@laser.nsc.ru, maximsh@ngs.ru, maks.mirash@gmail.com, helloanna999@mail.ru

Resonant opto-acoustic cells are used in some gas analysis applications such as SF₆LaserGasTest leak detector [1] and the Laser-Breeze gas analyzer [2]. Radiation sources in such case operates in pulse-periodic generation mode. Key factor of source operation in a resonant system is pulse repetition frequency, which must very well correspond to resonant frequency of the cell. The resonant frequency of the cell changes in case of temperature drift or gas composition variation. Misalignment of cell resonant frequency and radiation pulse repetition frequency dramatically reduces precision and stability of a device readings.

To determine the resonant frequency of the cell an auxiliary sound source was used [3]. Redefinition of the cell resonant frequency is possible only after interrupting of gas concentration measurement process. This fact is significant disadvantage of the method in use.

Designed data processing algorithm takes into account the phase of signal of resonant cell microphones. Special method was designed to adjust radiation source frequency to cell resonant frequency. Requirements for Fourier Transformation algorithm realization were revised and utilized in synthesized algorithm. Experimentally confirmed that the algorithm had been utilized in SF₆Laser-GasTest leak detector allows to measure the SF₆ concentration of 20 ppbv in the gas sample with an accuracy of $\pm 1.5\%$.

Acknowledgements

This research was supported by State Academies of Sciences through the Program of Basic Scientific Research of the 2013-2020, directions III.23, II.11.

References

1. I.V. Sherstov, Vadim Vasiliev, A.I. Karapuzikov, K. G. Zenov, R.V. Pustovalova, Instruments and Experimental Techniques 61(4), 2018 doi: 10.1134/S0020441218030259
2. A.A. Karapuzikov, I.V. Sherstov, D.B. Kolker, A.I. Karapuzikov, Y.V. Kistenev, D.A. Kuzmin, M.Y. Shtyrov, N.Y. Dukhovnikova, K.G. Zenov, A.A. Boyko, M.K. Starikova, I.I. Tikhonyuk, I.B. Miroshnichenko, M.B. Miroshnichenko, Y.B. Myakishev, V.N. Lokonov, Physics of Wave Phenomena 22(3), 2014 doi: 10.3103/S1541308X14030054
3. I.V. Sherstov, V.A. Vasiliev, A.M. Goncharenko, K.G. Zenov, R.V. Pustovalova, A.I. Karapuzikov Instruments and Experimental Techniques, 59(5), 2016 doi: 10.1134/S0020441216050079

EP 027

Thermal-wave resonant cavity model fitting in the complex plane for thermal diffusivity determination in liquids

Rubén Arturo MEDINA ESQUIVEL *, Caridad Guadalupe VALES PINZÓN,
Miguel Ángel ZAMBRANO ARJONA, Jorge Eduardo MAY AKE,
Francisco Ramón PEÑUÑURI ANGUIANO

*Facultad de Ingeniería-UADY, Av. Industrias no Contaminantes por Periférico Norte, Apdo. Postal 150 Cordemex, 97310 Mérida,
Yucatán, Mexico*

*ruben.medina@correo.uady.mx, caridad.vales@correo.uady.mx, miguel.zambrano@correo.uady.mx,
jmay@correo.uady.mx, francisco.pa@correo.uady.mx*

Thermal properties of different kind of liquids are obtained by fitting directly in the complex plane, the pyroelectric model of the thermal-wave resonant cavity signal. In this technique, it is a common practice to separately use the amplitude and phase of the complex signal to obtain the thermal diffusivity of the fluid sample, which must be compatible. However, the sensor signal is a complex function and metrological advantages are presented when the complex fitting of the signal as a function of sample thickness is used. To demonstrate the convenience of the proposed methodology, common liquids, such as distilled water, ethylene glycol, ethanol and a mixtures of ethanol water, were analyzed. With the use of this methodology we obtained that thermal diffusivity measurements was in good agreement with those reported in the literature.

Acknowledgements

This work was supported by SEP- CONACYT-CB-2015-256497 and Project CONACYT-SENER 254667.

Finite size and square geometry sensor effects in photothermal radiometry phase method

Miguel Ángel ZAMBRANO ARJONA, Rubén Arturo MEDINA ESQUIVEL *,
Caridad Guadalupe VALES PINZÓN, Francisco Ramón PEÑUÑURI ANGUIANO

*Facultad de Ingeniería-UADY, Av. Industrias no Contaminantes por Periférico Norte, Apdo. Postal 150 Cordemex, 97310 Mérida,
Yucatán, Mexico*

*miguel.zambrano@correo.uady.mx, ruben.medina@correo.uady.mx, caridad.vales@correo.uady.mx,
francisco.pa@correo.uady.mx*

Photothermal radiometry has been widely used to obtain lateral thermal diffusivity of solid materials. It is well known that thermal field phase has a linear behavior when measured as a function of the excitation source distance, particularly, inside the excitation source the signal phase is flat. In this work we analyze the effect of the size and square geometry of the IR sensor, on the temperature field measurement. Calculations showed that temperature field phase will remain flat when measured as a function of the distance to the excitation source, if sensor size is larger than the radius of the excitation source. On the other hand, to observe the linear behavior, measurements beyond half the size of the sensor have to be performed. The linear behavior is found in thermally thick and thin samples. Experimental results are performed using sensors of different sizes, particularly $50\ \mu\text{m} \times 50\ \mu\text{m}$, $1\ \text{mm} \times 1\ \text{mm}$ and $4\ \text{mm} \times 4\ \text{mm}$.

Acknowledgements

This work was supported by SEP- CONACYT-CB-2015-256497 and Project CONACYT-SENER 254667.

Graphene heat spreaders for a THz diode made of a vertical G-MGIM

E. Moreno ^{(1)*}, P. Cruz-Hernández ⁽²⁾, E.A. Michael ⁽¹⁾

1. Dept. of Electronic, U. of Chile, Av. Tupper 2007, Santiago, 8370451, Chile *enrique.moreno@raig.uchile.cl

2. Dept. of Mining Engineering, U. of Chile, Av. Tupper 2069, Santiago, 8370451, Chile

This work is focused on a vertical receiver made of Graphene-Metal-Graphene-Insulator-Metal junction (G-MGIM), which is a kind of Metal-Insulator-Metal (MIM) junction. MIM junctions are quantum diodes, which operate at room temperature and can sample infrared and even optical frequencies. G-MGIM is illuminated under Kretschmann and Reather’s configuration [2] which permits an external illumination distributed all along the MIM junction length. A well-established condition essential for this kind of illumination is given by the equation $\sqrt{\epsilon_{Glass}} \sin\theta = \frac{\epsilon_{Al} \epsilon_{Al_2O_3}}{\epsilon_{Al} + \epsilon_{Al_2O_3}}$ (Fig. 1a). The angle fits the incident p-wave momentum, outside the junction, to the momentum associated with the TM polarized SPP-TW inside the junction p-wave momentum, outside the junction, and to the momentum associated with the TM polarized SPP-W inside the junction [2]. A distributed illumination generated by the astigmatic lens is used in order to stimuli the entire MIM junction and harvest the current.

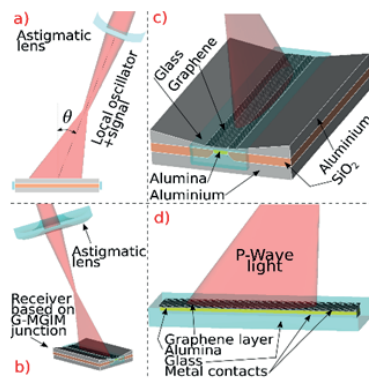


Fig. 1 (a) Inc. angle, (b) area, (c) setup, (d) g-MGIM junction.

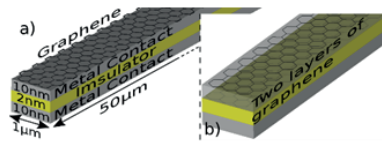


Fig. 2 (a) Geometry and dimensions, (b) location of graphene layers.

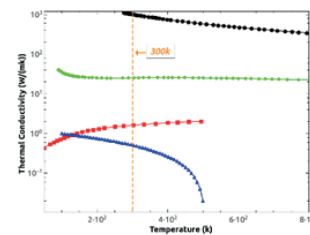


Fig. 3 Thermal conductivities versus Temperature $k(T(\vec{r}))$.

Figures 1 and 2 illustrate two layers of graphene, one in contact with metal and another in the region where the SPP-TW is induced. Graphene has been already employed in vertical quantum rectifiers [4]. The convenient illumination technique introduced above necessitates a metal layer. We consider a junction made with a sandwich-like of graphene-aluminum-graphene-alumina-aluminum. The high conductivity of the aluminum at 30THz together with graphene is physisorbed on Al justifies its election. The inner layer of graphene pursues boost the asymmetry in the current-voltage curve by means of an active barrier of electric potential induced by the Seebeck effect which is created in the graphene by the SSP-TW [4].

The goal of the present work is to study the top layer graphene as a spreader of heat [5]. At room temperature, Al follows the Wiedemann-Franz law and an increment in temperature means a reduction in the electric conductivity, also the calculated θ cannot agree on the desirable one, due to its dependency on the complex electric permittivity of the metal which varies with the temperature [6]. Here, we show how the top layer of graphene extracts heat from the top metal contact and moves it to the bulky lateral metal paddles which simply sink the heat.

The Model. First, we solve the curl Maxwell equations using auxiliary differential-equation difference-time-domain-technique (ADE-FDTD) and illuminating the structure [7]. We record the electromagnetic field in the top metal layer during a period of laser t_{rec} . Therefore, we determine the heat equation: $\nabla \cdot (k(T(\vec{r})) \nabla T(\vec{r})) = -\frac{1}{2t_{rec}} \int_0^{t_{rec}} Re([\epsilon_{Al}] |\vec{E}(\vec{r}, t)|^2 + \mu_0 |\vec{H}(\vec{r}, t)|^2) dt$. The thermal conductivity of the metal (Fig. 3), as well as the insulator value, are lower than in bulky block [8], also graphene thermal conductivity has been reduced assuming the same behavior. Electromagnetically, graphene is treated as a 2D conductivity layer as a boundary condition [9]. In [9] the range of frequency allows considering only intra-band conductivity. In mid-infrared the inter-band conductivity dominates and it cannot be removed from the calculation. We consider the first term of Taylor series

E Methodologies of Photothermics, PA/OA, and Related Techniques

$$\sigma_{inter} = \frac{-jq^2}{4\pi\hbar} \ln \left(\frac{2|\mu_c| - \hbar(\omega - j2\Gamma)}{2|\mu_c| + \hbar(\omega - j2\Gamma)} \right) = \frac{-jq^2}{4\pi\hbar} \ln \ln \left(\frac{1+\theta}{1-\theta} \right) = \frac{-jq^2}{4\pi\hbar} \sum_{n=1}^{\infty} \frac{\theta^{2n-1}}{2n-1},$$

$$\text{where } \theta = \frac{-\hbar(\omega - j2\Gamma)}{2|\mu_c|} \text{ and at } 30\text{THz } |\theta| \ll 1 \text{ and hence } \sigma_{inter} \approx \frac{q^2(j\omega + 2\Gamma)}{8\pi|\mu_c|}$$

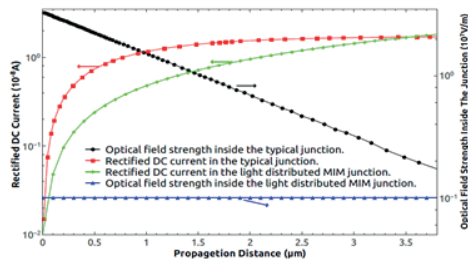


Fig. 4 Comparison of results taken of Fig. 6 of [11] with results produced by a distributed illumination based in [7] configuration.

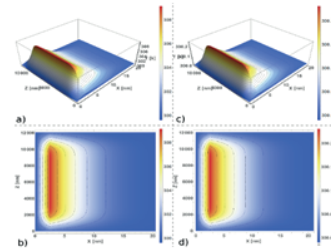


Fig. 5 ab) 3-2D temperature distribution from the top metal without graphene, cd) 3-2D temperature distribution from the top metal with graphene.

We compare the temperature distribution, from the top metal contact to the rest of the sandwich without graphene as it is portrayed in Figs.5, with the one same distribution when there is a layer of graphene on the metal. At room temperature we find in [7] a responsivity of $0.24 \frac{\mu\text{W}}{\text{W}}$ which is approximately twelve times the responsivity achieved by a traveling-wave in [10] at $10\mu\text{m}$ (see figure 6 in [10]). Fig.4 can explain this difference. To preserve a constant temperature on the top metal contact is important, and a simple layer of graphene works as a cooling system that guarantees this under an intense laser power.

References

- 1 S. G. "Applicability of Metal/Insulator/Metal (MIM) Diodes to Solar Rectennas" Photovoltaics, IEEE J., 2011.
- 2 C. D. Geddes, Reviews in Plasmonics 2016, C. D. E. Geddes, Ed.Springer, 2016.
- 3 M. S. et al., "High performance metal-insulator-graphene diodes for radio frequency power detection application" Nanoscale, 2017.
- 4 V. S. et al., "Plasmon induced thermoelectric effect in graphene" Nature Communications, 2018.
- 5 S. S. et al., "Graphene heat spreaders for thermal management of nanoelectronic circuits" IEEE, 2009.
- 6 A. M. et al., "Optical absorption in aluminium and the effect of temperature" J. of Physics F: Metal Physics.
- 7 https://drive.google.com/file/d/1Mr5EiwIICx6DAj_HkKbBI98wEZWEJ9Ow/view
- 8 C. et al., "Thermal study of multilayer resistive random access memories based on hfo2 and Al2O3 oxides" 2019, J. of V. S. & Technology B.
- 9 V. N. et al., "Modeling graphene in the finite-difference time-domain method using a surface boundary condition" Transaction on Antennas and Propagation, 2013.
- 10 S. G. et al., "Traveling-Wave Metal/Insulator/Metal Diodes for Improved Infrared Bandwidth and Efficiency of Antenna-Coupled Rectifiers" Nanotechnology, IEEE Transactions on, vol. 9, no. 6, pp. 716-722, Nov 2010.

EP 030

A Far-Field Thermal Diode: Preliminary Results

Juan José ALVARADO-GIL⁽¹⁾, Ivan Yecid FORERO-SANDOVAL⁽¹⁾, Cindy Lorena GOMEZ-HEREDIA⁽¹⁾, Jorge Andres RAMIREZ-RINCON⁽¹⁾, José ORDONEZ-MIRANDA^{(2)*}, Karl JOULIAN⁽²⁾, Yunez EZZAHARI⁽²⁾, Corinne CHAMPEAUX⁽³⁾, Frédéric DUMAS-BOUCHIAT⁽³⁾

1 Applied Physics Department, CINVESTAV-IPN Mérida, Mexico.

2 Institut Pprime, CNRS, Université de Poitiers, ISAE-ENSMA, F-86962, Futuroscope Chasseneuil, France.

3 Université de Limoges, CNRS, IRCER, UMR 7315, F-87000, Limoges, France

jjag09@yahoo.com

The management and control of heat flux require the design of high-efficient devices, such as rectifiers. The rectification of the radiative flow has been theoretically discussed in the literature and the use of VO₂ has been suggested for the construction of devices, mainly due to the possibility of taking advantage of thermal hysteresis and the dependence of emissivity with temperature [1-5]. In this work, the experimental design and preliminary results of a macroscopic VO₂-based thermal diode operating in the far-field regime are presented and discussed. Our system consists of two terminals, the first one is composed by a thin VO₂ film deposited on sapphire and the second consists of a heat flux meter, both terminals are attached to a temperature control system, in order to establish an appropriate temperature gradient between them, which allows us to record their temperatures and exchanged heat flux with high accuracy, stability, and reproducibility. By varying the temperature of the VO₂-based terminal around the transition temperature (68 °C) of VO₂, a rectification factor as high as 40% is obtained. As this rectification is driven by the radiative heat flux, higher rectification factors are expected for a thermal diode operating in vacuum, which is an ongoing work in our laboratory. Our design can also be the basis to extend the methodology to use a large variety of phase-change materials operating on a broad range of temperatures.

References

1. C. L. Gomez-Heredia, J. A. Ramirez-Rincon, J. Ordonez-Miranda, O. Ares, J. J. Alvarado-Gil, C. Champeaux, F. Dumas-Bouchiat, Y. Ezzahri, K. Joulain, *Scientific Reports* 8 8479 (2018) doi: 10.1038/s41598-018-26687-9
2. K. Ito, K. Nishikawa, H. Iizuka, and H. Toshiyoshi *Applied Physics Letters* 105 (25), 253503 (2014) doi: 10.1063/1.4905132
3. A. Fiorino, D. Thompson, L. Zhu, R. Mittapally, S. A. Biehs, O. Bezencenet, P. Reddy, *ACS Nano* 12 (6), 5174–5179 (2018) doi:10.1021/acsnano.8b01645
4. J. A. Ramirez-Rincon, C. L. Gomez-Heredia, A. Corvisier, J. Ordonez-Miranda, T. Girardeau, F. Paumier, C. Champeaux, F. Dumas-Bouchiat, Y. Ezzahri, K. Joulain, O. Ares, J. J. Alvarado-Gil, *Journal of Applied Physics* 124 (19) 195102 (2018) doi:10.1063/1.5049747
5. J. Ordonez-Miranda, Y. Ezzahri, J. Drevillon, and K. Joulain, *Physical Review Applied* 6 (5) 054003 (2016) doi: 0.1103/PhysRevApplied.6.054003

Deep neural network applied in calibration of transmission frequency gas-microphone photoacoustic

Miroslava I. JORDOVIC-PAVLOVIC⁽¹⁾, Dragan D.MARKUSHEV⁽²⁾, Aleksandar D. KUPUSINAC⁽³⁾, Katarina Lj. DJORDJEVIC⁽⁴⁾, Miodjub V. NESIC⁽⁵⁾, Slobodanka P.GALOVIC⁽⁵⁾, Marica N. Popovic⁽⁵⁾

1. College of Applied Sciences Uzice, Trg Svetog Save 34, Uzice

2. Institute of Physics, University of Belgrade, Pregrevica 118, 11080 Belgrade-Zemun, Serbia

3. Faculty of Technical Sciences, University of Novi Sad, Trg Dositeja Obradovića 6, 21000 Novi Sad, Serbia

4. Faculty of Physics, University of Belgrade, Studentski Trg 12, 11000 Belgrade, Serbia

5. Vinča Institute of Nuclear Sciences, P.O. Box 522, 11001 Belgrade, Serbia

Corresponding author: maricap@vin.bg.ac.rs

Calibration in gas-microphone photoacoustics is not easily achieved, mainly due to the impossibility of finding two identical microphones needed for the differential set-up (each of them introducing non-linear influence on the recorded PA response).

In this work, the methodology is developed which determines the influence of the used microphone, manifested through five characteristic frequencies which are functionally bonded to electronic and geometrical properties of the device. This is accomplished with the implementation of two-layer deep neural networks (fig. 1), enabling the filtration of the measured signal and thus removing the influence of the measurement chain on the photoacoustic response.

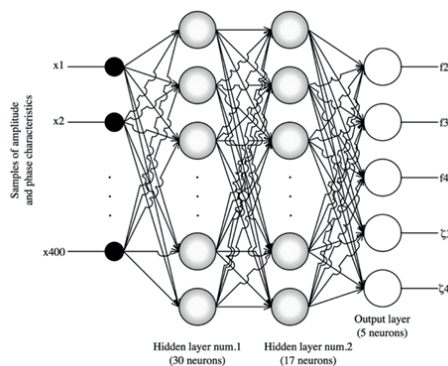


Fig. 1. An MLP with two hidden layers

Case study is done on PA measurements of laser-sintered polyamide (PA12), calibrated onto PA response of aluminum. Analysis of the obtained regression model for the prediction of the microphone parameters of PA response of aluminum is given in table 1.

Table 1. Analysis of the regression model for the prediction of the microphone parameters

	Accuracy		Cost		Numbers of epochs
Model 1	98.59%		0.000001		5000
Average deviation from the accurate value expressed in the percentage of the accurate value on the training set					
Parameter	f_2	f_3	f_4	ξ_3	ξ_4
Model 1	0.02025029	0.08571574	0.03485037	1.0117933	0.59135133
Average deviation from the accurate value expressed in the percentage of the accurate value on the validation set					
Parameter	f_2	f_3	f_4	ξ_3	ξ_4
Model 1	0.2028082	0.08540299	0.03530468	0.998583	0.60733956
Average deviation from the accurate value expressed in the percentage of the accurate value on the test set					
Parameter	f_2	f_3	f_4	ξ_3	ξ_4
Model 1	0.02026834	0.0861348	0.0351213	0.9855594	0.5777709
Prediction time					
	CPU time		Computation time		
Model 1	14 ms		31 ms		

E Methodologies of Photothermics, PA/OA, and Related Techniques

It is proven that this methodology successfully calibrates the measurement of examined samples onto a reference sample response, also filtrated from the measurement chain influence. It is also demonstrated that this procedure expands the frequency range for inverse solving of the PA problem, aiming at the estimation of thermal and optical sample properties, as well as improving their accuracy.

Acknowledgements

Authors wish to acknowledge the support of the Ministry of Education and Science of the Republic of Serbia for their support throughout the research projects III 45005 and OI 171016.

EP 032

Probing anisotropic heat transport using beam-offset method based on Time-Domain Thermoreflectance (TDTR)

Joan JAIME Puldon ^{(1)*}, David H. OLSON ⁽²⁾, John T. GASKINS ⁽²⁾, Ernesto MARIN ⁽²⁾,
Patrick E. HOPKINS ^(2, 3, 4)

1. *Instituto Politécnico Nacional, Centro de Investigación en Ciencia Aplicada y Tecnología Avanzada (CICATA) Unidad Legaria, Legaria 694, Colonia Irrigación, Delegación Miguel Hidalgo, Ciudad de México 11500, México.*
2. *Department of Mechanical and Aerospace Engineering, University of Virginia, Charlottesville, VA 22904, USA*
3. *Department of Materials Science and Engineering, University of Virginia, Charlottesville, Virginia 22904, USA*
4. *Department of Physics, University of Virginia, Charlottesville, Virginia 22904, USA*

jjaimepuldon@gmail.com

Anisotropic materials are ubiquitous in a wide range of applications such as electronics, thermoelectrics, and high-temperature superconductors, in all of which the thermal properties of the materials play a critical part. There are only a few experimental techniques that can be used to measure in-plane anisotropic thermal conductivity. An extension of time-domain thermoreflectance (TDTR) which utilizes offset pump and probe laser locations to measure in-plane thermal transport properties of multilayers materials was previously proposed [1-2]. In this work, we first conduct detailed signal sensitivity analyses for the beam-offset technique and show how it depends on the laser spot size and the modulation frequency. We use the full-width half-maxima of the out-of-phase beam offset sweep in a negative delay line position (e.g., -100ps), for calculating the in-plane thermal transport properties recommended by Feser et al. in [2]. The accuracy and limitations of the method are discussed based on measuring the in-plane thermal conductivity tensor of highly-oriented pyrolytic graphite (HOPG).

References

1. J. P. Feser and D. G. Cahill, *Rev. Sci. Instrum.* 83(10), 104901 (2012).
2. J. P. Feser, J. Liu, and D. G. Cahill, *Rev. Sci. Instrum.* 85(10), 104903 (2014).

EP 033

Angstrom configuration for measured absolute heat losses on metal sample by active thermography

Teodoro Cordova ^{(1)*}, Rosario L. Romero ⁽¹⁾, Rumen Ivanov ⁽²⁾, Jesús Villa ⁽³⁾, Daniel Alaniz ⁽³⁾

1. División de Ciencias e Ingenierías, Universidad de Guanajuato campuses León
Loma del Bosque N. 103, Lomas del Campestre, 37150 León, GTO, Mexico.

2. Facultad de Física, Universidad Autónoma de Zacatecas, Calz. Solidaridad Esquina Paseo
Bufa, s/n, Campus Universitario II, 98060 Zacatecas, ZAC, Mexico

3. Doctorado en Ciencias de la Ingeniería, Unidad Académica de Ingeniería Eléctrica,
Universidad Autónoma de Zacatecas, Antiguo Camino a la Bufa No. 1, Col. Centro.
98000, Zacatecas, ZAC. Mexico

Corresponding author: theo@fisica.ugto.mx

An experimental setup and optimized method for evaluating the heat loss coefficient averaged by the sample surface h_{average} are proposed in this work. A thermal camera along with the heat flow sensors were used to measure the heat loss coefficient in an absolute (non-relative) way. A numerical simulation was also done where minimum approximations are applied and no further adjustments with complicated theoretical models were necessary. Later, it was experimentally demonstrated that the heat loss coefficient does not depend on the thermal properties of the metal sample. The influence of the difference of the temperature of the sample with the room temperature, on the factor h is monotonously increasing independent from heating or cooling regime. The proposed method has the advantage that the value of heat loss coefficient is obtained experimentally, and the results are congruent with the COMSOL simulation outcomes.

Experiments were performed for the different samples with 12 heat flow values applied for each sample. Work was carried out in a steady state, in two modes: heating mode and cooling mode of the samples. Equality was always maintained for each measurement $\Phi_1 = \Phi_2$. Thermal relaxation time of the entire construction was also measured. Depending on the metal sample this time was from 30 sec to 45 sec. To ensure steady-state work for each measurement, the temperature was measured at least 30 minutes after changing the experimental conditions maintaining the equality between Φ_1 & Φ_2 .

The thermal camera along with the heat flow sensors can be used to measure the heat loss coefficient in an absolute (non-relative) way. An advantage of the proposed method is that the heat loss coefficient is obtained experimentally. Furthermore, in this procedure, minimum approximations are applied and no further adjustments with complicated theoretical models were necessary. It has been experimentally demonstrated that the heat loss coefficient does not depend on the thermal properties of the sample. The influence of the difference between the sample's temperature with the room temperature, on the factor h , is monotonously increasing without regard to the regime "to heat" or "to cool". Having knowledge of the heat loss coefficient can reduce errors in the results obtained from using this configuration to determine the thermal properties of the material.

References

- [1] : Emmanuel Rodriguez, Jorge Mireles, Cesar A.Terrazas, David Espalin, Mireya A.Perez, Ryan B.Wicker. Approximation of absolute surface temperature measurements of powder bed fusion additive manufacturing technology using in situ infrared thermography. *Additive Manufacturing*, 5, 31-39 (2015).
- [2] : Rubén Usamentiaga, Pablo Venegas, Jon Guerediaga, Laura Vega, Julio Molleda and Francisco G. Bulnes. Infrared Thermography for Temperature Measurement and Non-Destructive Testing. *Sensors*, 14(7): 12305-12348, (2014).
- [3] : Michael Vollmer, Klaus-Peter Möllmann. *Infrared Thermal Imaging: Fundamentals, Research and Applications*, Ed: "Wiley - VCH", 2-nd edition, Germany, (2018).
- [26] : Waldemar Minkina, Sebastian Dudzik, *Infrared Thermography: Errors and Uncertainties*, Ed.: John Wiley & Sons, Ltd, Chichester, UK
- [27] : D. Cárdenas-García, Emissivity measurement of high-emissivity black paint at CENAM, *Revista Mexicana de Física* 60 (2014) 305–308
- [28] <http://www.anape.es/pdf/ficha73.pdf>

Characteristic Analysis of Photoacoustic Sensing with Differential Torsion Beam

Rong LIANG*, Li CHEN

University of Electronic Science and Technology, Chengdu, China

201722050616@std.uestc.edu.cn

Photoacoustic spectroscopy (PAS) is a sensitive technique for trace gas detections [1-2]. The PAS signal is generated through the absorption of the modulated light by the samples inside the photoacoustic cell. This periodically varying pressure changes are detected with sensitive acoustic sensors, such as capacitive and electret microphones. Other types of acoustic sensor are developed to improve the detection sensitivity. Among them the most promising one is the optical sensor based on MEMS cantilever [3].

Since most PAS signals are in lower acoustic frequency range and the detection suffers from the environmental noises and vibrations. Therefore, only improving the sensitivity of the sensor may not yield optimal performance. The ability to suppress the environmental acoustic interference is very important for the detection system. This paper describes an optical PAS sensor based on a differential torsion beam design that has both high detection sensitivity for PAS signals and good performance on environmental noise suppression.

The differential torsion beam is firstly modeled with the finite element analysis as shown in Figure 1 (a). For comparison, Figure 1(b) shows the result for the cantilever design. The effects of air gap, beam length and other parameters on its frequency and amplitude characteristics are studied. For experiments, two types of MEMS sensor are fabricated with precision laser cutting on silicon wafers. The responses of the sensors are measured with a sensitive laser interferometry measurement system. The acoustic characteristics of the differential torsion beam are analyzed.

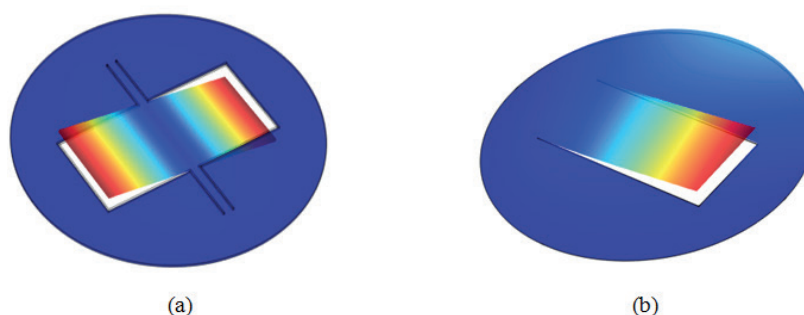


Fig. 1. Stimulation for two types of optical PAS sensors. (a) Differential torsion beam; (b) Cantilever.

References

1. J.Fonsen,V.Koskinen,K.Roth,et al,Vibrational Spectroscopy 50 (2), 214(2009)doi: 1 0.1016/j.vibspec.2008.12.001
2. V.Koskinen,J.Fonsen,K.Roth,et al,Applied Physics B,86(3),451(2007)doi:10.1007/s00340-006-2560-z
3. J. Kauppinen,K. Wilcken,I. Kauppinen, et al, Microchemical Journal 76(1-2),151(2004)doi:10.1016/j.micr--oc.2003.11.007

EP 035

A comparison of different techniques for photothermal super resolution image reconstruction

Samim AHMADI ^{(1)*}, Mathias ZIEGLER ⁽¹⁾, Erik THIEL ⁽¹⁾, Philipp HIRSCH ⁽¹⁾, Christina KARAGIANNI ⁽¹⁾, Peter BURGHOLZER ⁽²⁾, Günther MAYR ⁽³⁾, Peter JUNG ⁽⁴⁾, Giuseppe CAIRE ⁽⁴⁾

1. Bundesanstalt für Materialforschung und -prüfung (BAM), 12200 Berlin, Germany

2. RECENDT, Research Center for Non-Destructive Testing, Linz, Austria

3. Josef Ressel Center for Thermal NDE of Composites, University of Applied Sciences Upper Austria, Wels, Austria

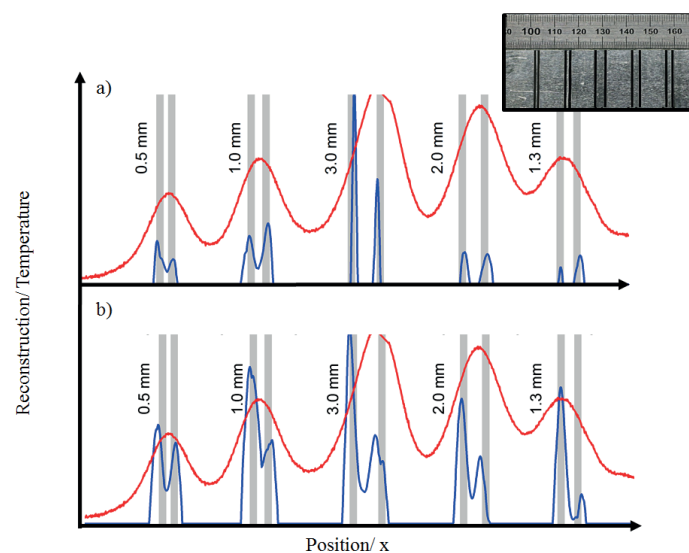
4. Technical University of Berlin, Department of Telecommunication System, Berlin, Germany

*samim.ahmadi@bam.de

The separation of two closely located defects in fields of Thermographic NDE is very challenging. The diffusive nature of thermal waves leads to a fundamental limitation in spatial resolution. Therefore, super resolution image reconstruction can be used. A new concerted ansatz based on spatially structured heating and joint sparsity of the signal ensemble allows an improved reconstruction of closely located defects [1,2]. This new technique has also been studied using 1D laser arrays in active thermography [3,4].

The post-processing can be roughly described by two steps: 1. Finding a sparse basis representation using a reconstruction algorithm such as the Fourier transform, 2. Application of an iterative joint sparsity (IJOSP) method to the firstly reconstructed data. For this reason, different methods in post-processing can be compared using the same measured data set.

The focus in this work was the variation of reconstruction algorithms in step 1 and its influence on the results from step 2. More precise, the measured thermal waves can be transformed to virtual (ultrasound) waves that can be processed by applying ultrasound reconstruction algorithms and finally the super resolution algorithm [1,3]. Otherwise, it is also possible to make use of a Fourier transform with a subsequent super resolution routine. These super resolution thermographic image reconstruction techniques in post-processing are discussed and evaluated regarding performance, accuracy and repeatability. The results of both methods are shown in Fig. 1.



References

1. P. Burgholzer, T. Berer, J. Gruber and G. Mayr, Applied Physics Letters, 111 (3), 031908 (2017)
2. T. W. Murray, M. Haltmeier, T. Berer, E. Leiss-Holzinger and P. Burgholzer, Optica, 4 (1), 17-22 (2017)
3. P. Burgholzer, T. Berer, J. Gruber, M. Ziegler, E. Thiel, S. Ahmadi and T. Studemund, QIRT Journal, submitted (2019)
4. M. Ziegler, E. Thiel and T. Studemund, Materials Testing, , 60 (7-8),749-757 (2018)

EP 036

The development of full-field material property characterization based on quantitative laser ultrasound visualization

Sheng-Po Tseng^{(1)*} and Che-Hua Yang⁽²⁾

Graduate Institute of Manufacture Technology, National Taipei University of Technology, Taipei, Taiwan

tseng3392@gmail.com

Motivation and Objective

This research employs a quantitative laser ultrasound visualization system (QLUVS) for the full-field mechanical property mapping in plate-like structures. The QLUVS has the advantage of fast, full-field and quantitative inspection. The QLUVS uses a pulsed laser generate acoustic waves with fast scanning mechanism to reach two dimensional scanning goal and then detected with a piezoelectric longitudinal transducer. By utilizing QLUVS, the spatial and temporal information of guided wave can be obtained with further signal processing, the velocity map can be extracted. Finally the analytical model and inversion algorithm will be integrated into QLUVS for the full-field mechanical property mapping purpose.

Methods

The ultrasound based technique, via generating with a pulsed laser and detecting with a transducer, quantitative laser ultrasound visualization (QLUV) system is developed. The QLUV system employs the pulsed laser to scan over the interested area on the surface of an arbitrary shape of material then detects with a piezoelectric transducer. With the aid of reciprocal theorem, dynamic behaviors of wave propagation can be reconstructed. With the QLUV system, the real image of Lamb wave propagation can be obtained and investigated. Further this research develops a novel algorithm called mechanical property mapping reconstruction algorithm, including spatial data interpolation method and database inversion method based on QLUVS to obtain the full-field mechanical property.

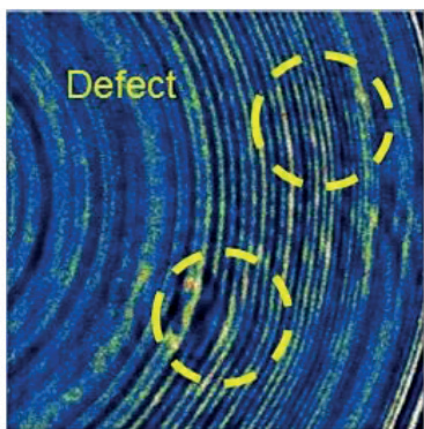


Fig. 1. The resolved wavefronts of aluminum plate with two defect.

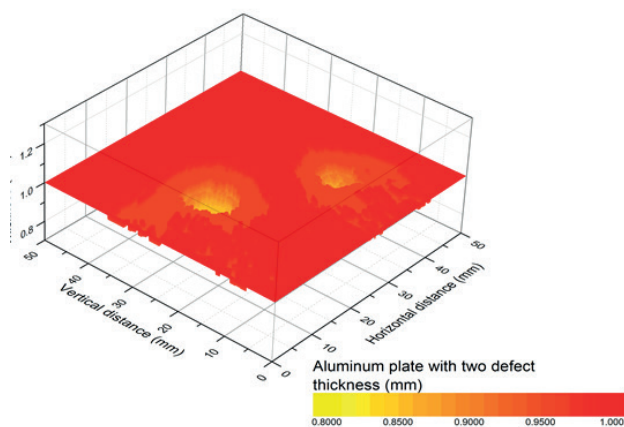


Fig. 2. Thickness's map for aluminum plate with two defect.

Results and discussion

The application of our algorithm to the thickness inversion of QLUVS data acquired on 1mm thick aluminum plate with machined defect. For aluminum with two defects, Fig. 1 shows the resolved wavefronts. According to these results, reflected wave and scattered wave can be observed obviously. Fig. 2 illustrates the application of our algorithm to the thickness inversion of QLUVS data acquired on 1mm thick aluminum plate with two machined defect. Utilizing the mechanical property mapping reconstruction algorithm, the thickness mapping can be reconstructed. It is shown thickness variation obviously.

Conclusions

This research demonstrates a inversion technique for the characterization of full-field material properties based on quantitative laser ultrasound visualization system. Utilizing the development of the full-field mechanical property inspection technology, full-field mechanical property measured by non-destructive, high-speed and high-precision measurements can be obtained in qualitative and quantitative results.

Acknowledgements

Financial support from the Featured Areas Research Center Program within the framework of the Higher Education Sprout Project by the Ministry of Education in Taiwan is gratefully acknowledgment.

E Methodologies of Photothermics, PA/OA, and Related Techniques

References

1. T. E. Michaels and J. E. Michaels, "Application of acoustic wavefield imaging to non contact ultrasonic inspection of bonded components," *Review of Progress in Quantitative Nondestructive Evaluation*, AIP, pp.1484-1491, 2006.
2. I. H. Liu and C.H. Yang, "An investigation on wedge waves and the interaction with a defect using a quantitative laser ultrasound visualization system," *IEEE Ultrasonics Symposium (IUS)*, 2010.
3. Hideo Nishino, Toshiro Tanaka, Kenichi Yoshida and Junji Takatsubo, "Simultaneous measurement of the phase and group velocities of Lamb waves in a laser generation based imaging method," *Ultrasonic*, 52, pp. 530-535, 2012.

Label-free molecule detection in 10^2 nm space by utilizing photothermal optical diffraction

Yoshiyuki Tsuyama, Kazuma Mawatari*

Graduate school of engineering, The University of Tokyo, Japan

tsuyama@icl.t.u-tokyo.ac.jp

Downscaling of analytical chemistry to nanofluidics (10^1 - 10^3 nm) provides ultra-sensitive analytical devices at single cell and single molecule level due to the ultra-small space [1], and sensitive detection method applicable to nanofluidics is strongly required. Label-free detection is also essential for targeting wide range of analytes. In our group, photothermal optical phase shift (POPS) detection method was developed and realized label-free protein molecule detection in $21 \mu\text{m} \times 900$ nm channel with LOD of 600 molecules [2]. However, for smaller channel than 900 nm, sensitivity of POPS rapidly decreases due to thermal diffusion to glass substrates. This physical limitation hinders POPS from applying to 10^1 - 10^2 nm channel. Here, we propose novel photothermal-based detection method for 10^1 - 10^2 nm channel: photothermal optical diffraction (POD). In this study, experimental setup was optimized and detection performance was evaluated. Also, signal enhancement by solvent effect was confirmed.

Figure. 1 shows the principle of POD. Because width of nanochannel (10^1 nm- 10^2 nm) is smaller than the focused probe beam spot ($\sim\mu\text{m}$), focused probe beam is diffracted by nanochannel, and diffracted light intensity (P_D) depends on the refractive index difference (Δn) between glass substrate ($n=1.46$) and water ($n=1.33$). Focused excitation beam induces photothermal effect of target molecules in the channel, followed by refractive index change of water and glass substrate due to the thermal diffusion. Refractive index response for temperature (dn/dT) of glass is 9.8×10^{-6} and dn/dT of water is -9.1×10^{-5} . Therefore, Δn becomes larger by photothermal effect, followed by diffracted light intensity change (ΔP_D) which is proportional to the number of molecules in the channel. In this detection principle, heat diffusion to the glass substrate also contributes to signal; POD is applicable to 102 nm channel.

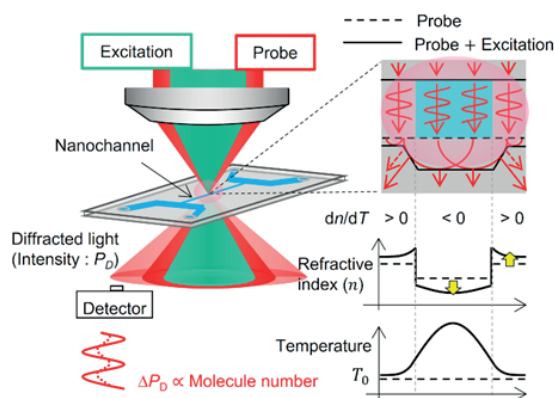


Fig.1. Principle of POD detection method

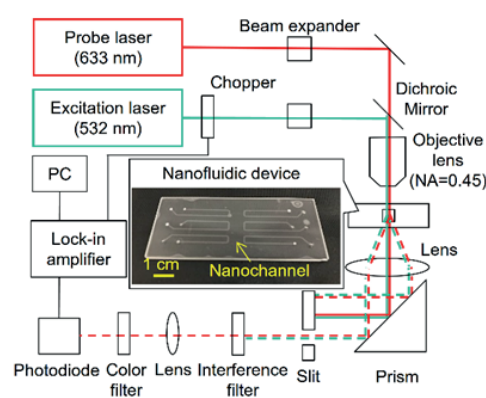


Fig.2. Experimental setup of POD detection method

Experiments and Results

Experimental setup is shown in Figure. 2. Width and depth of nanochannel were 400 nm, respectively. Sunset Yellow ($\epsilon=4800$ at 532 nm) aqueous solution was introduced to the channel. First, experimental conditions such as modulation frequency, laser intensity and detection position of diffracted light were optimized. Figure. 3 shows calibration curve for optimized experimental conditions. The limit of detection (LOD) is defined as a concentration that gives signal equivalent to background + 4σ , and σ is calculated from signal fluctuation of lowest concentration samples. The calculated LOD was $6.5 \mu\text{M}$, which corresponds to 900 molecules in a detection volume of 0.23 fL. Then, signal enhancement by solvent effect was confirmed. Sunset Yellow ethanol solution and SudanIV ($\epsilon=17700$ at 532 nm) acetonitrile solution was introduced to the channel, and sensitivities were compared with Sunset Yellow aqueous solution. Relative sensitivities for absorbance were shown in Figure. 4. By using ethanol solution and acetonitrile solution, sensitivities for absorbance were 1.9 and 3.9 times improved, respectively. The calculated LOD of SudanIV acetonitrile solution was $0.4 \mu\text{M}$ (60 molecules).

E Methodologies of Photothermics, PA/OA, and Related Techniques

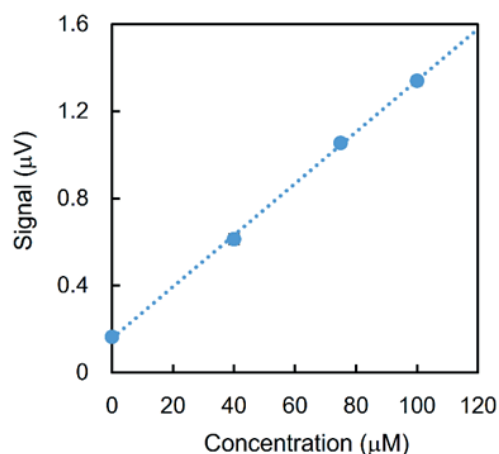


Fig.3. Calibration curve for Sunset Yellow aqueous solution.

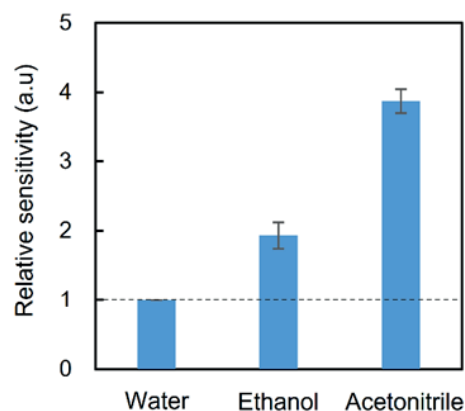


Fig.4. Comparison of relative sensitivity

Conclusions

By optimizing experimental condition of POD, LOD of 900 molecules was achieved in 10^2 nm channel. Furthermore, LOD of 60 molecules was achieved by using acetonitrile as a solution. Our method will be widely used for chemical and biological analyses in 10^2 - 10^3 nm space.

Acknowledgements

The authors gratefully acknowledge the financial support from the CREST (Core Research for Evolutional Science and Technology) of the Science and Technology Corporation (JST) of Japan

References

1. T. Nakao, Y. Kazoe, K. Morikawa, A. Yoshizaki, K. Mawatari and T. Kitamori, The Proceedings of TAS, 1, 133–134 (2018)
2. H. Shimizu, N. Miyawaki, Y. Asano, K. Mawatari, and T. Kitamori, Analytical Chemistry, 89 (11), 6043–6049 (2017) doi:10.1021/acs.analchem.7b00630

Determination of doping density and electrical resistivity of Si wafers with cavity ring-down technique

Qian WANG, Weiguo LIU, Lei GONG, Ligu Wang, Yaqing LI, Rong LIU

School of Optoelectronic Engineering, Xi'an Technological University, Xi'an 710021, China

qianwang@xatu.edu.cn

The four-point probe method and eddy current mapping is commonly used to measure resistivity (ρ) and doping density (N_d). [1] Recently, various contactless resistivity and doping density measurement methods based on photoluminescence (PL), such as dynamic PL [2], photocarrier radiometry [3] and lock-in carrierography [4] are also proposed. In this paper, a novel measurement method for doping density and resistivity of silicon wafers based on cavity ring-down (CRD) technique [5] is presented. The resistivity of wafers obtained by means of this methodology were compared with those obtained with conventional four-point probe measurements. The results indicated that the proposed method can be an alternative non-destructive tool for doping density and resistivity measurements.

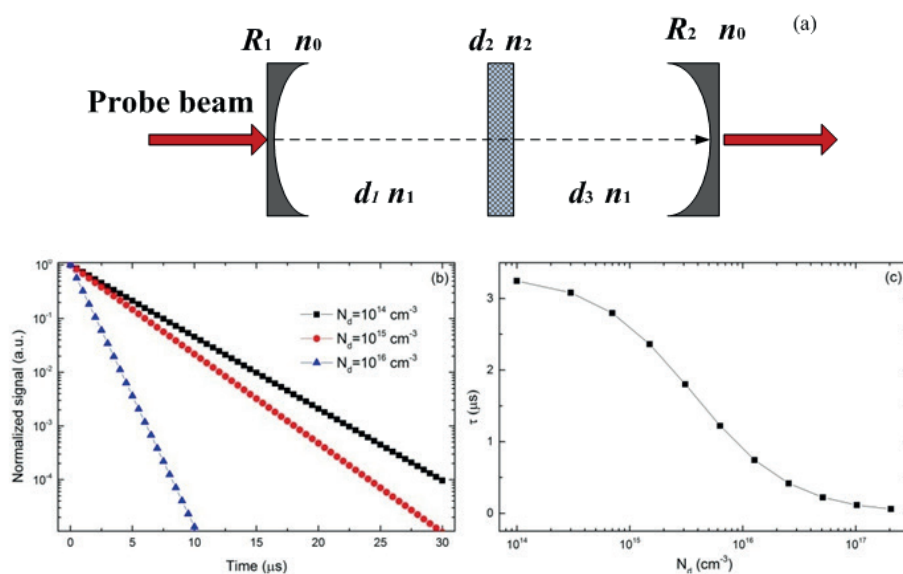


Fig. 1. (a) Configuration of a model cavity. (b) The normalized CRD signal for Si wafers with different doping density. (c) The decay time constant versus doping density of Si wafers.

Acknowledgements

The authors thank the financial support by the Natural Science Foundation of China (Grant Nos. 61704132, 61501363).

References

- [1] D. K. Schroder, Semiconductor Material and Device Characterization, Wiley New York, 2006, p. 34
- [2] J. A. Giesecke, M. C. Schubert, W. Warta, J. Appl. Phys. 112, 063704 (2012) doi: 10.1063/1.4752722
- [3] Q. M. Sun, A. Melnikov, J. Wang, A. Mandelis, J. Phys. D: Appl. Phys. 51,15LT01 (2018) doi: 10.1088/1361-6463/aab395
- [4] P. Song, A. Melnikov, Q. M. Sun, A. Mandelis, J. Y. Liu, Semicond. Sci. Technol. 33,12LT01 (2018) doi: 10.1088/1361-6641/aae810
- [5] A. Terasaki, T. Kondow and K. Egashira, J. Opt. Soc. Am. B 22, 675 (2005) doi: 10.1364/JOSAB.22.000675

EP 039

Comparison of techniques for multivariate analysis of photoacoustic spectra

Sander Vervoort^(1,2), Marcus Wolff^{(1)*}

1. Hamburg University of Applied Sciences, Hamburg, Germany

2. University of the West of Scotland, Paisley, UK

marcus.wolff@haw-hamburg.de

Photoacoustic Spectroscopy (PAS) is an extremely sensitive method for the detection of trace gases. It is based on the absorption of electromagnetic radiation and the non-radiating transfer of absorbed energy into heat. If the radiation is periodically modulated, expansion of the absorbing gas results in an acoustic wave with the modulation frequency [1]. We developed a photoacoustic analyzer for Volatile Organic Compounds (VOCs) that could serve in future breath tests for the detection of the lung cancer biomarkers 2-butanone, 1-propanol, isoprene, ethylbenzene, styrene and hexanal [2]. The analyzer is based on a continuous-wave Optical Parametric Oscillator (cw-OPO) as radiation source and an all-optical Mach-Zehnder modulator. The photoacoustic signal is detected by a digital MEMS microphone [3].

The concentrations of the single components are determined by multivariate analysis of the photoacoustic spectra. In this process it has to be considered that interdependencies of predictor variables (PA signal) could negatively affect the accuracy of the results. A variable selection or dimension reduction can prevent this [4]. Figure 1 illustrates the classification of the different approaches.

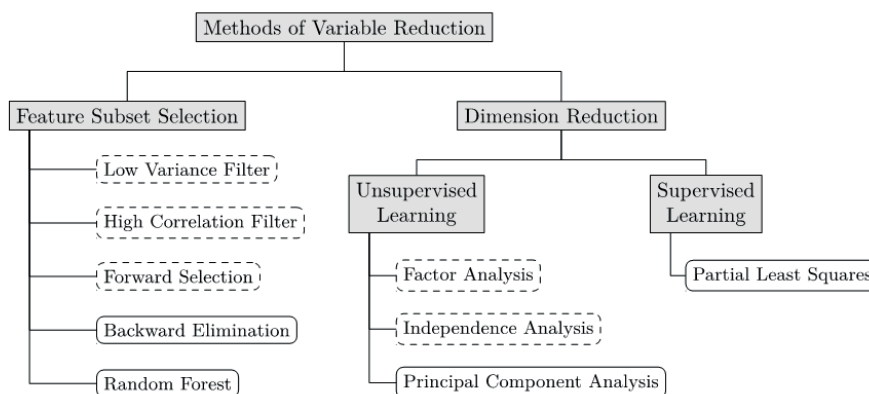


Fig. 1. Classification of variable reduction methods.

The following methods (circled with a solid line in Figure 1) were compared for the analysis of photoacoustic biomarker spectra:

- Multiple Linear Regression (MLR),
- Feature Subset Selection (FSS) by Random Forest approach (RF) or backward elimination and subsequent MLR,
- Dimension Reduction by Principal Component Analysis (PCA) and subsequent MLR,
- Partial Least Squares Regression (PLS).

FSS (RF+MLR), PCA and PLS showed increased accuracy (smaller error) and increased precision (higher cross-validation score) compared to MLR. PLS provided the best results.

A further approach could be to combine Feature Subset Selection with Dimension Reduction to further enhance the prediction.

References

1. K.H. Michaelian, Photoacoustic IR spectroscopy, Wiley-VCH, (2010)
2. Y. Saalberg, M. Wolff, VOC Breath Biomarkers in Lung Cancer, Clin. Chim. Acta 459, 5 (2016), doi:10.1016/j.cca.2016.05.013
3. Y. Saalberg, H. Bruhns, M. Wolff, Photoacoustic Spectroscopy for the Determination of Lung Cancer Biomarkers – A Preliminary Investigation, Sensors, 17 (1), 210 (2017) doi:10.3390/s17010210
4. H. Martens, M. Martens, Introduction to Multivariate Data Analysis for Understanding Quality, J. Wiley, (2000)

EP 040

Characterization of Material Properties for Additive Manufacture Parts using a Laser Ultrasound Technique

Che-Hua Yang ^{(1)*} and Sheng-Po Tseng ⁽²⁾

Graduate Institute of Manufacture Technology, National Taipei University of Technology, Taipei, Taiwan

yang3936@gmail.com

Motivation and Objective

In this research, a procedure employing a laser ultrasound technique (LUT) and an inversion algorithm is reported for nondestructive characterization of mechanical properties of 3D printed, or additive manufacture (AM) parts. For traditional subtraction manufacture (SM) such as milling or drilling, parts machined from relatively uniform bulk materials are stable and naturally exhibit higher strength. AM produces parts with a layer-by-layer way. As a consequence, these AM-manufactured parts suffer from inhomogeneity across layers and relatively lower strength. While used as load supporting components in critical applications, the AM parts need to demonstrate their stable mechanical properties. The research demonstrates that the additive manufacture parts is non-homogeneous for elastic modulus across the thickness direction. Laser ultrasound technique is used to characterize the inhomogeneous elastic property in a nondestructive way.

Methods

An ultrasonic method is employed to measure the elastic moduli of the 3DP samples in a nondestructive way. In the ultrasonic testing, a laser ultrasound technique is used to measure the dispersion spectra of guided waves propagating along the 3DP samples. Dispersion spectra of the guided waves are obtained. An inversion procedure is then employed to extract elastic moduli of the tested sample based on the measured dispersion spectra. Fig. 1 shows a schematic for the experimental configuration of the LUT system.

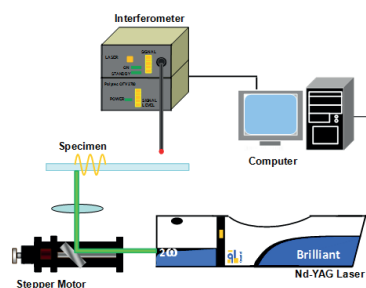


Fig. 1. A schematic showing the experimental configuration of laser ultrasound system.

Results and discussion

Fig. 2 shows the measured dispersion spectra with the LUT for the four 3DP samples with different thickness.

E Methodologies of Photothermics, PA/OA, and Related Techniques

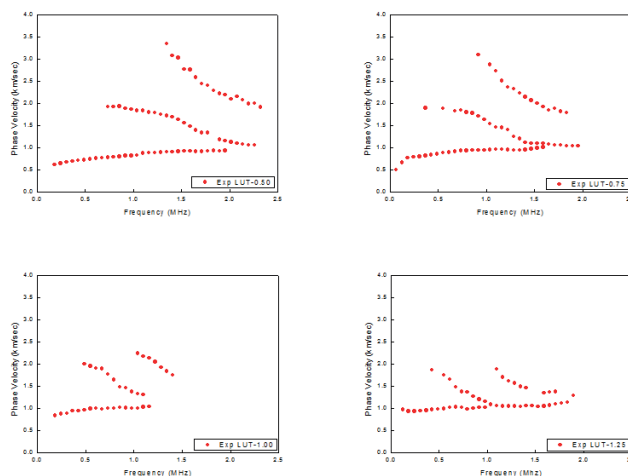


Fig. 2. Measured dispersion curves for the 4 3DP samples.

Conclusions

A procedure combining a laser ultrasound technique (LUT) and a simplex-based inversion algorithm is reported to characterize material and geometrical properties of 3DP tubes with different levels of hydrogen-charging. The reported procedure demonstrates its ability to obtain mechanical properties such as elastic moduli in a nondestructive way. The reported procedure is a remote, non-contact optical technique, and therefore is suitable to characterize 3DP tubes normally operated in irradiative and temperature-elevated environments.

Acknowledgements

Financial support from Ministry of Science and Technology, Taiwan, through grant No. 105-2221-E-027 -012 -MY3 is gratefully acknowledgment.

References

1. Ian Gibson, David W.Rosen, Brent Stucker Additive manufacturing technologies Boston, MA : Springer Science+Business Media, LLC , 2010
2. P. P. Kruth, "Material in excess manufacturing by rapid prototyping techniques," CIRP Annals—Manufacturing Technology, vol. 40, no. 2, pp. 603–614, 1991.
3. A.H Nickel, D.M Barnett, F.B Prinz "Thermal stresses and deposition patterns in layered manufacturing", Mater. Sci. Eng. A, 317 (2001), pp. 59–64
4. Berman, B. "3-D printing: the new industrial revolution.", 2012, Business Horizons 55(2): 155-162.

Laser Scanning Thermographic Inspection for IC Chip 3D Packaging

Kai ZHANG ^{(1)*}, Fei CHEN ⁽²⁾, Li CHEN ⁽¹⁾

1. University of Electronic Science and Technology, Chengdu, China

2. Nanjing University of Science and Technology, Nanjing, China

201722050629@std.uestc.edu.cn

3D chip packaging utilizes multi-layer stacking technology to greatly increase the density of the IC devices. The stacked IC chips are bonded between layers. The bonding quality is extremely important since any delamination between layers will severely affect the heat dissipation of the chips that may result in the failure of the devices. So in the production process, the detection of the delamination will be very desirable. At present, the most widely used tool in the industry is the scanning ultrasonic microscope, which has very slow detection speed and requires the samples to be immersed in water. So it's not suitable for inline production applications [1].

Laser scanning thermography has the potential to be applied to inline bonding inspection for IC chip 3D packaging. As a laser line is scanned across the chip, the absorbed heat will transmit into the under layers. Poor bonding will result in voids and delamination between chips that will affect the thermal conduction and can be detected. [2-3].

A two-dimensional model describes the surface temperature distribution of the sample under linear laser scanning is established. A laser scanning thermographic system is built for the experiments. Fig. 1 is the result for a sample with delaminated chip bonding. The affected areas are clearly shown in Fig.1 (b). For comparison, Fig.1 (c) shows the result from the ultrasonic microscope, which verified the delaminated areas.

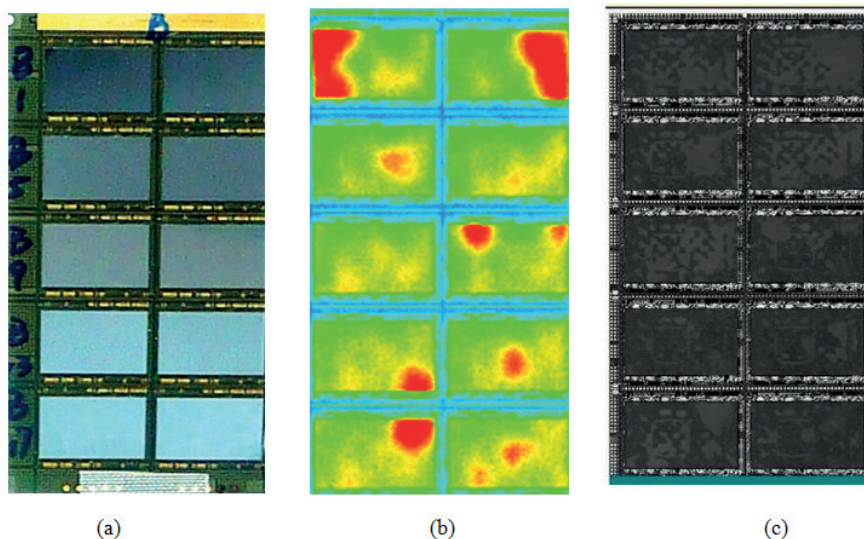


Fig. 1. The result of a sample test: (a) Optical image of the sample; (b) IR image by laser scanning thermography; (c) Image of the ultrasonic microscope.

References

1. Hui Guo. XIANG, Guang Xu. CHUN, Yang. LIU , Applied Mechanics and Materials ,(2014) doi: 10.4028/AWM.536-537.272.
2. Ley, Obdulia & Butera, Manny & Godinez, Valery. Proceedings of SPIE - The International Society for Optical Engineering , (2012) doi: 10.1117/12.919176.
3. Hai-Jun JIANG, Li CHEN, Nondestructive Testing 10(5), (2015) doi: 10.11973/wsjc201510002

EP 042

Improving the laser flash signal to noise ratio by multiple shots averaging

Giovanni Ferrarini ⁽¹⁾, Alessandro Bortolin ⁽¹⁾, Gianluca Cadelano ⁽¹⁾, Lorenzo Finesso ⁽²⁾, Paolo Bison ^{(1)*}

1. CNR-ITC, C.so Stati Uniti 4, 35127 Padova, Italy

2. CNR-IEIIT, via Gradenigo 6/B, 35131 Padova, Italy

paolo.bison@itc.cnr.it

The nondestructive evaluation of materials is a fundamental tool for the industrial production, as it can significantly contribute to improve the design of the components and to the assessment of the production quality [1,2]. Several methods and techniques are available to analyze material samples and investigate the chemical, structural, or thermal properties [3]. The latter are of great importance, for example during the design phase of a component. The thermal properties are used as input of simulation models [4] and providing accurate data to the models is the basic condition to obtain reliable predictions. A predetermined value of a thermal property could be also the desired requirement of an industrial component. The measurement on a component coming from different production batches could help the manufacturer to identify anomalous products [5]. Broadly speaking, the use of a nondestructive method is a great advantage, especially when dealing with real-size mockups [6] or when performing on-site evaluations [7].

Amongst all available methods for determining the thermal properties [8], one of the most popular is the Laser Flash Method (LFM) [9]. The LFM is a procedure where a heat flux is applied on the front face of a specimen and the temperature is measured on the back of the specimen [10–12]. The LFM is typically applied to small size disk-shaped specimens in order to measure their thermal diffusivity (α value). The main advantages of this method are simplicity, rapidity of measurement, and the possibility to measure the thermal diffusivity on a wide range of materials also within a wide temperature range. The LFM is chosen also because it gives the possibility of obtaining the thermal conductivity, if a procedure with adequate reference samples is used or if other thermal properties are measured. In the second case the knowledge of the density (ρ), that could be measured through the Archimedes principle, and of the specific heat (cp), that could be obtained through differential scanning calorimetry (DSC), makes it possible to calculate the thermal conductivity as the product of the density, the specific heat, and the thermal diffusivity [13].

The original LFM method has been widely studied and applied, especially for the characterization of thermal barrier coatings (TBC) [14–17]. Several modifications have been proposed, both from the mathematical [18] and from the experimental standpoint [19] to improve the results. One critical issue is limiting the input power, that for some ranges of thermal properties and thickness of the specimen may lead to an unwanted and nonuniform overheating [16]. Vozàr and Hohenauer [20] proposed to divide the energy of a single laser pulse across smaller repeated pulses, obtaining results comparable to the traditional technique. Recently, Ruffio et al. [21] explored the use of a high speed laser pulse train in order to improve the signal-to-noise ratio. This study proposes a novel experimental setup that allows the automatic repetition of single pulses with a user defined time delay between each pulse. This leads to an increase of the signal-to-noise ratio, depending on the number of replicas of the experiment as shown in Fig. 1.

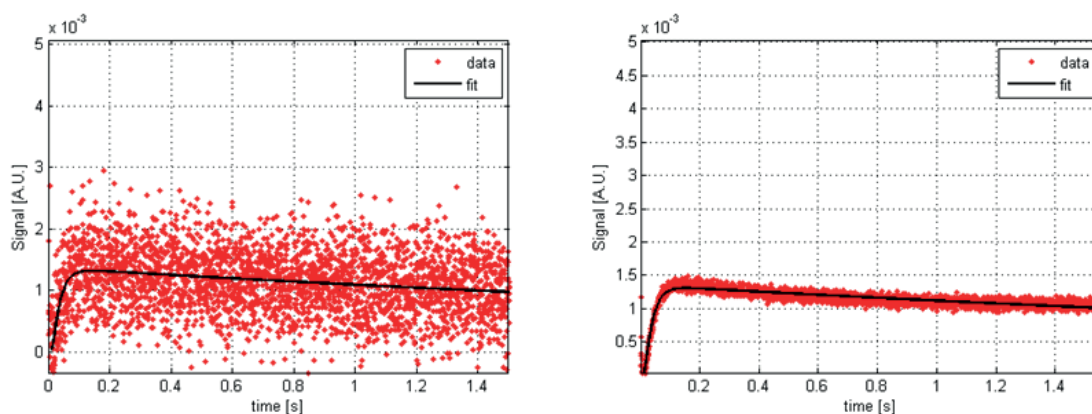


Fig. 1. Results of the AISI 304 specimen measurements. Experimental data and fitting curve for a single shot (a) and for the average of 100 shots (b).

E Methodologies of Photothermics, PA/OA, and Related Techniques

References

1. Shepard S M, Hou J, Lhota J R and Golden J M 2007 Automated processing of thermographic derivatives for quality assurance *Opt. Eng* 46 051008-051008-6
2. Cielo P, Lewak R and Balageas D L 1986 Thermal Sensing For Industrial Quality Control *Thermosense VIII: Thermal Infrared Sensing for Diagnostics and Control* vol 0581 pp 47-54
3. Achenbach J D 2000 Quantitative nondestructive evaluation *International Journal of Solids and Structures* 37 13-27
4. Bortolin A, Bison P, Cadelano G, Ferrarini G and Fortuna S 2015 Measurement of thermophysical properties coupled with LCA assessment for the optimization of a historical building retrofit *J. Phys.: Conf. Ser.* 655 012011
5. Ferrarini G, Bison P, Bortolin A, Cadelano G and Rossi S 2017 Thermal diffusivity measurement of ring specimens by infrared thermography *Thermosense: Thermal Infrared Applications Xxxix* vol 10214, ed P Bison and D Burleigh (Bellingham: Spie-Int Soc Optical Engineering) p UNSP 102140Z
6. Ferrarini G, Bison P, Bortolin A and Cadelano G 2016 Thermal response measurement of building insulating materials by infrared thermography *Energy and Buildings* 133 559-64
7. Cadelano G, Bison P, Bortolin A, Ferrarini G, Peron F, Girotto M and Volinia M 2015 Monitoring of historical frescoes by timed infrared imaging analysis *Opto-Electronics Review* 23 102-8
8. Jannot Y and Degiovanni A 2018 Thermal properties measurement of materials
9. Anon 2013 ASTM E1461 - 13 Standard Test Method for Thermal Diffusivity by the Flash Method
10. Parker W J, Jenkins R J, Butler C P and Abbott G L 1961 Flash Method of Determining Thermal Diffusivity, Heat Capacity, and Thermal Conductivity *Journal of Applied Physics* 32 1679-84
11. Bison P G, Marinetti S, Mazzoldi A, Grinzato E and Bressan C 2002 Cross-comparison of thermal diffusivity measurements by thermal methods *Infrared Physics & Technology* 43 127-32
12. Philippi I, Batsale J C, Maillat D and Degiovanni A 1995 Measurement of thermal diffusivities through processing of infrared images *Review of Scientific Instruments* 66 182-92
13. Bison P, Bortolin A, Cadelano G, Ferrarini G and Grinzato E 2012 Comparison of some thermographic techniques applied to thermal properties characterization of porous materials *Proc of 11th international conference on quantitative infrared thermography-QIRT2012*. Naples, Italy
14. Cernuschi F, Golosnoy I O, Bison P, Moscatelli A, Vassen R, Bossmann H-P and Capelli S 2013 Microstructural characterization of porous thermal barrier coatings by IR gas porosimetry and sintering forecasts *Acta Materialia* 61 248-62
15. Cernuschi F, Bison P, Mack D E, Merlini M, Boldrini S, Marchionna S, Capelli S, Concari S, Famengo A, Moscatelli A and Stamm W 2018 Thermo-physical properties of as deposited and aged thermal barrier coatings (TBC) for gas turbines: State-of-the art and advanced TBCs *Journal of the European Ceramic Society* 38 3945-61
16. Cernuschi F and Bison P 2008 The Influence of the Laser Energy on the Thermal Diffusivity Evaluation of TBC by Laser Flash *J Therm Spray Tech* 17 465-72
17. Taylor R E 1998 Thermal conductivity determinations of thermal barrier coatings *Materials Science and Engineering A* 245 160-7
18. Blumm J and Opfermann J 2002 Improvement of the mathematical modeling of flash measurements *High Temperatures-High Pressures* 34 515-21
19. Baba T and Ono A 2001 Improvement of the laser flash method to reduce uncertainty in thermal diffusivity measurements *Meas. Sci. Technol.* 12 2046
20. Vozár L and Hohenauer W 2001 Measurement of the thermal diffusivity by the laser-flash method with repeated pulses *High Temperatures - High Pressures* 33 9-16
21. Ruffio E, Pradere C, Sommier A, Batsale J-C, Kusiak A and Battaglia J-L 2018 Signal noise ratio improvement technique for bulk thermal diffusivity measurement *International Journal of Thermal Sciences* 129 385-95
22. Seber G A F and Wild C J 1989 *Nonlinear Regression* (New York; Chichester; Brisbane; Toronto; Singapore: John Wiley



Компания «Спектроника» - один из лидеров на рынке аналитического оборудования. Благодаря высочайшему качеству поставляемой нами продукции ведущих мировых производителей, адекватным ценам, а также полному спектру послепродажной поддержки лабораторного оборудования, мы заработали безупречную деловую репутацию.

Наш принцип - индивидуальный подход к каждому клиенту и помощь в решении его задач. Поэтому у нас работают настоящие профессионалы, досконально знающие возможности и особенности продаваемых нами лабораторных приборов.

Компания «Спектроника» - авторизованный дилер компаний Thermo Scientific, Bruker BioSpin, iThera Medical, Elementar, Biochrom, Miltenyi Biotec и ряда других мировых производителей аналитического и биохимического оборудования.

Оптоакустическая томография является совершенно новой в области молекулярной визуализации.

Компания «Спектроника» - эксклюзивный дистрибьютор компании iThera Medical, которая с 2010 года занимается поставками оборудования для доклинических исследований.

Мультиспектральная оптоакустическая томография (MSOT) позволяет проводить идентификацию спектральных характеристик большого числа специфичных соединений *in vivo* одновременно с получением контрастных изображений.

Данная технология молекулярной визуализации сочетает в себе получение изображения с высоким (20-200 мкм) разрешением, а также возможность работать с разнообразными метками и получать информацию о физиологических процессах в тканях на молекулярном и клеточном уровнях.



Визуализация с высоким разрешением поверхностной микроваскулярной системы очень важна для постановки диагноза и мониторинга терапии заболеваний, таких как рак кожи, ангиогенез опухоли и васкулярных заболеваний. Стандартные подходы позволяют оценить микроваскулятуру только с помощью контрастных агентов или с использованием инвазивных подходов.

Для формирования изображения с помощью метода RSOM используется излучение лазера и высокочастотная акустическая детекция, что обеспечивает оптический контраст ткани с разрешением до 10 мкм, на глубине до 5 мм. Реконструкция по диапазону частот позволяет детектировать крупные сосуды и мелкие сосуды с последующим наложением. Такие возможности метода обеспечивают визуализацию поверхностной микроваскулярной системы с высоким разрешением.

Система RSOM Explorer P50 может использоваться для доклинических исследований васкулярных заболеваний, рака кожи, ангиогенеза опухолей, заболеваний, при которых

нарушается накопление таких естественных абсорберов как гемоглобин и меланин на мезоскопическом уровне. В дополнение к естественным абсорберам могут исследоваться также молекулярные зонды.



LLC «SocTrade Co»
Russia, Moscow, ul. Ordzhonikidze, 11 bld.3
Postal address: 119071, Moscow, PO box 22
Tel.+7(495) 604-44-44
Fax: +7(495) 234-47-66
info@soctrade.com, soctrade@mail.ru
www.soctrade.com

Dear Colleagues!

Our company SocTrade, founded in 1986, one of major laboratory equipment suppliers on the Russian market, represents over 30 leading laboratory equipment manufacturers from all over the world.

Our mission is to serve our customers by helping them to solve analytical tasks efficiently and effectively, which helps us build long-term mutually beneficial relationships.

We provide a full range of services:

- consulting on the choice of equipment, selection of options, etc.,
- supply & delivery of equipment and consumables,
- equipment start-up & commissioning,
- technical support, warranty and post-warranty service,
- formulation of techniques, assistance in solving problems of equipment verification, certification and validation.

Our capabilities, experience and qualifications of our employees allow us to solve almost any task related to equipping quality control laboratories and research centers with high-tech reliable devices that fit our customers' tasks best and have an optimal price / quality ratio.

Equipment for all stages of analytical control and materials research is presented in our brochures and on the SocTrade website:

- equipment for research, counting and fractionation of nano- and microparticles,
- equipment for analyzing surface phenomena and studying wetting processes,
- tribology testers - equipment for studying the processes of friction and wear,
- wide range of furnaces, including special versions,
- chemical reactors, including those for supercritical processes,
- laboratory thermostats, drying cabinets, incubators,
- equipment for quality control in the oil and gas industry, agriculture, pharmaceutical industry
- automatic titrators, densitometers, viscometers, refractometers,
- general laboratory analytical equipment.

We maintain an active dialogue with manufacturers of laboratory equipment, certification bodies, leading scientists, industry specialists, we constantly monitor new developments of devices and changes in the regulatory framework. This allows us to provide our partners with high-quality equipment and maintain consistently high quality of our services for many years.

We will be glad to see you among our customers!

PhotoSound[®]
Imaging and Data Acquisition Solutions

Optical • PhotoAcoustic • UltraSound Imaging •
Preamplifiers • Analog-to-Digital Converters • Data
Acquisition Units

TRITOM



*Discover the power of
light and sound*

LEGION



*High Channel Count
Data Acquisition Units*

FLASH



*High Frame-Sample Rate
Data Acquisition Units*

www.pst-inc.com



ISBN 978-5-6041187-1-9



9 785604 118719